# Investigating the Applications of Neodymium Isotopic Compositions and Rare Earth Elements as Water Mass Tracers in the South Atlantic and North Pacific

Yingzhe Wu

Submitted in partial fulfillment of the
requirements for the degree of
Doctor of Philosophy
in the Graduate School of Arts and Sciences

COLUMBIA UNIVERSITY

2019

ABSTRACT

Investigating the Applications of Neodymium Isotopic Compositions and Rare Earth Elements as Water Mass Tracers in the South Atlantic and North Pacific

Yingzhe Wu

Neodymium (Nd) isotopes have been increasingly used to trace the modern and past ocean circulation. This assumes that seawater Nd isotope ratios (εNd) effectively fingerprint different water masses and approximate expected values from water mass mixing. However, the decoupling of Nd isotopes and Nd concentration (the "Nd paradox") in the water column, and the lack of understanding of sources and sinks of Nd, restrain our understanding of the "quasi-conservative" behavior of εNd in seawater. Nd is one of the lanthanide rare earth elements (REEs) with similar chemical characteristics that undergo some degree of fractionation. The shale-normalized REE patterns and REE ratios can be used to investigate potential sources/sinks of REEs. Combining REEs with εNd will provide additional information to study REE cycling in the ocean.

To better understand the reliability of εNd as a water mass tracer, 17 high-resolution seawater profiles were sampled meridionally in the Southwest Atlantic (GEOTRACES GA02 Leg 3; RRS James Cook 057) and measured for εNd. This region involves the major water masses in the Atlantic Meridional Overturning Circulation: southward flowing North Atlantic Deep Water (NADW), northward flowing Antarctic Intermediate Water (AAIW) and Antarctic Bottom Water (AABW). Along the cruise track, there are potential sources (eolian dusts, marginal sediments, oceanic volcanism,

and nepheloid layer) that could add external Nd to seawater and disturb the "quasi-conservative" behavior of εNd. Our results show strikingly that the Southwest Atlantic transect confirms "quasi-conservative" behavior of εNd in intermediate and deep water. Our evaluations of Nd isotopic deviations (ΔεNd) from conservative behavior show that out of 198 intermediate and deep samples, 49% of ΔεNd-values are within ± 0.25 εNd units (< analytical error: ± 0.30 εNd units) and 84% of ΔεNd-values are within ± 0.75 εNd units. Potential sources that could add external Nd to seawater from oceanic volcanism and the nepheloid layer do not show impact on seawater εNd. Terrigenous sources of Nd (e.g. eolian dusts from Africa and Patagonia, marginal sediments from South America) show influence on surface/subsurface water εNd but this εNd signature is not transferred to intermediate and deep water.

To better understand the conservative vs. non-conservative behavior of REEs in the ocean, the dissolved REE concentrations were analyzed for the 17 seawater profiles in the Southwest Meridional Atlantic Transect (GEOTRACES GA02 Leg 3). The shale-normalized REE patterns are consistent with typical seawater patterns. To investigate whether and how much REE concentrations deviate from conservative water mass mixing, the REE concentration deviations were calculated for the intermediate and deep water. It is shown that within the SAMT, the intermediate and deep water REEs generally reflect water mass mixing and nearly conservative behavior. Along this transect, the potential sources that could add external REEs to seawater are dissolution of REEs from eolian dust to the surface/subsurface water, REEs released from dissolution of Fe-Mn oxides in the oxygen depleted zone, REEs from sediments near the continental margin,

and dissolution of REEs from deep sea sediments. REEs and Nd isotopes of most intermediate and deep water masses passing the volcanic Rio Grande Rise (RGR) and Vitória-Trindade Ridge (VTR) do not show influence from RGR and VTR. REEs and Nd isotopes of the bottom water Lower Circumpolar Deep Water (LCDW) and AABW passing the RGR are influenced by dissolved REEs from the deep sea sediments. LCDW and AABW passing the VTR are influenced by dissolved REEs from the deep sea sediments as well as the volcanic VTR.

In order to better understand the oceanic Nd cycling in the North Pacific, its sources and sinks in seawater must be better characterized. The high εNd of North Pacific Deep Water (NPDW, ~ −4) has been difficult to reconcile with the eolian inputs as reflected in surface waters (e.g. Jones et al., 2008), which have much lower εNd (~ −10), indicating potential addition of a component from Pacific volcanism. In order to constrain the REE sources in the North Pacific, we measured εNd and REEs of seawater from five stations across the subarctic North Pacific sampled by the Innovative North Pacific Experiment (INOPEX) Cruise SO202 (2009). In the surface water (~10 m), the highest εNd is observed at the station closest to the Aleutian-Kamchatka volcanic margin (Northwest station SO202-5), suggesting higher contribution of external REEs from volcanic ashes compared to the other stations. In the shallow water (100-400 m, depending on location), remineralization of REEs from volcanic ashes prevails over Asian dusts at Northwest station SO202-5 and near Japan stations SO202-44, 41, and 39, whereas remineralization of REEs from Asian dusts prevails over volcanic ashes at the Northeast station SO202-32 in the open ocean of the Alaska Peninsula. From the depths

of North Pacific Intermediate Water (NPIW) to NPDW, seawater εNd and REEs show conservative water mass mixing of NPIW-NPDW. They also show conservative behavior along the water mass transport paths of NPIW and NPDW. Below the depths of NPDW, addition of external REEs is observed in the vertical profiles of εNd and REEs as well as along the transport path of LCDW. The potential sources that add external REEs to the bottom water are (1) sediments on the Kuril-Kamchatka-Aleutian volcanic margin along the LCDW transport path, and (2) sediments on the seafloor, both of which could interact with seawater and modify the seawater εNd and REE signatures.

Table of Contents

List of Tables

List of Figures

Acknowledgements

First, I want to thank my advisor Steve Goldstein for his guidance and support during the past few years of my PhD study. Thanks to Steve for giving me the opportunity to work on amazing research projects to understand seawater neodymium isotopes and rare earth elements. I deeply appreciate his dedication to discussions on data and research and modifications on my thesis chapters with great patience.

I am very thankful that Leo Pena and Bob Anderson are on my PhD committee. I thank Leo for teaching me the lab techniques essential for processing seawater and providing great advice on my research. I am very grateful for Bob's insightful inputs to my research and always feel greatly inspired by discussions with him. I thank Arnold Gordon for discussions on the water mass pathways and Rob Sherrell for helpful comments on my thesis.

Many thanks to Louise Bolge for spending enormous time setting up analyzing methods on the ICP-MS and patiently teaching me how to analyze samples. I thank Merry Cai for kindly teaching me analyzing techniques on the TIMS and providing great suggestions on presentation skills. Thanks to Martin Fleisher for his assistance to solve analytical difficulties. I also thank Chandranath Basak for his assistance in the lab and inspiring research discussions.

Thanks to the collaborators Alison Hartman, Chris Hayes, Micha Rijkenberg, Hein de Baar, and Rainer Gersonde for sample collecting, lab assistance and helpful discussions.

Finally, I want to thank my husband Xiaobo Li and my parents Gang Wu and Hong Cao for their love, encouragement, and support along this journey.

# Chapter 1. Introduction

## 1. General Introduction

The ocean circulation plays an essential role in the climate system because it is a major reservoir of heat and redistributes heat around the Earth (Fig. 1). The deep ocean circulation is especially important because it could potentially trigger global climate change (e.g. (Broecker and Denton, 1989)). A variety of tracers are used to study the modern ocean circulation such as salinity, oxygen, nutrient concentrations (e.g. nitrate, phosphate), and transient tracers (e.g. chlorofluorocarbons, sulphur hexafluoride). For example, the ocean circulation is clearly seen in the nutrient concentration section profiles (such as phosphate, Fig. 2), with southward flowing North Atlantic Deep Water (NADW) and northward Antarctic Intermediate Water (AAIW) and Antarctic Bottom Water (AABW) in the Atlantic basin and northward AAIW and AABW compensated by southward Pacific Deep Water (PDW) and in the Pacific basin (Fig. 2).

To reconstruct the ocean circulation in the past, paleoceanographic studies rely on archives accurately recording and preserving paleo-seawater signatures. For example, tracers such as carbon isotopes ($\delta^{13}C$) (e.g. (Curry et al., 1988; LeGrand and Wunsch, 1995; Curry and Oppo, 2005; Lynch-Stieglitz, 2006; Lynch-Stieglitz et al., 2007)) and Cd/Ca (e.g. (Boyle, 1988; Rosenthal et al., 1997; Lynch-Stieglitz, 2006; Marchitto and Broecker, 2006)) in benthic foraminifera are commonly used to study the paleo-ocean circulation based on their systematic variations in water masses. However, one limitation of using $\delta^{13}C$ is that they are affected by biological processes. Neodymium (Nd) isotopes, which have negligible biological and chemical fractionation effects, could be used to trace the past ocean circulation and are being increasingly used (e.g. (von Blanckenburg,

1999; Rutberg et al., 2000; Frank, 2002; Goldstein and Hemming, 2003; Thomas, 2004; Piotrowski et al., 2005; Gutjahr et al., 2008; Pahnke et al., 2008; Pena and Goldstein, 2014; van de Flierdt et al., 2016; Tachikawa et al., 2017)). For example, Piotrowski et al. (2005) showed that Nd isotopes vary along with both glacial-interglacial and millennial climate changes in a manner that is consistent with ocean circulation changes (Fig. 3). In the Southeast Atlantic, lower εNd values during warmer periods indicate stronger influence of NADW, whereas higher εNd values during cooler periods indicate the weakening of NADW strength (Piotrowski et al., 2005). The use of Nd isotopes as a paleo-ocean circulation proxy depends both on whether they accurately record deep water signature in sedimentary archives and whether they reflect water mass mixing. Thus, it is important to understand how well Nd isotopes trace the modern ocean circulation.

### *1.1. Nd isotopes in seawater*

Nd has 7 naturally occurring isotopes: $^{142}$Nd, $^{143}$Nd, $^{144}$Nd, $^{145}$Nd, $^{146}$Nd, $^{148}$Nd and $^{150}$Nd. In the Samarium (Sm)-Nd long-lived radioactive decay system, $^{147}$Sm decays to $^{143}$Nd by α-decay ($t_{1/2} = 1.06 \times 10^{11}$ year). The Nd isotopic composition is expressed as the $^{143}$Nd/$^{144}$Nd ratio. The $^{143}$Nd/$^{144}$Nd ratio of a sample is often expressed as the deviation from the bulk earth (chondritic uniform reservoir – CHUR) ratio in parts per $10^4$. This normalization is defined as the εNd (DePaolo and Wasserburg, 1976): $\varepsilon Nd = [(^{143}Nd/^{144}Nd_{sample}) / (^{143}Nd/^{144}Nd_{CHUR}) - 1] \times 10^4$, where $^{143}Nd/^{144}Nd_{CHUR} = 0.512638$ (Jacobsen and Wasserburg, 1980). During mantle melting, Nd is more incompatible than Sm, meaning that during melting of the mantle Nd is more preferentially partitioned into magmas which form continental crust. As a result, continental crustal rocks generally

have low Sm/Nd ratios and low εNd values (e.g. Archean rocks of West Greenland, εNd < −20), whereas young mantle-derived rocks generally have high Sm/Nd ratios and high εNd values (e.g. Aleutian arcs, εNd = +7 to +9) (e.g. compilation by (Jeandel et al., 2007)).

Seawater acquires its Nd isotopic signature from weathering of the continents. The deep water in the North Atlantic, which is surrounded by old continents, has εNd = −14 to −13 (e.g. (Piepgras and Wasserburg, 1980; Piepgras and Wasserburg, 1987)). The deep water in the North Pacific, which is surrounded by young volcanics, has εNd = −4 to −2 (e.g. (Piepgras and Wasserburg, 1980; Piepgras and Wasserburg, 1987)). The Southern Ocean has intermediate εNd = −9 to −8 (e.g. (Piepgras and Wasserburg, 1982; Stichel et al., 2012)), reflecting influence from both Atlantic and Pacific Ocean. The residence time of Nd in the ocean (200-1000 years; (Tachikawa et al., 1999; Tachikawa et al., 2003; Siddall et al., 2008; Arsouze et al., 2009; Rempfer et al., 2011)) is less than the mixing time of deep ocean (~1500 years; (Broecker and Peng, 1982)), which is long enough to allow Nd signal to be advected by water masses but short enough to prevent homogenization. This explains the distinctive deep water εNd values in different ocean basins and water masses.

Previous studies showed that intermediate and deep seawater εNd is correlated with conservative water mass tracers such as salinity (reviewed in (Goldstein and Hemming, 2003)). For example, εNd covaries with salinity in the Atlantic Basin and shows the mixing of North Atlantic and Southern Ocean water masses (Fig. 4). In addition, Nd isotopic variations approximate expected values based on water mass

mixing. For example, the vertical profile of εNd in the South Atlantic approximates isotopic variations expected from mixing of AAIW and NADW from ~1500 m to ~3000 m and mixing of NADW and AABW from ~3000 m to ~4000 m (Fig. 5). These observations imply a system where εNd in intermediate and deep waters could potentially be used as a water mass tracer.

### *1.2. Rare earth elements in seawater*

Nd is one of the lanthanide rare earth elements (REEs), a group of 15 elements from lanthanum (La, atomic number 57) to lutetium (Lu, atomic number 71). In the lanthanide series, the electrons are progressively filled in the 4f orbitals with increasing atomic number. The REEs have similar outer electronic configuration, which shields electrons in the 4f orbitals and results in similar chemical characteristics of REEs. However, the decrease of ionic radius with increasing atomic number results in differences in the behavior of REEs. Relative abundances of REEs are calculated by normalizing the concentration of each element to its concentration in a reference standard, such as chondrites (e.g. (Masuda et al., 1973; Nakamura, 1974)) or shales (e.g. (Gromet et al., 1984; Taylor and McLennan, 1985)). Seawater REEs are usually normalized to Post-Archean Australian Shale (PAAS; (Taylor and McLennan, 1985)) because REEs are mainly brought to the oceans by materials eroded from continents (Section 1.3).

The REEs mostly complex with carbonate ion in seawater (e.g. (Byrne and Kim, 1990; Byrne, 2002; Luo and Byrne, 2004)). From La to Lu, the stability of REE complexes in seawater increases with decreasing radii (e.g. (Elderfield et al., 1988; Lee

and Byrne, 1993)). In addition, the light REEs (LREEs) with larger radii are more preferentially scavenged onto particles compared to heavy REEs (HREEs) (Byrne and Kim, 1990). As a result, typical PAAS-normalized REE pattern of seawater shows relatively enriched HREEs compared to LREEs (Fig. 6).

The REEs show 3+ valence in their oxidation states, although cerium (Ce) and europium (Eu) also exist in 4+ valence and 2+ valence, respectively. Ce with 4+ valence will form if the system is sufficiently oxidized and is insoluble in oxic seawater. Thus it shows a very low relative abundance compared to the other REEs in the seawater REE pattern (Fig. 6). This is often described as the "Ce anomaly ($Ce/Ce^*$)", determined by comparing sample Ce concentration with hypothetical Ce concentration interpolated from its neighbors La and Praseodymium (Pr). An equation is $Ce/Ce^* = 2\times Ce_n/(La_n + Pr_n)$, where $Ce_n$, $La_n$, and $Pr_n$ are PAAS-normalized Ce, La, and Pr concentrations of the samples. $Ce/Ce^*$ could potentially be used to study oxidation/reduction processes in seawater and sediments.

The vertical seawater concentration profiles of dissolved REEs are similar to that of nutrients and show increasing concentrations with depth in the water column (e.g. Fig. 7 in red). Previous studies have proposed that these are resulted from scavenging onto particles in the surface water and remineralization of sinking particles at depth (e.g. (Elderfield et al., 1988; Byrne and Kim, 1990)). In the deep water, the dissolved REE concentrations are similar to nutrients and accumulate with aging of water masses. They increase along the water mass transport path from the Atlantic to Pacific Ocean (e.g. (De Baar et al., 1985)) (Fig. 6).

Fractionation within the REEs occurs between the deep Atlantic and Pacific Ocean (e.g. (Osborne et al., 2017)). For example, the fractionation between PAAS-normalized Yb and Nd abundances in the deep Atlantic is smaller than that in the deep Pacific, resulting in lower PAAS-normalized Yb/Nd ratio in the deep Atlantic (Fig. 6). The deep water PAAS-normalized HREE/LREE ratio increases from the Atlantic to Pacific Ocean (e.g. (Bertram and Elderfield, 1993; Osborne et al., 2017)) as a result of preferential removal of LREEs onto particles relative to HREEs (e.g. (Elderfield and Greaves, 1982; Elderfield et al., 1988)) along the deep water pathway from the Atlantic to Pacific Ocean (e.g. (Bertram and Elderfield, 1993)).

Some studies have suggested that the intermediate and deep water REEs behave conservatively based on water mass mixing (e.g. (Elderfield et al., 1988; German et al., 1995; Haley et al., 2014; Zheng et al., 2016)). For example, dissolved REEs were studied in a full-depth zonal transect from the CoFeMUG (cobalt, iron and micro-organisms from the upwelling zone to the gyre) cruise across the South Atlantic Ocean at ~10°S (Zheng et al., 2016). This is a GEOTRACES approved compliant data cruise (GAc01). This zonal transect crosses a full-depth meridional transect from the GEOTRACES cruise GA02 Leg 3 in the Southwest Atlantic Ocean (Section 3), where dissolved εNd and REEs were studied in this thesis (Chapter 2 and 3). Zheng et al. (2016) showed that > 75% of the REEs below 1000 m are dominantly controlled by advective water mass mixing. Therefore, the seawater REEs could potentially be used as indicators of intermediate and deep water masses. In addition, the seawater REE characteristics can be combined with

εNd and this will provide additional information to study different chemical processes in the ocean.

### *1.3. Complications of using εNd*

A poorly understood aspect of seawater Nd is the mismatch of εNd and Nd concentration in the water column, which is called "Nd paradox" (Goldstein and Hemming, 2003). While εNd values show "quasi-conservative" behavior, that is, generally reflecting values expected from water mass mixing (Fig. 5), Nd concentrations appear to behave like nutrients (Fig. 7). Nutrient concentrations are depleted in shallow water and they increase with depth due to biomineralization. They accumulate as water mass ages and increase along water mass transport path. Some studies based on modeling have proposed reversible scavenging to explain the mismatch of Nd concentration and εNd (e.g. (Nozaki and Alibo, 2003; Siddall et al., 2008; Arsouze et al., 2009; Rempfer et al., 2011)). For example, Siddall et al. (2008) have proposed a combination of reversible scavenging and lateral advection to explain "Nd paradox". When particles are transported down the water column, Nd scavenged at surface is dissolved from particles such that Nd concentration increases with depth (Siddall et al., 2008). Sinking particles exchange some Nd with seawater, but it is advected away before it can impact greater depths, thus keeping the εNd profile intact (Siddall et al., 2008). In contrast, other studies have suggested that the intermediate and deep water REEs are dominantly controlled by water mass mixing (e.g. (Elderfield et al., 1988; German et al., 1995; Haley et al., 2014; Zheng et al., 2016)) (Section 1.2).

Another complication is our lack of understanding of Nd sources and sinks. It has been suggested that Nd isotopes approximate end-member water mass mixing (e.g. (Frank, 2002; Goldstein and Hemming, 2003; van de Flierdt et al., 2016; Tachikawa et al., 2017)). But Nd is brought to the oceans all over the Earth from eolian dusts (e.g. (Goldstein et al., 1984)), rivers (e.g. (Goldstein and Jacobsen, 1987)), pore water (e.g. (Elderfield and Sholkovitz, 1987; Haley et al., 2017)), ground water (e.g. (Johannesson and Burdige, 2007)), and "boundary exchange" (e.g. (Lacan and Jeandel, 2005)). A major process to remove Nd from seawater is the scavenging onto particles. It has been suggested that "boundary exchange", which is the Nd exchange between seawater and sediments from continental margins, can change εNd without significantly modifying Nd concentrations in seawater (Lacan and Jeandel, 2001; Lacan and Jeandel, 2005; Jeandel et al., 2007). Interaction of seawater with continental margins also allows removal of Nd from seawater (Lacan and Jeandel, 2001; Lacan and Jeandel, 2005; Jeandel et al., 2007). Thus, the continental margins can serve as a source as well as a sink for Nd (Lacan and Jeandel, 2001; Lacan and Jeandel, 2005; Jeandel et al., 2007; Grasse et al., 2012; Grenier et al., 2013; Garcia-Solsona et al., 2014), and the exchange between seawater and marginal sediments could result in non-conservative behavior of seawater εNd.

This thesis addresses the above questions by evaluating whether εNd deviates from conservative water mass mixing (Chapter 2) and whether REE concentration vertical profiles show conservative water mass mixing or reversible scavenging (Chapter 3). This thesis also addresses exchange processes at continental margins and in the

bottom seawater and investigates its influence on the seawater εNd and REE signatures (Chapter 3 and 4).

**2. Major Research Questions**

This thesis addresses some key questions associated with the application of εNd in seawater to trace water masses, and with the REE cycling in the ocean. Investigating the following research questions will help us better understand the behavior of εNd and REEs in seawater and serve as a basis for reconstructions of paleo-ocean circulation.

(1) To what extent εNd can be used as a conservative water mass tracer? We focus on whether seawater εNd deviates from conservative water mass mixing with increasing distance from the water mass source regions, and along the transport paths of different water masses.

(2) What are the sources that add external REEs to seawater? What are the sinks that remove REEs from seawater? We focus on whether seawater REEs deviate from conservative water mass mixing and whether they are influenced by potential sources/sinks such as eolian dusts, nepheloid layers, continental margins, and oceanic volcanism.

(3) How does REE signal transfer to seawater? What conditions promote the exchange of REEs between seawater and potential sources? We focus on chemical processes in the oxygen depleted zone (ODZ) (e.g. in the equatorial Atlantic Ocean), in the bottom seawater, and near continental margins.

## 3. Objectives

To address the reliability of using εNd as a conservative water mass tracer, Chapter 2 investigates a suite of seawater samples collected meridionally in the Southwest Atlantic Ocean (GEOTRACES GA02 Leg 3; RRS James Cook 057) and analyzed for εNd. The mission of the international GEOTRACES program is "to identify processes and quantify fluxes that control the distributions of key trace elements and isotopes in the ocean, and to establish the sensitivity of these distributions to changing environmental conditions", where εNd is listed as one of the key parameters to trace natural sources of trace elements and isotopes to the ocean and to reconstruct ocean circulation in the past (www.geotraces.org). Chapter 2 evaluates how well Nd isotopes trace the major water masses involved in the Atlantic Meridional Overturning Circulation at intermediate and deep depths in the Southwest Atlantic Meridional Transect (SAMT). Our results of seawater εNd show strikingly that the SAMT confirms the "quasi-conservative" behavior of εNd in intermediate and deep water in the Southwest Atlantic. We further quantify the intermediate and deep water Nd isotopic deviations from conservative water mass mixing. The very small Nd isotopic deviations from conservative behavior indicate that the measured εNd can be effectively predicted by water mass mixing calculations. Potential sources that could add external Nd to seawater from oceanic volcanism and nepheloid layer do not show impact on seawater εNd. Terrigenous sources of Nd (e.g. eolian dusts from Africa and Patagonia, marginal sediments from South America) show influence on surface/subsurface water εNd but this εNd signature is not transferred to intermediate and deep water.

To gain a better understanding of REE cycling in the ocean, Chapter 3 focuses on the REE distributions in the SAMT. Chapter 3 discusses the potential sources/sinks of REEs such as eolian dusts, nepheloid layers, continental margins, and volcanic Rio Grande Rise (RGR) and Vitória-Trindade Ridge (VTR). Combining REEs and εNd, Chapter 3 also discusses sources of external REEs that alter seawater Nd isotopic signature. Our analyzed seawater REE concentrations show that within the SAMT, the intermediate and deep water REEs generally reflect water mass mixing and nearly conservative behavior. Along this transect, the potential sources that could add external REEs to seawater are: dissolution of REEs from eolian dust to the surface/subsurface water, REEs released from dissolution of Fe-Mn oxides in the oxygen depleted zone, REEs from sediments near the continental margin, and dissolution of REEs from deep sea sediments. REEs and Nd isotopes of most intermediate and deep water masses passing the RGR and VTR do not show influence from RGR and VTR. REEs and Nd isotopes of the bottom water Lower Circumpolar Deep Water (LCDW) and AABW passing the RGR are influenced by dissolved REEs from the deep sea sediments. LCDW and AABW passing the VTR are influenced by dissolved REEs from the deep sea sediments as well as the volcanic VTR.

Chapter 4 investigates REE and Nd isotopic distributions of vertical seawater profiles sampled across the North Pacific Ocean by the INOPEX (Innovative North Pacific Experiment) SO202 cruise in 2009. It is observed that the North Pacific Deep Water (NPDW) has the highest εNd (−4 to −2, (Piepgras and Wasserburg, 1980; Piepgras and Wasserburg, 1987)) compared to the deep water in other oceans. However, this high

εNd signal has been difficult to reconcile with the eolian inputs as reflected in surface waters (Jones et al., 2008), which have much lower εNd (≈ −10, (Jones et al., 1994)). The main research objective of this study is to investigate the source of the high εNd in the deep North Pacific Ocean and how this signal is added to the seawater. In the surface water (~10 m), the highest εNd is observed at the station closest to the Aleutian-Kamchatka volcanic margin (Northwest station SO202-5), suggesting higher contribution of external REEs from volcanic ashes compared to the other stations. In the shallow water (100-400 m, depending on location), remineralization of REEs from volcanic ashes prevails over Asian dusts at Northwest station SO202-5 and near Japan stations SO202-44, 41, and 39, whereas remineralization of REEs from Asian dusts prevails over volcanic ashes at the Northeast station SO202-32 in the open ocean of the Alaska Peninsula. From the depths of North Pacific Intermediate Water (NPIW) to NPDW, seawater εNd and REEs show conservative water mass mixing of NPIW-NPDW. They also show conservative behavior along the water mass transport paths of NPIW and NPDW. Below the depths of NPDW, addition of external REEs is observed in the vertical profiles of εNd and REEs as well as along the transport path of LCDW. The potential sources that add external REEs to the bottom water are (1) sediments on the Kuril-Kamchatka-Aleutian volcanic margin along the LCDW transport path, and (2) sediments on the seafloor, both of which could interact with seawater and modify the seawater εNd and REE signatures.

## References


Arsouze, T., Dutay, J.C., Lacan, F. and Jeandel, C. (2009) Reconstructing the Nd oceanic cycle using a coupled dynamical-biogeochemical model. Biogeosciences 6, 2829-2846.

Behrens, M.K., Muratli, J., Pradoux, C., Wu, Y., Böning, P., Brumsack, H.-J., Goldstein, S.L., Haley, B., Jeandel, C. and Paffrath, R. (2016) Rapid and precise analysis of rare earth elements in small volumes of seawater-Method and intercomparison. Marine Chemistry 186, 110-120.

Bertram, C.J. and Elderfield, H. (1993) The geochemical balance of the rare earth elements and neodymium isotopes in the oceans. Geochimica et Cosmochimica Acta 57, 1957-1986.

Boyle, E.A. (1988) Cadmium: Chemical tracer of deepwater paleoceanography. Paleoceanography 3, 471-489.

Broecker, W.S. and Denton, G.H. (1989) The role of ocean-atmosphere reorganizations in glacial cycles. Geochimica et Cosmochimica Acta 53, 2465-2501.

Broecker, W.S. and Peng, T.H. (1982) Tracers in the Sea. Eldigio Press, Palisades, NY.

Byrne, R.H. (2002) Inorganic speciation of dissolved elements in seawater: the influence of pH on concentration ratios. Geochemical Transactions 3, 11.

Byrne, R.H. and Kim, K.-H. (1990) Rare earth element scavenging in seawater. Geochimica et Cosmochimica Acta 54, 2645-2656.

Curry, W.B., Duplessy, J.-C., Labeyrie, L.D. and Shackleton, N.J. (1988) Changes in the distribution of δ13C of deep water ΣCO2 between the last glaciation and the Holocene. Paleoceanography 3, 317-341.

Curry, W.B. and Oppo, D.W. (2005) Glacial water mass geometry and the distribution of δ13C of ΣCO2 in the western Atlantic Ocean. Paleoceanography 20.

De Baar, H.J.W., Bacon, M.P., Brewer, P.G. and Bruland, K.W. (1985) Rare earth elements in the Pacific and Atlantic Oceans. Geochimica et Cosmochimica Acta 49, 1943-1959.

DePaolo, D.J. and Wasserburg, G.J. (1976) Nd isotopic variations and petrogenetic models. Geophysical Research Letters 3, 249-252.

Elderfield, H. and Greaves, M.J. (1982) The rare earth elements in seawater. Nature 296, 214-219.

Elderfield, H. and Sholkovitz, E.R. (1987) Rare earth elements in the pore waters of reducing nearshore sediments. Earth and Planetary Science Letters 82, 280-288.

Elderfield, H., Whitfield, M., Burton, J.D., Bacon, M.P. and Liss, P.S. (1988) The oceanic chemistry of the rare-earth elements [and discussion]. Philosophical Transactions of the Royal Society of London A: Mathematical, Physical and Engineering Sciences 325, 105-126.

Frank, M. (2002) Radiogenic isotopes: tracers of past ocean circulation and erosional input. Reviews of geophysics 40.

Garcia-Solsona, E., Jeandel, C., Labatut, M., Lacan, F., Vance, D., Chavagnac, V. and Pradoux, C. (2014) Rare earth elements and Nd isotopes tracing water mass mixing and particle-seawater interactions in the SE Atlantic. Geochimica et Cosmochimica Acta 125, 351-372.

German, C.R., Masuzawa, T., Greaves, M.J., Elderfield, H. and Edmond, J.M. (1995) Dissolved rare earth elements in the Southern Ocean: Cerium oxidation and the influence of hydrography. Geochimica et Cosmochimica Acta 59, 1551-1558.

Goldstein, S.J. and Jacobsen, S.B. (1987) The Nd and Sr isotopic systematics of river-water dissolved material: Implications for the sources of Nd and Sr in seawater. Chemical Geology: Isotope Geoscience section 66, 245-272.

Goldstein, S.L. and Hemming, S.R. (2003) Long-lived isotopic tracers in oceanography, paleoceanography, and ice-sheet dynamics. Treatise on geochemistry 6, 453-489.

Goldstein, S.L., O'Nions, R.K. and Hamilton, P.J. (1984) A Sm-Nd isotopic study of atmospheric dusts and particulates from major river systems. Earth and planetary Science letters 70, 221-236.

Grasse, P., Stichel, T., Stumpf, R., Stramma, L. and Frank, M. (2012) The distribution of neodymium isotopes and concentrations in the Eastern Equatorial Pacific: Water mass advection versus particle exchange. Earth and Planetary Science Letters 353, 198-207.

Grenier, M., Jeandel, C., Lacan, F., Vance, D., Venchiarutti, C., Cros, A. and Cravatte, S. (2013) From the subtropics to the central equatorial Pacific Ocean: Neodymium isotopic composition and rare earth element concentration variations. Journal of Geophysical Research: Oceans 118, 592-618.

Gromet, L.P., Haskin, L.A., Korotev, R.L. and Dymek, R.F. (1984) The “North American shale composite”: its compilation, major and trace element characteristics. Geochimica et Cosmochimica Acta 48, 2469-2482.

Gutjahr, M., Frank, M., Stirling, C.H., Keigwin, L.D. and Halliday, A.N. (2008) Tracing the Nd isotope evolution of North Atlantic deep and intermediate waters in the Western North Atlantic since the Last Glacial Maximum from Blake Ridge sediments. Earth and Planetary Science Letters 266, 61-77.

Haley, B.A., Du, J., Abbott, A.N. and McManus, J. (2017) The impact of benthic processes on rare earth element and neodymium isotope distributions in the oceans. Frontiers in Marine Science 4, 426.

Haley, B.A., Frank, M., Hathorne, E. and Pisias, N. (2014) Biogeochemical implications from dissolved rare earth element and Nd isotope distributions in the Gulf of Alaska. Geochimica et Cosmochimica Acta 126, 455-474.

Jacobsen, S.B. and Wasserburg, G.J. (1980) Sm-Nd isotopic evolution of chondrites. Earth and Planetary Science Letters 50, 139-155.

Jeandel, C., Arsouze, T., Lacan, F., Techine, P. and Dutay, J.-C. (2007) Isotopic Nd compositions and concentrations of the lithogenic inputs into the ocean: A compilation, with an emphasis on the margins. Chemical Geology 239, 156-164.

Johannesson, K.H. and Burdige, D.J. (2007) Balancing the global oceanic neodymium budget: evaluating the role of groundwater. Earth and Planetary Science Letters 253, 129-142.

Jones, C.E., Halliday, A.N., Rea, D.K. and Owen, R.M. (1994) Neodymium isotopic variations in North Pacific modern silicate sediment and the insignificance of detrital REE contributions to seawater. Earth and Planetary Science Letters 127, 55-66.

Jones, K.M., Khatiwala, S.P., Goldstein, S.L., Hemming, S.R. and van de Flierdt, T. (2008) Modeling the distribution of Nd isotopes in the oceans using an ocean general circulation model. Earth and Planetary Science Letters 272, 610-619.

Lacan, F. and Jeandel, C. (2001) Tracing Papua New Guinea imprint on the central Equatorial Pacific Ocean using neodymium isotopic compositions and Rare Earth Element patterns. Earth and Planetary Science Letters 186, 497-512.

Lacan, F. and Jeandel, C. (2005) Neodymium isotopes as a new tool for quantifying exchange fluxes at the continent–ocean interface. Earth and Planetary Science Letters 232, 245-257.

Lee, J.H. and Byrne, R.H. (1993) Complexation of trivalent rare earth elements (Ce, Eu, Gd, Tb, Yb) by carbonate ions. Geochimica et Cosmochimica Acta 57, 295-302.

LeGrand, P. and Wunsch, C. (1995) Constraints from paleotracer data on the North Atlantic circulation during the last glacial maximum. Paleoceanography 10, 1011-1045.

Luo, Y.-R. and Byrne, R.H. (2004) Carbonate complexation of yttrium and the rare earth elements in natural waters. Geochimica et Cosmochimica Acta 68, 691-699.

Lynch-Stieglitz, J. (2006) Tracers of past ocean circulation. Treatise on geochemistry 6, 433-451.

Lynch-Stieglitz, J., Adkins, J.F., Curry, W.B., Dokken, T., Hall, I.R., Herguera, J.C., Hirschi, J.J.-M., Ivanova, E.V., Kissel, C. and Marchal, O. (2007) Atlantic meridional overturning circulation during the Last Glacial Maximum. science 316, 66-69.

Marchitto, T.M. and Broecker, W.S. (2006) Deep water mass geometry in the glacial Atlantic Ocean: A review of constraints from the paleonutrient proxy Cd/Ca. Geochemistry, Geophysics, Geosystems 7.

Masuda, A., Nakamura, N. and Tanaka, T. (1973) Fine structures of mutually normalized rare-earth patterns of chondrites. Geochimica et Cosmochimica Acta 37, 239-248.

Nakamura, N. (1974) Determination of REE, Ba, Fe, Mg, Na and K in carbonaceous and ordinary chondrites. Geochimica et Cosmochimica Acta 38, 757-775.

Nozaki, Y. and Alibo, D.S. (2003) Importance of vertical geochemical processes in controlling the oceanic profiles of dissolved rare earth elements in the northeastern Indian Ocean. Earth and Planetary Science Letters 205, 155-172.

Osborne, A.H., Hathorne, E.C., Schijf, J., Plancherel, Y., Böning, P. and Frank, M. (2017) The potential of sedimentary foraminiferal rare earth element patterns to trace water masses in the past. Geochemistry, Geophysics, Geosystems 18, 1550-1568.

Pahnke, K., Goldstein, S.L. and Hemming, S.R. (2008) Abrupt changes in Antarctic Intermediate Water circulation over the past 25,000 years. Nature Geoscience 1, 870.

Pena, L.D. and Goldstein, S.L. (2014) Thermohaline circulation crisis and impacts during the mid-Pleistocene transition. Science 345, 318-322.

Piepgras, D.J. and Wasserburg, G.J. (1980) Neodymium isotopic variations in seawater. Earth and Planetary Science Letters 50, 128-138.

Piepgras, D.J. and Wasserburg, G.J. (1982) Isotopic Composition of Neodymium in Waters from the Drake Passage. Science 217.

Piepgras, D.J. and Wasserburg, G.J. (1987) Rare earth element transport in the western North Atlantic inferred from Nd isotopic observations. Geochimica et Cosmochimica Acta 51, 1257-1271.

Piotrowski, A.M., Goldstein, S.L., Hemming, S.R. and Fairbanks, R.G. (2005) Temporal relationships of carbon cycling and ocean circulation at glacial boundaries. Science 307, 1933-1938.

Rempfer, J., Stocker, T.F., Joos, F., Dutay, J.-C. and Siddall, M. (2011) Modelling Nd-isotopes with a coarse resolution ocean circulation model: Sensitivities to model parameters and source/sink distributions. Geochimica et cosmochimica acta 75, 5927-5950.

Rosenthal, Y., Boyle, E.A. and Labeyrie, L. (1997) Last glacial maximum paleochemistry and deepwater circulation in the Southern Ocean: Evidence from foraminiferal cadmium. Paleoceanography 12, 787-796.

Rutberg, R.L., Hemming, S.R. and Goldstein, S.L. (2000) Reduced North Atlantic Deep Water flux to the glacial Southern Ocean inferred from neodymium isotope ratios. Nature 405, 935.

Siddall, M., Khatiwala, S., van de Flierdt, T., Jones, K., Goldstein, S.L., Hemming, S. and Anderson, R.F. (2008) Towards explaining the Nd paradox using reversible scavenging in an ocean general circulation model. Earth and Planetary Science Letters 274, 448-461.

Stichel, T., Frank, M., Rickli, J. and Haley, B.A. (2012) The hafnium and neodymium isotope composition of seawater in the Atlantic sector of the Southern Ocean. Earth and Planetary Science Letters 317, 282-294.

Tachikawa, K., Arsouze, T., Bayon, G., Bory, A., Colin, C., Dutay, J.-C., Frank, N., Giraud, X., Gourlan, A.T. and Jeandel, C. (2017) The large-scale evolution of neodymium isotopic composition in the global modern and Holocene ocean revealed from seawater and archive data. Chemical Geology 457, 131-148.

Tachikawa, K., Athias, V. and Jeandel, C. (2003) Neodymium budget in the modern ocean and paleo‐oceanographic implications. Journal of Geophysical Research: Oceans 108.

Tachikawa, K., Jeandel, C. and Roy-Barman, M. (1999) A new approach to the Nd residence time in the ocean: the role of atmospheric inputs. Earth and Planetary Science Letters 170, 433-446.

Talley, L.D. (2013) Closure of the global overturning circulation through the Indian, Pacific, and Southern Oceans: Schematics and transports. Oceanography 26, 80-97.

Taylor, S.R. and McLennan, S.M. (1985) The continental crust: its composition and evolution. Blackwell Scientific Pub.,Palo Alto, CA, United States.

Thomas, D.J. (2004) Evidence for deep-water production in the North Pacific Ocean during the early Cenozoic warm interval. Nature 430, 65.

van de Flierdt, T., Griffiths, A.M., Lambelet, M., Little, S.H., Stichel, T. and Wilson, D.J. (2016) Neodymium in the oceans: a global database, a regional comparison and implications for palaeoceanographic research. Phil. Trans. R. Soc. A 374, 20150293.

van de Flierdt, T., Pahnke, K., Amakawa, H., Andersson, P., Basak, C., Coles, B., Colin, C., Crocket, K., Frank, M. and Frank, N. (2012) GEOTRACES intercalibration of neodymium isotopes and rare earth element concentrations in seawater and suspended particles. Part 1: reproducibility of results for the international intercomparison. Limnology and Oceanography: Methods 10, 234-251.

von Blanckenburg, F. (1999) Tracing past ocean circulation? Science 286, 1862-1863.

Zheng, X.-Y., Plancherel, Y., Saito, M.A., Scott, P.M. and Henderson, G.M. (2016) Rare earth elements (REEs) in the tropical South Atlantic and quantitative deconvolution of their non-conservative behavior. Geochimica et Cosmochimica Acta 177, 217-237.

Figure 1. Pathways of global overturning circulation (Talley, 2013).

Figure 2. Sections of phosphate concentration in the Atlantic and Pacific Ocean (figure source: http://www.ewoce.org). The upper panel clearly shows the southward NADW and northward AAIW and AABW. The lower panel shows the northward AAIW and AABW compensated by the southward PDW.

Figure 3. Climate records of GISP2 oxygen isotopic ratio (black), εNd (red), benthic $\delta^{13}C$ (blue and black) and Vostok ice core deuterium isotopic ratio (green) for the last 90,000 years (Piotrowski et al., 2005). εNd and benthic $\delta^{13}C$ records are from the southeast Atlantic cores RC11-83 (40.6°S, 9.8°E, 4718 m) and TNO57-21 (41.1°S, 7.8°E, 4981 m). Lower εNd values during warmer periods indicate stronger influence of NADW, whereas higher εNd values during cooler periods indicate the weakening of NADW strength. The εNd variations showing ocean circulation changes are consistent with the other climate records.

Figure 4. Diagram of εNd vs. salinity in the deep ocean (Goldstein and Hemming, 2003). Nd isotopes are highly correlated with the conservative water mass tracer salinity.

Figure 5. Diagram of εNd vs. depth in the Atlantic Ocean (modified after Goldstein and Hemming, 2003). The depth profiles are representative of North Atlantic, Southern Ocean and southwest Atlantic. The εNd depth profile in southwest Atlantic shows the influence from northern-sourced NADW at ~3000 m and southern-sourced AAIW at ~1000 m and AABW at ~4000 m.

Figure 6. PAAS-normalized REE concentrations of deep waters from the North Atlantic and North Pacific Ocean. The analyzed seawater is from two GEOTRACES intercalibration stations BATS (Bermuda Atlantic Time-series; 31.7°N, 64.1°W) in the North Atlantic and SAFe (Sampling and Analysis of Fe; 30°N, 140°W) in the North Pacific. The average REE concentrations at 2000 m water depth of BATS (van de Flierdt et al., 2012) and 3000 m water depth of SAFe (Behrens et al., 2016) are shown in blue and red, respectively. The PAAS-normalized seawater REE patterns show relatively enriched HREEs compared to LREEs and negative Ce anomalies. REE concentrations are higher in the North Pacific than in the North Atlantic Ocean. The PAAS-normalized REE patterns are often shown with a logarithmic scale. Here they are shown with a linear scale to demonstrate the difference between deep waters from the North Atlantic and North Pacific Ocean.

Figure 7. Diagram of Nd concentration vs. depth in different ocean basins (modified after Goldstein and Hemming, 2003). Nd concentrations generally increase with depth.

Figure 1. Pathways of global overturning circulation

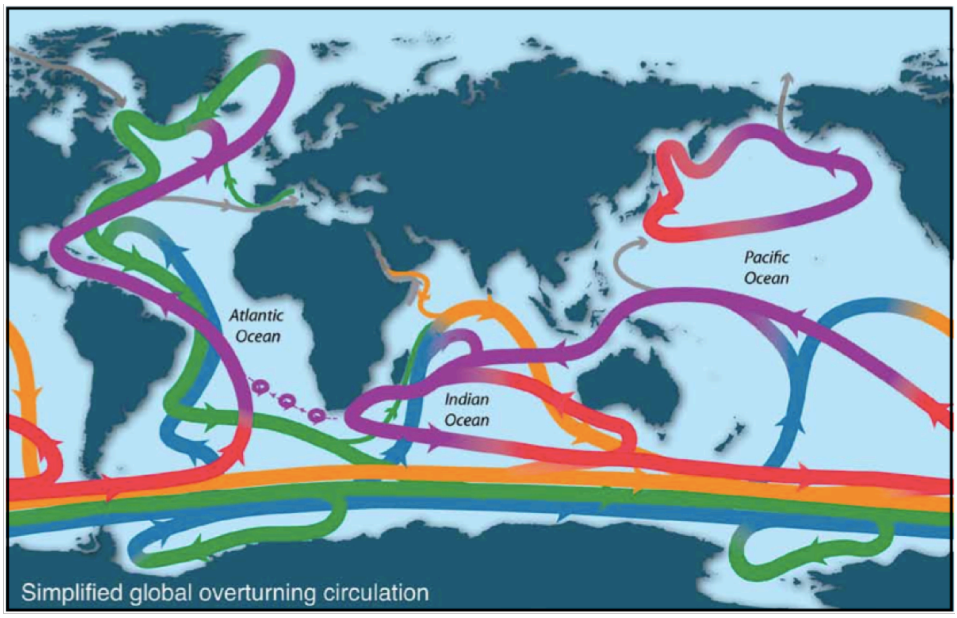


Purple: upper ocean and thermocline.
Red: denser thermocline and intermediate water.
Orange: Indian Deep Water and Pacific Deep Water.
Green: North Atlantic Deep Water.
Blue: Antarctic Bottom Water.
Gray: Bering Strait components and Mediterranean and Red Sea inflows.

Figure 2. Sections of phosphate concentration in the Atlantic and Pacific Ocean

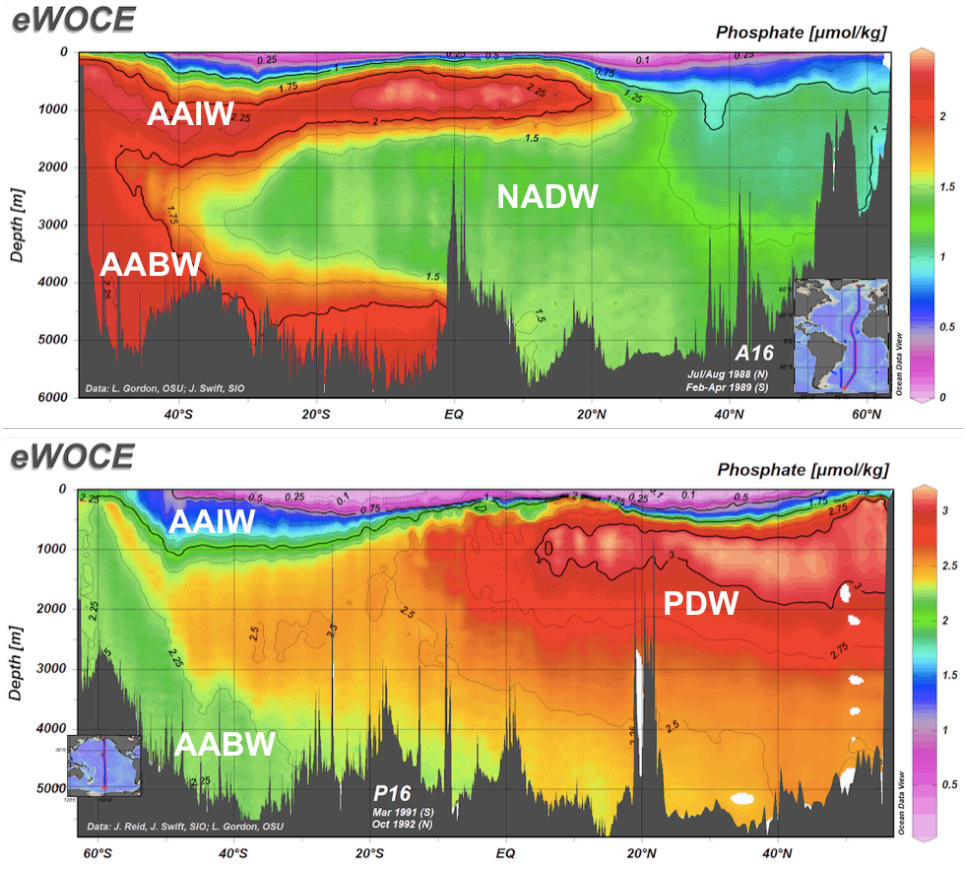

Figure 3. Climate records of GISP2 oxygen isotopic ratio, εNd, benthic $\delta^{13}C$ and Vostok ice core deuterium isotopic ratio for the last 90,000 years

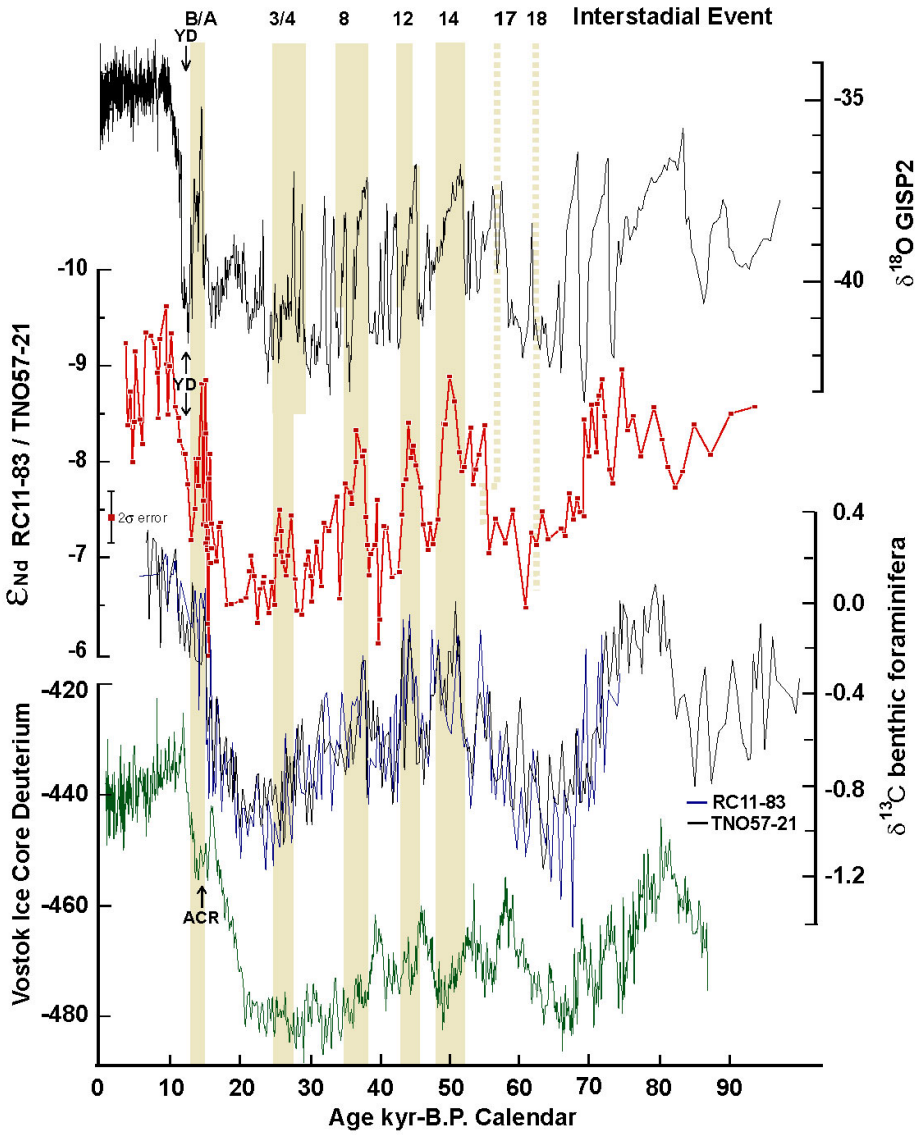

Figure 4. Diagram of εNd vs. salinity in the deep ocean

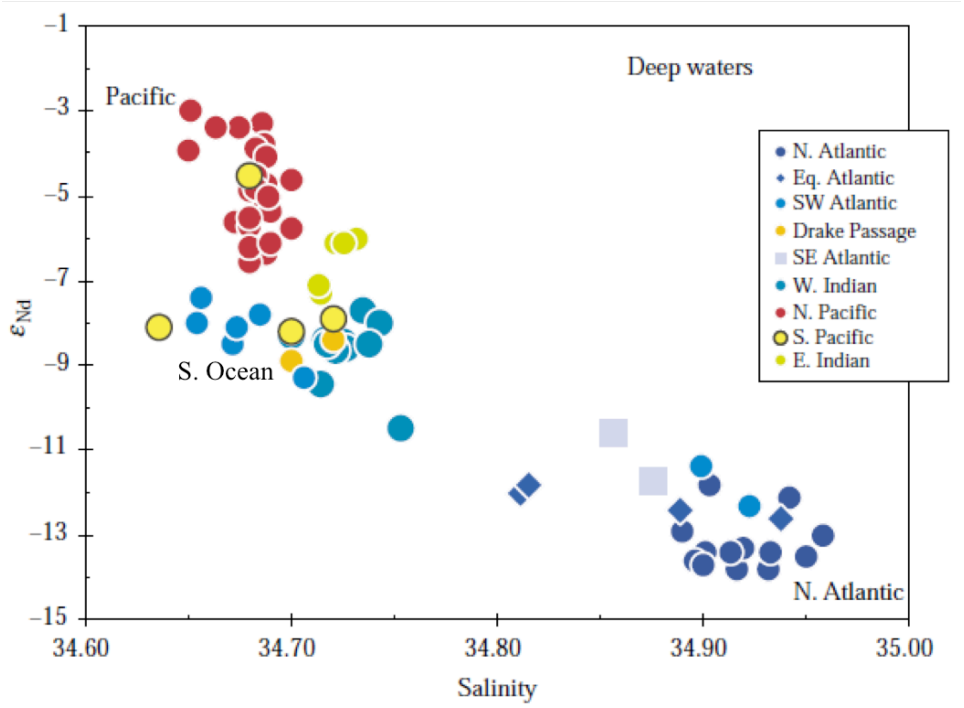

Figure 5. Diagram of εNd vs. depth in the Atlantic Ocean

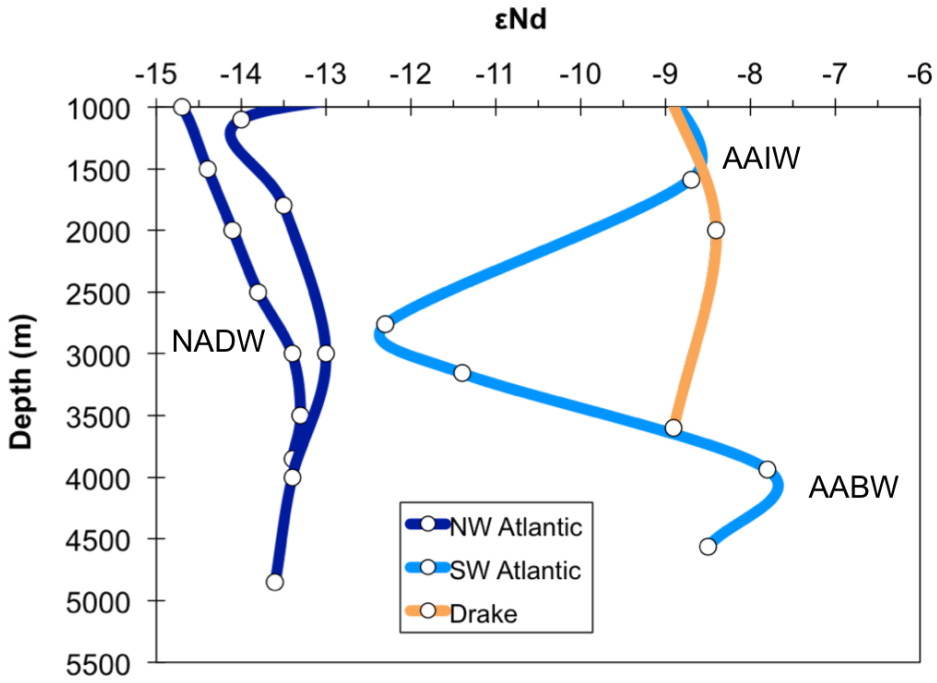

Figure 6. PAAS-normalized REE concentrations of deep waters from the North Atlantic and North Pacific Ocean

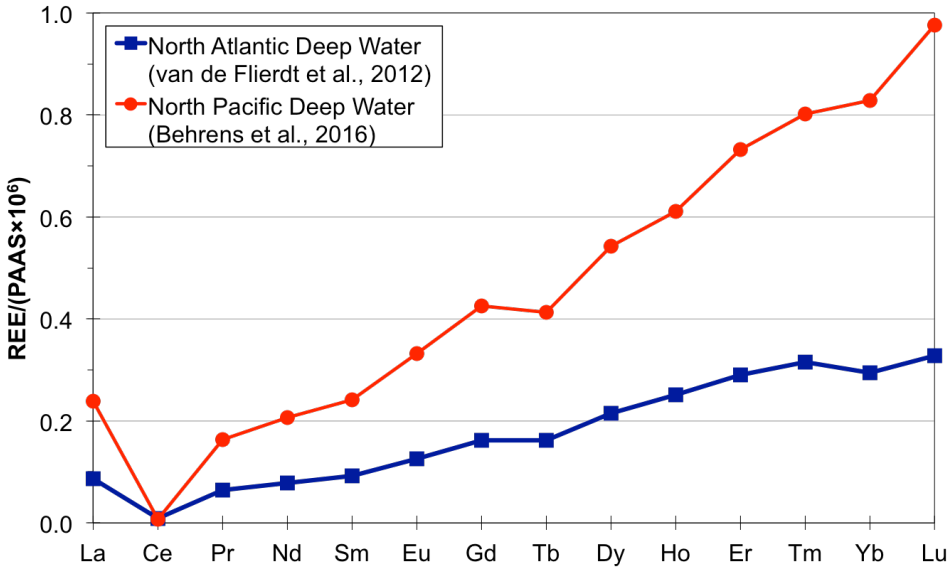

Figure 7. Diagram of Nd concentration vs. depth in different ocean basins

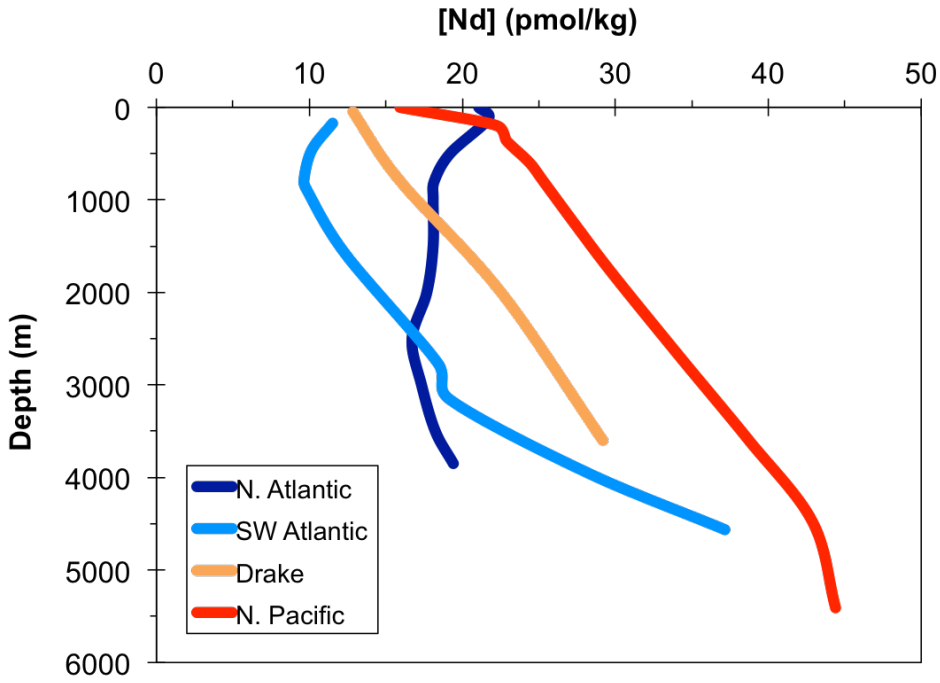

## Chapter 2. How Well Do Neodymium Isotopes Trace Atlantic Meridional Ocean Circulation Mixing?

Yingzhe Wu[1,2], Steven L. Goldstein[1,2], Leopoldo D. Pena[1,3], Robert F. Anderson[1,2], Alison E. Hartman[4], Louise L. Bolge[1], Chandranath Basak[5], Micha J.A. Rijkenberg[6], Hein J.W. de Baar[6]

[1] Lamont-Doherty Earth Observatory of Columbia University, Palisades, New York 10964, USA

[2] Department of Earth and Environmental Sciences, Columbia University, New York 10027, USA

[3] GRC Geociències Marines, Department of Earth and Ocean Dynamics, University of Barcelona, Barcelona 08028, Spain

[4] USGS Columbia Environmental Research Center, Columbia, Missouri 65201, USA

[5] California State University, 9001 Stockdale Highway, Bakersfield, CA 93311, USA

[6] Royal Netherlands Institute for Sea Research, Den Burg, The Netherlands

manuscript in preparation for *Nature Geoscience*

**The deep ocean circulation plays an important role in the global climate by storing and redistributing heat around the Earth. The South Atlantic is a critical region to study ocean circulation because it includes the major Atlantic water masses in the Atlantic Meridional Overturning Circulation (AMOC). AMOC changes in the present and past provide us important information to understand the modern and paleo-climate changes. Neodymium isotopic compositions (expressed in εNd notation) have been suggested to behave "quasi-conservatively" in the intermediate and deep water, where they approximate values expected from water mass mixing in the modern oceans and have been increasingly used to trace global ocean circulation in the present and past. However, recent studies have focused on processes (e.g. interaction between seawater and particulates) that potentially interfere with the "quasi-conservative" behavior of Nd isotopes. To establish its reliability as a water mass tracer and its application to trace paleo-ocean circulation, here we show results from 17 high-resolution seawater profiles (272 samples) collected along the Southwest Atlantic Meridional Transect (SAMT; GEOTRACES GA02 Leg 3) and analyzed for dissolved Nd isotopes. The Southwest Atlantic region includes potential sources (eolian dusts, marginal sediments, oceanic volcanism, and nepheloid layer) that could add external Nd to seawater and impact its εNd, hence an ideal test bed for investigating integrity of εNd as a water mass tracer. We here report that deviations (expressed as ΔεNd) of Nd isotopic values in seawater from the theoretical values (assuming conservative behavior) are negligible. Out of 198 intermediate and deep samples, 49% of ΔεNd-values are**

**within ± 0.25 εNd units (< analytical error: ± 0.30 εNd units) and 84% of ΔεNd-values are within ± 0.75 εNd units. Our results show that dissolved Nd isotopes along the SAMT behave as a "quasi-conservative" water mass tracer for intermediate and deep water masses and confirm the potential of using Nd isotopes to reconstruct changes of the AMOC through time. This is the first high-resolution study in the critical South Atlantic establishing the viability of using Nd isotopes as a water mass tracer.**

The deep ocean circulation plays an essential role in the climate system because it holds and redistributes heat around the Earth, thus it could potentially trigger the global climate change. Nd isotopes are used as a "quasi-conservative" proxy to trace paleo-ocean circulation, based on the modern ocean observations that seawater Nd isotopes effectively "fingerprint" different water masses, and that over long water mass transport distances in deep seawater they mainly reflect values expected from water mass mixing[1-8]. Over the past several years, studies have increasingly focused on the potential of external addition of Nd along water mass transport paths (e.g., through "boundary exchange" with particulates or addition from groundwaters[9-12]), thus challenging the idea that Nd isotopes behave "quasi-conservatively" in the oceans.

The Southwest Atlantic Ocean is one of the best locations on Earth to evaluate how well Nd isotopic composition resembles a conservative water mass tracer in the modern ocean, because it involves the major water masses in the Atlantic Meridional Overturning Circulation: southward flowing North Atlantic Deep Water (NADW), northward flowing Antarctic Intermediate Water (AAIW) and Antarctic Bottom Water

(AABW) (the hydrographic properties and circulations of water masses in the Atlantic Ocean are described in the Supplementary Information Section 1 and their transport paths are shown in Fig. S1). Seawater profiles from 17 stations, with 16 samples at different depths for each station, were collected in the Southwest Atlantic Ocean between 49.5°S and 0.2°S (Fig. 1a) in the South Atlantic Meridional GEOTRACES cruise (GA02 Leg 3; RRS James Cook 057) and measured for Nd isotopes. Most stations were sampled in the open ocean, providing a test of whether Nd isotopic composition shows "quasi-conservative" mixing systematics away from continental margins. The cruise section also provides several opportunities to test the potential effects of external Nd input. For example, it transects the continental shelf in the far south (~50°S), the volcanic Rio Grande Rise (RGR; ~30°S), and the volcanic Trindade seamount chain (Trindade; ~20°S). It crosses the major geological age boundaries of South America, where sediments show decreasing Nd isotopic compositions from south (eroded from young continental crust with high Nd isotopic composition) to north (eroded from Precambrian craton with low Nd isotopic composition)[13]. It also crosses the major Southern Hemisphere wind zones (westerlies from ~60°S to ~35°S and eastward trade winds from ~35°S to the equator[14]), allowing us to test the impacts of eolian input. In addition, a nepheloid layer with resuspended particles is observed within 500 m of the seafloor from ~50°S to ~40°S. All of these features have the potential to modify the seawater Nd isotopic compositions, allowing us to determine if they add external Nd that would change the Nd isotopic compositions of the seawater.

The Southwest Atlantic hydrography along the SAMT is reflected in the salinity

section profile (Fig. 1b) and hydrographic property diagrams of potential temperature vs. salinity (Fig. 2a) and phosphate star ($PO_4^*$) vs. salinity (Fig. 2b). $PO_4^*$ is the preformed phosphate in the ocean ($PO_4^* = PO_4 + O_2/175 - 1.95$) and considered as a conservative water mass tracer[15]. The North Atlantic-sourced NADW turns eastward at ~40°S[16], which is reflected in the salinity section profile of the SAMT where it starts to disappear at ~35°S (Fig. 1b). The Southern Ocean-sourced South Atlantic Central Water (SACW) occurs at shallow depth from ~40°S to the equator[17]. There are two types of the Southern Ocean-sourced AAIW[18]: (1) the AAIW formed in the Atlantic sector of the Southern Ocean (here labeled aAAIW), which flows northward to ~40°S before moving eastward around the South Atlantic Gyre; (2) the AAIW originating from the Indian sector of the Southern Ocean (here labeled iAAIW), which moves northwest and then westward at ~20°S before it reaches the western boundary and separates into two directions (southward from ~20°S to ~40°S and northward to the North Atlantic). These two types of AAIW and their mixing are clearly seen in the hydrographic diagrams (Fig. 2a,2b,3a,3c). The other southern-sourced water masses Upper Circumpolar Deep Water (UCDW), Lower Circumpolar Deep Water (LCDW), and AABW show decreasing thicknesses as they move northward (Fig. 1b). The hydrographic properties and transport pathways (Fig. S1) of the above water masses are described in detail in Supplementary Information Section 1.

**Nd Isotopic compositions of the Southwest Atlantic Meridional Transect**

The Nd isotopic composition is expressed as the $^{143}Nd/^{144}Nd$ ratio. The

$^{143}Nd/^{144}Nd$ ratio of a sample is often expressed as the deviation from the bulk earth (chondritic uniform reservoir – CHUR) ratio in parts per $10^4$. This normalization is defined as the εNd: $\varepsilon Nd = [(^{143}Nd/^{144}Nd_{sample}) / (^{143}Nd/^{144}Nd_{CHUR}) - 1] \times 10^4$, where $^{143}Nd/^{144}Nd_{CHUR} = 0.512638$[19]. The εNd section profile of the SAMT (Fig. 1c) strikingly resembles the salinity section (Fig. 1b) at intermediate and deep depths. From northern to southern stations, εNd strongly reflects the southward thinning NADW wedge, and thickening AAIW and AABW (Fig. 1c), closely following the salinity changes with latitude (Fig. 1b). Stations from 0.2°S to 22.5°S (Station 18 to 12; here labeled SAMT-18 and SAMT-12, respectively) are dominated by NADW and the influence of AABW increases from north to south (Fig. 1b,c). The thickness of NADW decreases from 26.1°S to 35.0°S (SAMT-11 to SAMT-8), whereas the influence of AABW continues to increase (Fig. 1b,c). Stations from 37.8°S to 46.9°S (SAMT-7 to SAMT-3) show thickening of AAIW, UCDW, LCDW and AABW as well as sniffs of NADW signal at ~2500 m (Fig. 1b,c). The southernmost stations at ~50°S (SAMT-1 and SAMT-2) are dominated by the southern sourced AAIW, UCDW, LCDW and AABW (Fig. 1b,c). The seawater εNd-values of SAMT-1 and SAMT-2 range from −9.0 to −7.8 except for the surface samples (Fig. 1c, Table 1), consistent with published data in previous studies near the Drake Passage[2,20].

The SAMT intermediate and deep water below the depths of AAIW (300−1000 m, depending on location) show systematic changes with latitude in the hydrographic diagrams (Fig. 2a,b). When compared with potential temperature and neutral density ($\gamma^n$), εNd-values also change systematically with latitude (Fig. 2c,d). To a first order, seawater

εNd-values below the depths of AAIW reflect mixtures of the main water masses upper NADW (UNADW), middle NADW (MNADW), lower NADW (LNADW), aAAIW, iAAIW, UCDW, LCDW, and AABW (Fig. 2c,d). Here the water mass end-member compositions were defined based on the extreme values from the SAMT (Fig. S2; Table 2). These extreme values from the SAMT allow us to evaluate how well εNd reflects water mass mixing within the transect. Most of the water mass end-member compositions based on SAMT are similar to that of the formation regions. However, small differences in some water mass end-member compositions could impact the mixing calculations that investigate how much εNd deviates from conservative water mass mixing.

The εNd-values of intermediate and deep water below the depths of AAIW are compared with $PO_4^*$ in more detail (Fig. 3). Each station shows a minimum $PO_4^*$ that also is the maximum salinity, indicating the strongest influence of northern-sourced NADW at that station (Fig. 2b). In order to illustrate mixing between southern-sourced waters and NADW, samples were separated into two groups: (1) from the depths of AAIW to depths of minimum $PO_4^*$/maximum salinity for each station (Fig. 3a,b); (2) from depths of minimum $PO_4^*$/maximum salinity for each station to the bottom (Fig. 3c,d). For group (1) samples, the $PO_4^*$ vertical profiles show systematic changes from northern to southern stations and indicate mixtures of water mass end-members aAAIW, iAAIW, UCDW, UNADW, and MNADW (Fig. 3a), which are also observed in the εNd vs. $PO_4^*$ diagram (Fig. 3b). They show iAAIW-UNADW mixing in the northern-most stations, aAAIW-UCDW mixing in the southern-most stations, and intermediate values between the above mixing curves in the mid-latitude stations (Fig. 3a,b). For group (2)

samples, the systematic changes from northern to southern stations and mixtures of water mass end-members UNADW, MNADW, LNADW, LCDW, and AABW are shown in the εNd vs. $PO_4^*$ diagram (Fig. 3d), consistent with observations in the vertical profiles of $PO_4^*$ (Fig. 3c). They show NADW-AABW mixing in the northern-most stations, LCDW-AABW mixing in the southern-most stations, and intermediate values between the above mixing curves in the mid-latitude stations (Fig. 3c,d). While we use $PO_4^*$, salinity could also be used to show the same relationships (Supplementary Information Section 4; Fig. S13). The εNd also covaries with salinity below the depths of AAIW and shows water mass end-member mixing (Supplementary Information Section 4; Fig. S13).

**Nd Isotopic deviations from conservative behavior**

To further investigate to what extent Nd isotopes behave conservatively in seawater, predicted εNd-values for each sample were calculated based on water mass mixing and compared with measured εNd-values. Smaller differences between measured and predicted εNd-values indicate smaller deviations from conservative mixing behavior. To define the water mass end-member compositions, the neutral densities were defined according to the hydrographic characteristics of each water mass: the salinity minimum for aAAIW, the oxygen minimum for UCDW, the salinity maximum for UNADW, the oxygen minimum for MNADW in the northernmost SAMT-17 and SAMT-18, the oxygen maximum for LNADW in the northernmost SAMT-17 and SAMT-18, the salinity maximum for LCDW in the southernmost SAMT-1 and SAMT-2, and the lowest potential temperature for AABW (Supplementary Information Section 2 and 3; Fig. S2-

S11). Then the values for the other parameters (salinity, potential temperature, $PO_4^*$, silicate, and oxygen concentration) corresponding to the neutral densities of these water masses were used as end-member compositions (Supplementary Information Section 2 and 3; Fig. S2-S11). We defined the water mass end-member compositions based on the SAMT data that best represents it, and we compared these values to published εNd and rare earth element (REE) data in the formation regions of each water mass (Supplementary Information Section 2 and 3; Fig. S2-S11, Table 2). Most water mass end-members have similar compositions in the SAMT and the formation regions except that εNd and REEs of AABW and iAAIW are modified between the formation regions and the SAMT stations (Fig. S12; Table 2). In the formation regions, AABW has εNd of −9.0 and [Nd] of 26.07 pmol/kg and iAAIW has εNd of −9.2 and [Nd] of 11.19 pmol/kg (Fig. S12; Table 2). When they reach the SAMT stations, AABW has εNd of −8.0 and [Nd] of 36.99 pmol/kg and iAAIW has εNd of −10.3 and [Nd] of 12.38 pmol/kg (Fig. S12; Table 2). Therefore, we used water mass end-member compositions defined from SAMT data (Fig. S2; Table 2) for deviation calculations because they show εNd and REE signatures when the water masses reach the SAMT stations and are more representative of the processes occurring within the SAMT.

To determine the contribution from each end-member for each sample, the fractional contributions of different water masses for each sample were calculated based on potential temperature and salinity using the following three component mixing equations assuming that each sample reflects mixing of three water mass end-members:

$$f_1 \times \theta_1 + f_2 \times \theta_2 + f_3 \times \theta_3 = \theta$$

$$f_1 \times S_1 + f_2 \times S_2 + f_3 \times S_3 = S$$

$$f_1 + f_2 + f_3 = 1$$

$$f_i > 0$$

where $f_i$, $\theta_i$ and $S_i$ are the fractional contributions, potential temperature and salinity values of water mass i, respectively. The expected εNd-values were then calculated as:

$$\varepsilon Nd_{predicted} = \frac{\varepsilon Nd_1 \times [Nd]_1 \times f_1 + \varepsilon Nd_2 \times [Nd]_2 \times f_2 + \varepsilon Nd_3 \times [Nd]_3 \times f_3}{[Nd]_1 \times f_1 + [Nd]_2 \times f_2 + [Nd]_3 \times f_3}$$

where $\varepsilon Nd_i$, $[Nd]_i$ and $f_i$ are the Nd isotopic composition, Nd concentration, and fractional contribution of water mass i, respectively. The εNd deviations were calculated as:

$$\Delta\varepsilon Nd = \varepsilon Nd_{measured} - \varepsilon Nd_{predicted}$$

where $\varepsilon Nd_{measured}$ and $\varepsilon Nd_{predicted}$ are measured and predicted values, respectively.

The ΔεNd section profile shows very small deviations from predicted εNd-values (Fig. 4a). The ΔεNd calculated based on salinity and potential temperature ranges from −3.1 to 2.0 with a median of −0.06 and an average of −0.15 ± 0.60 (1σ) εNd units (Fig. 4b). Fully 49% of ΔεNd-values are within the range of −0.25 to 0.25 εNd units (the typical measurement error) and about 84% of ΔεNd-values are within the range of −0.75 to 0.75 εNd units (Fig. 4c). The data demonstrate that the seawater εNd-values in the intermediate and deep Southwest Atlantic Ocean can be effectively predicted by water mass mixing. ΔεNd-values for each sample were also calculated based on (i) $PO_4^*$ and potential temperature; and (ii) $PO_4^*$ and salinity and show similarly small deviations from conservative mixing (Supplementary Information Section 5; Fig. S14,S15). The ΔεNd

calculated based on $PO_4^*$ and potential temperature ranges from −3.3 to 1.9 with a median of −0.22 and an average of −0.32 ± 0.63 (1σ) εNd units (Fig. S14b). 45% of ΔεNd-values are within the range of −0.25 to 0.25 εNd units and 83% of ΔεNd-values are within the range of −0.75 to 0.75 εNd units (Fig. S14c). The ΔεNd calculated based on $PO_4^*$ and salinity ranges from −3.1 to 2.0 with a median of −0.13 and an average of −0.22 ± 0.58 (1σ) εNd units (Fig. S15b). 48% of ΔεNd-values are within the range of −0.25 to 0.25 εNd units and 86% of ΔεNd-values are within the range of −0.75 to 0.75 εNd units (Fig. S15c).

ΔεNd-values were further separated into three groups using the neutral densities of the water mass end-members to investigate where the data show the most conservative behavior and the largest deviations from conservative behavior: (1) from depths of AAIW to UNADW (27.15 to 27.90 kg/m$^3$); (2) from depths of UNADW to LNADW (27.90 to 28.11 kg/m$^3$); (3) from depths of LNADW to the bottom (>28.11 kg/m$^3$) (Fig. 4c). From depths of AAIW to UNADW, negative ΔεNd values are seen at 750-1000 m from SAMT-15 to SAMT-18 (Fig. 4a,b). ΔεNd-values of these samples have an average of −0.75 ± 0.77 (1σ) εNd units. Stations SAMT-15 to SAMT-18 in the trade wind zone could receive eolian dusts from Africa with low εNd (−19 to −8)[21,22]. Low εNd-values are observed in SAMT-15 to SAMT-18 at 25-100 m (Fig. 5a,b). Samples at 750-1000 m from SAMT-15 to SAMT-18 are in the oxygen depleted zone (Fig. S2e), where Nd could be released when Fe-Mn oxides dissolve in the reducing condition[23-27]. Therefore, the negative deviation of ΔεNd-values may be explained by the release of Nd with low εNd signal from the dissolution of Fe-Mn oxides in the oxygen depleted zone. From depths of

UNADW to LNADW, the northward flowing UCDW from SAMT-1 to SAMT-5 shows very slight positive deviations (Fig. 4a,b). ΔεNd-values based on (θ, S) of these samples have an average of 0.44 ± 0.28 (1σ) εNd units. But ΔεNd-values based on ($PO_4^*$, θ) and ($PO_4^*$-S) have an average of 0.12 ± 0.20 (1σ) εNd units and 0.24 ± 0.23 (1σ) εNd units (Supplementary Information Section 6), which indicate almost no Nd isotopic deviations from conservative behavior. These stations in the far south are close to the continental margin, where marginal sediments from Patagonia with high εNd (−4.4 to +4.8)[13,21,28-33] could release Nd and alter εNd signal of seawater. Therefore, dissolved Nd from marginal sediments probably has very slight or no impact on εNd of the above samples. For seawater from depths of LNADW to the bottom, the ΔεNd distribution is skewed to more negative values (Fig. 4c), corresponding to samples below 4000 m at SAMT-11 to SAMT-18 (Fig. 4a,b). ΔεNd-values of these samples have an average of −0.83 ± 0.68 (1σ) εNd units. These stations in the trade wind zone could receive eolian dusts from Africa with low εNd (−19 to −8)[21,28,34,35]. It is observed that the shallow water (25-100 m) shows low εNd-values in these stations (Fig. 5a,b). Dissolved Nd with this low εNd signature might be scavenged in the shallow water and released by sediments at the bottom of the ocean after they sink to the sea floor. Therefore, the deviation to more negative values of the bottom water may be due to addition of low εNd signal from dissolved Nd from deep sea sediments.

**Potential sources to add external Nd to seawater**

Two potential sources that could add external Nd to seawater are eolian dusts

from Africa with low εNd (−19 to −8)[21,22] between the equator and ~35°S (wind zone of eastward trade winds) and from Patagonia and Falkland Island with high εNd (−4.4 to +4.8)[13,21,28-33] south of ~35°S (wind zone of westerlies) (Fig. 5a,b). From ~35°S to the equator, εNd-values of the surface and subsurface water from SAMT-8 to SAMT-16 (−17.7 to −11.4) are consistent with that of surface sediments eroded from Africa (−19 to −8)[21,22] (Fig. 5a,b). εNd-values of these samples from ~35°S to the equator (−17.7 to −11.4) are also consistent with that of surface sediments eroded from Rio de La Plata, Brazil, and Amazon (−17.1 to −7.5)[13,21,29,32] (Fig. 5a,b). In addition to eolian input from Africa, it is possible that boundary exchange between seawater and South American marginal sediments also influence εNd-values of the surface and subsurface water from ~35°S to the equator. South of ~35°S, εNd-values of the surface (25 m) and subsurface (100 m) water from SAMT-1 to SAMT-7 (−11.3 to −6.9) are lower than that of surface sediments eroded from Patagonia and Falkland Island (−4.4 to +4.8)[13,21,28-33] (Fig. 5a,b). They have similar εNd-values compared to that of surface sediments eroded from Rio de La Plata and Brazil between ~25°S and ~35°S (Fig. 5a,b). Since the Brazil current transports southwestward along South America (Fig. S1d), it can bring Nd isotopic signal from Rio de La Plata and Brazil between ~25°S and ~35°S to the surface and subsurface water south of ~35°S (Fig. 5a). In general, surface/subsurface εNd-values are consistent with terrigenous contributions of Nd to surface/subsurface seawater. The εNd variability of the surface/subsurface water is larger than that of intermediate and deep water (Fig. 5c). For example, the surface/subsurface water εNd-values of SAMT-11 to 14 and SAMT-16 (εNd as low as −18) exceed the lower side of the extreme values of

intermediate and deep water (εNd as low as −13) (Fig. 5c). The surface/subsurface water εNd-values of SAMT-3 and SAMT-5 (εNd as high as −7) exceed the higher side of the extreme values of intermediate and deep water (εNd as high as −8) (Fig. 5c). ΔεNd-values of intermediate and deep water from the above stations show that 48% of ΔεNd-values are within the range of −0.25 to 0.25 εNd units and 89% of ΔεNd-values are within the range of −0.75 to 0.75 εNd units (Fig. 5d). This indicates very small deviations to conservative mixing for the above intermediate and deep water samples. Therefore, the surface/subsurface water εNd signature is not transferred to intermediate and deep water.

Another potential source of external Nd is oceanic volcanism with very high εNd-values (e.g. Mid-Atlantic Ridge basalts in the Atlantic Ocean, with average εNd = 8.6 ± 2.5[36], 1σ, n = 844). Oceanic basalts in this transect are the volcanic Rio Grande Rise (RGR) and the Trindade seamount chain. Based on the largest currently available geochemical data set, EarthChem (www.earthchem.org/portal), including PetDB[37], GEOROC[38] and SedDB[39], 11 volcanic rocks from RGR have εNd values averaging −3.7 ± 2.4 (1σ) and 1 sediment sample from RGR has an εNd value of −5.5, which is similar to the values of the volcanic rocks. εNd values of 55 volcanic rocks from Trindade extracted from EarthChem (www.earthchem.org/portal) have an average of +2.9 ± 0.6 (1σ). Seawater samples near RGR and Trindade have lower εNd values than that of the above rock and sediment samples. However, this evidence is not sufficient to prove that seawater Nd isotopes near RGR and Trindade are not influenced by volcanic components. It is necessary to investigate if there is any change in the εNd deviation when a water mass passes the volcanic RGR and the Trindade chain. If the oceanic

basalts influence the seawater εNd signal, εNd deviations should be observed near the volcanic RGR (SAMT-9 and SAMT-10) and the Trindade seamount (SAMT-12 and SAMT-13) due to the directions of the water mass flow. The northward flowing water masses would show deviations to higher εNd values north of RGR/Trindade, whereas the southward flowing water masses would show deviations to higher εNd values south of RGR/Trindade. εNd-values of the northward flowing AAIW and UCDW would deviate to higher values at SAMT-10 (north of RGR). εNd-values of the southward flowing NADW would deviate to higher values at SAMT-9 (south of RGR) and SAMT-12 (south of Trindade). εNd-values of the northward flowing LCDW and AABW would deviate to higher values at SAMT-10 (north of RGR) and SAMT-13 (north of Trindade). However, seawater ΔεNd-values near RGR and Trindade do not show any discernable positive deviations, indicating negligible influence from the volcanic rocks (Fig. 4a).

Nepheloid layers near the seafloor sometimes have very high particle concentrations (100s-1000s μg/L)[40]. Thick nepheloid layers (100s-1000s m) are observed in the North Atlantic, South Atlantic and Western Indian Ocean[40]. Resuspended particles in the nepheloid layer could also potentially add external Nd to the seawater. For example, in the Northeast Atlantic the bottom water in the nepheloid layer has lower εNd-values and higher Nd concentrations compared to other bottom water from the GEOTRACES North Atlantic Zonal Transect (GA03)[41]. From SAMT-2 to SAMT-5 (~49°S to ~42°S), resuspended particles in the nepheloid layer could potentially interact with the bottom water and modify εNd signature of the bottom water. However, ΔεNd-values of the bottom water samples from SAMT-2 to SAMT-5 are all very close to 0

(Fig. 4a,b). The very small deviations from conservative water mass mixing indicate that resuspended particles in the nepheloid layer do not show impact on the bottom water εNd-values. Although the distribution of ΔεNd-values of all bottom water show negative deviations (Fig. 4c), this is due to the dominance of negative εNd deviations of the bottom water from SAMT-11 to SAMT-18, which is probably influenced by the deep sea sediments as mentioned in the previous section.

**Nd isotopic compositions of the GEOTRACES Atlantic Meridional Transect (Leg 1 and 3)**

The SAMT is a part of the GEOTRACES Atlantic Meridional Transect from ~60°N to ~50°S (GEOTRACES GA02)[42] (Fig. 6a). The εNd section of GEOTRACES GA02 is shown using εNd data from the GEOTRACES GA02 Leg 1[43] and from the GEOTRACES GA02 Leg 3 (SAMT; this study) (Fig. 6c). The agreement between the εNd section (Fig. 6c) and salinity section (Fig. 6b) of GEOTRACES GA02 is stunningly good with clear indication of the main water masses AAIW, NADW and AABW.

**Conclusions**

Our analyses of dissolved εNd in the SAMT confirm its use as a "quasi-conservative" water mass tracer at intermediate and deep depths. When compared with tracers such as salinity and $PO_4^*$, the intermediate and deep εNd-values show systematic changes from northern to southern stations and reflect mixtures of the main water masses. Our evaluations of Nd isotopic deviations from conservative behavior show that out of

198 intermediate and deep samples, 49% of ΔεNd-values are within ± 0.25 εNd units (< analytical error: ± 0.30 εNd units) and 84% of ΔεNd-values are within ± 0.75 εNd units. Potential sources that could add external Nd to seawater from oceanic volcanism and nepheloid layer do not show impact on seawater εNd. Terrigenous sources of Nd (e.g. eolian dusts from Africa and Patagonia, marginal sediments from South America) show influence on surface/subsurface water εNd but this εNd signature is not transferred to intermediate and deep water. This study confirms that εNd effectively trace water mass mixing of the AMOC and can be used to reconstruct past changes of the AMOC, which is important for us to understand climate changes in the present and past.

**Methods**

Seawater samples were collected in the GEOTRACES GA02 Cruise Leg 3 from Punta Arenas (Chile) to Las Palmas (Spain), March-April 2011. 5-10 L of water were collected depending on the sample depth and stored in a cubitainer for each sample. The samples were filtered using 0.2 μm Sartobran® cartridges and acidified using ultrapure Seastar® hydrochloric acid (HCl) to pH ~ 2 shortly after collection.

We preconcentrated rare earth elements (REEs) from seawater using C18 cartridges (Waters Corp., Sep-Pak classic, 360 mg, 55-105 μm) loaded with complexing agent of 2-ethylhexyl hydrogen phosphate (HDEHP) and 2-ethylhexyl dihydrogen phosphate ($H_2$MEHP), which was first proposed by Shabani et al. (1992)[44]. In this study, we followed the methods by Jeandel et al. (1998)[45], Lacan and Jeandel (2001)[46], and Pahnke et al. (2012)[47]. Specifically, C18 cartridges were first cleaned in a 0.5 N HCl bath

overnight, passed through 10 mL of 6 N HCl and then flushed with >500 mL of Milli-Q water. Cartridges were stored in Milli-Q water after cleaning. 300 μL of complexing agent HDEHP/$H_2$MEHP was loaded on a clean cartridge for a 5 L sample. Seawater samples were adjusted to pH ≈ 3.5 by adding Optima® ammonium hydroxide before pumped through the cartridges at 20 mL/min by a peristaltic pump in the ultra-clean chemistry laboratory at Lamont-Doherty Earth Observatory (LDEO) of Columbia University. Cartridges were then eluted with 10 mL of 0.01 N HCl to remove barium. After barium elution, cartridges were eluted with 35 mL of 6 N HCl at 10 mL/min by a peristaltic pump to collect REEs. REEs were dried and further purified by Eichrom RE-spec column chemistry. Nd fractions were extracted from REEs by LN-spec column chemistry and dried. They were redissolved in 0.5-1 mL of 3% nitric acid ($HNO_3$) for the Nd isotope analysis depending on the Nd amount in each sample (~3 to ~75 ng).

The Nd isotopic compositions were measured by a Thermo Scientific Neptune-Plus® multicollector-inductively coupled plasma-mass spectrometer (MC-ICP-MS) at LDEO. The instrument was coupled with a desolvation introduction system (a Cetac Aridus® nebulizer). All measured Nd isotopic compositions were corrected for mass fractionation using an exponential law with $^{146}Nd/^{144}Nd = 0.7219$. For each analyzing session, standard JNdi-1 was measured between every sample. For each sample, the Nd isotopic composition is calculated as $^{143}Nd/^{144}Nd_{sample} = {}^{143}Nd/^{144}Nd_{sample\_measured} \times ({}^{143}Nd/^{144}Nd_{JNdi\_measured} / {}^{143}Nd/^{144}Nd_{JNdi\_recommended})$, where $^{143}Nd/^{144}Nd_{sample\_measured}$ is the average of the measured ratios for the sample, $^{143}Nd/^{144}Nd_{JNdi\_measured}$ is the average of JNdi-1 standards in that analyzing session, and $^{143}Nd/^{144}Nd_{JNdi\_recommended} = 0.512115$[48] is

the recommended value of JNdi-1 standard. Analyses of 30 ng JNdi-1 standards (~40 ppb solutions) yielded an average $^{143}Nd/^{144}Nd$ of 0.512067 ± 0.000007 (± 0.13 εNd units; 2σ, external reproducibility; n = 24). Analyses of 15 ng JNdi-1 standards (~20 ppb solutions) yielded an average $^{143}Nd/^{144}Nd$ of 0.512080 ± 0.000012 (± 0.23 εNd units; 2σ, external reproducibility; n = 122). Analyses of 10 ng JNdi-1 standards (~15 ppb solutions) yielded an average $^{143}Nd/^{144}Nd$ of 0.512079 ± 0.000012 (± 0.23 εNd units; 2σ, external reproducibility; n = 183). Analyses of 7 ng JNdi-1 standards (~10 ppb solutions) yielded an average $^{143}Nd/^{144}Nd$ of 0.512058 ± 0.000022 (± 0.43 εNd units; 2σ, external reproducibility; n = 37).

**Acknowledgements**

We thank Captain Bill Richardson and the crew of the RRS James Cook Cruise JC057. We thank Arnold Gordon for discussions on the water mass pathways and Alan Shiller for providing GEOTRACES GA03 REE data. Y.W. thanks Karla Knudson for help with editing the manuscript. This study is funded by U.S. NSF grant OCE-12-60514.

**References**

1 Piepgras, D. J. & Wasserburg, G. Neodymium isotopic variations in seawater. *Earth and Planetary Science Letters* **50**, 128-138 (1980).

2 Piepgras, D. J. & Wasserburg, G. Isotopic Composition of Neodymium in Waters from the Drake Passage. *Science* **217** (1982).

3 Jeandel, C. Concentration and isotopic composition of Nd in the South Atlantic Ocean. *Earth and Planetary Science Letters* **117**, 581-591 (1993).

4 von Blanckenburg, F. Tracing past ocean circulation? *Science* **286**, 1862-1863 (1999).

5 Frank, M. Radiogenic isotopes: tracers of past ocean circulation and erosional input. *Reviews of geophysics* **40** (2002).

6 Goldstein, S. L. & Hemming, S. R. Long-lived isotopic tracers in oceanography, paleoceanography, and ice-sheet dynamics. *Treatise on geochemistry* **6**, 453-489 (2003).

7 van de Flierdt, T. *et al.* Neodymium in the oceans: a global database, a regional comparison and implications for palaeoceanographic research. *Phil. Trans. R. Soc. A* **374**, 20150293 (2016).

8 Tachikawa, K. *et al.* The large-scale evolution of neodymium isotopic composition in the global modern and Holocene ocean revealed from seawater and archive data. *Chemical Geology* **457**, 131-148 (2017).

9 Lacan, F. & Jeandel, C. Neodymium isotopes as a new tool for quantifying exchange fluxes at the continent–ocean interface. *Earth and Planetary Science Letters* **232**, 245-257 (2005).

10 Jeandel, C., Arsouze, T., Lacan, F., Techine, P. & Dutay, J.-C. Isotopic Nd compositions and concentrations of the lithogenic inputs into the ocean: A compilation, with an emphasis on the margins. *Chemical Geology* **239**, 156-164 (2007).

11 Johannesson, K. H. & Burdige, D. J. Balancing the global oceanic neodymium budget: Evaluating the role of groundwater. *Earth and Planetary Science Letters* **253**, 129-142 (2007).

12 Johannesson, K. H. *et al.* Submarine groundwater discharge is an important net source of light and middle REEs to coastal waters of the Indian River Lagoon, Florida, USA. *Geochimica et Cosmochimica Acta* **75**, 825-843 (2011).

13 de Mahiques, M. M. *et al.* Nd and Pb isotope signatures on the Southeastern South American upper margin: Implications for sediment transport and source rocks. *Marine Geology* **250**, 51-63 (2008).

14 Hellerman, S. & Rosenstein, M. Normal monthly wind stress over the world ocean with error estimates. *Journal of Physical Oceanography* **13**, 1093-1104 (1983).

15 Broecker, W. S., Blanton, S., Smethie, W. M. & Ostlund, G. Radiocarbon decay and oxygen utilization in the Deep Atlantic Ocean. *Global Biogeochemical Cycles* **5**, 87-117, doi:10.1029/90GB02279 (1991).

16 Stramma, L. & England, M. On the water masses and mean circulation of the South Atlantic Ocean. *Journal of Geophysical Research-Oceans* **104**, 20863-20833 (1999).

17 Talley, L. D. *Descriptive physical oceanography: an introduction*. (Academic press, 2011).

18 Gordon, A. L., Weiss, R. F., Smethie, W. M. & Warner, M. J. Thermocline and intermediate water communication between the South Atlantic and Indian Oceans. *Journal of Geophysical Research: Oceans* **97**, 7223-7240 (1992).

19 Jacobsen, S. B. & Wasserburg, G. Sm-Nd isotopic evolution of chondrites. *Earth and Planetary Science Letters* **50**, 139-155 (1980).

20 Stichel, T., Frank, M., Rickli, J. & Haley, B. A. The hafnium and neodymium isotope composition of seawater in the Atlantic sector of the Southern Ocean. *Earth and Planetary Science Letters* **317**, 282-294 (2012).

21 Goldstein, S. L., O'Nions, R. K. & Hamilton, P. J. A Sm-Nd isotopic study of atmospheric dusts and particulates from major river systems. *Earth and planetary Science letters* **70**, 221-236 (1984).

22 Dia, A., Allegre, C. J. & Erlank, A. J. The development of continental crust through geological time: the South African case. *Earth and Planetary Science Letters* **98**, 74-89 (1990).

23 de Baar, H. J. W., German, C. R., Elderfield, H. & Van Gaans, P. Rare earth element distributions in anoxic waters of the Cariaco Trench. *Geochimica et Cosmochimica Acta* **52**, 1203-1219 (1988).

24 Sholkovitz, E. R., Shaw, T. J. & Schneider, D. L. The geochemistry of rare earth elements in the seasonally anoxic water column and porewaters of Chesapeake Bay. *Geochimica et Cosmochimica Acta* **56**, 3389-3402 (1992).

25 German, C. R. & Elderfield, H. Rare earth elements in Saanich Inlet, British Columbia, a seasonally anoxic basin. *Geochimica et Cosmochimica Acta* **53**, 2561-2571 (1989).

26 German, C. R., Holliday, B. P. & Elderfield, H. Redox cycling of rare earth elements in the suboxic zone of the Black Sea. *Geochimica et Cosmochimica Acta* **55**, 3553-3558 (1991).

27 Schijf, J., De Baar, H. J. W. & Millero, F. J. Vertical distributions and speciation of dissolved rare earth elements in the anoxic brines of Bannock Basin, eastern Mediterranean Sea. *Geochimica et Cosmochimica Acta* **59**, 3285-3299 (1995).

28 McLennan, S. M., Taylor, S. R., McCulloch, M. T. & Maynard, J. B. Geochemical and Nd-Sr isotopic composition of deep-sea turbidites: Crustal evolution and plate tectonic associations. *Geochimica et Cosmochimica Acta* **54**, 2015-2050 (1990).

29 Henry, F., Probst, J.-L., Thouron, D., Depetris, P. J. & Garçon, V. Nd-Sr isotopic compositions of dissolved and particulate material transported by the Parana and Uruguay rivers during high (december 1993) and low (september 1994) water periods. *Sciences Géologiques, Bulletin* **49**, 89-100 (1996).

30 Basile, I. *et al.* Patagonian origin of glacial dust deposited in East Antarctica (Vostok and Dome C) during glacial stages 2, 4 and 6. *Earth and Planetary Science Letters* **146**, 573-589 (1997).

31 Gaiero, D. M., Brunet, F., Probst, J.-L. & Depetris, P. J. A uniform isotopic and chemical signature of dust exported from Patagonia: Rock sources and occurrence in southern environments. *Chemical Geology* **238**, 107-120 (2007).

32 Rousseau, T. C. C. *et al.* Rapid neodymium release to marine waters from lithogenic sediments in the Amazon estuary. *Nature communications* **6**, 7592 (2015).

33 Gili, S. *et al.* Glacial/interglacial changes of Southern Hemisphere wind circulation from the geochemistry of South American dust. *Earth and Planetary Science Letters* **469**, 98-109 (2017).

34 Franzese, A. M., Hemming, S. R., Goldstein, S. L. & Anderson, R. F. Reduced Agulhas Leakage during the Last Glacial Maximum inferred from an integrated provenance and flux study. *Earth and Planetary Science Letters* **250**, 72-88 (2006).

35 Bayon, G., German, C. R., Burton, K. W., Nesbitt, R. W. & Rogers, N. Sedimentary Fe–Mn oxyhydroxides as paleoceanographic archives and the role of aeolian flux in regulating oceanic dissolved REE. *Earth and Planetary Science Letters* **224**, 477-492 (2004).

36 Class, C. & Lehnert, K. PetDB Expert MORB (Mid-Ocean Ridge Basalt) Compilation. EarthChem Library. (2012).

37 Lehnert, K., Su, Y., Langmuir, C., Sarbas, B. & Nohl, U. A global geochemical database structure for rocks. *Geochemistry, Geophysics, Geosystems* **1** (2000).

38 GEOROC. GEOROC, Geochemistry of rocks of the oceans and continents, database. *Max-Planck-Institut für Chemie* (2007).

39 Johansson, A., Lehnert, K. & Hsu, L. Status report on the SedDB sediment geochemistry database. *GeoPRISMS Newsletter* **28**, 21 (2012).

40 Gardner, W. D., Richardson, M. J. & Mishonov, A. V. Global assessment of benthic nepheloid layers and linkage with upper ocean dynamics. *Earth and Planetary Science Letters* **482**, 126-134 (2018).

41 Stichel, T. *et al.* Separating biogeochemical cycling of neodymium from water mass mixing in the Eastern North Atlantic. *Earth and Planetary Science Letters* **412**, 245-260 (2015).

42 Rijkenberg, M. J. *et al.* The distribution of dissolved iron in the West Atlantic Ocean. *PloS one* **9**, e101323 (2014).

43 Lambelet, M. *et al.* Neodymium isotopic composition and concentration in the western North Atlantic Ocean: Results from the GEOTRACES GA02 section. *Geochimica et Cosmochimica Acta* **177**, 1-29 (2016).

44 Shabani, M. B., Akagi, T. & Masuda, A. Preconcentration of trace rare-earth elements in seawater by complexation with bis (2-ethylhexyl) hydrogen phosphate and 2-ethylhexyl dihydrogen phosphate adsorbed on a C18 cartridge and determination by inductively coupled plasma mass spectrometry. *Analytical Chemistry* **64**, 737-743 (1992).

45 Jeandel, C., Thouron, D. & Fieux, M. Concentrations and isotopic compositions of neodymium in the eastern Indian Ocean and Indonesian straits. *Geochimica et Cosmochimica Acta* **62**, 2597-2607 (1998).

46 Lacan, F. & Jeandel, C. Tracing Papua New Guinea imprint on the central Equatorial Pacific Ocean using neodymium isotopic compositions and Rare Earth Element patterns. *Earth and Planetary Science Letters* **186**, 497-512 (2001).

47 Pahnke, K. *et al.* GEOTRACES intercalibration of neodymium isotopes and rare earth element concentrations in seawater and suspended particles. Part 2: Systematic tests and baseline profiles. *Limnology and Oceanography: Methods* **10**, 252-269 (2012).

48 Tanaka, T. *et al.* JNdi-1: a neodymium isotopic reference in consistency with LaJolla neodymium. *Chemical Geology* **168**, 279-281 (2000).

49 Vanicek, M. & Siedler, G. Zonal fluxes in the deep water layers of the western South Atlantic Ocean. *Journal of Physical Oceanography* **32**, 2205-2235 (2002).

50 Schlitzer, R. (2012).

Figure 1. Sampling locations and section profiles of the Southwest Atlantic Meridional Transect (SAMT). (a) Map of the Southwest Atlantic Ocean with sampling stations (black dots). Numbers are station numbers. (b) Salinity section profile with contours of neutral density ($\gamma^n$). The water masses are upper North Atlantic Deep Water (UNADW, $\gamma^n$ = 27.75-27.98 kg/m$^3$ [49]), middle North Atlantic Deep Water (MNADW, $\gamma^n$ = 27.98-28.07 kg/m$^3$ [49]), lower North Atlantic Deep Water (LNADW, $\gamma^n$ = 28.07-28.12 kg/m$^3$ [49]), South Atlantic Central Water (SACW, $\gamma^n$ = 26.6-27.15 kg/m$^3$ [49]), Antarctic Intermediate Water from the Atlantic section of the Southern Ocean (aAAIW, $\gamma^n$ = 27.15-27.55 kg/m$^3$ [49]), Antarctic Intermediate Water from the Indian section of the Southern Ocean (iAAIW, $\gamma^n$ = 27.15-27.55 kg/m$^3$ [49]), Upper Circumpolar Deep Water (UCDW, $\gamma^n$ = 27.55-27.88 kg/m$^3$ [49]), Lower Circumpolar Deep Water (LCDW, $\gamma^n$ = 28.12-28.24 kg/m$^3$ [49]), and Antarctic Bottom Water (AABW, $\gamma^n$ > 28.24 kg/m$^3$ [49]). The Rio Grande Rise (RGR) and Trindade seamount chain (Trindade) are labeled. (c) εNd section profile. The legend numbers are station numbers from Station 1 (SAMT-1) in the south to Station 18 (SAMT-18) at the equator. The diagrams were made using ODV software[50].

Figure 2. SAMT seawater samples below the depths of AAIW. (a) Potential temperature vs. salinity. (b) $PO_4^*$ vs. salinity. (c) Potential temperature vs. εNd. (d) Neutral density vs. εNd. The legend numbers are station numbers from SAMT-1 in the south to SAMT-18 at the equator. Black crosses are water mass end-members defined from the SAMT and listed in Table 2. SAMT seawater samples show systematic changes with latitude following violet, blue, yellow, and red curves from stations in the south to stations at the equator. To a first order, seawater εNd-values below the depths of AAIW reflect mixtures of the main water masses.

Figure 3. Intermediate and deep water samples from depths of AAIW to depths of minimum $PO_4^*$ of each station (a and b) and from depths of minimum $PO_4^*$ of each station to the bottom (c and d). (a) and (c) are diagrams of neutral density vs. $PO_4^*$. (b) and (d) are diagrams of εNd vs. $PO_4^*$. The legend numbers are station numbers from SAMT-1 in the south to SAMT-18 at the equator. Black crosses are water mass end-members defined and listed in Table 2. SAMT seawater samples show systematic changes with latitude following violet, blue, yellow, and red curves from stations in the south to stations at the equator. (a) and (b) show iAAIW-UNADW mixing in the northern-most stations, aAAIW-UCDW mixing in the southern-most stations, and intermediate values between the above mixing curves in the mid-latitude stations. (c) and (d) show NADW-AABW mixing in the northern-most stations, LCDW-AABW mixing in the southern-most stations, and intermediate values between the above mixing curves in the mid-latitude stations.

Figure 4. εNd deviations (ΔεNd = measured εNd – predicted εNd) calculated based on water mass mixing using potential temperature and salinity. (a) ΔεNd section profile. The legend numbers are station numbers from Station 1 in the south to Station 18 at the equator. The section diagram was made using ODV software[50]. (b) ΔεNd vs. neutral density. The average ΔεNd = −0.15 ± 0.60 (1σ) εNd units. (c) Histogram of ΔεNd. The y-

axis on the left is the number of calculated samples. The y-axis on the right is the percentage of calculated samples. ΔεNd-values were separated into three groups using the neutral densities of the water mass end-members defined from the SAMT (Table 2). Green columns include samples from the depths of AAIW to UNADW ($\gamma^n$ = 27.15-27.90 kg/m$^3$). Red columns include samples from the depths of UNADW to LNADW ($\gamma^n$ = 27.90-28.11 kg/m$^3$). Blue columns include samples from the depths of LNADW to AABW ($\gamma^n$ =28.11-28.30 kg/m$^3$). The numbers above the columns are percentage values within each interval from depths of AAIW to the bottom. These diagrams show that the intermediate and deep seawater εNd-values in the SAMT can be effectively predicted by water mass mixing.

Figure 5. (a) εNd of surface water from the SAMT (with black marker lines) and surface sediments near South America[13,21,28-33] and Africa[21,22]. Horizontal arrows indicate wind directions of westerlies from ~60°S to ~35°S and trade winds from ~35°S to the equator[14]. The dash line is the boundary for westerlies and trade winds. The map was made using ODV software[50]. (b) Latitude vs. εNd of shallow seawater of the top 100 m from the SAMT (symbols in color) and surface sediments (symbols in black). These shallow water εNd-values are consistent with that of surface sediments eroded from South America (SAMT-1 to SAMT-7; south of ~35°S) and Africa (SAMT-8 to SAMT-16; ~35°S to the equator), indicating terrigenous contributions of Nd to surface seawater. (c) εNd vs. depth of selected stations SAMT-3, 5, 11, 12, 13, 14, and 16. The shallow water εNd varies from −18 to −7 (in the light blue area). The intermediate and deep water εNd varies from −13 to −8 (between grey dashed lines). (d) Histogram of ΔεNd-values of intermediate and deep water from stations in (c). It shows very small deviations from conservative mixing for these intermediate and deep water samples. These diagrams indicate that the shallow water εNd signature is not transferred to intermediate and deep water.

Figure 6. Sampling locations and section profiles of GEOTRACES GA02 from Leg 1[43] to Leg 3 (SAMT; this study). (a) Map of the Atlantic Ocean with sampling stations (black dots). Numbers are station numbers. (b) Salinity section profile. (c) εNd section profile. The GEOTRACES GA02 sections of salinity and εNd agree with each other very well. The diagrams were made using ODV software[50].

Figure 1. Sampling locations and section profiles of the Southwest Atlantic Meridional Transect (SAMT)

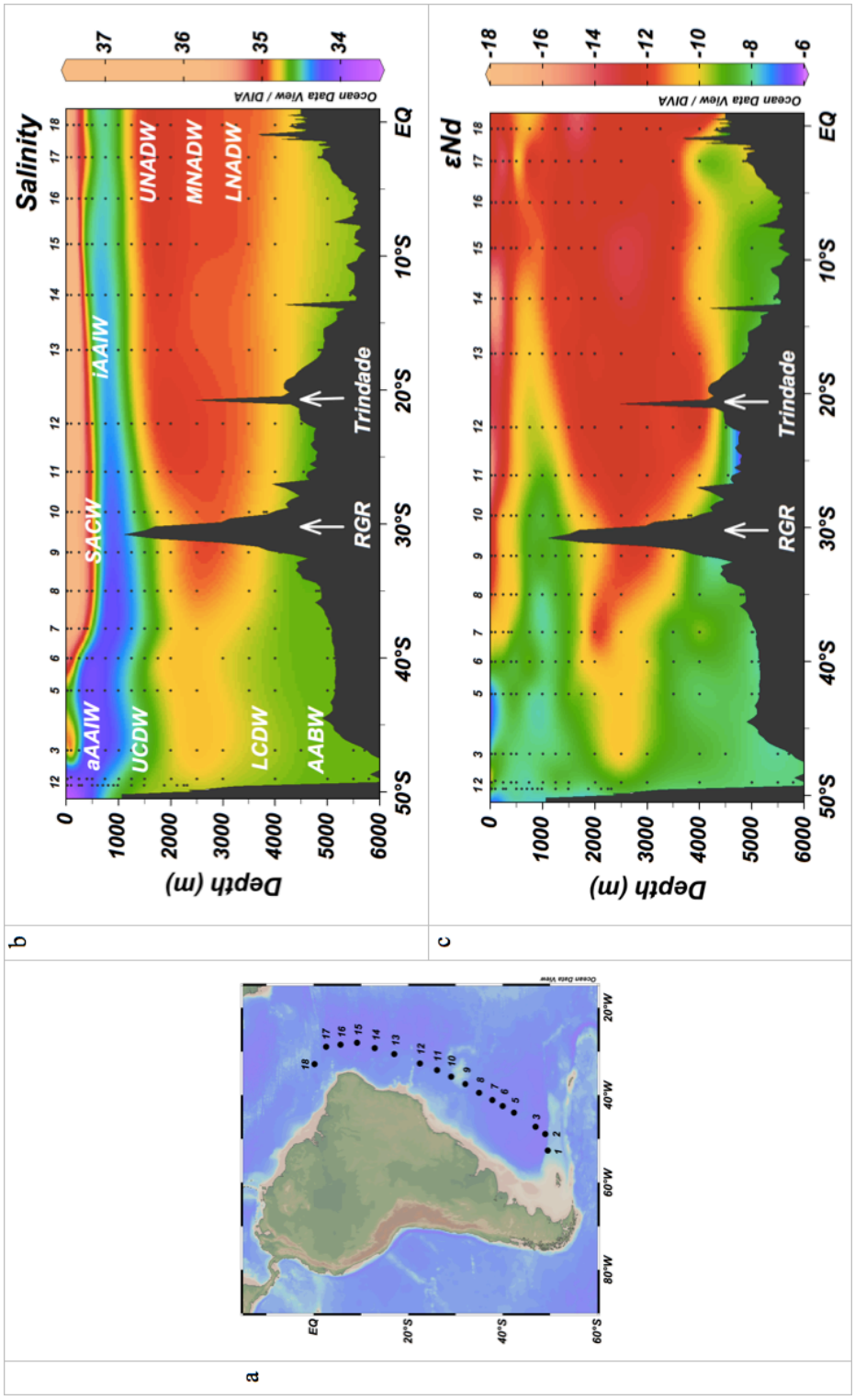

Figure 2. SAMT seawater samples below the depths of AAIW

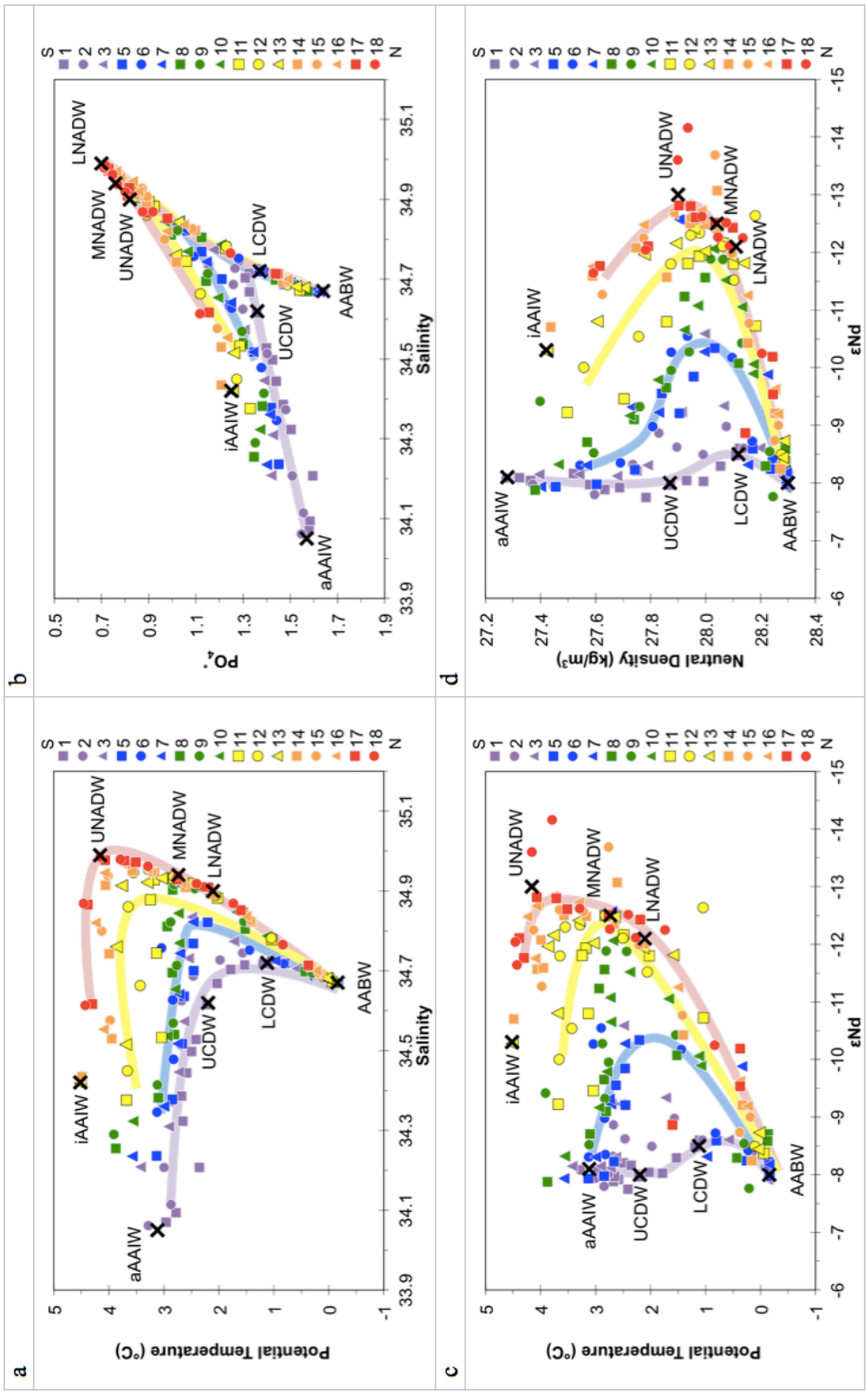

Figure 3. Intermediate and deep water samples from depths of AAIW to depths of minimum $PO_4^*$ of each station and from depths of minimum $PO_4^*$ of each station to the bottom

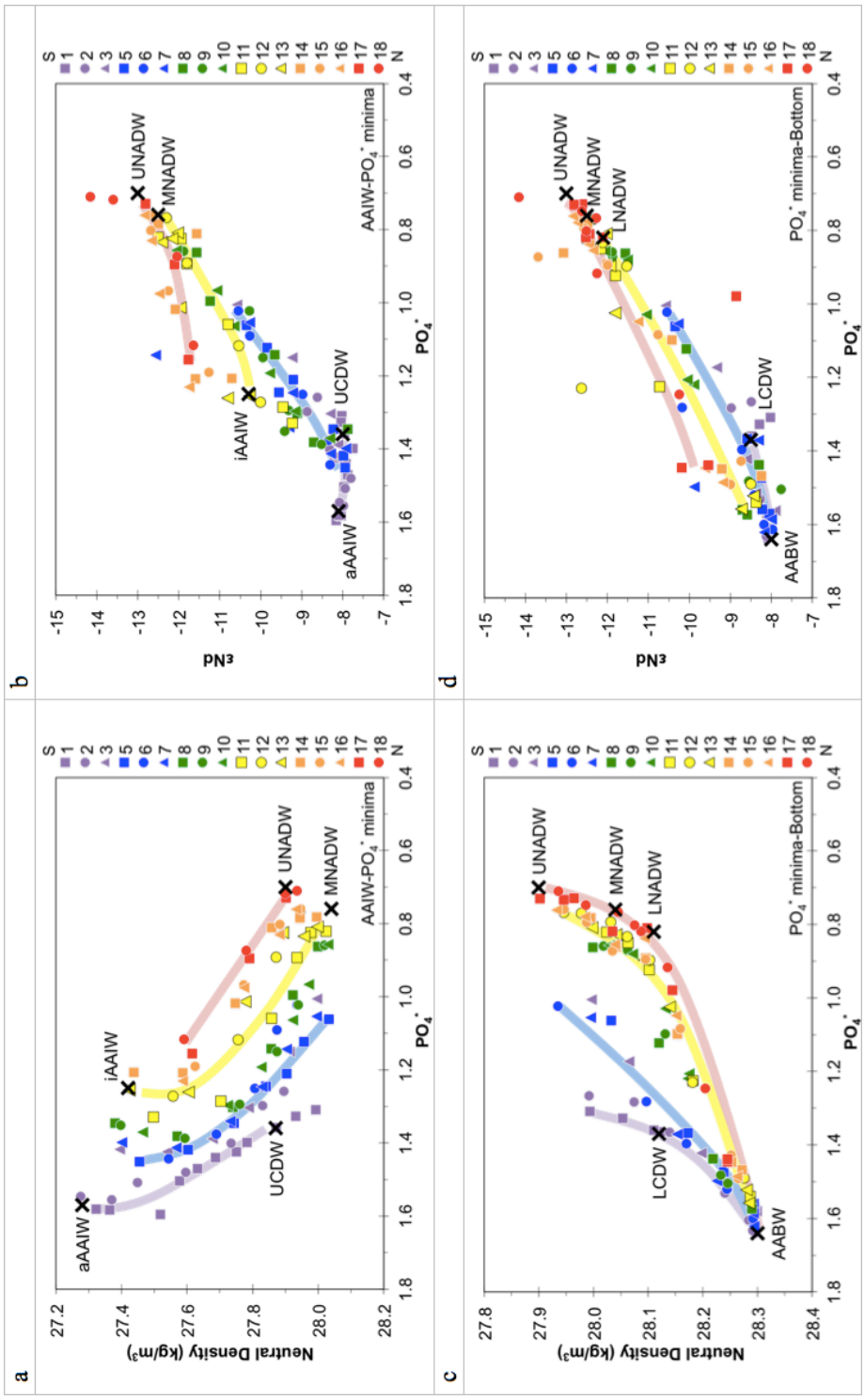

Figure 4. εNd deviations calculated based on water mass mixing using potential temperature and salinity

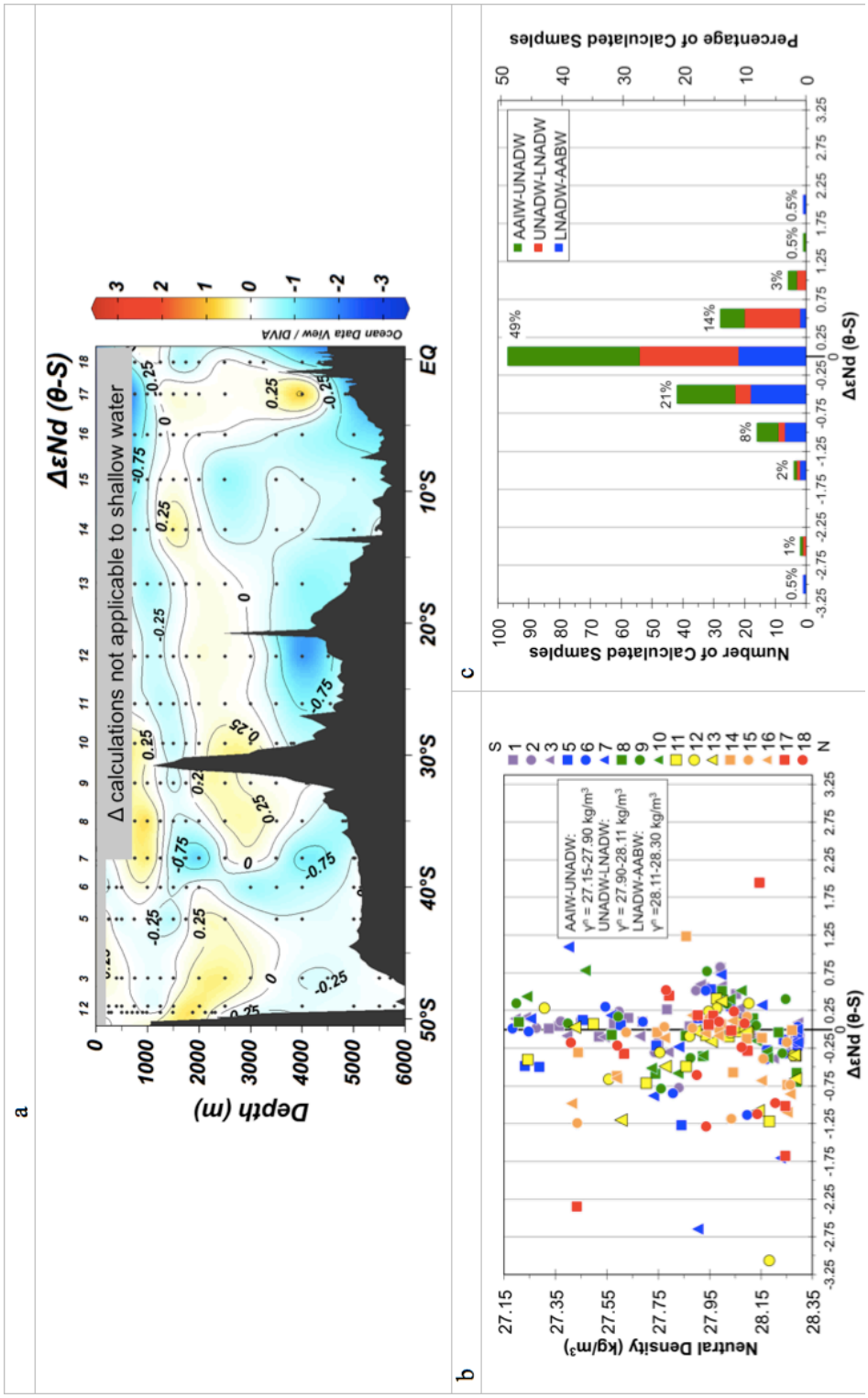

Figure 5. εNd of surface water from the SAMT and surface sediments near South America and Africa

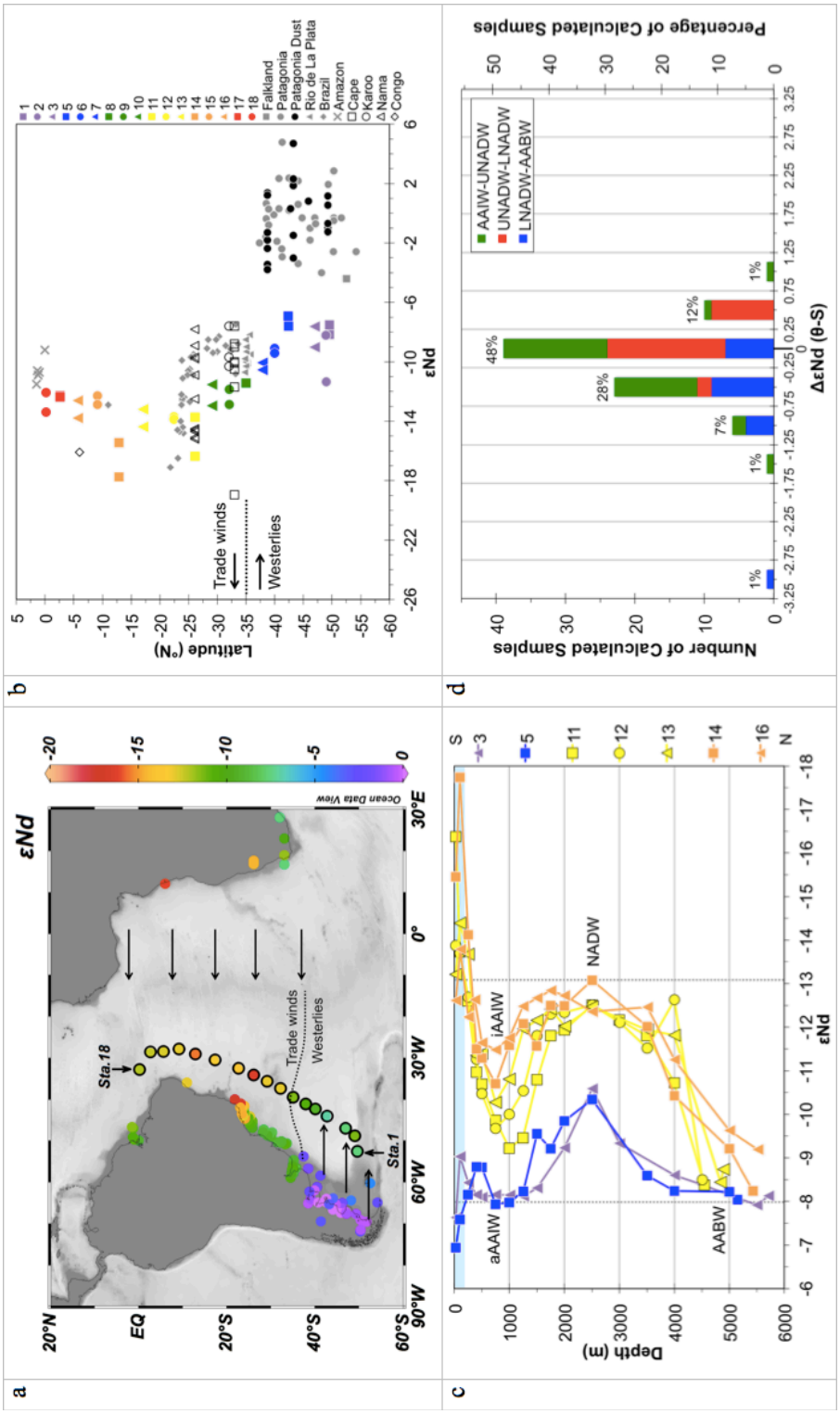

Figure 6. Sampling locations and section profiles of GEOTRACES GA02 from Leg 1 to Leg 3

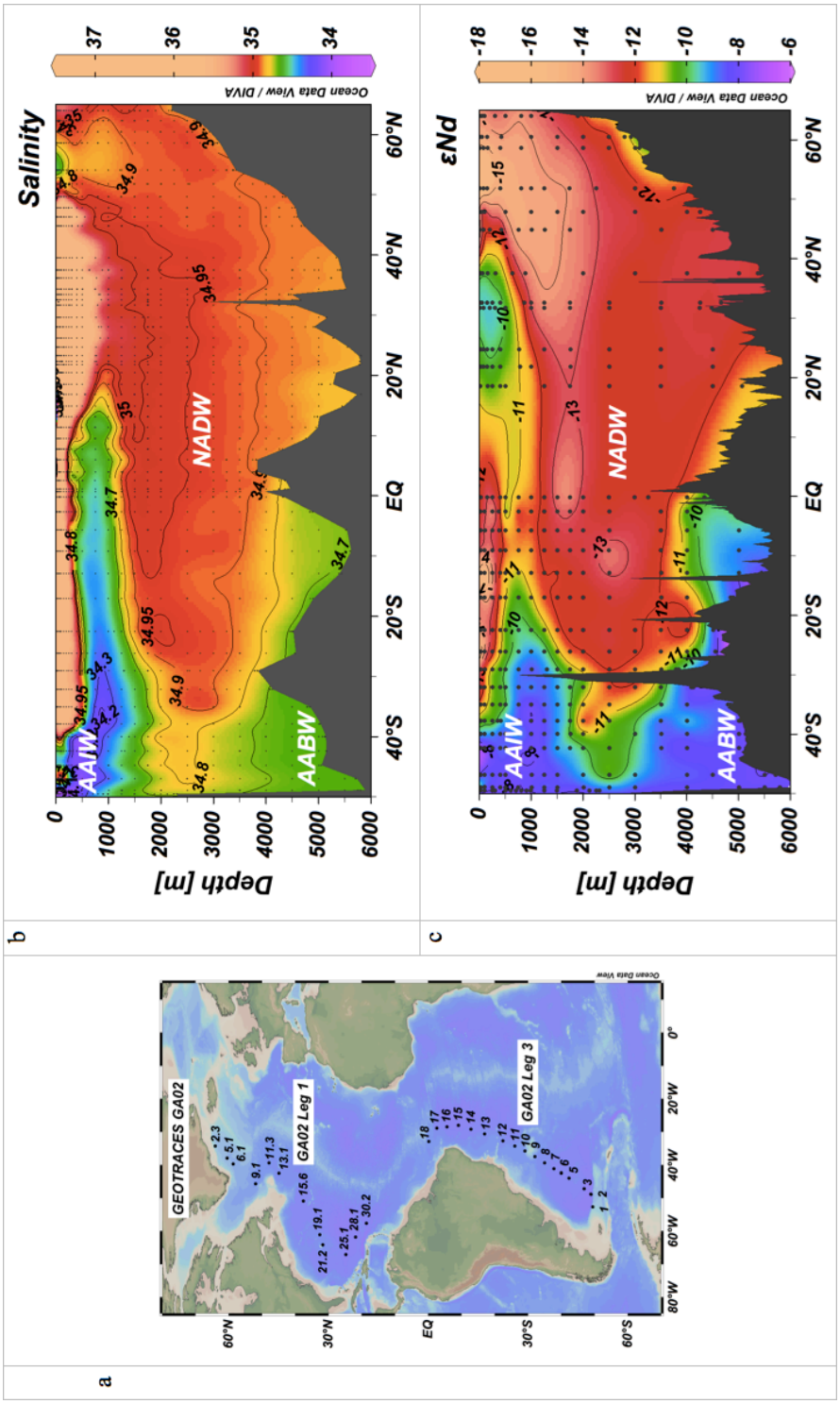

Table 1. Data for the 17 seawater profiles collected from the Southwest Atlantic Meridional Transect (SAMT). Sampling location, depth, salinity, potential temperature, neutral density, oxygen concentration, silicate concentration, nutrient concentration, εNd, external 2 standard deviation of εNd, fractional contributions of water masses calculated based on potential temperature and salinity, predicted εNd based on water mass mixing calculations, and ΔεNd-value (= measured εNd – expected εNd). Table 1 is in the Appendix 1.

Table 2. (a) Water mass end-member compositions based on data from the SAMT. (b) Water mass end-member compositions based on hydrographic data from World Ocean Atlas 2013 and published εNd and REE data in the water mass formation regions.

Table 2. South Atlantic water mass end-member compositions

| | Salinity | Potential Temperature | $PO_4^*$ | Silicate | Oxygen | Neutral Density | εNd | [La] | [Nd] | [Er] | [Yb] |
|---|---|---|---|---|---|---|---|---|---|---|---|
| | | °C | µmol/kg | µmol/kg | µmol/kg | kg/m$^3$ | | pmol/kg | pmol/kg | pmol/kg | pmol/kg |
| a | | | | | | | | | | | |
| UNADW | 34.99 | 4.16 | 0.70 | 16 | 242 | 27.90 | −13.0 | 23.35 | 18.00 | 5.23 | 5.05 |
| MNADW | 34.94 | 2.74 | 0.76 | 27 | 247 | 28.04 | −12.5 | 26.45 | 19.47 | 5.51 | 5.35 |
| LNADW | 34.90 | 2.11 | 0.82 | 32 | 255 | 28.11 | −12.1 | 29.91 | 22.69 | 5.77 | 5.81 |
| SACW | 34.31 | 6.26 | 1.05 | 8 | 255 | 27.10 | −8.6 | 14.09 | 10.39 | 3.86 | 3.66 |
| aAAIW | 34.05 | 3.12 | 1.57 | 15 | 295 | 27.28 | −8.1 | 15.38 | 10.32 | 4.37 | 4.14 |
| iAAIW | 34.42 | 4.52 | 1.25 | 30 | 175 | 27.42 | −10.3 | 17.34 | 12.38 | 4.71 | 5.06 |
| UCDW | 34.62 | 2.20 | 1.36 | 81 | 168 | 27.87 | −8.0 | 24.93 | 14.85 | 5.82 | 6.14 |
| LCDW | 34.72 | 1.12 | 1.37 | 108 | 195 | 28.12 | −8.5 | 33.60 | 21.45 | 6.91 | 7.27 |
| AABW | 34.67 | -0.16 | 1.64 | 127 | 225 | 28.30 | -8.0 | 50.49 | 36.99 | 8.50 | 8.79 |
| b | | | | | | | | | | | |
| UNADW | 35.02 | 4.35 | 0.69 | 13 | 250 | 27.90 | −13.2 | 23.27 | 17.49 | 5.01 | 4.74 |
| MNADW | 34.96 | 3.01 | 0.78 | 19 | 263 | 28.02 | −12.6 | 23.94 | 18.27 | 5.00 | 4.82 |
| LNADW | 34.92 | 2.23 | 0.81 | 25 | 266 | 28.10 | −12.2 | 29.72 | 23.63 | 5.61 | 5.47 |
| SACW | 34.65 | 9.27 | 0.59 | 5 | 240 | 26.89 | − | 14.10 | 10.19 | 3.56 | 3.40 |
| aAAIW | 34.16 | 3.27 | 1.52 | 22 | 285 | 27.37 | −8.0 | − | 10.79 | − | − |
| iAAIW | 34.38 | 4.78 | 1.17 | 26 | 214 | 27.35 | −9.2 | 17.97 | 11.19 | 4.55 | 4.69 |
| UCDW | 34.60 | 2.22 | 1.36 | 75 | 175 | 27.85 | −8.4 | 22.65 | 13.94 | 5.05 | 5.61 |
| LCDW | 34.71 | 1.05 | 1.37 | 109 | 198 | 28.13 | −8.4 | 34.38 | 22.50 | 6.66 | 7.33 |
| AABW | 34.66 | -0.35 | 1.65 | 122 | 235 | 28.33 | −9.0 | 39.50 | 26.07 | 7.38 | 7.81 |

## Supplementary Information

## Chapter 2. How Well Do Neodymium Isotopes Trace Atlantic Meridional Ocean Circulation Mixing?

This supplementary information includes (1) a description of hydrographic properties of shallow to deep water masses and their pathways in the Atlantic Ocean, (2) an explanation of how we defined the water mass end-member compositions based on data from the Southwest Atlantic Meridional Transect (SAMT), (3) an explanation of how we defined the water mass end-member compositions based on data from the water mass source regions, (4) comparison of εNd with salinity, (5) calculations of ΔεNd based on (i) $PO_4^*$, potential temperature and (ii) $PO_4^*$, salinity, and (6) discussions on distributions and deviations of ΔεNd.

## 1. Water masses and their transport paths in the Atlantic Ocean

### *1.1. Northern-sourced water masses*

North Atlantic Deep Water (NADW) consists of three layers: upper NADW (UNADW), middle NADW (MNADW), and lower NADW (LNADW) (Rhein et al., 1995; Schmitz Jr, 1996; Smethie et al., 2000; Stramma and England, 1999). UNADW forms as follows (Fig. S1a): Labrador Sea Water (LSW) formed in the Labrador Sea is characterized by low salinity and high oxygen concentration (Talley and McCartney, 1982). LSW propagates to three directions after it leaves the Labrador Sea (Sy et al., 1997): northeastward into the Irminger Sea, southeastward across the Charlie Gibbs Fracture Zone (~53°N), and southward along the western boundary of the North Atlantic. The southward branch forms UNADW and it continues to flow southward along the western boundary. At ~30°N, UNADW shows influence from the westward

Mediterranean Outflow Water (MOW) characterized by high salinity and high potential temperature (Schmitz Jr, 1996).

For MNADW (Fig. S1b), Iceland Scotland Overflow Water (ISOW) moves southwestward from the Norwegian Sea and separates into two directions. The eastern branch continues to flow southward along the east side of the Mid-Atlantic Ridge (MAR) and the other branch moves westward and enters the western basin through the Charlie Gibbs Fracture Zone at ~53°N (Schott and Brandt, 2007). ISOW mixes with the modified Antarctic Bottom Water (AABW) moving north up in the eastern Atlantic, LSW, and modified North Atlantic Water (a water mass with high salinity and temperature originating from Subtropical Atlantic) to form MNADW (Schmitz Jr, 1996). It moves southward along the western boundary after it leaves the Labrador Sea. MNADW is marked by high salinity and low oxygen concentration.

For LNADW (Fig. S1c), Denmark Strait Overflow Water (DSOW) is characterized by low salinity and maximum oxygen concentration (Dickson and Brown, 1994; Smethie et al., 2000). It overflows the Denmark Strait west of Iceland and enters the Labrador Sea. DSOW mixes with modified AABW moving north up in the western Atlantic, LSW and Subpolar Mode Water to form LNADW (Schmitz Jr, 1996).

NADW, comprising the three layers, enters the western basin of South Atlantic Ocean along the western boundary and turns eastward at ~40°S (Larqué et al., 1997; Reid, 1994; Stramma and England, 1999) (Fig. S1a-c). It also enters the eastern basin of South Atlantic through the Romanche Fracture Zone at the equator (Larqué et al., 1997; Reid, 1994; Stramma and England, 1999) (Fig. S1a-c).

In the SAMT section, the northern-sourced NADW with high salinity (S > 34.90) flows between 1500 m and 4500 m at the equator, becoming thinner southward, and starts to disappear at ~35°S (where it turns east) near Station 8 of the SAMT (SAMT-8) (Fig. 1b,S2). UNADW, at a neutral density ($\gamma^n$) layer of 27.75-27.98 kg/m$^3$ (Vanicek and Siedler, 2002), is identified by the salinity maximum and low silicate concentration between the equator and ~26°S (Fig. 1b,S2a,S2d). At the equator, MNADW ($\gamma^n$ = 27.98-28.07 kg/m$^3$; (Vanicek and Siedler, 2002)) is indicated by an oxygen minimum (Fig. S2e) and LNADW ($\gamma^n$ = 28.07-28.12 kg/m$^3$; (Vanicek and Siedler, 2002)) is indicated by an oxygen maximum (Fig. S2e).

***1.2. Southern-sourced water masses***

*1.2.1. South Atlantic Central Water*

South Atlantic Central Water (SACW) (Fig. S1d) originates from subducted surface water and has a range of salinities and potential temperatures (θ) (Talley, 2011) with $\gamma^n$ of 26.6-27.15 kg/m$^3$ (Vanicek and Siedler, 2002). The θ-S curve of SACW is characterized by a linear line between points (θ = 5°C, S = 34.3) and (θ = 20°C, S = 36.0) (Stramma and England, 1999) (Fig. S6b). It is formed in the Brazil-Malvinas confluence zone and recirculates within the South Atlantic Gyre (Stramma and England, 1999). SACW is transported in the Benguela Current toward the Brazilian shelf and separates into two directions when it reaches the Brazilian shelf: the northward North Brazil Current and the southward Brazil Current (Stramma and England, 1999). SACW also flows northward from the Benguela Current in the Southern South Equatorial Current toward the Brazilian shelf which turns eastward at ~10°S and joins the Angola Gyre in

the eastern South Atlantic (Stramma and England, 1999). The eastward Equatorial Undercurrent flows southward after it reaches Africa and joins the Angola Gyre (Stramma and England, 1999).

In the SAMT section, Stations SAMT-5 and SAMT-6 are in the SACW formation region (Fig. S1d). The southward Brazil Current from ~20°S to ~40°S passes from SAMT-12 to SAMT-7 (Fig. S1d). The northward North Brazil Current passes stations from SAMT-13 to SAMT-18 (Fig. S1d).

*1.2.2. Antarctic Intermediate Water*

Antarctic Intermediate Water (AAIW) (Fig. S1e) is characterized by low salinity and a high oxygen concentration, with $\gamma^n$ from 27.15 kg/m$^3$ to 27.55 kg/m$^3$ (Vanicek and Siedler, 2002; Whitworth and Nowlin, 1987). Two types of AAIW are reported (Gordon et al., 1992): one from the Atlantic Ocean (here labeled aAAIW) and the other from the Indian Ocean (here labeled iAAIW). aAAIW originates from the Pacific sector of the Southern Ocean and enters the South Atlantic from the Drake Passage (McCartney, 1977). aAAIW flows northward to the Brazil-Malvinas Current confluence at ~40°S (near SAMT-6; Fig. S1e) (McCartney, 1977; Piola and Gordon, 1989; Talley, 2011). There it moves eastward around the South Atlantic Gyre (Larqué et al., 1997; Reid, 1994; Stramma and England, 1999). iAAIW enters the South Atlantic via the Agulhas leakage before moving northwest and then westward at ~20°S (Gordon et al., 1992). When it reaches the western boundary at ~20°S (between SAMT-12 and SAMT-13; Fig. S1e), it moves in two directions: southward from ~20°S to ~40°S and northward along the western boundary (Larqué et al., 1997; Reid, 1994; Stramma and England, 1999).

In the SAMT section, aAAIW is recognized by the salinity minimum and oxygen maximum at ~50°S (Fig. S2a,e). It sinks from ~300 m depth at ~50°S to ~1000 m at the equator (Fig. 1b). Stations SAMT-1 to SAMT-5 are on the northward aAAIW transport path from ~50°S to ~40°S (Fig. S1e). The southward branch of iAAIW from ~20°S to ~40°S passes from SAMT-6 to SAMT-12 (Fig. S1e). SAMT-13 to SAMT-18 are on the northward branch of iAAIW from ~20°S northward (Fig. S1e). The two types of AAIW are also clearly seen in diagrams of potential temperature vs. εNd (Fig. 2c) and neutral density vs. εNd (Fig. 2d), where iAAIW is ~2 εNd units lower than aAAIW.

*1.2.3. Circumpolar Deep Water*

Circumpolar Deep Water (CDW) at $\gamma^n$ = 27.55-28.24 kg/m$^3$ (Vanicek and Siedler, 2002) is the major water mass of Antarctic Circumpolar Current, which flows eastward around Antarctica. It is a thick layer extending from just below the Antarctic Surface Water or AAIW to above AABW. CDW enters the Argentine Basin from the Drake Passage (Fig. S1f,g). It is penetrated by NADW and separated into upper CDW (UCDW) and lower CDW (LCDW).

UCDW in the SAMT is observed between 1000 m and 2000 m ($\gamma^n$ = 27.55-27.88 kg/m$^3$; (Vanicek and Siedler, 2002)) at ~50°S, and its thickness decreases as it moves northward (Fig. 1b). UCDW lies beneath AAIW and above NADW and indicated by low oxygen and high silicate concentrations (Orsi et al., 1999; Rintoul et al., 2001; Whitworth III et al., 1998) (Fig. S2d,e). It moves northward to ~20°S in the western basin (near SAMT-12; Fig. S1f) and most of it returns southward to the eastern basin (Larqué et al., 1997; Reid, 1994).

LCDW is observed at $\gamma^n$ of 28.12-28.24 kg/m$^3$ (Vanicek and Siedler, 2002) in the SAMT (Fig. 1b). LCDW lies beneath NADW and above AABW and has high salinity from the influence of NADW (Reid, 1994; Reid and Lynn, 1971) (Fig. S2a). In the western basin, it progresses northward to the equator (Larqué et al., 1997; Reid, 1994) (Fig. S1g).

*1.2.4. Antarctic Bottom Water*

The densest water mass AABW ($\gamma^n$ = 28.24-28.4 kg/m$^3$, e.g. (Heywood and King, 2002; Klatt et al., 2005; Orsi et al., 1999; Orsi et al., 2002; Vanicek and Siedler, 2002)), is characterized by very low potential temperature ($\theta < 0$°C) and high silicate (Fig. S2b,d). AABW formed in the Weddell Sea enters the Argentine Basin along the South Sandwich Trench and then flows northeastward along the western boundary (Larqué et al., 1997; Reid, 1994; Stramma and England, 1999) (Fig. S1h). After it enters the North Atlantic, it moves northward in the western basin and extends up to ~40°N (Talley, 2011) (Fig. S1h). An arm of it turns eastward at the equator and passes the Romanche Fracture Zone (Larqué et al., 1997; Reid, 1994; Stramma and England, 1999) (Fig. S1h). It also turns eastward at ~10°N and passes the Vema Fraction Zone (Talley, 2011) (Fig. S1h). AABW in the SAMT is observed below $\gamma^n$ of 28.24 kg/m$^3$ (Fig. S2). Its thickness decreases moving northward and it disappears at SAMT-18 (~0.2°N) (Fig. 1b).

**2. How the water mass end-member compositions are defined based on data from the SAMT**

To calculate the predicted εNd-values based on conservative water mass mixing,

the intermediate and deep water mass end-member compositions have been defined below the depths of SACW. We show our results based on water mass end-member compositions defined from the SAMT instead of that defined from the water mass formation regions (WMFR; Section 3) because (1) the SAMT end-members are the extreme values within the transect which allows us to evaluate how well εNd reflects water mass mixing within the SAMT, especially for AABW and iAAIW which are somewhat different from that in the formation regions (discussed in Section 3, Fig. S12b); (2) the published εNd and REE data for the southern-sourced water masses are limited especially for aAAIW (discussed in Section 3).

For the shallow SACW, the end-member was defined at SAMT-5 in the formation region of SACW. Two samples at ~100 m and ~250 m at SAMT-5 are within the $\gamma^n$ of SACW (26.6-27.15 kg/m$^3$) (Fig. 1b). The sample at ~250 m was used as the SACW end-member since the sample at ~100 m is too shallow and influenced by surface water εNd and REE signatures. Then the corresponding salinity, potential temperature, $PO_4^*$, silicate, oxygen, εNd, and REE concentrations were used as the end-member compositions of SACW, which are shown in Fig. S2 and listed in Table 2a.

For the intermediate and deep water masses, aAAIW is characterized by the salinity minimum (Fig. S2a), UCDW by the oxygen minimum (Fig. S2e), UNADW by the salinity maximum (Fig. S2a), MNADW by the oxygen minimum in the northernmost SAMT-17 and SAMT-18 (Fig. S2e), LNADW by the oxygen maximum in the northernmost SAMT-17 and SAMT-18 (Fig. S2e), LCDW by the salinity maximum in the southernmost SAMT-1 and SAMT-2 (Fig. S2a), and AABW by the lowest potential

temperature and the highest $PO_4^*$ (Fig. S2b,c). The neutral densities of these water masses were defined according to the above hydrographic characteristics (Fig. S2). Then the salinity, potential temperature, $PO_4^*$, silicate, oxygen, εNd, and REE concentrations corresponding to the neutral densities of the above water masses were used as the end-member compositions, which are shown in Fig. S2 and listed in Table 2a. Because a nepheloid layer is observed between and including SAMT-2 and SAMT-6, the εNd and REE concentrations of samples at ~5500 m of SAMT-2 and SAMT-3 were used instead of the bottommost samples for the AABW εNd and REE end-member values (Fig. 2d,S2f; Table 2a).

**3. Defining water mass end-member compositions in water mass formation regions based on published εNd and REE data**

The water mass end-member compositions have also been defined from the WMFR. The water mass hydrographic properties were defined using World Ocean Atlas (WOA) 2013 (Garcia et al., 2013a; Garcia et al., 2013b; Locarnini et al., 2013; Zweng et al., 2013) in the WMFR. εNd and REE end-member values for the WMFR were defined from the published data of filtered seawater samples in the western subtropical North Atlantic where the North Atlantic-sourced water masses are formed and in the Southern Ocean where the southern-sourced water masses are formed. The εNd and REE end-member values for the SAMT were defined within the transect (Section 2).

The published εNd and REE data of filtered Atlantic seawater samples used in this evaluation are from 17°N to 65°N ((Filippova et al., 2017; Lacan and Jeandel, 2004;

Lacan and Jeandel, 2005; Lambelet et al., 2016; Pahnke et al., 2012; Rickli et al., 2009; Sholkovitz and Schneider, 1991; Sholkovitz et al., 1994; Stichel et al., 2015; van de Flierdt et al., 2012); GEOTRACES GA03 REE data) and from 37°S to 67°S ((Garcia-Solsona et al., 2014; Hathorne et al., 2015; Stichel et al., 2012); GEOTRACES GA10 REE data) (Fig. S3-S11). GEOTRACES GA03 consists of two sections in the subtropical North Atlantic: the first section was completed in 2010 (henceforth labeled GA03-2010) from Lisbon to ~32°N, ~22°W, then southward to 18°N (meridional), then westward from the coast of Mauritania to ~18°N, ~25°W (zonal); the second section was completed in 2011 (henceforth labeled GA03-2011) from Woods Hole to Bermuda then southeastward to ~18°N, ~25°W. The GEOTRACES GA10 (henceforth labeled GA10) section is a zonal transect at ~40°S in the South Atlantic. The cruise reports for these GEOTRACES cruises are available in www.geotraces.org. REE data of GEOTRACES GA03 and GEOTRACES GA10 are available in the GEOTRACES Intermediate Data Product 2017 (http://www.bodc.ac.uk/geotraces/data/idp2017/). The water masses of these samples were defined based on the same hydrographic properties as the SAMT end-members: the salinity minimum for aAAIW in the South Atlantic, the oxygen minimum for UCDW in the South Atlantic, the salinity maximum for UNADW in the North Atlantic, the oxygen minimum for MNADW in the North Atlantic, the oxygen maximum for LNADW in the North Atlantic, the salinity maximum for LCDW in the South Atlantic, and the lowest potential temperature for AABW in the South Atlantic. Then the corresponding εNd and REE data of these samples were used to define the end-member compositions.

### *3.1. Defining the North Atlantic-sourced water masses*

For the North Atlantic-sourced water masses UNADW, MNADW and LNADW, we used published εNd and REE data from 17°N to 65°N to define the WMFR end-member compositions (Fig. S3-S5). The published data were separated into two groups for comparison: (1) western basin, data from the west of the MAR; (2) eastern basin, data from the east of the MAR (Fig. S3-S5; Table S1).

Station BATS (Bermuda Atlantic Time-series; 31.67°N, 64.17°W) is a well-intercalibrated GEOTRACES intercalibration station (Pahnke et al., 2012; van de Flierdt et al., 2012). Station 21.2 (31.67°N, 64.17°W) from (Lambelet et al., 2016), and Station 10 from GEOTRACES GA03 2011 (GA03-2011-10; 31.75°N, 64.16°W) have almost the same location as BATS. These stations are close to the region where UNADW, MNADW and LNADW are formed and are on their transport paths (Fig. S1). Therefore, it is reasonable to choose these stations to define the end-member values for UNADW, MNADW and LNADW.

For the water mass hydrographic end-members, we used the WOA 2013 (Garcia et al., 2013a; Garcia et al., 2013b; Locarnini et al., 2013; Zweng et al., 2013) constrained in the western subtropical North Atlantic to define the end-member values based on hydrographic properties: the salinity maximum for UNADW, the oxygen minimum for MNADW, and the oxygen maximum for LNADW. We used the εNd and REE data from BATS and a few other stations in close by locations as the end-member values for UNADW, MNADW and LNADW. The WMFR end-member compositions of UNADW, MNADW and LNADW are shown in Fig. S12 and listed in Table 2b. These WMFR end-

members were compared with SAMT end-members in diagrams of potential temperature vs. salinity and Nd concentration ([Nd]) vs. εNd (Fig. S12). The WMFR end-member compositions of are very close to the SAMT end-member compositions (Fig. S12).

### *3.2. Defining the southern-sourced water masses*

For the shallow SACW, we used published REE data from GEOTRACES GA10 (data available in the GEOTRACES Intermediate Data Product 2017) along ~40°S to define end-member compositions in the WMFR (Fig. S6). For the intermediate and deep water masses aAAIW, iAAIW, UCDW, LCDW and AABW, we used published εNd and REE data from 37°S to 67°S to define the WMFR end-member compositions (Fig. S7-S11). For SACW, aAAIW, UCDW and LCDW, the published data were separated into western basin and eastern basin groups (Fig. S6,S7,S9,S10; Table 2b). The published stations are in the eastern basin for iAAIW and in the western basin for AABW (Fig. S8,S11; Table 2b).

#### *3.2.1. Comparison of εNd and REE data from the SAMT and stations in the WMFR*

For SACW, Station 18 of GEOTRACES GA10 (GA10-18; REE data available in the GEOTRACES Intermediate Data Product 2017) is in the SACW formation region with Nd concentrations available (Fig. S6). The Nd concentration of SACW at this station (10.19 pmol/kg, measurement error is not reported) is very close to that at SAMT-5 and SAMT-6 (10.39 ± 0.11 pmol/kg; the error is one standard deviation of multiple samples), which are also in the SACW formation region. Thus, SACW Nd concentrations are similar in the SAMT and WMFR whereas no published εNd data in the WMFR can be compared with that in the SAMT.

For aAAIW, Stations PS71/244 and PS71/250 (Stichel et al., 2012) are in the aAAIW formation region, in the Drake Passage, with Nd concentrations published (Fig. S7). The εNd (−8.0 ± 0.1) and Nd concentration (10.79 ± 0.11 pmol/kg; the error is measurement error and labeled ME since only one sample is available) of aAAIW in these stations are nearly the same as values at SAMT-2 where εNd = −8.1 ± 0.3 (ME) and [Nd] = 10.32 ± 0.29 (ME) pmol/kg. In the following paragraphs, the errors labeled ME are measurement errors whereas the errors without labeling are one standard deviations of multiple samples. Thus, the SAMT and WMFR have almost the same Nd concentrations and εNd-values for aAAIW (Fig. S12b).

For iAAIW, Stations GA10-1, GA10-2, S2, PS71/101, PS71/102 ((Garcia-Solsona et al., 2014; Hathorne et al., 2015; Stichel et al., 2012); GA10 REE data available in the GEOTRACES Intermediate Data Product 2017) are on the iAAIW pathway from the Indian Ocean to SAMT-13 (Fig. S8). The εNd of iAAIW decreases from the published stations (−9.2 ± 0.2) to SAMT-13 (−10.3 ± 0.2; ME). Nd concentrations slightly increase from 11.19 (± 1.20) pmol/kg to 12.38 (± 0.35; ME) pmol/kg and Yb concentrations increase from 4.69 (± 0.51) pmol/kg to 5.06 (± 0.23; ME) pmol/kg. Thus, the SAMT has similar Nd concentrations and lower εNd-values compared to that in the WMFR for iAAIW (Fig. S12b).

For UCDW, Stations PS71/230, PS71/236, PS71/241, and PS71/244 (Hathorne et al., 2015; Stichel et al., 2012) are on the pathway of UCDW from the Drake Passage to SAMT-1 (Fig. S9). Station PS71/241 has all the REE concentrations published (Hathorne et al., 2015), whereas the other stations only have Nd concentrations published (Stichel et

al., 2012). The εNd of UCDW does not change much from the Drake Passage (−8.4 ± 0.3) to SAMT-1 (−8.0 ± 0.3; ME), whereas Nd concentration increases from 13.94 (± 1.53) pmol/kg to 14.85 (± 0.42; ME) pmol/kg and Yb concentration increases from 5.61 (± 0.13) pmol/kg to 6.14 (± 0.28; ME) pmol/kg. Thus, the SAMT and WMFR have similar Nd concentrations and εNd-values for UCDW (Fig. S12b).

For LCDW, Stations PS71/230, PS71/236, PS71/241, PS71/244, and PS71/250 (Hathorne et al., 2015; Stichel et al., 2012) in the Drake Passage and PS71/193 farther east in the Circum-Antarctic are in the LCDW source regions (Fig. S10). Stations PS71/193 and PS71/241 have all the REE concentrations published, whereas only Nd concentrations are available for the other stations. The εNd of LCDW is −8.4 (± 0.2) in the LCDW source regions and −8.5 (± 0.3; ME) at SAMT-1. Nd concentration is 22.50 (± 3.26) pmol/kg in the LCDW source regions and 21.45 (± 0.60; ME) pmol/kg at SAMT-1. Yb concentration is 7.33 (± 0.80) pmol/kg in the LCDW source regions and 7.27 (± 0.33; ME) pmol/kg at SAMT-1. Although the source regions have large range of REE concentrations, REE concentrations of SAMT-1 and average WMFR are close to each other. Thus, the SAMT and WMFR have similar Nd concentrations and εNd-values for LCDW (Fig. S12b).

For AABW, Station PS71/193 (Hathorne et al., 2015; Stichel et al., 2012) with all REE concentrations is in the water mass formation region in the Weddell Sea (Fig. S11). Since we used samples at ~5500 m of SAMT-2 and SAMT-3 instead of the bottommost samples to define the AABW within the SAMT, we also excluded the bottommost samples from the published εNd and REE values of AABW samples. The εNd of AABW

increases from Weddell Sea (−9.0 ± 0.1) to SAMT-2 and SAMT-3 (−8.0 ± 0.1). Nd concentration increases from 26.07 (± 1.08) pmol/kg to 36.99 (± 1.49) pmol/kg and Yb concentration increases from 7.81 (± 0.22) pmol/kg to 8.79 (± 0.18) pmol/kg. Both εNd and Nd concentration changed from Weddell Sea to SAMT-2 and SAMT-3 probably due to addition of radiogenic Nd along the transport path of AABW. Thus, the SAMT has higher Nd concentrations and higher εNd-values compared to that in the WMFR for AABW (Fig. S12b).

The WMFR end-member compositions of aAAIW, iAAIW, UCDW, LCDW, and AABW are shown in Fig. S12 and listed in Table 2b. These southern-sourced WMFR end-members were compared with SAMT end-members in diagrams of potential temperature vs. salinity and [Nd] vs. εNd (Fig. S12). The SACW is not included in Fig. S12 because there is no published εNd data in the WMFR. For water masses aAAIW, UCDW and LCDW, εNd and [Nd] end-member values defined from the WMFR are very close to that of the SAMT (Fig. S12b). The AABW values defined from the southernmost stations of SAMT are higher in εNd and [Nd] than that of the WMFR Drake Passage (Fig. S12b). The iAAIW defined from the SAMT has lower εNd and slightly higher [Nd] compared to the WMFR end-member values (Fig. S12b).

*3.2.2. Comparison of εNd and REE data from the SAMT and GEOTRACES GA10*

The GEOTRACES GA10 (REE data available in the GEOTRACES Intermediate Data Product 2017) is a zonal transect in the South Atlantic with most of the stations along ~40°S (Fig. S6-S11), where Station GA10-18 crosses the SAMT at ~40°S (SAMT-6). For SACW, the REE concentrations of SAMT-5 and SAMT-6 are very close to that of

GA10-18, as mentioned in Section 3.2.1. For aAAIW, the REE concentrations of SAMT-1 and SAMT-2 (e.g. [Nd] = 10.40 ± 0.10 pmol/kg) are very close to that of GEOTRACES GA10 in the western basin (e.g. [Nd] = 10.19 ± 0.28 pmol/kg) (Fig. S7; Table S1). The REE concentrations of iAAIW from SAMT-13 (e.g. [Nd] = 12.38 ± 0.35 pmol/kg; ME) are slightly higher than that of GEOTRACES GA10 in the eastern basin (e.g. [Nd] = 11.49 ± 0.74 pmol/kg) (Fig. S8; Table S1). The REE concentrations of UCDW from SAMT-1 (e.g. [Nd] = 13.94 ± 0.39 pmol/kg; ME) are slightly higher than that of GEOTRACES GA10 in the western basin (e.g. [Nd] = 12.97 ± 0.84 pmol/kg) (Fig. S9; Table S1). The REE concentrations of LCDW from SAMT-1 (e.g. [Nd] = 21.45 ± 0.60 pmol/kg; ME) are lower than that of GEOTRACES GA10 in the western basin (e.g. [Nd] = 25.85 ± 2.08 pmol/kg) (Fig. S10; Table S1). For AABW, the REE concentrations of SAMT-2 and SAMT-3 (e.g. [Nd] = 36.99 ± 1.49 pmol/kg) and GEOTRACES GA10 in the western basin (e.g. [Nd] = 34.26 ± 1.64 pmol/kg) have REE concentrations within one standard deviation of each other (Fig. S11; Table S1).

**4. Comparison of εNd with salinity**

Each station shows a maximum salinity at depth, representing strongest influence of northern-sourced NADW at that station (Fig. 2a,2b,S13a,S13c). In order to more easily distinguish data trends, samples shallower and deeper than this maximum were separated into two groups: (1) from the depths of AAIW to depths of maximum salinity for each station (Fig. S13a,b); (2) from depths of maximum salinity for each station to the bottom (Fig. S13c,d). For the shallower samples, the salinity vertical profiles show systematic

changes from northern to southern stations, and indicate mixing of water mass end-members aAAIW, iAAIW, UCDW, UNADW, and MNADW (Fig. S13a). These same mixtures are also observed in the εNd vs. salinity diagram (Fig. S13b). They show iAAIW-UNADW mixing in the northern-most stations, aAAIW-UCDW mixing in the southern-most stations, and intermediate values between the above mixing curves in the mid-latitude stations (Fig. S13a,b). For the deeper samples, systematic changes from northern to southern stations and mixing of water mass end-members UNADW, MNADW, LNADW, LCDW, and AABW are shown in the εNd vs. salinity diagram (Fig. S13d), consistent with observations in the vertical profiles of salinity (Fig. S13c). They show NADW-AABW mixing in the northern-most stations, LCDW-AABW mixing in the southern-most stations, and intermediate values between the above mixing curves in the mid-latitude stations (Fig. S13c,d).

A separation is shown between stations south and north of ~35°S where SAMT-8 is (Fig. S13c). The deep water samples south of SAMT-8 show mixing of AABW and LCDW, whereas the deep water samples north of SAMT-8 show mixing of AABW and NADW. Since NADW moves eastward at ~35°S (Talley, 2011) where SAMT-8 is (Fig. S1a-c,S3-S5), the separation could probably explained by the influence of NADW. Stations north of ~35°S (SAMT-8) show influence of NADW before it turns eastward, whereas stations south of ~35°S (SAMT-8) show very little influence of NADW (Fig. S13c).

**5. Calculations of ΔεNd based on (i) $PO_4^*$, potential temperature and (ii) $PO_4^*$, salinity**

While the main section of this study uses salinity and potential temperature to evaluate ΔεNd and water mass mixing, we also used different combinations of conservative water mass tracers to calculate ΔεNd, in order to investigate whether ΔεNd will be different from results based on salinity and potential temperature. Here we calculated predicted εNd-values for each sample were calculated based on (i) $PO_4^*$ and potential temperature; (ii) $PO_4^*$ and salinity. Then ΔεNd-values were calculated with measured εNd-values subtracting predicted εNd-values. The water mass end-member compositions are based on data from the SAMT (Table 2a).

The fractional contributions of different water masses for each sample were calculated based on $PO_4^*$ and potential temperature using three component mixing equations:

$$f_1 \times PO_{4_1}^* + f_2 \times PO_{4_2}^* + f_3 \times PO_{4_3}^* = PO_4^*$$

$$f_1 \times \theta_1 + f_2 \times \theta_2 + f_3 \times \theta_3 = \theta$$

$$f_1 + f_2 + f_3 = 1$$

$$f_i > 0$$

where $PO_{4_i}^*$, $\theta_i$, and $f_i$ are the phosphate star, potential temperature, and fractional contribution of water mass i, respectively. The fractions of different water masses for each sample were also calculated based on $PO_4^*$ and salinity using three component mixing equations:

$$f_1 \times PO_{4_1}^* + f_2 \times PO_{4_2}^* + f_3 \times PO_{4_3}^* = PO_4^*$$

$$f_1 \times S_1 + f_2 \times S_2 + f_3 \times S_3 = S$$

$$f_1 + f_2 + f_3 = 1$$

$$f_i > 0$$

where $PO_{4_i}^*$, $S_i$ and $f_i$ are the phosphate star, salinity, and fractional contribution of water mass i, respectively. The expected εNd-values were calculated as:

$$\varepsilon Nd_{predicted} = \frac{\varepsilon Nd_1 \times [Nd]_1 \times f_1 + \varepsilon Nd_2 \times [Nd]_2 \times f_2 + \varepsilon Nd_3 \times [Nd]_3 \times f_3}{[Nd]_1 \times f_1 + [Nd]_2 \times f_2 + [Nd]_3 \times f_3}$$

where $\varepsilon Nd_i$, $[Nd]_i$ and $f_i$ are the Nd isotopic composition, Nd concentration, and fractional contribution of water mass i, respectively.

**6. Distributions and deviations of ΔεNd**

The ΔεNd section profiles show very small deviations from predicted εNd-values (Fig. S14a,S15a). The εNd deviation calculated based on $PO_4^*$ and potential temperature, here labeled ΔεNd ($PO_4^*$-θ), ranges from −3.3 to 1.9 with a median of −0.22 and an average ΔεNd = −0.32 ± 0.63 (1σ) εNd units (Fig. S14b). 45% of ΔεNd ($PO_4^*$-θ) are within the range of −0.25 to 0.25 εNd units, that is, within the measurement error of ± 0.3 εNd units, and 83% of ΔεNd ($PO_4^*$-θ) are within the range of −0.75 to 0.75 εNd units (Fig. S14b). The εNd deviation calculated based on $PO_4^*$ and salinity, here labeled ΔεNd ($PO_4^*$-S), ranges from −3.1 to 2.0 with a median of −0.13 and an average ΔεNd = −0.22 ± 0.58 (1σ) εNd units (Fig. S15b). 48% of ΔεNd ($PO_4^*$-S) are within the range of −0.25 to 0.25 εNd units and 86% of ΔεNd ($PO_4^*$-S) are within the range of −0.75 to 0.75 εNd units (Fig. S15b). The very small deviations from predicted εNd-values are reflected in the

section profiles of ΔεNd (Fig. S14c,S15c), and show that the seawater εNd-values in the intermediate and deep Southwest Atlantic Ocean can be effectively predicted by water mass mixing.

A small proportion of ΔεNd-values are outside the range of −0.75 to 0.75 εNd units, which are 17% for ΔεNd ($PO_4^*$-θ) values and 14% for ΔεNd ($PO_4^*$-S) values. ΔεNd-values were further separated into three groups using the neutral densities of the water mass end-members listed in Table 2a: (1) from depths of AAIW to UNADW ($\gamma^n$ = 27.15-27.90 kg/m$^3$); (2) from depths of UNADW to LNADW ($\gamma^n$ = 27.90-28.11 kg/m$^3$); (3) from depths of LNADW to the bottom ($\gamma^n$ > 28.11 kg/m$^3$) (Fig. S14c,S15c). This will allow us to investigate ΔεNd distributions within each depth range.

From depths of AAIW to UNADW, negative ΔεNd ($PO_4^*$-θ) values with an average of −1.40 ± 0.67 (1σ) εNd units and negative ΔεNd ($PO_4^*$-S) with an average of −0.78 ± 0.73 (1σ) εNd units are shown at 750-1000 m from SAMT-15 to SAMT-18 (Fig. S14a,b;S15a,b), similar to that in the section of ΔεNd (θ-S) (−0.75 ± 0.77; 1σ) (Fig. 4a,b). As mentioned in the main text of this study, stations SAMT-15 to SAMT-18 in the trade wind zone could receive eolian dusts from Africa with low εNd (−19 to −18) (Dia et al., 1990; Goldstein et al., 1984). Low εNd-values are observed in SAMT-15 to SAMT-18 at 25-100 m (Fig. 5a,b). Samples at 750-1000 m from SAMT-15 to SAMT-18 are in the oxygen depleted zone (Fig. S2e), where Nd could be released when Fe-Mn oxides dissolve in reducing conditions (e.g. (de Baar et al., 1988; German and Elderfield, 1989; German et al., 1991; Schijf et al., 1995; Sholkovitz et al., 1992)). Therefore, the negative deviation of ΔεNd ($PO_4^*$-θ) values could probably be explained by the release of Nd with

low εNd signal from the dissolution of Fe-Mn oxides in the oxygen depleted zone.

From depths of UNADW to LNADW, the northward UCDW from SAMT-1 to SAMT-5 show very slight positive ΔεNd (θ-S) values (0.44 ± 0.28; 1σ) (Fig. 4a,b). But ΔεNd ($PO_4^*$-θ) with an average of 0.12 ± 0.20 (1σ) εNd units and ΔεNd ($PO_4^*$-S) values with an average of 0.24 ± 0.23 (1σ) εNd units indicate almost no Nd isotopic deviations from conservative behavior (Fig. S14a,b;S15a,b). As mentioned in the main section of this study, these stations in the far south are close to the continental margin, where marginal sediments from Patagonia with high εNd (−4.4 to 4.8) (Basile et al., 1997; de Mahiques et al., 2008; Gaiero et al., 2007; Gili et al., 2017; Goldstein et al., 1984; Henry et al., 1996; McLennan et al., 1990; Rousseau et al., 2015) could release Nd and alter εNd signal of seawater. Therefore, dissolved Nd from marginal sediments probably has very slight or no impact on εNd of the above samples.

From depths of LNADW to the bottom, the ΔεNd ($PO_4^*$-θ) and ΔεNd ($PO_4^*$-S) distributions (Fig. S14c,S15c) are similar to the ΔεNd (θ-S) distribution (Fig. 4c). They are all skewed to more negative values (Fig. 4c,S14c,S15c), most of which correspond to samples below 4000 m at SAMT-11 to SAMT-18 (Fig. 4a,S14a,S15a). These samples show negative deviation of ΔεNd ($PO_4^*$-θ) with an average of −0.71 ± 0.70 (1σ) εNd units and negative deviation of ΔεNd ($PO_4^*$-S) with an average of −0.68 ± 0.65 (1σ) εNd units (Fig. S14a,b;S15a,b), similar to the negative deviation of ΔεNd (θ-S) (−0.67 ± 0.65; 1σ) (Fig. 4a,b). As mentioned in the main section of this study, these stations in the trade wind zone could receive eolian dusts from Africa with low εNd (−24.9 to −11.2) (Bayon et al., 2004; Franzese et al., 2006; Goldstein et al., 1984; McLennan et al., 1990), where

they show low εNd-values at 25-100 m (Fig. 5a,b). Dissolved Nd with low εNd signature could be scavenged in the shallow water and released from sediments at the bottom of the ocean after they sink to the sea floor. Therefore, the negative deviations of the bottom water could probably be due to addition of low εNd signal from dissolved Nd from deep sea sediments.

**References**


Basile, I., Grousset, F.E., Revel, M., Petit, J.R., Biscaye, P.E., Barkov, N.I., 1997. Patagonian origin of glacial dust deposited in East Antarctica (Vostok and Dome C) during glacial stages 2, 4 and 6. Earth and Planetary Science Letters 146, 573-589.

Bayon, G., German, C.R., Burton, K.W., Nesbitt, R.W., Rogers, N., 2004. Sedimentary Fe–Mn oxyhydroxides as paleoceanographic archives and the role of aeolian flux in regulating oceanic dissolved REE. Earth and Planetary Science Letters 224, 477-492.

de Baar, H.J.W., German, C.R., Elderfield, H., Van Gaans, P., 1988. Rare earth element distributions in anoxic waters of the Cariaco Trench. Geochimica et Cosmochimica Acta 52, 1203-1219.

de Mahiques, M.M., Tassinari, C.C.G., Marcolini, S., Violante, R.A., Figueira, R.C.L., da Silveira, I.C.A., Burone, L., e Sousa, S.H.d.M., 2008. Nd and Pb isotope signatures on the Southeastern South American upper margin: Implications for sediment transport and source rocks. Marine Geology 250, 51-63.

Dia, A., Allegre, C.J., Erlank, A.J., 1990. The development of continental crust through geological time: the South African case. Earth and Planetary Science Letters 98, 74-89.

Dickson, R.R., Brown, J., 1994. The production of North Atlantic Deep Water: sources, rates, and pathways. Journal of Geophysical Research: Oceans 99, 12319-12341.

Elderfield, H., Greaves, M.J., 1982. The rare earth elements in seawater. Nature 296, 214-219.

Filippova, A., Frank, M., Kienast, M., Rickli, J., Hathorne, E., Yashayaev, I.M., Pahnke, K., 2017. Water mass circulation and weathering inputs in the Labrador Sea based on coupled Hf–Nd isotope compositions and rare earth element distributions. Geochimica et Cosmochimica Acta 199, 164-184.

Franzese, A.M., Hemming, S.R., Goldstein, S.L., Anderson, R.F., 2006. Reduced Agulhas Leakage during the Last Glacial Maximum inferred from an integrated provenance and flux study. Earth and Planetary Science Letters 250, 72-88.

Gaiero, D.M., Brunet, F., Probst, J.-L., Depetris, P.J., 2007. A uniform isotopic and chemical signature of dust exported from Patagonia: Rock sources and occurrence in southern environments. Chemical Geology 238, 107-120.

Garcia, H.E., Boyer, T.P., Locarnini, R.A., Antonov, J.I., Mishonov, A.V., Baranova, O.K., Zweng, M.M., Reagan, J.R., Johnson, D.R., 2013a. World Ocean Atlas 2013, Volume 3: Dissolved Oxygen, Apparent Oxygen Utilization, and Oxygen Saturation. NOAA Atlas NESDIS 75, 27.

Garcia, H.E., Locarnini, R.A., Boyer, T.P., Antonov, J.I., Baranova, O.K., Zweng, M.M., Reagan, J.R., Johnson, D.R., 2013b. World Ocean Atlas 2013, Volume 4: Dissolved Inorganic Nutrients (phosphate, nitrate, silicate). NOAA Atlas NESDIS 76, 25.

Garcia-Solsona, E., Jeandel, C., Labatut, M., Lacan, F., Vance, D., Chavagnac, V., Pradoux, C., 2014. Rare earth elements and Nd isotopes tracing water mass mixing and particle-seawater interactions in the SE Atlantic. Geochimica et Cosmochimica Acta 125, 351-372.

German, C.R., Elderfield, H., 1989. Rare earth elements in Saanich Inlet, British Columbia, a seasonally anoxic basin. Geochimica et Cosmochimica Acta 53, 2561-2571.

German, C.R., Holliday, B.P., Elderfield, H., 1991. Redox cycling of rare earth elements in the suboxic zone of the Black Sea. Geochimica et Cosmochimica Acta 55, 3553-3558.

Gili, S., Gaiero, D.M., Goldstein, S.L., Chemale Jr, F., Jweda, J., Kaplan, M.R., Becchio, R.A., Koester, E., 2017. Glacial/interglacial changes of Southern Hemisphere wind circulation from the geochemistry of South American dust. Earth and Planetary Science Letters 469, 98-109.

Goldstein, S.L., O'Nions, R.K., Hamilton, P.J., 1984. A Sm-Nd isotopic study of atmospheric dusts and particulates from major river systems. Earth and planetary Science letters 70, 221-236.

Gordon, A.L., Weiss, R.F., Smethie, W.M., Warner, M.J., 1992. Thermocline and intermediate water communication between the South Atlantic and Indian Oceans. Journal of Geophysical Research: Oceans 97, 7223-7240.

Hathorne, E.C., Stichel, T., Brück, B., Frank, M., 2015. Rare earth element distribution in the Atlantic sector of the Southern Ocean: the balance between particle scavenging and vertical supply. Marine Chemistry 177, 157-171.

Henry, F., Probst, J.-L., Thouron, D., Depetris, P.J., Garçon, V., 1996. Nd-Sr isotopic compositions of dissolved and particulate material transported by the Parana and Uruguay rivers during high (december 1993) and low (september 1994) water periods. Sciences Géologiques, Bulletin 49, 89-100.

Heywood, K.J., King, B.A., 2002. Water masses and baroclinic transports in the South Atlantic and Southern oceans. Journal of Marine Research 60, 639-676.

Klatt, O., Fahrbach, E., Hoppema, M., Rohardt, G., 2005. The transport of the Weddell Gyre across the Prime Meridian. Deep Sea Research Part II: Topical Studies in Oceanography 52, 513-528.

Lacan, F., Jeandel, C., 2004. Subpolar Mode Water formation traced by neodymium isotopic composition. Geophysical Research Letters 31.

Lacan, F., Jeandel, C., 2005. Neodymium isotopes as a new tool for quantifying exchange fluxes at the continent–ocean interface. Earth and Planetary Science Letters 232, 245-257.

Lambelet, M., van de Flierdt, T., Crocket, K., Rehkämper, M., Kreissig, K., Coles, B., Rijkenberg, M.J., Gerringa, L.J., de Baar, H.J., Steinfeldt, R., 2016. Neodymium isotopic composition and concentration in the western North Atlantic Ocean: Results from the GEOTRACES GA02 section. Geochimica et Cosmochimica Acta 177, 1-29.

Larqué, L., Maamaatuaiahutapu, K., Garçon, V., 1997. On the intermediate and deep water flows in the South Atlantic Ocean. Journal of Geophysical Research: Oceans 102, 12425-12440.

Locarnini, R.A., Mishonov, A.V., Antonov, J.I., Boyer, T.P., Garcia, H.E., Baranova, O.K., Zweng, M.M., Paver, C.R., Reagan, J.R., Johnson, D.R., Hamilton, M., Seidov, D., 2013. World Ocean Atlas 2013, Volume 1: Temperature. NOAA Atlas NESDIS 73, 40.

McCartney, M.S., 1977. Subantarctic Mode Water, A Voyage of Discovery, George Deacon 70th Anniversary Volume M. Angel, 103–119. Pergamon, New York.

McLennan, S.M., Taylor, S.R., McCulloch, M.T., Maynard, J.B., 1990. Geochemical and Nd-Sr isotopic composition of deep-sea turbidites: Crustal evolution and plate tectonic associations. Geochimica et Cosmochimica Acta 54, 2015-2050.

Orsi, A.H., Johnson, G.C., Bullister, J.L., 1999. Circulation, mixing, and production of Antarctic Bottom Water. Progress in Oceanography 43, 55-109.

Orsi, A.H., Smethie, W.M., Bullister, J.L., 2002. On the total input of Antarctic waters to the deep ocean: A preliminary estimate from chlorofluorocarbon measurements. Journal of Geophysical Research: Oceans 107.

Pahnke, K., Van de Flierdt, T., Jones, K.M., Lambelet, M., Hemming, S.R., Goldstein, S.L., 2012. GEOTRACES intercalibration of neodymium isotopes and rare earth element concentrations in seawater and suspended particles. Part 2: Systematic tests and baseline profiles. Limnology and Oceanography: Methods 10, 252-269.

Piola, A.R., Gordon, A.L., 1989. Intermediate waters in the southwest South Atlantic. Deep Sea Research Part A. Oceanographic Research Papers 36, 1-16.

Reid, J.L., 1994. On the total geostrophic circulation of the North Atlantic Ocean: Flow patterns, tracers, and transports. Progress in Oceanography 33, 1-92.

Reid, J.L., Lynn, R.J., 1971. On the influence of the Norwegian-Greenland and Weddell seas upon the bottom waters of the Indian and Pacific oceans, Deep Sea Research and Oceanographic Abstracts. Elsevier, pp. 1063IN31067IN51077-10661076IN10681088.

Rhein, M., Stramma, L., Send, U., 1995. The Atlantic deep western boundary current: water masses and transports near the equator. Journal of Geophysical Research: Oceans 100, 2441-2457.

Rickli, J., Frank, M., Halliday, A.N., 2009. The hafnium–neodymium isotopic composition of Atlantic seawater. Earth and Planetary Science Letters 280, 118-127.

Rintoul, S., Hughes, C., Olbers, D., 2001. The Antarctic circumpolar current system, In: Ocean Circulation and Climate/G. Siedler, J. Church and J. Gould, eds. New York: Academic Press. p., pp. 271-302.

Rousseau, T.C.C., Sonke, J.E., Chmeleff, J., Van Beek, P., Souhaut, M., Boaventura, G., Seyler, P., Jeandel, C., 2015. Rapid neodymium release to marine waters from lithogenic sediments in the Amazon estuary. Nature communications 6, 7592.

Schijf, J., De Baar, H.J.W., Millero, F.J., 1995. Vertical distributions and speciation of dissolved rare earth elements in the anoxic brines of Bannock Basin, eastern Mediterranean Sea. Geochimica et Cosmochimica Acta 59, 3285-3299.

Schlitzer, R., 2012. Ocean data view.

Schmitz Jr, W.J., 1996. On the World Ocean Circulation. Volume 1. Some Global Features/North Atlantic Circulation. Woods Hole Oceanographic Institution, MA.

Schott, F.A., Brandt, P., 2007. Circulation and deep water export of the subpolar North Atlantic during the 1990's. Ocean Circulation: Mechanisms and Impacts-Past and Future Changes of Meridional Overturning, 91-118.

Sholkovitz, E., Schneider, D., 1991. Cerium redox cycles and rare earth elements in the Sargasso Sea. Geochimica et Cosmochimica Acta 55, 2737-2743.

Sholkovitz, E.R., Landing, W.M., Lewis, B.L., 1994. Ocean particle chemistry: the fractionation of rare earth elements between suspended particles and seawater. Geochimica et Cosmochimica Acta 58, 1567-1579.

Sholkovitz, E.R., Shaw, T.J., Schneider, D.L., 1992. The geochemistry of rare earth elements in the seasonally anoxic water column and porewaters of Chesapeake Bay. Geochimica et Cosmochimica Acta 56, 3389-3402.

Smethie, W.M., Fine, R.A., Putzka, A., Jones, E.P., 2000. Tracing the flow of North Atlantic Deep Water using chlorofluorocarbons. Journal of Geophysical Research: Oceans 105, 14297-14323.

Stichel, T., Frank, M., Rickli, J., Haley, B.A., 2012. The hafnium and neodymium isotope composition of seawater in the Atlantic sector of the Southern Ocean. Earth and Planetary Science Letters 317, 282-294.

Stichel, T., Hartman, A.E., Duggan, B., Goldstein, S.L., Scher, H., Pahnke, K., 2015. Separating biogeochemical cycling of neodymium from water mass mixing in the Eastern North Atlantic. Earth and Planetary Science Letters 412, 245-260.

Stramma, L., England, M., 1999. On the water masses and mean circulation of the South Atlantic Ocean. Journal of Geophysical Research-Oceans 104, 20863-20833.

Sy, A., Rhein, M., Lazier, J.R., Koltermann, K.P., Meincke, J., Putzka, A., Bersch, M., 1997. Surprisingly rapid spreading of newly formed intermediate waters across the North Atlantic Ocean. Nature 386, 675.

Talley, L., McCartney, M., 1982. Distribution and circulation of Labrador Sea water. Journal of Physical Oceanography 12, 1189-1205.

Talley, L.D., 2011. Descriptive physical oceanography: an introduction. Academic press.

van de Flierdt, T., Pahnke, K., Amakawa, H., Andersson, P., Basak, C., Coles, B., Colin, C., Crocket, K., Frank, M., Frank, N., Goldstein, S.L., Goswami, V., Haley, B.A., Hathorne, E.C., Hemming, S.R., Henderson, G.M., Jeandel, C., Jones, K., Kreissig, K., Lacan, F., Lambelet, M., Martin, E.E., Newkirk, D.R., Obata, H., Pena, L., Piotrowski, A.M., Pradoux, C., Scher, H.D., Schöberg, H., Singh, S.K., Stichel, T., Tazoe, H., Vance, D., Yang, J., 2012. GEOTRACES intercalibration of neodymium isotopes and rare earth element concentrations in seawater and suspended particles. Part 1: reproducibility of results for the international intercomparison. Limnology and Oceanography: Methods 10, 234-251.

Vanicek, M., Siedler, G., 2002. Zonal fluxes in the deep water layers of the western South Atlantic Ocean. Journal of Physical Oceanography 32, 2205-2235.

Whitworth III, T., Orsi, A.H., Kim, S.J., Nowlin, W.D., Locarnini, R.A., 1998. Water masses and mixing near the Antarctic Slope Front. Ocean, ice, and atmosphere: interactions at the Antarctic continental margin, 1-27.

Whitworth, T., Nowlin, W.D., 1987. Water masses and currents of the Southern Ocean at the Greenwich Meridian. Journal of Geophysical Research: Oceans 92, 6462-6476.

Zweng, M.M., Reagan, J.R., Antonov, J.I., Locarnini, R.A., Mishonov, A.V., Boyer, T.P., Garcia, H.E., Baranova, O.K., Johnson, D.R., Seidov, D., Biddle, M.M., 2013. World Ocean Atlas 2013, Volume 2: Salinity. NOAA Atlas NESDIS 74, 39.

Figure S1. Maps showing sampling locations of the Southwest Atlantic Meridional Transect (SAMT), stations with published εNd and REE data in the Atlantic Ocean to define the end-member compositions, and water mass pathways (white). Sampling locations in red (filled and empty squares) are stations from the SAMT. The red filled squares are stations chosen to define the end-member compositions within the SAMT. Sampling location in black is station BATS. Sampling locations in other colors are stations with εNd and REE data of filtered seawater samples from previous studies. (a) Upper North Atlantic Deep Water (UNADW) pathway (after (Larqué et al., 1997; Reid, 1994; Schott and Brandt, 2007; Talley, 2011)). The station numbers are shown in Figure S3. (b) Middle North Atlantic Deep Water (MNADW) pathway (after (Larqué et al., 1997; Reid, 1994; Schott and Brandt, 2007; Talley, 2011)). The station numbers are shown in Figure S4. (c) Lower North Atlantic Deep Water (LNADW) pathway (after (Larqué et al., 1997; Reid, 1994; Schott and Brandt, 2007; Talley, 2011)). The station numbers are shown in Figure S5. (d) South Atlantic Central Water (SACW) pathway (after (Stramma and England, 1999)). The station numbers are shown in Figure S6. (e) Antarctic Intermediate Water (AAIW) pathway (after (Gordon et al., 1992; Piola and Gordon, 1989; Reid, 1994; Stramma and England, 1999)). The station numbers are shown in Figures S7 and S8. (f) Upper Circumpolar Deep Water (UCDW) pathway (after (Larqué et al., 1997; Reid, 1994)). The station numbers are shown in Figure S9. (g) Lower Circumpolar Deep Water (LCDW) pathway (after (Larqué et al., 1997; Reid, 1994; Talley, 2011)). The station numbers are shown in Figure S10. (h) Antarctic Bottom Water (AABW) pathway (after (Orsi et al., 1999; Reid, 1994; Stramma and England, 1999)). The station numbers are shown in Figure S11. The maps were made using ODV software (Schlitzer, 2012).

Figure S2. Hydrographic diagrams of samples from the SAMT. (a) Salinity (S) vs. neutral density ($\gamma^n$). (b) Potential temperature (θ) vs. neutral density. (c) $PO_4^*$ vs. neutral density. (d) Silicate vs. neutral density. (e) Oxygen vs. neutral density. (f) Nd concentration vs. neutral density. The black crosses are water mass end-members defined from the SAMT and listed in Table 2a. The legend numbers are station numbers from Station 1 (SAMT-1) in the south to Station 18 (SAMT-18) at the equator.

Figure S3. Comparison of REE end-members of the SAMT with published REE data of filtered seawater samples between 17°N and 65°N for UNADW. (a) Map of stations with UNADW REE data. SAMT-17 and SAMT-18 in red are stations from the SAMT. The other stations are from (Elderfield and Greaves, 1982) (dark green), (Lacan and Jeandel, 2004; Lacan and Jeandel, 2005) (violet), (Rickli et al., 2009) (light blue), (van de Flierdt et al., 2012) (grey), (Pahnke et al., 2012) (black), (Lambelet et al., 2016) (yellow), (Filippova et al., 2017) (light green), GEOTRACES GA03 2010 (orange), and GEOTRACES GA03 2011 (brown). The UNADW pathways are shown in white. The map was made using ODV software (Schlitzer, 2012). (b) UNADW REE patterns for stations shown in (a). (c) UNADW REE patterns for stations in the western basin. (d) UNADW REE patterns for stations in the eastern basin. (e) UNADW REE patterns for

station BATS and stations in the same location. UNADW REE patterns of SAMT-17 and SAMT-18 are plotted in (b) to (e) for comparison.

Figure S4. Comparison of REE end-members of the SAMT with published REE data of filtered seawater samples between 17°N and 65°N for MNADW. (a) Map of stations with MNADW REE data. SAMT-17 and SAMT-18 in red are stations from the SAMT. The other stations are from (Lacan and Jeandel, 2004; Lacan and Jeandel, 2005) (violet), (Rickli et al., 2009) (light blue), (Pahnke et al., 2012) (black), (Lambelet et al., 2016) (yellow), (Filippova et al., 2017) (light green), GEOTRACES GA03 2010 (orange), and GEOTRACES GA03 2011 (brown). The MNADW pathways are shown in white. The map was made using ODV software (Schlitzer, 2012). (b) MNADW REE patterns for stations shown in (a). (c) MNADW REE patterns for stations in the western basin. (d) MNADW REE patterns for stations in the eastern basin. (e) MNADW REE patterns for station BATS and stations in the same location. MNADW REE patterns of SAMT-17 and SAMT-18 are plotted in (b) to (e) for comparison.

Figure S5. Comparison of REE end-members of the SAMT with published REE data of filtered seawater samples between 17°N and 65°N for LNADW. (a) Map of stations with LNADW REE data. SAMT-17 and SAMT-18 in red are stations from the SAMT. The other stations are from (Elderfield and Greaves, 1982) (dark green), (Lacan and Jeandel, 2004; Lacan and Jeandel, 2005) (violet), (Rickli et al., 2009) (light blue), (Pahnke et al., 2012) (black), (Lambelet et al., 2016) (yellow), (Filippova et al., 2017) (light green), GEOTRACES GA03 2010 (orange), and GEOTRACES GA03 2011 (brown). The LNADW pathways are shown in white. The map was made using ODV software (Schlitzer, 2012). (b) LNADW REE patterns for stations shown in (a). (c) LNADW REE patterns for stations in the western basin. (d) LNADW REE patterns for stations in the eastern basin. (e) LNADW REE patterns for station BATS and stations in the same location. LNADW REE patterns of SAMT-17 and SAMT-18 are plotted in (b) to (e) for comparison.

Figure S6. Comparison of REE end-members of the SAMT with published REE data of filtered seawater samples along ~40°S for SACW. (a) Map of stations with SACW REE data. SAMT-5 and SAMT-6 in red are stations from the SAMT. The other stations are from (Garcia-Solsona et al., 2014) (dark blue) and GEOTRACES GA10 (light blue). The SACW pathways are shown in white. The map was made using ODV software (Schlitzer, 2012). (b) Potential temperature vs. salinity of samples from the SAMT. SACW is characterized by a linear line between points ($\theta$ = 5°C, S = 34.3) and ($\theta$ = 20°C, S = 36.0). (c) SACW REE patterns for stations shown in (a). (d) SACW REE patterns for stations in the western basin. (e) SACW REE patterns for stations in the eastern basin. SACW REE patterns of SAMT-5 and SAMT-6 are plotted in (c) to (e) for comparison.

Figure S7. Comparison of REE end-members of the SAMT with published REE data of filtered seawater samples between 37°S and 67°S for aAAIW. (a) Map of stations with aAAIW REE data. SAMT-1 and SAMT-2 in red are stations from the SAMT. The other

stations are from (Stichel et al., 2012) (dark green), (Garcia-Solsona et al., 2014) (dark blue), (Hathorne et al., 2015) (violet), and GEOTRACES GA10 (light blue). The aAAIW pathways are shown in white. The map was made using ODV software (Schlitzer, 2012). (b) aAAIW REE patterns for stations shown in (a). (c) aAAIW REE patterns for stations in the western basin. (d) aAAIW REE patterns for stations in the eastern basin. aAAIW REE patterns of SAMT-1 and SAMT-2 are plotted in (b) to (d) for comparison.

Figure S8. Comparison of REE end-members of the SAMT with published REE data of filtered seawater samples between 37°S and 67°S for iAAIW. (a) Map of stations with iAAIW REE data. SAMT-13 and SAMT-14 in red are from the SAMT. The other stations are from (Stichel et al., 2012) (dark green), (Garcia-Solsona et al., 2014) (dark blue), (Hathorne et al., 2015) (violet), and GEOTRACES GA10 (light blue). The iAAIW pathways are shown in white. The map was made using ODV software (Schlitzer, 2012). (b) iAAIW REE patterns for stations shown in (a). iAAIW REE patterns of SAMT-13 and SAMT-14 are plotted in (b) for comparison.

Figure S9. Comparison of REE end-members of the SAMT with published REE data of filtered seawater samples between 37°S and 67°S for UCDW. (a) Map of stations with UCDW REE data. SAMT-1 and SAMT-2 in red are stations from the SAMT. The other stations are from (Stichel et al., 2012) (dark green), (Garcia-Solsona et al., 2014) (dark blue), (Hathorne et al., 2015) (violet), and GEOTRACES GA10 (light blue). The UCDW pathways are shown in white. The map was made using ODV software (Schlitzer, 2012). (b) UCDW REE patterns for stations shown in (a). (c) UCDW REE patterns for stations in the western basin. (d) UCDW REE patterns for stations in the eastern basin. UCDW REE patterns of SAMT-1 and SAMT-2 are plotted in (b) to (d) for comparison.

Figure S10. Comparison of REE end-members of the SAMT with published REE data of filtered seawater samples between 37°S and 67°S for LCDW. (a) Map of stations with LCDW REE data. SAMT-1 and SAMT-2 in red are stations from the SAMT. The other stations are from (Stichel et al., 2012) (dark green), (Garcia-Solsona et al., 2014) (dark blue), (Hathorne et al., 2015) (violet), and GEOTRACES GA10 (light blue). The LCDW pathways are shown in white. The map was made using ODV software (Schlitzer, 2012). (b) LCDW REE patterns for stations shown in (a). (c) LCDW REE patterns for stations in the western basin. (d) LCDW REE patterns for stations in the eastern basin. LCDW REE patterns of SAMT-1 and SAMT-2 are plotted in (b) to (d) for comparison.

Figure S11. Comparison of REE end-members of the SAMT with published REE data of filtered seawater samples between 37°S and 67°S for AABW. (a) Map of stations with AABW REE data. SAMT-2 and SAMT-3 in red are stations from the SAMT. The other stations are from (Stichel et al., 2012) (dark green), (Garcia-Solsona et al., 2014) (dark blue), (Hathorne et al., 2015) (violet), and GEOTRACES GA10 (light blue). The AABW pathways are shown in white. The map was made using ODV software (Schlitzer, 2012). (b) AABW REE patterns for stations shown in (a). (c) AABW REE patterns excluding

the bottommost samples. AABW REE patterns of SAMT-2 and SAMT-3 are plotted in (b) and (c) for comparison.

Figure S12. Comparison of water mass end-member compositions defined from the SAMT (circles) and in the water mass formation regions (WMFR; triangles). (a) Potential temperature vs. salinity. Potential temperature and salinity end-members in the WMFR (triangles) are defined using the World Ocean Atlas (WOA) 2013. (b) Nd concentration vs. εNd. The WMFR for the northern-sourced water masses UNADW (red), MNADW (orange) and LNADW (yellow) is near station BATS.

Figure S13. Intermediate and deep water SAMT samples from depths of AAIW to depths maximum salinity of each station (a and b) and from depths of maximum salinity to the bottom (c and d). (a) and (c) are diagrams of neutral density vs. salinity. (b) and (d) are diagrams of εNd vs. salinity. The legend numbers are station numbers from SAMT-1 in the south to SAMT-18 at the equator. Black crosses are water mass end-members defined from the SAMT and listed in Table 2a.

Figure S14. εNd deviations (ΔεNd = measured εNd – predicted εNd) calculated based on water mass mixing using $PO_4^*$ and potential temperature. (a) ΔεNd section profile. The legend numbers are station numbers from SAMT-1 in the south to SAMT-18 at the equator. The section diagram was made using ODV software (Schlitzer, 2012). (b) ΔεNd vs. neutral density. The average ΔεNd = −0.29 ± 0.61 (1σ) εNd units. (c) Histogram of ΔεNd. The y-axis on the left is the count number of calculated samples. The y-axis on the right is the percentage of calculated samples. The y-axis on the right is the percentage of calculated samples. ΔεNd-values were separated into three groups using the neutral densities of the water mass end-members defined from the SAMT (Table 2a). Green columns include samples from the depths of AAIW to UNADW ($\gamma^n$ = 27.28-27.90 kg/m$^3$). Red columns include samples from the depths of UNADW to LNADW ($\gamma^n$ = 27.90-28.11 kg/m$^3$). Blue columns include samples from the depths of LNADW to AABW ($\gamma^n$ =28.11-28.30 kg/m$^3$). The numbers above the columns are percentage values within each interval from depths of AAIW to the bottom.

Figure S15. εNd deviations (ΔεNd = measured εNd – predicted εNd) calculated based on water mass mixing using $PO_4^*$ and salinity. (a) ΔεNd section profile. The legend numbers are station numbers from SAMT-1 in the south to SAMT-18 at the equator. The section diagram was made using ODV software (Schlitzer, 2012). (b) ΔεNd vs. neutral density. The average ΔεNd = −0.26 ± 0.62 (1σ) εNd units. (c) Histogram of ΔεNd. The y-axis on the left is the count number of calculated samples. The y-axis on the right is the percentage of calculated samples. The y-axis on the right is the percentage of calculated samples. ΔεNd-values were separated into three groups using the neutral densities of the water mass end-members defined from the SAMT (Table 2a). Green columns include samples from the depths of AAIW to UNADW ($\gamma^n$ = 27.28-27.90 kg/m$^3$). Red columns include samples from the depths of UNADW to LNADW ($\gamma^n$ = 27.90-28.11 kg/m$^3$). Blue columns include samples from the depths of LNADW to AABW ($\gamma^n$ =28.11-28.30

kg/$m^3$). The numbers above the columns are percentage values within each interval from depths of AAIW to the bottom.

Figure S1. Maps showing sampling locations of the SAMT, stations with published εNd and REE data in the Atlantic Ocean to define the end-member compositions, and water mass pathways

a

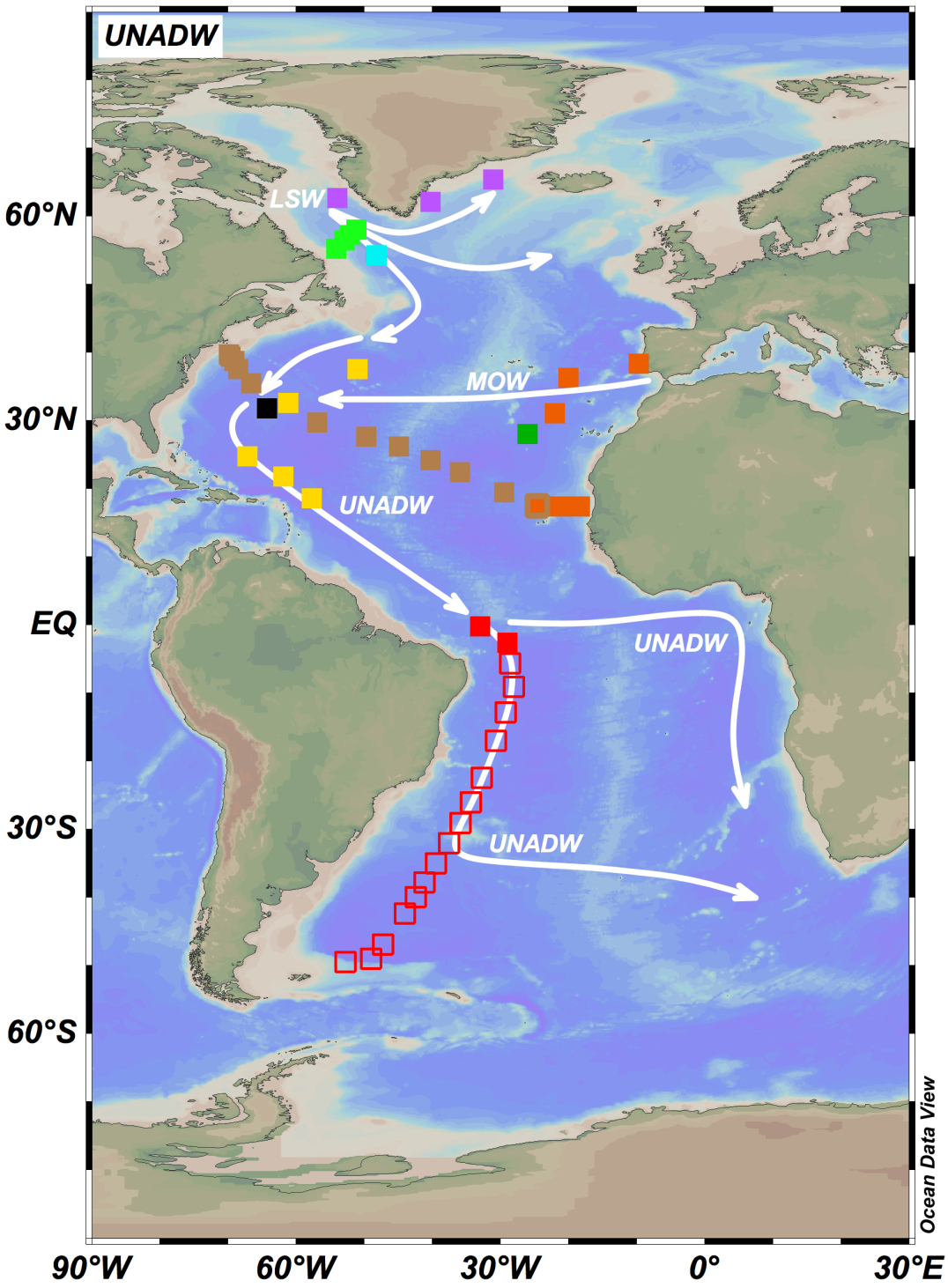

Figure S1. continued

b

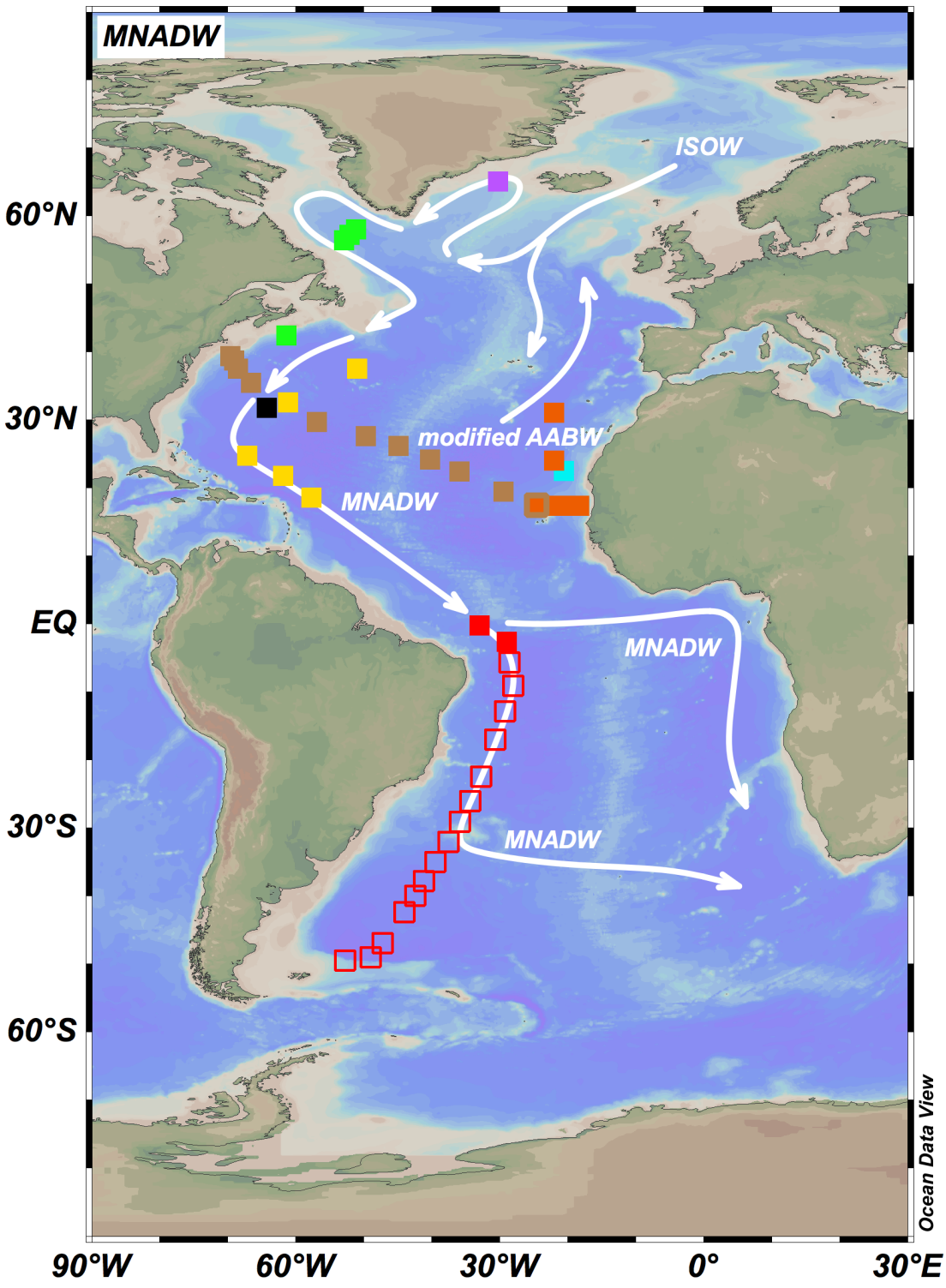

Figure S1. continued

c

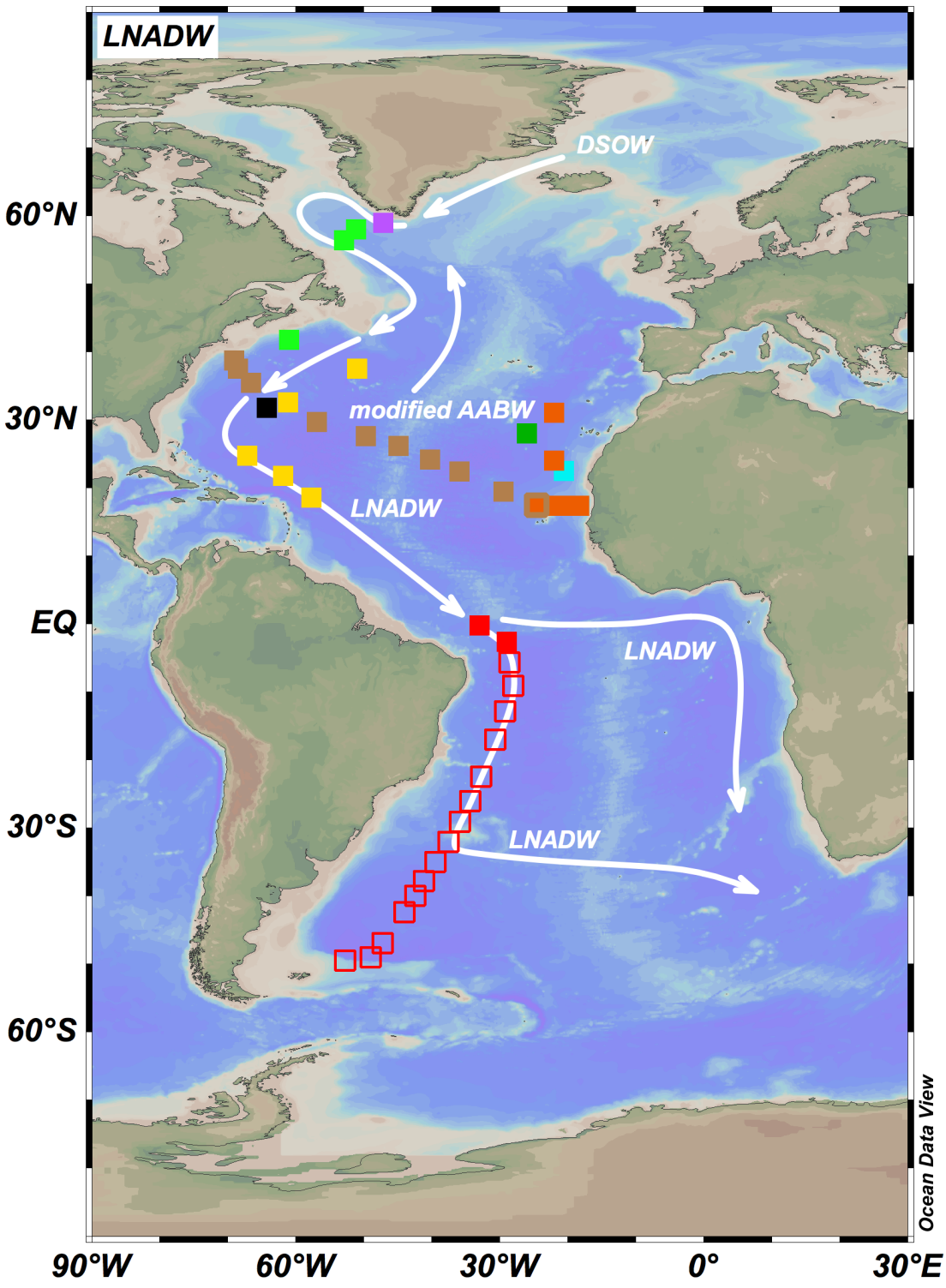

Figure S1. continued

d

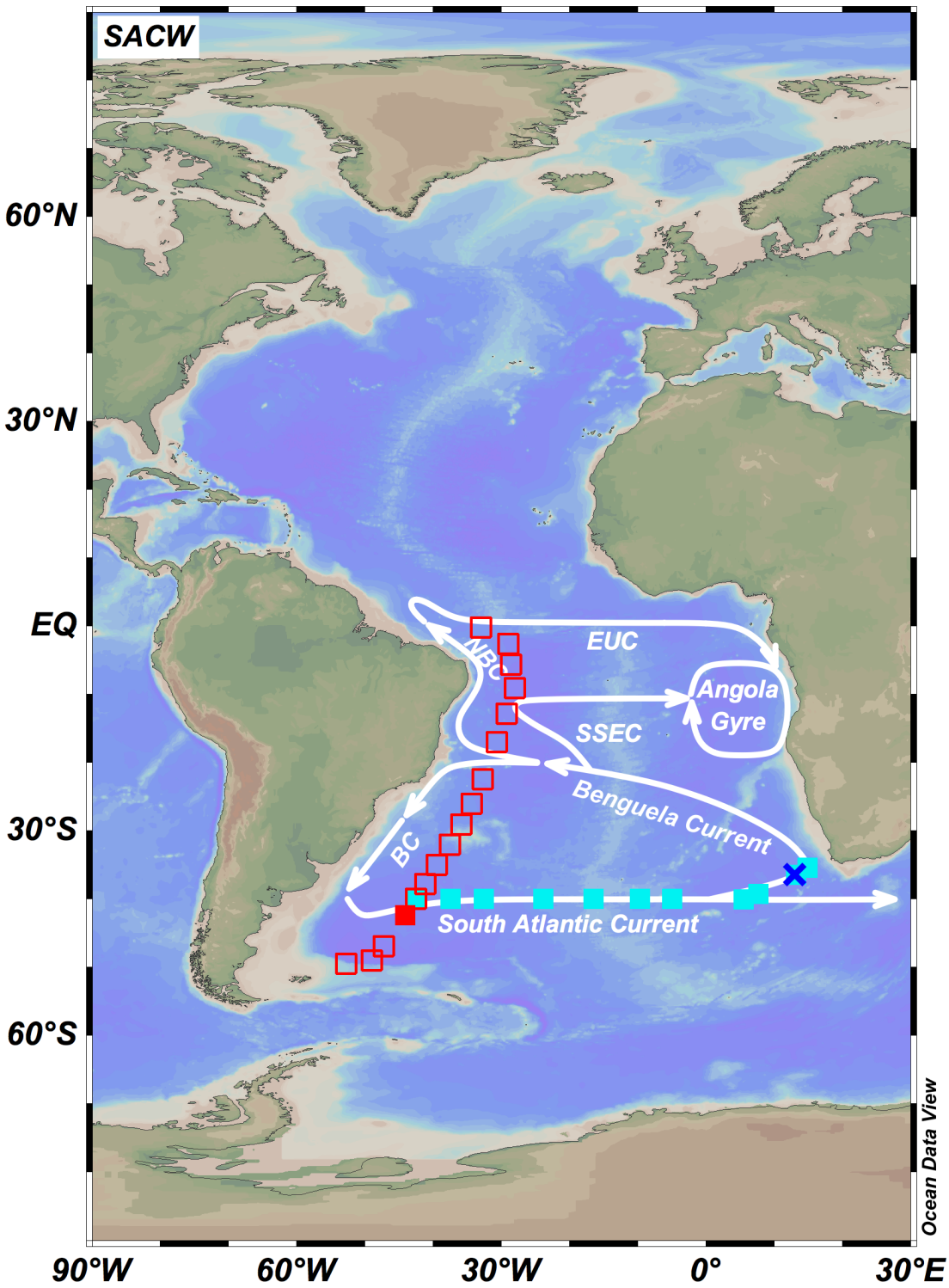

Figure S1. continued

e

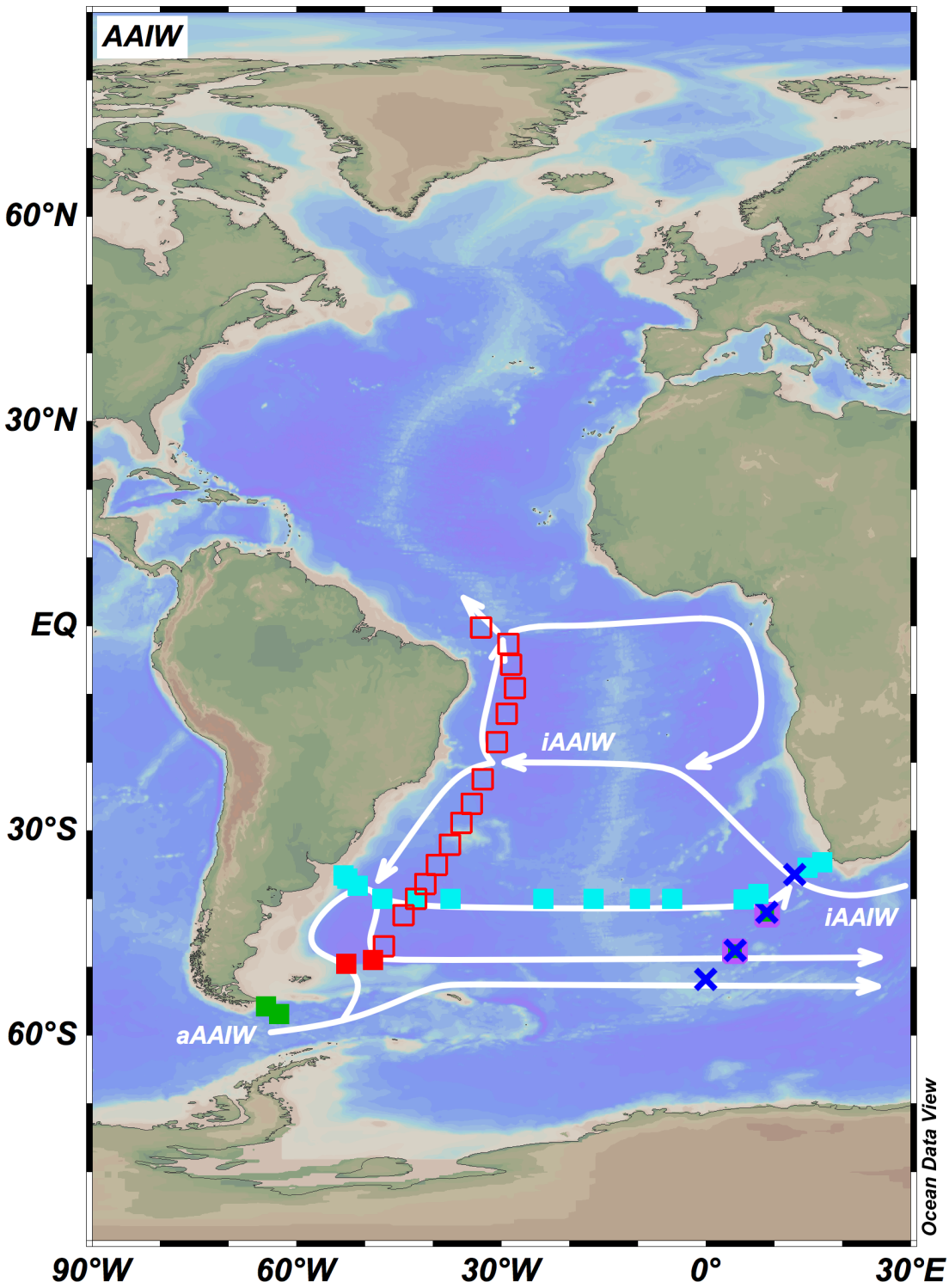

Figure S1. continued

f

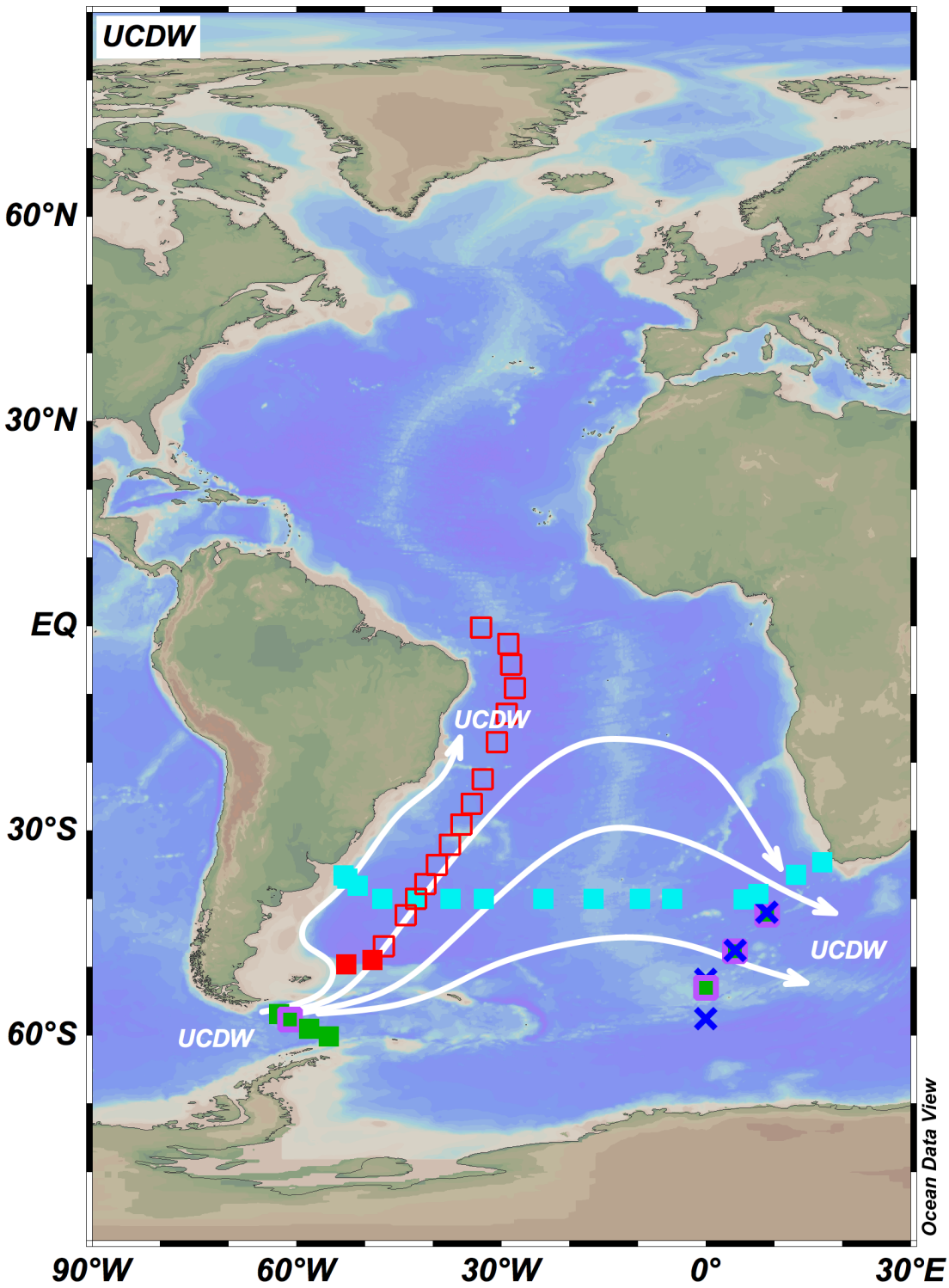

Figure S1. continued

g

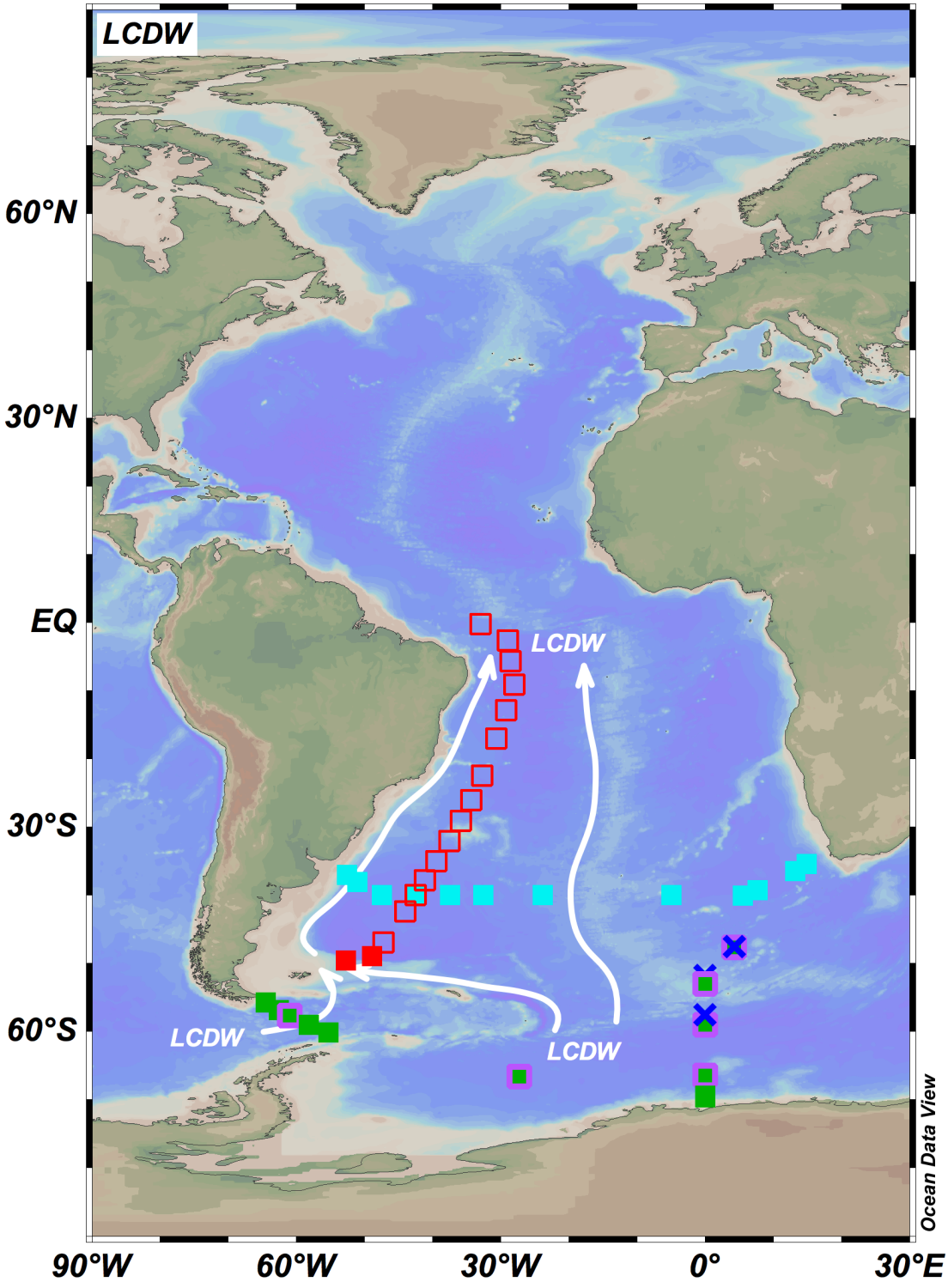

Figure S1. continued

h

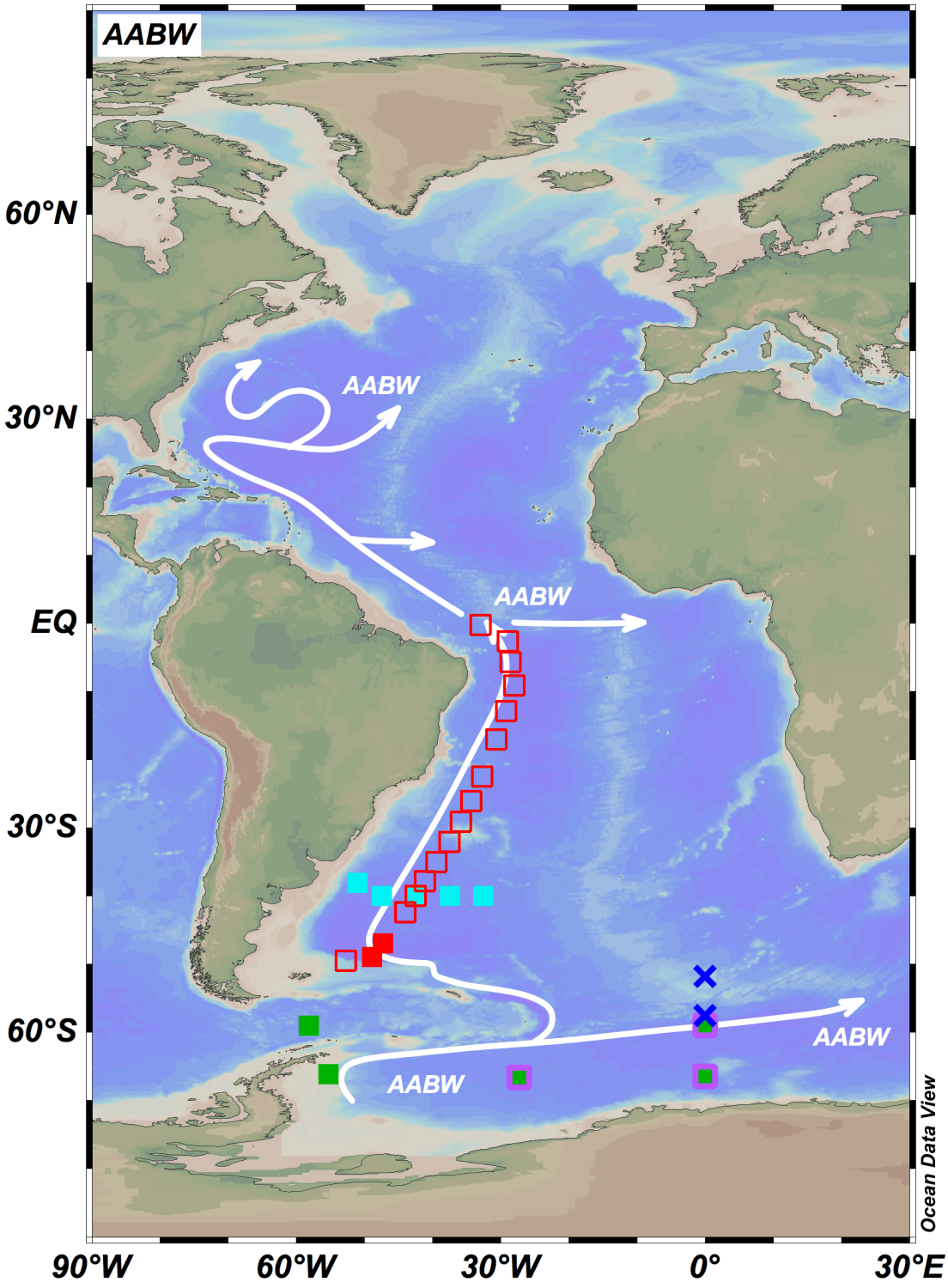

Figure S2. Hydrographic diagrams of samples from the SAMT

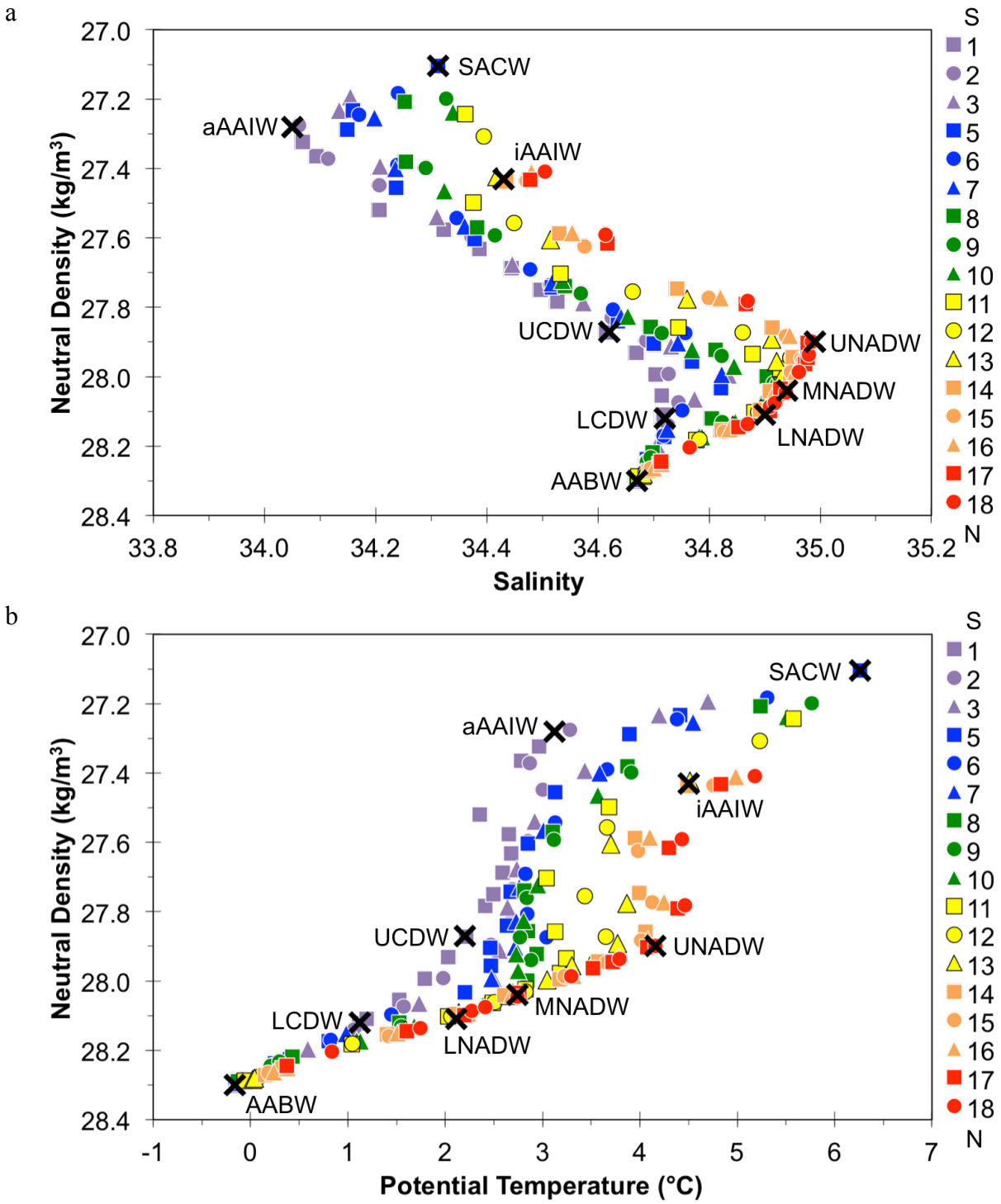

Figure S2. continued

c

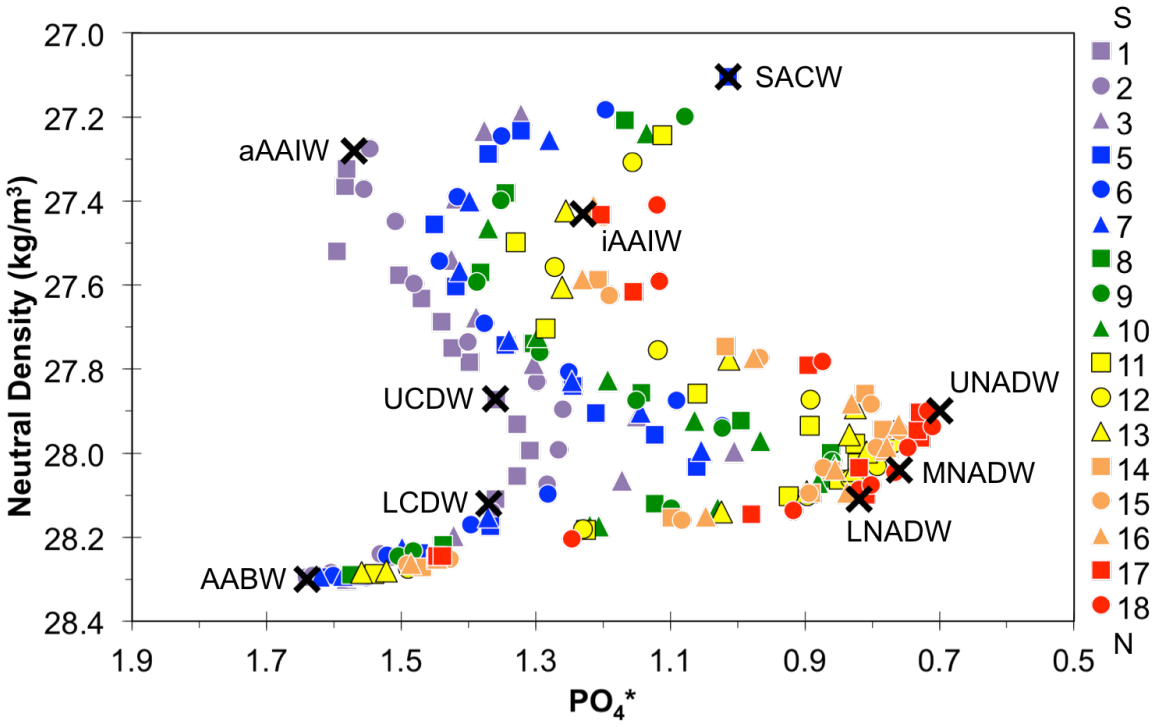


d

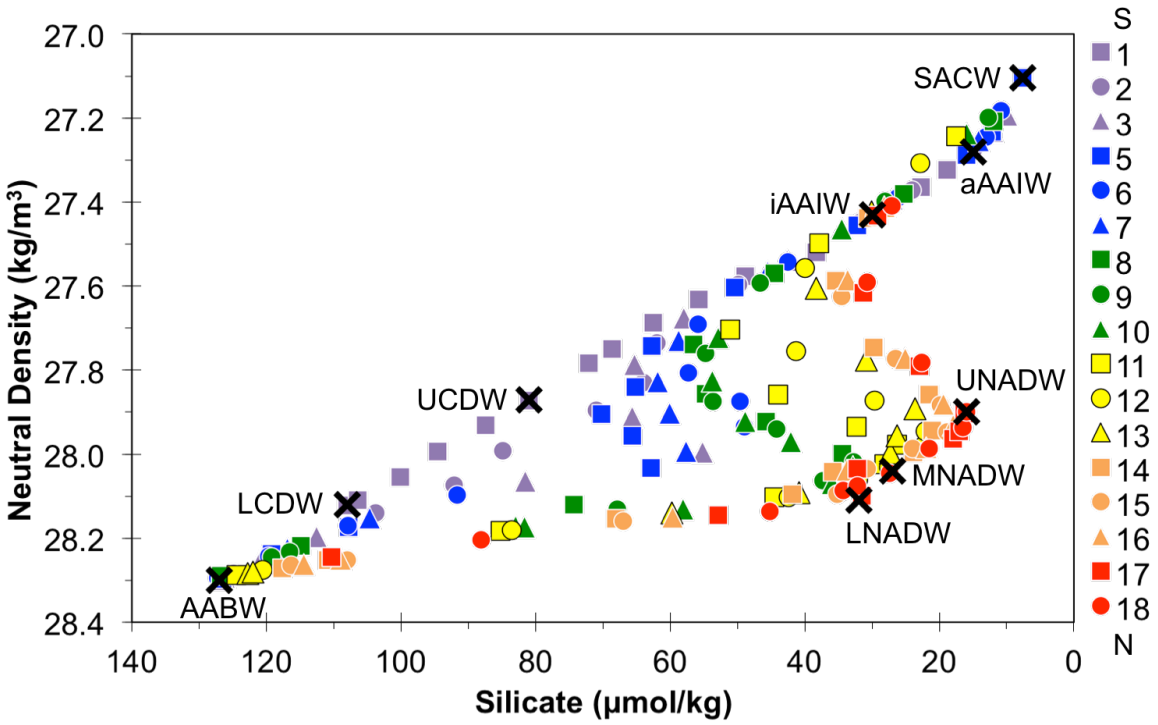

Figure S2. continued

e

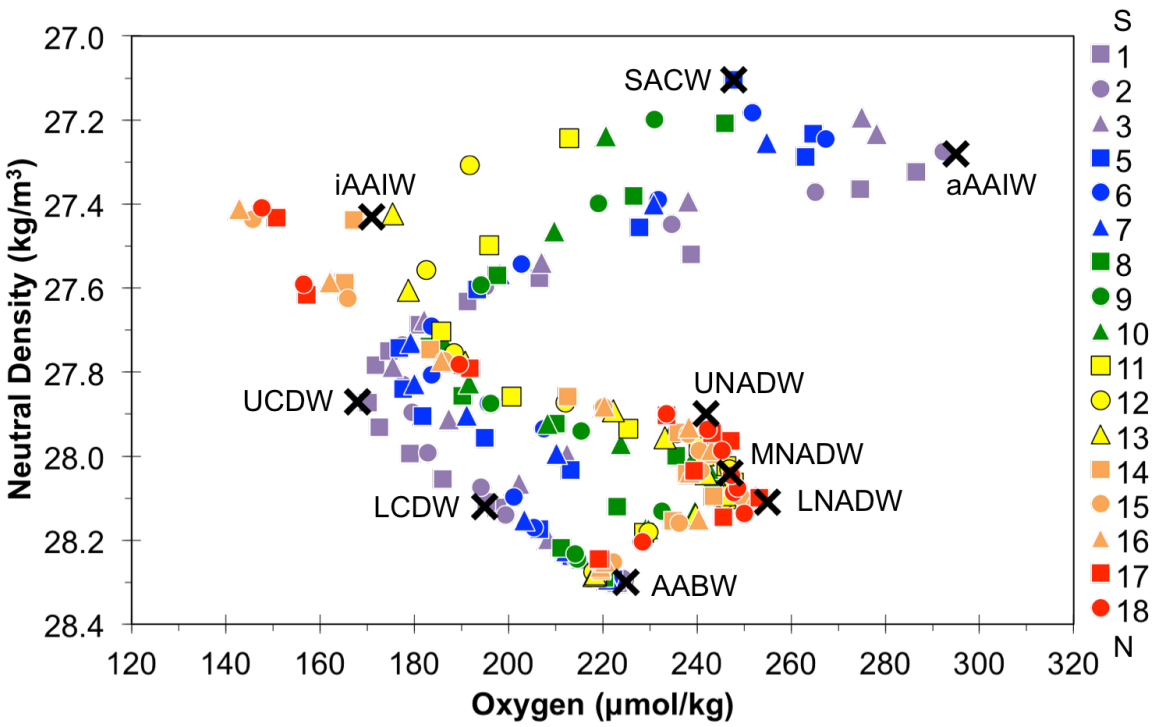


f

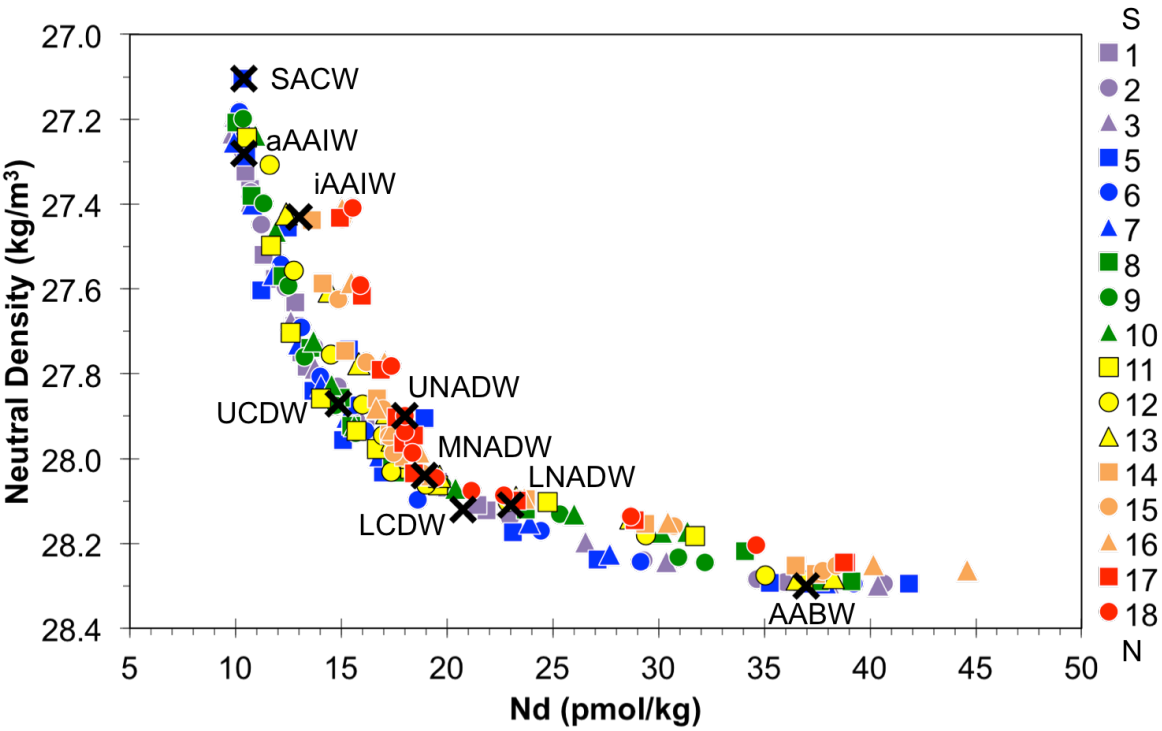

Figure S3. Comparison of REE end-members of the SAMT with published REE data for UNADW

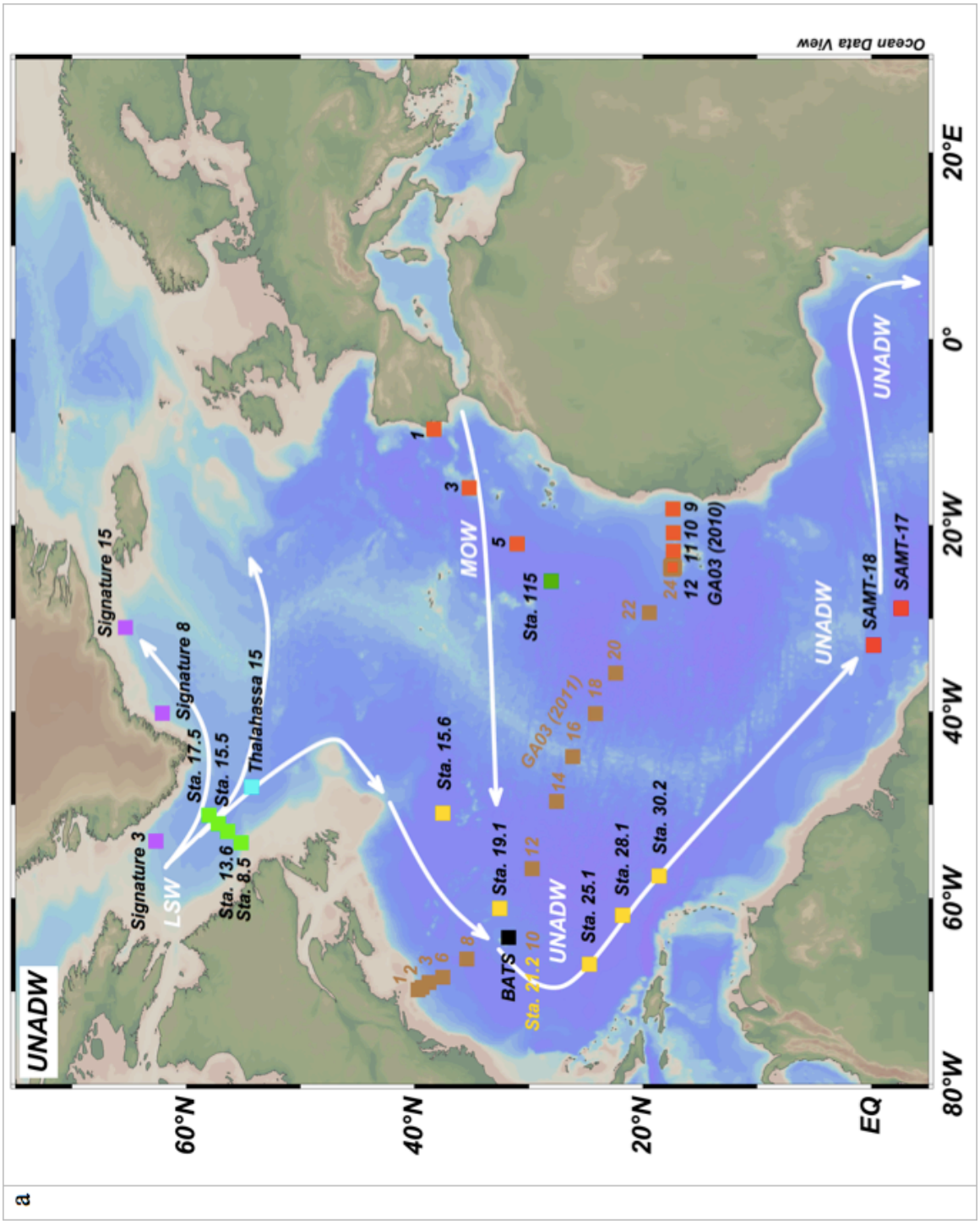

Figure S3. continued

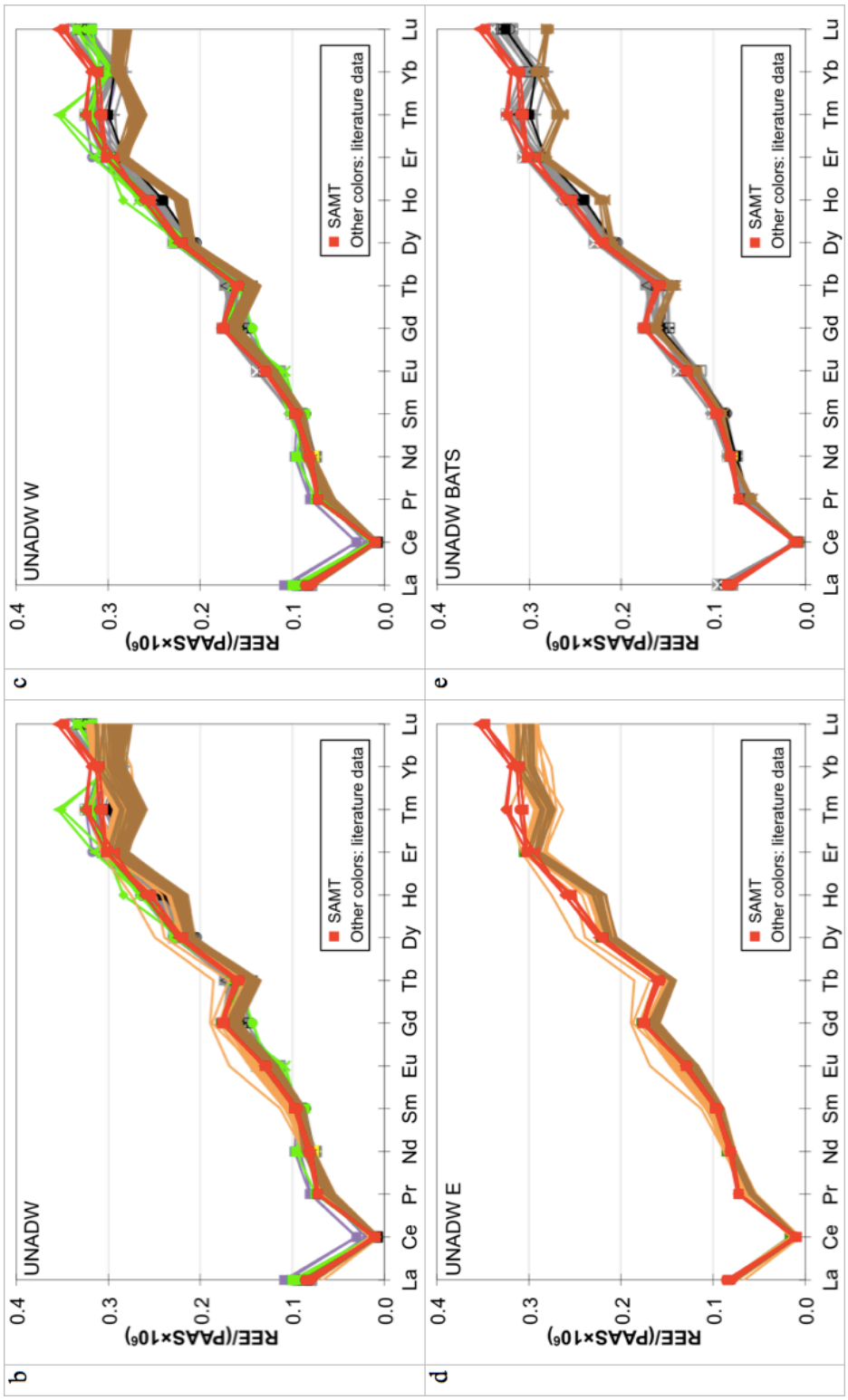

Figure S4. Comparison of REE end-members of the SAMT with published REE data for MNADW

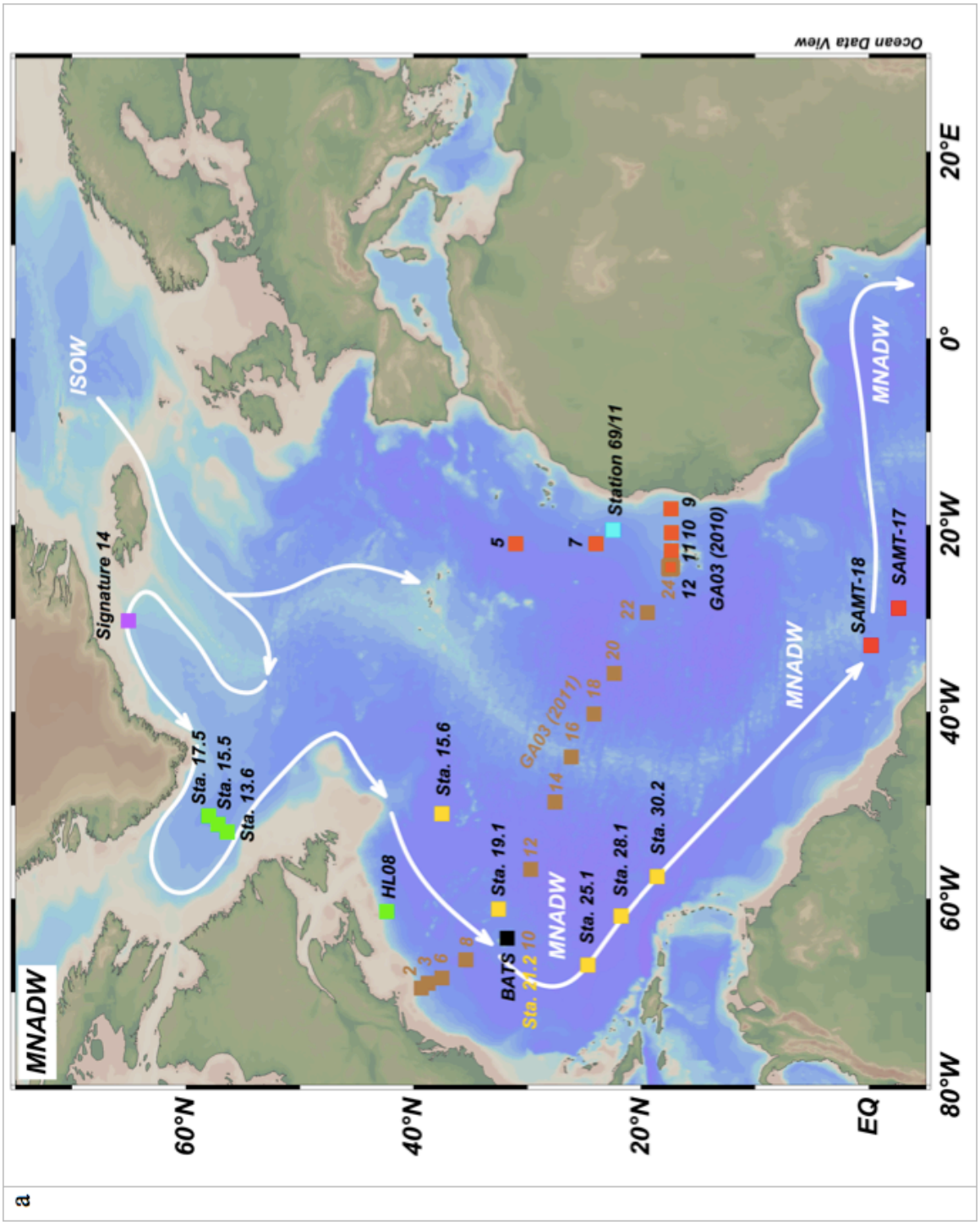

Figure S4. continued

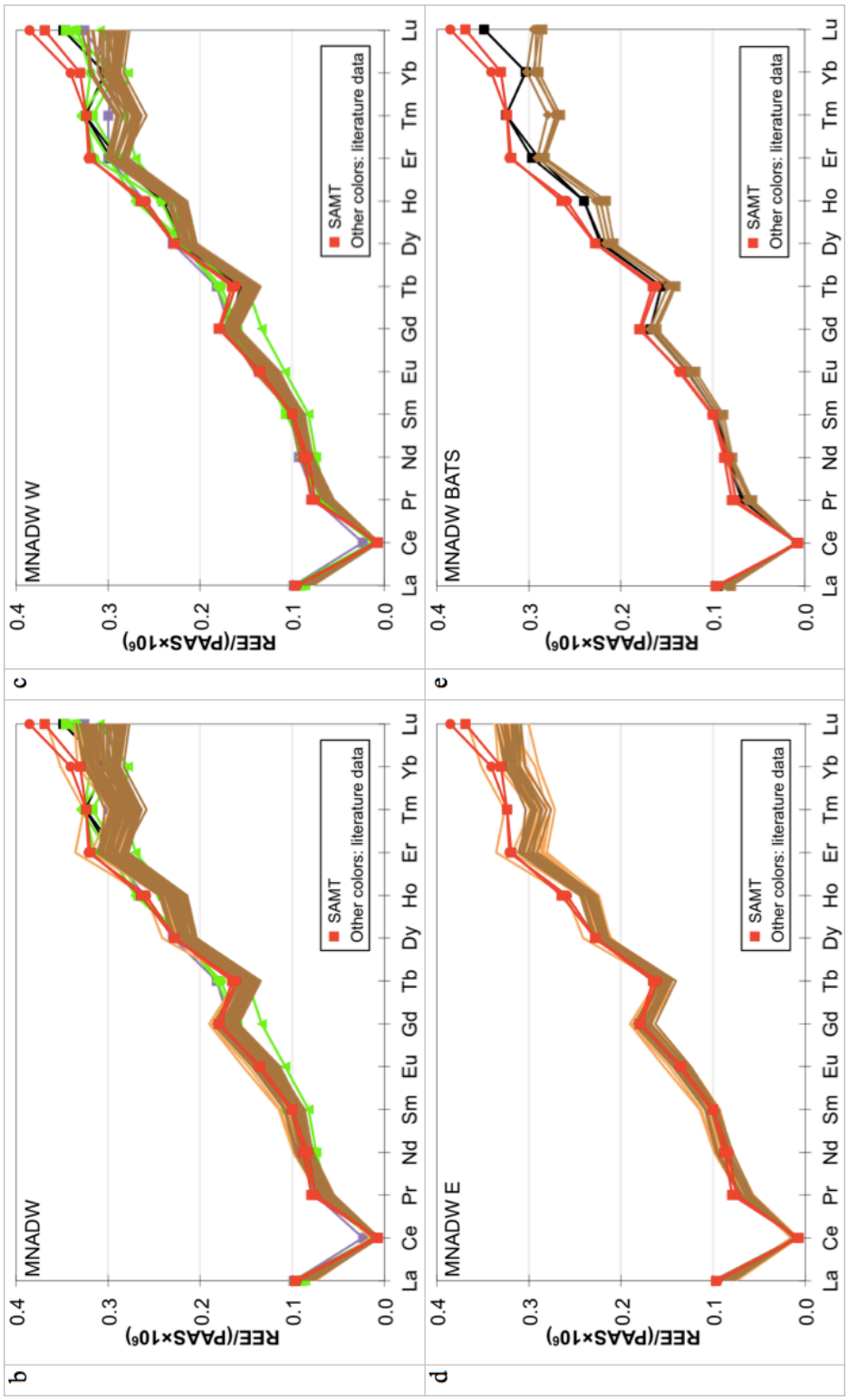

Figure S5. Comparison of REE end-members of the SAMT with published REE data for LNADW

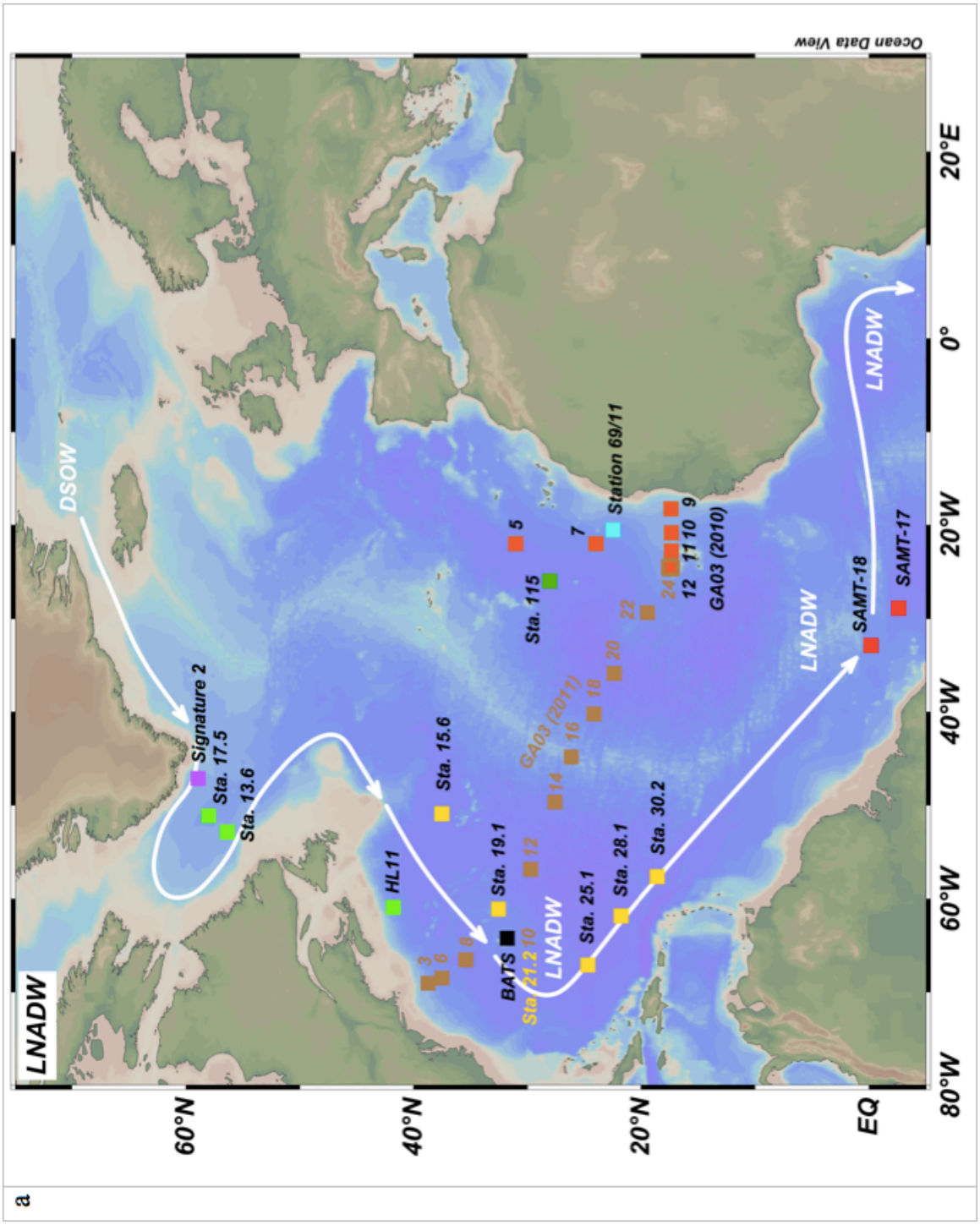

Figure S5. continued

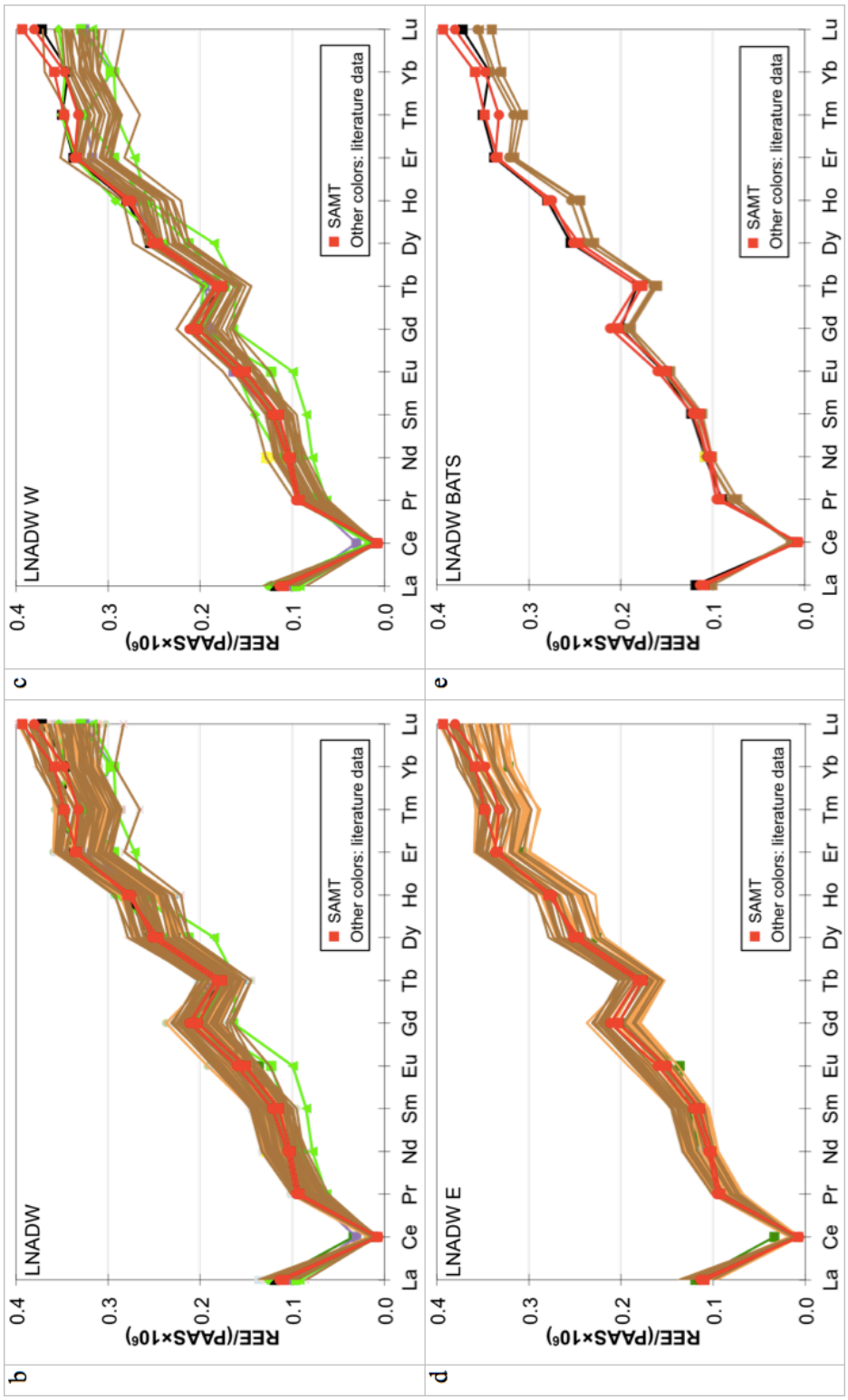

Figure S6. Comparison of REE end-members of the SAMT with published REE data for SACW

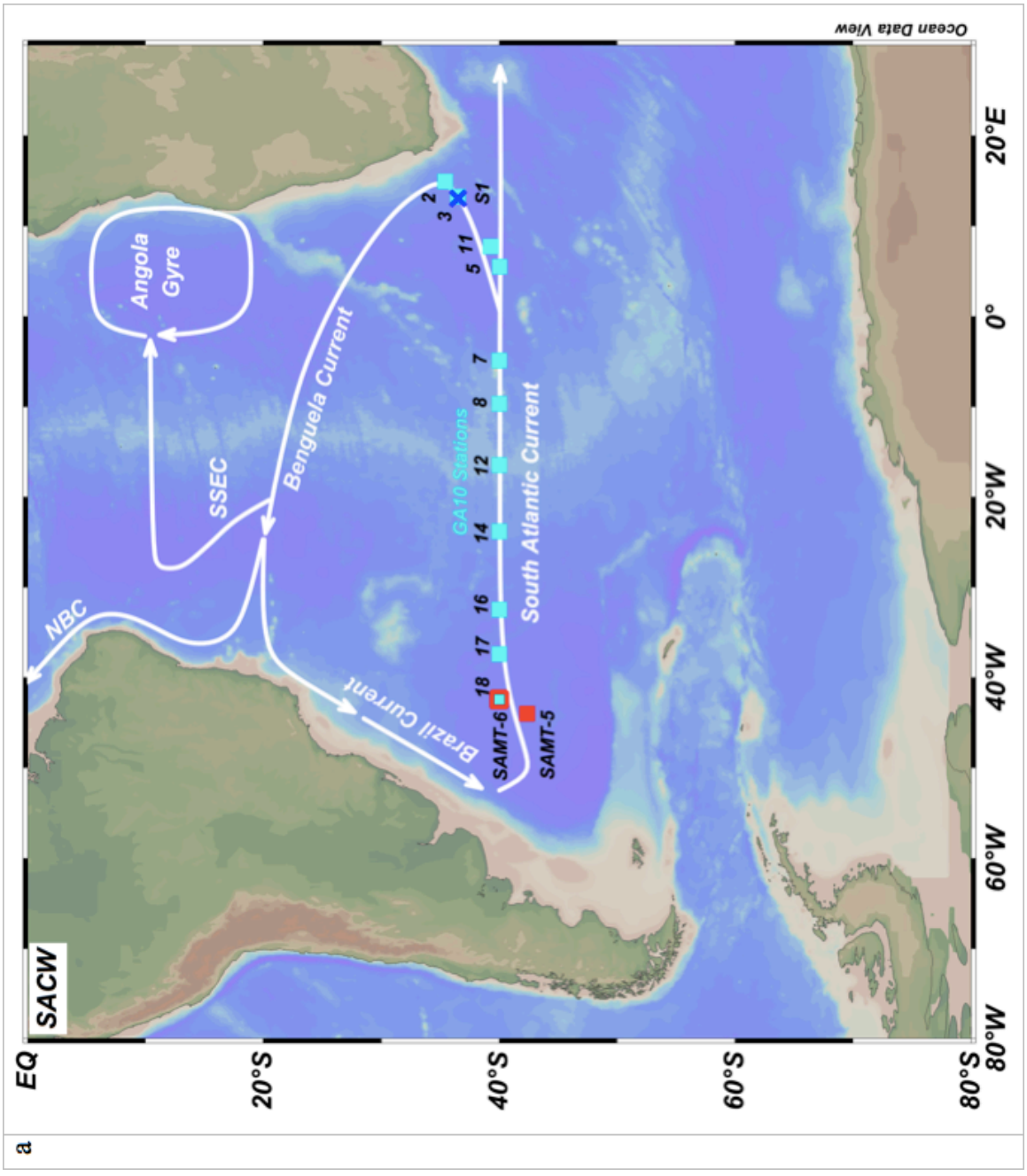

Figure S6. continued

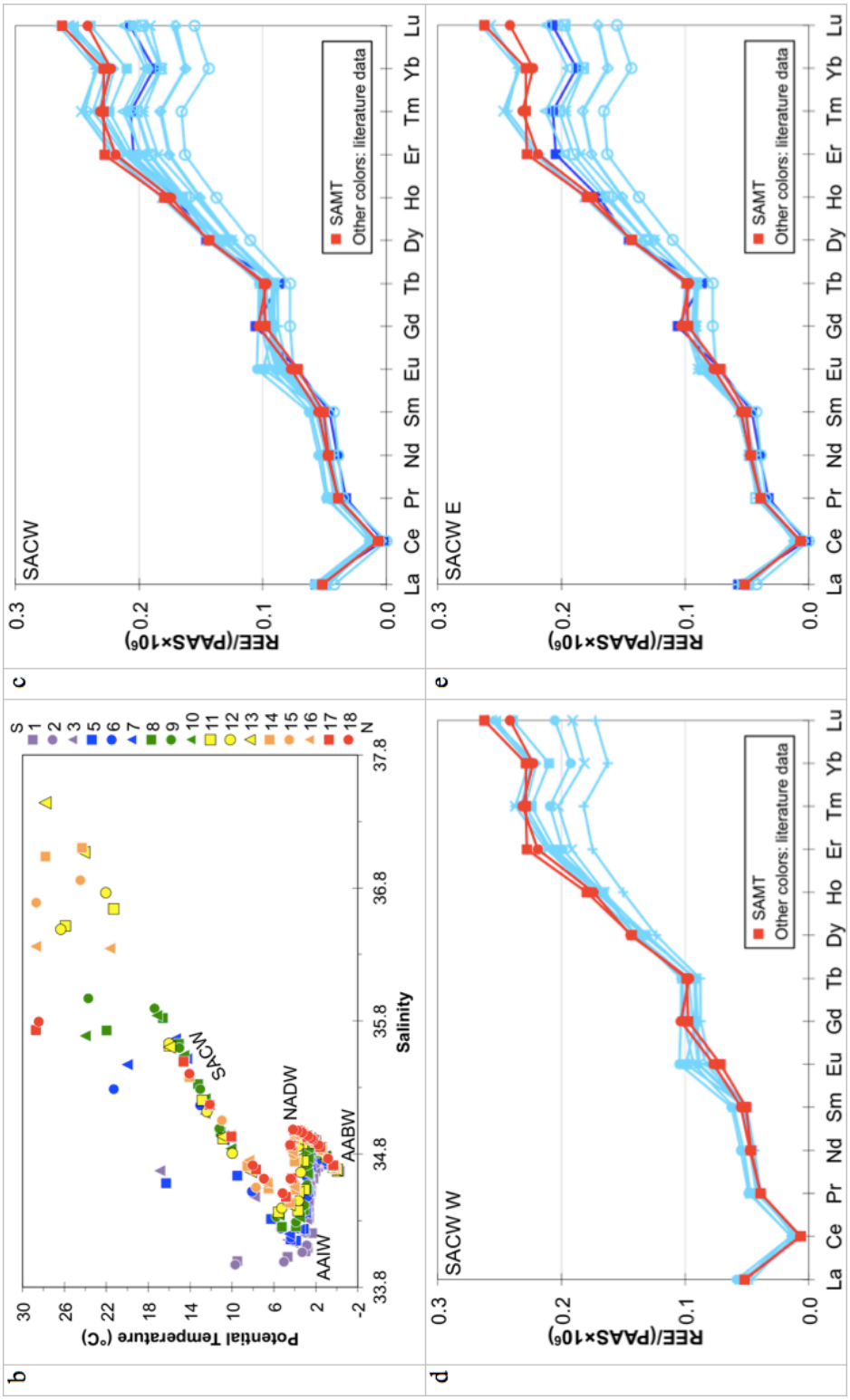

Figure S7. Comparison of REE end-members of the SAMT with published REE data for aAAIW

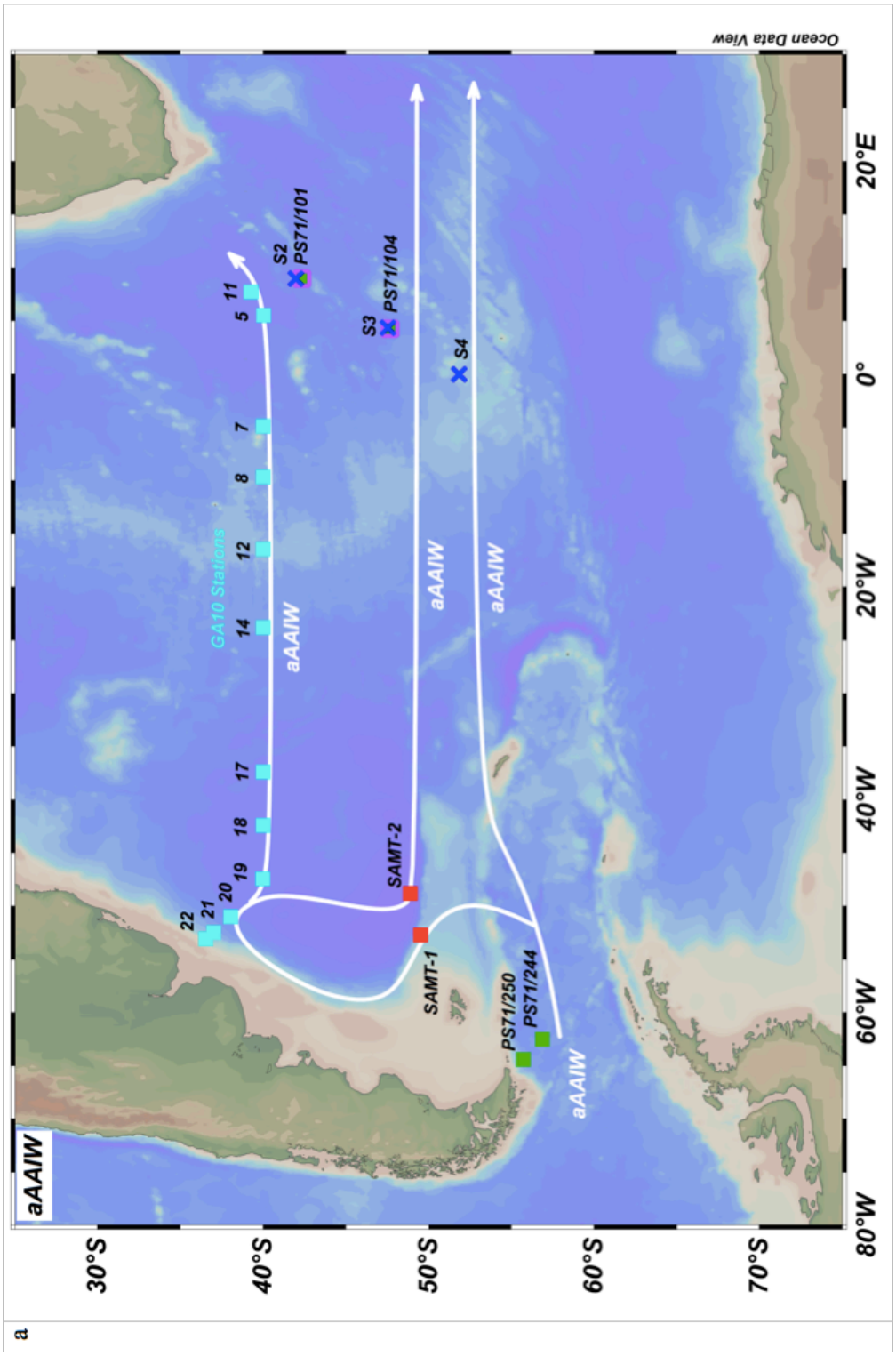

Figure S7. continued

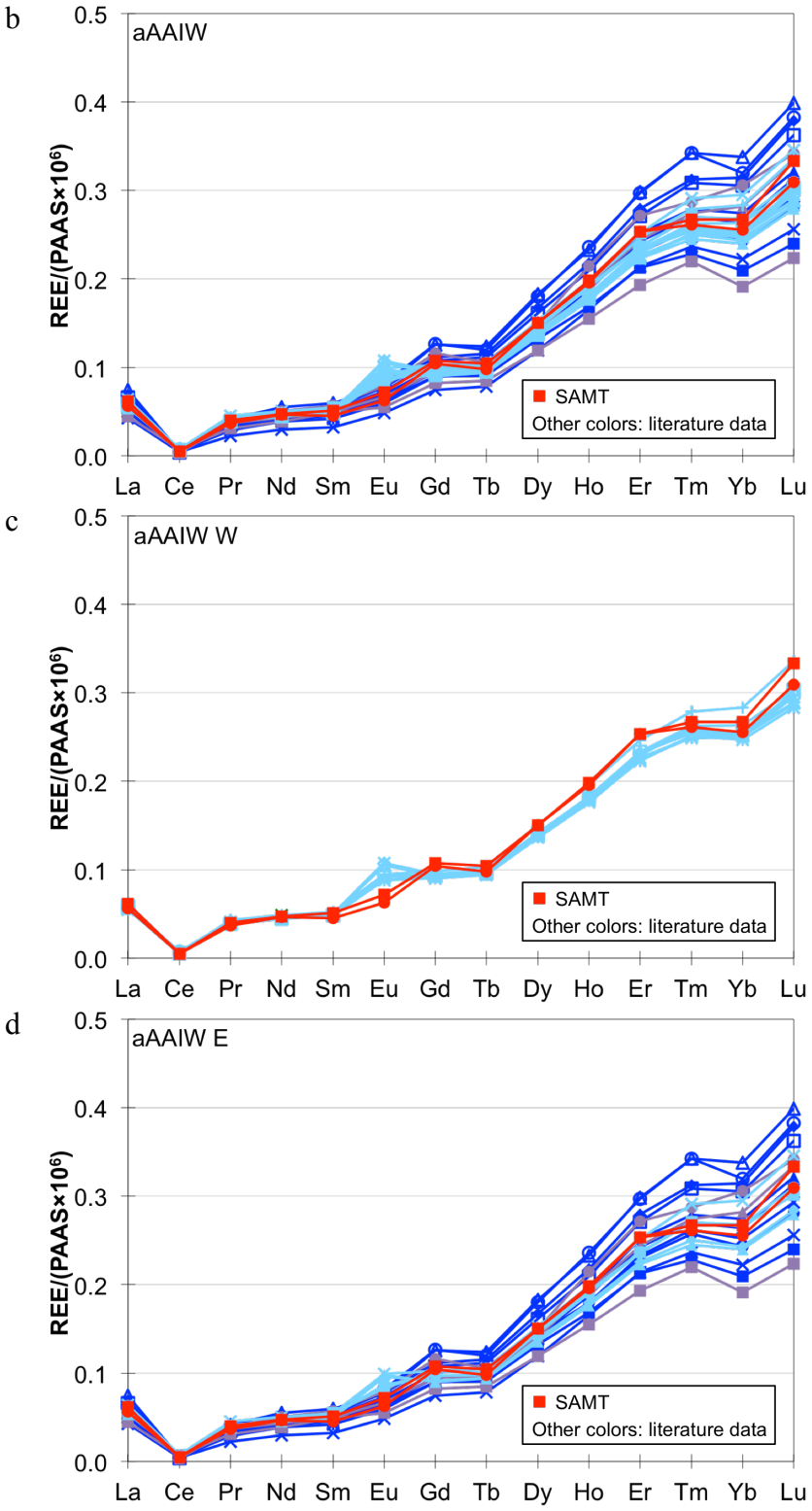

Figure S8. Comparison of REE end-members of the SAMT with published REE data for iAAIW

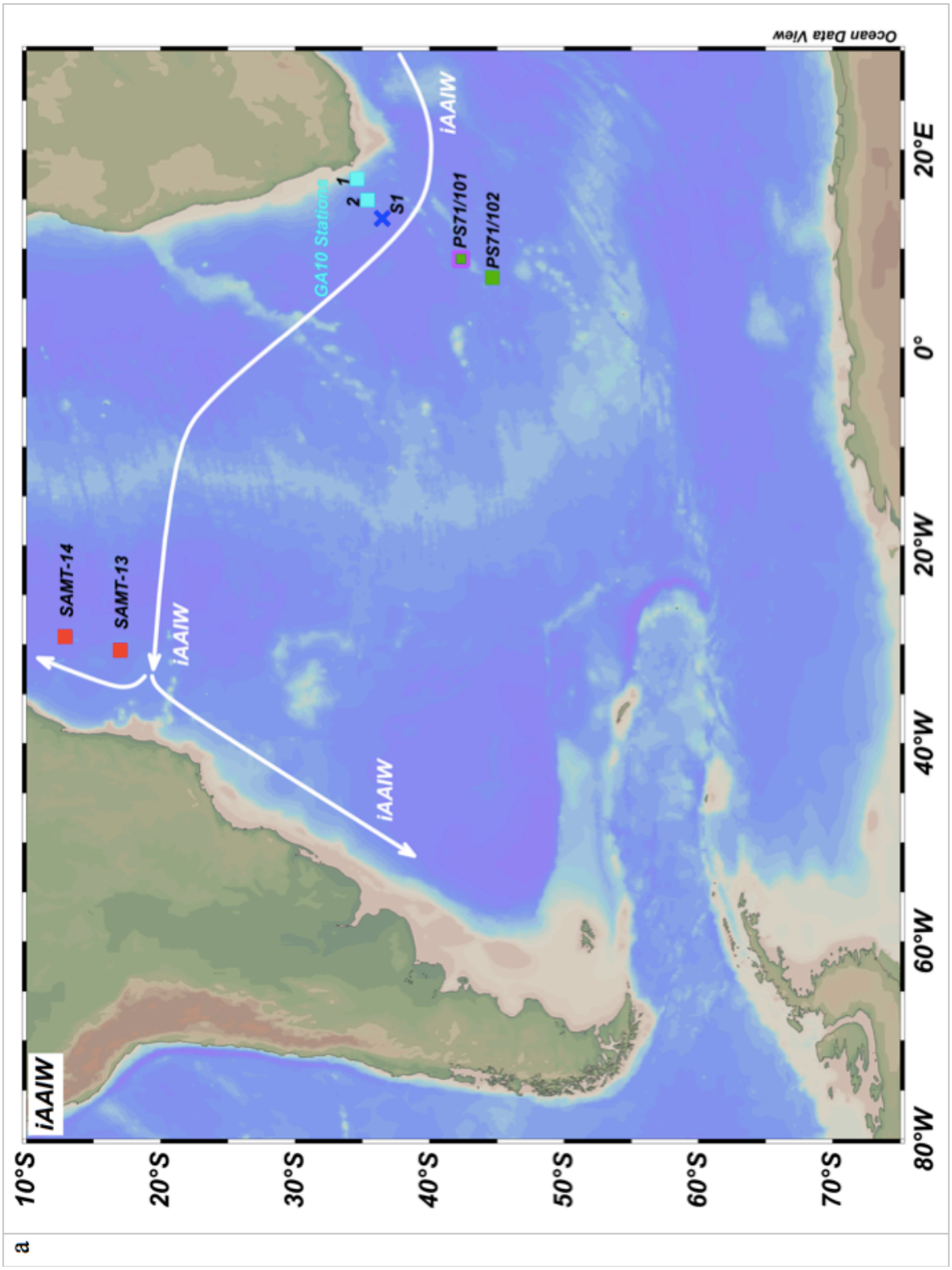

Figure S8. continued

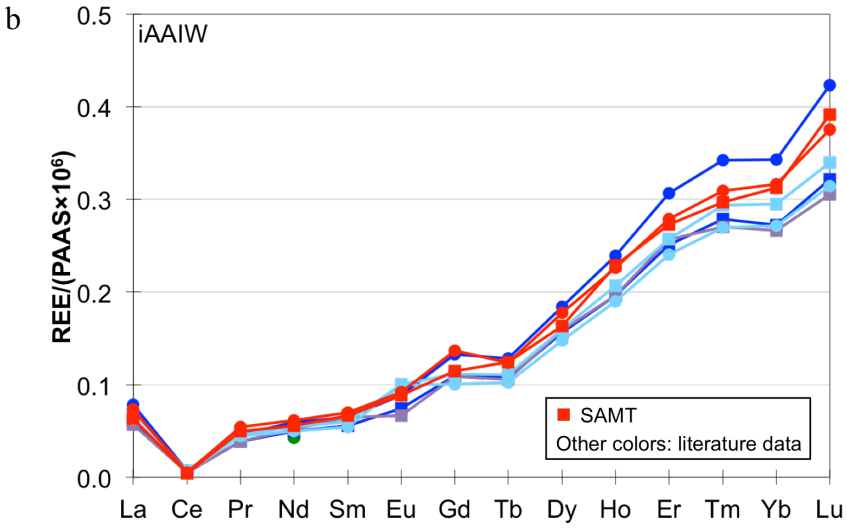

Figure S9. Comparison of REE end-members of the SAMT with published REE data for UCDW

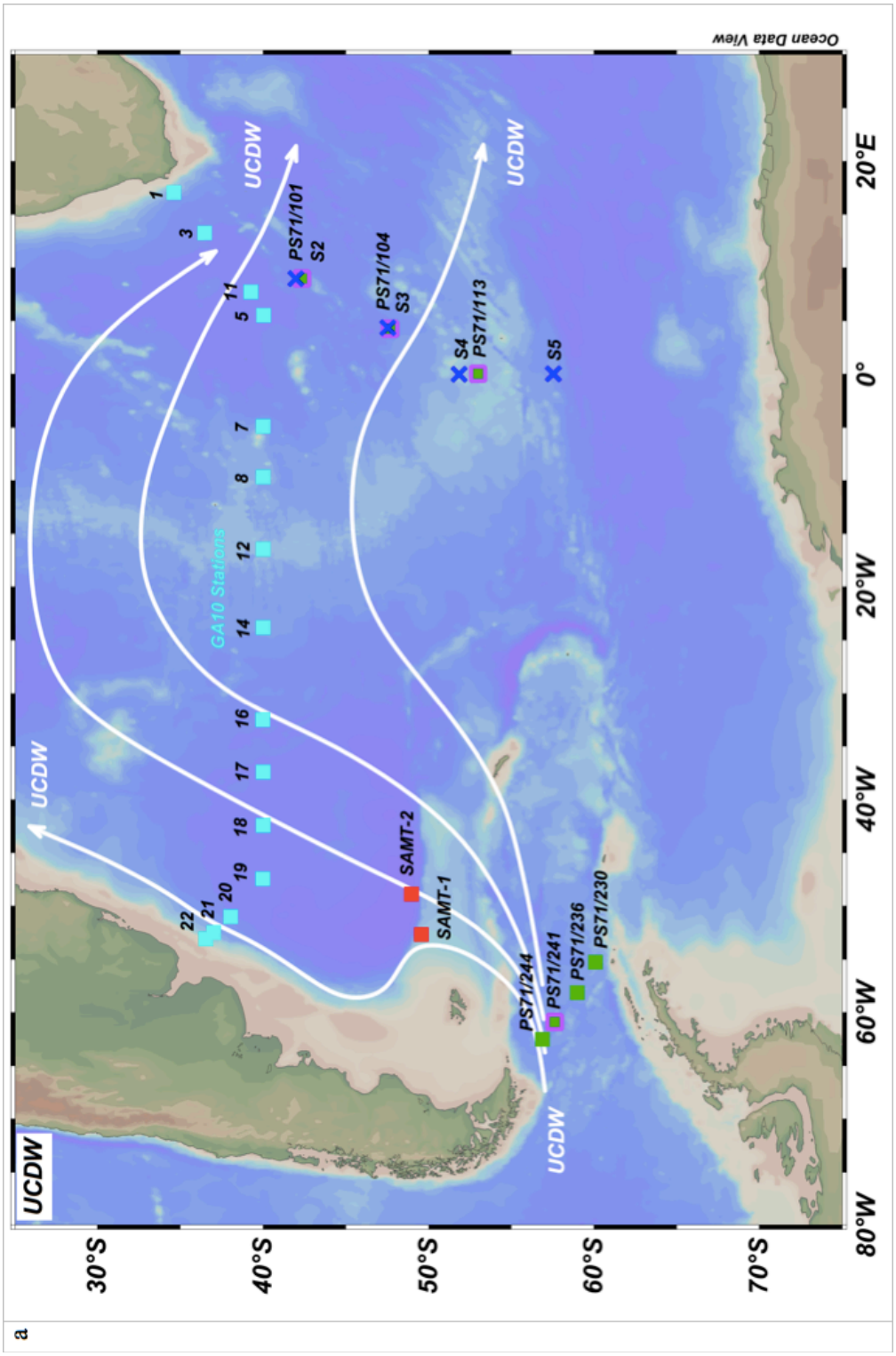

Figure S9. continued

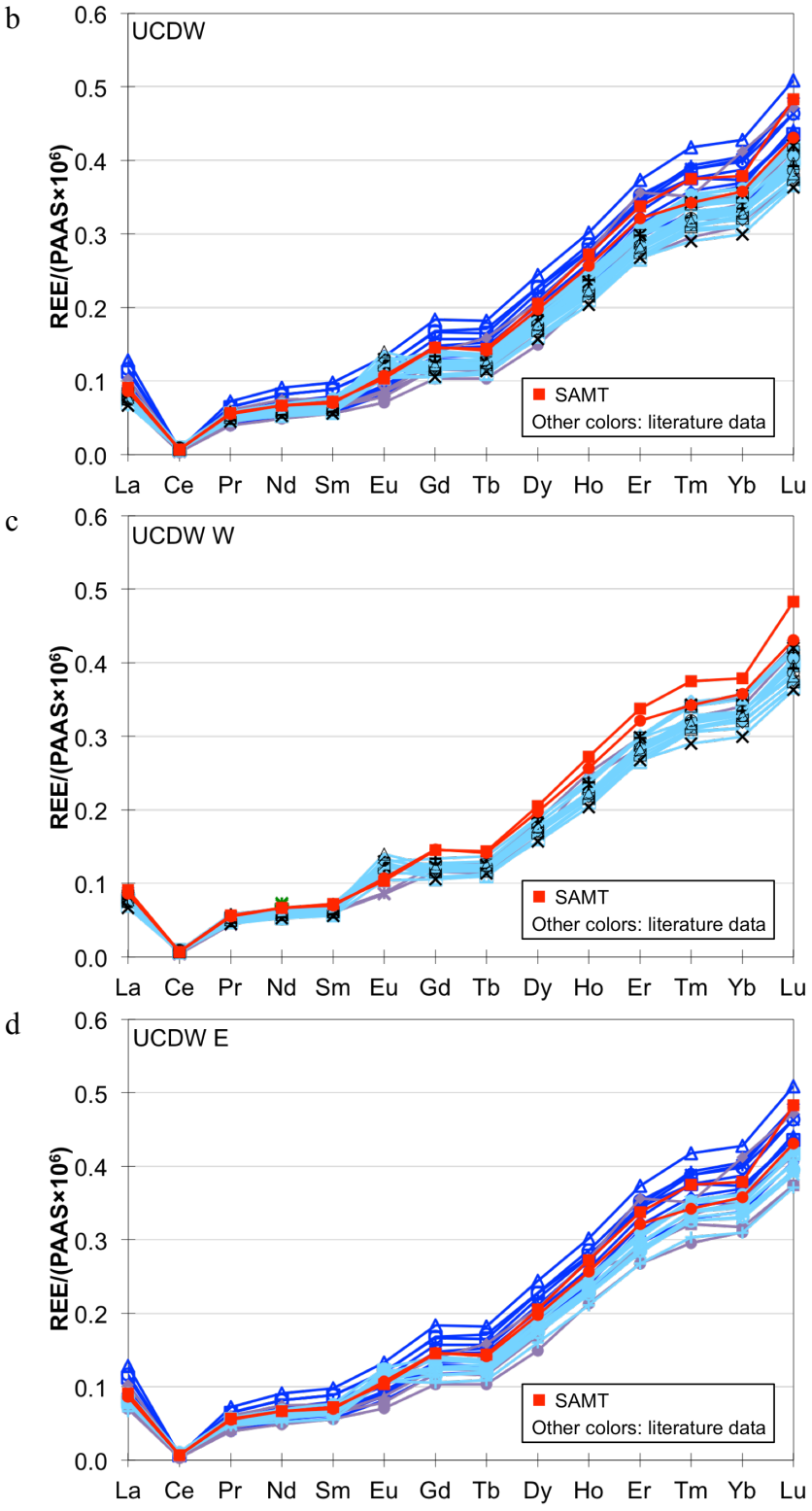

Figure S10. Comparison of REE end-members of the SAMT with published REE data for LCDW

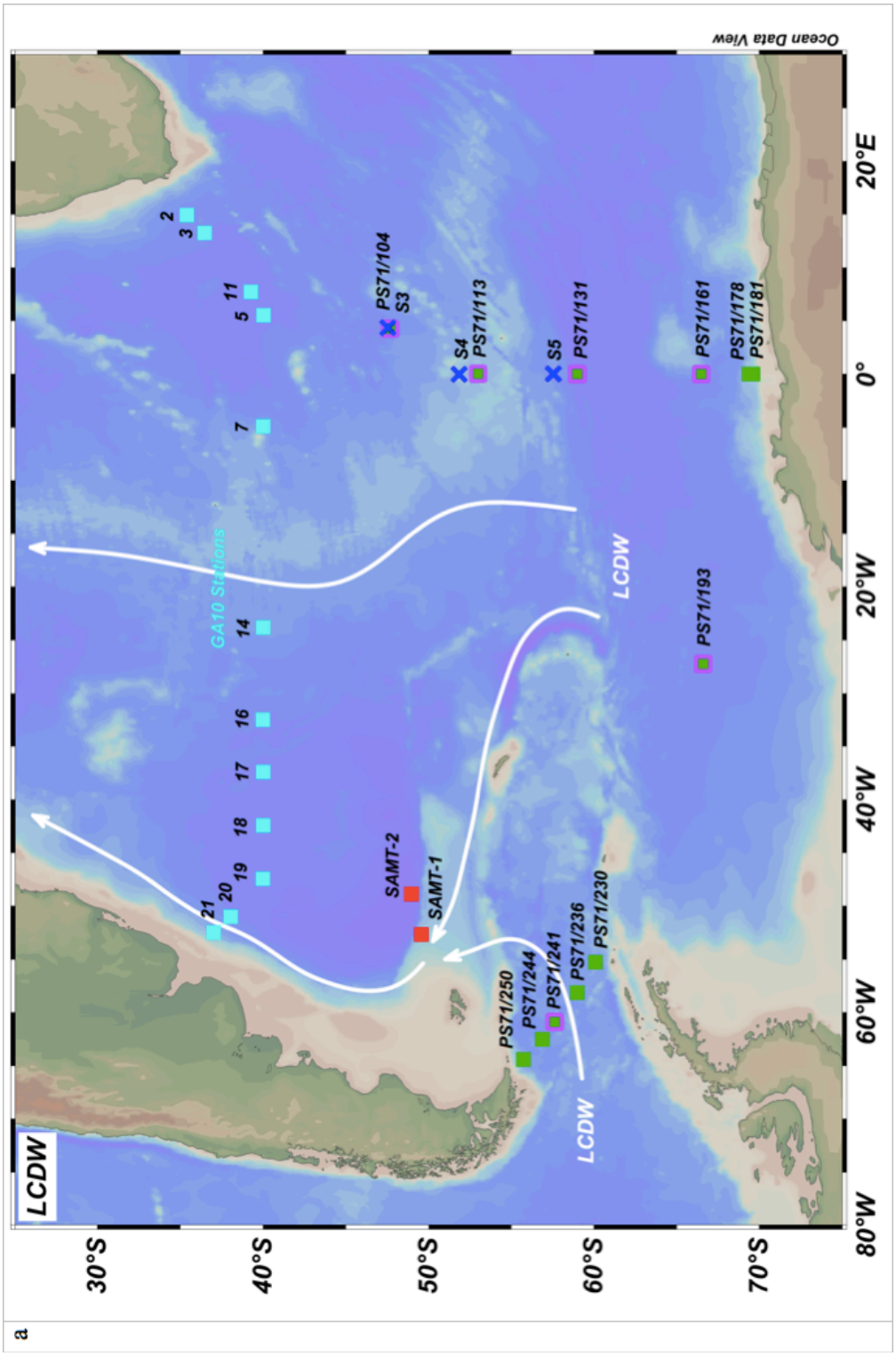

Figure S10. continued

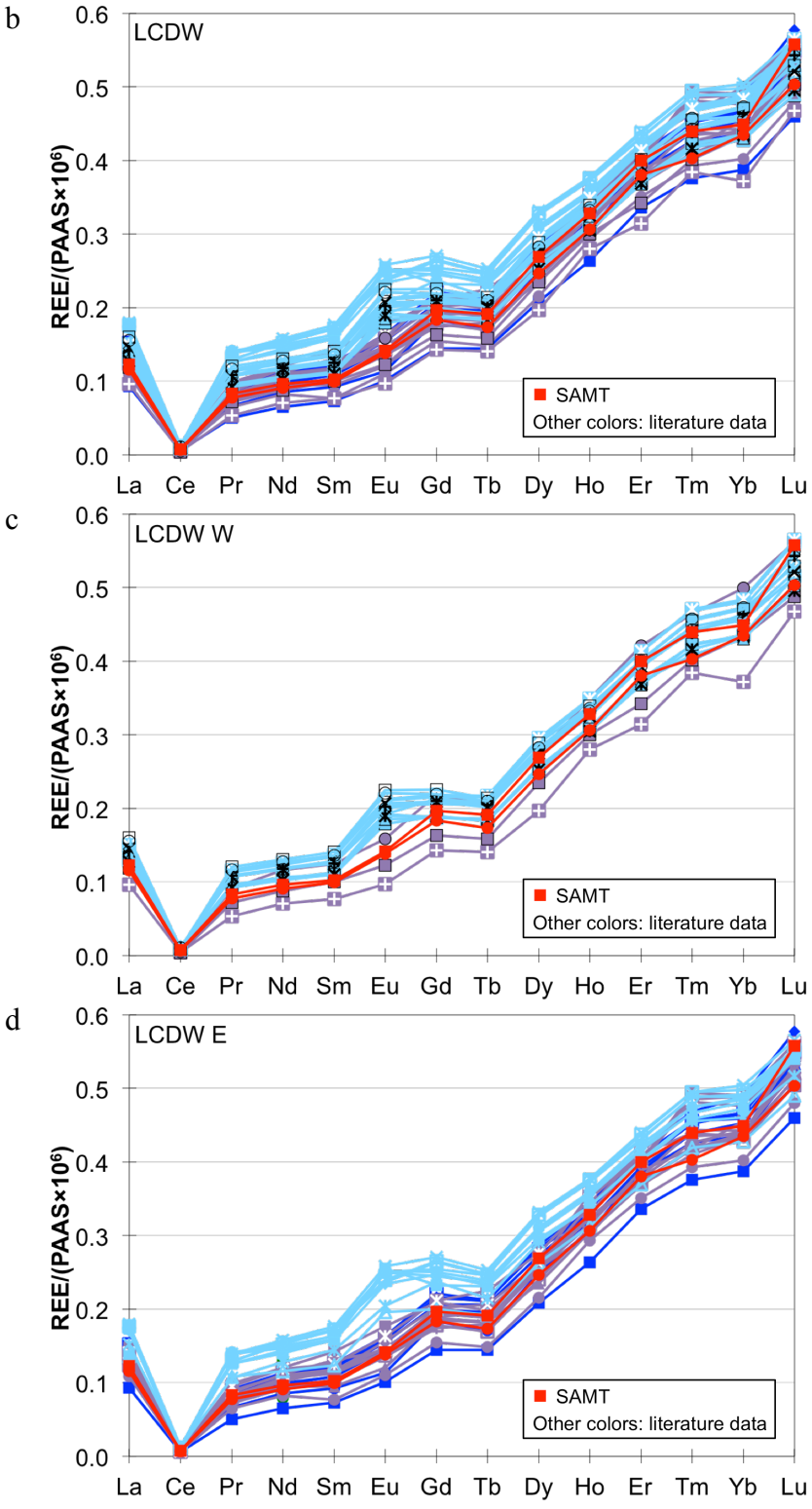

Figure S11. Comparison of REE end-members of the SAMT with published REE data for AABW

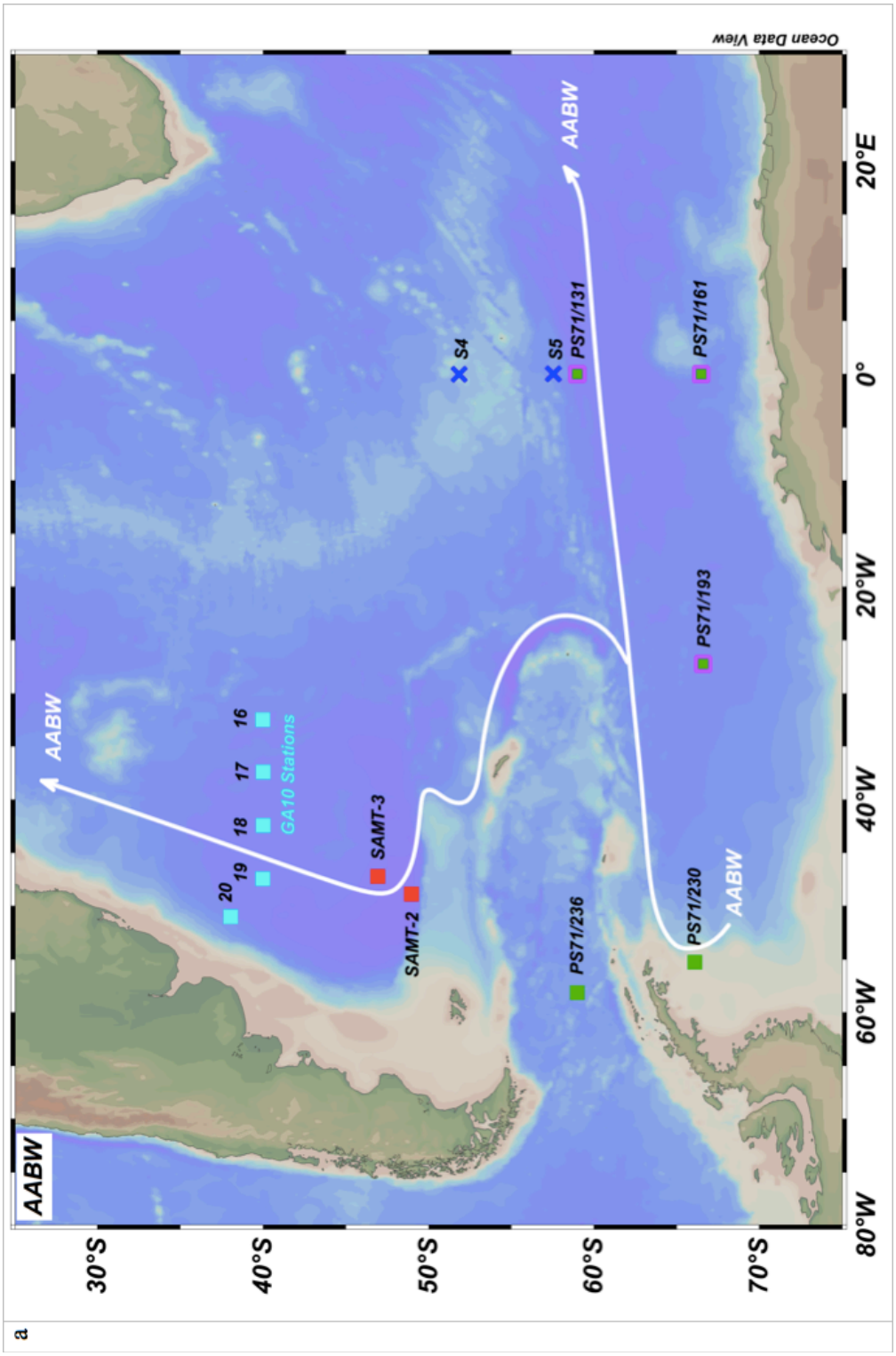

Figure S11. continued

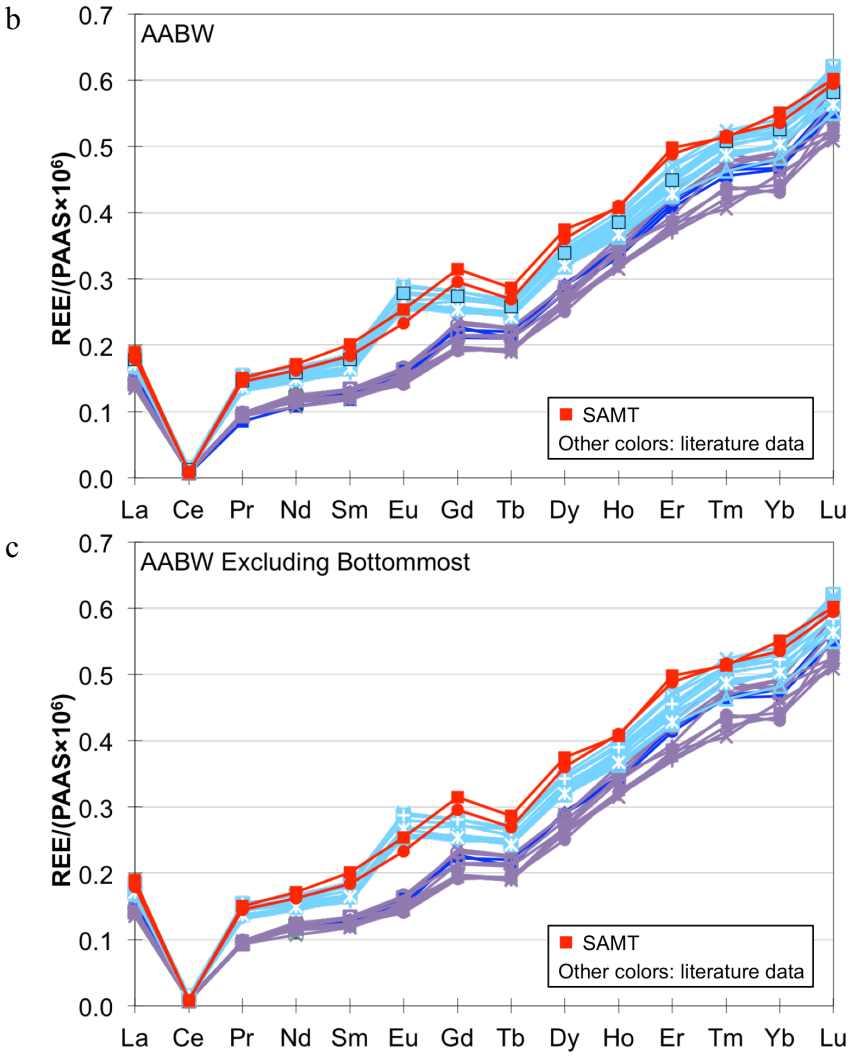

Figure S12. Comparison of water mass end-member compositions defined from the SAMT and in the water mass formation regions

a

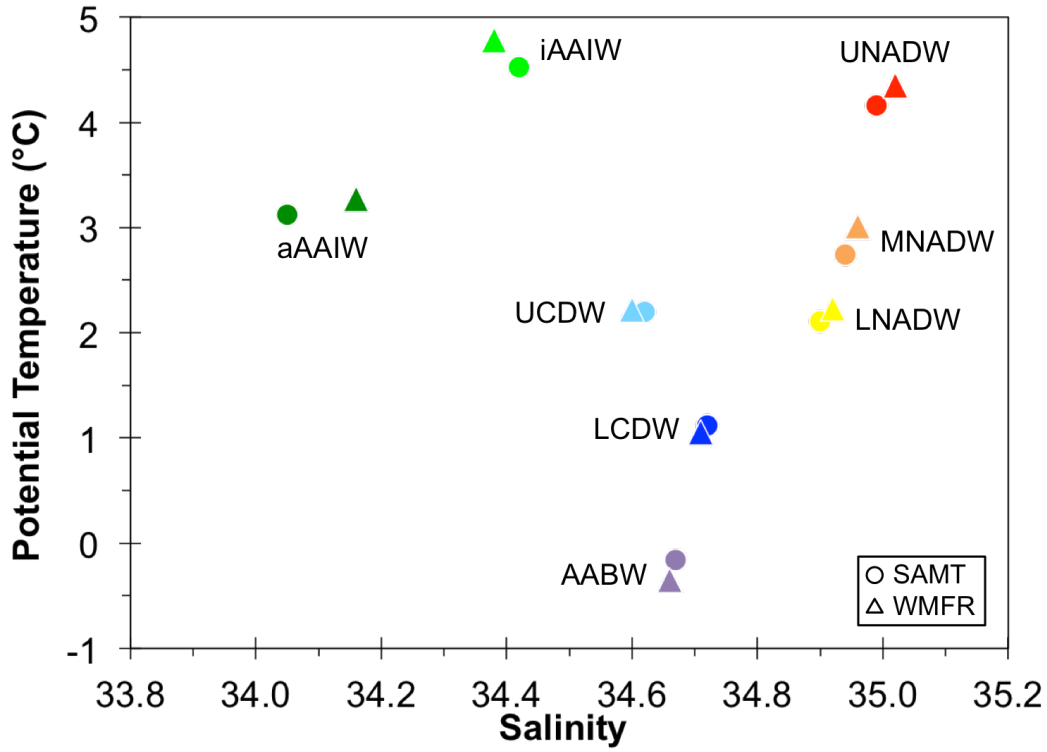


b

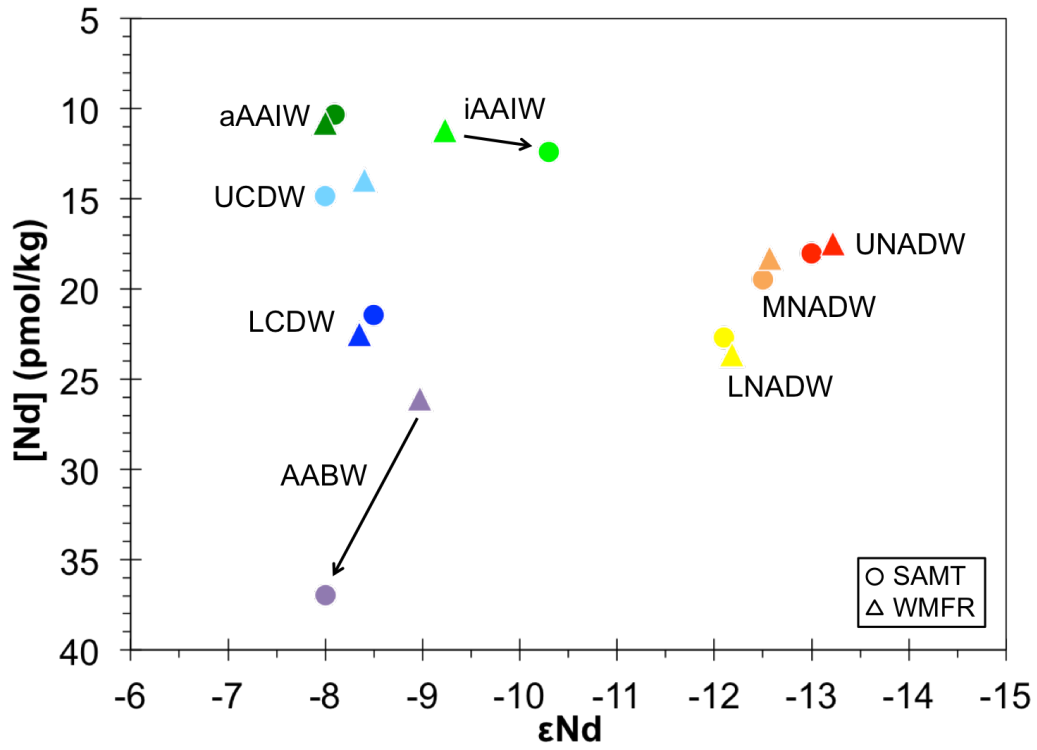

Figure S13. Intermediate and deep water SAMT samples from depths of AAIW to depths maximum salinity of each station and from depths of maximum salinity to the bottom

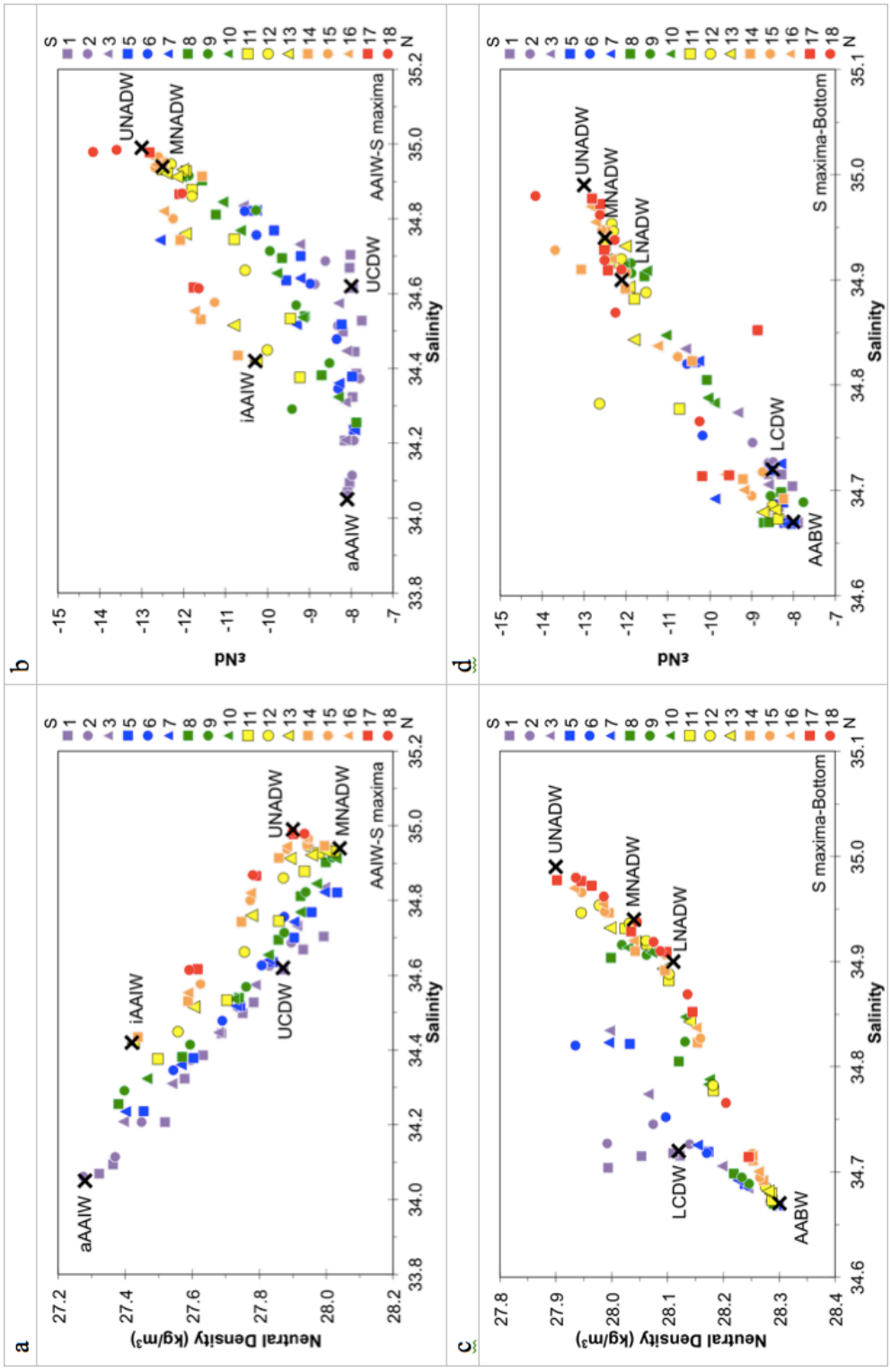

Figure S14. εNd deviations calculated based on water mass mixing using $PO_4^*$ and potential temperature

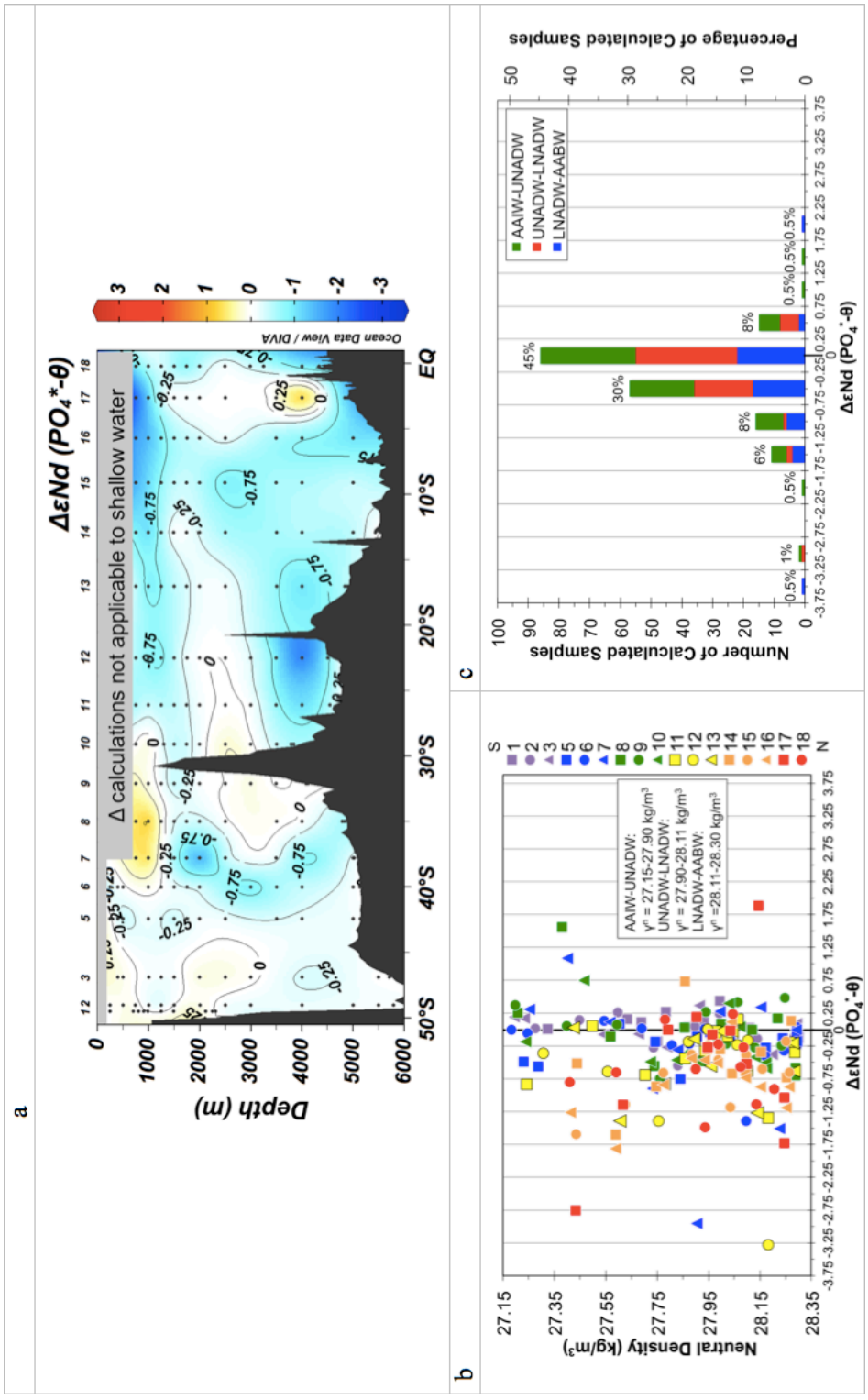

Figure S15. εNd deviations calculated based on water mass mixing using $PO_4^*$ and salinity

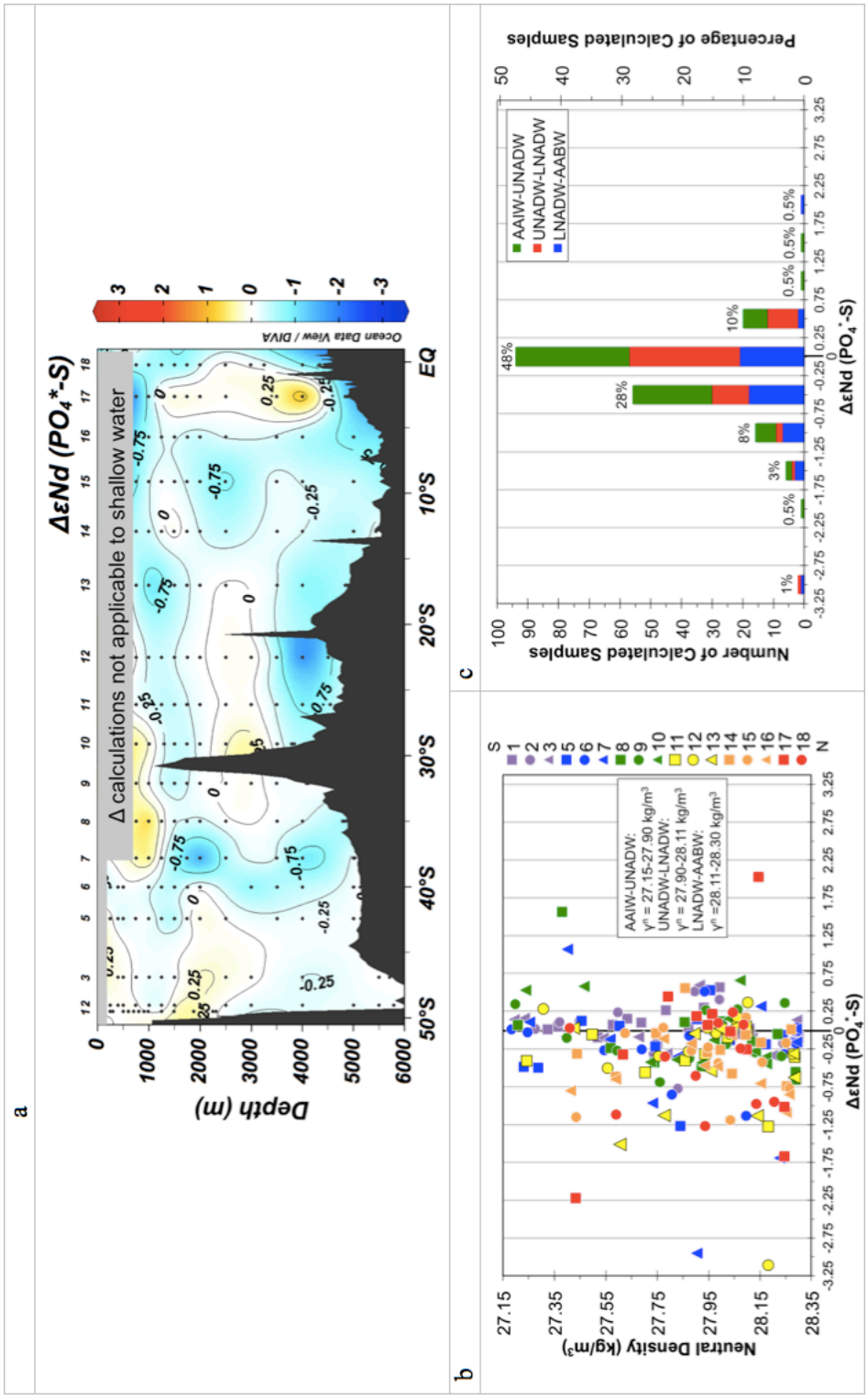

Table S1. (a) Published εNd and REE data from 17°N to 65°N in the Atlantic Ocean, in the western basin, and in the eastern basin. (b) Published εNd and REE data south of 50°S in the Atlantic Ocean (SACW data are from GEOTRACES GA10 stations along ~40°S and iAAIW data are from stations at 34-45°S), in the western basin, and in the eastern basin. (c) GEOTRACES GA10 REE data, in the western basin, and in the eastern basin. The error is one standard deviation. The εNd and REE data for AABW exclude the bottommost samples.

Table S1. Published εNd and REE data from 17°N to 65°N and south of 50°S in the Atlantic Ocean and GEOTRACES GA10 REE data

| | εNd | | | [Nd] pmol/kg | | | [Yb] pmol/kg | | |
|---|---|---|---|---|---|---|---|---|---|
| a | | | | | | | | | |
| | 17°-65°N | W | E | 17°-65°N | W | E | 17°-65°N | W | E |
| UNADW | −12.94 ± 0.96 | −13.32 ± 0.60 | −11.45 ± 0.57 | 18.03 ± 0.92 | 17.96 ± 0.94 | 18.20 ± 0.84 | 4.77 ± 0.16 | 4.70 ± 0.09 | 4.91 ± 0.16 |
| MNADW | −12.20 ± 0.52 | −12.41 ± 0.40 | −11.65 ± 0.39 | 18.80 ± 1.23 | 18.18 ± 1.00 | 19.54 ± 1.07 | 4.96 ± 0.22 | 4.82 ± 0.16 | 5.11 ± 0.18 |
| LNADW | −12.17 ± 0.68 | −12.49 ± 0.38 | −11.62 ± 0.72 | 24.31 ± 2.81 | 23.31 ± 2.71 | 25.17 ± 2.64 | 5.46 ± 0.34 | 5.26 ± 0.30 | 5.59 ± 0.30 |
| b | | | | | | | | | |
| | >50°S | W | E | >50°S | W | E | >50°S | W | E |
| SACW | – | – | – | 10.28 ± 0.90 | 10.67 ± 0.87 | 9.94 ± 0.83 | 3.17 ± 0.45 | 3.28 ± 0.39 | 3.08 ± 0.51 |
| aAAIW | −7.85 ± 0.19 | −8.00 ± 0.14 | −7.70 ± 0.00 | 11.42 ± 0.72 | 10.79 | 11.73 ± 0.68 | 5.32 ± 0.21 | – | 5.32 ± 0.21 |
| iAAIW | −9.23 ± 0.17 | – | −9.23 ± 0.17 | 11.19 ± 1.20 | – | 11.19 ± 1.20 | 4.69 ± 0.51 | – | 4.69 ± 0.51 |
| UCDW | −8.29 ± 0.26 | −8.40 ± 0.30 | −8.20 ± 0.23 | 15.26 ± 2.22 | 13.94 ± 1.53 | 16.42 ± 2.44 | 6.26 ± 0.44 | 5.61 ± 0.13 | 6.39 ± 0.32 |
| LCDW | −8.51 ± 0.40 | −8.52 ± 0.31 | −8.46 ± 0.69 | 22.46 ± 2.66 | 22.67 ± 2.67 | 21.21 ± 2.43 | 7.27 ± 0.47 | 7.25 ± 0.48 | 7.43 ± 0.45 |
| AABW | −9.29 ± 0.46 | −9.29 ± 0.46 | – | 26.02 ± 0.89 | 26.02 ± 0.89 | – | 7.54 ± 0.34 | 7.54 ± 0.34 | – |
| c | | | | | | | | | |
| | | | | GA10 | W | E | GA10 | W | E |
| SACW | | | | 10.28 ± 0.90 | 10.67 ± 0.87 | 9.94 ± 0.83 | 3.17 ± 0.45 | 3.28 ± 0.39 | 3.08 ± 0.51 |
| aAAIW | | | | 10.27 ± 0.35 | 10.19 ± 0.28 | 10.40 ± 0.44 | 4.19 ± 0.26 | 4.15 ± 0.19 | 4.24 ± 0.36 |
| iAAIW | | | | 11.49 ± 0.74 | – | 11.49 ± 0.74 | 4.59 ± 0.26 | – | 4.59 ± 0.26 |
| UCDW | | | | 13.14 ± 0.94 | 12.97 ± 0.81 | 13.43 ± 1.11 | 5.41 ± 0.28 | 5.33 ± 0.26 | 5.54 ± 0.27 |
| LCDW | | | | 28.51 ± 3.94 | 25.85 ± 2.08 | 31.41 ± 3.35 | 7.56 ± 0.36 | 7.40 ± 0.29 | 7.79 ± 0.35 |
| AABW | | | | 34.26 ± 1.64 | 34.26 ± 1.64 | – | 8.35 ± 0.30 | 8.35 ± 0.30 | – |

# Chapter 3. The Rare Earth Element Distribution of Seawater in the Southwest Atlantic Meridional Transect (GEOTRACES GA02 Leg 3)

Yingzhe Wu[1,2], Steven L. Goldstein[1,2], Robert F. Anderson[1,2], Leopoldo D. Pena[1,3], Alison E. Hartman[4], Louise L. Bolge[1], Micha J.A. Rijkenberg[5], Hein J.W. de Baar[5]

[1] Lamont-Doherty Earth Observatory of Columbia University, Palisades, New York 10964, USA

[2] Department of Earth and Environmental Sciences, Columbia University, New York 10027, USA

[3] GRC Geociències Marines, Department of Earth and Ocean Dynamics, University of Barcelona, Barcelona 08028, Spain

[4] USGS Columbia Environmental Research Center, Columbia, Missouri 65201, USA

[5] Royal Netherlands Institute for Sea Research, Den Burg, The Netherlands

manuscript in preparation for *Geochimica et Cosmochimica Acta*

**Abstract**

To better understand the conservative vs. non-conservative behavior of rare earth elements (REEs) in the ocean, dissolved REE concentrations were analyzed for 17 seawater vertical profiles in the Southwest Atlantic Meridional Transect (SAMT; GEOTRACES GA02 Leg 3; RRS James Cook 057). The SAMT includes the main water masses involved in the Atlantic Meridional Overturning Circulation and provides a great opportunity to test impacts of water mass mixing and open system processes on REEs at intermediate and deep depths. The shale-normalized REE patterns are consistent with typical seawater patterns, showing enrichments of heavy REEs compared to light REEs and negative cerium anomalies. In the intermediate and deep water, REE concentrations appear to behave like nutrients and increase with depth, whereas neodymium (Nd) isotopic compositions approximate expected values based on water mass mixing. This mismatch of Nd concentrations and Nd isotopes is called "Nd paradox". This transect provides an excellent opportunity to examine "Nd paradox" and the effects of conservative mixing vs. open system behavior. To investigate whether and how much intermediate and deep water REEs reflect water mass mixing, deviations of REE concentrations and ratios from predicted values based on water mass mixing were calculated. Our results show that within the SAMT, the intermediate and deep water REEs generally reflect water mass mixing and nearly conservative behavior. Out of 198 intermediate and deep samples, 51-68% of deviations of REE concentrations are within ± 5% of predicted values and 96-98% of them are within ± 15% of predicted values.

This transect also provides the opportunity to explore where and how the deviations are formed. Along the transect, there are potential sources that could add external REEs and cause non-conservative behavior of REEs and Nd isotopes, such as eolian dust, marginal sediments, deep sea sediments, nepheloid layers, and oceanic volcanism. In the surface (25 m) and subsurface (100 m) water, REEs and Nd isotopic compositions reflect contributions of eolian sources from Africa and South America. However, the surface/subsurface water εNd signature is not transferred to intermediate and deep water. In the oxygen depleted zone (250-500 m, between ~10°S and the equator), increased REE concentrations (except Ce) and low Nd isotopic compositions likely result from the dissolution of Fe-Mn oxides in reducing condition. Near the continental margin (1500-3000 m), slight REE additions and small Nd isotopic deviations from water mass mixing suggest dissolution of REEs from marginal sediments. In the bottom water (~35°S to ~0°S), REE additions and negative Nd isotopic deviations from water mass mixing are likely due to dissolution of REEs from sediments on the seafloor. In the nepheloid layers (~49°S to ~42°S), the bottom water REEs and Nd isotopes are not significantly influenced by resuspended particles and show almost conservative behavior. Near the Rio Grande Rise (RGR) and the Vitoria Trindade Ridge (VTR) hotspot tracks in this transect, most intermediate and deep water masses passing the RGR and VTR show no influence on deviations of Nd isotopes and REE concentrations from RGR and VTR. LCDW and AABW show decreasing values of Nd isotopic deviations and REE additions when they pass the RGR indicating influence by dissolved REEs from the deep sea

sediments. LCDW and AABW passing the VTR are influenced by dissolved REEs from the deep sea sediments as well as the volcanic VTR.

## 1. Introduction

The rare earth elements (REEs) and neodymium (Nd) isotopic compositions in the ocean are important tools to investigate lithogenic sources of trace elements and to trace water mass mixing (e.g. (Elderfield and Greaves, 1982; Elderfield et al., 1988; Sholkovitz et al., 1994; Frank, 2002; Goldstein and Hemming, 2003; van de Flierdt et al., 2016; Osborne et al., 2017; Tachikawa et al., 2017)). This study focuses on the REEs in seawater profiles from 17 stations, with 16 samples at different depths for each station, collected meridionally in the Southwest Atlantic Ocean between 49.5°S and 0.2°S (Fig. 1) in the GEOTRACES cruise GA02 Leg 3 (RRS James Cook 057). The Southwest Atlantic Meridional Transect (SAMT), including major Atlantic water masses and crossing potential sources that could add external REEs, provides an excellent opportunity to investigate the conservative vs. non-conservative behavior of REEs.

The lanthanide REEs are a group of 15 elements from lanthanum (La, atomic number 57) to lutetium (Lu, atomic number 71). In the lanthanide series, the electrons progressively fill the 4f orbitals with increasing atomic number. REEs have a similar outer electronic configuration, which results in similar chemical characteristics. However, the decrease of ionic radius with increasing atomic number results in systematic fractionation of REEs.

In seawater, REEs mostly complex with carbonate ion (e.g. (Byrne and Kim, 1990; Byrne, 2002; Luo and Byrne, 2004)) with increasing stability of REE complexes as ionic radius decreases from La to Lu (e.g. (Elderfield et al., 1988; Lee and Byrne, 1993)). In addition, the dissolved light REEs (LREEs) with larger radii are more preferentially

scavenged onto particles compared to the heavy REEs (HREEs) (Byrne and Kim, 1990). As a result, relative abundances of seawater REEs normalized to Post-Archean Australian Shale (PAAS; (Taylor and McLennan, 1985)) show enrichments of HREEs compared to LREEs (Elderfield et al., 1988). Here the relative abundances are calculated by normalizing the concentration of each element to its concentration in a reference standard, such as chondrites (e.g. (Masuda et al., 1973; Nakamura, 1974)) or shales (e.g. (Gromet et al., 1984; Taylor and McLennan, 1985)). Seawater REEs are usually normalized to PAAS (Taylor and McLennan, 1985) because it is logical for seawater to compare the REE abundances to their continental sources. The REEs show 3+ valence in their oxidation states although cerium (Ce) and europium (Eu) also exist in 4+ valence and 2+ valence, respectively. Ce with 4+ valence will form if the system is sufficiently oxidized and is insoluble in oxic seawater. Thus Ce shows very low relative abundances compared to the other REEs in PAAS-normalized seawater REE pattern (Elderfield et al., 1988).

The vertical seawater profiles of dissolved REE concentrations are similar to that of nutrients and show increasing concentrations with depth in the water column. Early studies proposed that they result from scavenging onto particles in the surface water and remineralization of sinking particles at depth (e.g. (Elderfield et al., 1988; Byrne and Kim, 1990)). REEs also accumulate with aging of water masses, increasing along the water mass transport paths from the Atlantic to Pacific Ocean (e.g. (De Baar et al., 1985)). REE patterns show fractionation between the deep Atlantic and Pacific Ocean (e.g. (Osborne et al., 2017)). The deep water PAAS-normalized HREE/LREE ratios increase from the

Atlantic to Pacific Ocean as a result of preferential removal of LREEs onto particles relative to HREEs (e.g. (Elderfield and Greaves, 1982; Elderfield et al., 1988)) along the deep water pathway from the Atlantic to Pacific Ocean (e.g. (Bertram and Elderfield, 1993)).

Some studies have suggested that the intermediate and deep water REEs behave conservatively based on water mass mixing (e.g. (German et al., 1995; Haley et al., 2014; Zheng et al., 2016)). Recently, dissolved REEs were studied in the South Atlantic in a full-depth zonal transect from the CoFeMUG (cobalt, iron and micro-organisms from the upwelling zone to the gyre) cruise across the South Atlantic Ocean along ~10°S (Zheng et al., 2016). This is a GEOTRACES approved compliant data cruise (GAc01). This zonal transect crosses the SAMT at ~10°S near Station 14 and 15 of the SAMT (SAMT-14 and 15). Zheng et al. (2016) concluded that >75% of the REEs below 1000 m are dominantly controlled by advective water mass mixing. Therefore, the seawater REE characteristics could potentially be used as indicators of intermediate and deep water masses.

The isotopic composition of Nd (one of the REEs) has been used to trace the water masses in modern and past ocean circulation studies (e.g. (Frank, 2002; Goldstein and Hemming, 2003; van de Flierdt et al., 2016; Tachikawa et al., 2017)). The use of seawater Nd isotopes is based on the observation that they effectively "fingerprint" different water masses and behave "quasi-conservatively", that is, they mainly reflect values expected from water mass mixing over long water mass transport distances in intermediate and deep water (Frank, 2002; Goldstein and Hemming, 2003). The Nd

isotopic composition is expressed as the $^{143}Nd/^{144}Nd$ ratio. The $^{143}Nd/^{144}Nd$ ratio of a sample is often expressed as the deviation from the bulk earth (chondritic uniform reservoir – CHUR) ratio in parts per $10^4$. This normalization is defined as the εNd (DePaolo and Wasserburg, 1976): $\varepsilon Nd = [(^{143}Nd/^{144}Nd_{sample}) / (^{143}Nd/^{144}Nd_{CHUR}) - 1] \times 10^4$, where $^{143}Nd/^{144}Nd_{CHUR} = 0.512638$ (Jacobsen and Wasserburg, 1980).

While Nd isotopes generally show "quasi-conservative" behavior in seawater, that is, reflecting values expected from water mass mixing, Nd concentrations appear to behave like nutrients and increase with depth. This apparent mismatch of εNd-values and Nd concentration in the water column is called "Nd paradox" (Goldstein and Hemming, 2003). Reversible scavenging, first proposed by (Bacon and Anderson, 1982), have been used by some modeling studies to explain "Nd paradox" (e.g. (Nozaki and Alibo, 2003; Siddall et al., 2008; Arsouze et al., 2009; Rempfer et al., 2011)). For example, Siddall et al. (2008) have proposed a combination of reversible scavenging and lateral advection to explain "Nd paradox". When particles are transported down the water column, Nd scavenged at surface is dissolved from particles such that Nd concentration increases with depth (Siddall et al., 2008). Sinking particles exchange some Nd with seawater, but it is advected away before it can impact greater depths, thus keeping the εNd profile intact (Siddall et al., 2008). In contrast, other studies have suggested that the intermediate and deep water REEs are dominantly controlled by water mass mixing (e.g. (Elderfield et al., 1988; German et al., 1995; Haley et al., 2014; Zheng et al., 2016)).

REEs are brought to the oceans from eolian dust (e.g. (Goldstein et al., 1984)), rivers (e.g. (Goldstein and Jacobsen, 1987)), pore water (e.g. (Elderfield and Sholkovitz,

1987; Haley et al., 2017)), ground water (e.g. (Johannesson and Burdige, 2007)), and "boundary exchange" (e.g. (Lacan and Jeandel, 2005)). It has been suggested that "boundary exchange", which is the REE exchange between seawater and sediments from continental margins, can change εNd without significantly modifying Nd concentrations in seawater (Lacan and Jeandel, 2001; Lacan and Jeandel, 2005; Jeandel et al., 2007). Interaction between seawater and particles at continental margins also allows removal of Nd from seawater (Lacan and Jeandel, 2001; Lacan and Jeandel, 2005; Jeandel et al., 2007). Thus, the continental margins can serve as both a source and a sink of REEs (e.g. (Lacan and Jeandel, 2001; Lacan and Jeandel, 2005; Jeandel et al., 2007; Grasse et al., 2012; Grenier et al., 2013; Garcia-Solsona et al., 2014)). The "boundary exchange" process between seawater and sediments could disturb the "quasi-conservative" behavior of Nd isotopes in the ocean (Lacan and Jeandel, 2001; Lacan and Jeandel, 2005; Jeandel et al., 2007).

The SAMT provides an excellent opportunity to investigate the REE cycling in the ocean. The REEs of this transect are expected to show increasing concentrations with depth. The SAMT includes the major water masses in the Atlantic Meridional Overturning Circulation (AMOC): southward North Atlantic Deep Water (NADW), northward Antarctic Intermediate Water (AAIW) and Antarctic Bottom Water (AABW) (Fig. 2). REE abundances and PAAS-normalized HREE/LREE ratios of these water masses are expected to increase along the water mass transport paths if there is no influence from the external sources of REEs. The cruise section provides several opportunities to test the potential effects of external REE input from eolian dusts,

nepheloid layer, oceanic basalts, and continental margins. All of these features have the potential to change the seawater REE concentrations or Nd isotopic compositions. The REE and Nd isotopic distributions in the SAMT will allow us to investigate to what extent they could be used as conservative water mass tracers and their implications in reconstructing paleo-ocean circulation in this region.

## 2. South Atlantic Hydrography

The water mass hydrographic properties and their circulation are described in detail in the Supplementary Information Section 1 (Fig. S1-S11). The northern-sourced water masses observed in the SAMT are upper NADW (UNADW) with neutral density ($\gamma^n$) of 27.75-27.98 kg/m$^3$, middle NADW (MNADW; $\gamma^n$ = 27.98-28.07 kg/m$^3$), and lower NADW (LNADW; $\gamma^n$ = 28.07-28.12 kg/m$^3$) ($\gamma^n$ all from (Vanicek and Siedler, 2002)), which are characterized by high salinity (S = 34.9-35.0 for UNADW, MNADW and LNADW). NADW enters the western basin of South Atlantic Ocean along the western boundary and turns eastward at ~40°S (Reid, 1994; Larqué et al., 1997; Stramma and England, 1999), which is reflected in the salinity section profile of the SAMT where it starts to disappear at ~35°S near Station 8 of the SAMT (SAMT-8) (Fig. 2a).

In the shallow Southwest Atlantic Ocean, the southern-sourced South Atlantic Central Water (SACW) originates from subducted surface water and has a range of salinities and potential temperatures (Talley, 2011). The neutral density of SACW ranges from 26.6 kg/m$^3$ to 27.15 kg/m$^3$ (Vanicek and Siedler, 2002). It is recognized as the long linear branch on the potential temperature vs. salinity diagram (Stramma and England,

1999) (Fig. 3a). The southern-sourced AAIW ($\gamma^n$ = 27.15-27.55 kg/m$^3$; (Vanicek and Siedler, 2002)) is characterized by the salinity minimum (Fig. 2a,3). Two types of the southern-sourced AAIW are formed (Gordon et al., 1992) (Fig. S1e): (1) in the Atlantic sector of the Southern Ocean (here labeled aAAIW), where it flows northward to ~40°S before moving eastward around the South Atlantic Gyre; and (2) in the Indian sector of the Southern Ocean (here labeled iAAIW), where it moves northwest and then westward at ~20°S before it reaches the western boundary and separates into two directions (southward from ~20°S to ~40°S and northward forward). These two types of AAIW and their mixing are clearly seen in the hydrographic diagrams (Fig. 3b). The southern-sourced water mass Circumpolar Deep Water (CDW) is penetrated by the NADW and separated into upper CDW (UCDW; $\gamma^n$ = 27.55-27.88 kg/m$^3$) and lower CDW (LCDW; $\gamma^n$ = 28.12-28.24 kg/m$^3$) ($\gamma^n$ both from (Vanicek and Siedler, 2002)). In the SAMT, UCDW and LCDW show decreasing thicknesses as they move northward (Fig. 2). The southern-sourced water mass Antarctic Bottom Water (AABW; $\gamma^n$ = 28.24-28.4 kg/m$^3$; (Orsi et al., 1999; Heywood and King, 2002; Orsi et al., 2002; Vanicek and Siedler, 2002; Klatt et al., 2005)) enters the Argentine Basin along the South Sandwich Trench and then flows northward along the western boundary (Reid, 1994; Larqué et al., 1997; Stramma and England, 1999). In the SAMT, the thickness of AABW decreases as it moves northward (Fig. 2).

## 3. Methods

### *3.1. Sampling*

Seventeen vertical profiles of seawater samples, with 16 samples at different depths for each station, were collected in the GEOTRACES GA02 Cruise Leg 3 from Punta Arenas (Chile) to Las Palmas (Spain), March-April 2011. 5-10 L of seawater samples were collected depending on the sample depth and stored in acid-cleaned cubitainers for each sample. The samples were filtered using 0.2 μm Sartobran cartridges and acidified using ultrapure Seastar hydrochloric acid (HCl) to pH ~ 2 shortly after sampling.

### *3.2. REE concentrations*

Aliquots of ~50 mL were taken from each sample for REE concentration analyses. About 10 mL of each filtered sample was weighed and 30-300 mg of a mixed REE spike in 1N $HNO_3$ was added. The spike was diluted (1:36744) from a mixed REE spike enriched in $^{142}$Ce, $^{145}$Nd, $^{149}$Sm (samarium), $^{153}$Eu, $^{155}$Gd (gadolinium), $^{161}$Dy (dysprosium), $^{167}$Er (erbium), and $^{171}$Yb (ytterbium) (Table 1) made and calibrated by Professor Gilbert Hanson at The State University of New York at Stony Brook. The diluted spike was recalibrated against Nd standard (High Purity Standards) using reverse isotope dilution. The mixed sample-spike solutions were stored in acid-cleaned 30 mL HDPE bottles and left to sit for at least 24 hours for equilibration.

The REEs were pre-concentrated using the ESI SC-DX seaFast®-pico system (purchased in June 2013) in offline mode (Behrens et al., 2016). The seaFast® system uses a chelating resin with ethylenediaminetriacetic acid and iminodiacetic acid

functional groups to preconcentrate trace metals and remove anions and alkali and alkaline earth cations (http://www.icpms. com/pdf/seaFAST-seawater-analysis.pdf). This system consists of an autosampler, a preconcentration column (200 μL of chelating resin), a cleanup column (200 μL of chelating resin), triple 6-port valves, Teflon plumbing and sample loop reservoir, all-Teflon syringe pumps, an ultra-low particulate air enclosure, and reservoirs of buffer solution, elution acid and high purity water (http://www.icpms.com/PDF/seaFAST-pico-open-ocean seawater.pdf). The solutions for the seaFast® system were prepared with high purity chemicals (Optima™ quality, Fisher Chemical) and high purity water (18.2 MΩ cm, from a MilliQ® ICP Advantage A10 System). The buffer solution (pH = 6.0 ± 0.2) was prepared using 834 mL of high purity water, 70 mL of 17.5 N high purity glacial acetic acid (Optima™ quality, Fisher Chemical), and 96 mL of high purity 11.4 N ammonium hydroxide (Optima™ quality, Fisher Chemical). The 1.6 N nitric acid ($HNO_3$) elution acid was made from double distilled concentrated nitric acid (Certified ACS Plus grade, Fisher Chemical). For each sample, the mixed sample-spike solution (~10 mL) was loaded into the sample loop and mixed with buffer solution to maintain a pH = 6. The mixing solution was pumped through the preconcentration column at a flow rate of 0.5 mL/min. Then the column was cleaned by passing buffer solution and high purity water to remove the seawater matrix. The REEs were then eluted into acid-cleaned 2 mL vials in three steps each of 100 μL of 1.6 N $HNO_3$ at an initial flow rate of 0.1 mL/min and a final flow rate of 0.5 mL/min. The offline mode of REE preconcentration for ~10 mL of seawater sample took ~15 minutes for each sample.

REE concentrations were measured on a VG PQ ExCell® quadrupole inductively coupled plasma-mass spectrometer (ICP-MS) at Lamont-Doherty Earth Observatory (LDEO) of Columbia University. The instrument was coupled to a desolvation introduction system (CETAC Aridus) that minimized molecular oxide ion formation with a self-aspirated Apex ST PFA micro flow nebulizer (Elemental Scientific ESI). The instrument was optimized for sensitivity and operated in pulse counting mode with 10 ms of dwell time for all isotopes. For each sample, 250 µL of 300 µL was used during 280 s of aspiration of sample for the analysis. Procedural blanks (n = 5) of 1% $HNO_3$ represent ≤ 0.9% of the sample intensities except for Ce (≤ 1.7%). To measure the total procedural blank, we processed 10 mL of ultrapure 1% $HNO_3$ through the seaFAST® the same way as the samples. At least 5 procedural blanks were processed during each seaFAST® session. Sample intensities were corrected by subtracting the procedural blank using $I_{meas} = I_{raw} - I_{procedural\_blk}$, where $I_{raw}$ is the raw intensity of the sample, $I_{procedural\_blk}$ is the intensity of the procedural blank and $I_{meas}$ is the intensity after procedural blank correction.

To correct for molecular oxide formation and interference at REE isotope masses, we did oxide calibration analysis by measuring masses of M and MO in pure, single element solutions of Ba and REE. This analysis was only needed once. The oxide calibration value is expressed as the ratio of $\frac{^{MO}I_{cal}}{^{M}I_{cal}}$, where $^{M}I_{cal}$ is the intensity of

mass M and ${}^{MO}I_{cal}$ is the intensity of mass MO measured during the calibration. For an unknown sample, the oxide interference for any mass M is calculated as ${}^{MO}I_{\text{int}} = \frac{{}^{MO}I_{cal}}{{}^{M}I_{cal}} \times {}^{M}I_{meas}$, where ${}^{M}I_{meas}$ is the measured intensity for any mass and ${}^{MO}I_{\text{int}}$ is the intensity of its oxide interference.

The oxide calibration values are not constant and need to be adjusted each time REEs are measured. However, the degrees to which the interfering elements form oxides are proportional to each other. Therefore, we analyzed $^{157}$PrO/$^{141}$Pr ratio of a 100 ng/L Pr solution during each session of REE measurement to get the correction factor $C = \frac{(\frac{{}^{157}\text{Pr}O}{{}^{141}\text{Pr}})_{today}}{(\frac{{}^{157}\text{Pr}O}{{}^{141}\text{Pr}})_{cal}}$, where $(\frac{{}^{157}\text{Pr}O}{{}^{141}\text{Pr}})_{cal}$ was measured during the oxide calibration analysis and $(\frac{{}^{157}\text{Pr}O}{{}^{141}\text{Pr}})_{today}$ was measured each time we analyzed REEs. Then the oxide interference is expressed as ${}^{MO}I_{\text{int}} = C \times \frac{{}^{MO}I_{cal}}{{}^{M}I_{cal}} \times {}^{M}I_{meas}$. The final true intensity without oxide interference is calculated as ${}^{MO}I_{ox\_cor} = {}^{MO}I_{meas} - C \times \frac{{}^{MO}I_{cal}}{{}^{M}I_{cal}} \times {}^{M}I_{meas}$.

We used the exponential law $R_c = R_m * (\frac{m_i}{m_j})^{\beta}$ to correct for mass fractionation, where $R_c$ is the mass fractionation corrected isotope ratio in the sample, $R_m$ is the measured isotope ratio in the sample, $m_i$ is the atomic mass of the numerator spike isotope, usually the one enriched in the spike, $mj$ is the atomic mass of reference isotope. To calculate $\beta$, we prepared a mass bias solution in which each REE has concentration of 100 ng/L and measured it during each REE measurement session. $\beta$ is expressed as $\beta = \frac{Ln(\frac{R_n}{R_{mb}})}{Ln(\frac{m_i}{m_j})}$, where $R_n$ is the ratio in natural samples, and $R_{mb}$ is the measured ratio in the mass bias solution.

The concentrations of spiked elements were calculated using isotope dilution equations. Taking Nd as an example, Nd concentration was calculated as $[Nd] = \frac{(\frac{^{143}Nd}{^{145}Nd})_{spk} - (\frac{^{143}Nd}{^{145}Nd})_{meas}}{(\frac{^{143}Nd}{^{145}Nd})_{meas} - (\frac{^{143}Nd}{^{145}Nd})_{nat}} * \frac{[^{145}Nd]_{spk}}{^{145Nd}Ab_{nat}} * \frac{m_{spk}}{m_{smpl}} * M_{Nd}$, where $(\frac{^{143}Nd}{^{145}Nd})_{spk}$ is the isotope ratio in the spike, $(\frac{^{143}Nd}{^{145}Nd})_{meas}$ is the isotope ratio in the measured sample-spike mixture, $(\frac{^{143}Nd}{^{145}Nd})_{nat}$ is the natural isotope ratio, $[^{145}Nd]_{spk}$ is the concentration of $^{145}$Nd in the spike (mol/g), $^{145Nd}Ab_{nat}$ is the natural abundance of $^{145}$Nd, $m_{spk}$ and $m_{smpl}$ are

spike and sample weights (g), and $M_{Nd}$ is the atomic mass of Nd (144.24 g/mol). Other elements calculated using the isotope dilution equation are Sm, Eu, Gd, Dy, Er, and Yb and henceforth will be called "ID elements".

Since $^{142}$Ce has an isobaric interference from Nd, $^{142}$Ce in the sample was calculated by subtracting interference of $^{142}$Nd from the sample and the spike using $^{142Ce}I_{smpl} = {}^{142Total}I_{smpl} - {}^{143Nd}I_{smpl} * (\frac{^{142}Nd}{^{143}Nd})_{nat} - {}^{143Nd}I_{spk} * (\frac{^{142}Nd}{^{143}Nd})_{spk}$, where $^{142Total}I_{smpl}$ is the intensity of mass 142 in the sample, $^{143Nd}I_{smpl}$ is the intensity of $^{143}$Nd in the sample, $(\frac{^{142}Nd}{^{143}Nd})_{nat}$ is the natural isotope ratio, $^{143Nd}I_{spk}$ is the intensity of $^{143}$Nd in the spike, and $(\frac{^{142}Nd}{^{143}Nd})_{spk}$ is the isotope ratio in the spike. Then the Ce concentration was calculated using the isotope dilution equation.

For mono-isotopic elements Pr, Tb, Ho and Tm, their concentrations were calculated by comparing their intensities to intensities of non-spike isotopes of ID elements. To calculate intensities of non-spike isotopes of ID elements, contributions from the spike need to be subtracted. Taking Nd as an example, the spike-free intensity for $^{143}$Nd was calculated as

$$^{143Nd}I_{spkfree} = {}^{143Nd}I_{total} - {}^{143Nd}I_{spk} = {}^{143Nd}I_{total} - \frac{(\frac{^{143}Nd}{^{145}Nd})_{nat} * {}^{145Nd}I_{total} - {}^{143Nd}I_{total}}{\frac{(\frac{^{143}Nd}{^{145}Nd})_{nat}}{(\frac{^{143}Nd}{^{145}Nd})_{spk}} - 1},$$

where $^{143Nd}I_{total}$ is the intensity of $^{143}$Nd in total, $^{143Nd}I_{spk}$ is the intensity of $^{143}$Nd in the spike, $^{145Nd}I_{total}$ is the intensity of $^{145}$Nd in total, $(\frac{^{143}Nd}{^{145}Nd})_{nat}$ is the natural isotope ratio, and $(\frac{^{143}Nd}{^{145}Nd})_{spk}$ is the isotope ratio in the spike. Then the relationship between ID element and mono-isotopic element was established by comparing their sensitivities in the mass bias standard solution. For Nd, the sensitivity of $^{143}$Nd was calculated as $^{143}Nd_{sens} = \frac{^{143Nd}I_{std}}{[Nd]_{std} * {}^{143Nd}Ab_{nat}}$, where $^{143Nd}I_{std}$ is the intensity of $^{143}$Nd in the standard solution, $[Nd]_{std}$ is the Nd concentration in the standard solution, and $^{143Nd}Ab_{nat}$ is the natural fractional abundance of $^{143}$Nd. For Pr, the sensitivity of $^{141}$Pr was calculated as $^{141}\mathrm{Pr}_{sens} = \frac{^{141\mathrm{Pr}}I_{std}}{[\mathrm{Pr}]_{std} * {}^{141\mathrm{Pr}}Ab_{nat}}$, where $^{141Pr}I_{std}$ is the intensity of $^{141}$Pr in the standard solution, $[\mathrm{Pr}]_{std}$ is the Pr concentration in the standard solution, and

$^{141Pr}Ab_{nat}$ is the natural abundance of $^{141}$Pr (=1). Then the sensitivity ratio $\frac{^{143}Nd_{sens}}{^{141}\mathrm{Pr}_{sens}}$ in the standard solution was used to calculate the Pr concentration in the sample using $[\mathrm{Pr}]_{smpl} = \frac{^{143}Nd_{sens}}{^{141}\mathrm{Pr}_{sens}} * \frac{^{141Pr}I_{smpl}}{^{143Nd}I_{smpl\_spkfree}} * \frac{[Nd]_{smpl} * ^{143Nd}Ab_{nat}}{^{141Pr}Ab_{nat}}$, where $^{141Pr}I_{smpl}$ is the intensity of $^{141}$Pr in the sample, $^{143Nd}I_{smpl\_spkfree}$ is the spike-free intensity for $^{143}$Nd in the sample, $[Nd]_{smpl}$ is the Nd concentration in the sample, $^{143Nd}Ab_{nat}$ is the natural abundance of $^{143}$Nd, and $^{141Pr}Ab_{nat}$ is the natural abundance of $^{141}$Pr (=1).

For spiked elements La and Lu, their spike isotopes $^{138}$La and $^{176}$Lu have very low abundances in both the DKM spike and natural samples. Their spike isotope/non-spike isotope ratios ($^{138}$La/$^{139}$La and $^{176}$Lu/$^{175}$Lu, respectively) in the DKM spike and natural samples have very small differences, which is not ideal for using isotope dilution calculations. Therefore, La and Lu were treated as mono-isotopic elements and were calculated using equations for mono-isotopic elements.

To ensure the accuracy of our method, seawater samples from a GEOTRACES intercalibration station BATS in the North Atlantic (Bermuda Atlantic Time-series; 31.7°N, 64.1°W) at 20 m and 2000 m have been repeatedly analyzed. Our measured REE concentrations of BATS at 20 m (n = 16) and BATS at 2000 m (n = 14) are listed in Table 2. The long-term external reproducibilities (2σ RSD%) for BATS at 20 m are 3.5% for Nd, 3.4% for Yb, and an average of 5.6% (± 1.1%, 1 σ) for the other REEs. The long-

term external reproducibilities for BATS at 2000 m are 2.8% for Nd, 4.6% for Yb, and an average of 4.1% (± 1.3%, 1 σ) for the other REEs. The results for BATS at 2000 m measured in this study are compared with GEOTRACES intercalibration values (van de Flierdt et al., 2012) and they agree with each other very well (Table 2). We participated in an international intercomparison study of seawater REEs where four labs analyzed seawater from a GEOTRACES station SAFe in the North Pacific (Sampling and Analysis of Fe; 30°N, 140°W) at 3000 m (Behrens et al., 2016). Our analyzed REE concentrations of SAFe at 3000 m agree well with values from the other labs. The REE concentrations of SAFe at 3000 m from four labs show great agreement with < 7% reproducibility for all REEs (2σ SD), except for Ce (71%, 2σ SD), Gd (14%, 2σ SD) and Lu (12%, 2σ SD) (Behrens et al., 2016). Our results of seawater REE concentrations from the SAMT are presented in Table 3.

### *3.3. Calculating REE deviations*

To investigate how much REEs deviate from conservative behavior, we compared the measured REE concentrations with predicted values calculated from conservative water mass mixing of end-members. The first step to calculate the predicted REEs is to define the water mass end-member compositions. The shallow water above the depths of SACW has not been taken into account because REEs and εNd at these depths (0-250 m) do not behave conservatively. The neutral densities are defined according to the hydrographic characteristics of each water mass: the salinity maximum for UNADW (Fig. 2a), the oxygen minimum for MNADW in the northernmost SAMT-17 and SAMT-18 (Fig. 2c), the oxygen maximum for LNADW in the northernmost SAMT-17 and

SAMT-18 (Fig. 2c), the salinity minimum for aAAIW (Fig. 2a), the oxygen minimum for UCDW (Fig. 2c), the salinity maximum for LCDW in the southernmost SAMT-1 and SAMT-2 (Fig. 2a), and the lowest potential temperature for AABW (Fig. 2b). Then the values for the other parameters (salinity, potential temperature, $PO_4^*$, silicate, and oxygen concentration) corresponding to the neutral densities of these water masses were used as end-member compositions (Supplementary Information Section 2; Fig. S2-S11).

We defined the water mass end-members based on the SAMT data that best represents it as well as published εNd and REE data in the water mass formation regions (WMFR) (Supplementary Information Section 2 and 3; Fig. S2-S11; Table 4). The end-members defined from SAMT and WMFR were compared in diagrams of potential temperature vs. salinity and Nd concentration ([Nd]) vs. εNd (Fig. S12; Table 4). For the northern-sourced water masses, end-members defined from the northernmost stations of the SAMT have values very close to end-member values in the WMFR near a GEOTRACES intercalibration station BATS in the North Atlantic (Fig. S12). For the southern-sourced water masses, aAAIW, UCDW and LCDW values defined from SAMT are close to values defined from published data in the WMFR (Fig. S12). The AABW values defined from the southernmost stations of SAMT are higher in εNd (= −8.0) and [Nd] (= 36.99 pmol/kg) than AABW values in the Drake Passage (εNd = −9.0, [Nd] = 26.07 pmol/kg) (Fig. S12), its WMFR, which indicates that a high εNd signal is added to AABW along its transport path from the Drake Passage to the southernmost stations of SAMT (Supplementary Information Section 2 and 3). The iAAIW end-member values of SAMT and WMFR are similar in [Nd] but different in εNd (Fig. S12). Along the iAAIW

pathway from southeast Atlantic to SAMT-13, the εNd signal of iAAIW is modified without [Nd] change (Supplementary Information Section 2 and 3). Therefore, we used water mass end-member compositions defined from the SAMT data (Fig. 3b,S2; Table 4) for deviation calculations because they show εNd and REE signatures when the water masses reach the stations of the SAMT (especially for AABW and iAAIW) and are more representative of the processes occurring within the SAMT.

The calculation of fractional contribution from different water masses discussed below is based on salinity and potential temperature (Fig. 3b) using the following three component mixing equations assuming that each sample reflects mixing of three water mass end-members:

$$f_1 \times \theta_1 + f_2 \times \theta_2 + f_3 \times \theta_3 = \theta$$

$$f_1 \times S_1 + f_2 \times S_2 + f_3 \times S_3 = S$$

$$f_1 + f_2 + f_3 = 1$$

$$f_i > 0$$

where $f_i$, $\theta_i$ and $S_i$ are the fractional contributions, potential temperature and salinity values of water mass i, respectively. Then the predicted REE concentrations (e.g. Nd and Yb) were calculated as:

$$[Nd]_{predicted} = [Nd]_1 \times f_1 + [Nd]_2 \times f_2 + [Nd]_3 \times f_3$$

$$[Yb]_{predicted} = [Yb]_1 \times f_1 + [Yb]_2 \times f_2 + [Yb]_3 \times f_3$$

where $[Nd]_i$ and $[Nd]_i$ are the Nd and Yb concentrations of water mass i, and $f_i$ is the fractional contribution of water mass i. The predicted $Yb_n/Nd_n$ values were calculated as:

$$(\mathrm{Yb_n/Nd_n})_{\mathrm{predicted}} = \frac{[\mathrm{Yb}]_{\mathrm{predicted}}/[\mathrm{Yb}]_{\mathrm{PAAS}}}{[\mathrm{Nd}]_{\mathrm{predicted}}/[\mathrm{Nd}]_{\mathrm{PAAS}}}$$

where n stands for the concentration of an element in the sample normalized to its concentration in PAAS (Taylor and McLennan, 1985), $[\mathrm{Yb}]_{\mathrm{predicted}}$ and $[\mathrm{Nd}]_{\mathrm{predicted}}$ are the predicted concentrations, and $[\mathrm{Yb}]_{\mathrm{PAAS}}$ and $[\mathrm{Nd}]_{\mathrm{PAAS}}$ are the Yb and Nd concentrations in PAAS. The deviations for the measured values were calculated by subtracting the predicted values:

$$\Delta[\mathrm{Nd}] = [\mathrm{Nd}]_{\mathrm{measured}} - [\mathrm{Nd}]_{\mathrm{predicted}}$$

$$\Delta[\mathrm{Yb}] = [\mathrm{Yb}]_{\mathrm{measured}} - [\mathrm{Yb}]_{\mathrm{predicted}}$$

$$\Delta(\mathrm{Yb_n/Nd_n}) = (\mathrm{Yb_n/Nd_n})_{\mathrm{measured}} - (\mathrm{Yb_n/Nd_n})_{\mathrm{predicted}}$$

Delta values close to zero mean that the measured values are close to the predicted values and indicate conservative behavior. The above delta REE concentrations (Δ[REE]) and delta REE ratios (Δ(REE ratio)) were compared with predicted values based on conservative water mass mixing as the percent deviations of the measured value from the predicted value, i.e. Δ[REE]/Predicted [REE]×100 and Δ(REE ratio)/Predicted (REE ratio)×100. Here we define Δ[REE]/Predicted [REE] and Δ(REE ratio)/Predicted (REE ratio) as Δ[REE](%) and Δ(REE ratio)(%), respectively.

The REE deviations have also been calculated based on two other combinations of conservative water mass tracers: (i) $PO_4^*$ and potential temperature; (ii) $PO_4^*$ and salinity. This will allow us to investigate whether REE deviations will be different from results calculated based on salinity and potential temperature. The calculations based on

(i) $PO_4^*$ and potential temperature; (ii) $PO_4^*$ and salinity are shown in Supplementary Information Section 6.

## 4. Results and Discussions

### *4.1. REE patterns*

PAAS-normalized seawater REE patterns from the SAMT are consistent with typical seawater REE patterns, with negative Ce anomalies, increasing REE concentrations with depth, and relative enrichment of HREEs compared to LREEs (Fig. S34). Seawater REE patterns of three SAMT stations SAMT-18, SAMT-8, and SAMT-2 are shown in Fig. 4 to represent stations at the equator, in the mid-latitude, and in the far south, respectively. REE patterns are usually shown on logarithmic scales of y-axis. Here we show them in a linear y-axis to emphasize similarities and differences. These three stations show typical seawater REE patterns and their patterns increasingly fan out from SAMT-18 to SAMT-8 to SAMT-2 (Fig. 4).

The SAMT seawater REE patterns also show that the relative abundances of REEs gradually increase with increasing atomic number from praseodymium (Pr) to ytterbium (Yb) (Fig. 4). Therefore, we are particularly interested in Ce, Nd, and Yb as well as the following related REE ratios. The Ce anomaly ($Ce/Ce^*$) is calculated as $2\times Ce_n/(La_n + Pr_n)$ with low $Ce/Ce^*$ values close to 0 indicating strong negative Ce anomalies. Here $REE_n$ stands for PAAS-normalized REE concentrations of the samples. To investigate the fractionation within the REE group, $Yb_n/Nd_n$ is calculated as an

indicator of HREE/LREE with higher $Yb_n/Nd_n$ values corresponding to stronger Yb enrichment.

REEs accumulate along the water mass transport paths from the North Atlantic, to the Southern Ocean, and then to the North Pacific. The REE patterns of the intermediate and deep water masses defined from end-member compositions of the SAMT are compared with that in the North Atlantic and North Pacific (Fig. 5). REE data for NADW in the North Atlantic are based on published data in the GEOTRACES calibration station BATS ((Pahnke et al., 2012; van de Flierdt et al., 2012; Lambelet et al., 2016); GEOTRACES GA03 REE data). REE data for NPIW, NPDW, and LCDW in the North Pacific are average values of each water mass from Wu et al. (Chapter 4 of this thesis). For the intermediate water, aAAIW and iAAIW from the SAMT show lower REE concentrations than NPIW in the North Pacific (Fig. 5a). For the deep water, NADW from the SAMT show similar REE concentrations compared to that in the North Atlantic and much lower REE concentrations than NPDW in the North Pacific (Fig. 5b). For the bottom water, LCDW and AABW from the SAMT have much lower REE concentrations than LCDW in the North Pacific (Fig. 5c). PAAS-normalized REE patterns for intermediate and deep water show that REE abundances increase from the North Atlantic to the North Pacific (Fig. 5).

### *4.2. Vertical changes of REEs*

Vertical profiles of SAMT-18 at the equator, SAMT-8 in the mid-latitude and SAMT-2 in the far south are shown in Fig. 6 to illustrate the mismatch of Nd concentration and εNd. Nd concentrations appear to behave like nutrients and increase

with depth below ~100 m ($\gamma^n$ > 27.15 kg/m$^3$) (Fig. 6a,7a). Other REEs (except Ce) also show increasing concentrations with depth below ~100 m (e.g. Yb; Fig. 7b). However, εNd-values behave "quasi-conservatively" and show mixing of different water masses. For example, SAMT-8 shows the mixing of NADW and CDW between natural densities of 27.75 and 28.12 kg/m$^3$ (Fig. 6b).

Low $Yb_n/Nd_n$ values are observed at the surface of all stations (1.9-3.5; Fig. 9c), which are consistent with observations in previous studies (e.g. (Jeandel et al., 2013)). Then $Yb_n/Nd_n$ values increase to the maximum values at ~1000 m (4.4-6.0; Fig. 9c) before decreasing with increasing depth (Fig. 8a). We further investigate whether these vertical changes of $Yb_n/Nd_n$ values result from water mass mixing or lithogenic input in Section 4.6.

Ce concentrations are the highest at the surface for all stations and they sharply decrease to < 8 pmol/kg below ~250 m (Fig. 7c). The highest $Ce/Ce^*$ values are also observed at surface for all stations and they sharply decrease to < 0.16 below ~500 m (Fig. 8b). These results are consistent with observations in previous studies and indicate rapid Ce oxidation and removal in the shallow water in the open oceans as well as oxidative removal of Ce from the deep ocean (e.g. (German et al., 1995)).

### *4.3. Advective changes of REEs*

The REE changes along the lateral advection of water masses are observed in the vertical profiles of the SAMT. For example, Nd concentrations of NADW between neutral densities of 27.75 and 28.12 kg/m$^3$ gradually decrease along the NADW pathway from the equator (SAMT-18) to ~17°S (SAMT-13) to ~35°S (SAMT-8) (Fig. 6c). εNd-

values of NADW ($\gamma^n$ = 27.75-28.12 kg/m$^3$) gradually increase along the transport path of NADW (Fig. 6d). $Yb_n/Nd_n$ ratios also change systematically along the water mass transport paths. For example, $Yb_n/Nd_n$ ratios of UNADW (e.g. ~1500 m) increase from northern to southern stations (Fig. 8a). The above observations indicate the weakening of the NADW signal and increasing influence of the southern-sourced water masses along the NADW transport path from the equator to the south.

We further investigate how REEs change for each intermediate and deep water mass along their transport paths in Supplementary Information Section 4 (Fig. S14-S22). For each intermediate and deep water mass, Yb concentrations show the strongest conservative behavior with an average of 91% (± 8%, 1σ) of the values falling within the mixing triangles of water mass end-members. Nd concentrations and $Yb_n/Nd_n$ ratios, with averages of 81% (± 17%, 1σ) and 77% (± 19%, 1σ) of the values falling within the mixing triangles of water mass end-members, show less conservative behavior compared to Yb concentrations. An explanation for stronger conservative behavior of Yb is that Yb is more soluble in seawater and less preferentially scavenged compared to Nd. The resulting $Yb_n/Nd_n$ ratios are similar to Nd concentrations and they are more sensitive to test conservative mixing vs. external addition processes compared to Yb concentrations. εNd-values of the above intermediate and deep water masses show conservative behavior with an average of 86% (± 12%, 1σ) of the values falling within the mixing triangles of water mass end-members. Therefore, REEs of each intermediate and deep water mass generally show conservative mixing along water mass advective pathways (Supplementary Information Section 4).

### *4.4. Source of REEs to the surface water*

Nd concentrations of most stations from the SAMT are enriched near the surface (~25 m) compared to the subsurface (~100 m) (Fig. 9a), whereas Yb concentrations of most stations increase with depth from ~25 m to ~100 m (Fig. 9b). In addition, the highest Ce concentrations, the highest $Ce/Ce^*$ ratios and very low $Yb_n/Nd_n$ values are also observed in near surface water at ~25 m (Fig. 9c,10a,10b). These REE characteristics of the surface water reflect lithogenic contributions, from which LREEs are more preferentially released compared to HREEs (e.g.(Zhang and Nozaki, 1998)). This is further supported by the following εNd isotope evidence of surface/subsurface water.

Eolian dusts are lithogenic sources that could add external REEs to the surface seawater. The trade winds between the equator and ~35°S transport eolian dusts with low εNd (−19 to −8) from Africa (Goldstein et al., 1984; Dia et al., 1990) (Fig. 11a). The westerlies south of ~35°S transport eolian dusts with high εNd (−4.0 to +4.8) from South America to the ocean (Goldstein et al., 1984; McLennan et al., 1990; Henry et al., 1996; Basile et al., 1997; Gaiero et al., 2007; de Mahiques et al., 2008; Rousseau et al., 2015; Gili et al., 2017) (Fig. 11a). From ~35°S to the equator, εNd-values (−17.7 to −11.4) of the surface/subsurface seawater (25-100 m) from SAMT-8 to SAMT-16 (~35°S to the equator) are consistent with that of surface sediments eroded from Africa (−19 to −8) (Goldstein et al., 1984; Dia et al., 1990) (Fig. 11a,b). εNd-values of these samples from ~35°S to the equator (−17.7 to −11.4) are also consistent with that of surface sediments eroded from Rio de La Plata, Brazil, and Amazon (−17.1 to −7.5) (Goldstein et al., 1984; Henry et al., 1996; de Mahiques et al., 2008; Rousseau et al., 2015) (Fig. 11a,b). In

addition to eolian input from Africa, it is possible that boundary exchange between seawater and South American marginal sediments also influence εNd-values of the surface and subsurface water from ~35°S to the equator. South of ~35°S, εNd-values of the surface/subsurface water (25-100 m) from SAMT-1 to SAMT-7 (−11.3 to −6.9) are lower than that of surface sediments eroded from Patagonia and Falkland Island (−4.4 to +4.8) (Goldstein et al., 1984; McLennan et al., 1990; Henry et al., 1996; Basile et al., 1997; Gaiero et al., 2007; de Mahiques et al., 2008; Rousseau et al., 2015; Gili et al., 2017) (Fig. 11a,b). They have similar εNd-values compared to that of surface sediments eroded from Rio de La Plata and Brazil between ~25°S and ~35°S (Fig. 11a,b). Since the Brazil current transports southwestward along South America (Fig. S1d), it can bring Nd isotopic signal from Rio de La Plata and Brazil between ~25°S and ~35°S to the surface/subsurface water south of ~35°S (Fig. 11a). In general, surface/subsurface εNd-values are consistent with terrigenous contributions of Nd to surface/subsurface seawater. The εNd variability of surface/subsurface water is larger than that of intermediate and deep water (Fig. 11c). For example, the surface/subsurface water εNd-values of SAMT-11 to 14 and SAMT-16 (εNd as low as −18) are lower than the lowest values of intermediate and deep water (εNd as low as −13) (Fig. 11c). The surface/subsurface water εNd-values of SAMT-3 and SAMT-5 (εNd as high as −7) exceed the highest values of intermediate and deep water (εNd as high as −8) (Fig. 11c). ΔεNd-values of intermediate and deep water from the above stations show that 48% of ΔεNd-values are within the range of −0.25 to +0.25 εNd units and 89% of ΔεNd-values are within the range of −0.75 to +0.75 εNd units (Fig. 11d). This indicates very small deviations to conservative mixing

for intermediate and deep water samples. Therefore, the surface/subsurface water εNd signature is not transferred to intermediate and deep water.

### *4.5. Influence of oxygen on REEs in the shallow water*

SACW occurs at 250-500 m (depending on location) between SAMT-5 (~42°S) and SAMT-18 (~0°S) (Fig. 2). From SAMT-15 (~9°S) to SAMT-18 (~0°S), low oxygen concentrations (Fig. 9d) and high Nd concentrations (Fig. 9a) are observed between 250 m and 500 m in the oxygen depleted zone (ODZ). Both Nd and Yb concentrations show negative correlations with oxygen concentrations (Fig. 12a,b). Since REEs are released when Fe-Mn oxides dissolve in reducing conditions (e.g. (de Baar et al., 1988; German and Elderfield, 1989; German et al., 1991; Sholkovitz et al., 1992; Schijf et al., 1995)), it is likely that the increased Nd and Yb concentrations in the ODZ reflect addition of these elements with dissolution of Fe-Mn oxides.

Ce is very insoluble in oxic conditions, therefore Ce abundances are expected to increase under anoxic conditions due to reductive regeneration. However, Ce concentrations still decrease in the ODZ from SAMT-15 (~9°S) to SAMT-18 (~0°S) (Fig. 10a), indicating that the oxidative removal of Ce exceeds reductive regeneration. Estimates of the threshold oxygen concentrations enabling reductive regeneration of REEs range from 15 to 40 μmol/kg (German and Elderfield, 1990; Stichel et al., 2015; Zheng et al., 2016). The oxygen concentrations in the ODZ of SAMT (90-125 μmol/kg; Fig. 9d) are much higher than the above threshold value (15 to 40 μmol/kg) and are not low enough for the reduction of Ce.

Increasing REE concentrations (except Ce) of the shallow water in the ODZ indicate external addition of these elements from dissolution of Fe-Mn oxides in reducing conditions. However, the oxygen concentration in the ODZ from this transect is still much higher than the threshold value for the reduction of Ce. Therefore, we do not observe increasing Ce of the shallow water in the ODZ from this transect.

### *4.6. Conservative vs. non-conservative behavior of REEs in the SAMT intermediate and deep water*

To investigate whether increasing REE concentrations with depth for intermediate and deep water result from water mass mixing or other processes such as scavenging in the shallow water and remineralization in the deep layers, we first compare REE concentrations and ratios with water mass tracers below, and found that to a first order, they reflect water mass mixing and conservative behavior of REEs (Section 4.6.1). To further differentiate the conservative and non-conservative components of the REEs, predicted REE concentrations and ratios based on conservative water mass mixing are calculated and compared with measured values. We will discuss below to what extent intermediate and deep water REEs behave conservatively, and identifying locations where they deviate from conservative water mass mixing.

#### *4.6.1. Comparison of REEs with water mass tracers*

Nd and Yb concentrations are compared with salinity and $PO_4^*$ below the depths of AAIW (Fig. 13). Each station shows a maximum salinity that also is the minimum $PO_4^*$, indicating the strongest influence of northern-sourced NADW at that station (Fig. 13). They show mixing of iAAIW-NADW-AABW in the northern-most stations, mixing

of aAAIW-UCDW-LCDW-AABW in the southern-most stations, and intermediate values between the above mixing curves in the mid-latitude stations (Fig. 13). A gap is seen between stations south and north of ~35°S (SAMT-8) in the above diagrams (Fig. 13). Deep water south of SAMT-8 shows mixing of AABW and LCDW, whereas deep water north of SAMT-8 shows mixing of AABW and NADW (Fig. 13).

$Yb_n/Nd_n$ ratios are compared with salinity, $PO_4^*$, and εNd below the depths of AAIW (Fig. 14). Similar to diagrams of REE concentrations vs. tracers, diagrams of $Yb_n/Nd_n$ ratios vs. tracers also show mixing of iAAIW-NADW-AABW in the northern-most stations, mixing of aAAIW-UCDW-LCDW-AABW in the southern-most stations, and intermediate values between the above mixing curves in the mid-latitude stations (Fig. 14). The gap between stations south and north of ~35°S (SAMT-8) is also observed, where deep water shows AABW-LCDW mixing south of SAMT-8 and AABW-NADW mixing north of SAMT-8 (Fig. 14).

Diagrams of $Yb_n/Nd_n$ vs. 1/[Nd] (Fig. 15a) and $Nd_n/Yb_n$ (reversed scale) vs. 1/[Yb] (Fig. 15b) are used to investigate how conservative Yb and Nd is, respectively and which one is more sensitive to test conservative mixing vs. external addition processes. Averages of the concentrations are used to calculate water mass end-member ratios (black crosses in Fig. 15) so they might not be in the middle of the samples. Mixing between water mass end-members should be linear in these diagrams (grey lines in Fig. 15). Most of the samples fall within the area made by the mixing lines indicating their conservative behavior (Fig. 15). Samples falling out of the area made by the mixing lines indicate their non-conservative behavior (Fig. 15). If there are less samples falling within

the area made by the mixing lines in $Nd_n/Yb_n$ vs. 1/[Yb] (Fig. 15b) compared to that in $Yb_n/Nd_n$ vs. 1/[Nd] (Fig. 15a), it means that Nd is more sensitive to test conservative mixing vs. external addition processes compared to Yb. Here it is not very easy to observe which one is more sensitive than the other. So we further discuss their sensitivity to test conservative mixing vs. external addition processes based on the calculations of their deviations from conservative water mass mixing in Section 4.6.2 (Fig. 16). Samples showing non-conservative behavior are intermediate water samples at SAMT-1 to SAMT-5 (higher $Yb_n/Nd_n$ or lower $Nd_n/Yb_n$ values than the mixing line of aAAIW-UCDW) and bottom water samples at most of the stations (lower $Yb_n/Nd_n$ values or higher $Nd_n/Yb_n$ values than the mixing line of AABW-LNADW) (Fig. 15), which are further discussed in Section 4.6.3. The separation of the data from stations south and north of ~35°S is also observed. Deep water shows mixing of AABW and LCDW from SAMT-1 to SAMT-7 and mixing of AABW and NADW from SAMT-8 to SAMT-18 (Fig. 15).

Southward flowing NADW shifts eastward at ~35°S (Talley, 2011) at station SAMT-8 (Fig. S1a-c,S3-S5), and the gap in the above diagrams (Fig. 13-15) reflect this eastward shift of NADW. That is, stations north of ~35°S show influence of NADW before it turns eastward, whereas stations south of ~35°S show very little influence of NADW (Fig. 13-15).

*4.6.2. Intermediate and deep water dominantly controlled by conservative mixing*

The REE deviations from conservative water mass mixing are calculated to evaluate conservative vs. non-conservative behavior of REEs. Here we show Δ[REE](%)

and Δ(REE ratio)(%) of the Southwest Atlantic seawater samples calculated based on salinity and potential temperature (Fig. 16-18). The following discussion refers to REE concentrations, REE ratios, and εNd-values as "too high" if measured values are higher than predicted by the water mass mixtures, and "too low" if they are lower than predicted by the water mass mixtures. Δ[REE](%) and Δ(REE ratio)(%) values within ± 5% are considered conservative. ΔεNd-values within ± 0.25 εNd units are considered conservative.

Out of 198 intermediate and deep samples, 51% of the Δ[Nd](%) values are within ± 5% and 96% of the Δ[Nd](%) values are within ± 15% (Fig. 16a). 68% of the Δ[Yb](%) values are within ± 5% and 98% of the Δ[REE](%) values are within ± 15% (Fig. 16b). 54% of the $\Delta(Yb_n/Nd_n)$(%) values are within ± 5% and 99.5% of the $\Delta(Yb_n/Nd_n)$(%) values are within ± 15% (Fig. 16c). Δ[Nd](%) values have a median of −2% and an average of 0% ± 8% (1σ) (Table 5). Δ[Yb](%) values have a median of +1% and an average of +1% ± 6% (1σ) (Table 5). $\Delta(Yb_n/Nd_n)$(%) values have a median of +3% and an average of +2% ± 6% (1σ) (Table 5). Lower number of intermediate and deep samples considered conservative (within ± 5% of Δ[REE](%)) means higher sensitivity to test conservative mixing vs. external addition processes. Compared to Yb, Nd and $Yb_n/Nd_n$ are more sensitive to test conservative mixing vs. external addition processes. Evaluation of conservative behavior of REEs based on salinity and potential temperature shows small deviations from conservative water mass mixing.

The REE deviations for each sample are also calculated based on (i) $PO_4^*$ and potential temperature; (ii) $PO_4^*$ and salinity (Supplementary Information Section 6). They

both show similarly small deviations from conservative water mass mixing (Supplementary Information Section 7; Fig. S28-S33). Deviation calculations based on $PO_4^*$ and potential temperature show that 50% of the Δ[Nd](%) values are within ± 5% and 88% of the Δ[Nd](%) values are within ± 15% (Fig. S28a). 70% of the Δ[Yb](%) values are within ± 5% and 97% of the Δ[REE](%) values are within ± 15% (Fig. S28b). 55% of the $\Delta(Yb_n/Nd_n)$(%) values are within ± 5% and 98% of the $\Delta(Yb_n/Nd_n)$(%) values are within ± 15% (Fig. S28c). Deviation calculations based on $PO_4^*$ and salinity show that 52% of the Δ[Nd](%) values are within ± 5% and 93% of the Δ[Nd](%) values are within ± 15% (Fig. S29a). 74% of the Δ[Yb](%) values are within ± 5% and 97% of the Δ[REE](%) values are within ± 15% (Fig. S29b). 56% of the $\Delta(Yb_n/Nd_n)$(%) values are within ± 5% and 97% of the $\Delta(Yb_n/Nd_n)$(%) values are within ± 15% (Fig. S29c). Therefore, evaluations of conservative behavior of REEs based on three combinations of tracers show that REEs in the intermediate and deep water are dominantly controlled by conservative water mass mixing.

The section profile of Δ[Nd](%) shows very slight [Nd] subtraction (−5% to 0%, almost conservative) in the northward flowing aAAIW, UCDW and LCDW and the southward flowing UNADW and MNADW (Fig. 17b). Most ΔεNd values of these samples are within ± 0.25 (Fig. 18c), which is within the analytical error (± ~0.3). Small amounts of [Nd] addition (0% to +5%, almost conservative) are observed in the northward flowing iAAIW and AABW and the southward flowing LNADW (Fig. 17b). Most ΔεNd values of these samples range from –0.75 to 0, indicating εNd-values equal to or lower than predicted values based on water mass mixing (Fig. 18c). The section

profile of Δ[Yb](%) is similar to that of Δ[Nd](%), although slight [Yb] addition is observed in the southward flowing UNADW (0% to +5%, almost conservative) (Fig. 17c). The section profile of $\Delta(Yb_n/Nd_n)(\%)$ shows values > 0 in the northward aAAIW, iAAIW, UCDW, and LCDW and values < 0 in the southward NADW and the northward AABW (Fig. 18b).

*4.6.3. Non-conservative behavior of REEs in different water masses*

Delta values were further separated into three groups using the neutral densities of the water mass end-members (Table 4a) to investigate deviations from conservative mixing for REE concentrations and ratios within each depth range: (1) from depths of AAIW to UNADW ($\gamma^n$ = 27.15-27.90 kg/m$^3$); (2) from depths of UNADW to LNADW ($\gamma^n$ = 27.90-28.11 kg/m$^3$); (3) from depths of LNADW to the bottom ($\gamma^n$ > 28.11 kg/m$^3$) (Fig. 16). This will allow us to investigate where in the water column the data show the most conservative behavior and the largest deviations from conservative behavior.

From depths of AAIW to UNADW, high Δ[Nd](%) (+11% ± 5%; 1σ) and high Δ[Yb](%) (+8% ± 4%; 1σ) are observed at 750-1000 m from SAMT-15 to SAMT-18 (Fig. 17b,c). ΔεNd-values of these samples have an average of −0.75 ± 0.77 (1σ) εNd units (Fig. 18c). Samples at 750-1000 m from SAMT-15 to SAMT-18 are in the ODZ (Fig. 2c,10c), where REEs could be released by dissolution of Fe-Mn oxides due to the reducing condition (e.g. (de Baar et al., 1988; German and Elderfield, 1989; German et al., 1991; Sholkovitz et al., 1992; Schijf et al., 1995)). Stations SAMT-15 to SAMT-18 in the trade wind zone receive eolian dusts from Africa with low εNd (−19 to −8) (Goldstein et al., 1984; Dia et al., 1990). Low εNd-values (−12.71 ± 0.60, 1σ) are observed in

SAMT-15 to SAMT-18 at 25-100 m (Fig. 11a,b). The low εNd signal in the surface water might influence samples at 750-1000 m from SAMT-15 to SAMT-18 with ΔεNd of −0.75 (± 0.77, 1σ). Therefore, high Δ[REE](%) and slightly low ΔεNd of the above samples reflect REEs with low εNd signal released by dissolution of Fe-Mn oxides in the ODZ.

From depths of UNADW to LNADW, ΔεNd-values of the northward flowing UCDW and LCDW from SAMT-1 to SAMT-3 have an average of 0.44 ± 0.28 (1σ) εNd units (Fig. 18c). These samples have slightly high Δ[Yb](%) = (+5% ± 2%; 1σ) and do not show high Δ[Nd](%) values (0% ± 2%; 1σ) (Fig. 17b,c). These stations in the far south are close to the continental margin, where marginal sediments from Patagonia are potential sources with high εNd (−4 to +5) (Goldstein et al., 1984; McLennan et al., 1990; Henry et al., 1996; Basile et al., 1997; Gaiero et al., 2007; de Mahiques et al., 2008; Rousseau et al., 2015; Gili et al., 2017). High ΔεNd of the above samples likely reflect small amounts of REEs added from these marginal sediments without significantly changing REE concentrations.

From depths of LNADW to the bottom, the Δ[REE](%) distributions are skewed to high values (Fig. 16a,b). They correspond to REE additions for samples in the bottom water from SAMT-8 to SAMT-18 in the Δ[REE](%) section profiles (Fig. 17b,c). The strongest additions of Nd and Yb (+20% and +17%, respectively) are seen at the bottom of SAMT-16 (~6°S) (Fig. 17b,c). ΔεNd-values of these samples have an average of −0.67 ± 0.65 (1σ) εNd units (Fig. 17c). These stations in the trade wind zone receive eolian dusts from Africa with low εNd (−19 to −8) (Goldstein et al., 1984; Dia et al., 1990). It is

observed that the surface (25 m) and subsurface (100 m) water show low εNd-values in these stations (Fig. 11a,b). The data suggest that REEs dissolved from dusts with this low εNd signature are scavenged in the shallow water and released by sediments at the bottom of the ocean after they sink to the sea floor. Therefore, high Δ[REE](%) and low ΔεNd of the above bottom water samples could be attributed to addition of dissolved REEs from deep sea sediments with low εNd signal.

### *4.7. Sources of REEs in the nepheloid layer*

A nepheloid layer with resuspended particles is observed within 500 m of the seafloor from SAMT-2 to SAMT-5 (~49°S to ~42°S). The particles in the nepheloid layer could potentially react with the bottom water by exchanging Nd and modify εNd signature of the bottom water. For example, in the Northeast Atlantic from the GEOTRACES North Atlantic Zonal Transect (GA03), the bottom water in the nepheloid layer shows elevated Nd concentrations ([Nd] increases 2.4 pmol/kg in the bottom 80 m) compared to the water above the nepheloid layer (slope of increasing [Nd] is ~1 pmol/kg per 235 m) (Stichel et al., 2015). εNd shifts from −11.8 above the nepheloid layer to −12.7 at 390 m above the seafloor (Stichel et al., 2015). If this process also occurs in the nepheloid layer in the SAMT, the bottom water from SAMT-2 to SAMT-5 is expected to show addition of REEs and εNd different from the predicted values (assuming resuspended particles and the bottom water have very different εNd signatures).

From SAMT-2 to SAMT-5, the average Δ[REE](%) values of the bottom water samples are high by 0% to 6% (Fig. 16b,c), which indicates almost conservative behavior (± 5%). ΔεNd-values of these bottom water samples show an average of −0.09 ± 0.10

(1σ) εNd units (Fig. 17c), which indicates almost no deviations from conservative water mass mixing. Therefore, REEs and εNd of the bottom water from SAMT-2 to SAMT-5 are not significantly impacted by resuspended particles in the nepheloid layer.

### *4.8. Influence on REEs and εNd from oceanic volcanism*

Oceanic basalts is a potential source that could add external Nd with high εNd-values (e.g. Mid-Atlantic Ridge basalts in the South Atlantic, with average εNd = +8.6 ± 2.5, 1σ, n = 844 (Class and Lehnert, 2012)) to seawater. Oceanic basalts in this transect are the volcanic Rio Grande Rise (RGR) and a seamount chain on the Vitória-Trindade Ridge (VTR) (Fig. 1,2a). Based on the largest available geochemical data set, EarthChem (www.earthchem.org/portal), including PetDB (Lehnert et al., 2000), GEOROC (GEOROC, 2007) and SedDB (Johansson et al., 2012), 11 volcanic rocks from RGR have εNd values of −3.7 ± 2.4 (1σ) and 1 sediment sample from RGR has an εNd value of −5.5 which is similar to the values of the volcanic rocks. εNd values of 55 volcanic rocks from VTR extracted from EarthChem (www.earthchem.org/portal) have an average of +2.9 ± 0.6 (1σ). Seawater samples near RGR and VTR have lower εNd values than that of the above rock and sediment samples. However, this evidence is not sufficient to prove that seawater Nd isotopes near RGR and VTR are not influenced by volcanic components. It is necessary to investigate if there is any change in the εNd deviation when a water mass passes the volcanic RGR and VTR. If the oceanic basalts influence the seawater εNd signal, εNd deviations might be observed near the volcanic RGR (between SAMT-9 and SAMT-10) and VTR (between SAMT-12 and SAMT-13) in the directions of water mass flow (Fig. 1,2a). The northward flowing water masses would

show deviations to higher εNd values north of RGR and VTR, whereas the southward flowing water masses would show deviations to higher εNd values south of RGR and VTR. For the northward flowing AAIW and UCDW, εNd-values would deviate to higher values at SAMT-10 (north of RGR). For the southward flowing NADW, εNd-values would deviate to higher values at SAMT-9 (south of RGR) and SAMT-12 (south of VTR). For the northward flowing LCDW and AABW, εNd-values would deviate to higher values at SAMT-10 (north of RGR) and SAMT-13 (north of VTR). We investigate whether there is any influence of these volcanics by calculating εNd and [Nd] deviations from conservative water mass mixing.

Since the top of the VTR seamount along the transect is about 2000 m under surface water and at greater depths than AAIW and UCDW (Fig. 2a), for these water masses we only discuss εNd and [Nd] deviations at RGR (its top is about 1000 m beneath the surface water; Fig. 2a). South of RGR, northward flowing AAIW and UCDW have ΔεNd-values of −0.79 to +0.17 εNd units and Δ[Nd](%) of −8% to −5% at SAMT-9 (Fig. 16b,17c). North of RGR, AAIW and UCDW have ΔεNd of −0.58 to +0.78 εNd units and Δ[Nd](%) of −5% to −3% at SAMT-10 (Fig. 16b,17c). From SAMT-9 to SAMT-10, ΔεNd-values increase 0.2 to 0.6 εNd units (analytical error ≈ 0.3 εNd units) and Δ[Nd](%) increase 2% to 3% (analytical error ≈ 3%). The very small changes of ΔεNd-values and Δ[Nd](%) indicate almost no influence on seawater εNd and REEs from RGR when northward flowing AAIW and UCDW pass RGR.

Southward flowing NADW passes VTR from SAMT-13 to SAMT-12 and then passes RGR from SAMT-10 to SAMT-9 (Fig. 2a). At SAMT-13, NADW has ΔεNd-

values of −1.08 to +0.37 εNd units and Δ[Nd](%) of −3% to +11% (Fig. 16b,17c). At SAMT-12, NADW has ΔεNd-values of −0.09 to +0.34 εNd units and Δ[Nd](%) of −10% to +1% (Fig. 16b,17c). From SAMT-13 to SAMT-12, ΔεNd-values increase 0 to 1.0 εNd units and Δ[Nd](%) decrease 7% to 10%. When southward flowing NADW passes VTR, radiogenic Nd from the volcanic VTR could be added to seawater resulting in increasing ΔεNd. Then REEs could be scavenged by VTR after NADW passes VTR resulting in decreasing Δ[Nd](%). At SAMT-10, NADW has ΔεNd-values of −0.15 to +0.51 εNd units and Δ[Nd](%) of −7% to +5% (Fig. 16b,17c). At SAMT-9, NADW has ΔεNd-values of +0.02 to +0.77 εNd units and Δ[Nd](%) of −8% to +4% (Fig. 16b,17c). From SAMT-10 to SAMT-9, ΔεNd-values increase 0.2 to 0.3 εNd units and Δ[Nd](%) decrease 1%, indicating no influence on seawater εNd and REEs from RGR when southward flowing NADW passes RGR.

Northward flowing LCDW and AABW pass the RGR from SAMT-9 to SAMT-10 and then pass the VTR from SAMT-12 to SAMT-13 (Fig. 2a). At SAMT-9, LCDW and AABW have ΔεNd-values of −0.04 to +0.40 εNd units and Δ[Nd](%) of +2% to +3% (Fig. 16b,17c). At SAMT-10, LCDW and AABW have ΔεNd-values of −0.38 to −0.30 εNd units and Δ[Nd](%) of +9% to +13% (Fig. 16b,17c). From SAMT-9 to SAMT-10, ΔεNd-values decrease 0.1 to 0.7 εNd units and Δ[Nd](%) increase 12% to 15%. Since the volcanic RGR has high εNd, they cannot be the source contributing to the decreasing ΔεNd-values of LCDW and AABW. This low εNd signal could be the dissolved Nd released from the sediments on the sea floor, which also results in the increasing Δ[Nd](%) (addition of Nd). At SAMT-12, LCDW and AABW have ΔεNd-

values of −3.06 to −0.35 εNd units and Δ[Nd](%) of +2% to +3% (Fig. 16b,17c). At SAMT-13, LCDW and AABW have ΔεNd-values of −0.66 to −0.34 εNd units and Δ[Nd](%) of +5% to +10% (Fig. 16b,17c). Here all ΔεNd-values are < 0 and all Δ[Nd](%) are > 0 indicating addition of low εNd signal which could come from the dissolved Nd released from the sediments on the sea floor. From SAMT-12 to SAMT-13, ΔεNd-values increase 0 to 2.4 εNd units and Δ[Nd](%) increase 3% to 7%, indicating addition of radiogenic Nd from the volcanic VTR when northward LCDW and AABW pass VTR. LCDW and AABW are influenced by REEs released from deep sea sediments as well as the volcanic VTR when LCDW and AABW pass the VTR.

AAIW, UCDW, and NADW passing the volcanic RGR show almost no influence on ΔεNd-values and Δ[Nd](%) from RGR. NADW passing the volcanic VTR indicates addition of radiogenic Nd and then scavenging of REEs. LCDW and AABW passing the RGR are influenced by dissolved REEs from the deep sea sediments. LCDW and AABW passing the VTR are influenced by dissolved REEs from the deep sea sediments and the volcanic VTR.

**5. Conclusions**

The SAMT, including main water masses involved in the AMOC, provides an excellent opportunity to study conservative vs. non-conservative behavior of seawater REEs as well as potential sources and sinks of seawater REEs. To investigate whether intermediate and deep water REEs reflect water mass mixing or open system processes such as reversible scavenging, we calculated REE deviations from predicted values based

on conservative water mass mixing of end-member compositions. Our results show that the REE abundances within the SAMT are dominated by water mass mixing for the intermediate and deep water. This result is also observed with REE ratios compared with water mass tracers such as salinity and $PO_4^*$. The potential sources that could add external REEs to seawater are: dissolution of REEs from eolian dust to the surface/subsurface water, REEs released from dissolution of Fe-Mn oxides in the ODZ, REEs from sediments near the continental margin, and dissolution of REEs from deep sea sediments. REEs and Nd isotopes of most intermediate and deep water masses passing the volcanic RGR and VTR do not show influence from RGR and VTR. REEs and Nd isotopes of the bottom water LCDW and AABW passing the RGR are influenced by dissolved REEs from the deep sea sediments. LCDW and AABW passing the VTR are influenced by dissolved REEs from the deep sea sediments as well as the volcanic VTR.

**Acknowledgements**

We thank Captain Bill Richardson and the crew of the RRS James Cook Cruise JC057. We thank Arnold Gordon for discussions on the water mass pathways and Alan Shiller for providing GEOTRACES GA03 REE data. Y.W. thanks Chandranath Basak for general research discussions. This study is funded by U.S. NSF grant OCE-12-60514.

**References**

Arsouze, T., Dutay, J.C., Lacan, F. and Jeandel, C. (2009) Reconstructing the Nd oceanic cycle using a coupled dynamical-biogeochemical model. Biogeosciences 6, 2829-2846.

Bacon, M.P. and Anderson, R.F. (1982) Distribution of thorium isotopes between dissolved and particulate forms in the deep sea. Journal of Geophysical Research: Oceans 87, 2045-2056.

Basile, I., Grousset, F.E., Revel, M., Petit, J.R., Biscaye, P.E. and Barkov, N.I. (1997) Patagonian origin of glacial dust deposited in East Antarctica (Vostok and Dome C) during glacial stages 2, 4 and 6. Earth and Planetary Science Letters 146, 573-589.

Behrens, M.K., Muratli, J., Pradoux, C., Wu, Y., Böning, P., Brumsack, H.-J., Goldstein, S.L., Haley, B., Jeandel, C. and Paffrath, R. (2016) Rapid and precise analysis of rare earth elements in small volumes of seawater-Method and intercomparison. Marine Chemistry 186, 110-120.

Bertram, C.J. and Elderfield, H. (1993) The geochemical balance of the rare earth elements and neodymium isotopes in the oceans. Geochimica et Cosmochimica Acta 57, 1957-1986.

Byrne, R.H. (2002) Inorganic speciation of dissolved elements in seawater: the influence of pH on concentration ratios. Geochemical Transactions 3, 11.

Byrne, R.H. and Kim, K.-H. (1990) Rare earth element scavenging in seawater. Geochimica et Cosmochimica Acta 54, 2645-2656.

Class, C. and Lehnert, K. (2012) PetDB Expert MORB (Mid-Ocean Ridge Basalt) Compilation. EarthChem Library.

De Baar, H.J.W., Bacon, M.P., Brewer, P.G. and Bruland, K.W. (1985) Rare earth elements in the Pacific and Atlantic Oceans. Geochimica et Cosmochimica Acta 49, 1943-1959.

de Baar, H.J.W., German, C.R., Elderfield, H. and Van Gaans, P. (1988) Rare earth element distributions in anoxic waters of the Cariaco Trench. Geochimica et Cosmochimica Acta 52, 1203-1219.

de Mahiques, M.M., Tassinari, C.C.G., Marcolini, S., Violante, R.A., Figueira, R.C.L., da Silveira, I.C.A., Burone, L. and e Sousa, S.H.d.M. (2008) Nd and Pb isotope signatures on the Southeastern South American upper margin: Implications for sediment transport and source rocks. Marine Geology 250, 51-63.

DePaolo, D.J. and Wasserburg, G.J. (1976) Nd isotopic variations and petrogenetic models. Geophysical Research Letters 3, 249-252.

Dia, A., Allegre, C.J. and Erlank, A.J. (1990) The development of continental crust through geological time: the South African case. Earth and Planetary Science Letters 98, 74-89.

Elderfield, H. and Greaves, M.J. (1982) The rare earth elements in seawater. Nature 296, 214-219.

Elderfield, H. and Sholkovitz, E.R. (1987) Rare earth elements in the pore waters of reducing nearshore sediments. Earth and Planetary Science Letters 82, 280-288.

Elderfield, H., Whitfield, M., Burton, J.D., Bacon, M.P. and Liss, P.S. (1988) The oceanic chemistry of the rare-earth elements [and discussion]. Philosophical Transactions of the Royal Society of London A: Mathematical, Physical and Engineering Sciences 325, 105-126.

Frank, M. (2002) Radiogenic isotopes: tracers of past ocean circulation and erosional input. Reviews of geophysics 40.

Gaiero, D.M., Brunet, F., Probst, J.-L. and Depetris, P.J. (2007) A uniform isotopic and chemical signature of dust exported from Patagonia: Rock sources and occurrence in southern environments. Chemical Geology 238, 107-120.

Garcia-Solsona, E., Jeandel, C., Labatut, M., Lacan, F., Vance, D., Chavagnac, V. and Pradoux, C. (2014) Rare earth elements and Nd isotopes tracing water mass mixing and particle-seawater interactions in the SE Atlantic. Geochimica et Cosmochimica Acta 125, 351-372.

GEOROC (2007) GEOROC, Geochemistry of rocks of the oceans and continents, database. Max-Planck-Institut für Chemie.

German, C.R. and Elderfield, H. (1989) Rare earth elements in Saanich Inlet, British Columbia, a seasonally anoxic basin. Geochimica et Cosmochimica Acta 53, 2561-2571.

German, C.R. and Elderfield, H. (1990) Rare earth elements in the NW Indian Ocean. Geochimica et Cosmochimica Acta 54, 1929-1940.

German, C.R., Holliday, B.P. and Elderfield, H. (1991) Redox cycling of rare earth elements in the suboxic zone of the Black Sea. Geochimica et Cosmochimica Acta 55, 3553-3558.

German, C.R., Masuzawa, T., Greaves, M.J., Elderfield, H. and Edmond, J.M. (1995) Dissolved rare earth elements in the Southern Ocean: Cerium oxidation and the influence of hydrography. Geochimica et Cosmochimica Acta 59, 1551-1558.

Gili, S., Gaiero, D.M., Goldstein, S.L., Chemale Jr, F., Jweda, J., Kaplan, M.R., Becchio, R.A. and Koester, E. (2017) Glacial/interglacial changes of Southern Hemisphere wind circulation from the geochemistry of South American dust. Earth and Planetary Science Letters 469, 98-109.

Goldstein, S.J. and Jacobsen, S.B. (1987) The Nd and Sr isotopic systematics of river-water dissolved material: Implications for the sources of Nd and Sr in seawater. Chemical Geology: Isotope Geoscience section 66, 245-272.

Goldstein, S.L. and Hemming, S.R. (2003) Long-lived isotopic tracers in oceanography, paleoceanography, and ice-sheet dynamics. Treatise on geochemistry 6, 453-489.

Goldstein, S.L., O'Nions, R.K. and Hamilton, P.J. (1984) A Sm-Nd isotopic study of atmospheric dusts and particulates from major river systems. Earth and planetary Science letters 70, 221-236.

Gordon, A.L., Weiss, R.F., Smethie, W.M. and Warner, M.J. (1992) Thermocline and intermediate water communication between the South Atlantic and Indian Oceans. Journal of Geophysical Research: Oceans 97, 7223-7240.

Grasse, P., Stichel, T., Stumpf, R., Stramma, L. and Frank, M. (2012) The distribution of neodymium isotopes and concentrations in the Eastern Equatorial Pacific: Water mass advection versus particle exchange. Earth and Planetary Science Letters 353, 198-207.

Grenier, M., Jeandel, C., Lacan, F., Vance, D., Venchiarutti, C., Cros, A. and Cravatte, S. (2013) From the subtropics to the central equatorial Pacific Ocean: Neodymium isotopic composition and rare earth element concentration variations. Journal of Geophysical Research: Oceans 118, 592-618.

Gromet, L.P., Haskin, L.A., Korotev, R.L. and Dymek, R.F. (1984) The "North American shale composite": its compilation, major and trace element characteristics. Geochimica et Cosmochimica Acta 48, 2469-2482.

Haley, B.A., Du, J., Abbott, A.N. and McManus, J. (2017) The impact of benthic processes on rare earth element and neodymium isotope distributions in the oceans. Frontiers in Marine Science 4, 426.

Haley, B.A., Frank, M., Hathorne, E. and Pisias, N. (2014) Biogeochemical implications from dissolved rare earth element and Nd isotope distributions in the Gulf of Alaska. Geochimica et Cosmochimica Acta 126, 455-474.

Hellerman, S. and Rosenstein, M. (1983) Normal monthly wind stress over the world ocean with error estimates. Journal of Physical Oceanography 13, 1093-1104.

Henry, F., Probst, J.-L., Thouron, D., Depetris, P.J. and Garçon, V. (1996) Nd-Sr isotopic compositions of dissolved and particulate material transported by the Parana and Uruguay rivers during high (december 1993) and low (september 1994) water periods. Sciences Géologiques, Bulletin 49, 89-100.

Heywood, K.J. and King, B.A. (2002) Water masses and baroclinic transports in the South Atlantic and Southern oceans. Journal of Marine Research 60, 639-676.

Hoernle, K., Rohde, J., Hauff, F., Garbe-Schönberg, D., Homrighausen, S., Werner, R. and Morgan, J.P. (2015) How and when plume zonation appeared during the 132 Myr evolution of the Tristan Hotspot. Nature communications 6, 7799.

Jacobsen, S.B. and Wasserburg, G.J. (1980) Sm-Nd isotopic evolution of chondrites. Earth and Planetary Science Letters 50, 139-155.

Jeandel, C., Arsouze, T., Lacan, F., Techine, P. and Dutay, J.-C. (2007) Isotopic Nd compositions and concentrations of the lithogenic inputs into the ocean: A compilation, with an emphasis on the margins. Chemical Geology 239, 156-164.

Jeandel, C., Delattre, H., Grenier, M., Pradoux, C. and Lacan, F. (2013) Rare earth element concentrations and Nd isotopes in the Southeast Pacific Ocean. Geochemistry, Geophysics, Geosystems 14, 328-341.

Johannesson, K.H. and Burdige, D.J. (2007) Balancing the global oceanic neodymium budget: evaluating the role of groundwater. Earth and Planetary Science Letters 253, 129-142.

Johansson, A., Lehnert, K. and Hsu, L. (2012) Status report on the SedDB sediment geochemistry database. GeoPRISMS Newsletter 28, 21.

Klatt, O., Fahrbach, E., Hoppema, M. and Rohardt, G. (2005) The transport of the Weddell Gyre across the Prime Meridian. Deep Sea Research Part II: Topical Studies in Oceanography 52, 513-528.

Lacan, F. and Jeandel, C. (2001) Tracing Papua New Guinea imprint on the central Equatorial Pacific Ocean using neodymium isotopic compositions and Rare Earth Element patterns. Earth and Planetary Science Letters 186, 497-512.

Lacan, F. and Jeandel, C. (2005) Neodymium isotopes as a new tool for quantifying exchange fluxes at the continent–ocean interface. Earth and Planetary Science Letters 232, 245-257.

Lambelet, M., van de Flierdt, T., Crocket, K., Rehkämper, M., Kreissig, K., Coles, B., Rijkenberg, M.J., Gerringa, L.J., de Baar, H.J. and Steinfeldt, R. (2016) Neodymium isotopic composition and concentration in the western North Atlantic Ocean: Results from the GEOTRACES GA02 section. Geochimica et Cosmochimica Acta 177, 1-29.

Larqué, L., Maamaatuaiahutapu, K. and Garçon, V. (1997) On the intermediate and deep water flows in the South Atlantic Ocean. Journal of Geophysical Research: Oceans 102, 12425-12440.

Lee, J.H. and Byrne, R.H. (1993) Complexation of trivalent rare earth elements (Ce, Eu, Gd, Tb, Yb) by carbonate ions. Geochimica et Cosmochimica Acta 57, 295-302.

Lehnert, K., Su, Y., Langmuir, C., Sarbas, B. and Nohl, U. (2000) A global geochemical database structure for rocks. Geochemistry, Geophysics, Geosystems 1.

Luo, Y.-R. and Byrne, R.H. (2004) Carbonate complexation of yttrium and the rare earth elements in natural waters. Geochimica et Cosmochimica Acta 68, 691-699.

Masuda, A., Nakamura, N. and Tanaka, T. (1973) Fine structures of mutually normalized rare-earth patterns of chondrites. Geochimica et Cosmochimica Acta 37, 239-248.

McLennan, S.M., Taylor, S.R., McCulloch, M.T. and Maynard, J.B. (1990) Geochemical and Nd-Sr isotopic composition of deep-sea turbidites: Crustal evolution and plate tectonic associations. Geochimica et Cosmochimica Acta 54, 2015-2050.

Nakamura, N. (1974) Determination of REE, Ba, Fe, Mg, Na and K in carbonaceous and ordinary chondrites. Geochimica et Cosmochimica Acta 38, 757-775.

Nozaki, Y. and Alibo, D.S. (2003) Importance of vertical geochemical processes in controlling the oceanic profiles of dissolved rare earth elements in the northeastern Indian Ocean. Earth and Planetary Science Letters 205, 155-172.

Orsi, A.H., Johnson, G.C. and Bullister, J.L. (1999) Circulation, mixing, and production of Antarctic Bottom Water. Progress in Oceanography 43, 55-109.

Orsi, A.H., Smethie, W.M. and Bullister, J.L. (2002) On the total input of Antarctic waters to the deep ocean: A preliminary estimate from chlorofluorocarbon measurements. Journal of Geophysical Research: Oceans 107.

Osborne, A.H., Hathorne, E.C., Schijf, J., Plancherel, Y., Böning, P. and Frank, M. (2017) The potential of sedimentary foraminiferal rare earth element patterns to trace water masses in the past. Geochemistry, Geophysics, Geosystems 18, 1550-1568.

Pahnke, K., Van de Flierdt, T., Jones, K.M., Lambelet, M., Hemming, S.R. and Goldstein, S.L. (2012) GEOTRACES intercalibration of neodymium isotopes and rare earth element concentrations in seawater and suspended particles. Part 2: Systematic tests and baseline profiles. Limnology and Oceanography: Methods 10, 252-269.

Peyve, A. and Skolotnev, S. (2014) Systematic variations in the composition of volcanic rocks in tectono-magmatic seamount chaines in the Brazil Basin. Geochemistry International 52, 111-130.

Reid, J.L. (1994) On the total geostrophic circulation of the North Atlantic Ocean: Flow patterns, tracers, and transports. Progress in Oceanography 33, 1-92.

Rempfer, J., Stocker, T.F., Joos, F., Dutay, J.-C. and Siddall, M. (2011) Modelling Nd-isotopes with a coarse resolution ocean circulation model: Sensitivities to model parameters and source/sink distributions. Geochimica et cosmochimica acta 75, 5927-5950.

Rousseau, T.C.C., Sonke, J.E., Chmeleff, J., Van Beek, P., Souhaut, M., Boaventura, G., Seyler, P. and Jeandel, C. (2015) Rapid neodymium release to marine waters from lithogenic sediments in the Amazon estuary. Nature communications 6, 7592.

Schijf, J., De Baar, H.J.W. and Millero, F.J. (1995) Vertical distributions and speciation of dissolved rare earth elements in the anoxic brines of Bannock Basin, eastern Mediterranean Sea. Geochimica et Cosmochimica Acta 59, 3285-3299.

Schlitzer, R. (2012) Ocean data view.

Sholkovitz, E.R., Landing, W.M. and Lewis, B.L. (1994) Ocean particle chemistry: the fractionation of rare earth elements between suspended particles and seawater. Geochimica et Cosmochimica Acta 58, 1567-1579.

Sholkovitz, E.R., Shaw, T.J. and Schneider, D.L. (1992) The geochemistry of rare earth elements in the seasonally anoxic water column and porewaters of Chesapeake Bay. Geochimica et Cosmochimica Acta 56, 3389-3402.

Siddall, M., Khatiwala, S., van de Flierdt, T., Jones, K., Goldstein, S.L., Hemming, S. and Anderson, R.F. (2008) Towards explaining the Nd paradox using reversible scavenging in an ocean general circulation model. Earth and Planetary Science Letters 274, 448-461.

Stichel, T., Hartman, A.E., Duggan, B., Goldstein, S.L., Scher, H. and Pahnke, K. (2015) Separating biogeochemical cycling of neodymium from water mass mixing in the Eastern North Atlantic. Earth and Planetary Science Letters 412, 245-260.

Stramma, L. and England, M. (1999) On the water masses and mean circulation of the South Atlantic Ocean. Journal of Geophysical Research-Oceans 104, 20863-20833.

Tachikawa, K., Arsouze, T., Bayon, G., Bory, A., Colin, C., Dutay, J.-C., Frank, N., Giraud, X., Gourlan, A.T. and Jeandel, C. (2017) The large-scale evolution of neodymium isotopic composition in the global modern and Holocene ocean revealed from seawater and archive data. Chemical Geology 457, 131-148.

Talley, L.D. (2011) Descriptive physical oceanography: an introduction. Academic press.

Taylor, S.R. and McLennan, S.M. (1985) The continental crust: its composition and evolution.

van de Flierdt, T., Griffiths, A.M., Lambelet, M., Little, S.H., Stichel, T. and Wilson, D.J. (2016) Neodymium in the oceans: a global database, a regional comparison and implications for palaeoceanographic research. Phil. Trans. R. Soc. A 374, 20150293.

van de Flierdt, T., Pahnke, K., Amakawa, H., Andersson, P., Basak, C., Coles, B., Colin, C., Crocket, K., Frank, M., Frank, N., Goldstein, S.L., Goswami, V., Haley, B.A., Hathorne, E.C., Hemming, S.R., Henderson, G.M., Jeandel, C., Jones, K., Kreissig, K., Lacan, F., Lambelet, M., Martin, E.E., Newkirk, D.R., Obata, H., Pena, L., Piotrowski, A.M., Pradoux, C., Scher, H.D., Schöberg, H., Singh, S.K., Stichel, T., Tazoe, H., Vance, D. and Yang, J. (2012) GEOTRACES intercalibration of neodymium isotopes and rare earth element concentrations in seawater and suspended particles. Part 1: reproducibility of results for the international intercomparison. Limnology and Oceanography: Methods 10, 234-251.

Vanicek, M. and Siedler, G. (2002) Zonal fluxes in the deep water layers of the western South Atlantic Ocean. Journal of Physical Oceanography 32, 2205-2235.

Zhang, J. and Nozaki, Y. (1998) Behavior of rare earth elements in seawater at the ocean margin: a study along the slopes of the Sagami and Nankai troughs near Japan. Geochimica et Cosmochimica Acta 62, 1307-1317.

Zheng, X.-Y., Plancherel, Y., Saito, M.A., Scott, P.M. and Henderson, G.M. (2016) Rare earth elements (REEs) in the tropical South Atlantic and quantitative deconvolution of their non-conservative behavior. Geochimica et Cosmochimica Acta 177, 217-237.

Figure 1. Map of the Southwest Atlantic Ocean with sampling stations of the Southwest Atlantic Meridional Transect (SAMT) (black dots). The numbers are station numbers from Station 1 (SAMT-1) in the south to Station 18 (SAMT-18) at the equator. The Rio Grande Rise (RGR) and Vitória-Trindade Ridge (VTR) are labeled. The map was made using ODV software (Schlitzer, 2012).

Figure 2. Section profiles of the SAMT. (a) Salinity section profile with contours of neutral density ($\gamma^n$). (b) $PO_4^*$ section profile with contours of potential temperature. (c) Oxygen section profile with contours of silicate. The water masses are upper North Atlantic Deep Water (UNADW, $\gamma^n$ = 27.75-27.98 kg/m$^3$; (Vanicek and Siedler, 2002)), middle North Atlantic Deep Water (MNADW, $\gamma^n$ = 27.98-28.07 kg/m$^3$; (Vanicek and Siedler, 2002)), lower North Atlantic Deep Water (LNADW, $\gamma^n$ = 28.07-28.12 kg/m$^3$; (Vanicek and Siedler, 2002)), South Atlantic Central Water (SACW, $\gamma^n$ = 26.6-27.15 kg/m$^3$; (Vanicek and Siedler, 2002)), Antarctic Intermediate Water from the Atlantic section of the Southern Ocean (aAAIW, $\gamma^n$ = 27.15-27.55 kg/m$^3$; (Vanicek and Siedler, 2002)), Antarctic Intermediate Water from the Indian section of the Southern Ocean (iAAIW, $\gamma^n$ = 27.15-27.55 kg/m$^3$; (Vanicek and Siedler, 2002)), Upper Circumpolar Deep Water (UCDW, $\gamma^n$ = 27.55-27.88 kg/m$^3$; (Vanicek and Siedler, 2002)), Lower Circumpolar Deep Water (LCDW, $\gamma^n$ = 28.12-28.24 kg/m$^3$; (Vanicek and Siedler, 2002)), and Antarctic Bottom Water (AABW, $\gamma^n$ > 28.24 kg/m$^3$; (Vanicek and Siedler, 2002)). The legend numbers are station numbers from SAMT-1 in the south to SAMT-18 at the equator. The diagrams were made using ODV software (Schlitzer, 2012).

Figure 3. Potential temperature vs. salinity diagrams for seawater profiles of the SAMT. Diagram (b) is enlargement of diagram (a). The numbers are station numbers from SAMT-1 in the south to SAMT-18 at the equator. Black crosses are water mass end-members defined from the SAMT and listed in Table 4. SAMT seawater samples show systematic changes with latitude following violet, blue, yellow, and red stations from south to the equator.

Figure 4. PAAS-normalized REE patterns of selected stations from the SAMT. (a) SAMT-18. (b) SAMT-8. (c) SAMT-2. Each REE generally shows increasing concentration with depth. REEs also show systematical changes with latitude. For example, Yb concentrations of UNADW (1250-1750 m) gradually increase along the NADW pathway from the equator (SAMT-18; Fig. 4a) to mid-latitude (SAMT-8; Fig. 4b) to the far south (SAMT-2; Fig. 4c).

Figure 5. REE patterns of intermediate and deep water in the North Atlantic (blue), South Atlantic (green), and North Pacific (red). (a) Intermediate water (square). (b) Deep water (circle). (c) Bottom water: LCDW (triangle) and AABW (diamond). REE patterns show that REE abundances increase from the North Atlantic to North Pacific.

Figure 6. Vertical profiles of Nd concentration ([Nd]) and Nd isotopic composition (εNd) at SAMT-2, SAMT-8, SAMT-13 and SAMT-18. (a) and (c) are $\gamma^n$ vs. [Nd]. (b) and (d)

are $\gamma^n$ vs. εNd. Nd concentrations appear to behave like nutrients and increase with depth, whereas εNd values reflect water mass mixing.

Figure 7. REE concentration section profiles. (a) [Nd]. (b) [Yb]. (c) [Ce]. The numbers above each section diagram are station numbers. The sections were made using the ODV software (Schlitzer, 2012). They generally show increasing concentrations with depth.

Figure 8. REE ratio section profiles. (a) $Yb_n/Nd_n$. (b) $Ce/Ce^*$. The numbers above each section plot are station numbers. The sections were made using the ODV software (Schlitzer, 2012).

Figure 9. Depth profiles of (a) [Nd], (b) [Yb], (c) $Yb_n/Nd_n$, and (d) [Oxygen] from the surface to depths of AAIW. The numbers are station numbers from SAMT-1 in the south to SAMT-18 at the equator.

Figure 10. Depth profiles of (a) [Ce] and (b) $Ce/Ce^*$ from the surface to depths of AAIW. The numbers are station numbers from SAMT-1 in the south to SAMT-18 at the equator.

Figure 11. (a) εNd of surface water from the SAMT (with black marker lines) and surface sediments near South America (Goldstein et al., 1984; McLennan et al., 1990; Henry et al., 1996; Basile et al., 1997; Gaiero et al., 2007; de Mahiques et al., 2008; Rousseau et al., 2015; Gili et al., 2017) and Africa (Goldstein et al., 1984; Dia et al., 1990). Horizontal arrows indicate wind directions of westerlies from ~60°S to ~35°S and trade winds from ~35°S to the equator (Hellerman and Rosenstein, 1983). The dash line is the boundary for westerlies and trade winds. The map was made using ODV software (Schlitzer, 2012). (b) Latitude vs. εNd of shallow seawater of the top 100 m from the SAMT (symbols in color), surface sediments (grey and empty symbols), and eolian dusts (black dots). These shallow water εNd-values are consistent with that of surface sediments/eolian dusts eroded from South America (SAMT-1 to SAMT-7; south of ~35°S) and Africa (SAMT-8 to SAMT-16; ~35°S to the equator), indicating terrigenous contributions of Nd to surface seawater. (c) εNd vs. depth of selected stations of the SAMT. The shallow water εNd varies from −18 to −7 (in the light blue area). The intermediate and deep water εNd ranges from −13 to −8 (between grey dashed lines). The εNd variability of shallow water is larger than that of intermediate and deep water, which indicates that the shallow water εNd signature is not transferred to intermediate and deep water.

Figure 12. REE concentrations vs. oxygen concentration within SACW. (a) [Nd] vs. [Oxygen]. (b) [Yb] vs. [Oxygen]. They both show increasing concentrations with decreasing oxygen concentrations.

Figure 13. Compare REE concentrations with salinity and $PO_4^*$. (a) [Nd] vs. salinity. (b) [Nd] vs. $PO_4^*$. (c) [Yb] vs. salinity. (d) [Yb] vs. $PO_4^*$.

Figure 14. Compare $Yb_n/Nd_n$ with salinity, $PO_4^*$, and εNd below the depths of AAIW. (a) $Yb_n/Nd_n$ vs. salinity. (b) $Yb_n/Nd_n$ vs. $PO_4^*$. (c) $Yb_n/Nd_n$ vs. εNd. The black crosses are water mass end-members. The numbers are station numbers from SAMT-1 in the south to SAMT-18 at the equator. They show mixing of aAAIW, UCDW, LCDW and AABW in the northernmost stations and mixing of iAAIW, NADW, and AABW in the southernmost stations.

Figure 15. Compare $Yb_n/Nd_n$ with 1/[Nd] and $Nd_n/Yb_n$ with 1/[Yb] below the depths of AAIW. (a) $Yb_n/Nd_n$ vs. 1/[Nd]. (b) $Nd_n/Yb_n$ vs. 1/[Yb]. The black crosses are water mass end-members. The numbers are station numbers from SAMT-1 in the south to SAMT-18 at the equator. Mixing lines (grey) are linear in these diagrams. Samples showing non-conservative behavior are intermediate water at SAMT-1 to SAMT-5 (higher $Yb_n/Nd_n$ values than the aAAIW-UCDW mixing line) and bottom water at most of the stations (lower $Yb_n/Nd_n$ values than the AABW-LNADW mixing line).

Figure 16. Histograms of Δ[REE] (%), $\Delta(Yb_n/Nd_n)$ (%) and ΔεNd calculated based on water mass mixing using salinity and potential temperature. (a) Δ[Nd] (%). (b) Δ[Yb] (%). (c) $\Delta(Yb_n/Nd_n)$ (%). (d) ΔεNd. The y-axis on the left is the number of calculated samples. The y-axis on the right is the percentage of calculated samples. Delta values were separated into three groups using the neutral densities of the water mass end-members defined from the SAMT (Table 4a). Green columns include samples from the depths of AAIW to UNADW ($\gamma^n$ = 27.15-27.90 kg/m$^3$). Red columns include samples from the depths of UNADW to LNADW ($\gamma^n$ = 27.90-28.11 kg/m$^3$). Blue columns include samples from the depths of LNADW to AABW ($\gamma^n$ =28.11-28.30 kg/m$^3$). The numbers above the columns are percentage values within each interval from depths of AAIW to the bottom.

Figure 17. Section profiles of (a) Salinity with contours of neutral density, (b) Δ[Nd] (%), (c) Δ[Yb] (%). Δ[REE] (%) are calculated based on water mass mixing using salinity and potential temperature. The numbers above each section plot are station numbers. The sections were made using the ODV software (Schlitzer, 2012).

Figure 18. Section profiles of (a) $PO_4^*$ with contours of neutral density, (b) $\Delta(Yb_n/Nd_n)$ (%), (c) ΔεNd. $\Delta(Yb_n/Nd_n)$ (%) and ΔεNd are calculated based on water mass mixing using salinity and potential temperature. The numbers above each section plot are station numbers. The sections were made using the ODV software (Schlitzer, 2012).

Figure 1. Map of the Southwest Atlantic Ocean with sampling stations of the SAMT

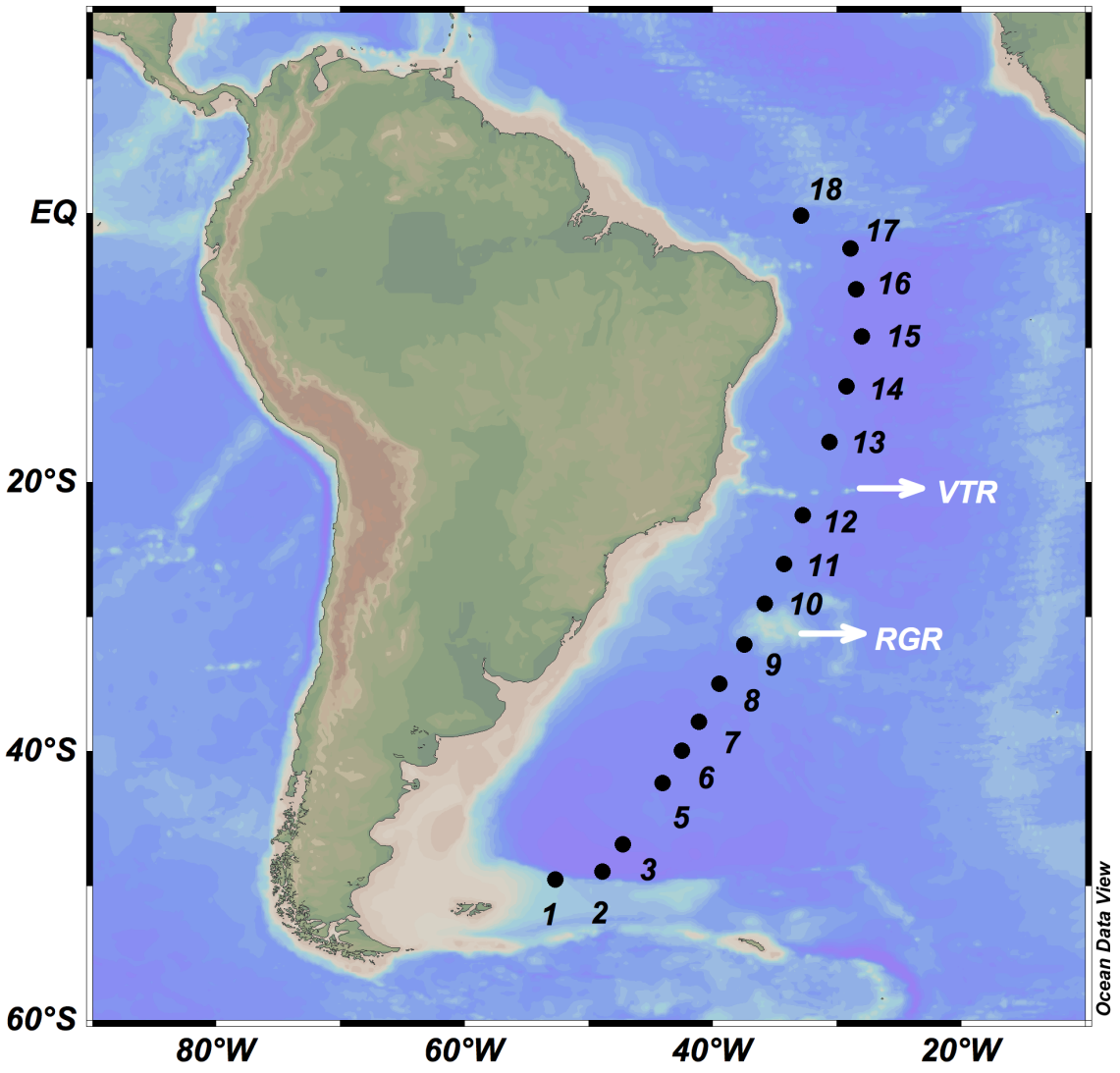

Figure 2. Section profiles of the SAMT

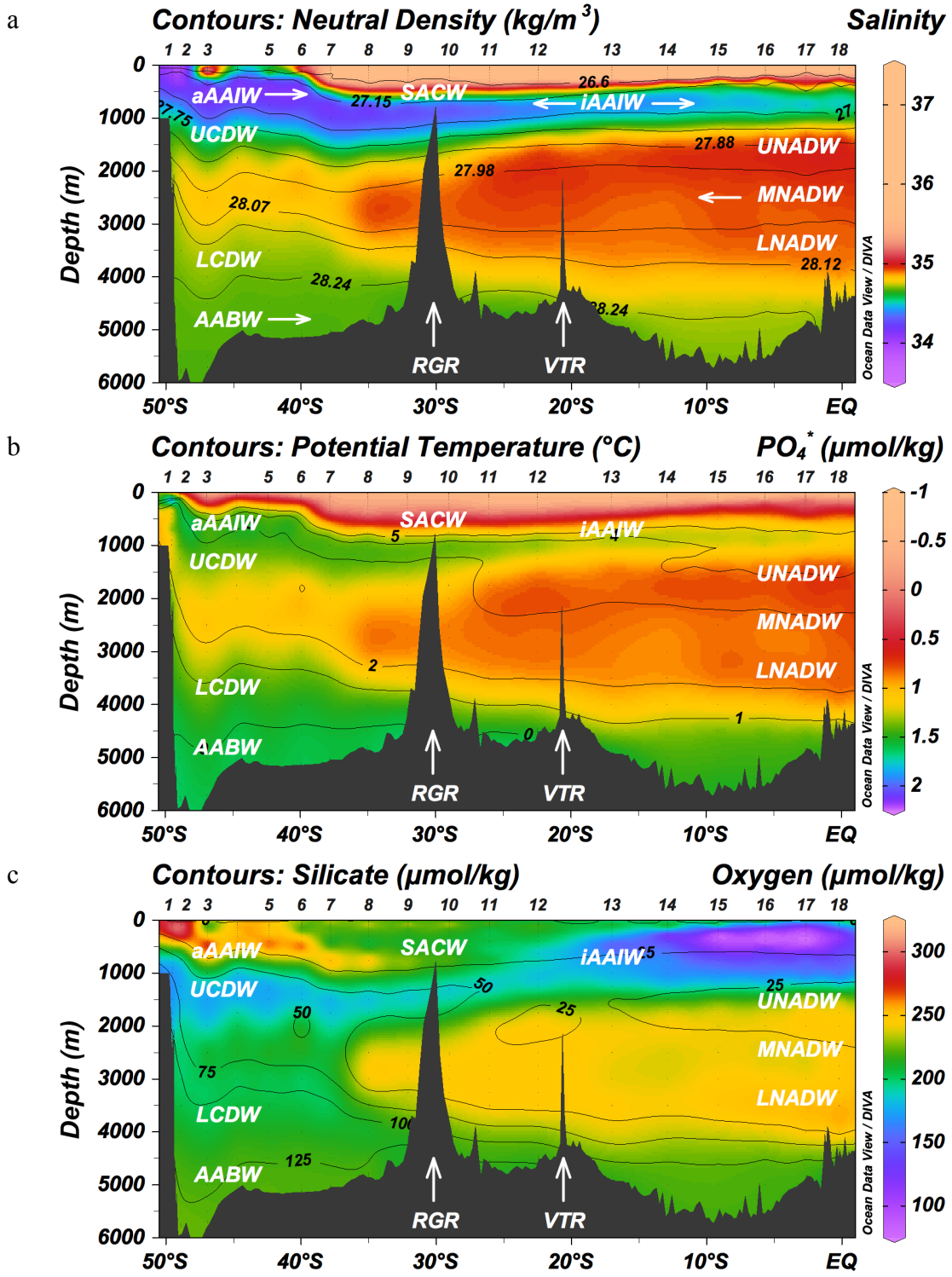

Figure 3. Potential temperature vs. salinity diagrams for seawater profiles of the SAMT

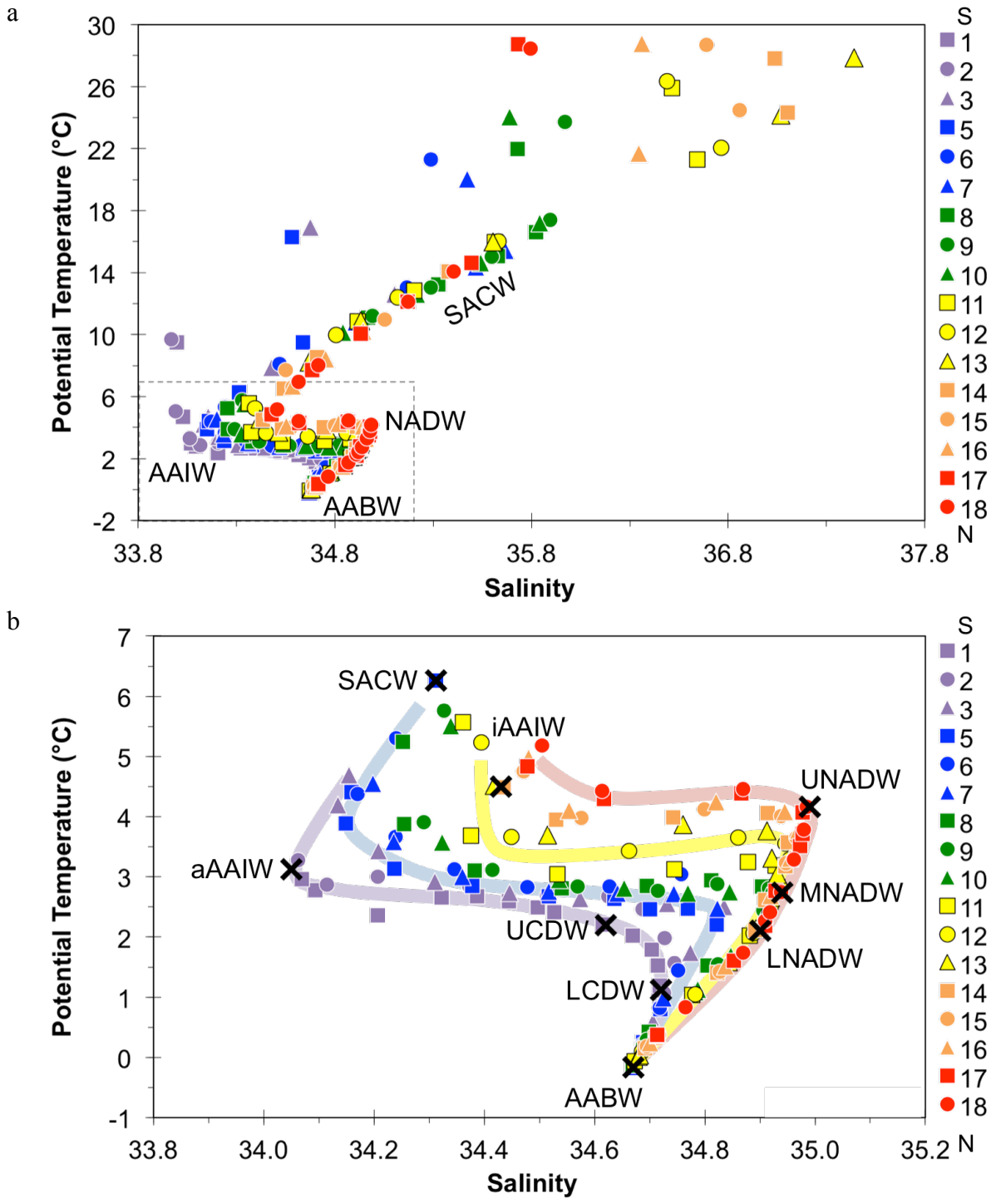

Figure 4. PAAS-normalized REE patterns of selected stations from the SAMT

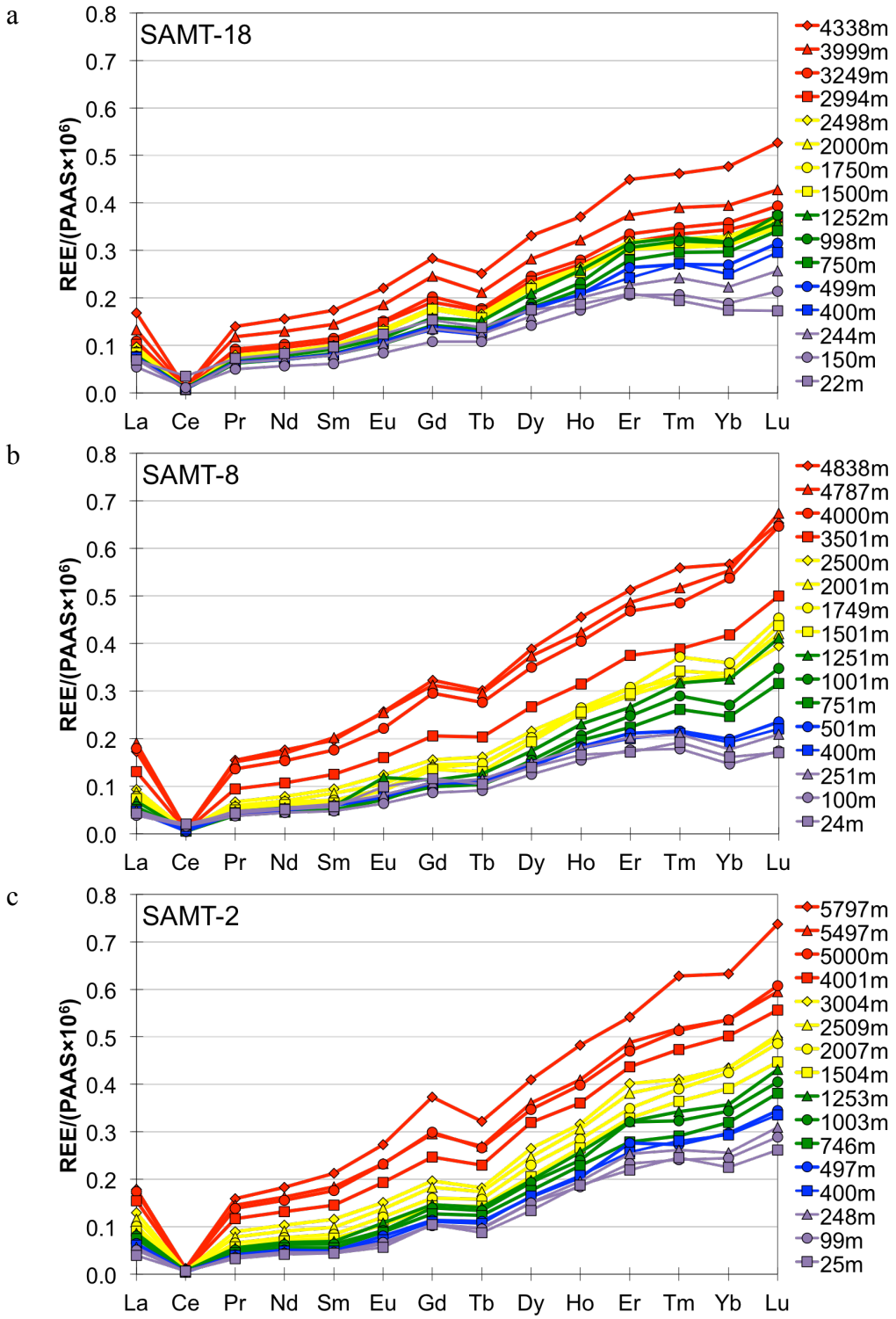

Figure 5. REE patterns of intermediate and deep water in the North Atlantic, South Atlantic, and North Pacific

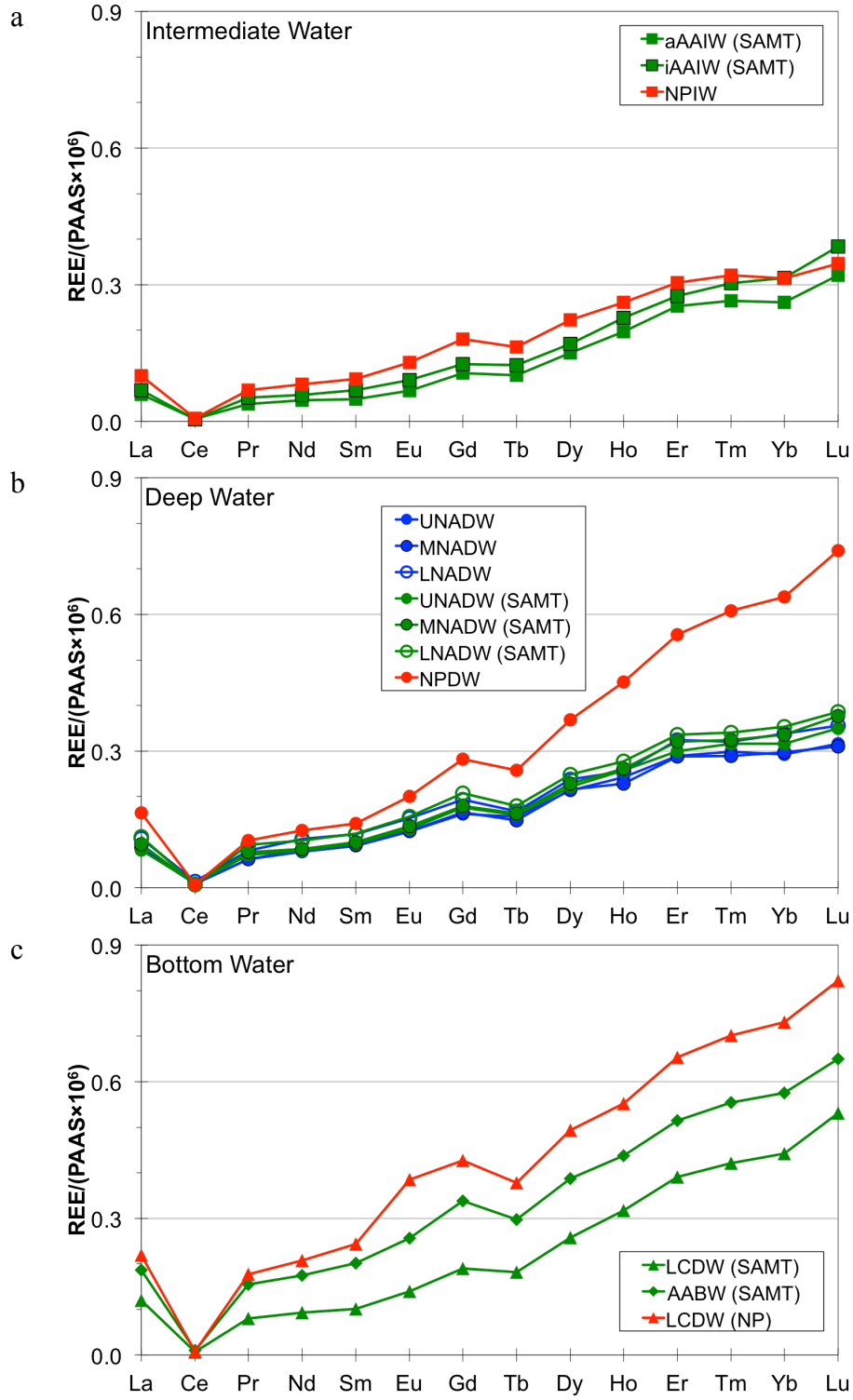

Figure 6. Vertical profiles of [Nd] and εNd at SAMT-2, SAMT-8, SAMT-13 and SAMT-18

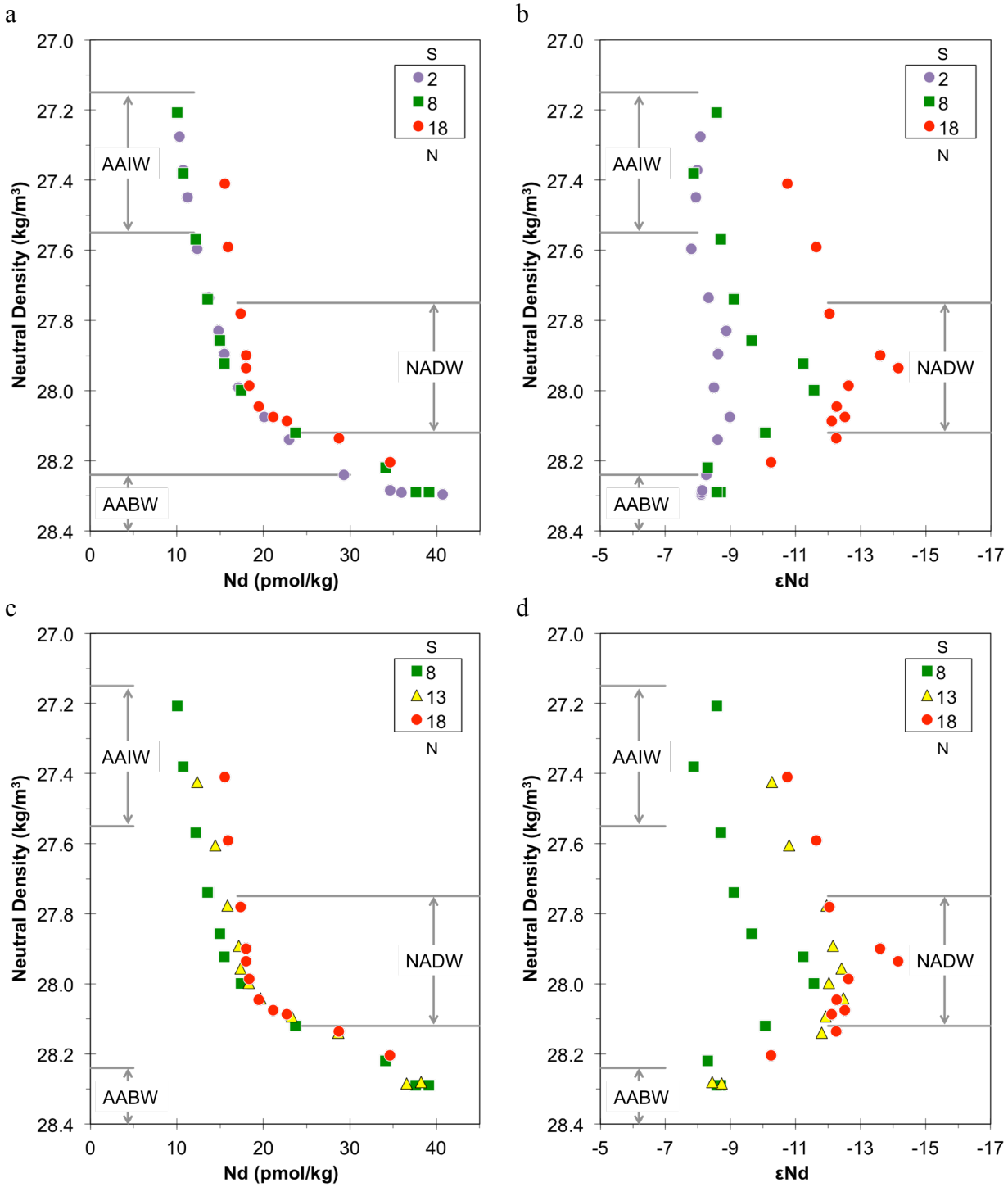

Figure 7. REE concentration section profiles

a

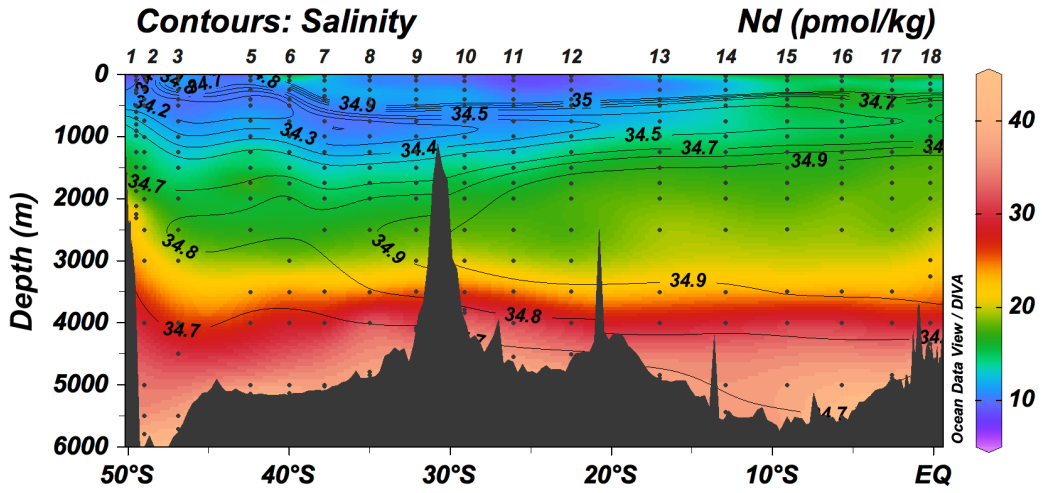


b

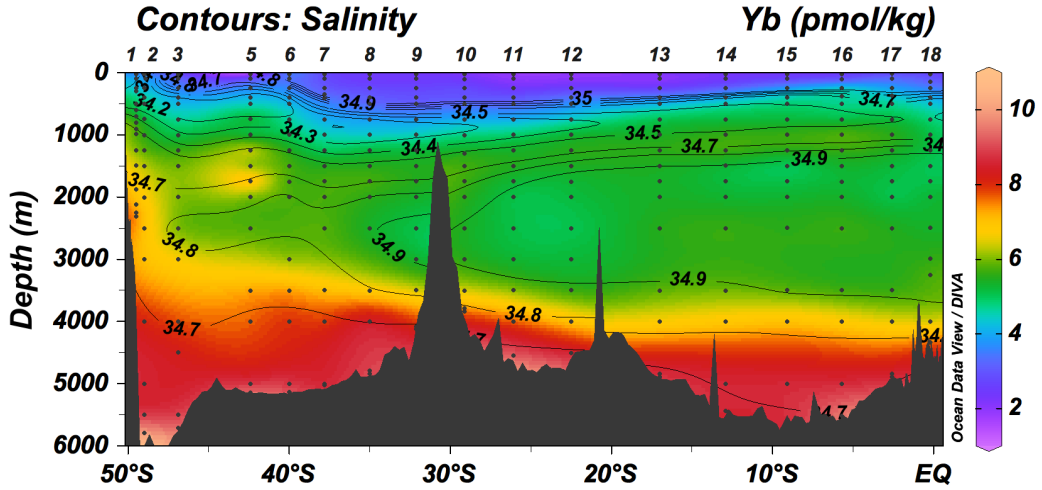


c

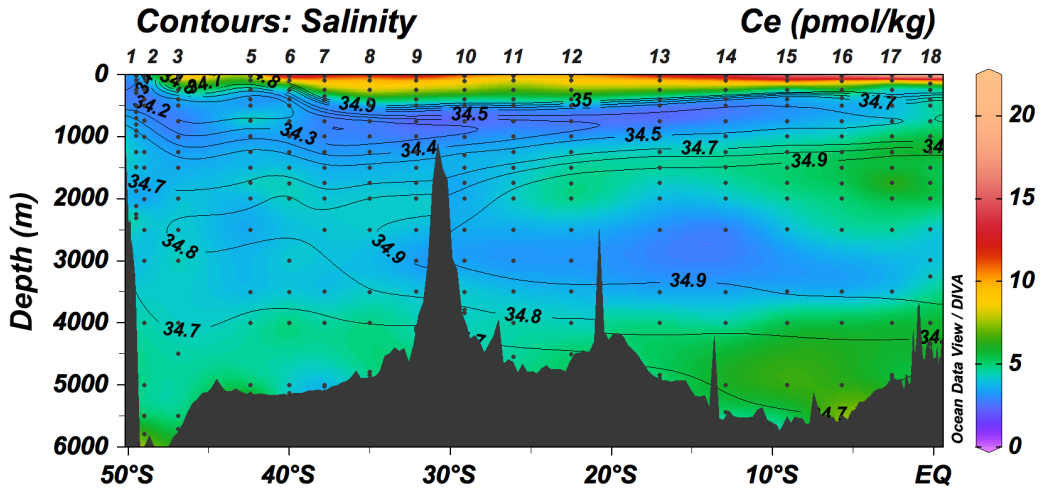

Figure 8. REE ratio section profiles

a

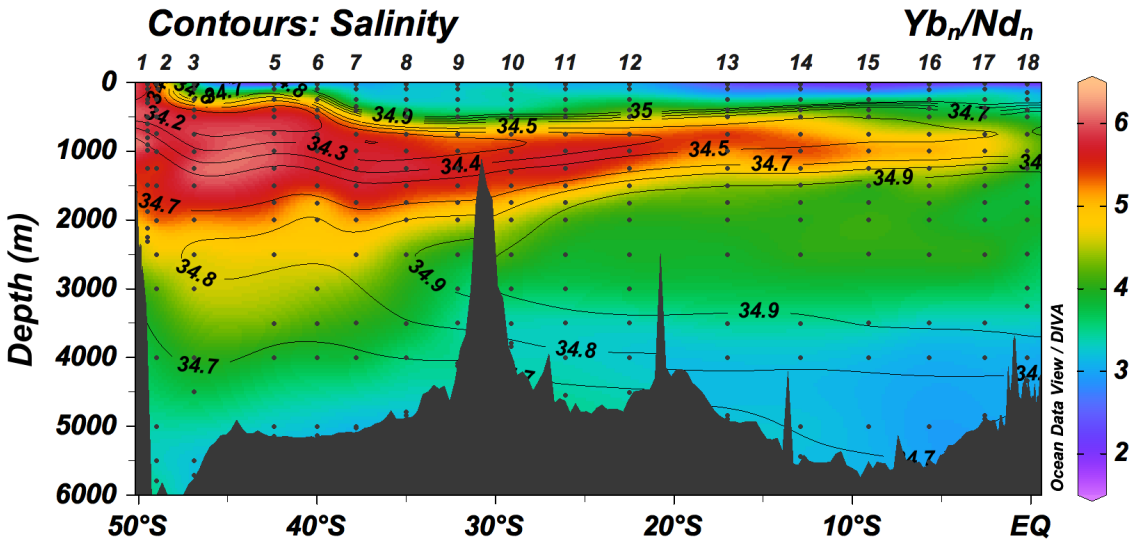


b

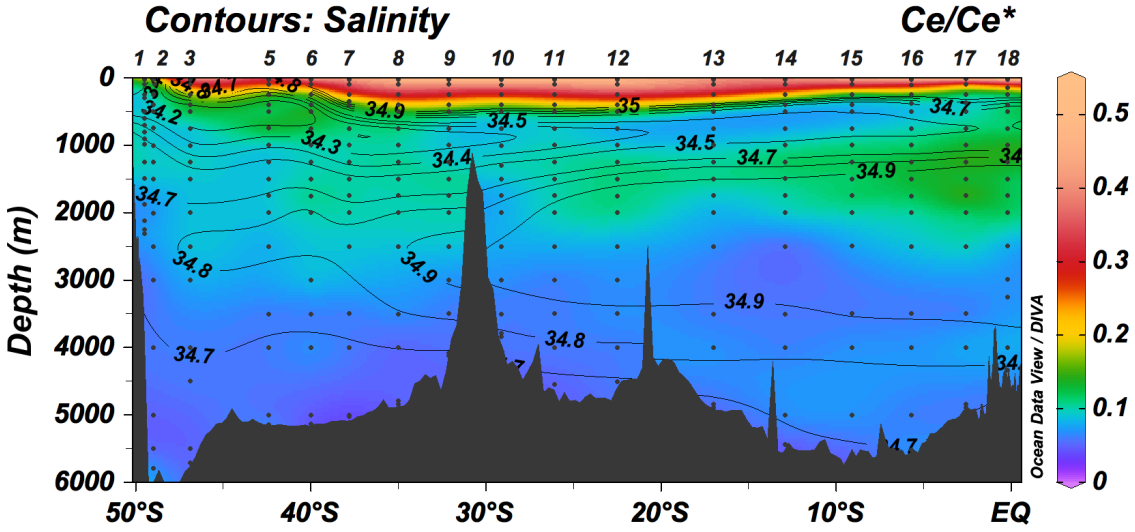

Figure 9. Depth profiles of [Nd], [Yb], $Yb_n/Nd_n$, and [Oxygen] from the surface to depths of AAIW

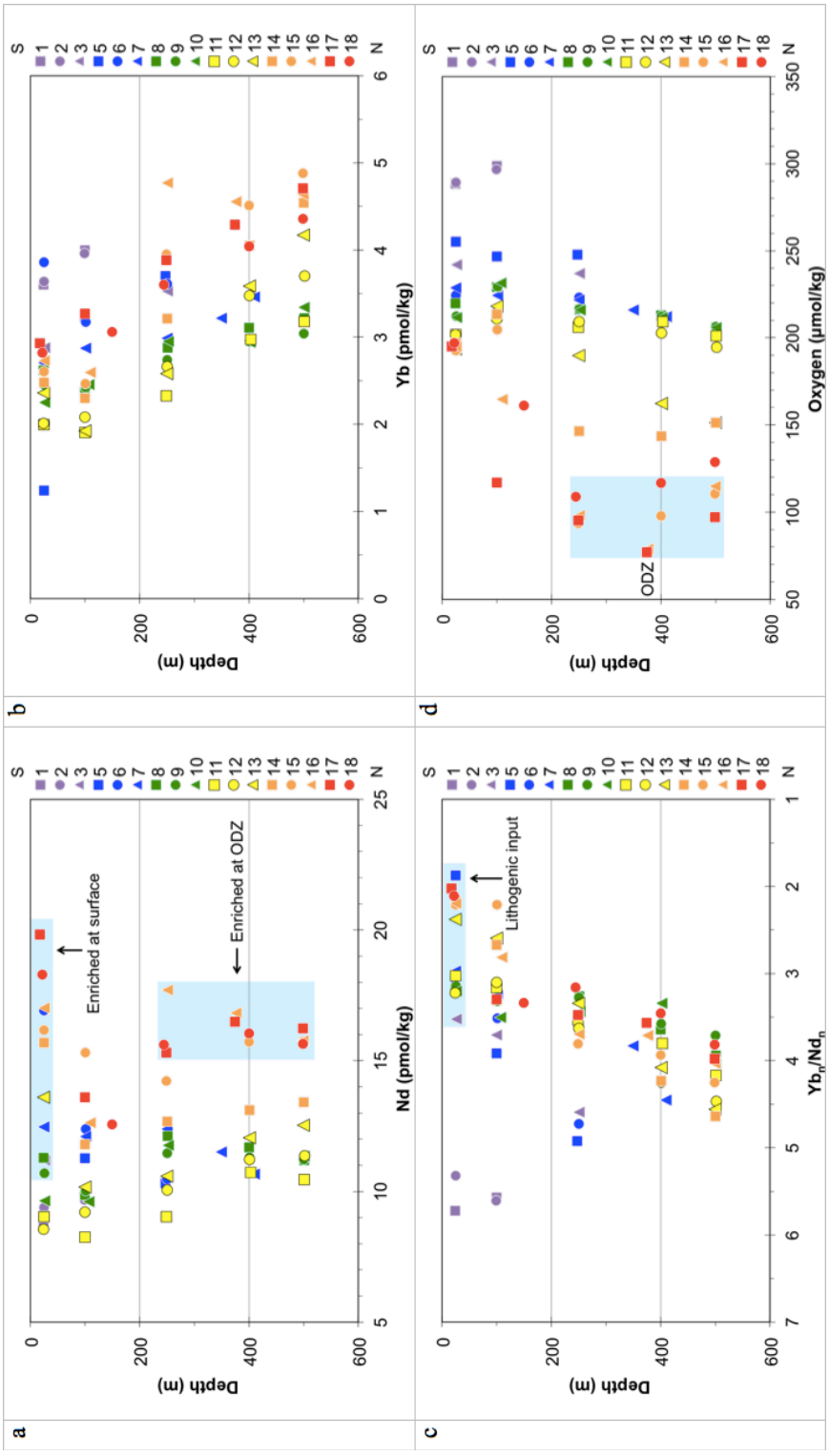

Figure 10. Depth profiles of [Ce] and Ce/Ce* from the surface to depths of AAIW

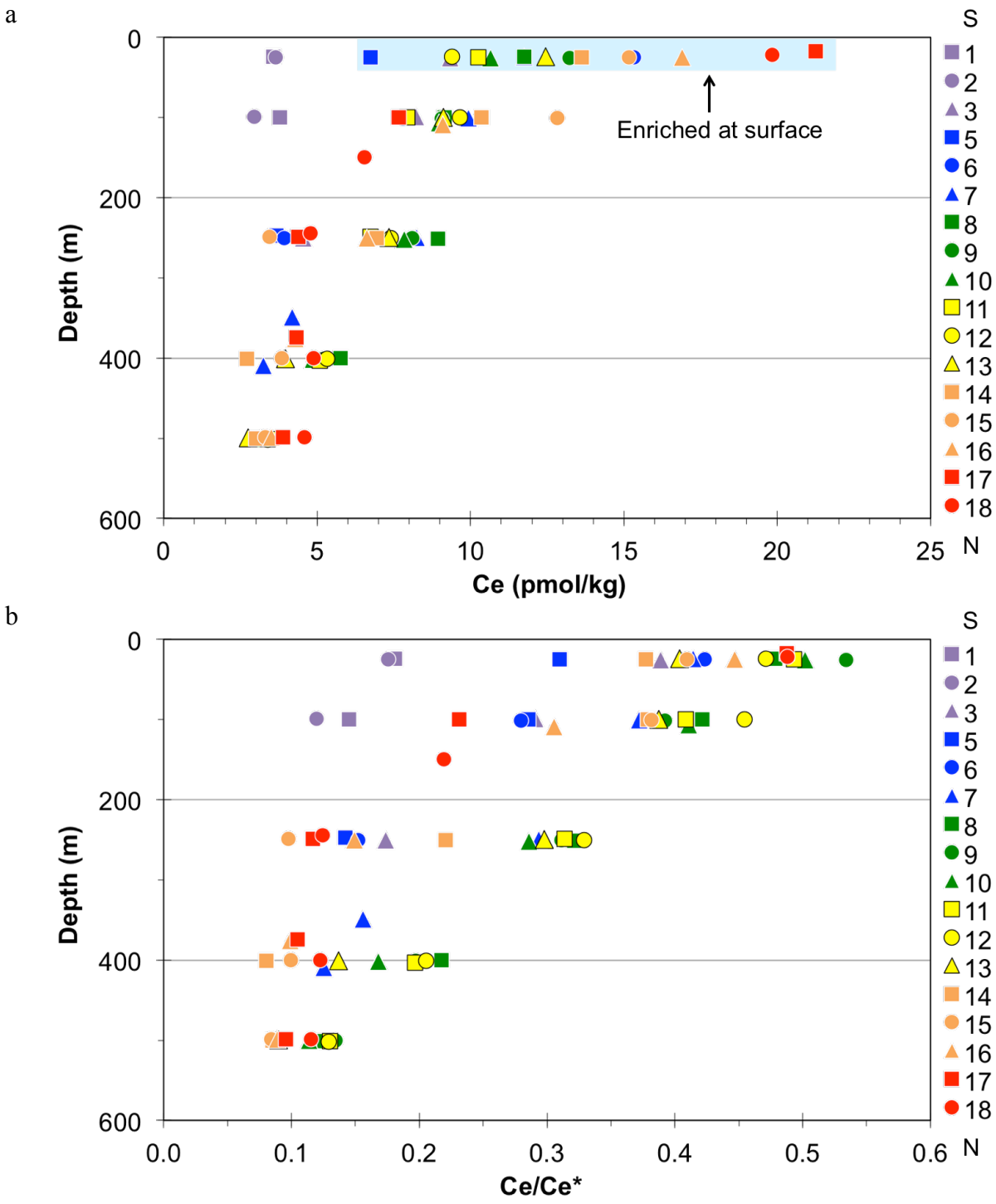

Figure 11. εNd of surface water from the SAMT and surface sediments near South America and Africa

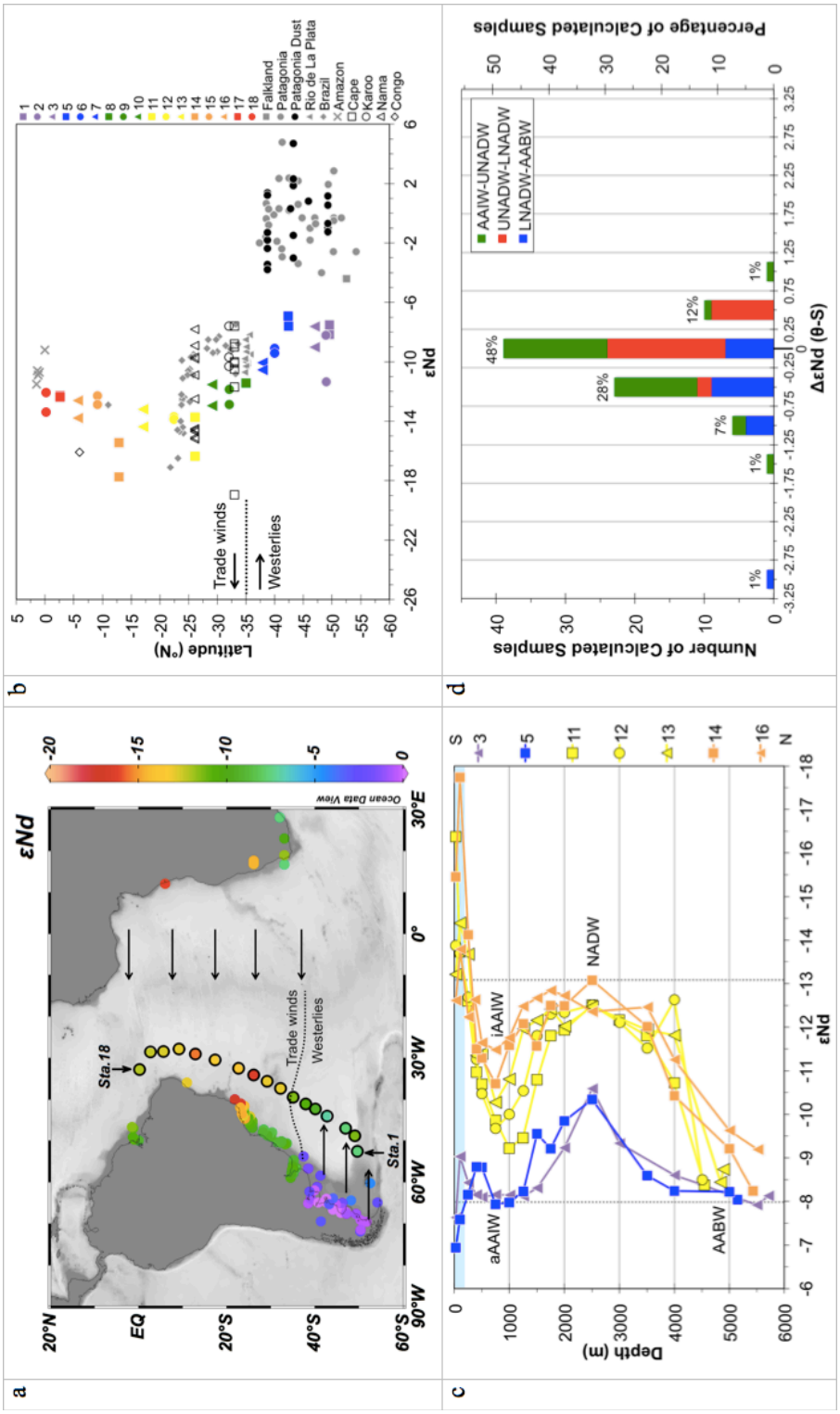

Figure 12. REE concentrations vs. oxygen concentration within SACW

a

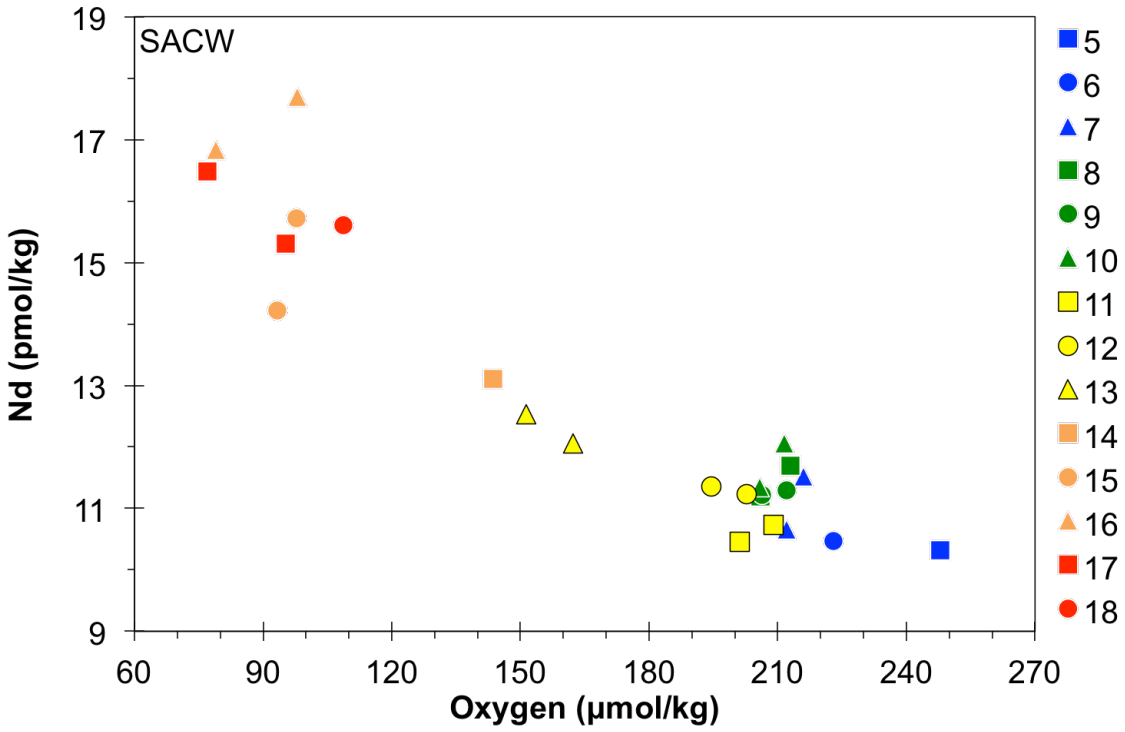


b

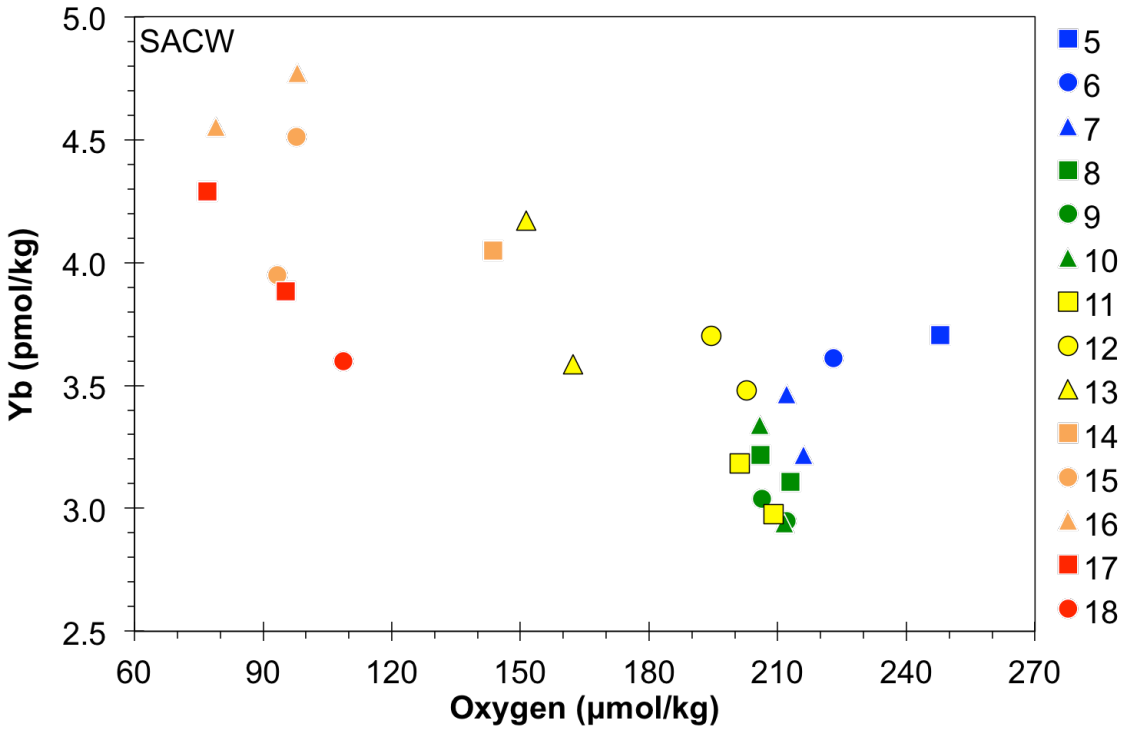

Figure 13. Compare REE concentrations with salinity and $PO_4^*$

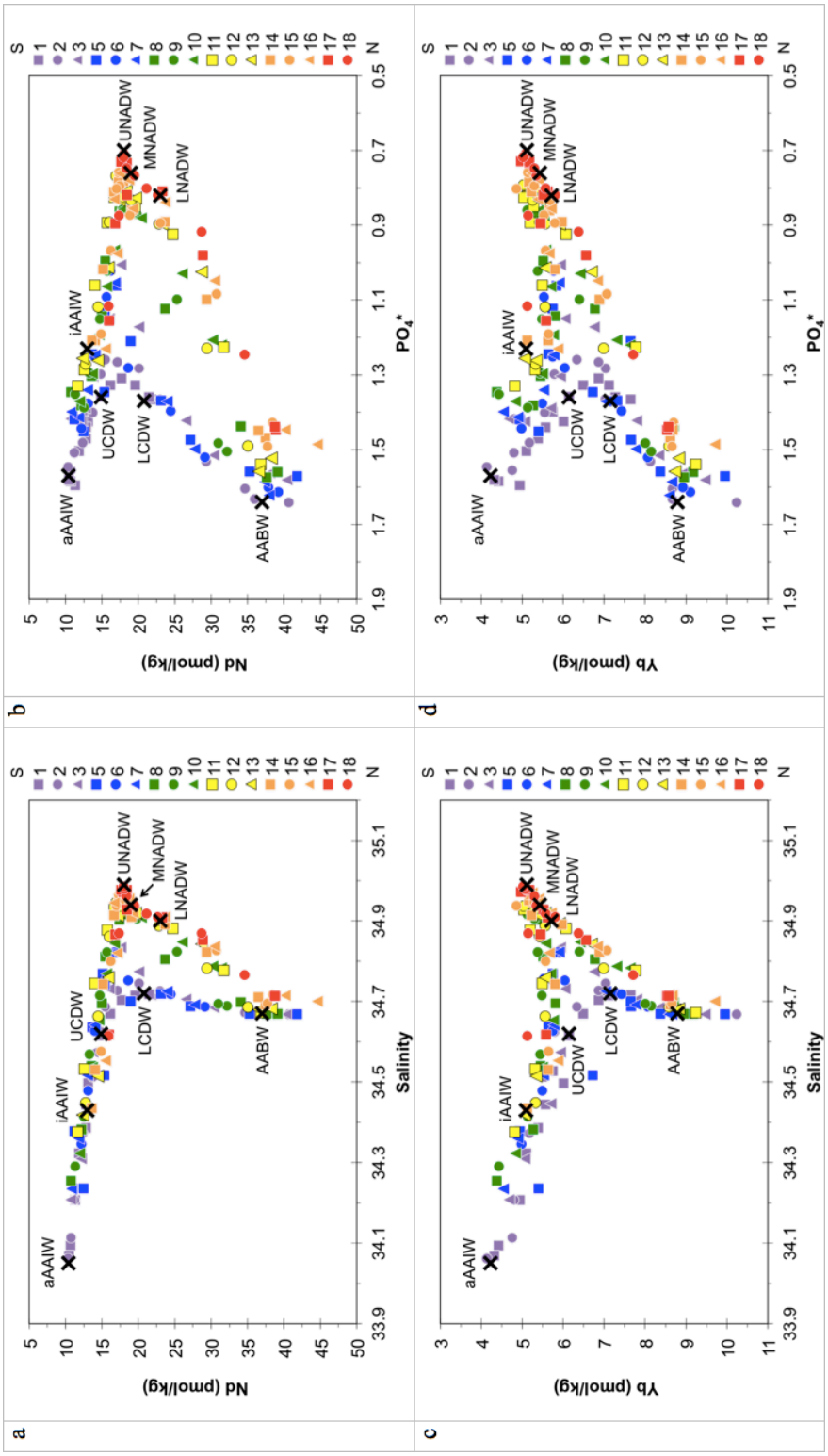

Figure 14. Compare $Yb_n/Nd_n$ with salinity, $PO_4^*$, and εNd below the depths of AAIW

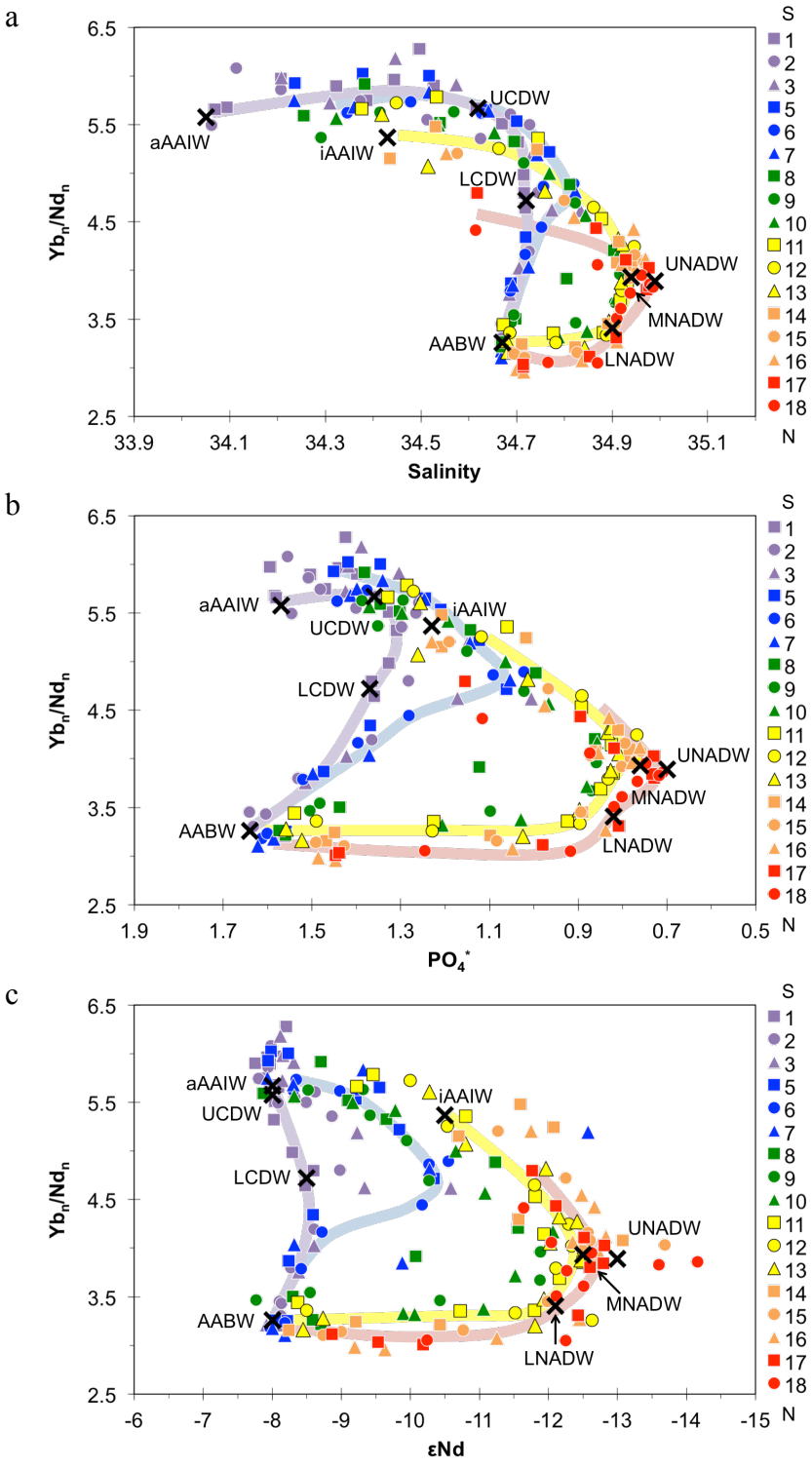

Figure 15. Compare $Yb_n/Nd_n$ with 1/[Nd] and $Nd_n/Yb_n$ with 1/[Yb] below the depths of AAIW

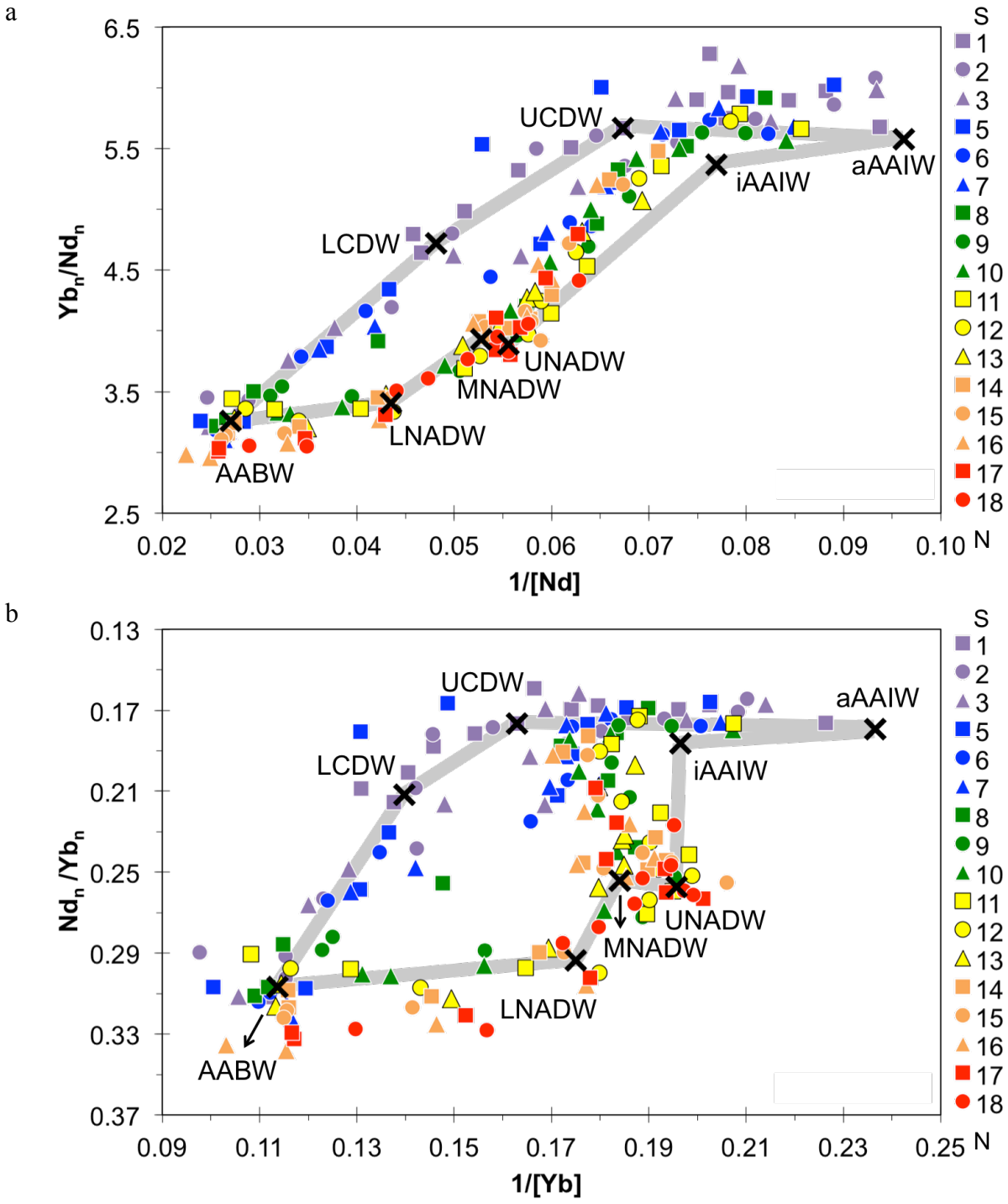

Figure 16. Histograms of Δ[REE](%), $\Delta(Yb_n/Nd_n)$(%) and ΔεNd calculated based on water mass mixing using salinity and potential temperature

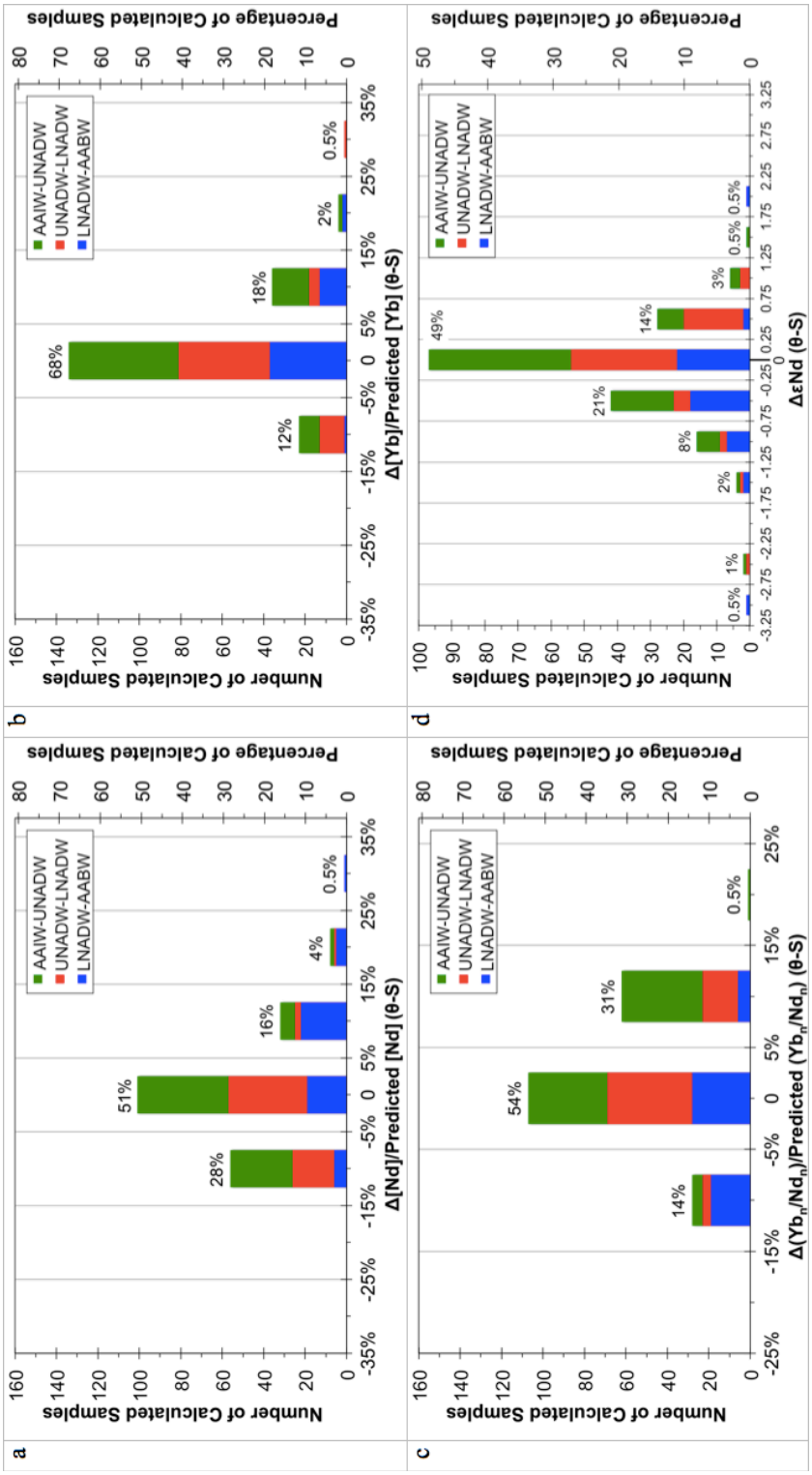

Figure 17. Section profiles of salinity with contours of neutral density, Δ[Nd](%), and Δ[Yb](%) based on salinity and potential temperature

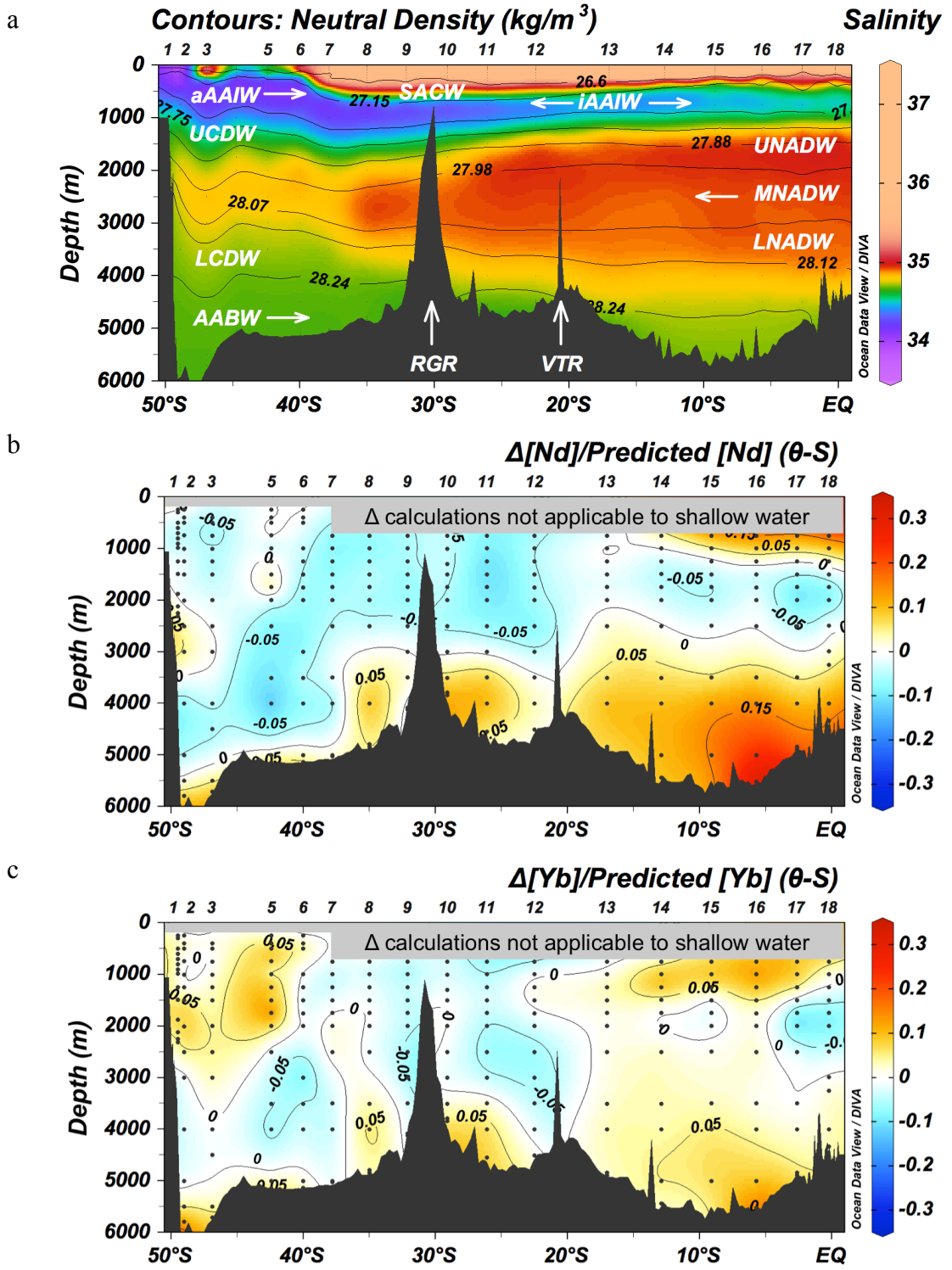

Figure 18. Section profiles of $PO_4^*$ with contours of neutral density, $\Delta(Yb_n/Nd_n)(\%)$, and $\Delta\varepsilon Nd$ based on salinity and potential temperature

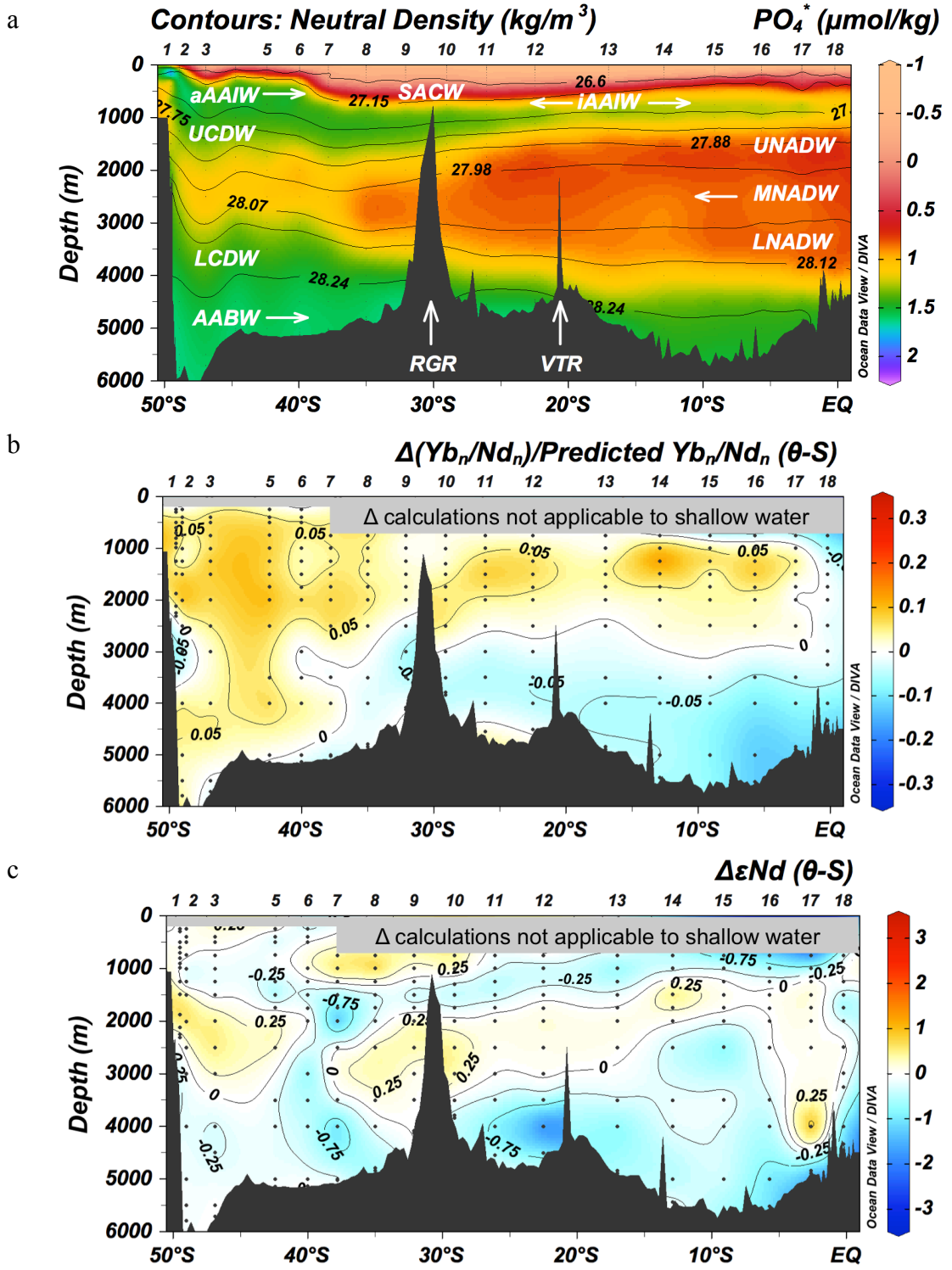

Table 1. Isotope concentrations and natural abundances for DKM spike and diluted spike solution (dilution factor = 36744).

Table 2. Seawater REE concentrations of GEOTRACES station BATS at 20 m and 2000 m analyzed in this study with two standard deviations (2σ SD) and relative two standard deviations (2σ RSD). REE concentrations at 2000 m of BATS analyzed in this study are compared with GEOTRACES intercalibration values (van de Flierdt et al., 2012).

Table 3. Sampling location, depth, REE concentration, Ce anomaly, and $Yb_n/Nd_n$ for the 17 seawater profiles collected from the Southwest Atlantic Meridional Transect (SAMT). Table 3 is in the Appendix 2.

Table 4. (a) Water mass end-member compositions based on data from the SAMT. (b) Water mass end-member compositions based on hydrographic data from World Ocean Atlas 2013 and published εNd and REE data in the water mass formation regions.

Table 5. Median, mean and one standard deviation (1σ SD) values of calculated Δ[REE](%), Δ(REE ratio)(%), and ΔεNd based on (a) salinity, potential temperature; (b) $PO_4^*$, potential temperature; and (c) $PO_4^*$, salinity.

Table 1. Isotope concentrations and natural abundances for DKM spike and diluted spike solution

| Isotope | DKM Spike Concentration | Diluted Spike Concentration | Natural Abundance |
|---|---|---|---|
| | μmol/g | μmol/g | |
| $^{138}$La | 5.64E-04 | 1.53E-08 | 0.0009 |
| $^{139}$La | 7.77E-03 | 2.12E-07 | 0.9991 |
| $^{140}$Ce | 1.27E-02 | 3.46E-07 | 0.8848 |
| $^{142}$Ce | 1.45E-01 | 3.95E-06 | 0.1108 |
| $^{143}$Nd | 7.46E-04 | 2.03E-08 | 0.1218 |
| $^{144}$Nd | 8.93E-02 | 2.43E-06 | 0.0830 |
| $^{147}$Sm | 1.82E-04 | 4.94E-09 | 0.1500 |
| $^{149}$Sm | 4.81E-02 | 1.31E-06 | 0.1380 |
| $^{151}$Eu | 7.92E-04 | 2.16E-08 | 0.4780 |
| $^{153}$Eu | 1.39E-02 | 3.77E-07 | 0.5220 |
| $^{155}$Gd | 2.72E-02 | 7.39E-07 | 0.1480 |
| $^{157}$Gd | 3.73E-04 | 1.02E-08 | 0.1565 |
| $^{161}$Dy | 2.84E-02 | 7.74E-07 | 0.1889 |
| $^{163}$Dy | 4.55E-04 | 1.24E-08 | 0.2490 |
| $^{166}$Er | 4.38E-04 | 1.19E-08 | 0.3360 |
| $^{167}$Er | 1.38E-02 | 3.74E-07 | 0.2295 |
| $^{171}$Yb | 1.52E-02 | 4.12E-07 | 0.1430 |
| $^{174}$Yb | 1.55E-04 | 4.23E-09 | 0.3180 |
| $^{175}$Lu | 1.22E-04 | 3.32E-09 | 0.9741 |
| $^{176}$Lu | 3.08E-04 | 8.38E-09 | 0.0259 |

Table 2. Seawater REE concentrations of GEOTRACES station BATS at 20 m and 2000 m

| | La | Ce | Pr | Nd | Sm | Eu | Gd | Tb | Dy | Ho | Er | Tm | Yb | Lu |
|---|---|---|---|---|---|---|---|---|---|---|---|---|---|---|
| BATS 20 m | | | | | | | | | | | | | | |
| Average of this study (pmol/kg) (n = 16) | 14.30 | 10.33 | 3.28 | 14.09 | 3.15 | 0.87 | 4.33 | 0.77 | 5.99 | 1.45 | 4.80 | 0.64 | 4.20 | 0.66 |
| 2σ SD (pmol/kg) | 0.72 | 0.50 | 0.22 | 0.49 | 0.16 | 0.06 | 0.27 | 0.04 | 0.28 | 0.09 | 0.21 | 0.03 | 0.14 | 0.05 |
| 2σ RSD (%) | 5.00 | 4.81 | 6.77 | 3.49 | 5.13 | 6.84 | 6.13 | 5.32 | 4.72 | 6.35 | 4.35 | 4.03 | 3.43 | 7.22 |
| | | | | | | | | | | | | | | |
| BATS 2000 m | | | | | | | | | | | | | | |
| Average of this study (pmol/kg) (n = 14) | 23.54 | 4.24 | 4.21 | 17.23 | 3.38 | 0.87 | 4.20 | 0.74 | 5.76 | 1.44 | 4.91 | 0.68 | 4.72 | 0.78 |
| 2σ SD (pmol/kg) | 1.21 | 0.15 | 0.07 | 0.49 | 0.13 | 0.05 | 0.25 | 0.03 | 0.25 | 0.03 | 0.23 | 0.02 | 0.22 | 0.03 |
| 2σ RSD (%) | 5.14 | 3.45 | 1.71 | 2.83 | 3.98 | 5.51 | 5.94 | 4.69 | 4.39 | 2.29 | 4.78 | 3.28 | 4.57 | 4.35 |
| GEOTRACES intercalibration value (pmol/kg) | 23.61 | 5.12 | 4.03 | 17.32 | 3.45 | 0.91 | 4.84 | 0.79 | 5.80 | 1.52 | 5.04 | 0.74 | 4.76 | 0.81 |
| 2σ SD (pmol/kg) | 2.79 | 2.27 | 0.36 | 1.22 | 0.34 | 0.10 | 0.53 | 0.08 | 0.38 | 0.09 | 0.25 | 0.05 | 0.25 | 0.04 |
| 2σ RSD (%) | 11.83 | 44.42 | 8.88 | 7.04 | 9.74 | 11.17 | 10.91 | 9.69 | 6.53 | 5.83 | 4.97 | 6.82 | 5.28 | 4.53 |

Table 4. South Atlantic water mass end-member compositions

| | Salinity | Potential Temperature | $PO_4^*$ | Silicate | Oxygen | Neutral Density | εNd | [La] | [Nd] | [Er] | [Yb] |
|---|---|---|---|---|---|---|---|---|---|---|---|
| | | °C | μmol/kg | μmol/kg | μmol/kg | $kg/m^3$ | | pmol/kg | pmol/kg | pmol/kg | pmol/kg |
| a | | | | | | | | | | | |
| UNADW | 34.99 | 4.16 | 0.70 | 16 | 242 | 27.90 | −13.0 | 23.35 | 18.00 | 5.23 | 5.05 |
| MNADW | 34.94 | 2.74 | 0.76 | 27 | 247 | 28.04 | −12.5 | 26.45 | 19.47 | 5.51 | 5.35 |
| LNADW | 34.90 | 2.11 | 0.82 | 32 | 255 | 28.11 | −12.1 | 29.91 | 22.69 | 5.77 | 5.81 |
| SACW | 34.31 | 6.26 | 1.05 | 8 | 255 | 27.10 | −8.6 | 14.09 | 10.39 | 3.86 | 3.66 |
| aAAIW | 34.05 | 3.12 | 1.57 | 15 | 295 | 27.28 | −8.1 | 15.38 | 10.32 | 4.37 | 4.14 |
| iAAIW | 34.42 | 4.52 | 1.25 | 30 | 175 | 27.42 | −10.3 | 17.34 | 12.38 | 4.71 | 5.06 |
| UCDW | 34.62 | 2.20 | 1.36 | 81 | 168 | 27.87 | −8.0 | 24.93 | 14.85 | 5.82 | 6.14 |
| LCDW | 34.72 | 1.12 | 1.37 | 108 | 195 | 28.12 | −8.5 | 33.60 | 21.45 | 6.91 | 7.27 |
| AABW | 34.67 | -0.16 | 1.64 | 127 | 225 | 28.30 | −8.0 | 50.49 | 36.99 | 8.50 | 8.79 |
| b | | | | | | | | | | | |
| UNADW | 35.02 | 4.35 | 0.69 | 13 | 250 | 27.90 | −13.2 | 23.27 | 17.49 | 5.01 | 4.74 |
| MNADW | 34.96 | 3.01 | 0.78 | 19 | 263 | 28.02 | −12.6 | 23.94 | 18.27 | 5.00 | 4.82 |
| LNADW | 34.92 | 2.23 | 0.81 | 25 | 266 | 28.10 | −12.2 | 29.72 | 23.63 | 5.61 | 5.47 |
| SACW | 34.65 | 9.27 | 0.59 | 5 | 240 | 26.89 | − | 14.10 | 10.19 | 3.56 | 3.40 |
| aAAIW | 34.16 | 3.27 | 1.52 | 22 | 285 | 27.37 | −8.0 | − | 10.79 | − | − |
| iAAIW | 34.38 | 4.78 | 1.17 | 26 | 214 | 27.35 | −9.2 | 17.97 | 11.19 | 4.55 | 4.69 |
| UCDW | 34.60 | 2.22 | 1.36 | 75 | 175 | 27.85 | −8.4 | 22.65 | 13.94 | 5.05 | 5.61 |
| LCDW | 34.71 | 1.05 | 1.37 | 109 | 198 | 28.13 | −8.4 | 34.38 | 22.50 | 6.66 | 7.33 |
| AABW | 34.66 | -0.35 | 1.65 | 122 | 235 | 28.33 | −9.0 | 39.50 | 26.07 | 7.38 | 7.81 |

Table 5. Median, mean and one standard deviation values of calculated Δ[REE](%), Δ(REE ratio)(%), and ΔεNd

| | Δ[Nd](%) | Δ[Yb](%) | $\Delta(Yb_n/Nd_n)$(%) | ΔεNd |
|---|---|---|---|---|
| | % | % | % | εNd unit |
| (a) θ-S | | | | |
| Median | −2 | 1 | 3 | −0.06 |
| Mean | 0 | 1 | 2 | −0.15 |
| 1σ SD | 8 | 6 | 6 | +0.60 |
| (b) $PO_4^*$-θ | | | | |
| Median | 0 | 1 | 1 | −0.22 |
| Mean | 2 | 2 | 0 | −0.32 |
| 1σ SD | 9 | 6 | 7 | +0.63 |
| (c) $PO_4^*$-S | | | | |
| Median | −1 | 1 | 2 | −0.13 |
| Mean | 0 | 1 | 2 | −0.22 |
| 1σ SD | 8 | 5 | 6 | +0.58 |

## Supplementary Information

# Chapter 3. The Rare Earth Element Distribution of Seawater in the Southwest Atlantic Meridional Transect (GEOTRACES GA02 Leg 3)

This supplementary information includes (1) a description of hydrographic properties of shallow to deep water masses and their pathways in the Atlantic Ocean, (2) an explanation of how we defined the water mass end-member compositions based on data from the Southwest Atlantic Meridional Transect (SAMT), (3) an explanation of how we defined the water mass end-member compositions based on data from the water mass source regions, (4) a description of how εNd and REEs change for each water mass along their transport paths, (5) a description of how εNd and REEs change zonally for NADW (~10°S) , LCDW (~40°S), and AABW (~40°S and ~10°S), (6) calculations of Δ[REE](%) and Δ(REE ratio)(%) based on (i) $PO_4^*$, potential temperature and (ii) $PO_4^*$, salinity in the SAMT intermediate and deep water, and (7) evaluations on conservative vs. non-conservative behavior of REEs based on calculations in (6).

**1. Water masses and their transport paths in the Atlantic Ocean**

This section is the same as Supplementary Information Section 1 of Chapter 2.

**2. How the water mass end-member compositions are defined based on data from the SAMT**

This section is the same as Supplementary Information Section 2 of Chapter 2.

**3. Defining water mass end-member compositions in water mass formation regions based on published εNd and REE data**

This section is the same as Supplementary Information Section 3 of Chapter 2.

**4. How εNd and REEs change along the water mass transport paths**

For each water mass, how REEs and εNd change along its water mass transport path has important implications for whether REEs and εNd behave conservatively along the advective pathways and where they show deviations from conservative water mass mixing. The SAMT crosses a zonal transect CoFeMUG (cobalt, iron and micro-organisms from the upwelling zone to the gyre) cruise at ~10°S (Fig. S13). This is a GEOTRACES compliant data cruise (GAc01). The SAMT also crosses another zonal transect GEOTRACES cruise GA10 at ~40°S (Fig. S13). The cruise reports for the above cruises are available in www.geotraces.org. The water masses of GAc01 and GA10 were defined in this study based on the same hydrographic properties as the SAMT end-members: the salinity minimum for aAAIW in the South Atlantic, the oxygen minimum for UCDW in the South Atlantic, the salinity maximum for UNADW in the North Atlantic, the oxygen minimum for MNADW in the North Atlantic, the oxygen maximum for LNADW in the North Atlantic, the salinity maximum for LCDW in the South Atlantic, and the lowest potential temperature for AABW in the South Atlantic. Then the corresponding εNd and REE data of these samples were used to show how they change along the water mass pathways. Hydrographic properties of the above samples for different water masses are shown in diagrams of potential temperature vs. salinity (Fig. S14b-S22b).

The transport paths with increasing location numbers for each water mass are shown in Fig. S14a-S22a. Here location numbers are not station numbers. They are

locations where REEs and εNd data are available. Changes of REEs and εNd along each water mass pathway are shown in Fig. S14c-g to S22c-g. For each water mass, REEs and εNd are compared with its water mass fraction (Fig. S14h-l to S22h-l). The mixing lines/curves between this water mass and related water masses show mixing triangles where predicted values should fall (Fig. S14h-l to S22h-l). 5% errors for the upper and lower limit of the mixing triangles are also shown in Fig. S14h-l to S22h-l (dashed grey lines/curves). Samples fall in the mixing triangles (including 5% errors) are considered conservative. For samples falling outside of the mixing triangles, it is important to understand how much they deviate from predicted values based on water mass mixing. They indicate where and how much they deviate from conservative behavior along the water mass transport paths. These deviations from predicted values are discussed in the main text Section 4.6 and Supplementary Information Section 6 and 7.

### *4.1. Northern-sourced water masses*

#### *4.1.1. Upper North Atlantic Deep Water*

UNADW is transported to the south along the western boundary and starts to disappear at ~22°S (location 1 to 11; Fig. S14a). Along the southward transport path of UNADW, Nd concentrations show a decreasing trend (Fig. S14c) whereas Yb concentrations show an increasing trend (Fig. S14d). The resulting $Yb_n/Nd_n$ ratios of UNADW increase from the WMFR to ~22°S (Fig. S14e). Oxidation of Ce(III) to insoluble Ce(IV) in the ocean results in Ce removal and lower $Ce/Ce^*$. $Ce/Ce^*$ ratios of UNADW tend to decrease from the WMFR to ~22°S (Fig. S14f), probably due to continuous removal of insoluble Ce(IV) along the water mass transport path. εNd-values

of UNADW increase along the transport path (Fig. S14g) due to increasing influence of the southern-sourced water masses (εNd = −10.3 to −8.0).

Water masses mixing with UNADW are iAAIW, UCDW, and MNADW (Fig. S14h-l). Out of 22 samples, the percentages of samples falling within the mixing triangles of water mass end-members and indicating conservative behavior are 91% for Nd concentrations (Fig. S14h), 91% for Yb concentrations (Fig. S14i), 73% for $Yb_n/Nd_n$ ratios (Fig. S14j), and 45% for $Ce/Ce^*$ ratios (Fig. S14k). For εNd-values, 86% of the samples are within the mixing triangles of the water mass end-members (Fig. S14l) indicating conservative water mass mixing.

*4.1.2. Middle North Atlantic Deep Water*

MNADW moves southward from the WMFR along the western boundary and turns eastward at ~35°S before flowing eastward along ~40°S (location 1 to 21; Fig. S15a). The samples along ~40°S are from the zonal transect GA10 (REE data available in the GEOTRACES Intermediate Data Product 2017). Nd concentrations (Fig. S15c) and Yb concentrations (Fig. S15d) of MNADW do not change much from the WMFR to ~35°S in the western basin (location 1 to 15; Fig. S15a). After MNADW turns eastward and flows along ~40°S (location 16 to 21; Fig. S15a), Nd concentrations are lower (Fig. S15c) whereas Yb concentrations are higher (Fig. S15d) in the eastern basin than that in the western basin. The resulting $Yb_n/Nd_n$ ratios of MNADW are higher in the eastern basin than that in the western basin (Fig. S15e). Similar to UNADW, $Ce/Ce^*$ ratios of MNADW tend to decrease from the WMFR to ~35°S (Fig. S15f). Then $Ce/Ce^*$ ratios

increase after MNADW turns eastward and flows along ~40°S (Fig. S15f). Similar to UNADW, εNd-values of MNADW increase along the transport path (Fig. S15g).

Water masses mixing with MNADW are UCDW, UNADW, LNADW, and LCDW (Fig. S15h-l). Out of 23 samples, the percentages of samples falling within the mixing triangles of water mass end-members and indicating conservative behavior are 96% for Nd concentrations (Fig. S15h), 96% for Yb concentrations (Fig. S15i), 100% for $Yb_n/Nd_n$ ratios (Fig. S15j), and 52% for $Ce/Ce^*$ ratios (Fig. S15k). For εNd-values, 91% of the samples are within the mixing triangles of the water mass end-members (Fig. S15l) indicating conservative water mass mixing.

*4.1.3. Lower North Atlantic Deep Water*

LNADW has the same transport path as MNADW-southward path from the WMFR to ~35°S and then eastward along ~40°S (location 1 to 21; Fig. S16a). Nd concentrations of LNADW (Fig. S16c) do not change much and Yb concentrations of LNADW (Fig. S16d) slightly increase from the WMFR to ~26°S in the western basin (location 1 to 12; Fig. S16a). After LNADW turns eastward and moves along ~40°S (location 16 to 21; Fig. S16a), Nd concentrations are lower (Fig. S16c) whereas Yb concentrations do not change much (Fig. S16d) in the eastern basin compared to that in the western basin. $Yb_n/Nd_n$ ratios of LNADW in the eastern basin are about the same as that in the western basin (Fig. S16e). Similar to UNADW and MNADW, $Ce/Ce^*$ ratios of LNADW tend to decrease from the WMFR to ~35°S (Fig. S16f). $Ce/Ce^*$ ratios increase after LNADW turns eastward and transports along ~40°S (Fig. S16f). Similar to

UNADW and MNADW, εNd-values of LNADW indicate conservative water mass mixing with increasing values along the transport path (Fig. S16g,l).

Water masses mixing with LNADW are MNADW, LCDW, and AABW (Fig. S16h-l). Out of 22 samples, the percentages of samples falling within the mixing triangles of water mass end-members and indicating conservative behavior are 77% for Nd concentrations (Fig. S16h), 100% for Yb concentrations (Fig. S16i), 82% for $Yb_n/Nd_n$ ratios (Fig. S16j), and 82% for $Ce/Ce^*$ ratios (Fig. S16k). For εNd-values, 91% of the samples are within the mixing triangles of the water mass end-members (Fig. S16l) indicating conservative water mass mixing.

### *4.2. Southern-Sourced water masses*

#### *4.2.1. South Atlantic Central Water*

After SACW is formed in the Brazil-Malvinas confluence zone (location 1; Fig. S17a), it moves eastward to southern Africa (location 2 to 11; Fig. S17a) and then northwestward towards Brazil. It separates into southward (location 12S to 17S; Fig. S17a) and northward (location 12N to 17N; Fig. S17a) directions after it reaches the western boundary at ~20°S. Nd concentrations (8.6 to 12.2 pmol/kg) do not change much from the WMFR towards the east along ~40°S (Fig. S17c). After SACW turns around and reaches the western boundary, the southward branch does not show much change in Nd concentrations (8.6 to 12.2 pmol/kg) whereas the northward branch shows increasing Nd concentrations (Fig. S17c). Yb concentrations range from 2.3 to 3.8 pmol/kg and do not show a trend from the WMFR towards east along ~40°S (Fig. S17d). The southward branch generally shows lower Yb concentrations than that of the northward branch (Fig.

S17d). $Yb_n/Nd_n$ ratios scatter between 3.5 and 4.9 from the WMFR towards east along ~40°S (Fig. S17e). After SACW reaches the western boundary, $Yb_n/Nd_n$ ratios decrease in both southward and northward directions (Fig. S17e). $Ce/Ce^*$ ratios do not show an obvious trend along the SACW pathway (Fig. S17f). The southward branch of SACW shows increasing εNd (Fig. S17g) indicating influence of the southern-sourced water masses. The northward branch of SACW shows decreasing εNd (Fig. S17g) indicating influence of the northern-sourced water masses.

At depths of SACW, samples from the zonal transect GAc01 along ~10°S (Zheng et al., 2016) (location 13.5 to 24.5; Fig. S17a) show increasing Nd concentrations (Fig. S17c), increasing Yb concentrations (Fig. S17d), decreasing $Yb_n/Nd_n$ ratios (Fig. S17e) and increasing $Ce/Ce^*$ ratios (Fig. S17f) from the western basin to the eastern basin. These have been explained by the release of REEs from reduction of Fe-Mn oxides in the ODZ (Zheng et al., 2016).

*4.2.2. Antarctic Intermediate Water from the Atlantic Ocean*

aAAIW flows northward to the Brazil-Malvinas Current confluence at ~40°S and then eastward along ~40°S (location 1 to 14; Fig. S18a). Due to higher depth resolution of sampling at the SAMT, aAAIW from the SAMT has larger ranges of Nd and Yb concentrations than that from GA10 along ~40°S (Fig. S18c,d). $Yb_n/Nd_n$ of aAAIW from the SAMT has a larger range than that from the zonal transect GA10 along ~40°S but does not show obvious trend along the water mass transport path (Fig. S18e). $Ce/Ce^*$ ratios increase from the WMFR to ~40°S and then show a decreasing trend along ~40°S (Fig. S18f). εNd-values do not change much along the aAAIW pathway (Fig. S18g).

Water masses mixing with aAAIW are SACW, iAAIW, and UCDW (Fig. S18h-l). Out of 11 samples, the percentages of samples falling within the mixing triangles of water mass end-members and indicating conservative behavior are 91% for Nd concentrations (Fig. S18h), 82% for Yb concentrations (Fig. S18i), 45% for $Yb_n/Nd_n$ ratios (Fig. S18j), and 64% for $Ce/Ce^*$ ratios (Fig. S18k). All εNd-values are within the mixing triangles of the water mass end-members (Fig. S18l) indicating conservative water mass mixing.

*4.2.3. Antarctic Intermediate Water from the Indian Ocean*

iAAIW enters the South Atlantic via the Agulhas leakage before moving northwest and then westward at ~20°S (location 1 to 2; Fig. S19a). When it reaches the western boundary, it moves in two directions: southward direction from ~20°S to ~40°S (location 2S to 7S; Fig. S19a) and northward toward along the western boundary (location 2N to 7N; Fig. S19a). Nd and Yb concentrations both increase from the WMFR to the western boundary (Fig. S19c,d). Then the southward branch shows decreasing Nd and Yb concentrations, whereas the northward branch shows increasing Nd and Yb concentrations (Fig. S19c,d). Both southward and northward branches of iAAIW show decreasing $Yb_n/Nd_n$ (Fig. S19e) and increasing $Ce/Ce^*$ (Fig. S19f) along the iAAIW transport path. The southward branch of iAAIW shows increasing εNd, whereas the northward branch shows decreasing εNd (Fig. S19g).

Water masses mixing with iAAIW are SACW, aAAIW, UCDW, and UNADW (Fig. S19h-l). Out of 16 samples, the percentages of samples falling within the mixing triangles of water mass end-members and indicating conservative behavior are 75% for

Nd concentrations (Fig. S19h), 81% for Yb concentrations (Fig. S19i), 94% for $Yb_n/Nd_n$ ratios (Fig. S19j), and 62.5% for $Ce/Ce^*$ ratios (Fig. S19k). 37.5% of the $Ce/Ce^*$ ratios are higher than the iAAIW-SACW mixing curve (Fig. S19k). For εNd-values, 62.5% of the samples fall within the mixing triangles of water mass end-members (Fig. S19l) indicating conservative water mass mixing.

*4.2.4. Upper Circumpolar Deep Water*

UCDW moves northward to ~20°S in the western basin and most of it returns southward to the eastern basin (Fig. S20a). Nd concentrations do not show much change (Fig. S20c) whereas Yb concentrations show a decreasing trend (Fig. S20d) on the northward path of UCDW (location 1 to 12; Fig. S20a). The resulting $Yb_n/Nd_n$ ratios also tend to decrease along the UCDW pathway (Fig. S20e). $Ce/Ce^*$ ratios show an increasing trend along the UCDW pathway (Fig. S20f). εNd-values decrease when UCDW moves northward (Fig. S20g) and indicate increasing influence of the northern-sourced water masses.

Water masses mixing with UCDW are aAAIW, iAAIW, UNADW, MNADW, and LCDW (Fig. S20h-l). Out of 40 samples, the percentages of samples falling within the mixing triangles of water mass end-members and indicating conservative behavior are 90% for Nd concentrations (Fig. S20h), 93% for Yb concentrations (Fig. S20i), 77.5% for $Yb_n/Nd_n$ ratios (Fig. S20j), and 95% for $Ce/Ce^*$ ratios (Fig. S20k). 90% of the εNd-values are within the mixing triangles of the water mass end-members (Fig. S20l) indicating conservative water mass mixing.

On the eastward transport path of UCDW (location 6E to 16E; Fig. S20a), both Nd and Yb concentrations slightly increase for the zonal transect GA10 along ~40°S (Fig. S20c,d). $Yb_n/Nd_n$ ratios do not change much whereas $Ce/Ce^*$ ratios tend to increase along the eastward pathway of UCDW (Fig. S20e,f).

*4.2.5. Lower Circumpolar Deep Water*

LCDW moves northward to the equator mainly in the western basin (location 1 to 7; Fig. S21a). Nd concentrations increase whereas Yb concentrations do not change much along the LCDW pathway (Fig. S21c,d). The resulting $Yb_n/Nd_n$ ratios decrease along the northward transport path of LCDW (Fig. S21e). $Ce/Ce^*$ ratios do not show much change along the LCDW pathway (Fig. S21f). εNd-values also do not show much change along the LCDW pathway (Fig. S21g).

Water masses mixing with LCDW are UCDW, MNADW, LNADW, and AABW (Fig. S21h-l). Out of 12 samples, the percentages of samples falling within the mixing triangles of water mass end-members and indicating conservative behavior are 83% for Nd concentrations (Fig. S21h), Yb concentrations (Fig. S21i), 92% for $Yb_n/Nd_n$ ratios (Fig. S21j), and 67% for $Ce/Ce^*$ ratios (Fig. S21k). 92% of the εNd-values are within the mixing triangles of the water mass end-members (Fig. S20l) indicating conservative water mass mixing.

*4.2.6. Antarctic Bottom Water*

AABW formed in the Weddell Sea enters the Argentine Basin along the South Sandwich Trench and then flows northward along the western boundary (location 1 to 17; Fig. S22a). The bottommost samples of AABW (grey symbols in Fig. S22c-l) are not

discussed here due to potential influence from the dissolution of REEs from the sediments on the seafloor. Nd concentrations increase whereas Yb concentrations do not change much along the AABW pathway (Fig. S22c,d). The resulting $Yb_n/Nd_n$ ratios decrease along the northward transport path of AABW (Fig. S22e). $Ce/Ce^*$ ratios do not show much change along the AABW pathway (Fig. S22f). εNd-values also do not show much change from the WMFR to ~32°S and decrease from ~32°S to the equator (Fig. S22g).

Water masses mixing with AABW are LCDW and LNADW (Fig. S22h-l). Out of 17 samples (excluding the bottommost samples), the percentages of samples falling within the mixing triangle of AABW-LCDW-LNADW and indicating conservative behavior are 41% for Nd concentrations (Fig. S22h), 100% for Yb concentrations (Fig. S22i), 53% for $Yb_n/Nd_n$ ratios (Fig. S22j), and 53% for $Ce/Ce^*$ ratios (Fig. S22k). 76.5% of the εNd-values are within the mixing triangle of AABW-LCDW-LNADW (Fig. 22l) indicating conservative water mass mixing.

***4.3. Summary***

For each intermediate and deep water mass mentioned above, REEs generally show conservative mixing along water mass advective pathways. Yb concentrations show the strongest conservative behavior with an average of 91% (± 8%, 1σ) of the values falling within the mixing triangles of water mass end-members. Nd concentrations and $Yb_n/Nd_n$ ratios, with averages of 81% (± 17%, 1σ) and 77% (± 19%, 1σ) of the values falling within the mixing triangles of water mass end-members, show less conservative behavior compared to Yb concentrations. An average of 64% (± 17%, 1σ) of $Ce/Ce^*$

ratios fall within the mixing triangles of water mass end-members and show conservative water mass mixing. A possible explanation for stronger conservative behavior of Yb is that Yb is more soluble in seawater and less preferentially scavenged compared to Nd. The resulting $Yb_n/Nd_n$ ratios are more sensitive to test conservative mixing vs. external addition processes. εNd-values of the above intermediate and deep water masses show conservative behavior with an average of 86% (± 12%, 1σ) of the values falling within the mixing triangles of water mass end-members.

## 5. How REEs change zonally for NADW (~10°S), LCDW (~40°S), and AABW (~40°S and ~10°S)

### *5.1. Northern-sourced NADW*

NADW enters the western basin of South Atlantic Ocean along the western boundary (Stramma and England, 1999). It also enters the eastern basin of South Atlantic through the Romanche Fracture Zone at the equator and moves southward along the eastern boundary (Stramma and England, 1999). Along ~10°S, eastward flow of NADW from the western boundary is observed but it does not reach into the eastern Angola Basin (Koltermann et al., 2011). Along ~15°S, westward flow of NADW from the eastern boundary is observed and it recirculates within the Angola Basin (Stramma and England, 1999). Therefore, both eastward and westward NADW towards the Mid-Atlantic Ridge (MAR) are seen along the zonal transect of 10-15°S (Fig. S14a-S16a).

At depths of UNADW (1000-2000 m), the eastward UNADW from the zonal transect GAc01 along ~10°S (Zheng et al., 2016) (Fig. S14a) shows no obvious trend for

Nd concentrations (Fig. S23a), increasing Yb concentrations (Fig. S23b), no obvious trend for $Yb_n/Nd_n$ ratios (Fig. S23c) and $Ce/Ce^*$ ratios (Fig. S23d) from the west to the MAR (location 8.5 to 13.5). The westward UNADW (Fig. S14a) shows decreasing Nd concentrations (Fig. S23a), decreasing Yb concentrations (Fig. S23b), slightly increasing $Yb_n/Nd_n$ ratios (Fig. S23c) and decreasing $Ce/Ce^*$ ratios (Fig. S23d) from the east to the MAR (location 18.5 to 13.5). Zheng et al. (2016) deconvolved conservative and non-conservative components for samples below 1000 m for the zonal transect GAc01 along ~10°S. For samples at depths of UNADW, REEs behave conservatively from the west to the MAR and additions of non-conservative REEs increase from the MAR to the east (Zheng et al., 2016). Zheng et al. (2016) ruled out the explanation of release of REEs from Fe-Mn oxides for these samples because the water is well oxygenated below 1000 m. Since the highest addition of non-conservative REEs are observed close to the margin, the source of REEs is attributed to the release of REEs from marginal sediments in the Angola Basin (Zheng et al., 2016).

At depths of MNADW (2000-3000 m), the eastward MNADW from the zonal transect GAc01 along ~10°S (Zheng et al., 2016) (Fig. S15a) shows no obvious trends for Nd concentrations (Fig. S24a), Yb concentrations (Fig. S24b), $Yb_n/Nd_n$ ratios (Fig. S24c) and $Ce/Ce^*$ ratios (Fig. S24d) from the west to the MAR (location 8.5 to 13.5). The westward MNADW (Fig. S15a) shows decreasing Nd concentrations (Fig. S24a), decreasing Yb concentrations (Fig. S24b), no obvious trend for $Yb_n/Nd_n$ ratios (Fig. S24c) and decreasing $Ce/Ce^*$ ratios (Fig. S24d) from the east to the MAR (location 18.5 to 13.5). Similar to UNADW, the zonal change of REEs for MNADW can also be

explained by the release of REEs from marginal sediments in the Angola Basin (Zheng et al., 2016).

At depths of LNADW (3000-4000 m), the eastward LNADW from the zonal transect GAc01 along ~10°S (Zheng et al., 2016) (Fig. S16a) shows no obvious trends for Nd concentrations (Fig. S25a), Yb concentrations (Fig. S25b), $Yb_n/Nd_n$ ratios (Fig. S25c) and $Ce/Ce^*$ ratios (Fig. S25d) from the west to the MAR (location 8.5 to 13.5). The westward LNADW (Fig. S16a) shows decreasing Nd concentrations (Fig. S25a), decreasing Yb concentrations (Fig. S25b), slightly increasing $Yb_n/Nd_n$ ratios (Fig. S25c) and slightly decreasing $Ce/Ce^*$ ratios (Fig. S25d) from the east to the MAR (location 18.5 to 13.5). Similar to UNADW and MNADW, the zonal change of REEs for LNADW can also be explained by the release of REEs from marginal sediments in the Angola Basin (Zheng et al., 2016).

### *5.2. Southern-Sourced LCDW and AABW*

At depths of LCDW (3000-4000 m), samples from the zonal GA10 transect along ~40°S (location 6E to 9E; Fig. S22a) do not show obvious trends for Nd concentrations, Yb concentrations, $Yb_n/Nd_n$ ratios, and $Ce/Ce^*$ ratios from west to east (Fig. S26a-d). At depths of AABW (> 4000 m), samples from the zonal transect GA10 along ~40°S (location 6E to 8E; Fig. S23a) show similar Nd concentrations, Yb concentrations, $Yb_n/Nd_n$ ratios, and $Ce/Ce^*$ ratios compared to SAMT-6 at the same latitude (location 6) (Fig. S27a-d). Samples from the zonal transect GAc01 along ~10°S at depths of AABW (Zheng et al., 2016) (location 14.5 to 17.5; Fig. S23a) show similar Nd concentrations,

Yb concentrations, $Yb_n/Nd_n$ ratios, and $Ce/Ce^*$ ratios compared to nearby stations SAMT-14 and SAMT-15 (locations 14 and 15) (Fig. S27e-h).

**6. Calculations of Δ[REE](%) and Δ(REE ratio)(%) based on (i) $PO_4^*$, potential temperature and (ii) $PO_4^*$, salinity in the SAMT intermediate and deep water**

While the main section of this study uses salinity and potential temperature to evaluate Δ[REE] and Δ(REE ratio) and water mass mixing, we also used different combinations of conservative water mass tracers to calculate Δ[REE] and Δ(REE ratio), in order to investigate whether they will be different from results based on salinity and potential temperature. Here we calculated predicted REE concentrations for each sample were calculated based on (i) $PO_4^*$ and potential temperature; (ii) $PO_4^*$ and salinity. Then REE deviations were calculated with measured REE concentrations/ratios subtracting predicted REE concentrations/ratios. The water mass end-member compositions are based on data from the SAMT (Table 3a).

The fractional contributions of different water masses for each sample were calculated based on $PO_4^*$ and potential temperature using three component mixing equations:

$$f_1 \times PO_{4_1}^* + f_2 \times PO_{4_2}^* + f_3 \times PO_{4_3}^* = PO_4^*$$

$$f_1 \times \theta_1 + f_2 \times \theta_2 + f_3 \times \theta_3 = \theta$$

$$f_1 + f_2 + f_3 = 1$$

$$f_i > 0$$

where $PO_{4_i}^*$, $\theta_i$, and $f_i$ are the phosphate star, potential temperature, and fractional

contribution of water mass i, respectively. The fractions of different water masses for each sample were also calculated based on $PO_4^*$ and salinity using three component mixing equations:

$$f_1 \times PO_{4_1}^* + f_2 \times PO_{4_2}^* + f_3 \times PO_{4_3}^* = PO_4^*$$

$$f_1 \times S_1 + f_2 \times S_2 + f_3 \times S_3 = S$$

$$f_1 + f_2 + f_3 = 1$$

$$f_i > 0$$

where $PO_{4_i}^*$, $S_i$ and $f_i$ are the phosphate star, salinity, and fractional contribution of water mass i, respectively. Then the predicted REE concentrations (e.g. Nd and Yb) were calculated as:

$$[Nd]_{predicted} = [Nd]_1 \times f_1 + [Nd]_2 \times f_2 + [Nd]_3 \times f_3$$

$$[Yb]_{predicted} = [Yb]_1 \times f_1 + [Yb]_2 \times f_2 + [Yb]_3 \times f_3$$

where $[Nd]_i$ and $[Nd]_i$ are the Nd and Yb concentrations of water mass i, and $f_i$ is the fractional contribution of water mass i. The predicted $Yb_n/Nd_n$ values were calculated as:

$$(Yb_n/Nd_n)_{predicted} = \frac{[Yb]_{predicted}/[Yb]_{PAAS}}{[Nd]_{predicted}/[Nd]_{PAAS}}$$

where n stands for normalizing the concentration of an element in the sample to its concentration in Post Archean Australian Shale (PAAS) (Taylor and McLennan, 1985), $[Yb]_{predicted}$ and $[Nd]_{predicted}$ are predicted concentrations, and $[Yb]_{PAAS}$ and $[Nd]_{PAAS}$ are Yb and Nd concentrations in PAAS. The deviations were calculated using measured values subtracting predicted values:

$$\Delta[Nd] = [Nd]_{measured} - [Nd]_{predicted}$$

$$\Delta[\mathrm{Yb}] = [\mathrm{Yb}]_{\mathrm{measured}} - [\mathrm{Yb}]_{\mathrm{predicted}}$$

$$\Delta(\mathrm{Yb_n/Nd_n}) = (\mathrm{Yb_n/Nd_n})_{\mathrm{measured}} - (\mathrm{Yb_n/Nd_n})_{\mathrm{predicted}}$$

Delta values close to zero mean that the measured values are close to the predicted values and indicate conservative behavior. Δ[REE] and Δ(REE ratio) values were compared with predicted values based on conservative water mass mixing as the percent deviations of the measured value from the predicted value, i.e. Δ[REE]/Predicted [REE]×100 and Δ(REE ratio)/Predicted (REE ratio)×100. Here we define Δ[REE]/Predicted [REE] and Δ(REE ratio)/Predicted (REE ratio) as Δ[REE](%) and Δ(REE ratio)(%), respectively.

## 7. Evaluations on conservative vs. non-conservative behavior of REEs based on the above calculations

### *7.1. Intermediate and deep water dominantly controlled by conservative mixing*

We evaluate conservative vs. non-conservative behavior of REEs based on REE deviations from water mass mixing calculated by (i) $PO_4^*$ and potential temperature; (ii) $PO_4^*$ and salinity. Similar to the main text, the following discussion refers to REE concentrations, REE ratios, and εNd-values as "too high" if measured values are higher than predicted by the water mass mixtures, and "too low" if they are lower than predicted by the water mass mixtures. Δ[REE](%) and Δ(REE ratio)(%) values within ± 5% are considered conservative. ΔεNd-values within ± 0.25 εNd units are considered conservative.

Based on $PO_4^*$ and potential temperature, here labeled ($PO_4^*$-θ), Δ[Nd](%) values range from −15% to +33% with a median of 0% and an average of +2% ± 9% (1σ) (Fig.

S28a). 50% of the Δ[Nd](%) values are within ± 5% and 88% of the Δ[Nd](%) values are within ± 15% (Fig. S28a). Δ[Yb](%) values range from −11% to +33% with a median of 1% and an average of +2% ± 6% (1σ) (Fig. S28b). 70% of the Δ[Yb](%) values are within ± 5% and 97% of the Δ[Yb](%) values are within ± 15% (Fig. S28b). 55% of the $\Delta(Yb_n/Nd_n)$(%) values are within ± 5% and 98% of the $\Delta(Yb_n/Nd_n)$(%) values are within ± 15% (Fig. S28c).

Based on $PO_4^*$ and salinity, here labeled ($PO_4^*$-S), Δ[Nd](%) values range from −17% to +32% with a median of −1% and an average of 0% ± 8% (1σ) (Fig. S31a). 52% of the Δ[Nd](%) values are within ± 5% and 93% of the Δ[Nd](%) values are within ± 15% (Fig. S31a). Δ[Yb](%) values range from −13% to +31% with a median of 1% and an average of 1% ± 5% (1σ) (Fig. S31b). 74% of the Δ[Yb](%) values are within ± 5% and 97% of the Δ[Yb](%) values are within ± 15% (Fig. S31b). 56% of the $\Delta(Yb_n/Nd_n)$(%) values are within ± 5% and 97% of the $\Delta(Yb_n/Nd_n)$(%) values are within ± 15% (Fig. S31c).

The above evaluations of conservative behavior of REEs based on (i) $PO_4^*$ and potential temperature; (ii) $PO_4^*$ and salinity show small deviations from conservative water mass mixing. Evaluation of conservative behavior of REEs based on salinity and potential temperature shows similarly small deviations from conservative water mass mixing (main text Section 4.6.2). Therefore, evaluations of conservative behavior of REEs based on three combinations of tracers show that REEs in the intermediate and deep water are dominantly controlled by conservative water mass mixing.

### *7.2. Non-conservative behavior of REEs in different water masses*

Delta values were further separated into three groups using the neutral densities ($\gamma^n$) of the water mass end-members (Table 3a) to investigate deviations from conservative mixing for REE concentrations and ratios within each depth range: (1) from depths of AAIW to UNADW ($\gamma^n$ = 27.15-27.90 kg/m$^3$); (2) from depths of UNADW to LNADW ($\gamma^n$ = 27.90-28.11 kg/m$^3$); (3) from depths of LNADW to the bottom ($\gamma^n$ > 28.11 kg/m$^3$) (Fig. S28,S31). This will allow us to investigate where the data show the most conservative behavior and the largest deviations from conservative behavior.

From depths of AAIW to UNADW, high Δ[REE](%) ($PO_4^*$-θ) (average = +5% to +16%) and high Δ[REE](%) ($PO_4^*$-S) (average = +4% to +10%) are seen at 750-1000 m from SAMT-15 to SAMT-18 (Fig. S29b,c,S32b,c), similar to that in the sections of Δ[REE](%) (θ-S) (average = +8% to +11%) (Fig. 17b,c). These samples show low ΔεNd ($PO_4^*$-θ) with an average of −1.40 ± 0.67 (1σ) εNd units (Fig. S30c) and low ΔεNd ($PO_4^*$-S) with an average of −0.78 ± 0.73 (1σ) εNd units (Fig. S33c), similar to the low ΔεNd (θ-S) (−0.75 ± 0.77; 1σ) (Fig. 18c). As mentioned in the main text Section 4.6.3, SAMT-15 to SAMT-18 are in the trade wind zone and receive eolian dusts from Africa with low εNd (−19 to −8) (Goldstein et al., 1984; Dia et al., 1990). Low εNd-values are observed in SAMT-15 to SAMT-18 at 25-100 m (Fig. 11a,b). Samples at 750-1000 m from SAMT-15 to SAMT-18 are in the ODZ (Fig. 2c,10c), where REEs are released by dissolution of Fe-Mn oxides due to the reducing condition (e.g. (de Baar et al., 1988; German and Elderfield, 1989; German et al., 1991; Sholkovitz et al., 1992; Schijf et al.,

1995)). Therefore, high Δ[REE](%) and low ΔεNd of the above samples reflect REEs with low εNd signal released from the dissolution of Fe-Mn oxides in the ODZ.

From depths of UNADW to LNADW, slightly high Δ[REE](%) ($PO_4^*$-θ) (average = +2% to +5%) and slightly high Δ[Yb](%) ($PO_4^*$-S) (average = +2%) are seen in the northward UCDW and LCDW from SAMT-1 to SAMT-3 (Fig. S29b,c,S32c), similar to that in the sections of Δ[REE](%) (θ-S) (average = +0% to +5%) (Fig. 17b,c). These samples show slightly high ΔεNd ($PO_4^*$-θ) with an average of 0.13 ± 0.18 (1σ) εNd units (Fig. S30c) and slightly high ΔεNd ($PO_4^*$-S) with an average of 0.25 ± 0.24 (1σ) εNd units (Fig. S33c), slightly lower than the high ΔεNd (θ-S) (0.44 ± 0.28; 1σ) (Fig. 18c). As mentioned in the main text Section 4.6.3, SAMT-1 to SAMT-3 in the far south are close to the continental margin, where marginal sediments from Patagonia are potential sources with high εNd (−4 to +5) (Goldstein et al., 1984; McLennan et al., 1990; Henry et al., 1996; Basile et al., 1997; Gaiero et al., 2007; de Mahiques et al., 2008; Rousseau et al., 2015; Gili et al., 2017). Therefore, high ΔεNd of the above samples likely result from small amounts of REEs added from marginal sediments without significantly changing REE concentrations.

From depths of LNADW to the bottom, Δ[REE](%) ($PO_4^*$-θ) and Δ[REE](%) ($PO_4^*$-S) slightly skew to high values (Fig. S28a,b,S31a,b). They correspond to samples in the bottom water from SAMT-8 to SAMT-18 in sections of Δ[REE](%) ($PO_4^*$-θ) (average = +4% to +13%) and Δ[REE](%) ($PO_4^*$-S) (average = +4% to +10%) (Fig. S29b,c,S32b,c), similar to that in the sections of Δ[REE](%) (θ-S) (average = +4% to +11%) (Fig. 17b,c). These samples show low ΔεNd ($PO_4^*$-θ) with an average of −0.71 ±

0.70 (1σ) εNd units (Fig. S30c) and low ΔεNd ($PO_4^*$-S) with an average of −0.68 ± 0.65 (1σ) εNd units (Fig. S33c), similar to the low ΔεNd (θ-S) (−0.67 ± 0.65; 1σ) (Fig. 18c). As mentioned in the main text Section 4.6.3, stations SAMT-8 to SAMT-18 in the trade wind zone receive eolian dusts from Africa with low εNd (−19 to −8) (Goldstein et al., 1984; Dia et al., 1990). It is observed that the surface (25 m) and subsurface (100 m) water show low εNd-values in these stations (Fig. 11a,b). The data suggest that REEs dissolved from dusts with this low εNd signature are scavenged in the shallow water and released by sediments at the bottom of the ocean after they sink to the sea floor. Therefore, high Δ[REE](%) and low ΔεNd of the above bottom water samples could result from addition of dissolved REEs from deep sea sediments with low εNd signal.

**References**

Basile, I., Grousset, F.E., Revel, M., Petit, J.R., Biscaye, P.E. and Barkov, N.I. (1997) Patagonian origin of glacial dust deposited in East Antarctica (Vostok and Dome C) during glacial stages 2, 4 and 6. Earth and Planetary Science Letters 146, 573-589.

de Baar, H.J.W., German, C.R., Elderfield, H. and Van Gaans, P. (1988) Rare earth element distributions in anoxic waters of the Cariaco Trench. Geochimica et Cosmochimica Acta 52, 1203-1219.

de Mahiques, M.M., Tassinari, C.C.G., Marcolini, S., Violante, R.A., Figueira, R.C.L., da Silveira, I.C.A., Burone, L. and e Sousa, S.H.d.M. (2008) Nd and Pb isotope signatures on the Southeastern South American upper margin: Implications for sediment transport and source rocks. Marine Geology 250, 51-63.

Dia, A., Allegre, C.J. and Erlank, A.J. (1990) The development of continental crust through geological time: the South African case. Earth and Planetary Science Letters 98, 74-89.

Gaiero, D.M., Brunet, F., Probst, J.-L. and Depetris, P.J. (2007) A uniform isotopic and chemical signature of dust exported from Patagonia: Rock sources and occurrence in southern environments. Chemical Geology 238, 107-120.

German, C.R. and Elderfield, H. (1989) Rare earth elements in Saanich Inlet, British Columbia, a seasonally anoxic basin. Geochimica et Cosmochimica Acta 53, 2561-2571.

German, C.R., Holliday, B.P. and Elderfield, H. (1991) Redox cycling of rare earth elements in the suboxic zone of the Black Sea. Geochimica et Cosmochimica Acta 55, 3553-3558.

Gili, S., Gaiero, D.M., Goldstein, S.L., Chemale Jr, F., Jweda, J., Kaplan, M.R., Becchio, R.A. and Koester, E. (2017) Glacial/interglacial changes of Southern Hemisphere wind circulation from the geochemistry of South American dust. Earth and Planetary Science Letters 469, 98-109.

Goldstein, S.L., O'Nions, R.K. and Hamilton, P.J. (1984) A Sm-Nd isotopic study of atmospheric dusts and particulates from major river systems. Earth and planetary Science letters 70, 221-236.

Henry, F., Probst, J.-L., Thouron, D., Depetris, P.J. and Garçon, V. (1996) Nd-Sr isotopic compositions of dissolved and particulate material transported by the Parana and Uruguay rivers during high (december 1993) and low (september 1994) water periods. Sciences Géologiques, Bulletin 49, 89-100.

Koltermann, K.P., Gouretski, V. and Jancke, K. (2011) Hydrographic Atlas of the World Ocean Circulation Experiment (WOCE): volume 3: Atlantic Ocean. National Oceanography Centre.

McLennan, S.M., Taylor, S.R., McCulloch, M.T. and Maynard, J.B. (1990) Geochemical and Nd-Sr isotopic composition of deep-sea turbidites: Crustal evolution and plate tectonic associations. Geochimica et Cosmochimica Acta 54, 2015-2050.

Rousseau, T.C.C., Sonke, J.E., Chmeleff, J., Van Beek, P., Souhaut, M., Boaventura, G., Seyler, P. and Jeandel, C. (2015) Rapid neodymium release to marine waters from lithogenic sediments in the Amazon estuary. Nature communications 6, 7592.

Schijf, J., De Baar, H.J.W. and Millero, F.J. (1995) Vertical distributions and speciation of dissolved rare earth elements in the anoxic brines of Bannock Basin, eastern Mediterranean Sea. Geochimica et Cosmochimica Acta 59, 3285-3299.

Schlitzer, R. (2012) Ocean data view.

Sholkovitz, E.R., Shaw, T.J. and Schneider, D.L. (1992) The geochemistry of rare earth elements in the seasonally anoxic water column and porewaters of Chesapeake Bay. Geochimica et Cosmochimica Acta 56, 3389-3402.

Stramma, L. and England, M. (1999) On the water masses and mean circulation of the South Atlantic Ocean. Journal of Geophysical Research-Oceans 104, 20863-20833.

Taylor, S.R. and McLennan, S.M. (1985) The continental crust: its composition and evolution.

Zheng, X.-Y., Plancherel, Y., Saito, M.A., Scott, P.M. and Henderson, G.M. (2016) Rare earth elements (REEs) in the tropical South Atlantic and quantitative deconvolution of their non-conservative behavior. Geochimica et Cosmochimica Acta 177, 217-237.

Figure S1 to Figure S12 are the same as Figure S1 to Figure S12 in Supplementary Information of Chapter 2.

Figure S13. Map showing stations from GEOTRACES GA02 Leg 3 (SAMT; this study; in red), GEOTRACES compliant GAc01 ((Zheng et al., 2016); in purple) and GEOTRACES GA10 (REE data available in the GEOTRACES Intermediate Data Product 2017; in light blue) used in this study. The map was made using the ODV software (Schlitzer, 2012).

Figure S14. Changes of REEs and εNd along the UNADW pathway. (a) Map showing the transport path of UNADW. Location numbers are not station numbers. They indicate locations where REE and εNd data are available. The map was made using the ODV software (Schlitzer, 2012). (b) θ vs. S. (c) [Nd] vs. location number. (d) [Yb] vs. location number. (e) $Yb_n/Nd_n$ vs. location number. (f) $Ce/Ce^*$ vs. location number. (g) εNd vs. location number. Grey lines indicate εNd of southern-sourced water masses mixing with UNADW. (h) [Nd] vs. UNADW%. (i) [Yb] vs. UNADW%. (j) $Yb_n/Nd_n$ vs. UNADW%. (k) $Ce/Ce^*$ vs. UNADW%. (l) εNd vs. UNADW%. The x-axis in (h) to (l) is the fraction of UNADW in percent. Solid grey lines/curves in (h) to (l) are mixing lines/curves between different water mass end-members. Dashed grey lines/curves in (h) to (l) are mixing lines/curves 5% higher than the upper limit and 5% lower than the lower limit. Black crosses are water mass end-members.

Figure S15. Changes of REEs and εNd along the MNADW pathway. (a) Map showing the transport path of MNADW. Location numbers are not station numbers. They indicate locations where REE and εNd data are available. The map was made using the ODV software (Schlitzer, 2012). (b) θ vs. S. (c) [Nd] vs. location number. (d) [Yb] vs. location number. (e) $Yb_n/Nd_n$ vs. location number. (f) $Ce/Ce^*$ vs. location number. (g) εNd vs. location number. Grey lines indicate εNd of southern-sourced water masses mixing with MNADW. (h) [Nd] vs. MNADW%. (i) [Yb] vs. MNADW%. (j) $Yb_n/Nd_n$ vs. MNADW%. (k) $Ce/Ce^*$ vs. MNADW%. (l) εNd vs. MNADW%. The x-axis in (h) to (l) is the fraction of MNADW in percent. Solid grey lines/curves in (h) to (l) are mixing lines/curves between different water mass end-members. Dashed grey lines/curves in (h) to (l) are mixing lines/curves 5% higher than the upper limit and 5% lower than the lower limit. Black crosses are water mass end-members.

Figure S16. Changes of REEs and εNd along the LNADW pathway. (a) Map showing the transport path of LNADW. Location numbers are not station numbers. They indicate locations where REE and εNd data are available. The map was made using the ODV software (Schlitzer, 2012). (b) θ vs. S. (c) [Nd] vs. location number. (d) [Yb] vs. location number. (e) $Yb_n/Nd_n$ vs. location number. (f) $Ce/Ce^*$ vs. location number. (g) εNd vs. location number. Grey lines indicate εNd of southern-sourced water masses mixing with LNADW. (h) [Nd] vs. LNADW%. (i) [Yb] vs. LNADW%. (j) $Yb_n/Nd_n$ vs. LNADW%. (k) $Ce/Ce^*$ vs. LNADW%. (l) εNd vs. LNADW%. The x-axis in (h) to (l) is the fraction of LNADW in percent. Solid grey lines/curves in (h) to (l) are mixing lines/curves

between different water mass end-members. Dashed grey lines/curves in (h) to (l) are mixing lines/curves 5% higher than the upper limit and 5% lower than the lower limit. Black crosses are water mass end-members.

Figure S17. Changes of REEs and εNd along the SACW pathway. (a) Map showing the transport path of SACW. Location numbers are not station numbers. They indicate locations where REE and εNd data are available. The map was made using the ODV software (Schlitzer, 2012). (b) θ vs. S. (c) [Nd] vs. location number. (d) [Yb] vs. location number. (e) $Yb_n/Nd_n$ vs. location number. (f) $Ce/Ce^*$ vs. location number. (g) εNd vs. location number. The grey line indicates εNd of northern-sourced UNADW mixing with SACW. Black crosses are water mass end-members.

Figure S18. Changes of REEs and εNd along the aAAIW pathway. (a) Map showing the transport path of aAAIW. Location numbers are not station numbers. They indicate locations where REE and εNd data are available. The map was made using the ODV software (Schlitzer, 2012). (b) θ vs. S. (c) [Nd] vs. location number. (d) [Yb] vs. location number. (e) $Yb_n/Nd_n$ vs. location number. (f) $Ce/Ce^*$ vs. location number. (g) εNd vs. location number. (h) [Nd] vs. aAAIW%. (i) [Yb] vs. aAAIW%. (j) $Yb_n/Nd_n$ vs. aAAIW%. (k) $Ce/Ce^*$ vs. aAAIW%. (l) εNd vs. aAAIW%. The x-axis in (h) to (l) is the fraction of aAAIW in percent. Solid grey lines/curves in (h) to (l) are mixing lines/curves between different water mass end-members. Dashed grey lines/curves in (h) to (l) are mixing lines/curves 5% higher than the upper limit and 5% lower than the lower limit. Black crosses are water mass end-members.

Figure S19. Changes of REEs and εNd along the iAAIW pathway. (a) Map showing the transport path of iAAIW. Location numbers are not station numbers. They indicate locations where REE and εNd data are available. The map was made using the ODV software (Schlitzer, 2012). (b) θ vs. S. (c) [Nd] vs. location number. (d) [Yb] vs. location number. (e) $Yb_n/Nd_n$ vs. location number. (f) $Ce/Ce^*$ vs. location number. (g) εNd vs. location number. The grey line indicates εNd of northern-sourced UNADW mixing with iAAIW. (h) [Nd] vs. iAAIW%. (i) [Yb] vs. iAAIW%. (j) $Yb_n/Nd_n$ vs. iAAIW%. (k) $Ce/Ce^*$ vs. iAAIW%. (l) εNd vs. iAAIW%. The x-axis in (h) to (l) is the fraction of iAAIW in percent. Solid grey lines/curves in (h) to (l) are mixing lines/curves between different water mass end-members. Dashed grey lines/curves in (h) to (l) are mixing lines/curves 5% higher than the upper limit and 5% lower than the lower limit. Black crosses are water mass end-members.

Figure S20. Changes of REEs and εNd along the UCDW pathway. (a) Map showing the transport path of UCDW. Location numbers are not station numbers. They indicate locations where REE and εNd data are available. The map was made using the ODV software (Schlitzer, 2012). (b) θ vs. S. (c) [Nd] vs. location number. (d) [Yb] vs. location number. (e) $Yb_n/Nd_n$ vs. location number. (f) $Ce/Ce^*$ vs. location number. (g) εNd vs. location number. Grey lines indicate εNd of northern-sourced water masses mixing with UCDW. (h) [Nd] vs. UCDW%. (i) [Yb] vs. UCDW%. (j) $Yb_n/Nd_n$ vs. UCDW%. (k)

$Ce/Ce^*$ vs. UCDW%. (l) εNd vs. UCDW%. The x-axis in (h) to (l) is the fraction of UCDW in percent. Solid grey lines/curves in (h) to (l) are mixing lines/curves between different water mass end-members. Dashed grey lines/curves in (h) to (l) are mixing lines/curves 5% higher than the upper limit and 5% lower than the lower limit. Black crosses are water mass end-members.

Figure S21. Changes of REEs and εNd along the LCDW pathway. (a) Map showing the transport path of LCDW. Location numbers are not station numbers. They indicate locations where REE and εNd data are available. The map was made using the ODV software (Schlitzer, 2012). (b) θ vs. S. (c) [Nd] vs. location number. (d) [Yb] vs. location number. (e) $Yb_n/Nd_n$ vs. location number. (f) $Ce/Ce^*$ vs. location number. (g) εNd vs. location number. Grey lines indicate εNd of northern-sourced water masses mixing with LCDW. (h) [Nd] vs. LCDW%. (i) [Yb] vs. LCDW%. (j) $Yb_n/Nd_n$ vs. LCDW%. (k) $Ce/Ce^*$ vs. LCDW%. (l) εNd vs. LCDW%. The x-axis in (h) to (l) is the fraction of LCDW in percent. Solid grey lines/curves in (h) to (l) are mixing lines/curves between different water mass end-members. Dashed grey lines/curves in (h) to (l) are mixing lines/curves 5% higher than the upper limit and 5% lower than the lower limit. Black crosses are water mass end-members.

Figure S22. Changes of REEs and εNd along the AABW pathway. (a) Map showing the transport path of AABW. Location numbers are not station numbers. They indicate locations where REE and εNd data are available. The map was made using the ODV software (Schlitzer, 2012). (b) θ vs. S. (c) [Nd] vs. location number. (d) [Yb] vs. location number. (e) $Yb_n/Nd_n$ vs. location number. (f) $Ce/Ce^*$ vs. location number. (g) εNd vs. location number. The grey line indicates εNd of northern-sourced LNADW mixing with AABW. (h) [Nd] vs. AABW%. (i) [Yb] vs. AABW%. (j) $Yb_n/Nd_n$ vs. AABW%. (k) $Ce/Ce^*$ vs. AABW%. (l) εNd vs. AABW%. The x-axis in (h) to (l) is the fraction of AABW in percent. Solid grey lines/curves in (h) to (l) are mixing lines/curves between different water mass end-members. Dashed grey lines/curves in (h) to (l) are mixing lines/curves 5% higher than the upper limit and 5% lower than the lower limit. Black crosses are water mass end-members.

Figure S23. Changes of REEs and εNd along ~10°S for UNADW. (a) [Nd] vs. location number. (b) [Yb] vs. location number. (c) $Yb_n/Nd_n$ vs. location number. (d) $Ce/Ce^*$ vs. location number. The black arrows show flowing directions of UNADW. The grey dashed line indicates the location of Mid-Atlantic Ridge.

Figure S24. Changes of REEs and εNd along ~10°S for MNADW. (a) [Nd] vs. location number. (b) [Yb] vs. location number. (c) $Yb_n/Nd_n$ vs. location number. (d) $Ce/Ce^*$ vs. location number. The black arrows show flowing directions of MNADW. The grey dashed line indicates the location of Mid-Atlantic Ridge.

Figure S25. Changes of REEs and εNd along ~10°S for LNADW. (a) [Nd] vs. location number. (b) [Yb] vs. location number. (c) $Yb_n/Nd_n$ vs. location number. (d) $Ce/Ce^*$ vs.

location number. The black arrows show flowing directions of LNADW. The grey dashed line indicates the location of Mid-Atlantic Ridge.

Figure S26. Changes of REEs and εNd along ~40°S for LCDW. (a) [Nd] vs. location number. (b) [Yb] vs. location number. (c) $Yb_n/Nd_n$ vs. location number. (d) $Ce/Ce^*$ vs. location number.

Figure S27. Changes of REEs and εNd along ~40°S and ~10°S for AABW. (a) [Nd] vs. location number for GA10. (b) [Yb] vs. location number for GA10. (c) $Yb_n/Nd_n$ vs. location number for GA10. (d) $Ce/Ce^*$ vs. location number for GA10. (e) [Nd] vs. location number for GAc01. (f) [Yb] vs. location number for GAc01. (g) $Yb_n/Nd_n$ vs. location number for GAc01. (h) $Ce/Ce^*$ vs. location number for GAc01.

Figure S28. Histograms of Δ[REE]/Predicted [REE] and Δ(REE ratio)/Predicted (REE ratio) calculated based on water mass mixing using $PO_4^*$ and potential temperature. (a) Δ[Nd]/Predicted [Nd]. (b) Δ[Yb]/Predicted [Yb]. (c) $\Delta(Yb_n/Nd_n)$/Predicted $(Yb_n/Nd_n)$. (d) ΔεNd. The y-axis on the left is the number of calculated samples. The y-axis on the right is the percentage of calculated samples. Delta values were separated into three groups using the neutral densities of the water mass end-members defined from the SAMT (Table 3a). Green columns include samples from the depths of AAIW to UNADW ($\gamma^n$ = 27.15-27.90 $kg/m^3$). Red columns include samples from the depths of UNADW to LNADW ($\gamma^n$ = 27.90-28.11 $kg/m^3$). Blue columns include samples from the depths of LNADW to AABW ($\gamma^n$ =28.11-28.30 $kg/m^3$). The numbers above the columns are percentage values within each interval from depths of AAIW to the bottom.

Figure S29. Section profiles of (a) Salinity with contours of neutral density, (b) Δ[Nd]/Predicted [Nd], (c) Δ[Yb]/Predicted [Yb]. Δ[REE]/Predicted [REE] ratios are calculated based on water mass mixing using $PO_4^*$ and potential temperature. The numbers above each section plot are station numbers. The sections were made using the ODV software (Schlitzer, 2012).

Figure S30. Section profiles of (a) $PO_4^*$ with contours of neutral density, (b) $\Delta(Yb_n/Nd_n)$/Predicted $(Yb_n/Nd_n)$, (c) ΔεNd. $\Delta(Yb_n/Nd_n)$/Predicted $(Yb_n/Nd_n)$ and ΔεNd are calculated based on water mass mixing using $PO_4^*$ and potential temperature. The numbers above each section plot are station numbers. The sections were made using the ODV software (Schlitzer, 2012).

Figure S31. Histograms of Δ[REE]/Predicted [REE] and Δ(REE ratio)/Predicted (REE ratio) calculated based on water mass mixing using $PO_4^*$ and salinity. (a) Δ[Nd]/Predicted [Nd]. (b) Δ[Yb]/Predicted [Yb]. (c) $\Delta(Yb_n/Nd_n)$/Predicted $(Yb_n/Nd_n)$. (d) ΔεNd. The y-axis on the left is the number of calculated samples. The y-axis on the right is the percentage of calculated samples. Delta values were separated into three groups using the neutral densities of the water mass end-members defined from the SAMT (Table 3a). Green columns include samples from the depths of AAIW to UNADW ($\gamma^n$ = 27.15-27.90

kg/m$^3$). Red columns include samples from the depths of UNADW to LNADW ($\gamma^n$ = 27.90-28.11 kg/m$^3$). Blue columns include samples from the depths of LNADW to AABW ($\gamma^n$ =28.11-28.30 kg/m$^3$). The numbers above the columns are percentage values within each interval from depths of AAIW to the bottom.

Figure S32. Section profiles of (a) Salinity with contours of neutral density, (b) Δ[Nd]/Predicted [Nd], (c) Δ[Yb]/Predicted [Yb]. Δ[REE]/Predicted [REE] ratios are calculated based on water mass mixing using $PO_4^*$ and salinity. The numbers above each section plot are station numbers. The sections were made using the ODV software (Schlitzer, 2012).

Figure S33. Section profiles of (a) $PO_4^*$ with contours of neutral density, (b) $\Delta(Yb_n/Nd_n)$/Predicted $(Yb_n/Nd_n)$, (c) ΔεNd. $\Delta(Yb_n/Nd_n)$/Predicted $(Yb_n/Nd_n)$ and ΔεNd are calculated based on water mass mixing using $PO_4^*$ and salinity. The numbers above each section plot are station numbers. The sections were made using the ODV software (Schlitzer, 2012).

Figure S34. PAAS-normalized REE patterns of Southwest Atlantic seawater samples.

Figure S13. Map showing stations from GEOTRACES GA02 Leg 3, GEOTRACES compliant GAc01, and GEOTRACES GA10

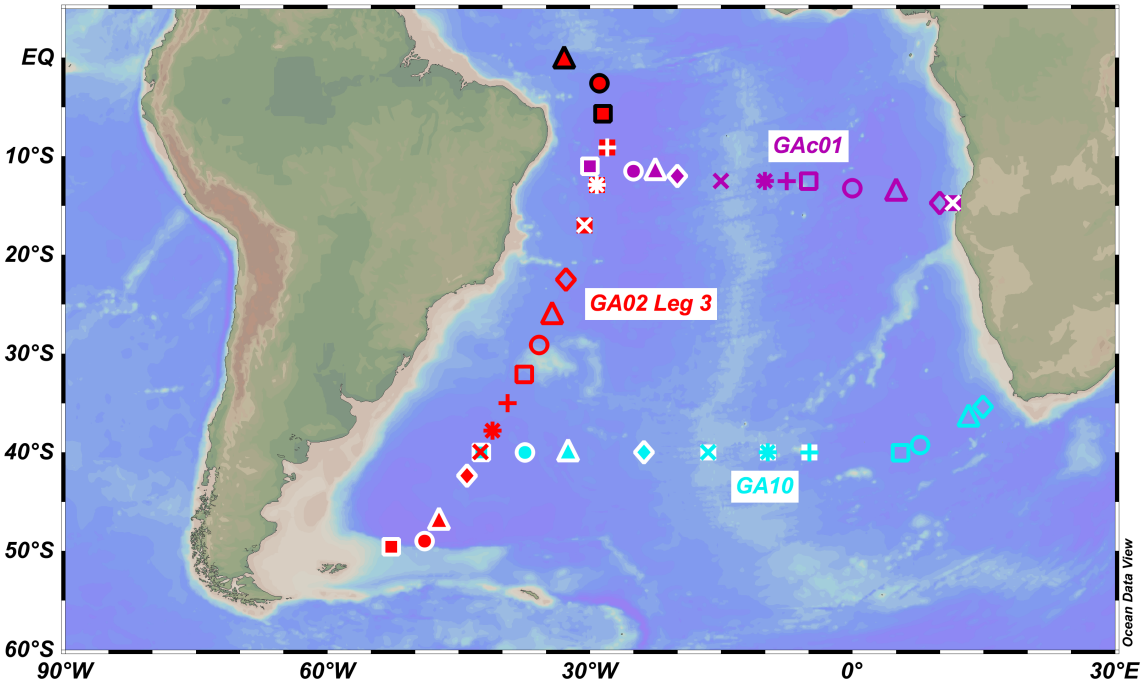

Figure S14. Changes of REEs and εNd along the UNADW pathway

a

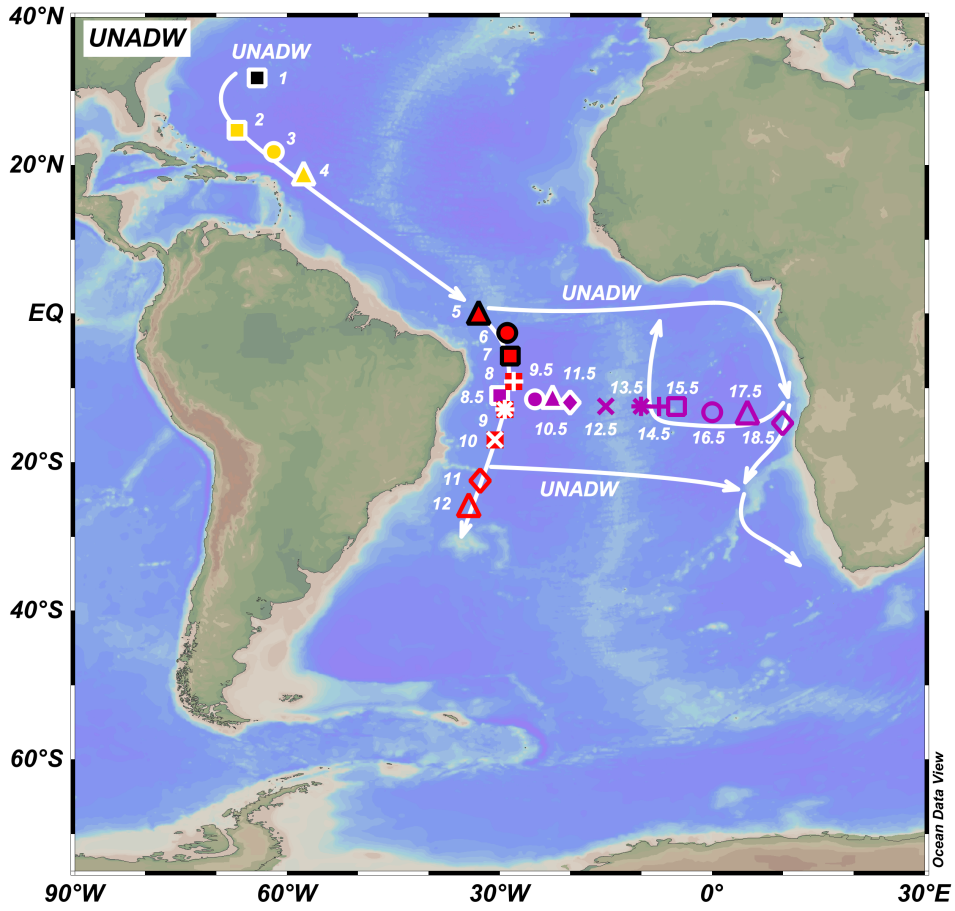


b

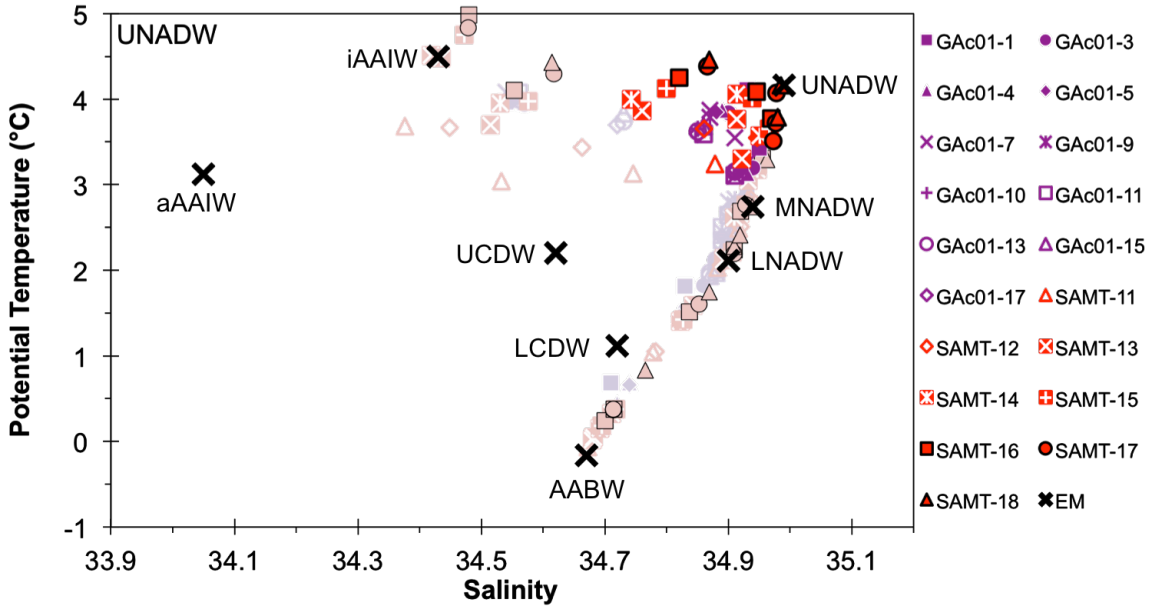

Figure S14. continued

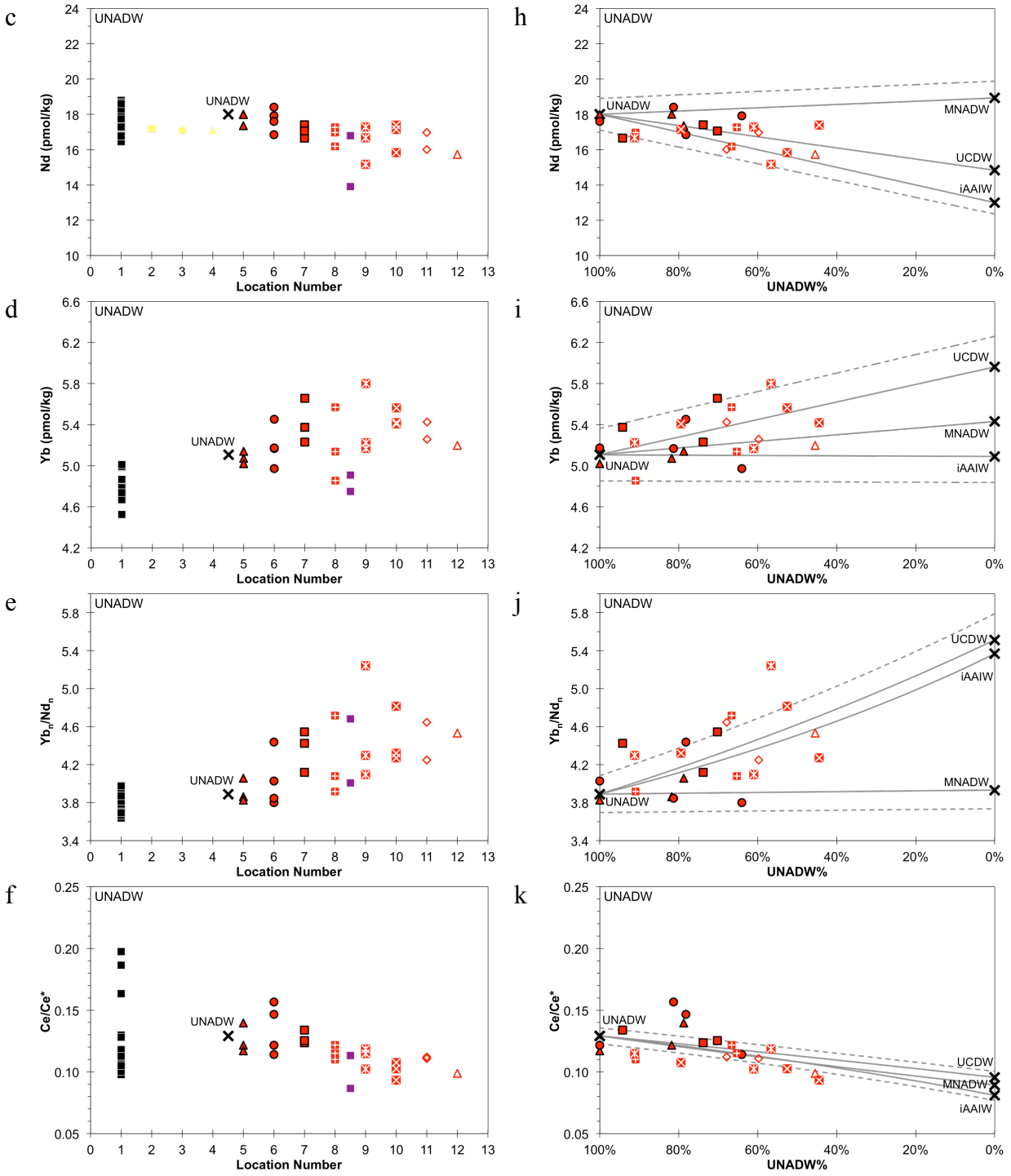

Figure S14. continued

g

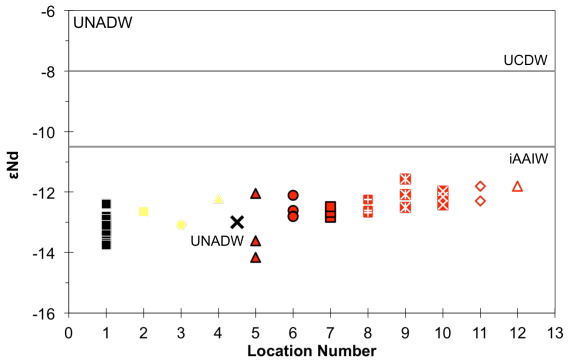


l

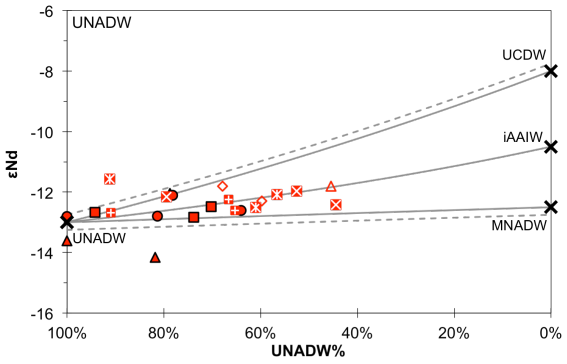

Figure S15. Changes of REEs and εNd along the MNADW pathway

a

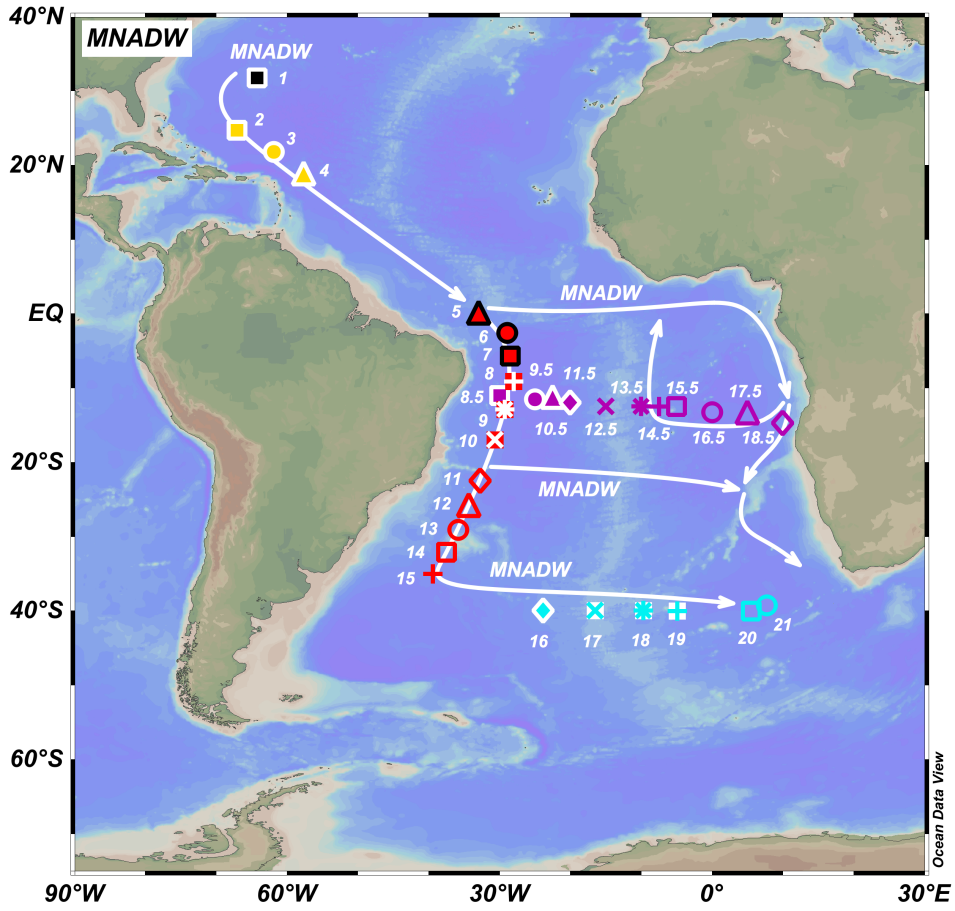


b

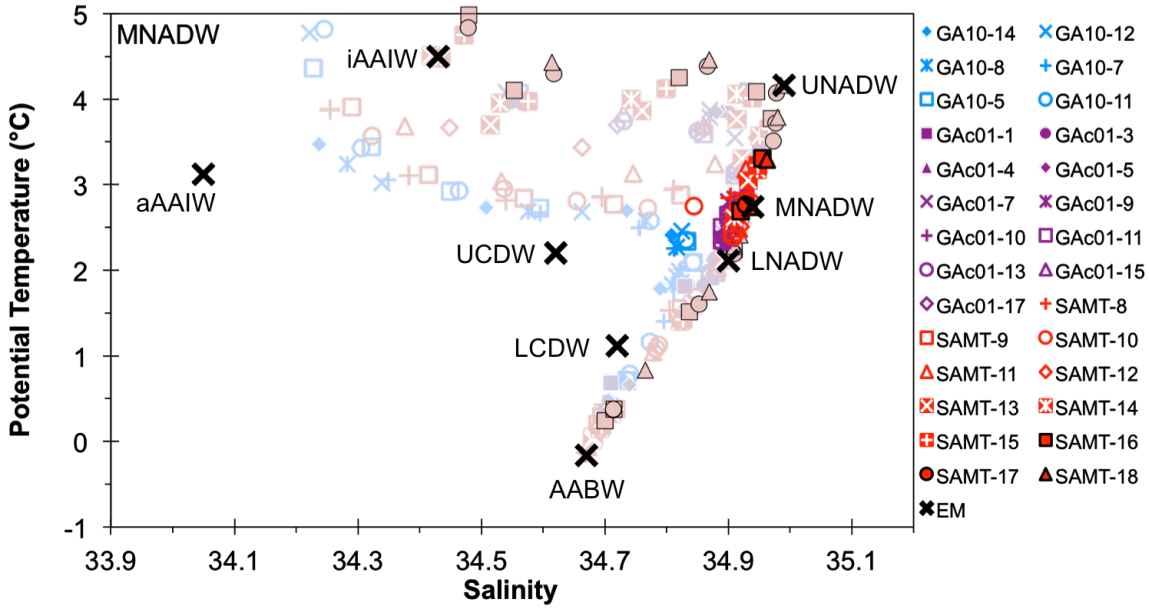

Figure S15. continued

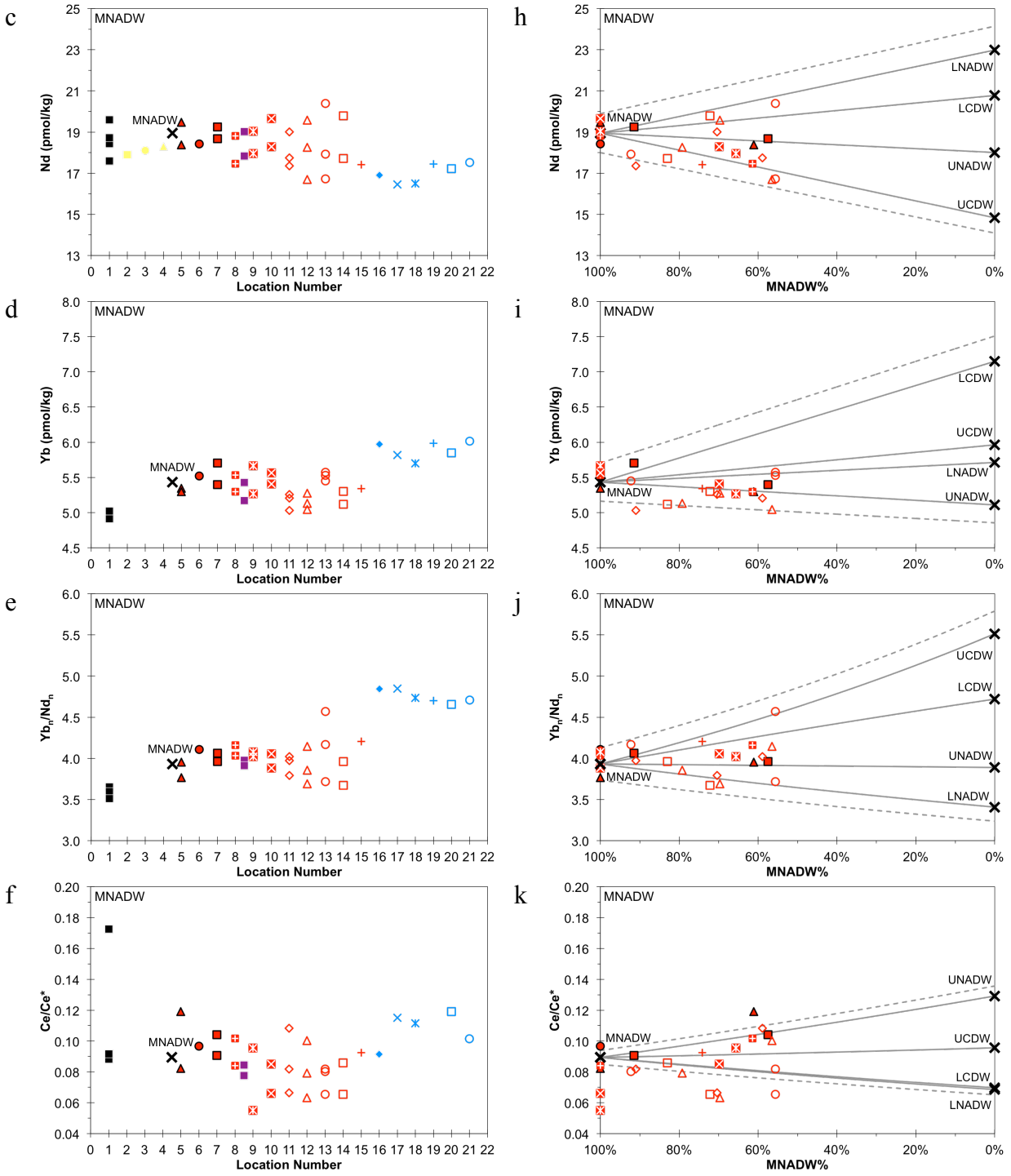

Figure S15. continued

g

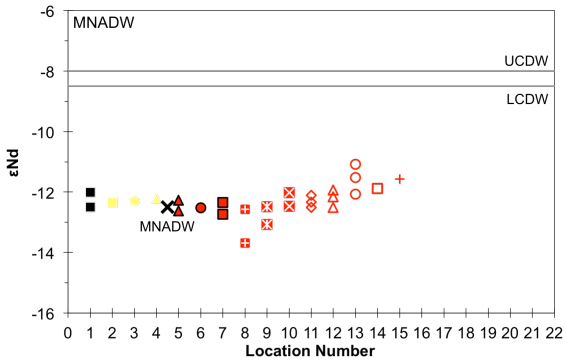


l

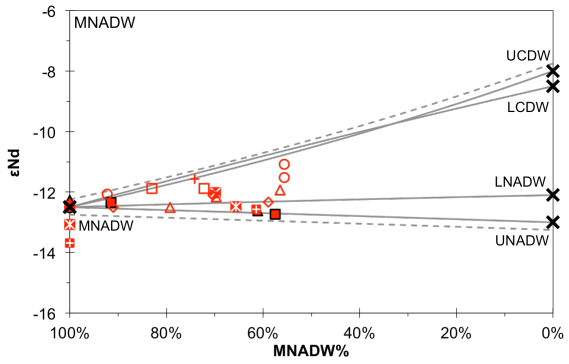

Figure S16. Changes of REEs and εNd along the LNADW pathway

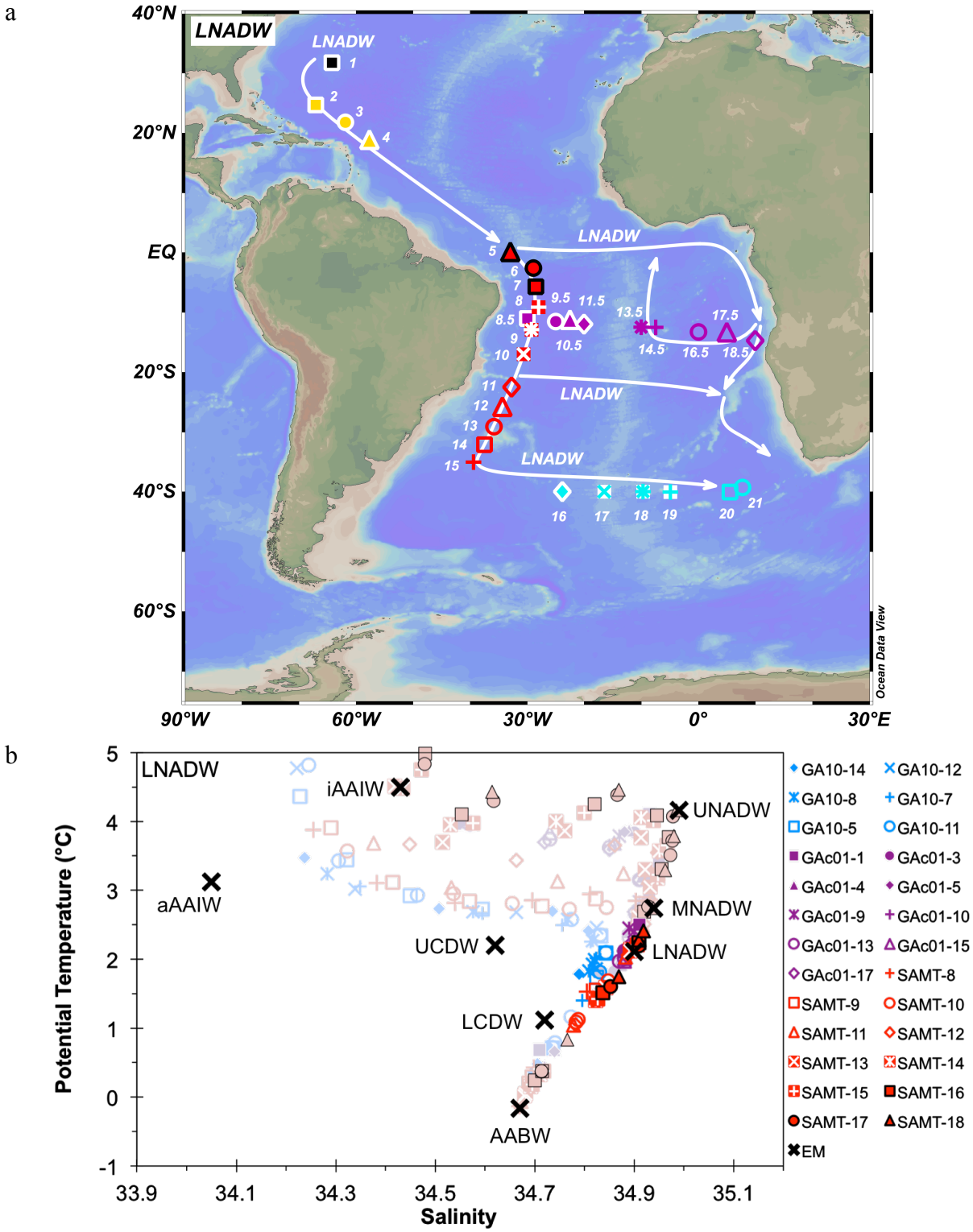

Figure S16. continued

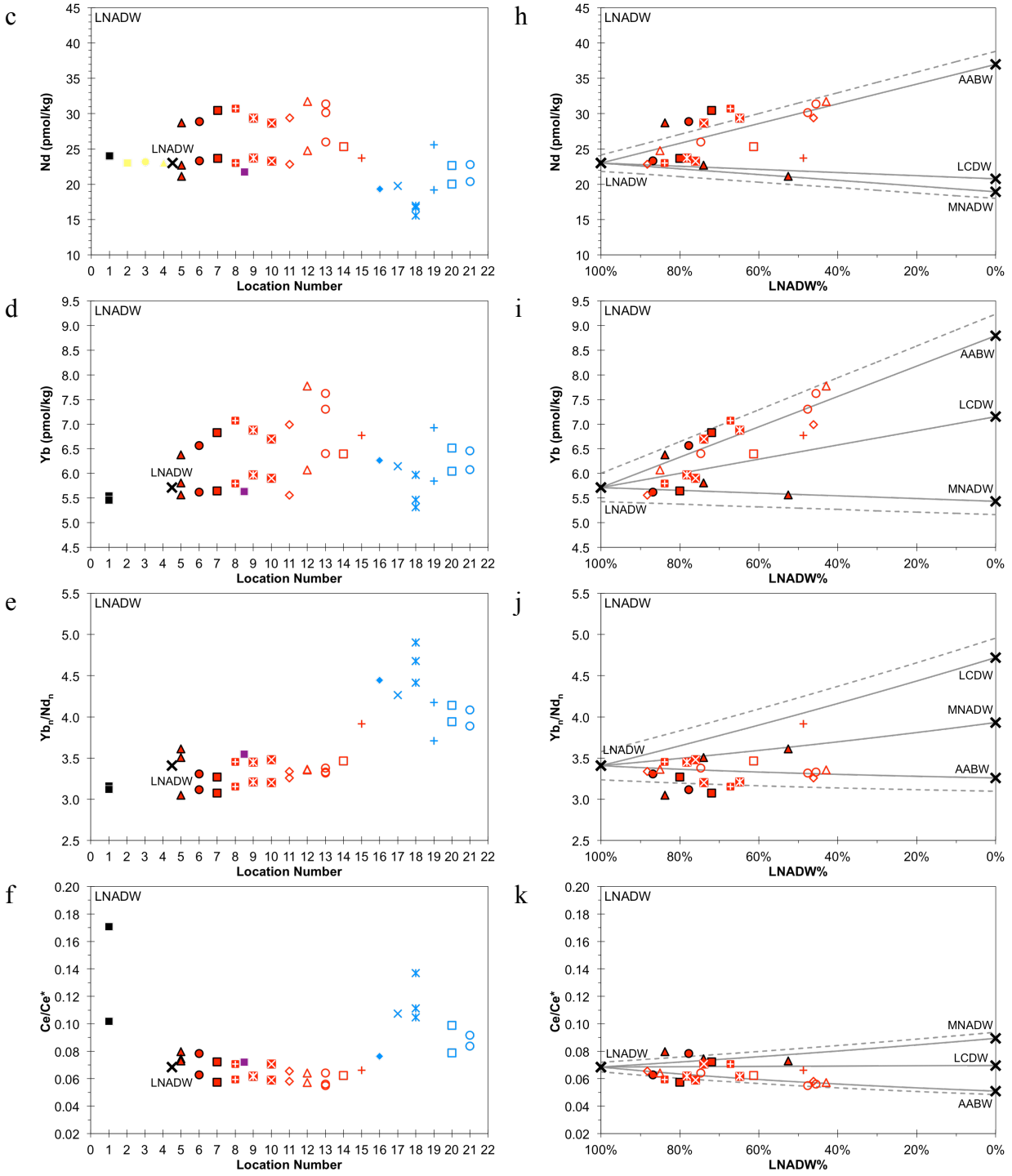

Figure S16. continued

g

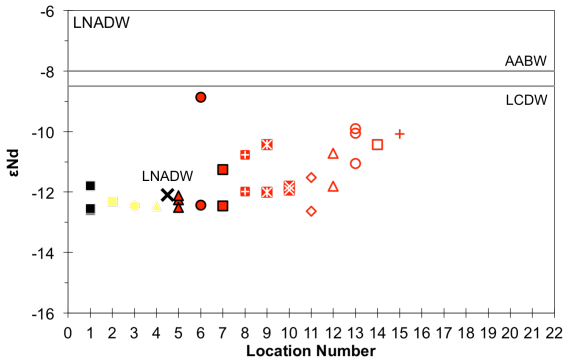


l

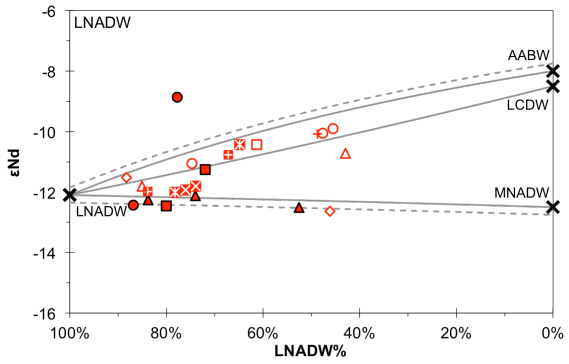

Figure S17. Changes of REEs and εNd along the SACW pathway

a

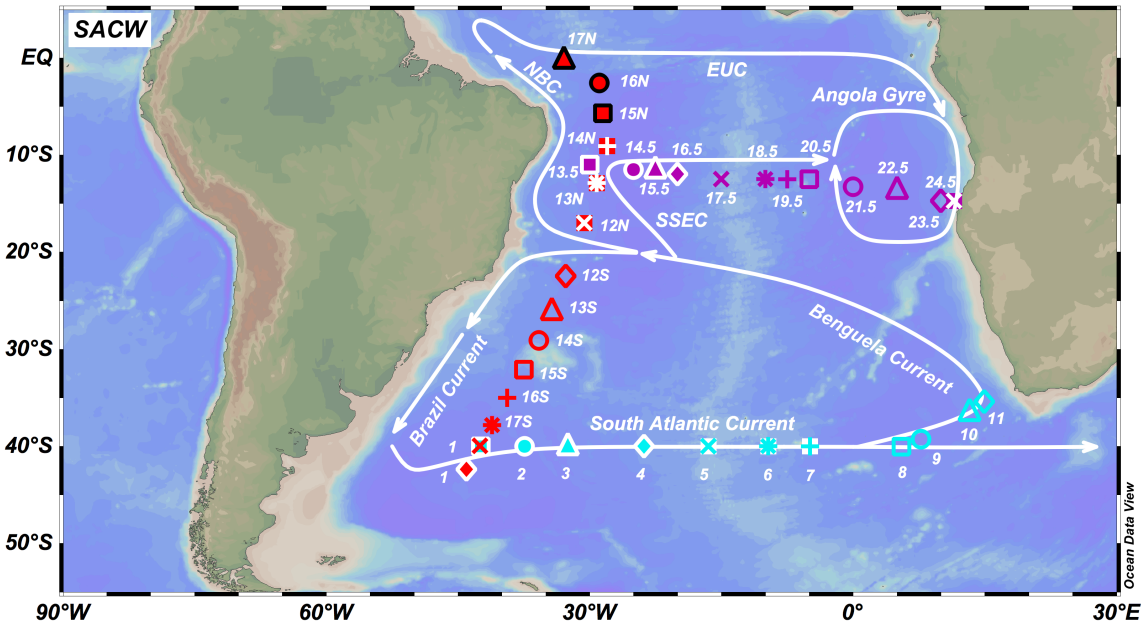


b

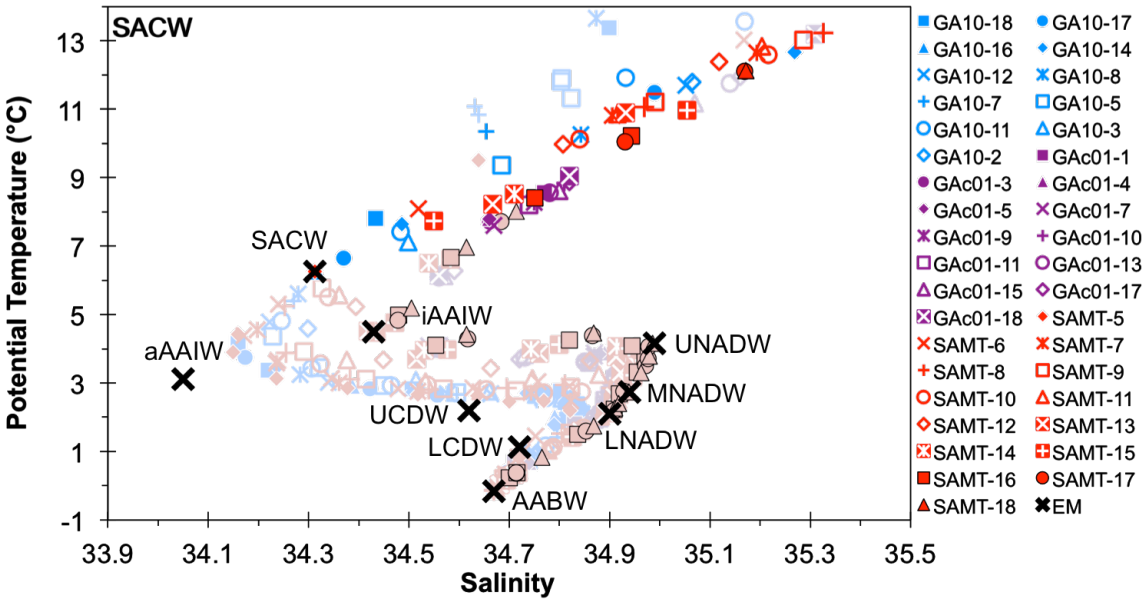

Figure S17. continued

c

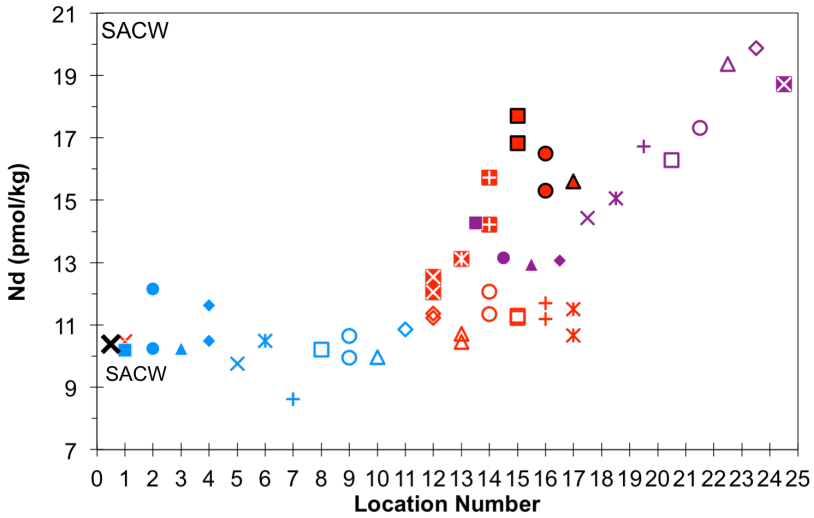


d

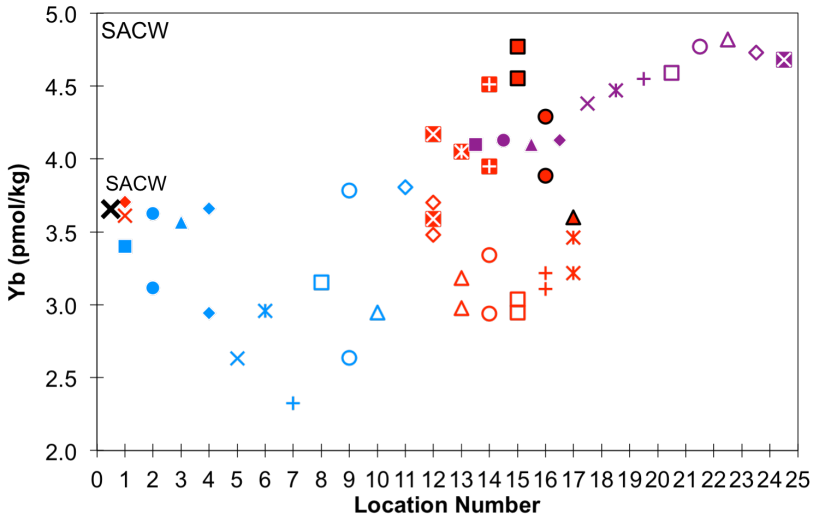


e

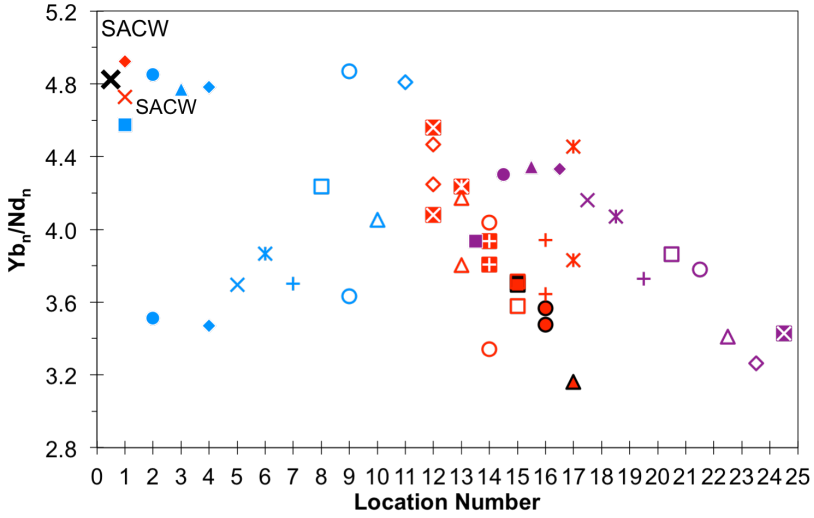

Figure S17. continued

f

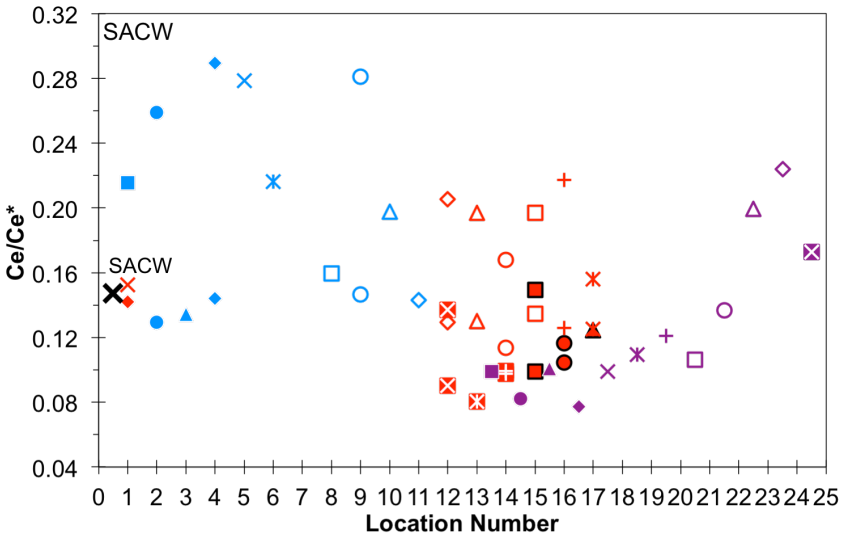


g

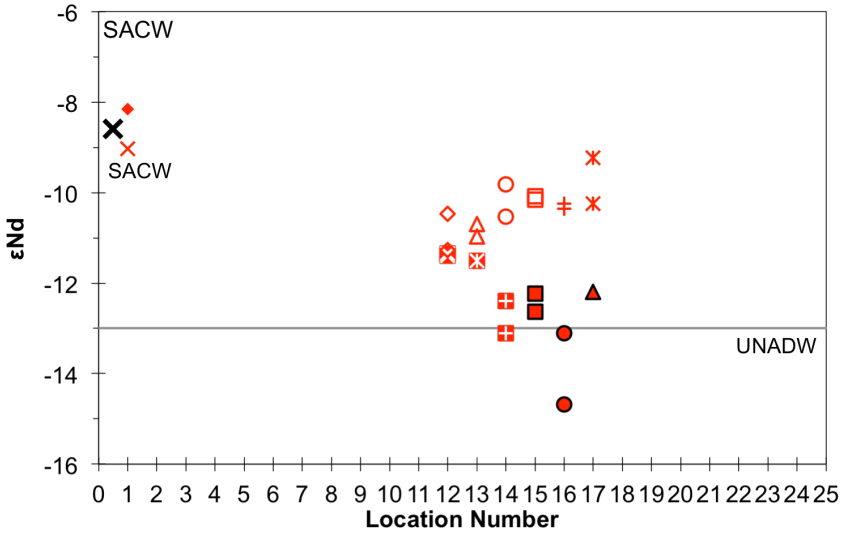

Figure S18. Changes of REEs and εNd along the aAAIW pathway

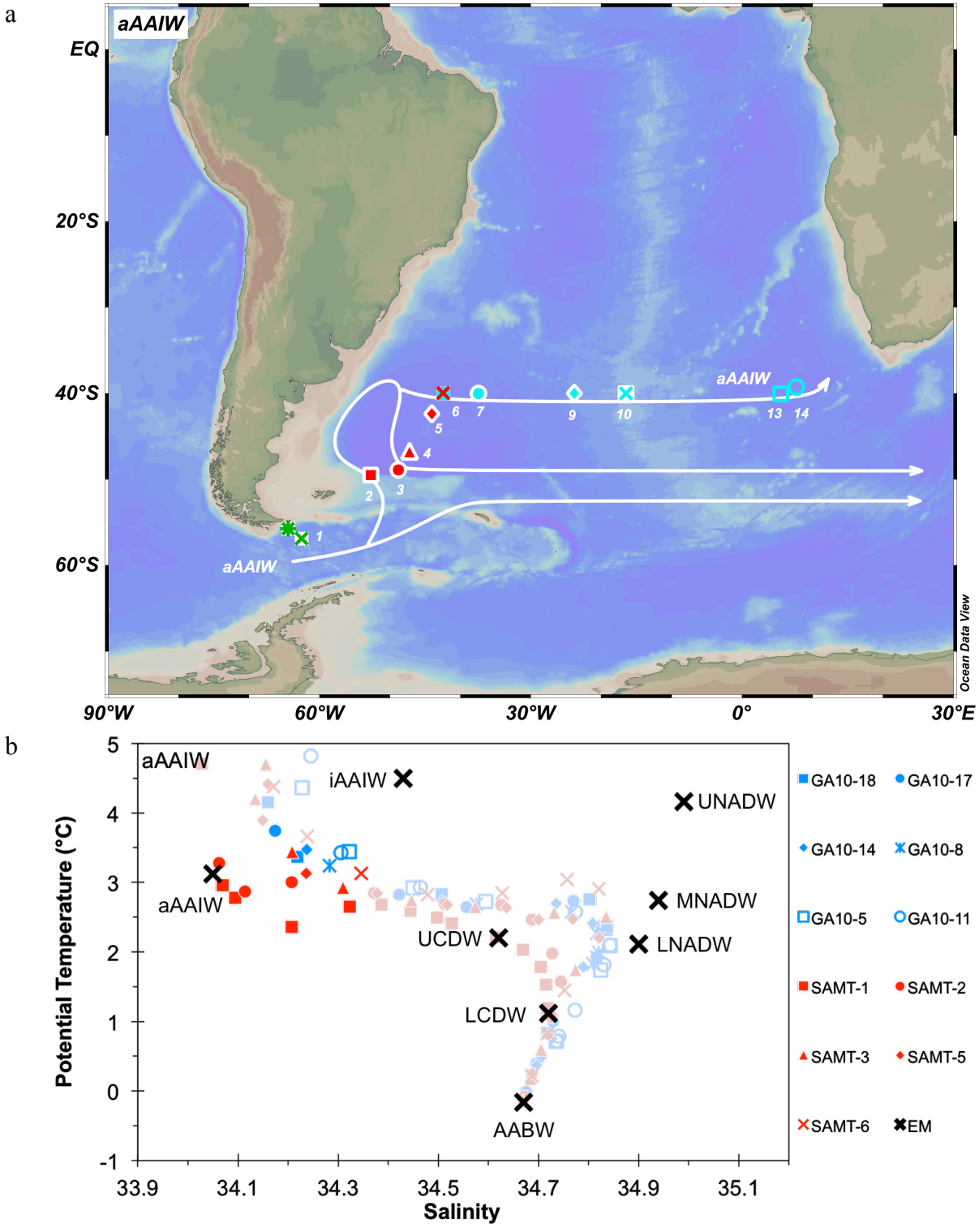

Figure S18. continued

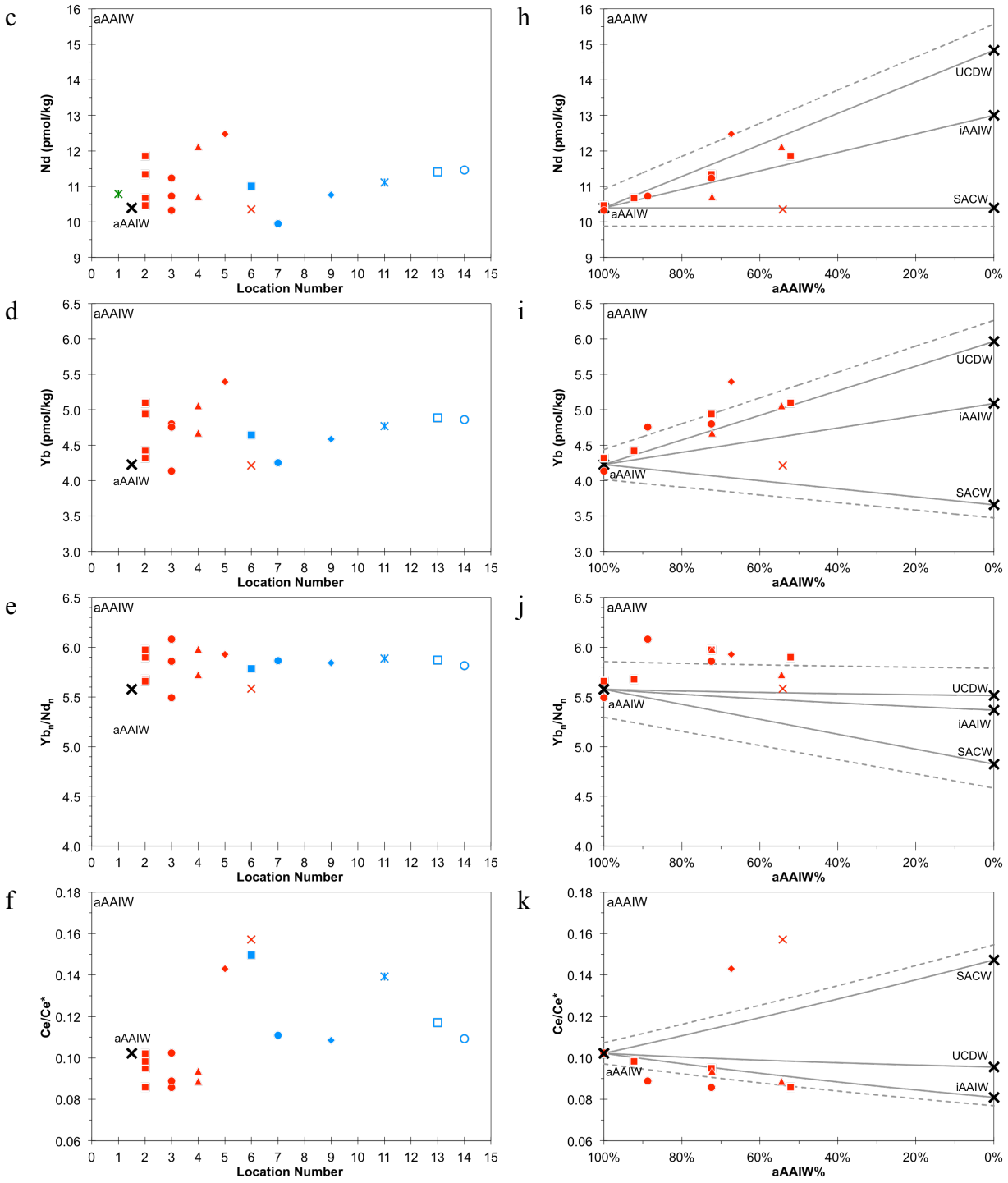

Figure S18. continued

g

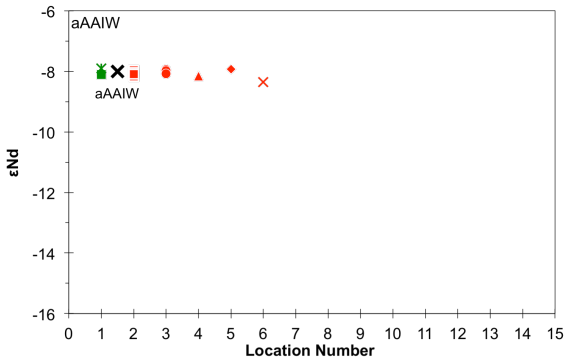


l

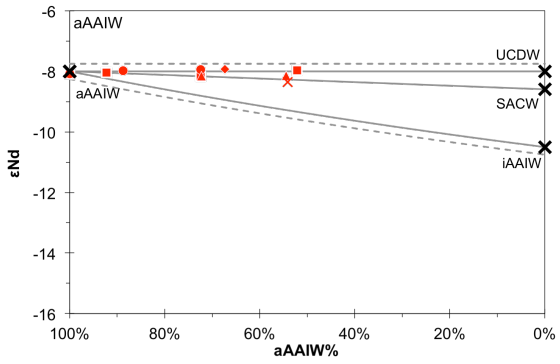

Figure S19. Changes of REEs and εNd along the iAAIW pathway

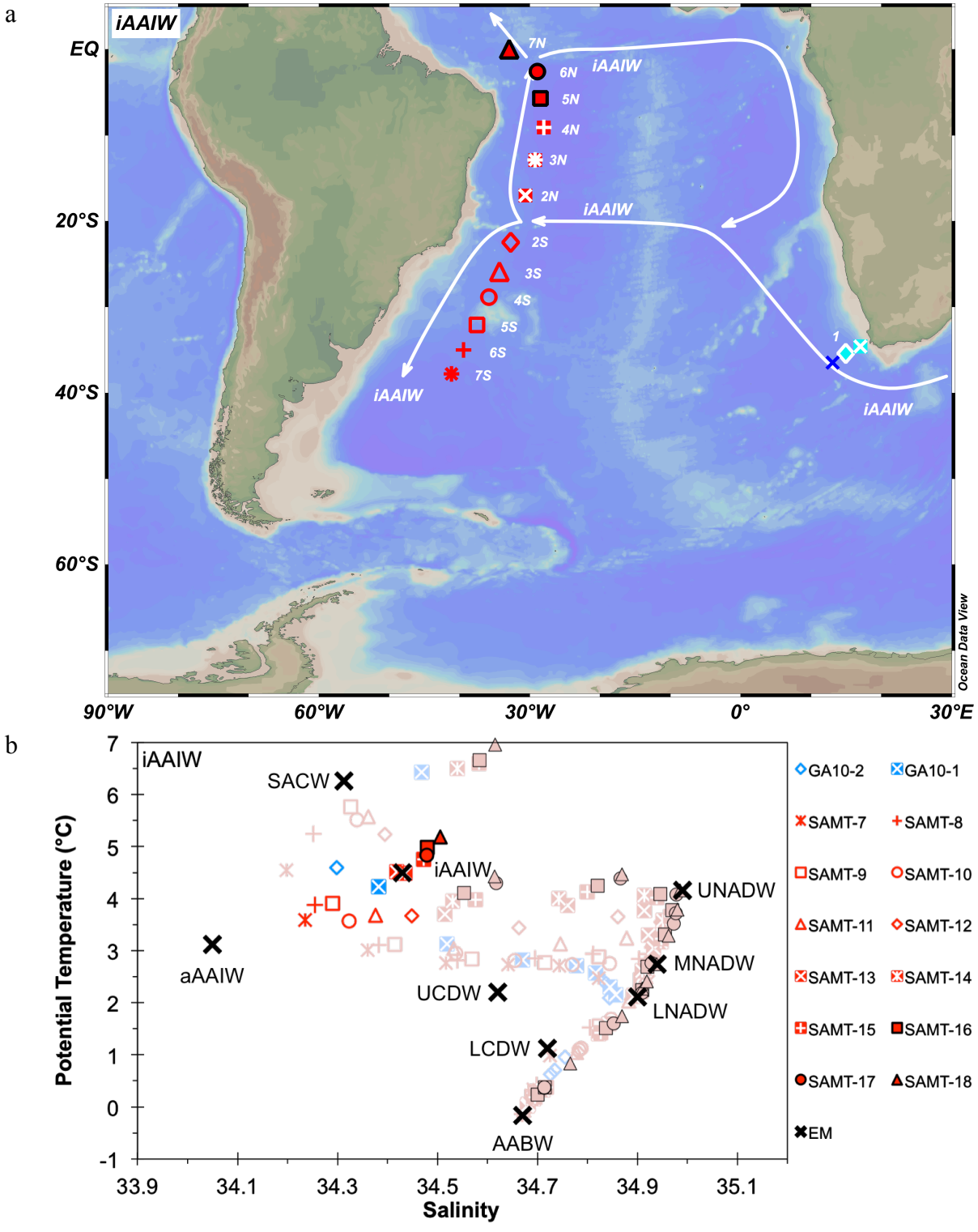

Figure S19. continued

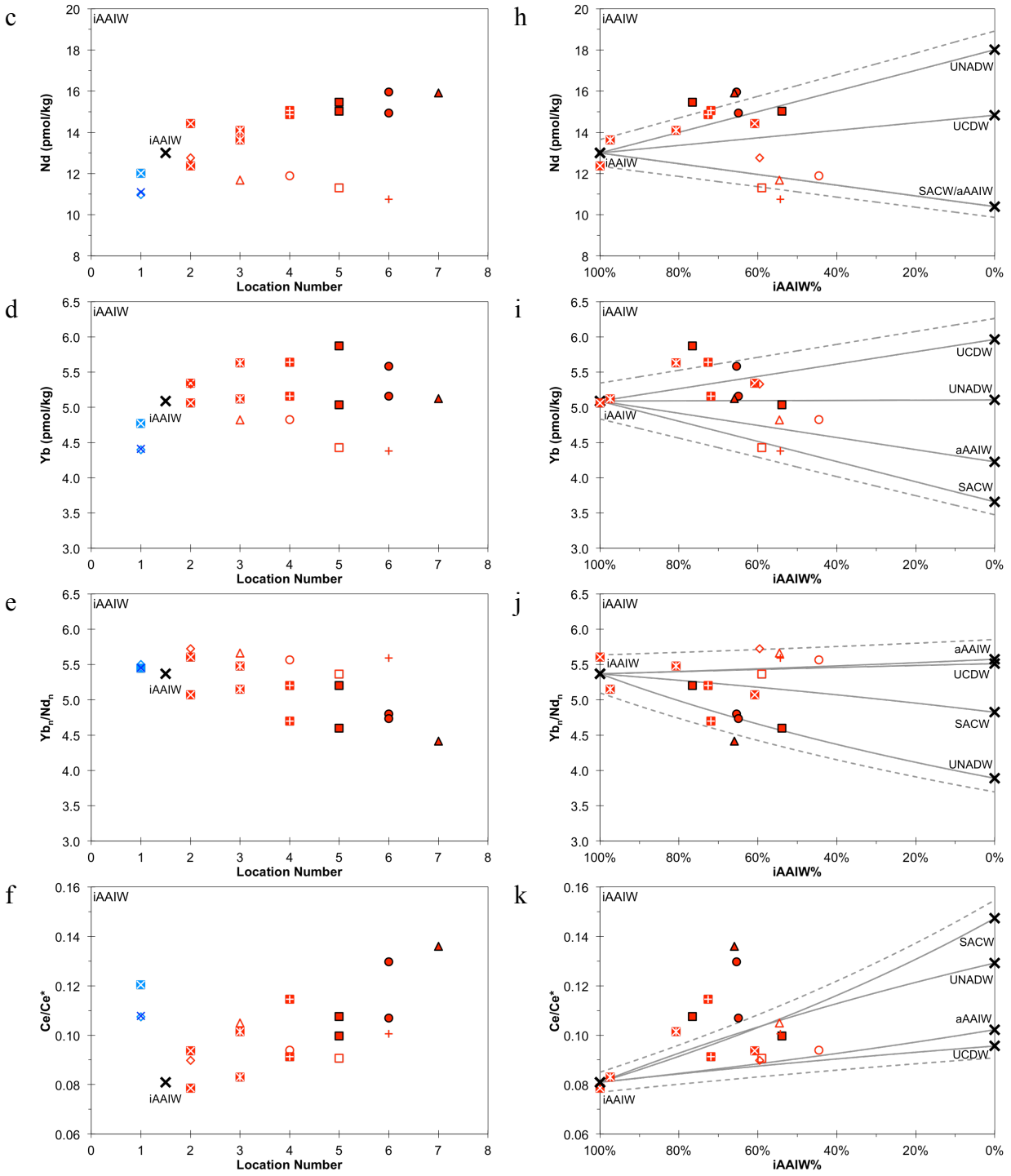

Figure S19. continued

g

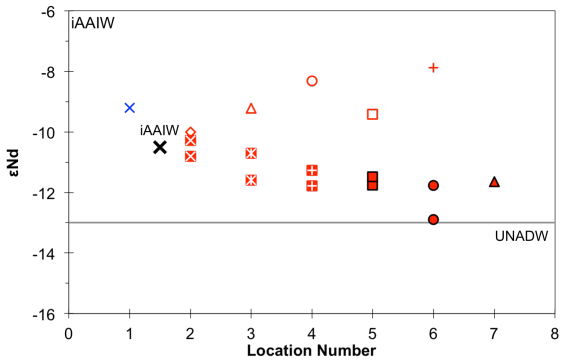


l

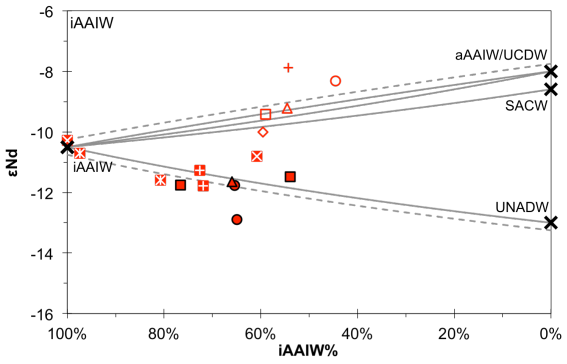

Figure S20. Changes of REEs and εNd along the UCDW pathway

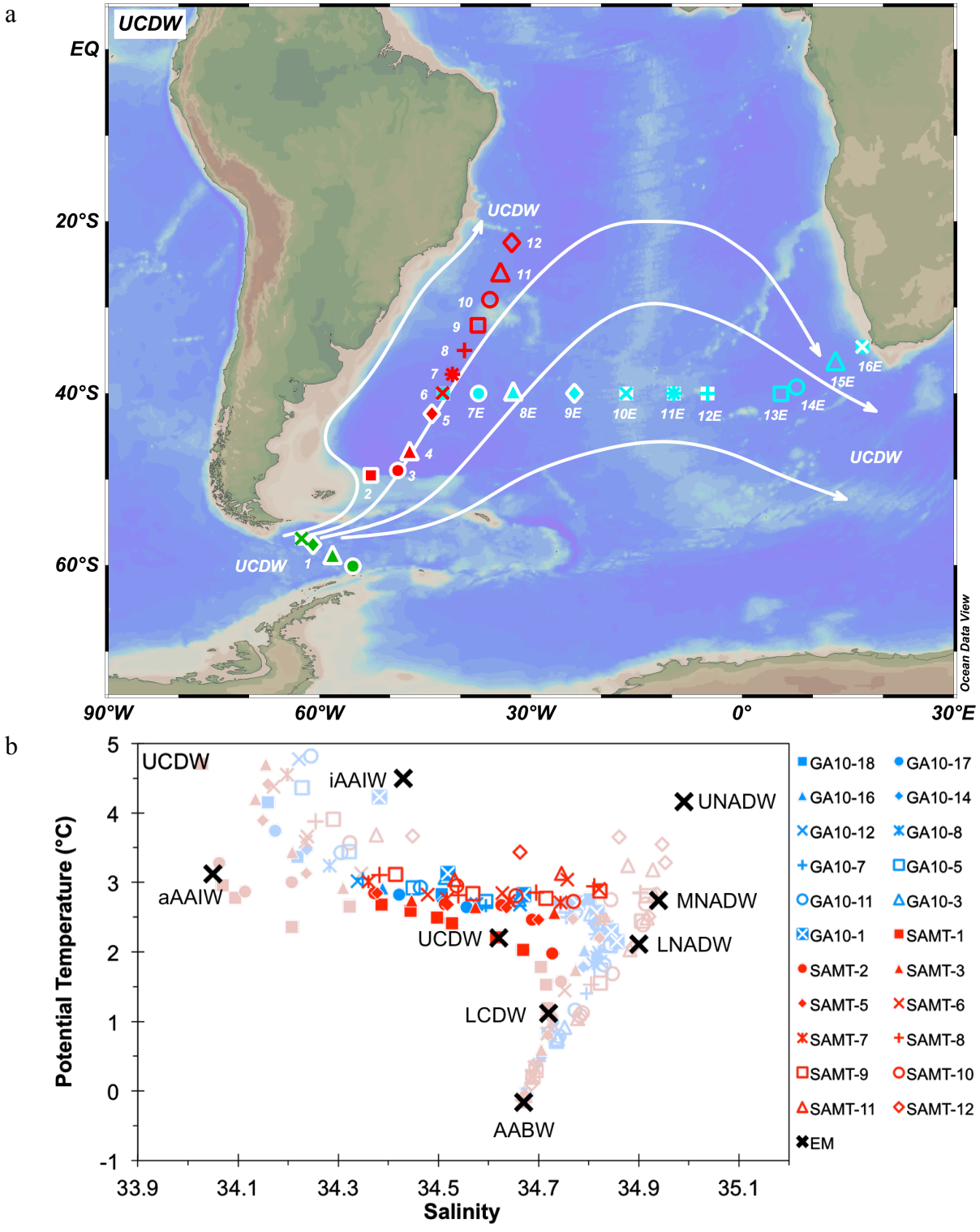

Figure S20. continued

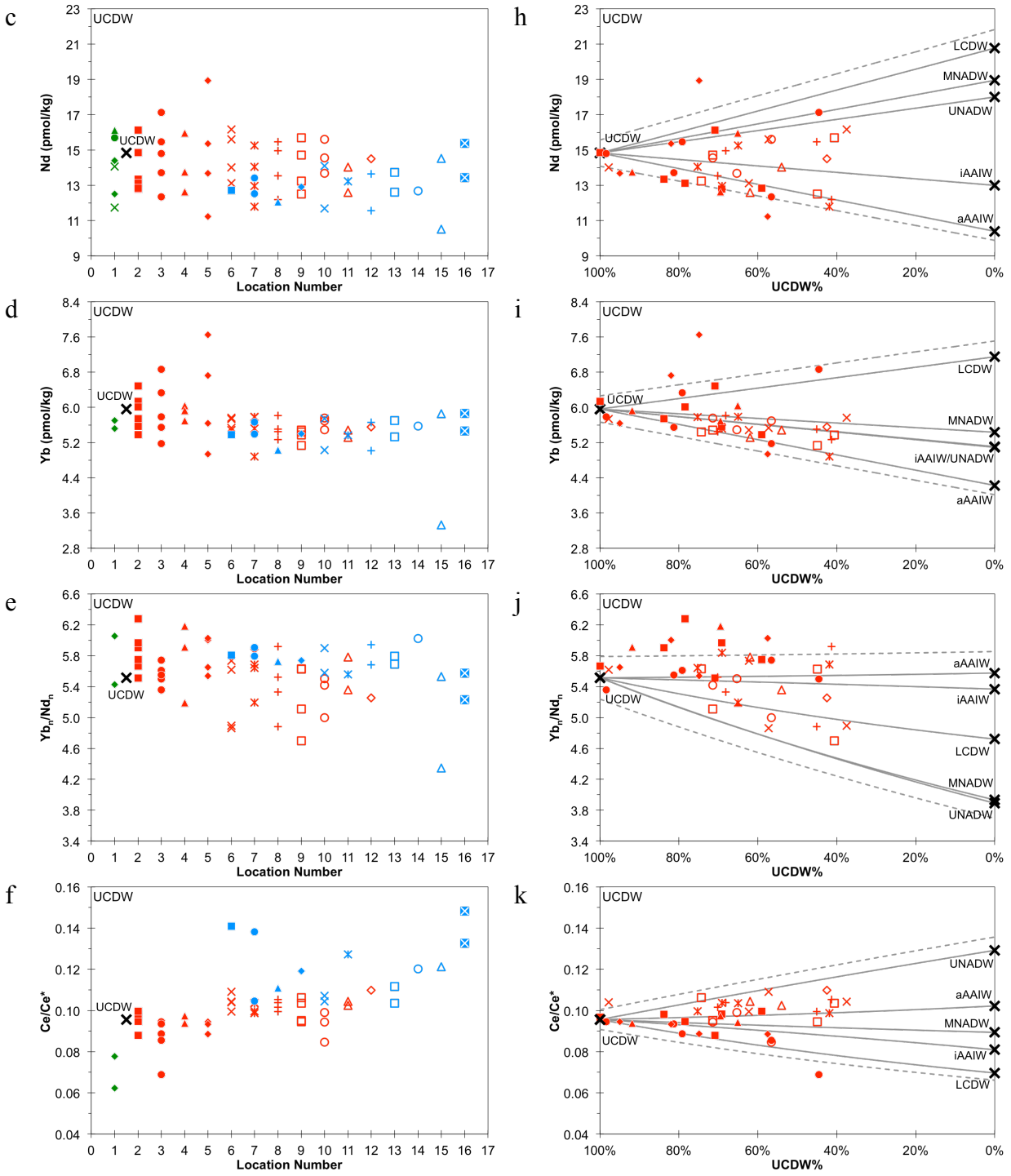

Figure S20. continued

g

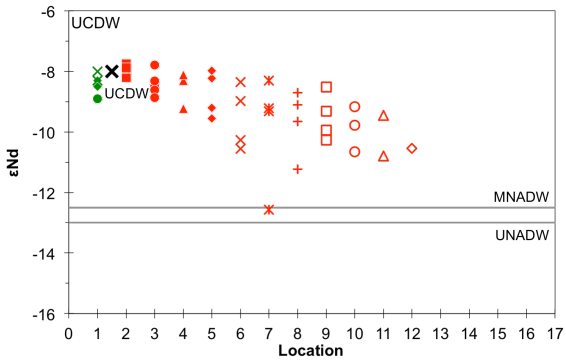


l

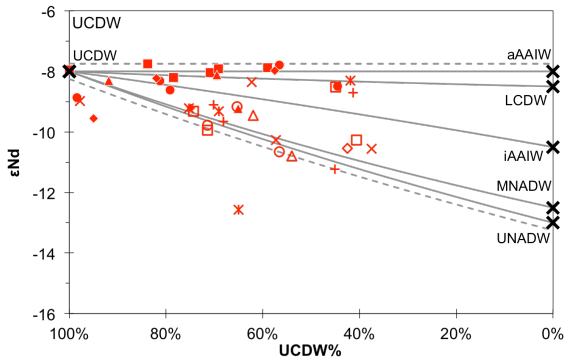

Figure S21. Changes of REEs and εNd along the LCDW pathway

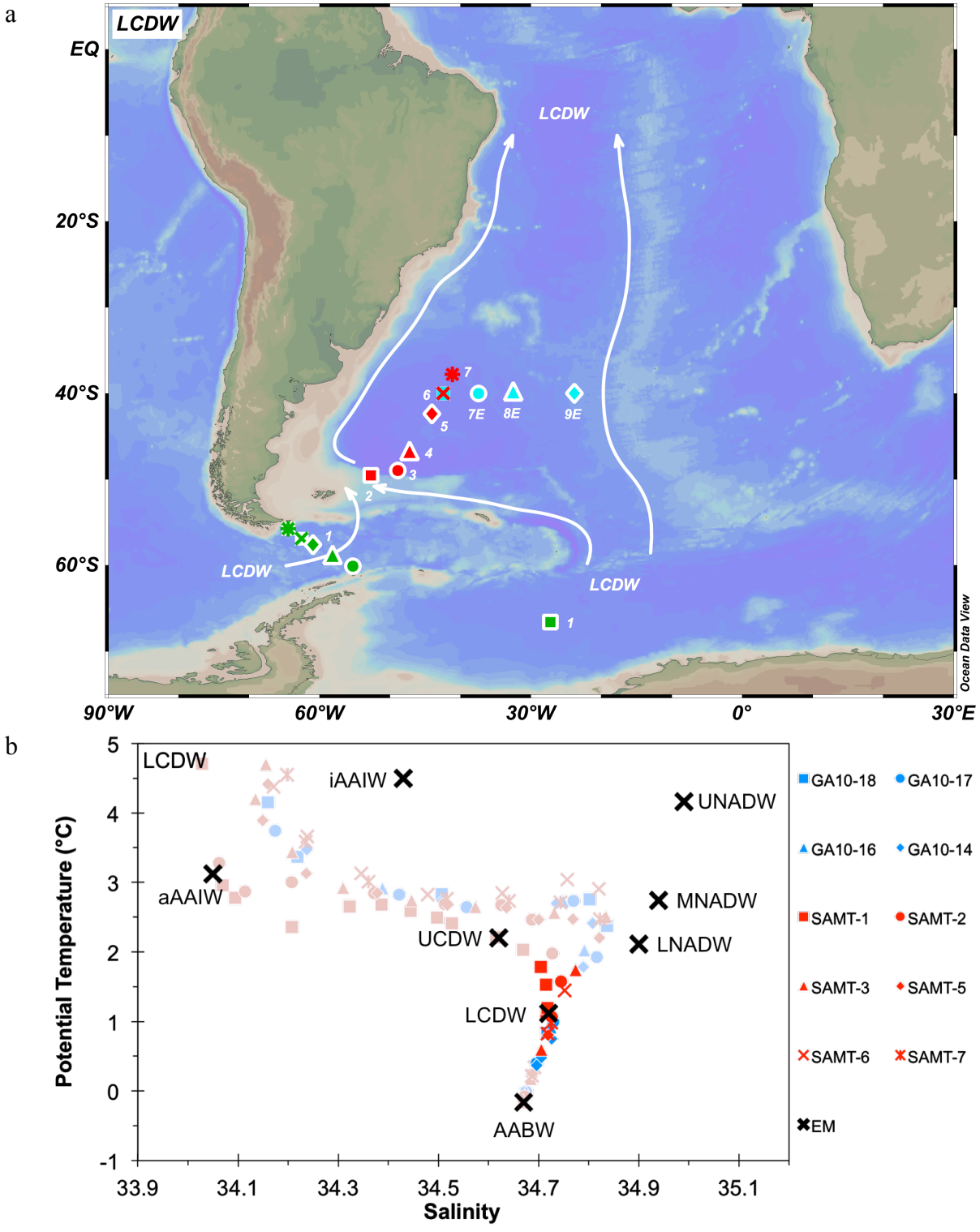

Figure S21. continued

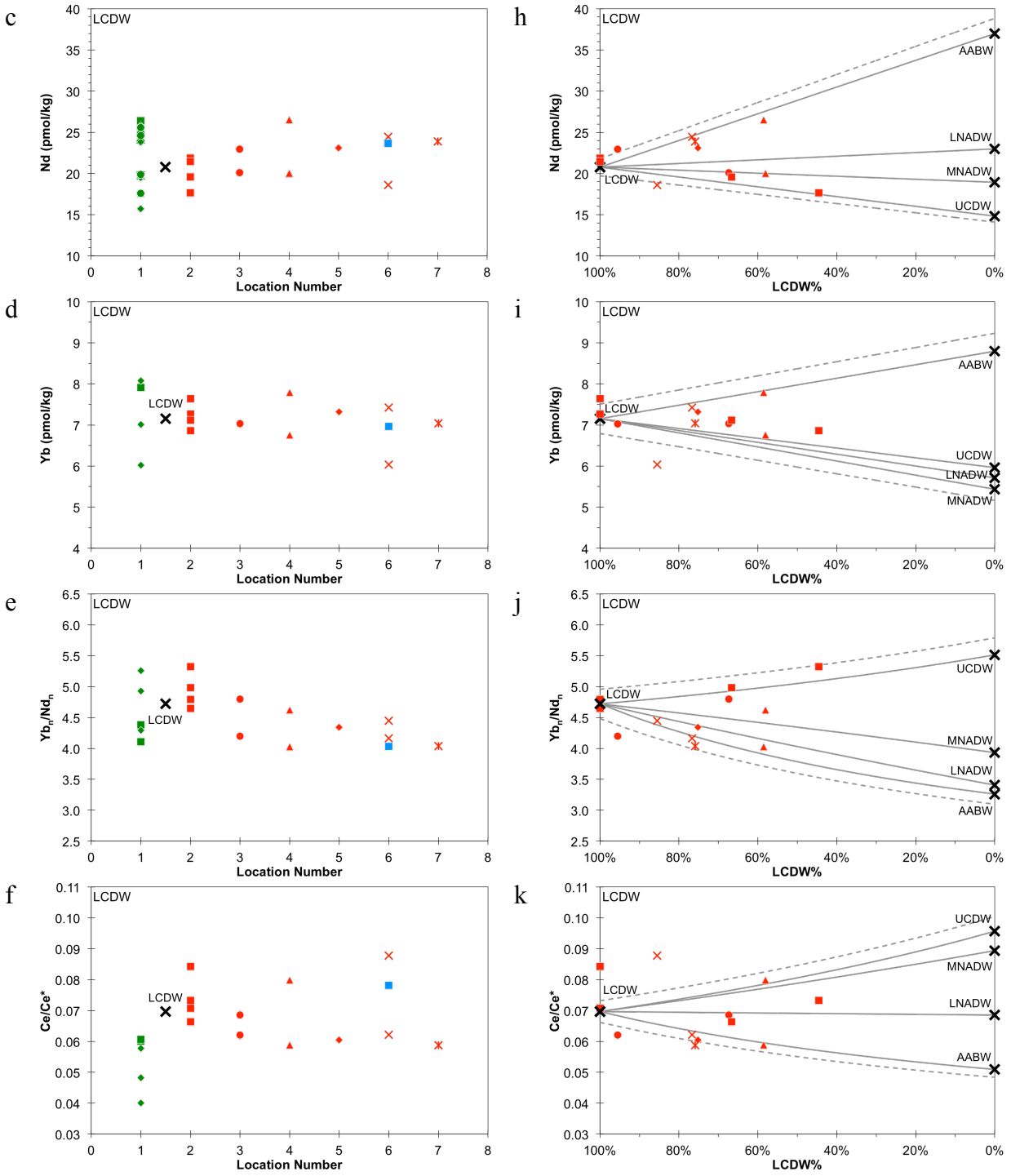

Figure S21. continued

g

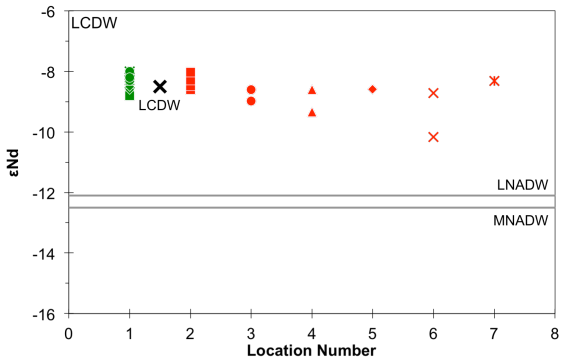


l

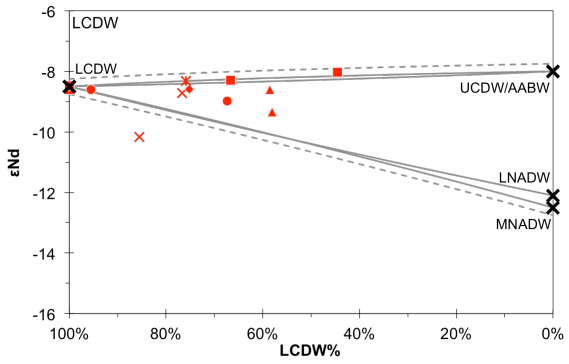

Figure S22. Changes of REEs and εNd along the AABW pathway

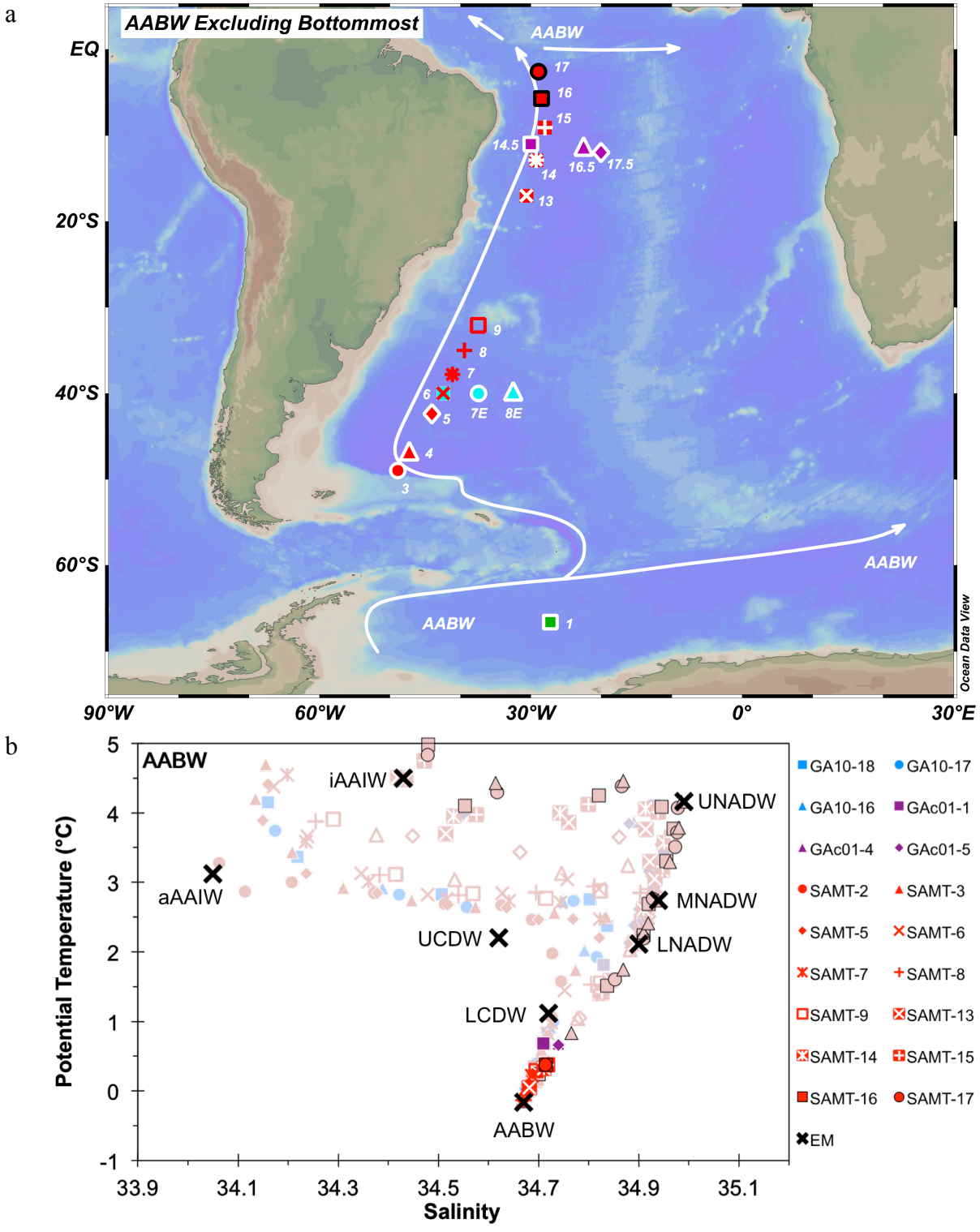

Figure S22. continued

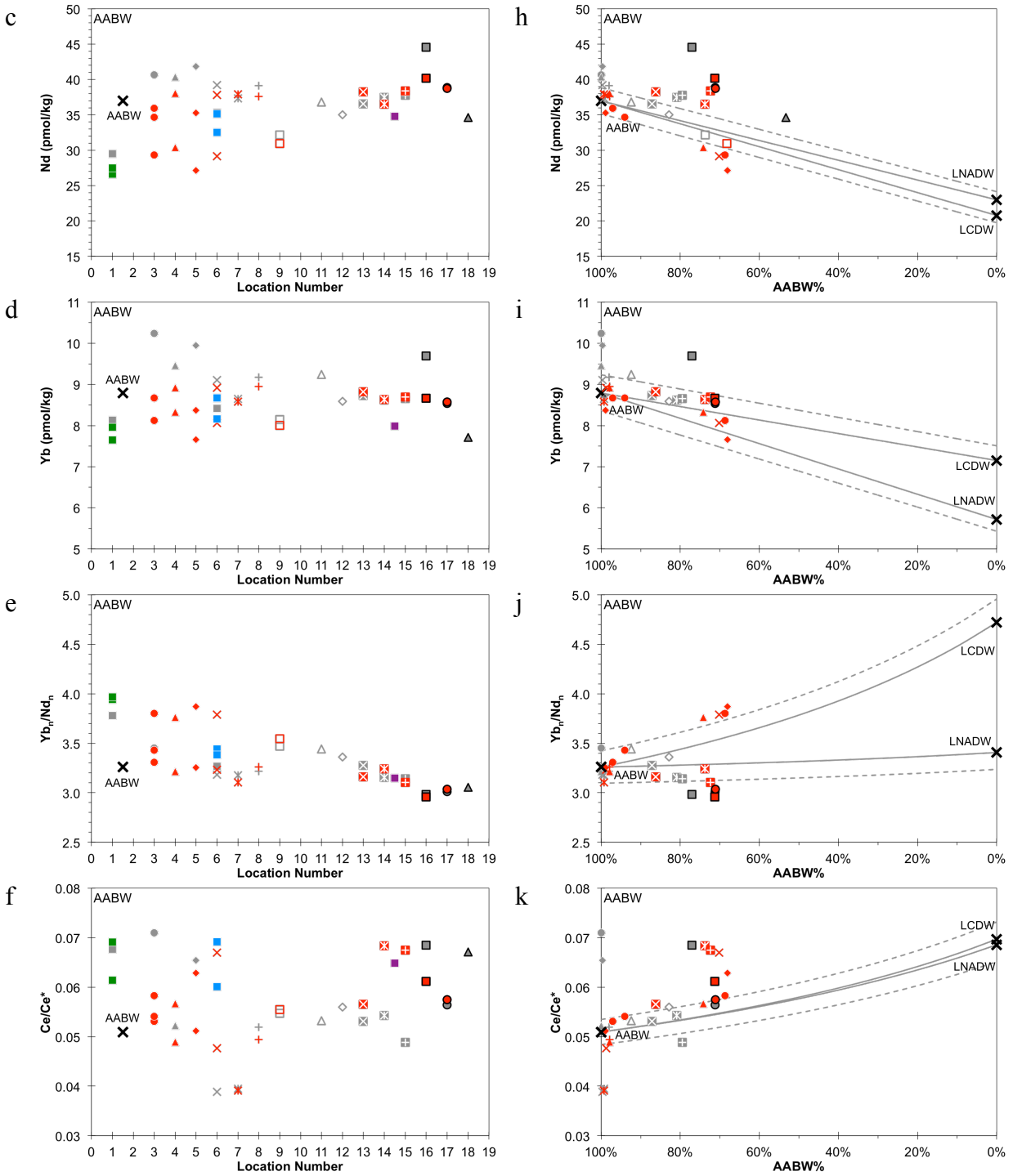

Figure S22. continued

g

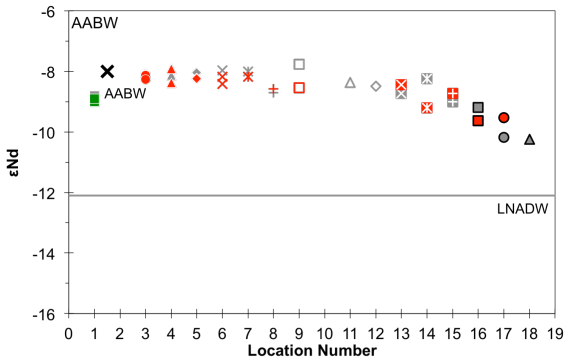


l

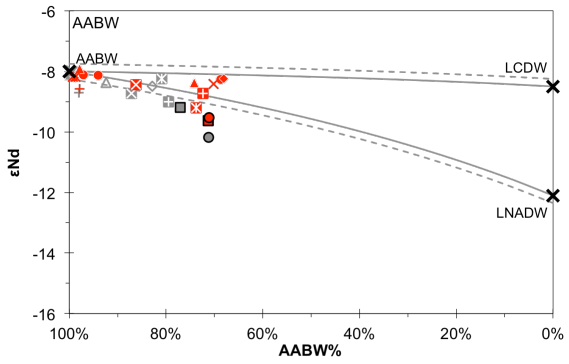

Figure S23. Changes of REEs and εNd along ~10°S for UNADW

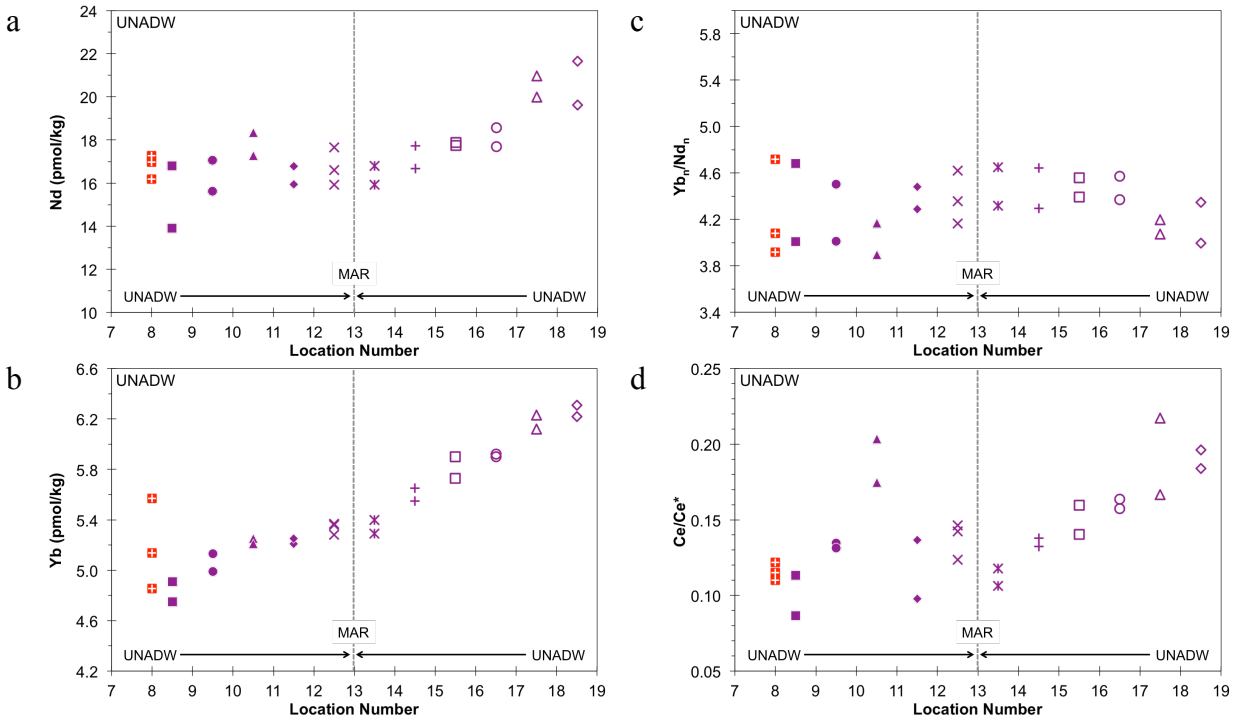

Figure S24. Changes of REEs and εNd along ~10°S for MNADW

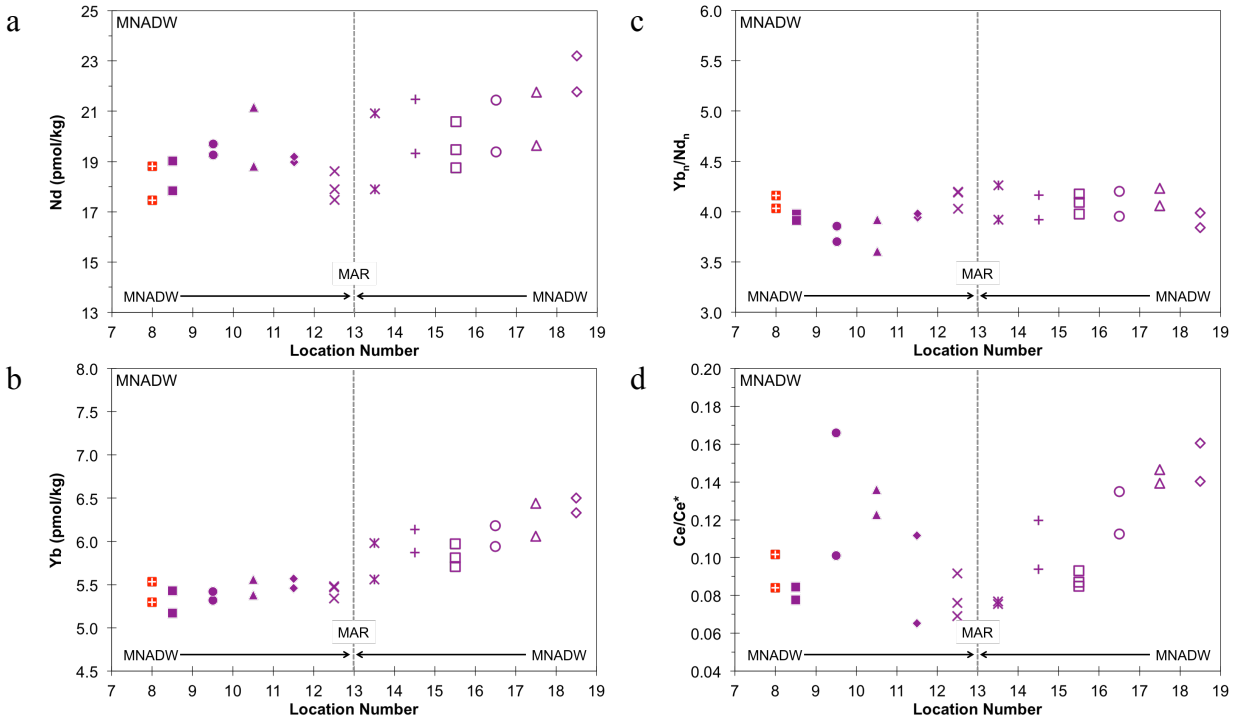

Figure S25. Changes of REEs and εNd along ~10°S for LNADW

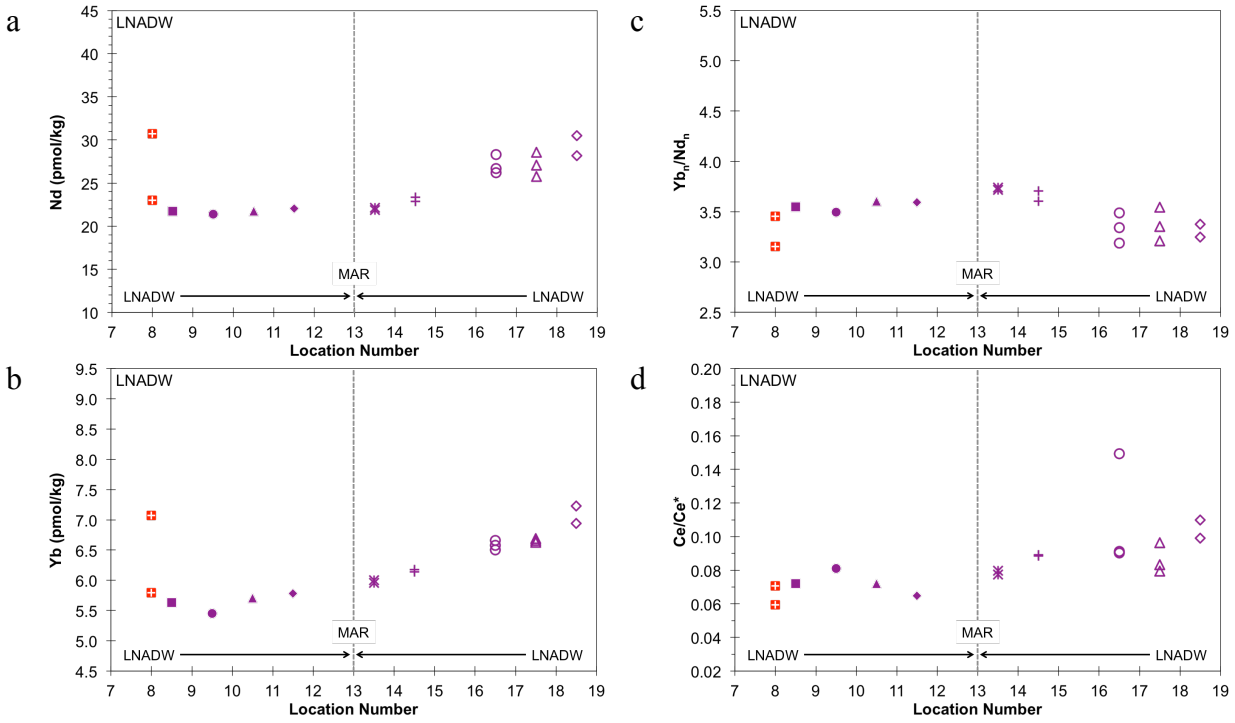

Figure S26. Changes of REEs and εNd along ~40°S for LCDW

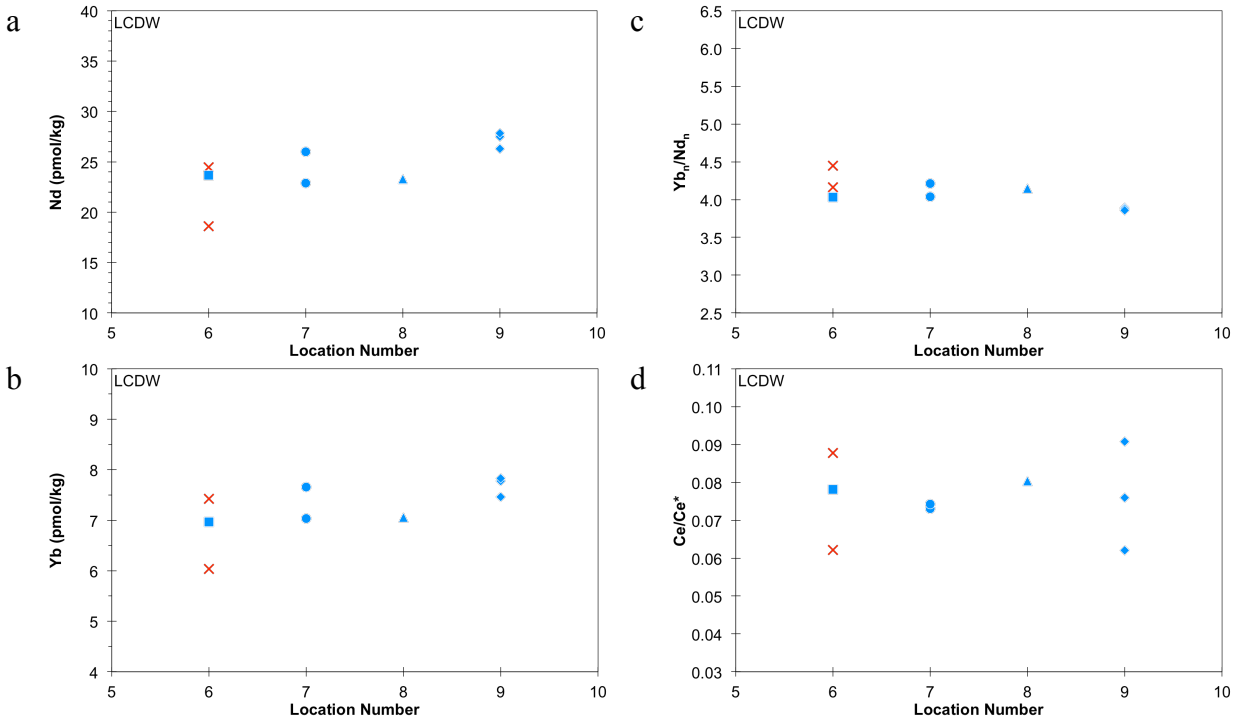

Figure S27. Changes of REEs and εNd along ~40°S and ~10°S for AABW

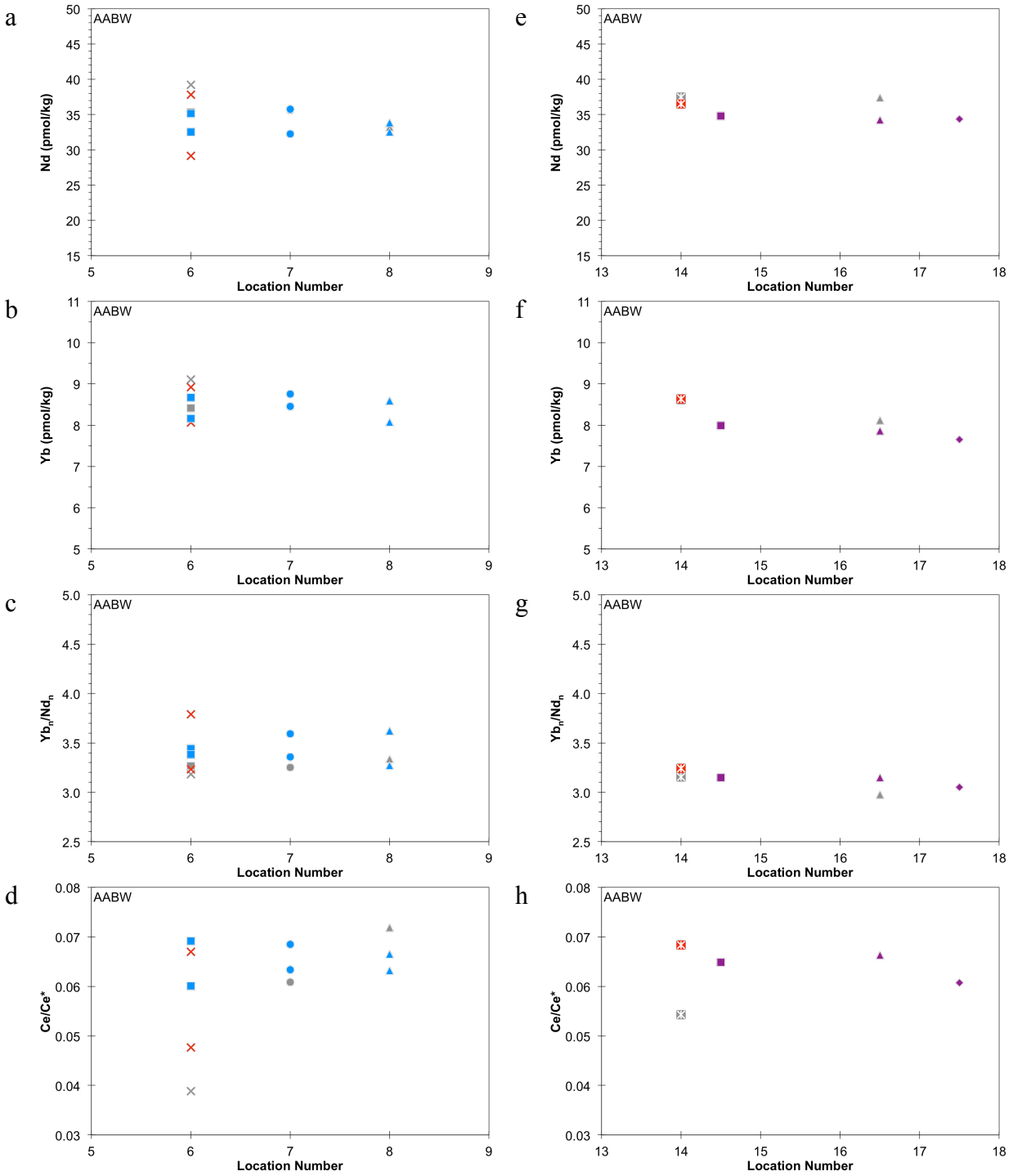

Figure S28. Histograms of Δ[REE]/Predicted [REE] and Δ(REE ratio)/Predicted (REE ratio) calculated based on water mass mixing using $PO_4^*$ and potential temperature

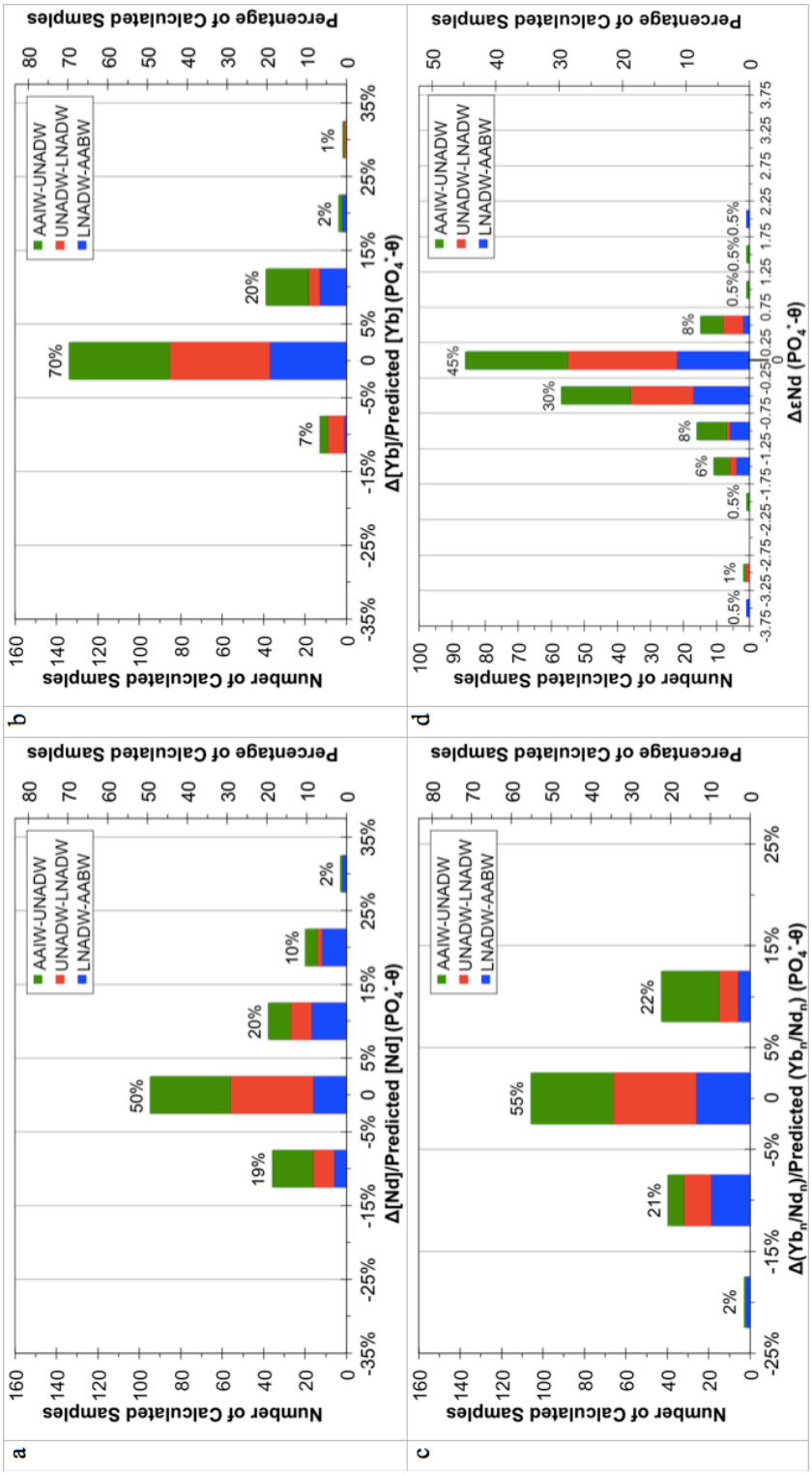

Figure S29. Section profiles of salinity with contours of neutral density, Δ[Nd]/Predicted [Nd], and Δ[Yb]/Predicted [Yb] based on $PO_4^*$ and potential temperature

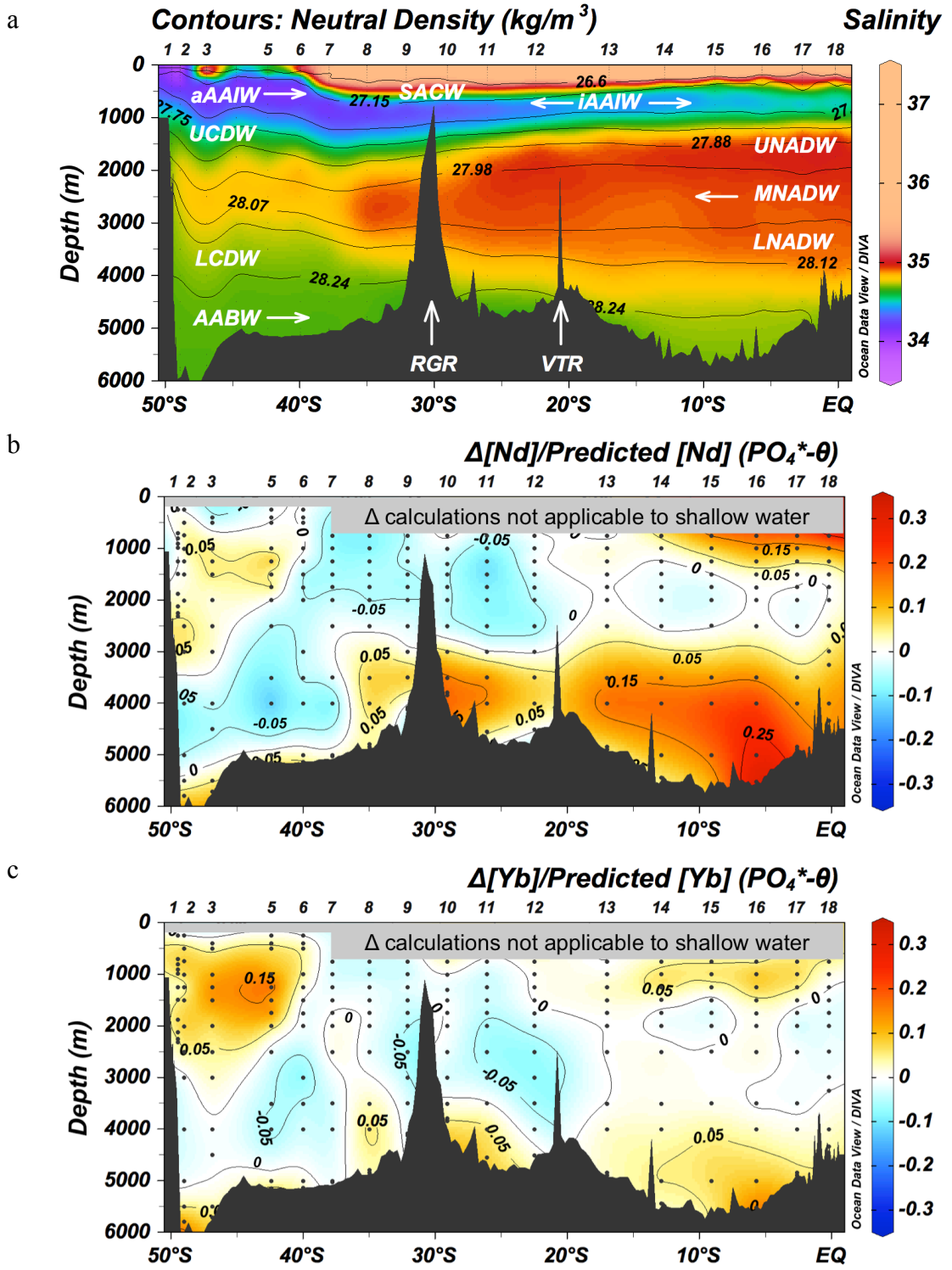

Figure S30. Section profiles of $PO_4^*$ with contours of neutral density, $\Delta(Yb_n/Nd_n)$/Predicted $(Yb_n/Nd_n)$, and $\Delta\varepsilon Nd$ based on $PO_4^*$ and potential temperature

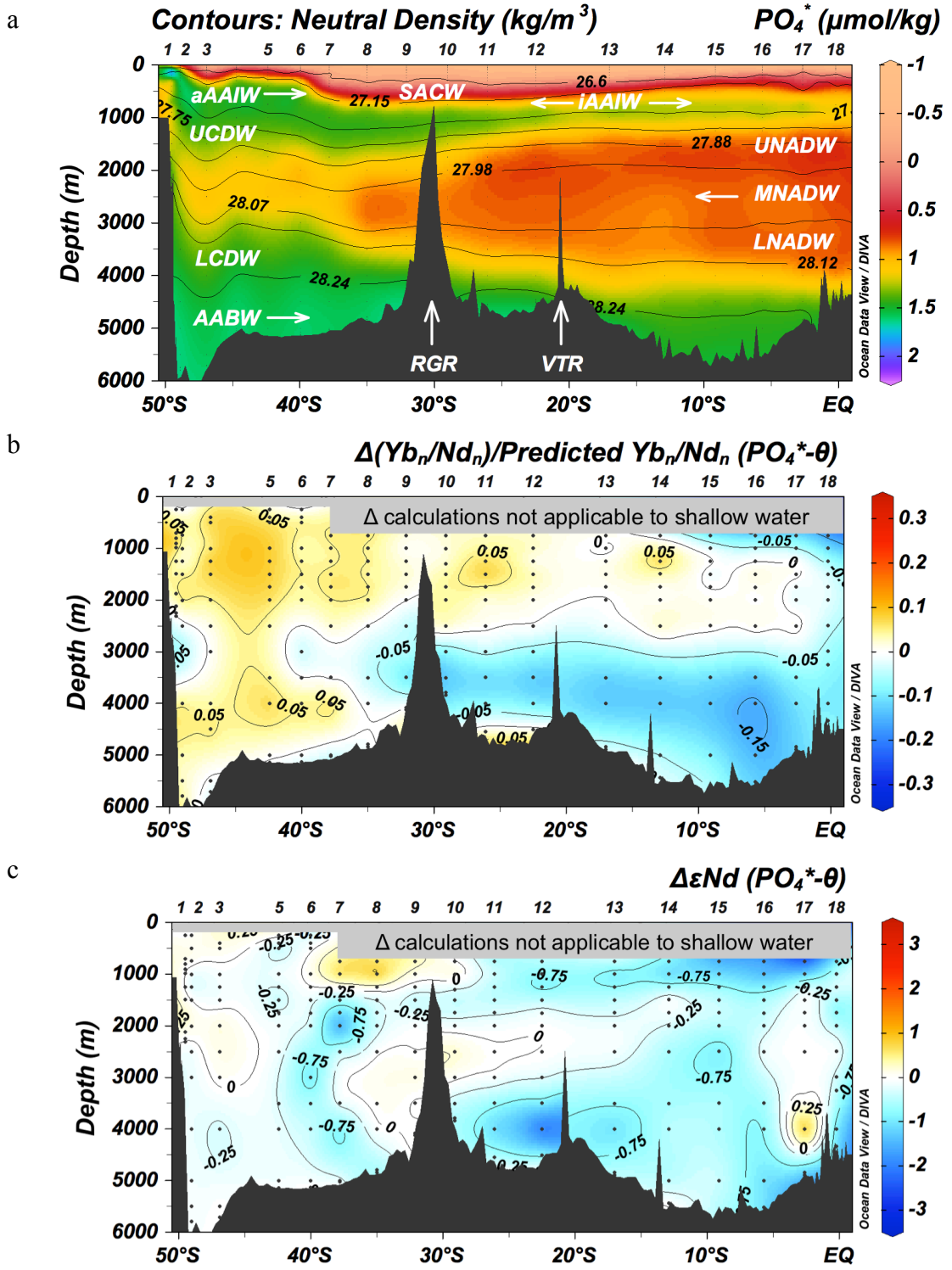

Figure S31. Histograms of Δ[REE]/Predicted [REE] and Δ(REE ratio)/Predicted (REE ratio) calculated based on water mass mixing using $PO_4^*$ and salinity

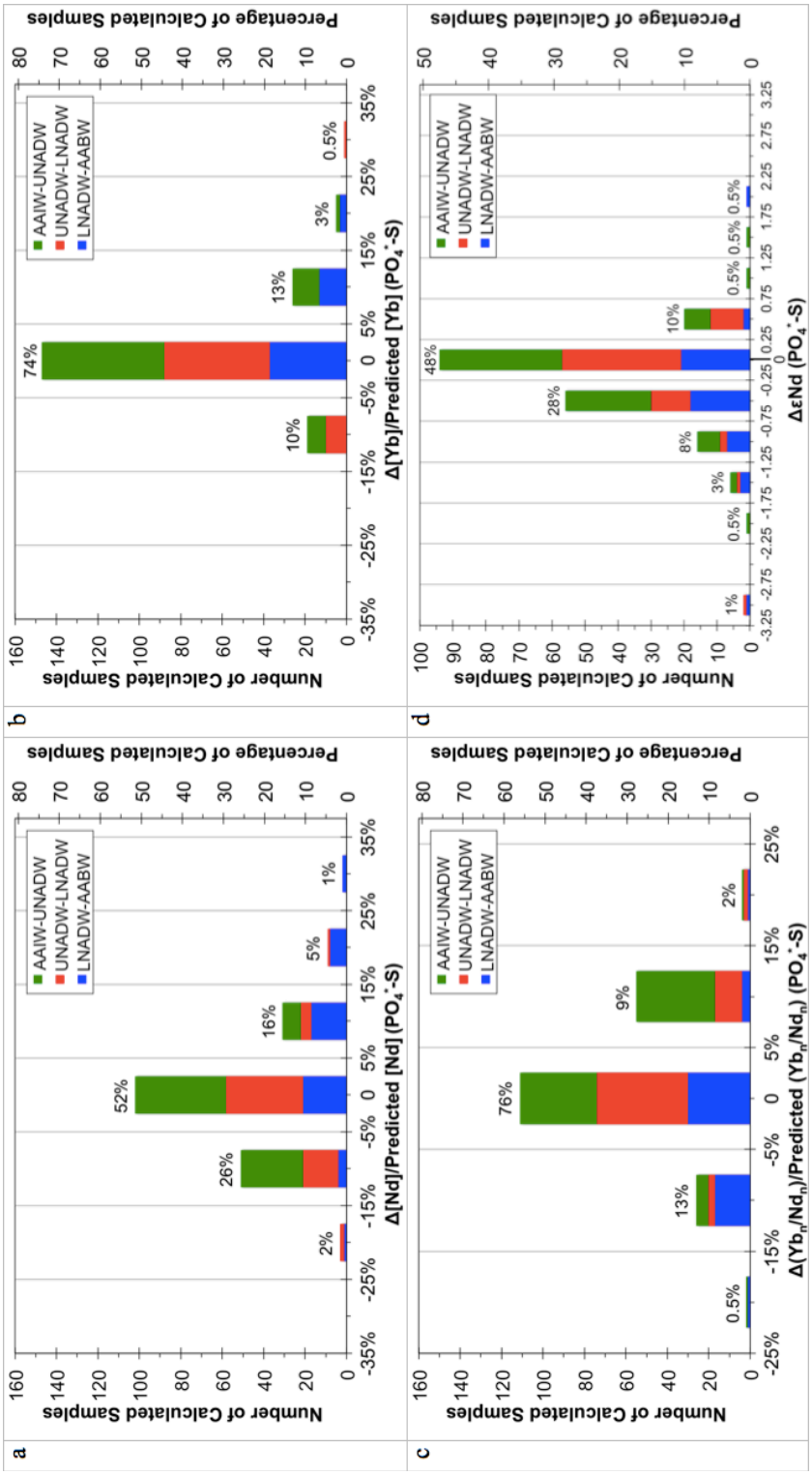

Figure S32. Section profiles of salinity with contours of neutral density, Δ[Nd]/Predicted [Nd], and Δ[Yb]/Predicted [Yb] based on $PO_4^*$ and salinity

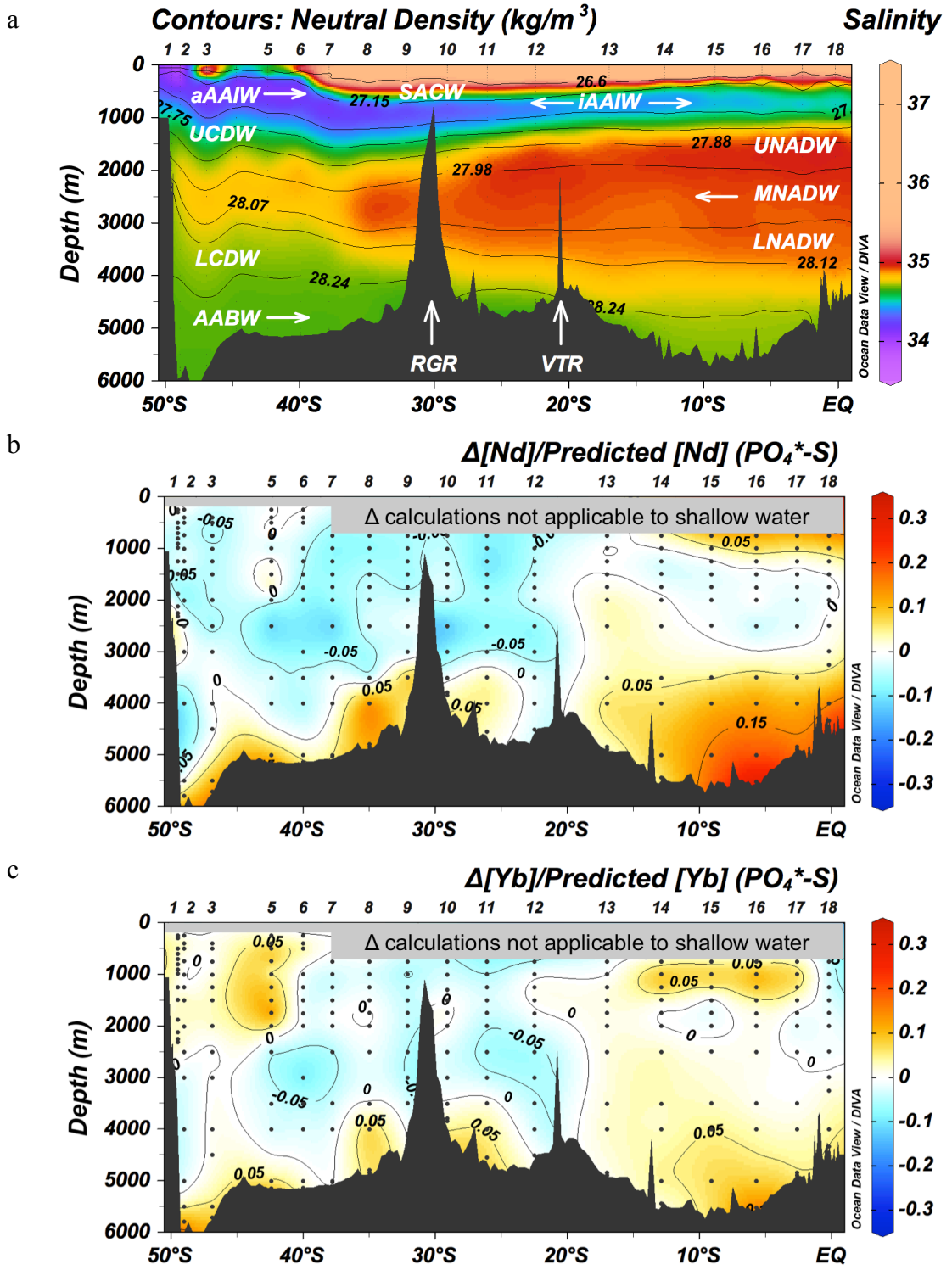

Figure S33. Section profiles of $PO_4^*$ with contours of neutral density, $\Delta(Yb_n/Nd_n)$/Predicted $(Yb_n/Nd_n)$, and $\Delta\varepsilon Nd$ based on $PO_4^*$ and salinity

a

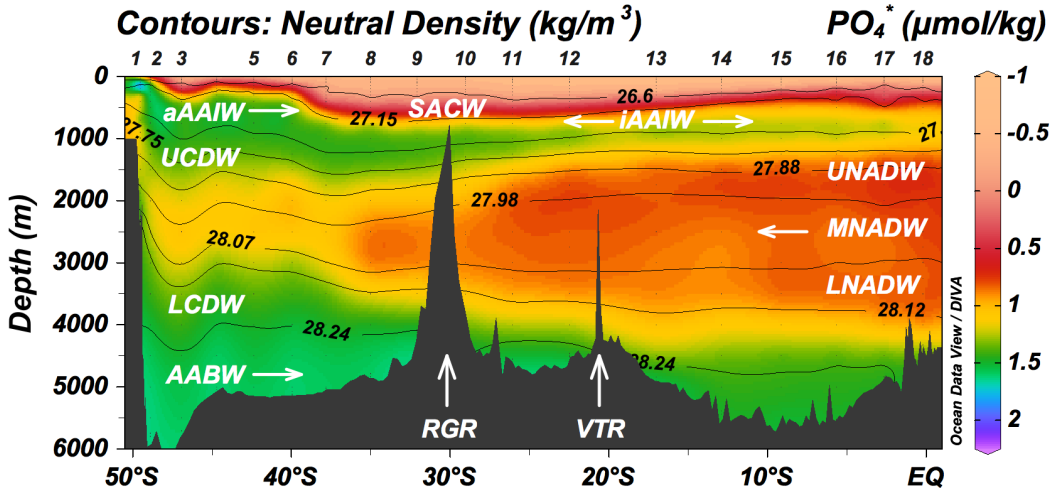


b

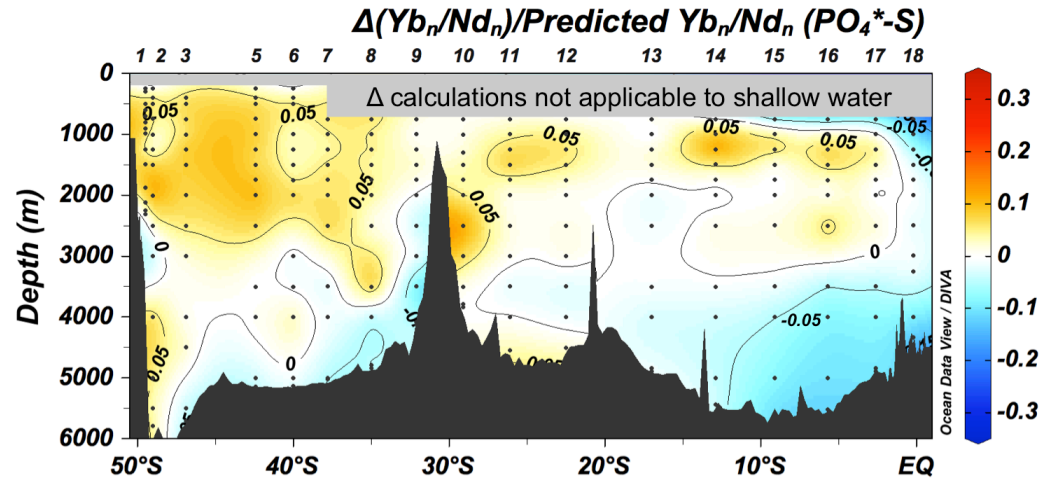


c

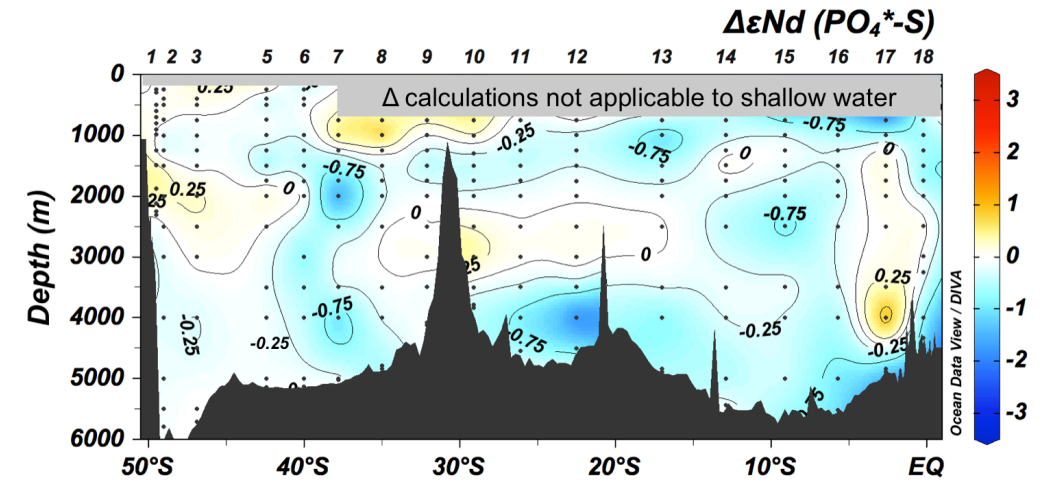

Figure S34. PAAS-normalized REE patterns of Southwest Atlantic seawater samples

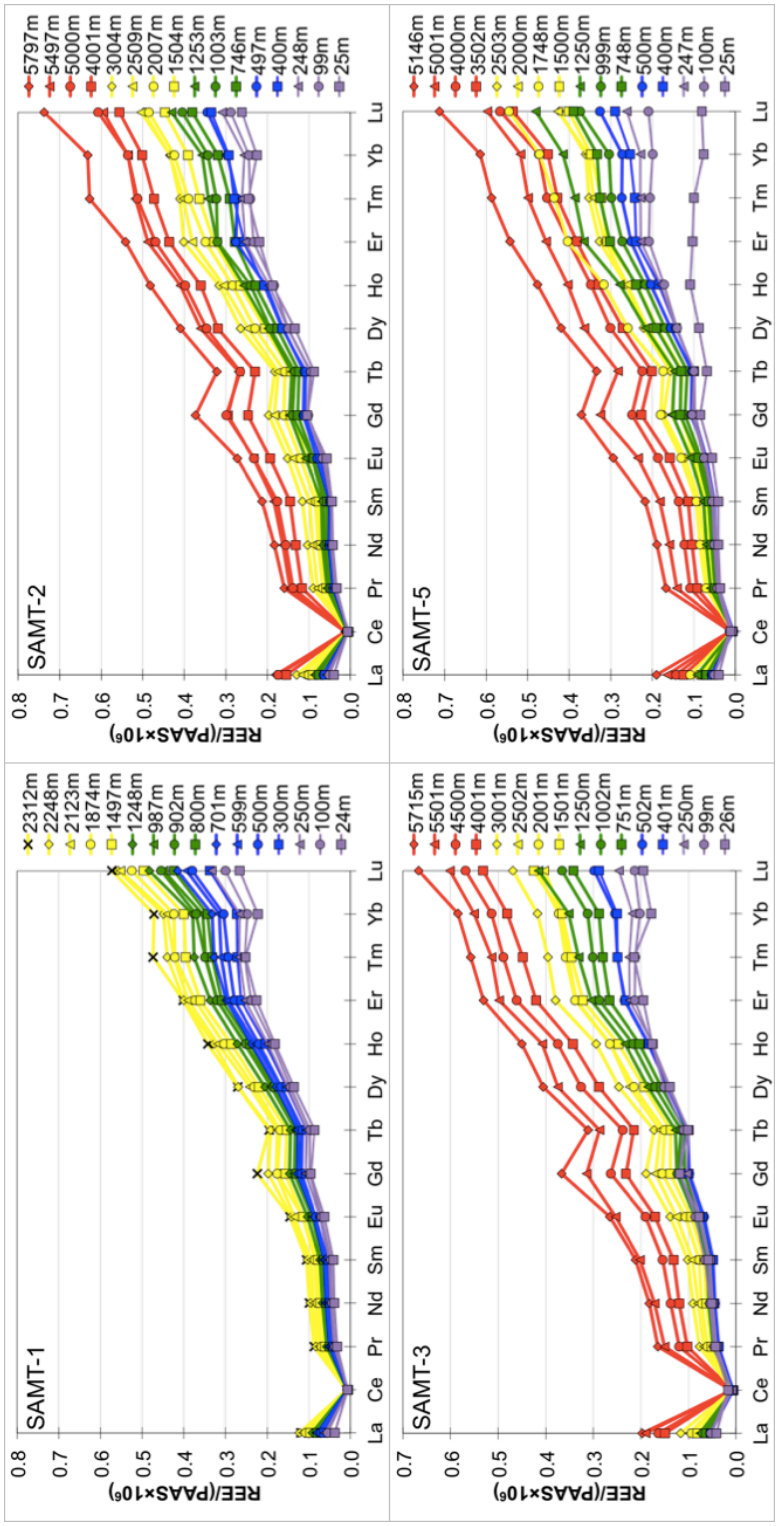

Figure S34. continued

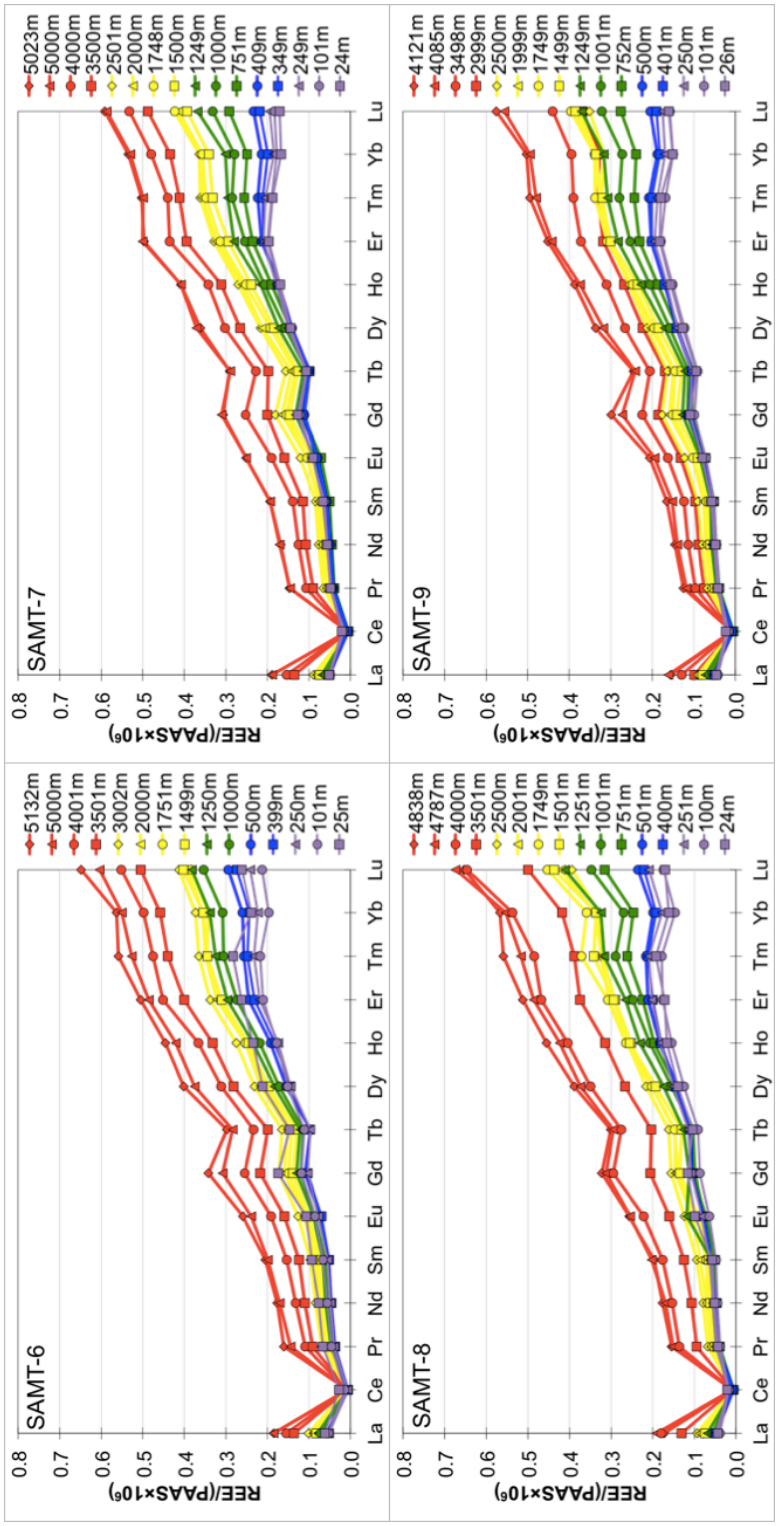

Figure S34. continued

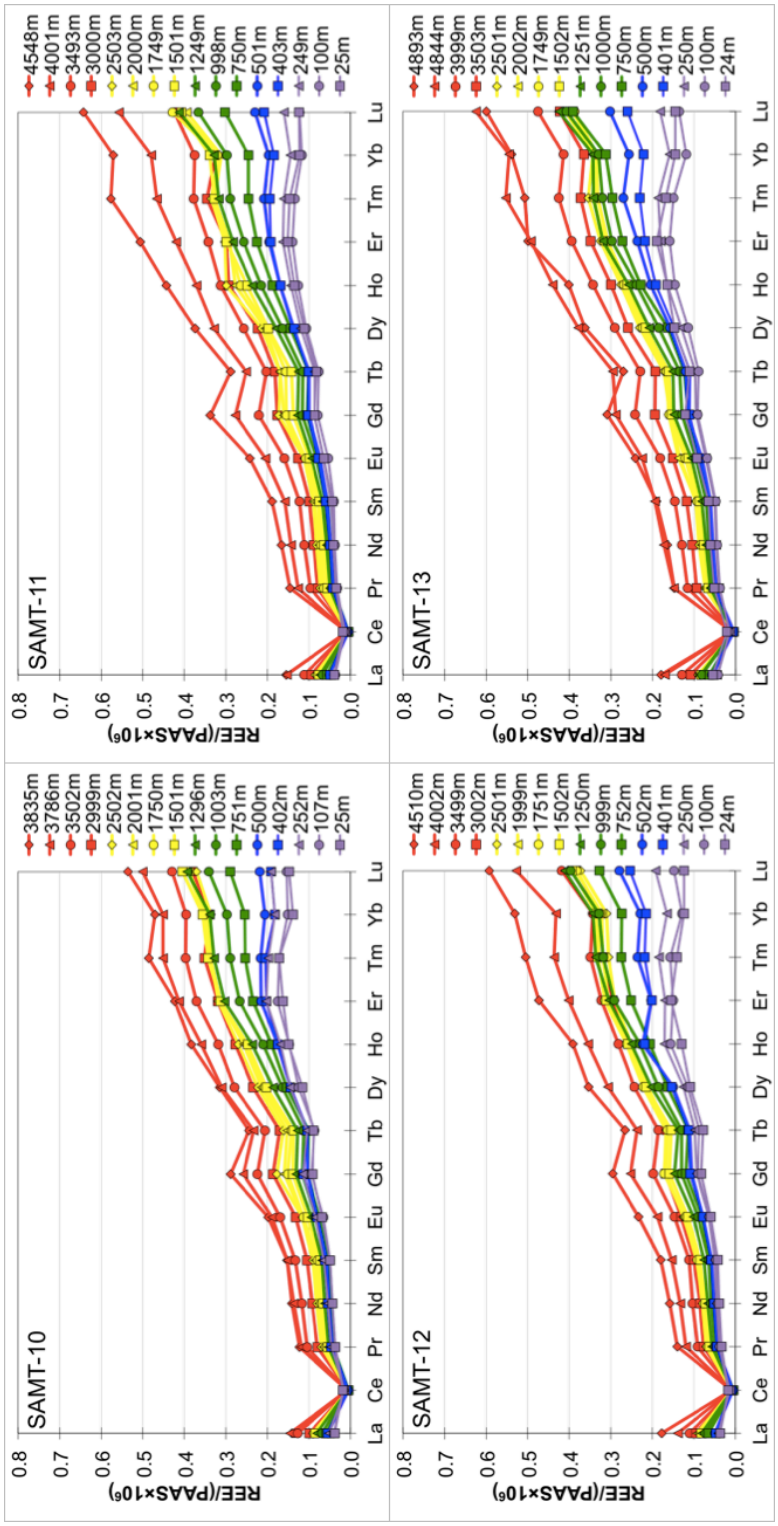

Figure S34. continued

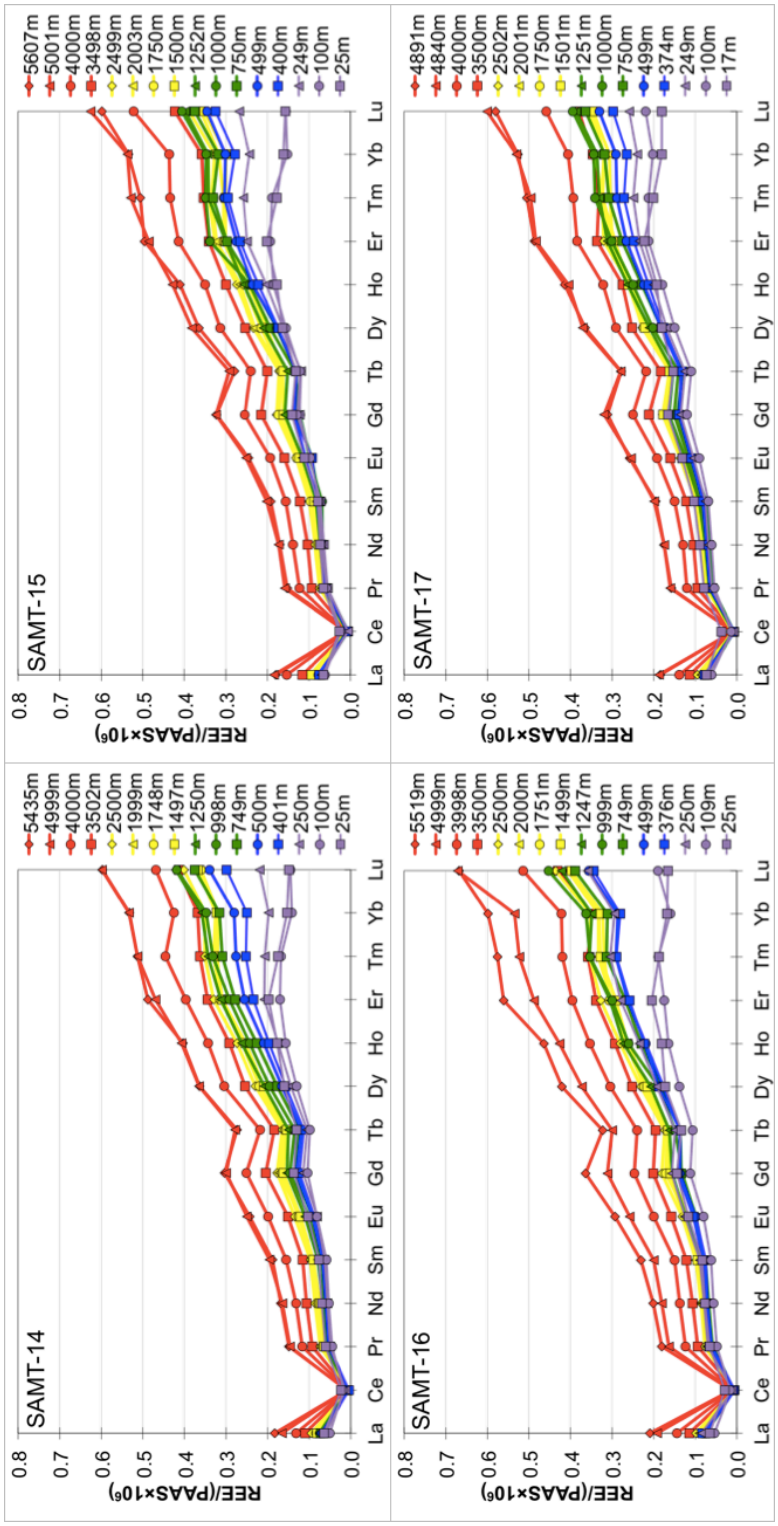

Figure S34. continued

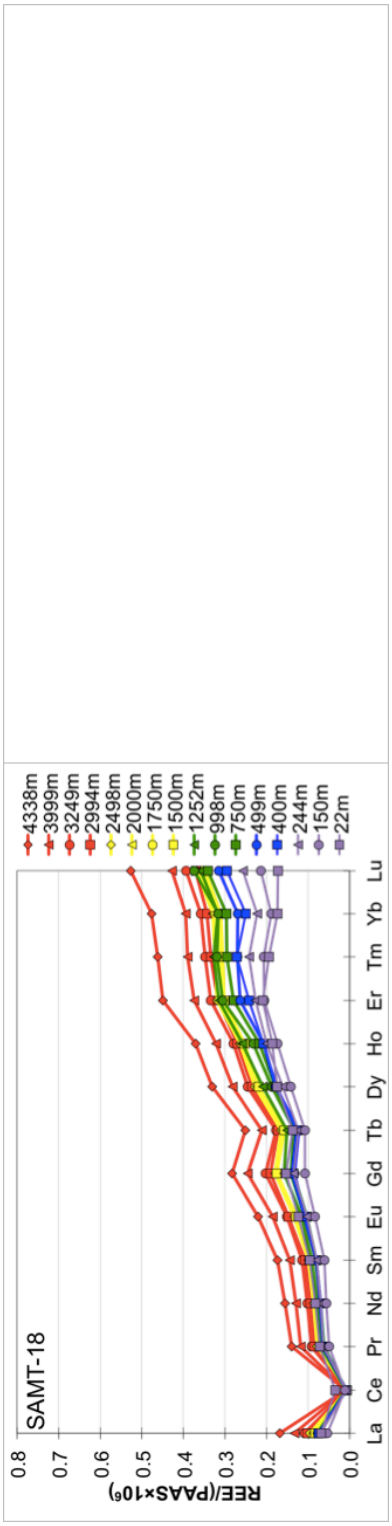

# Chapter 4. Constraining the Source of Neodymium Isotopic Composition in North Pacific Seawater

Yingzhe Wu[1,2], Steven L. Goldstein[1,2], Leopoldo D. Pena[1,3], Robert F. Anderson[1,2], Christopher T. Hayes[4], Louise Bolge[1], Yue Cai[1], Rainer Gersonde[5]

[1] Lamont-Doherty Earth Observatory of Columbia University, Palisades, New York 10964, USA

[2] Department of Earth and Environmental Sciences, Columbia University, New York 10027, USA

[3] GRC Geociències Marines, Department of Earth and Ocean Dynamics, University of Barcelona, Barcelona 08028, Spain

[4] Department of Marine Science, University of Southern Mississippi, Stennis Space Center, Mississippi 39529, USA

[5] Alfred Wegener Institute, Helmholtz Centre for Polar and Marine Research, Bremerhaven, Germany

manuscript in preparation for *Geochimica et Cosmochimica Acta*

**Abstract**

North Pacific Deep Water (NPDW) has the highest neodymium isotopic composition (expressed in εNd notation) in the oceans. However, the high εNd of NPDW (−4 to −2) has been difficult to reconcile with the eolian inputs of Asian dusts as reflected in surface waters, which have much lower εNd (≈ −10), indicating potential addition of a component from Pacific volcanism. In order to constrain the Nd sources in the North Pacific, we analyzed Nd isotopes and rare earth element concentrations (REEs) of seawater from five stations across the North Pacific sampled by the Innovative North Pacific Experiment (INOPEX) Cruise Sonne SO202. In the surface water (~10 m), the highest εNd is observed at the station closest to the Aleutian-Kamchatka volcanic margin (Northwest station SO202-5), suggesting higher contribution of external REEs from volcanic ashes compared to the other stations. In the shallow water (100-400 m, depending on location), remineralization of REEs from volcanic ashes prevails over Asian dusts at Northwest station SO202-5 and near Japan stations SO202-44, 41, and 39, whereas remineralization of REEs from Asian dusts prevails over volcanic ashes at the Northeast station SO202-32 in the open ocean of the Alaska Peninsula. From the depths of North Pacific Intermediate Water (NPIW) to NPDW, seawater εNd and REEs show conservative water mass mixing of NPIW-NPDW. They also show conservative behavior along the water mass transport paths of NPIW and NPDW. Below the depths of NPDW, addition of external REEs is observed in the vertical profiles of εNd and REEs as well as along the transport path of Lower Circumpolar Deep Water (LCDW). The potential sources that add external REEs to the bottom water are (1) sediments on the Kuril-

Kamchatka-Aleutian volcanic margin along the LCDW transport path, and (2) sediments on the seafloor, both of which could interact with seawater and modify the seawater εNd and REE signatures.

## 1. Introduction

In many regions of the oceans, neodymium (Nd) isotopic compositions of intermediate and deep water covary with conservative water mass tracers such as salinity and $PO_4^*$ (preformed phosphate; $PO_4^* = PO_4 + O_2/175 - 1.95$; (Broecker et al., 1991)), showing values approximating those expected based on water mass mixing (e.g. (Piepgras and Wasserburg, 1980; Jeandel, 1993; von Blanckenburg, 1999; Goldstein and Hemming, 2003; Jones et al., 2008; Rempfer et al., 2011; Stichel et al., 2012a; Stichel et al., 2012b; Molina-Kescher et al., 2014; Lambelet et al., 2016)). As a result, Nd isotopes are often described as behaving "quasi-conservatively" in the oceans. This quality makes Nd isotopes potentially useful to trace present and past ocean circulation independent of changes in nutrient cycling (Frank, 2002; Goldstein and Hemming, 2003; van de Flierdt et al., 2016), because Nd isotopic compositions are not significantly affected by biological productivity, air-sea gas exchange or temperature (unlike low atomic mass tracers such as benthic foraminiferal $\delta^{13}C$). Nevertheless, there are major gaps in our knowledge of Nd sources, sinks, and internal cycling that limit the utility of Nd isotopes as a tracer in the oceans.

The North Pacific plays a key role in the ocean Nd cycle as a voluminous end-member for mixing with the rest of the oceans. Based on limited available data, it appears that much of the deep North Pacific has a nearly uniform Nd isotopic composition, and a few published paleo-records indicate this uniformity has remained relatively stable for at least a few million years (Abouchami et al., 1997; Ling et al., 1997; Ling et al., 2005; Hu et al., 2012). Nevertheless, in contrast to the North Atlantic, the global complement to the

North Pacific, the question of how deep water in the north Pacific obtains its Nd isotopic composition is not understood. This study reports Nd isotopic compositions and rare earth element (REE) concentrations in full depth profiles from five stations across the subarctic North Pacific (Fig. 1), sampled by the INOPEX (Innovative North Pacific Experiment) cruise in 2009, to evaluate sources and sinks of Nd and other REEs in this region. The stations are located different distances from sources of REEs from Circum-Pacific volcanism and Asian eolian dust, in order to help us investigate the impacts of these potential sources. The stations are also on the transport paths of the major Northern Pacific intermediate and deep water masses, allowing us to investigate whether Nd isotopic compositions and REEs behave conservatively along the water mass pathways.

## 2. Background

### *2.1. Nd in the oceans*

Seawater acquires its Nd isotopic signature from weathering of the continents. The deep water in the North Atlantic has εNd = −14 to −13 (e.g. (Piepgras and Wasserburg, 1980; Piepgras and Wasserburg, 1987)). The deep water in the North Pacific has εNd = −4 to −2 (e.g. (Piepgras and Wasserburg, 1980; Piepgras and Wasserburg, 1987)). Here the Nd isotopic composition ($^{143}Nd/^{144}Nd$) is expressed as εNd = $[(^{143}Nd/^{144}Nd_{sample}) / (^{143}Nd/^{144}Nd_{CHUR}) - 1] \times 10^4$, where $^{143}Nd/^{144}Nd_{CHUR} = 0.512638$ (Jacobsen and Wasserburg, 1980). For the North Atlantic Ocean, the low εNd-values are consistent with weathering of the surrounding old North Atlantic continental crust. For vast areas of the North Pacific Ocean, the main sources of Nd are eolian dusts blown in

from Asia with values reflecting old continental crust (εNd ≈ −10; e.g. (Goldstein et al., 1984; Nakai et al., 1993; Jones et al., 1994)) and volcanic ashes from Circum-Pacific volcanism showing recent derivation from the mantle (e.g. in the North Pacific, the Aleutian, Kamchatka, and Kurile arcs). Based on the largest currently available geochemical data set, EarthChem (www.earthchem.org/portal), including PetDB (Lehnert et al., 2000) and GEOROC (GEOROC, 2007), 786 volcanic rocks from the Aleutian, Kamchatka, and Kurile arcs have average εNd values of +7.8 ± 1.3 (1σ). Thus, while the εNd of Pacific waters is between those of the major sources, range of εNd-values of these sources of Nd in the Pacific is very large, and the means by which the waters obtain their values is not understood.

For example, results of an ocean general circulation model (Jones et al., 2008) show that Nd isotopic compositions in the deep North Atlantic are those expected based on propagation of surface waters known surface ocean εNd-values conservatively propagated to the deep water (Jones et al., 2008). However, using the same set of conditions for the Pacific it predicts deep North Pacific εNd-values of ≈ −11, much lower than observed εNd-values of −4 to −2. Thus, while it is generally accepted that Circum-Pacific volcanism contributes to the high Nd isotopic composition in the North Pacific, it is unknown how this signature is added to seawater.

The five stations reported in this study sampled by INOPEX (RV Sonne 202, Fig. 1) were chosen to address the potential source of high εNd in the North Pacific and understand how this signal is added to the seawater. Four stations are in the west Pacific near Japan (stations SO202-44, 41, and 39 along ~40°N) and near the Aleutian-

Kamchatka intersection (Northwest station SO202-5), and one is in the open North Pacific Ocean far to the east, in the same longitude of the western Alaska Peninsula (Northeast station SO202-32).

### *2.2. REE geochemistry*

Nd is one of the rare earth elements (REEs), a group of 15 elements from lanthanum (La, atomic number 57) to lutetium (Lu, atomic number 71). In the lanthanide series, the electrons are progressively filled in the 4f orbitals with increasing atomic number. The REEs have similar outer electronic configurations, which the 6s electrons shield electrons in the 4f orbitals and results in similar chemical characteristics of REEs. However, the decrease of ionic radius with increasing atomic number results in slight chemical differences in the behavior of REEs. The REEs mostly complex with carbonate ion in seawater (e.g. (Byrne and Kim, 1990; Byrne, 2002; Luo and Byrne, 2004)). From La to Lu, the stability of REE complexes in seawater increases with decreasing radii (e.g. (Elderfield et al., 1988; Lee and Byrne, 1993)). In addition, the light REEs (LREEs) with larger radii are more preferentially scavenged onto particles compared to heavy REEs (HREEs) (e.g. (Byrne and Kim, 1990)). This systematic fractionation within the REEs is often seen in seawater REE patterns, where relative abundances of seawater REEs are calculated by normalizing the concentration of each element to its concentration in Post-Archean Australian Shale (PAAS; (Taylor and McLennan, 1985)). The REEs show 3+ valence in their oxidation states, although cerium (Ce) and europium (Eu) also exist in 4+ valence and 2+ valence, respectively. Ce with 4+ valence will form if the system is

sufficiently oxidized and is insoluble in oxic seawater. Thus it shows a very low relative abundance compared to the other REEs in the PAAS-normalized seawater REE pattern.

The vertical seawater profiles of dissolved REE concentrations are similar to that of nutrients and show increasing concentrations with depth in the water column. Previous studies have proposed that these are resulted from scavenging onto particles in the surface water and remineralization of sinking particles at depth (e.g. (Jeandel et al., 1995)). However, some studies have suggested that the intermediate and deep water REEs behave conservatively based on water mass mixing (e.g. (German et al., 1995; Haley et al., 2014; Zheng et al., 2016)).

In the deep water, the dissolved REEs accumulate with aging of water masses and increase along the water mass transport paths, for example, from the Atlantic to Pacific Ocean (e.g. (De Baar et al., 1985)). The deep water PAAS-normalized HREE/LREE ratio increases from the Atlantic to the Pacific Ocean as a result of preferential removal of LREEs onto particles (e.g. (Byrne and Kim, 1990)) as well as stronger complexation of HREEs (e.g. (Elderfield et al., 1988)) along the deep water pathway from the Atlantic to Pacific Ocean (e.g. (Bertram and Elderfield, 1993)).

Similar to εNd, REE ratios (e.g. HREE/LREE) can also be used to trace external addition of REEs to seawater, since virtually all rock sources have very different REE signatures compared to seawater, thus can be especially useful for the shallow and the bottommost water. If an external source has very different εNd and REE signatures from seawater, both εNd and REEs ratios of seawater could change when this external source

interacts with seawater. Therefore, REEs and εNd can be studied together to investigate potential sources/sinks and cycling of REEs in the ocean.

## 3. North Pacific Hydrography

### *3.1. Surface water*

In the subtropical North Pacific, the warm and saline Kuroshio Current moves northeastward along the western boundary of the North Pacific (Fig. 1a). After it leaves Japan coast at ~35°N and ~140°E, it continues to flow eastward as Kuroshio Extension (Fig. 1a). In the subarctic North Pacific, there are two wind-driven clockwise gyres: the Western Subarctic Gyre to the west and the Alaskan Gyre to the east ((Qiu, 2001; Harrison et al., 2004); Fig. 1a). These gyres are connected by Alaskan Stream flowing westward along the Aleutian Islands ((Qiu, 2001; Harrison et al., 2004); Fig. 1a). The East Kamchatka Current originating from the Bering Sea moves southwestward along the Kamchatka Peninsula and continues to flow southwestward along the Kuril Island as Oyashio Current ((Qiu, 2001; Harrison et al., 2004); Fig. 1a). The Kuroshio and Oyashio Currents mix at 35-40°N and continue to flow eastward (Fig. 1a). The Subarctic Front along ~45°N is formed in the mixing region (Harrison et al., 2004) (Fig. 1a). Near Japan stations SO202-44, 41, and 39 are located sequentially on the pathway of this mixture (Fig. 1a). Northwest station SO202-5 is on the transport path of the Alaskan Stream (Fig. 1a). Northeast station SO202-32 is on the transport path of the Subarctic Front (Fig. 1a).

### *3.2. Shallow water*

For near Japan stations SO202-44, 41, and 39, located eastward along ~40°N, the water at ~100 m is influenced by the North Pacific Subtropical Mode Water (NPSTMW, S ≈ 34.5; temperature T = 16-19 °C, potential density $\sigma_\theta$ ≈ 25.2 kg/m$^3$; (Hanawa and Talley, 2001; Talley, 2011)) (Fig. 2a). The shallow water below 100 m at these stations shows influence from North Pacific Central Water (NPCW, S = 34.1-34.4; T = 9-12 °C, $\sigma_\theta$ ≈ 26.2 kg/m$^3$; (Hanawa and Talley, 2001; Talley, 2011)) (Fig. 2a). For Northwest station SO202-5 and Northeast station SO202-32, the water at ~100 m reflects influence from Dichothermal Water (DTW), with low temperature and high oxygen (Talley, 2011) (Fig. 2a).

### *3.3. Intermediate water*

At intermediate depths, North Pacific Intermediate Water (NPIW) is formed in the mixed water region between the Kuroshio Extension and Oyashio front (Talley, 1993) (Fig. 1b). It is characterized by a salinity minimum in the subtropical North Pacific (Talley, 1993). NPIW circulates clockwise in the subtropical North Pacific at 300-800 m (You, 2003) (Fig. 1b). NPIW characterized by low salinity is observed at 300-500 m at Northeast station SO202-32 and near Japan stations SO202-44, 41, and 39 (S = 33.9-34.2; potential temperature $\theta$ = 2.2-7.6 °C; $\sigma_\theta$ = 26.6-27.4 kg/m$^3$; neutral density $\gamma^n$ = 26.5-27.4 kg/m$^3$ (You, 2003; Yasuda, 2004; Talley, 2011)) (Fig. 2a). NPIW is not observed in station SO202-5 in the far north west (Fig. 1b,2a). For SO202-5, Mesothermal Water (MTW) is observed beneath DTW with a temperature maximum (Talley, 2011) (Fig. 2a).

### *3.4. Deep and bottom water*

North Pacific Deep Water (NPDW) is formed from the upwelling water flowing in from the Southern Ocean (Kawabe and Fujio, 2010; Talley, 2011) (Fig. 1b). It is characterized by high salinity and low temperature and occupies depths of 1500-3000 m (Kawabe and Fujio, 2010; Talley, 2011). The deep water of all five stations shows hydrographic characteristics of NPDW (S = 34.5-34.68; $\theta$ = 1.2-2.4 °C; $\sigma_\theta$ = 27.6-27.77 kg/m$^3$; $\gamma^n$ = 27.7-28.0 kg/m$^3$ (Macdonald et al., 2009; Talley, 2011)) (Fig. 2a,b). Lower Circumpolar Deep Water (LCDW) with high oxygen and low nutrient concentrations flows into the mid- and high-latitude North Pacific at depths of > 4000 m (Orsi et al., 1999; Kawabe and Fujio, 2010). Hydrographic characteristics of LCDW are observed in Northeast station SO202-32 and near Japan stations SO202-44, 41, and 39 (S = 34.69-34.70; $\theta$ = 1.05-1.1 °C; $\sigma_\theta$ = 27.79-27.80 kg/m$^3$; $\gamma^n$ = 28.0-28.27 kg/m$^3$ (Orsi et al., 1995; Whitworth et al., 1998)) (Fig. 2a,b).

## 4. Methods

### *4.1. Sampling*

Seawater samples were collected during the Sonne Expedition SO202-INOPEX from Tomakomai, Japan to Busan, Korea, July-August 2009. All five stations are located in the subarctic North Pacific (Fig. 1). About 10 L of water were collected and stored in a cubitainer for each sample. The samples were filtered using Pall Acropak 0.45 μm cartridge filters and acidified to pH < 2 shortly after sampling. About 5 L of each sample were analyzed for REE concentrations and Nd isotopic compositions.

### *4.2. Nd Isotopic Compositions*

For Nd isotopic measurements, we preconcentrated REEs from 5 L of seawater using C18 cartridges (Waters Corp., Sep-Pak classic cartridges, 360 mg, 55-105 μm) loaded with complexing agent of 2-ethylhexyl hydrogen phosphate (HDEHP) and 2-ethylhexyl dihydrogen phosphate ($H_2$MEHP), which was first proposed by (Shabani et al., 1992). In this study, we followed established methods by (Jeandel et al., 1998; Lacan and Jeandel, 2004; Pahnke et al., 2012). Specifically, C18 cartridges were first cleaned in a 0.5 N hydrochloric acid (HCl) bath overnight, followed by passing through 10 mL of 6 N HCl, followed by flushing of the cartridge with >500 mL of Milli-Q water. Cartridges were stored in Milli-Q water after cleaning. 300 μL of complexing agent HDEHP/$H_2$MEHP was loaded on a clean cartridge for a 5 L sample. Seawater samples were adjusted to pH ≈ 3.5 by adding Optima® ammonium hydroxide before being pumped through the cartridges at 20 mL/min by a peristaltic pump in the ultra-clean chemistry laboratory at LDEO. Cartridges were then eluted with 10 mL of 0.01 N HCl to remove barium. After barium elution, cartridges were eluted with 35 mL of 6 N HCl at 10 mL/min by the peristaltic pump to collect the REEs. REEs were dried and further purified by Eichrom RE Resin column chemistry. Nd fractions were extracted from REEs by Eichrom Ln Resin column chemistry (if the total amount of Nd > 5 ng) or alpha-hydroxyisobutyric acid (α-HIBA) column chemistry (if the total amount of Nd < 5 ng). For isotopic ratio measurements, Nd fractions from Ln Resin column chemistry were dried by evaporation and redissolved in 800 μL of 3% $HNO_3$.

Nd isotopic compositions (samples with 8-45 ng of Nd) were measured by a Thermo Scientific Neptune-Plus® multicollector-ICP-MS (MC-ICP-MS) at LDEO. The instrument was coupled with a desolvation introduction system (a Cetac Aridus® nebulizer). All measured Nd isotopic compositions were corrected for mass fractionation using an exponential law with $^{146}Nd/^{144}Nd = 0.7219$. Analyses of 15 ng JNdi-1 standards (~20 ppb solutions) yielded an average $^{143}Nd/^{144}Nd$ of 0.512082 ± 0.000011 (± 0.21 εNd units; 2σ, external reproducibility; n = 41). Analyses of 10 ng JNdi-1 standards (~15 ppb solutions) yielded an average $^{143}Nd/^{144}Nd$ of 0.512061 ± 0.000010 (± 0.20 εNd units; 2σ, external reproducibility; n = 56). For each analyzing session, standard JNdi-1 was measured between every sample. For each sample, the Nd isotopic composition is calculated as $^{143}Nd/^{144}Nd_{sample} = {}^{143}Nd/^{144}Nd_{sample\_measured} \times (^{143}Nd/^{144}Nd_{JNdi\_measured} / {}^{143}Nd/^{144}Nd_{JNdi\_recommended})$, where $^{143}Nd/^{144}Nd_{sample\_measured}$ is the average of the measured ratios for the sample, $^{143}Nd/^{144}Nd_{JNdi\_measured}$ is the average of JNdi-1 standards in that analyzing session, and $^{143}Nd/^{144}Nd_{JNdi\_recommended} = 0.512115$ (Tanaka et al., 2000) is the recommended value of JNdi-1 standard.

Eleven surface/shallow seawater samples with low Nd concentrations (total amount of Nd < 5 ng) were dried at 120 °C after α-HIBA column chemistry, redissolved in 150 μL of 50% aqua regia, and dried again at 120 °C. Then they were dissolved in 2 μL of 3 N $HNO_3$, loaded on rhenium filaments and measured on a VG-54 thermal ionization mass spectrometer (TIMS) at LDEO as $NdO^+$ using faraday cups and $10^{11}$ ohm resistors on the amplifiers. All measured Nd isotopic compositions were corrected for mass fractionation using an exponential law with $^{146}Nd/^{144}Nd = 0.7219$. For each

analyzing session, 4-5 JNdi-1 standards were measured to verify the stability of TIMS before 2-3 samples were measured. For each sample, the Nd isotopic composition is calculated as $^{143}Nd/^{144}Nd_{sample} = {}^{143}Nd/^{144}Nd_{sample\_measured} \times (^{143}Nd/^{144}Nd_{JNdi\_measured} / {}^{143}Nd/^{144}Nd_{JNdi\_recommended})$, where $^{143}Nd/^{144}Nd_{sample\_measured}$ is the average of the measured ratios for the sample, $^{143}Nd/^{144}Nd_{JNdi\_measured}$ is the average of JNdi-1 standards in that analyzing session, and $^{143}Nd/^{144}Nd_{JNdi\_recommended} = 0.512115$ (Tanaka et al., 2000) is the recommended value of JNdi-1 standard. These surface/shallow seawater samples often yielded 0.1-0.3 volts of signal on $^{144}Nd$. For each sample, 200 isotope ratios were measured. JNdi-1 standards were also measured when they yielded 0.1-0.3 volts of signal on $^{144}Nd$. 39 analyses of JNdi-1 standard yield $^{143}Nd/^{144}Nd = 0.512068 \pm 0.000016$ (± 0.31 εNd units; 2σ, external reproducibility).

### *4.3. Rare Earth Element Concentrations*

Aliquots of ~50 mL were taken from each sample for REE concentration analyses. About 10 mL of each filtered sample was weighed and 20-100 mg of a mixed REE spike in 1N $HNO_3$ was added. The spike was diluted (1:16152) from a mixed REE spike enriched in $^{142}Ce$, $^{145}Nd$, $^{149}Sm$ (samarium), $^{153}Eu$, $^{155}Gd$ (gadolinium), $^{161}Dy$ (dysprosium), $^{167}Er$ (erbium), and $^{171}Yb$ (ytterbium) (Table 1) made and calibrated by Professor Gilbert Hanson at The State University of New York at Stony Brook. The diluted spike was recalibrated against Nd standard (High Purity Standards) using reverse isotope dilution. The mixed sample-spike solutions were stored in acid-cleaned 30 mL HDPE bottles and left to sit for at least 24 hours for equilibration.

The REEs were preconcentrated using the ESI SC-DX seaFast®-pico system (purchased in June 2013) in offline mode (Behrens et al., 2016). The seaFast® system uses a chelating resin with ethylenediaminetriacetic acid and iminodiacetic acid functional groups to preconcentrate trace metals and remove anions and alkali and alkaline earth cations (http://www.icpms. com/pdf/seaFAST-seawater-analysis.pdf). This system consists of an autosampler, a preconcentration column (200 µL of chelating resin), a cleanup column (200 µL of chelating resin), triple 6-port valves, Teflon plumbing and sample loop reservoir, all-Teflon syringe pumps, ultra-low particulate air enclosure, and reservoirs of buffer solution, elution acid and high purity water (http://www.icpms.com/PDF/seaFAST-pico-open-ocean seawater.pdf). The solutions for the seaFast® system were prepared with high purity chemicals (Optima™ quality, Fisher Chemical) and high purity water (18.2 MΩ cm, from a MilliQ® ICP Advantage A10 System). The buffer solution (pH = 6.0 ± 0.2) was prepared using 834 mL of high purity water, 70 mL of 17.5 N high purity glacial acetic acid (Optima™ quality, Fisher Chemical), and 96 mL of high purity 11.4 N ammonium hydroxide (Optima™ quality, Fisher Chemical). The 1.6 N nitric acid ($HNO_3$) elution acid was made from double distilled concentrated nitric acid (Certified ACS Plus grade, Fisher Chemical). For each sample, the mixed sample-spike solution (~10 mL) was loaded into the sample loop and mixed with buffer solution to maintain a pH = 6. The mixing solution was pushed through the preconcentration column at a flow rate of 0.5 mL/min. Then the column was cleaned by passing buffer solution and high purity water to remove the seawater matrix. The REEs were then eluted into acid-cleaned 2 mL vials in three steps each of 100 µL of

1.6 N $HNO_3$ at an initial flow rate of 0.1 mL/min and a final flow rate of 0.5 mL/min. The offline mode of REE preconcentration for ~10 mL of seawater sample took ~15 minutes for each sample.

REE concentrations were measured on a VG PQ ExCell® quadrupole inductively coupled plasma-mass spectrometer (ICP-MS) at Lamont-Doherty Earth Observatory (LDEO) of Columbia University. The instrument was coupled to a desolvation introduction system (CETAC Aridus) that minimized molecular oxide ion formation with a self-aspirated Apex ST PFA micro flow nebulizer (Elemental Scientific ESI). The instrument was optimized for sensitivity and operated in pulse counting mode with 10 ms of dwell time for all isotopes. For each sample, 250 µL of 300 µL was used during 280 s of aspiration of sample for the analysis. Procedural blanks (n = 5) of 1% $HNO_3$ represent ≤ 0.9% of the sample intensities except for Ce (≤ 1.7%). To measure the total procedural blank, we processed 10 mL of ultrapure 1% $HNO_3$ through the seaFAST® the same way as the samples. At least 5 procedural blanks were processed during each seaFAST® session. Sample intensities were corrected by subtracting the procedural blank using $I_{meas} = I_{raw} - I_{procedural\_blk}$, where $I_{raw}$ is the raw intensity of the sample, $I_{procedural\_blk}$ is the intensity of the procedural blank and $I_{meas}$ is the intensity after procedural blank correction.

To correct for molecular oxide formation and interference at REE isotope masses, we did oxide calibration analysis by measuring masses of M and MO in pure, single element solutions of Ba and REE. This analysis was only needed once. The oxide

calibration value is expressed as the ratio of $\frac{^{MO}I_{cal}}{^{M}I_{cal}}$, where $^{M}I_{cal}$ is the intensity of mass M and $^{MO}I_{cal}$ is the intensity of mass MO measured during the calibration. For an unknown sample, the oxide interference for any mass M is calculated as $^{MO}I_{\text{int}} = \frac{^{MO}I_{cal}}{^{M}I_{cal}} \times {}^{M}I_{meas}$, where $^{M}I_{meas}$ is the measured intensity for any mass and $^{MO}I_{\text{int}}$ is the intensity of its oxide interference.

The oxide calibration values are not constant and need to be adjusted each time REEs are measured. However, the degrees to which the interfering elements form oxides are proportional to each other. Therefore, we analyzed $^{157}$PrO/$^{141}$Pr ratio of a 100 ng/L Pr solution during each session of REE measurement to get the correction factor $C = \frac{(\frac{^{157}\text{Pr}O}{^{141}\text{Pr}})_{today}}{(\frac{^{157}\text{Pr}O}{^{141}\text{Pr}})_{cal}}$, where $(\frac{^{157}\text{Pr}O}{^{141}\text{Pr}})_{cal}$ was measured during the oxide calibration analysis and $(\frac{^{157}\text{Pr}O}{^{141}\text{Pr}})_{today}$ was measured each time we analyzed REEs. Then the oxide interference is expressed as $^{MO}I_{\text{int}} = C \times \frac{^{MO}I_{cal}}{^{M}I_{cal}} \times {}^{M}I_{meas}$. The final true

intensity without oxide interference is calculated as

$$^{MO}I_{ox\_cor} = {}^{MO}I_{meas} - C \times \frac{^{MO}I_{cal}}{^{M}I_{cal}} \times {}^{M}I_{meas}$$ .

We used the exponential law $R_c = R_m * (\frac{m_i}{m_j})^{\beta}$ to correct for mass fractionation, where $R_c$ is the mass fractionation corrected isotope ratio in the sample, $R_m$ is the measured isotope ratio in the sample, $m_i$ is the atomic mass of the numerator spike isotope, usually the one enriched in the spike, *mj* is the atomic mass of reference isotope. To calculate $\beta$, we prepared a mass bias solution in which each REE has concentration of 100 ng/L and measured it during each REE measurement session. $\beta$ is expressed as $\beta = \frac{Ln(\frac{R_n}{R_{mb}})}{Ln(\frac{m_i}{m_j})}$, where $R_n$ is the ratio in natural samples, and $R_{mb}$ is the measured ratio in the mass bias solution.

The concentrations of spiked elements were calculated using isotope dilution equations. Taking Nd as an example, Nd concentration was calculated as $[Nd] = \frac{(\frac{^{143}Nd}{^{145}Nd})_{spk} - (\frac{^{143}Nd}{^{145}Nd})_{meas}}{(\frac{^{143}Nd}{^{145}Nd})_{meas} - (\frac{^{143}Nd}{^{145}Nd})_{nat}} * \frac{[^{145}Nd]_{spk}}{^{145Nd}Ab_{nat}} * \frac{m_{spk}}{m_{smpl}} * M_{Nd}$, where $(\frac{^{143}Nd}{^{145}Nd})_{spk}$ is the isotope ratio in the spike, $(\frac{^{143}Nd}{^{145}Nd})_{meas}$ is the isotope ratio in the measured sample-

spike mixture, $(\frac{^{143}Nd}{^{145}Nd})_{nat}$ is the natural isotope ratio, $[^{145}Nd]_{spk}$ is the concentration of $^{145}$Nd in the spike (mol/g), $^{145Nd}Ab_{nat}$ is the natural abundance of $^{145}$Nd, $m_{spk}$ and $m_{smpl}$ are spike and sample weights (g), and $M_{Nd}$ is the atomic mass of Nd (144.24 g/mol). Other elements calculated using the isotope dilution equation are Sm, Eu, Gd, Dy, Er, and Yb and henceforth will be called "ID elements".

Since $^{142}$Ce has an isobaric interference from Nd, $^{142}$Ce in the sample was calculated by subtracting interference of $^{142}$Nd from the sample and the spike using $^{142Ce}I_{smpl} = {}^{142Total}I_{smpl} - {}^{143Nd}I_{smpl} * (\frac{^{142}Nd}{^{143}Nd})_{nat} - {}^{143Nd}I_{spk} * (\frac{^{142}Nd}{^{143}Nd})_{spk}$, where $^{142Total}I_{smpl}$ is the intensity of mass 142 in the sample, $^{143Nd}I_{smpl}$ is the intensity of $^{143}$Nd in the sample, $(\frac{^{142}Nd}{^{143}Nd})_{nat}$ is the natural isotope ratio, $^{143Nd}I_{spk}$ is the intensity of $^{143}$Nd in the spike, and $(\frac{^{142}Nd}{^{143}Nd})_{spk}$ is the isotope ratio in the spike. Then the Ce concentration was calculated using the isotope dilution equation.

For mono-isotopic elements Pr, Tb, Ho and Tm, their concentrations were calculated by comparing their intensities to intensities of non-spike isotopes of ID elements. To calculate intensities of non-spike isotopes of ID elements, contributions from the spike need to be subtracted. Taking Nd as an example, the spike-free intensity for $^{143}$Nd was calculated as

$$^{143Nd}I_{spkfree} = {}^{143Nd}I_{total} - {}^{143Nd}I_{spk} = {}^{143Nd}I_{total} - \frac{(\frac{^{143}Nd}{^{145}Nd})_{nat} * {}^{145Nd}I_{total} - {}^{143Nd}I_{total}}{\frac{(\frac{^{143}Nd}{^{145}Nd})_{nat}}{(\frac{^{143}Nd}{^{145}Nd})_{spk}} - 1},$$

where $^{143Nd}I_{total}$ is the intensity of $^{143}$Nd in total, $^{143Nd}I_{spk}$ is the intensity of $^{143}$Nd in the spike, $^{145Nd}I_{total}$ is the intensity of $^{145}$Nd in total, $(\frac{^{143}Nd}{^{145}Nd})_{nat}$ is the natural isotope ratio, and $(\frac{^{143}Nd}{^{145}Nd})_{spk}$ is the isotope ratio in the spike. Then the relationship between ID element and mono-isotopic element was established by comparing their sensitivities in the mass bias standard solution. For Nd, the sensitivity of $^{143}$Nd was calculated as $^{143}Nd_{sens} = \frac{^{143Nd}I_{std}}{[Nd]_{std} * {}^{143Nd}Ab_{nat}}$, where $^{143Nd}I_{std}$ is the intensity of $^{143}$Nd in the standard solution, $[Nd]_{std}$ is the Nd concentration in the standard solution, and $^{143Nd}Ab_{nat}$ is the natural fractional abundance of $^{143}$Nd. For Pr, the sensitivity of $^{141}$Pr was calculated as $^{141}\mathrm{Pr}_{sens} = \frac{^{141\mathrm{Pr}}I_{std}}{[\mathrm{Pr}]_{std} * {}^{141\mathrm{Pr}}Ab_{nat}}$, where $^{141\mathrm{Pr}}I_{std}$ is the intensity of $^{141}$Pr in the standard solution, $[\mathrm{Pr}]_{std}$ is the Pr concentration in the standard solution, and

$^{141Pr}Ab_{nat}$ is the natural abundance of $^{141}$Pr (=1). Then the sensitivity ratio $\frac{^{143}Nd_{sens}}{^{141}\mathrm{Pr}_{sens}}$ in the standard solution was used to calculate the Pr concentration in the sample using $[\mathrm{Pr}]_{smpl} = \frac{^{143}Nd_{sens}}{^{141}\mathrm{Pr}_{sens}} * \frac{^{141Pr}I_{smpl}}{^{143Nd}I_{smpl\_spkfree}} * \frac{[Nd]_{smpl} * ^{143Nd}Ab_{nat}}{^{141Pr}Ab_{nat}}$, where $^{141Pr}I_{smpl}$ is the intensity of $^{141}$Pr in the sample, $^{143Nd}I_{smpl\_spkfree}$ is the spike-free intensity for $^{143}$Nd in the sample, $[Nd]_{smpl}$ is the Nd concentration in the sample, $^{143Nd}Ab_{nat}$ is the natural abundance of $^{143}$Nd, and $^{141Pr}Ab_{nat}$ is the natural abundance of $^{141}$Pr (=1).

For spiked elements La and Lu, their spike isotopes $^{138}$La and $^{176}$Lu have very low abundances in both the DKM spike and natural samples. Their spike isotope/non-spike isotope ratios ($^{138}$La/$^{139}$La and $^{176}$Lu/$^{175}$Lu, respectively) in the DKM spike and natural samples have very small differences, which is not ideal for using isotope dilution calculations. Therefore, La and Lu were treated as mono-isotopic elements and were calculated using equations for mono-isotopic elements.

To ensure the accuracy of our method, seawater samples from a GEOTRACES intercalibration station BATS in the North Atlantic (Bermuda Atlantic Time-series; 31.7°N, 64.1°W) at 20 m and 2000 m have been repeatedly analyzed. Our measured REE concentrations of BATS at 20 m (n = 16) and BATS at 2000 m (n = 14) are listed in Table 2. The long-term external reproducibilities (2σ RSD%) for BATS at 20 m are 3.5% for Nd, 3.4% for Yb, and an average of 5.6% (± 1.1%, 1 σ) for the other REEs. The long-

term external reproducibilities for BATS at 2000 m are 2.8% for Nd, 4.6% for Yb, and an average of 4.1% (± 1.3%, 1 σ) for the other REEs. The results for BATS at 2000 m measured in this study are compared with GEOTRACES intercalibration values (van de Flierdt et al., 2012) and they agree with each other very well (Table 2). We participated in an international intercomparison study of seawater REEs where four labs analyzed seawater from a GEOTRACES station SAFe in the North Pacific (Sampling and Analysis of Fe; 30°N, 140°W) at 3000 m (Behrens et al., 2016). Our analyzed REE concentrations of SAFe at 3000 m agree well with values from the other labs. The REE concentrations of SAFe at 3000 m from four labs show great agreement with < 7% reproducibility for all REEs (2σ SD), except for Ce (71%, 2σ SD), Gd (14%, 2σ SD) and Lu (12%, 2σ SD) (Behrens et al., 2016).

## 5. Results

### *5.1. REE patterns*

REE concentration results are presented in Table 3. The PAAS-normalized REE patterns of five stations show typical seawater characteristics: increasing REE concentrations with depth, enriched HREEs relative to LREEs, and depleted Ce compared to La and praseodymium (Pr) (Fig. 3). The PAAS-normalized REE patterns show that La is slightly enriched compared to other LREEs (Pr and Nd) and Gd is enriched compared to its neighbors Eu and terbium (Tb) (Fig. 3). The enrichments of La and Gd are explained by the preferential solution of REEs with empty (La), half-filled (Gd), and completely filled (Lu) 4f electron shells (e.g. (De Baar et al., 1991; Byrne and

Li, 1995)). For Northeast SO202-32, Eu enrichment is observed in the seawater from ~4500 m to the bottom (Fig. 3b).

To investigate the differences of REEs patterns of intermediate and deep water masses in different ocean basins, REEs patterns of the intermediate and deep water masses in the North Pacific are compared with that in the North Atlantic and Southern Ocean (Fig. 4). Here REE data for the North Pacific water are average values from this study. REE data for North Atlantic Deep Water (NADW) are based on published data in a GEOTRACES calibration station BATS (Bermuda Atlantic Time-series; 31.7°N, 64.1°W) in the North Atlantic ((Pahnke et al., 2012; van de Flierdt et al., 2012; Lambelet et al., 2016); GEOTRACES GA03 REE data). REE data for Upper Circumpolar Deep Water (UCDW), LCDW and Antarctic Bottom Water (AABW) are based on published data in their formation regions in the Southern Ocean ((Stichel et al., 2012a; Hathorne et al., 2015); GEOTRACES GA10 REE data). For Antarctic Intermediate Water (AAIW), REEs are bashed on data from the southernmost stations of GEOTRACES GA02 Leg 3 at ~50°S (Wu et al., this thesis). REE data of GEOTRACES GA03 and GEOTRACES GA10 are available in the GEOTRACES Intermediate Data Product 2017 (http://www.bodc.ac.uk/geotraces/data/idp2017/).

For the intermediate water, NPIW in the North Pacific shows higher REE concentrations than AAIW in the Southern Ocean (Fig. 4a). For the deep water, NPDW in the North Pacific has much higher REE concentrations than NADW in the North Atlantic and UCDW in the Southern Ocean (Fig. 4b). For the bottom water, LCDW in the North Pacific shows higher REE concentrations than LCDW and AABW in the Southern

Ocean (Fig. 4c). PAAS-normalized REE patterns show that deep water masses generally have higher REE abundances than intermediate water masses and REE abundances in the North Pacific are higher than that in the North Atlantic and Southern Ocean (Fig. 4a-c).

### *5.2. Nd isotopic compositions*

The εNd values of the five stations range from −4.8 to −1.5 (Fig. 5b,6a). From the surface to ~1000 m ($\gamma^n$ = 22.50-27.66 kg/m$^3$), seawater samples at Northwest station SO202-5 near the Aleutian-Kamchatka intersection have higher εNd values (−2.4 to −1.5) than that at corresponding neutral density layers of the other stations (−4.8 to −2.6) (Fig. 5a,6f). For Northeast station SO202-32 and near Japan stations SO202-44, 41, and 39, εNd-values generally increase with depth except for some changes at the subsurface (200-300 m) (Fig. 5a,6f). On the other hand, the εNd values of Northwest station SO202-5 show a seesaw pattern over this interval (Fig. 5a,6f). From ~1500 m to ~2500 m ($\gamma^n$ = 27.77-28.00 kg/m$^3$), εNd-values of the five stations start to converge (Fig. 5b,6b). From ~3500m to ~4500 m ($\gamma^n$ = 28.07-28.11 kg/m$^3$), Northeast station SO202-32 in the open North Pacific Ocean shows higher εNd (−3.5 to −3.2) than that in the other stations at corresponding neutral density layers (εNd = −3.9 to −3.6) (Fig. 5b,6b). Below 5000 m, each near Japan station SO202-44, 41, and 39 has one bottom sample, Northwest station SO202-5 does not have samples, and Northeast station SO202-32 has seven samples (Fig. 5b). The bottom seawater εNd of SO202-44 (εNd = −4.3) is lower than that in the other stations (εNd = −3.1 to −3.6) (Fig. 5b).

### *5.3. REE concentrations*

Nd concentrations ([Nd]) of the five stations range from 7.3 to 12.5 pmol/kg at the

surface (~10 m; $\gamma^n$ = 22.50-25.43 kg/m$^3$) and generally increase with increasing depth with some exceptions (Fig. 5e,5f,6e,6f). From ~100 m to ~3500 m ($\gamma^n$ = 25.73-27.66 kg/m$^3$), Nd concentrations at the five stations have similar values at the same neutral density (Fig. 5e,5f,6e,6f). Below ~4500 m ($\gamma^n$ > 28.10 kg/m$^3$), Northeast station SO202-32 shows higher Nd concentrations (53.8 to 63.7 pmol/kg) than that in near Japan stations SO202-44, 41, and 39 (34.8 to 43.5 pmol/kg) (Fig. 5f,6f). The only exception is that Northeast station SO202-32 at ~5228 m ($\gamma^n$ = 28.10 kg/m$^3$) has a low Nd concentration of 20.3 pmol/kg (Fig. 5f,6f).

Ce concentrations of five stations are enriched at the surface (~10 m; $\gamma^n$ = 22.50-25.43 kg/m$^3$) (Fig. 7a,7b,8a,8b). They decrease to minimum values of 2.7 to 3.1 pmol/kg between ~150 m and ~500 m ($\gamma^n$ = 26.55-27.05 kg/m$^3$) (Fig. 7a,7b,8a,8b). Then they increase to 3.9 to 6.0 pmol/kg between ~1000 m and ~1500 m ($\gamma^n$ = 27.58-27.84 kg/m$^3$) (Fig. 7a,7b,8a,8b). Below ~2000 m ($\gamma^n$ > 27.94 kg/m$^3$), Ce concentrations of five stations range from 2.6 to 4.8 pmol/kg (Fig. 7b,8a). The only exceptions are at Northeast station SO202-32, where Ce concentrations are higher, with 6.5 pmol/kg at 4484 m and 7.2 pmol/kg at 5161 m (Fig. 7b).

### *5.4. REE ratios*

The Ce anomaly (Ce/Ce$^*$) is defined here as $2\times \mathrm{Ce_n}/(\mathrm{La_n}+\mathrm{Pr_n})$, where $\mathrm{Ce_n}$, $\mathrm{La_n}$, and $\mathrm{Pr_n}$ are the PAAS-normalized Ce, La, and Pr concentrations of the samples. Low Ce/Ce$^*$ close to 0 indicates a strong negative Ce anomaly. Typical sweater depth profiles have high Ce/Ce$^*$ values in the shallow water before rapidly decreasing to values < 0.10 in deeper water. It is explained by rapid oxidation from soluble Ce(III) to insoluble

Ce(IV) and removal of Ce(IV) in the shallow water (e.g. (Moffett, 1990; Sholkovitz and Schneider, 1991; German et al., 1995)). Here $Ce/Ce^*$ ratios of the five stations range from 0.14 to 0.42 at the surface (~10 m; $\gamma^n$ = 22.50-25.43 kg/m$^3$). Then they rapidly decrease with depth to 0.06 to 0.10 at ~500 m ($\gamma^n$ = 26.94-27.39 kg/m$^3$) and remain < 0.10 at depths deeper than 500 m (Fig. 7c,7d,8c,8d). The only exception is at Northeast station SO202-32 where $Ce/Ce^*$ (= 0.22) at 5294 m is much higher (Fig. 7d).

$Yb_n/Nd_n$ ratios reflect the fractionation between HREEs and LREEs. Higher values indicate larger fractionations. $Yb_n/Nd_n$ ratios in typical seawater depth profiles are low at the surface. This is explained by lithogenic input to the surface seawater, where LREEs (e.g. Nd) are more preferentially released from REE dissolution compared to HREEs (e.g. Yb) (e.g. (Zhang and Nozaki, 1998)). Then $Yb_n/Nd_n$ ratios increase with increasing depth because (1) HREEs are more soluble than LREEs and (2) LREEs are more preferentially scavenged onto the particles than HREEs in seawater. $Yb_n/Nd_n$ ratios increase along water mass transport paths because of preferential removal of LREEs compared to HREEs. Here $Yb_n/Nd_n$ ratios of the five stations range from 3.3 to 4.2 at the surface (~10 m; $\gamma^n$ = 22.50-25.43 kg/m$^3$) (Fig. 9a,9b,10a,10b). From ~100 m to ~2500 m ($\gamma^n$ = 25.73-28.00 kg/m$^3$), $Yb_n/Nd_n$ ratios increase with depth to 4.8-5.7 (Fig. 9a,9b,10a,10b). From ~2500 m to the bottom ($\gamma^n$ > 28.00 kg/m$^3$), $Yb_n/Nd_n$ ratios decrease with depth to 3.1-4.2 (Fig. 9a,9b,10a,10b).

$La_n/Nd_n$ is calculated to evaluate the fractionation between La and Nd with higher $La_n/Nd_n$ values corresponding to stronger La enrichment. The seawater REE patterns show that La is slightly enriched compared to Nd (Fig. 3). This is explained by the

preferential solution of REEs with empty (La), half-filled (Gd), and completely filled (Lu) 4f electron shells (e.g. (De Baar et al., 1991; Byrne and Li, 1995)). Here $La_n/Nd_n$ ratios of the five stations range from 0.7 to 1.3 at the surface (~10 m; $\gamma^n$ = 22.50-25.43 kg/m$^3$) (Fig. 9c,10c). For near Japan stations SO202-44, 41, and 39, $La_n/Nd_n$ ratios increase with depth to 1.3-1.4 at ~1000 m ($\gamma^n$ = 27.56-27.60 kg/m$^3$) (Fig. 9d,10c). Then they decrease with depth to 1.1-1.2 below ~5000 m ($\gamma^n$ > 28.10 kg/m$^3$) (Fig. 9d,10d). For Northwest station SO202-5, $La_n/Nd_n$ ratios range from 1.2 to 1.5 in the upper 400 m ($\gamma^n$ < 27.32 kg/m$^3$) and decrease with depth from ~500 m to the bottom ($\gamma^n$ > 27.39 kg/m$^3$) (Fig. 9c,9d,10c,10d). For Northeast station SO202-32, $La_n/Nd_n$ ratios decrease to 1.1 at ~200 m ($\gamma^n$ = 26.69 kg/m$^3$), then increase to the maximum value of 1.4 at ~1500 m ($\gamma^n$ = 27.79 kg/m$^3$) before decreasing again to 1.0 at ~4500 m ($\gamma^n$ = 28.10 kg/m$^3$) (Fig. 9c,9d,10c,10d). Below ~5000 m ($\gamma^n$ > 28.10 kg/m$^3$), $La_n/Nd_n$ ratios of Northeast SO202-32 range from 0.8 to 1.3 (Fig. 9d,10d).

MREE/MREE$^*$ can be used to indicate anomalies of middle REEs (MREEs) (e.g. (Osborne et al., 2015; Osborne et al., 2017)). MREE/MREE$^*$ is calculated as $(Gd_n + Dy_n)/(Nd_n + Yb_n)$, where $Gd_n$, $Dy_n$, $Nd_n$, and $Yb_n$ are PAAS-normalized Gd, Dy, Nd, and Yb concentrations of the samples. High values indicate stronger MREE enrichments. Typical seawater profiles have higher values in the surface water, which is explained by lithogenic contributions enriched in MREEs to the surface water (e.g. (Osborne et al., 2015)). Then they decrease with depth and remain ~1.0 in deeper water due to less influence from lithogenic sources away from the surface. Here MREE/MREE$^*$ ratios vary from 1.0 to 1.2 in the surface water (~10 m; $\gamma^n$ = 22.50-25.43 kg/m$^3$) (Fig.

11a,11b,12a,12b). From ~100 m to ~2500 m ($\gamma^n$ = 25.73-28.00 kg/m$^3$), MREE/MREE$^*$ ratios decrease with depth to 0.7 to 0.8 (Fig. 11a,11b,12a,12b). From ~2500 m to the bottom ($\gamma^n$ > 28.00 kg/m$^3$), MREE/MREE$^*$ ratios slightly increase with depth to 0.9 to 1.0 (Fig. 11a,11b,12a,12b).

The Eu anomaly (Eu/Eu$^*$) is defined here as $2\times \mathrm{Eu_n}/(\mathrm{Sm_n}+\mathrm{Gd_n})$, where $\mathrm{Eu_n}$, $\mathrm{Sm_n}$, and $\mathrm{Gd_n}$ are the PAAS-normalized Eu, Sm, and Gd concentrations of the samples. Eu/Eu$^*$ ratios are usually ~1.0 in seawater. If the seawater is influenced by addition of external REEs from basaltic sources enriched in Eu, the positive Eu anomaly would be observed in the seawater (e.g. (Grenier et al., 2013)). Here most of the Eu/Eu$^*$ values of the five stations range from 0.88 to 1.03 throughout the depth profiles except for the positive Eu anomalies observed at the surface of Northwest station SO202-5 and the bottom of the Northeast station SO202-32 (Fig. 11c,11d,12c,12d).

## 6. Discussion

In the following discussion, we use neutral density as the main vertical parameter rather than depth because the same neutral density at different stations can be at very different depths especially for shallow and intermediate water. It gives us insights about differences of the shallow water at five stations. We first discuss the potential sources of REEs to the surface water (Section 6.1) and remineralization of REEs in the shallow depths (Section 6.2). Then we investigate conservative vs. non-conservative behavior of εNd and REEs in the intermediate and deep water (Section 6.3). Comparisons between εNd and REEs and water mass tracers (Section 6.3.2) as well as advective changes of

εNd and REEs along the water mass transport paths (Section 6.3.3) show water mass mixing between the depths of NPIW and NPDW and non-conservative behavior of the bottom water. We further discuss potential sources of REEs to the bottom water (Section 6.3.4).

***6.1. Source of REEs to the surface water***

The surface (~10 m) water of the five stations shows lower $Yb_n/Nd_n$ ratios compared to the subsurface (~100 m) water (Fig. 9a). This is consistent with observations of the surface seawater influenced by lithogenic input, where LREEs (e.g. Nd) are more preferentially released from REE dissolution compared to HREEs (e.g. Yb) (e.g. (Zhang and Nozaki, 1998)). The surface water of the five stations shows higher MREE/MREE$^*$ ratios compared to the subsurface water (Fig. 11a), consistent with observations of the surface seawater influenced by lithogenic sources enriched in MREEs (e.g. (Osborne et al., 2015)).

The potential lithogenic sources of REEs to the surface seawater are eolian sources of Asian dusts and volcanic ashes. Asian dusts are sourced from the continents and have low εNd (≈ −10; (Goldstein et al., 1984; Nakai et al., 1993; Jones et al., 1994)) compared to Pacific seawater, whereas the volcanic ashes originate from young volcanics with high εNd (e.g. Aleutian, Kamchatka and Kurile basalts, εNd ≈ +7.8 ± 1.3, 1σ, based on data of 786 volcanic rocks extracted from EarthChem: www.earthchem.org/portal). Therefore, the Nd isotopic composition can help distinguish the lithogenic contribution from the Asian dusts and volcanic ashes. The surface seawater at Northwest station SO202-5, which is the closest to the Aleutian-Kamchatka margin, show higher εNd (≈

−2.0) than the other stations (εNd = −4.0 to −4.8) (Fig. 5a), indicating higher contribution of volcanic ashes compared to the other stations.

REE ratios can also be used to distinguish the differences between the Asian dusts and volcanics in the North Pacific. Continental rocks are relatively enriched in LREEs with larger ionic radii compared to volcanic rocks. Therefore, volcanic rocks have higher $Yb_n/Nd_n$ ratios, and lower $La_n/Nd_n$ ratios compared to continental rocks. Surface continental rocks are depleted in Eu because crystal fractionation of plagioclase (enriched in Eu) in the deep crust causes depletions of Eu in shallow granitic magmas, and during crustal melting plagioclase holds on to Eu. As a result, Asian dusts sourced from the continents usually have lower $Eu/Eu^*$ values compared to volcanic rocks. For example, $Yb_n/Nd_n$, $La_n/Nd_n$ and $Eu/Eu^*$ ratios are 1.0-1.1 in Asian dusts (e.g. (Ferrat et al., 2011; Serno et al., 2014)), whereas Aleutian, Kamchatka and Kurile volcanics have $Yb_n/Nd_n$ of 2.0, $La_n/Nd_n$ of 0.6, and $Eu/Eu^*$ of 1.5 (e.g. (Churikova et al., 2001; Singer et al., 2007; Dreyer et al., 2010)). REEs of core-top sediments were analyzed as a geochemical tracer of eolian dusts to study eolian dust input to the subarctic North Pacific in the same locations where seawater were sampled during the INOPEX SO202 cruise (Serno et al., 2014). Core-top sediments at Northwest station SO202-5 show higher $Yb_n/Nd_n$ (1.84) and higher $Eu/Eu^*$ (1.20) compared to the other stations ($Yb_n/Nd_n$ = 1.04-1.58, $Eu/Eu^*$ = 1.09-1.15). $La_n/Nd_n$ (0.77) of core-top sediments at Northwest station SO202-5 is lower than the other stations (0.93-0.98) except for Northeast station SO202-32 (0.75). The surface water at Northwest station SO202-5 shows higher $Yb_n/Nd_n$ (4.02) and higher $Eu/Eu^*$ (1.20) compared to the other stations ($Yb_n/Nd_n$ = 3.31-3.63, $Eu/Eu^*$ = 0.96-1.09). This is

consistent with observations in the core-top sediments and indicates higher contribution of volcanic ashes at Northwest station SO202-5 than the other stations. However, the surface water at Northwest station SO202-5 does not show lower $La_n/Nd_n$ than the other stations. One explanation is the La enrichment in seawater due to the preferential solution of REEs with empty (La), half-filled (Gd), and completely filled (Lu) 4f electron shells (e.g. (De Baar et al., 1991; Byrne and Li, 1995)).

REE patterns can also help distinguish Asian dusts and volcanics in the North Pacific (Fig. 13a). Here the PAAS-normalized REE abundances of each sample are further normalized to the average of the PAAS-normalized REE abundances as $REE_{PAAS}$/(Average $REE_{PAAS}$). It is the PAAS-normalized abundance of a single REE divided by the average of PAAS-normalized abundances of all the REEs. For example, $Nd_{PAAS}$/(Average $REE_{PAAS}$) = $Nd_{PAAS}$/Average ($La_{PAAS}$, $Ce_{PAAS}$, …, $Yb_{PAAS}$, $Lu_{PAAS}$). This double-normalization helps us to compare REE patterns without the effect of variation in REE abundances in different samples. Compared to Asian dusts, North Pacific volcanics show depletion of LREEs, enrichment of HREEs and positive Eu anomaly. REE pattern of core-top sediments at Northwest station SO202-5 shows more similarity to North Pacific volcanics compared to the other stations (Fig. 13b). REE patterns of the surface seawater of five stations do not resemble that of core-top sediments. Instead, they are overprinted by the seawater signatures with negative Ce anomalies and much higher enrichment of HREEs compared to North Pacific volcanics (Fig. 13c).

Serno et al. (2014) also used $^{4}He$ and $^{232}Th$ as geochemical tracers of eolian

sources together with grain size distribution data of core-top sediments to investigate the spatial distribution of Asian dust input. Serno et al. (2014) report that the open ocean sites are dominantly composed of Asian dusts (80-100%), whereas near margin sites show increased contribution from terrigenous input with volcanic signatures and have < 50% of Asian dusts (Serno et al., 2014). In particular, Northwest station SO202-5 has a much lower Asian dust fraction (10-16%; (Serno et al., 2014)) compared to the other four seawater stations (44-100%; (Serno et al., 2014)). This is consistent with our observations in the surface water εNd and REE ratios where Northwest station SO202-5 closest to the Aleutian-Kamchatka margin has higher εNd, higher $Yb_n/Nd_n$, and higher $Eu/Eu^*$ than the other stations (Fig. 1,5a,9a,11c).

### *6.2. Remineralization of REEs in the shallow water*

At the neutral densities between 25.73 and 26.69 $kg/m^3$ (100-400 m, depending on location), seawater εNd shows remineralization of Asian dusts vs. remineralization of volcanic ashes from the Aleutian-Kamchatka margin. At Northwest station SO202-5 and near Japan stations SO202-44, 41 and 39, increasing εNd with depth indicates remineralization of volcanic ashes prevailing over that of Asian dusts (Section 6.2.1 and 6.2.3). At Northeast station SO202-32, decreasing εNd with depth reflects remineralization of Asian dusts prevailing over that of volcanic ashes over the same interval (Section 6.2.2). REE signatures (increasing Nd concentration, increasing $Yb_n/Nd_n$, and increasing $Eu/Eu^*$ with depth) at Northwest station SO202-5 also indicate remineralization of volcanic ashes prevailing over that of Asian dusts, consistent with increasing εNd with depth (Section 6.2.1). For the other stations, remineralization of

Asian dusts or volcanic ashes that changes εNd is not reflected in REE signatures (Section 6.2.2 and 6.2.3).

*6.2.1. Northwest station SO202-5*

At the neutral densities between 25.73 and 26.69 kg/m$^3$ (100-400 m, depending on location), εNd-values of Northwest station SO202-5 increase to the maximum value of −1.5 at $\gamma^n \approx 26.56$ kg/m$^3$ (~100 m) (Fig. 5a,6a). This station shows increasing Nd concentrations (Fig. 5e,6e), increasing $Yb_n/Nd_n$ ratios (Fig. 9a,10a), and increasing $Eu/Eu^*$ ratios (Fig. 11c,12c) with increasing depth. The above εNd and REE signatures likely reflect the remineralization of volcanic ashes from the Aleutian-Kamchatka margin prevailing over that of Asian dusts. If this is the case, $La_n/Nd_n$ ratios are expected to decrease with depth at this interval. However, we observe almost no change in $La_n/Nd_n$ ratios with increasing depth (Fig. 9c,10c).

Hayes et al. (2013) used thorium (Th) isotopes to quantify lithogenic inputs to the North Pacific Ocean in the same seawater samples which we analyzed for Nd isotopes and REE concentrations. They found a dissolved $^{232}$Th peak at the subsurface of Northwest station SO202-5 (~100 m; $\gamma^n \approx 26.56$ kg/m$^3$) (Fig. 5c,6c), which indicates regeneration of $^{232}$Th from lithogenic input (Hayes et al., 2013). This $^{232}$Th peak coincides with our observations of the maximum εNd and peaks of $Yb_n/Nd_n$ and $Eu/Eu^*$ at the subsurface of Northwest station SO202-5.

*6.2.2. Northeast station SO202-32*

εNd-values of Northeast station SO202-32 decrease from −4.0 at $\gamma^n \approx 26.22$ kg/m$^3$ (~100 m) to the minimum value of −4.5 at $\gamma^n \approx 26.69$ kg/m$^3$ (~200 m) (Fig. 5a,6a),

indicating remineralization of Asian dusts prevailing over that of volcanic ashes from the Aleutian-Kamchatka margin. If this is the case, we would expect decreasing $Yb_n/Nd_n$ ratios, increasing $La_n/Nd_n$ ratios, and decreasing $Eu/Eu^*$ ratios with increasing depth. However, we observe slightly increasing $Yb_n/Nd_n$ ratios (Fig. 9a,10a) and no changes in $La_n/Nd_n$ ratios (Fig. 9c,10c) and $Eu/Eu^*$ ratios (Fig. 11c,12c) with increasing depth. Therefore, remineralization of Asian dusts prevailing over that of volcanic ashes based on observation from εNd is not reflected in the REE signatures.

Hayes et al. (2013) also observed a dissolved $^{232}Th$ peak at the subsurface of Northeast station SO202-32 (~200 m; $\gamma^n \approx 26.69$ kg/m$^3$) (Fig. 5c,6c), coinciding with our observation of the minimum εNd (Fig. 5a,6a). Although Northwest station SO202-5 and Northeast station SO202-32 both show $^{232}Th$ peaks at the subsurface, εNd-values differentiate the main sources: lower values corresponding to remineralization of Asian dusts prevailing over that of volcanic ashes and vice versa. This is further confirmed by Asian dust fraction analysis of these two stations where Northwest station SO202-5 (10-16%) has lower Asian dust fraction than Northeast station SO202-32 (81-100%) (Serno et al., 2014).

*6.2.3. Near Japan stations SO202-44, 41 and 39*

At the neutral densities between 25.73 and 26.69 kg/m$^3$ (100-400 m, depending on location), near Japan stations SO202-44, 41 and 39 show increasing εNd-values with depth except that the easternmost SO202-39 shows the minimum value of −4.2 at $\gamma^n \approx$ 26.44 kg/m$^3$ (~300 m) (Fig. 5a,6a). The increasing εNd-values with depth indicate the remineralization of volcanic ashes from the Aleutian-Kamchatka margin prevailing over

that of Asian dusts. If this is the case, we would expect increasing $Yb_n/Nd_n$ ratios, decreasing $La_n/Nd_n$ ratios, and increasing $Eu/Eu^*$ ratios with increasing depth. However, they show no changes in $Yb_n/Nd_n$ ratios (Fig. 9a,10a) and increasing $La_n/Nd_n$ ratios (Fig. 9c,10c) with increasing depth. $Eu/Eu^*$ ratios do not show any trends with increasing depth (Fig. 11c,12c). Therefore, remineralization of volcanic ashes prevailing over that of Asian dusts based on observation from εNd is not reflected in the REE signatures.

Hayes et al. (2013) found subsurface maxima of dissolved $^{232}Th$ between 100 m and 200 m ($\gamma^n$ = 25.73-26.69 kg/m$^3$) (Fig. 5c,6c) indicating regeneration of dissolved $^{232}Th$ from lithogenic input over this interval. We do not observe any maximum or minimum values of εNd and REE ratios over this interval.

***6.3. Conservative vs. non-conservative behavior of εNd and REEs in the intermediate and deep water***

In this section, we first investigate potential effect of filtration on εNd and REE data of the intermediate and deep water in the North Pacific (Section 6.3.1). Then we define the water mass end-member compositions for NPIW, NPDW, and LCDW using World Ocean Atlas 2013 and εNd and REE data of filtered seawater (Section 6.3.2). The water mass mixing curves based on the defined end-member compositions are used to illustrate whether the intermediate and deep water samples show conservative water mass mixing (Section 6.3.2). We also discuss the advective changes of εNd and REE along the transport path of NPIW, NPDW, and LCDW (Section 6.3.3). Based on the observations of non-conservative behavior in the bottom water, we discuss the potential sources of REEs to the bottom water (Section 6.3.4).

*6.3.1. Comparison of εNd and REEs for the intermediate and deep water masses from SO202 stations with published data from nearby locations*

To investigate whether filtration has any impact on εNd and REEs of seawater samples in the North Pacific, we compare our εNd and REE data of filtered seawater samples for NPIW, NPDW and LCDW from SO202 stations with published data of filtered and unfiltered samples in the North Pacific (Supplementary Information Section 1). This section will only discuss comparison between our data with published data in locations close to our stations (Fig. 14a,15a,16a).

For NPIW, samples with the minimum salinity values (33.9-34.5) of each station are chosen for comparison (Fig. 14b). εNd-values of NPIW at our stations range from −3.2 to −2.6, consistent with published εNd-values of filtered samples (−3.4 to −3.2, symbols with marker lines in Fig. 14c) and higher than the published εNd-values of unfiltered samples (−5.3 to −3.5, symbols without marker lines in Fig. 14c) in nearby stations. Nd concentrations of NPIW at our stations range from 16.9 to 19.8 pmol/kg (Fig. 14d). The published stations with Nd concentrations available (14.4 to 18.7 pmol/kg, Fig.14d) are along the slopes of the Sagami and Nankai troughs near Japan, where slope sediments could influence the seawater REEs (Zhang and Nozaki, 1998; Alibo and Nozaki, 1999).

For NPDW, samples with salinity of 34.48-34.68 and potential temperature of 1.3-2.6 °C at each station are chosen for comparison (Fig. 15b). εNd-values of NPDW at our stations range from −3.1 to −2.2, consistent with published εNd-values of filtered samples (−3.2 to −2.1, symbols with marker lines in Fig. 15c) and higher than the

published εNd-values of unfiltered samples (−4.7 to −3.0, symbols without marker lines in Fig. 15c) in nearby stations. Nd concentrations of NPDW at our stations range from 24.6 to 31.7 pmol/kg, consistent with published Nd concentrations in most of the nearby stations (23.4 to 34.2 pmol/kg) except for station BO-1 ([Nd] = 36.6 to 45.2 pmol/kg between 2000 m and 3000 m) (Fig. 15d).

For LCDW, samples between 4000 m and 6000 m with the lowest potential temperature are chosen for comparison (Fig. 16b). εNd-values of LCDW at our stations range from −4.2 to −3.1, consistent with published εNd-values of filtered samples (−3.8 to −3.3, symbols with marker lines in Fig. 16c) and higher than the published εNd-values of unfiltered samples (−5.7 to −3.3, symbols without marker lines in Fig. 16c) in nearby stations. Nd concentrations of LCDW at our stations range from 34.8 to 63.7 pmol/kg, consistent with published Nd concentrations in nearby stations (42.5 to 62.8 pmol/kg) (Fig. 16d).

In general, εNd-values for NPIW, NPDW and LCDW observed in our stations are consistent with that of filtered samples and higher than that of unfiltered samples in nearby published stations. Most Nd concentrations for NPIW, NPDW and LCDW observed in our stations are consistent with published data of filtered and unfiltered seawater in nearby stations. εNd of unfiltered seawater is the mixture between seawater and particle εNd signals. Lower εNd-values of the unfiltered seawater compared to the filtered seawater indicate release of unradiogenic Nd from particle leaching. Nd concentrations of the unfiltered seawater are expected to show higher values compared to the filtered seawater due to particle leaching. However, filtered and unfiltered seawater

show similar Nd concentrations suggesting that particle leaching does not impact Nd concentrations significantly. Therefore, the Nd isotopes are impacted by particle-water exchange reactions rather than simple addition of Nd.

*6.3.2. Water mass mixing vs. lithogenic input in the intermediate and deep water*

To investigate whether εNd and REEs reflect water mass mixing in the intermediate and deep water, εNd, Nd concentration and REE ratios are compared with water mass tracer salinity (Fig. 17,18). Mixing curves of water mass end-members are used to show water mass mixing of NPIW-NPDW and NPDW-LCDW (Fig. 17,18). Smaller deviations from these mixing curves indicate smaller deviations from conservative mixing behavior. Mixing curves of water mass end-members require the definition of water mass end-member compositions for NPIW, NPDW, and LCDW. NPIW and NPDW are defined in their formation regions, which are close to our SO202 stations. Since LCDW is gradually modified along its pathway from the Southern Ocean, LCDW end-member in this study is defined in the region after it enters the North Pacific and before it reaches our SO202 stations. According to the hydrographic characteristics of NPIW, NPDW, and LCDW (Section 3), the water mass hydrographic properties are defined using World Ocean Atlas 2013 (Garcia et al., 2013; Locarnini et al., 2013a, b; Zweng et al., 2013). εNd and REE end-member values are defined from filtered seawater samples in this study and published data in the above defined regions for NPIW, NPDW, and LCDW. The water mass end-member compositions are listed in Table 4.

Between the depths of NPIW and NPDW, most of the samples fall within the mixing envelope of NPIW-NPDW in the diagram of εNd vs. salinity (Fig. 17a). Similar

to εNd, Nd concentration and REE ratios of most samples also fall within the mixing envelope of NPIW-NPDW when compared with salinity (Fig. 17c,18). These observations indicate very small deviations from conservative water mass mixing between the depths of NPIW and NPDW. εNd, Nd concentration and REE ratios covary with salinity and show NPIW-NPDW end-member mixing. While we use salinity, potential temperature could also be used to show the same correlations (Fig. S10,S11). εNd, Nd concentration and REE ratios also covary with potential temperature between the depths of NPIW and NPDW and show NPIW-NPDW end-member mixing (Fig. S10,S11). These are consistent with observations from dissolved $^{232}$Th over the same interval, where they do not change with salinity/potential temperature and indicate no addition of $^{232}$Th from lithogenic input (Fig. 17b,S10b).

Below the depths of NPDW, εNd-values of all samples fall outside of the mixing envelope of NPDW-LCDW and are higher than expected values based on water mass mixing of NPDW-LCDW in the diagram of εNd vs. salinity (Fig. 17a). This indicates addition of high εNd signal from volcanic sources to seawater below the depths of NPDW. Nd concentrations and $Yb_n/Nd_n$ ratios also show values outside of the mixing envelope of NPDW-LCDW below 2500 m ($S > 34.64$, $\theta < 1.52°C$) (Fig. 17c,18a). Nd concentrations are higher than the mixing envelope of NPDW-LCDW (Fig. 17c) indicating addition of external Nd. $Yb_n/Nd_n$ ratios are lower than the mixing envelope of NPDW-LCDW (Fig. 18a). They indicate addition of external lithogenic sources of REEs since LREEs are more preferentially released from lithogenic sources compared to HREEs resulting in lower $Yb_n/Nd_n$ ratios. Most of the Eu/Eu$^*$ values below the depth of

NPDW fall within the mixing envelope of NPDW-LCDW except that they are higher at Northeast station SO202-32 (Fig. 18d). When εNd, Nd concentration and REE ratios are compared with potential temperature, they also show values outside of the mixing envelope of NPDW-LCDW below the depths of NPDW (Fig. S10,S11). The above observations are consistent with evidence from dissolved $^{232}$Th below the depths of NPDW, where they increase with increasing salinity/decreasing potential temperature and indicate addition of $^{232}$Th from lithogenic input (Fig. 17b,S10b). The potential volcanic sources of REEs to the bottom water are discussed in Section 6.3.4.

*6.3.3. Advective changes of εNd and REEs in the intermediate and deep water*

To investigate how well εNd and REEs trace the intermediate and deep water masses along the transport paths, we discuss the advective changes of εNd and REEs along each water mass transport path (Supplementary Information Section 2). Along the transport paths of NPIW and NPDW, εNd of the filtered samples do not change much and indicate conservative behavior. Their $Yb_n/Nd_n$ ratios show increasing trends along the transport paths, consistent with typical $Yb_n/Nd_n$ evolution along water mass pathway since Nd is more preferentially scavenged onto particles compared to Yb. Their $Eu/Eu^*$ ratios do not increase along the transport paths indicating no addition of lithogenic input from volcanic sources along the water mass pathways of NPIW and NPDW. Along the transport path of LCDW, the increasing εNd-values, decreasing $Yb_n/Nd_n$ ratios, and increasing $Eu/Eu^*$ ratios of the filtered samples indicate addition of external REEs from volcanic sources along the transport path of LCDW.

Therefore, NPIW and NPDW of the filtered samples show conservative behavior of εNd and REEs along their transport paths, whereas εNd and REEs of the filtered samples for LCDW indicate addition of external REEs from volcanic sources along the transport path of LCDW. The potential volcanic sources of REEs to the bottom water are discussed in Section 6.3.4.

*6.3.4. Potential sources of REEs to the bottom water*

One potential source that could add external REEs to seawater and influence its εNd and REE signatures is the sediments along the volcanic continental margin. Seawater influenced by these marginal sediments are expected to show higher εNd, higher Nd concentration, lower $Yb_n/Nd_n$ values than values predicted by conservative water mass mixing. Near Japan station SO202-44 and Northwest station SO202-5 are close to the volcanic continental margin. εNd and REE signatures of the bottom water observed in these two stations, that is, higher εNd, higher Nd concentration, lower $Yb_n/Nd_n$ values compared to the mixing envelope of NPDW-LCDW (Fig. 17a,17c,18a), could be explained by addition of REEs with high εNd signal from the volcanic marginal sediments.

Another potential source that could impact the bottom water εNd is the deep sea sediments (e.g. (Haley et al., 2017)). The interaction between seafloor sediments and the bottom water could modify the seawater εNd signal. Near Japan station SO202-41 and 39 are further away from the volcanic continental margin compared to near Japan station SO202-44 and Northwest station SO202-5. However, their bottom water shows the same εNd and REE signatures as that of station SO202-44 and 5 near the continental margin. It

is reported that εNd of the silicate fraction of sediments on the seafloor near stations SO202-41 and 39 is +0.9 (Nakai et al., 1993) (Fig. 19). Therefore, external REEs with high εNd signature from the seafloor sediments could be added to the bottom water at station SO202-41 and 39 resulting in higher εNd, higher Nd concentration, lower $Yb_n/Nd_n$ values of the bottom water.

Northeast station SO202-32 is in the open ocean far away from the volcanic continental margin. εNd of the silicate fraction of sediments on the seafloor near station SO202-32 is −8.4 (Jones et al., 1994) (Fig. 19). If the seafloor sediments are the only source affecting the bottom water, εNd-values of the bottom water at Northeast station SO202-32 are expected to be lower than predicted values based on conservative water mass mixing. However, the bottom water at Northeast station SO202-32 shows the same εNd and REE signatures as that of the above stations, suggesting addition of external REEs from volcanic sources with high εNd. North of 40°N, the northward branch of LCDW moves along the volcanic Kuril-Kamchatka-Aleutian margin, turns southeastward at 50°N and 160°W, and then moves towards station SO202-32 (Fig. 19). Along this LCDW pathway, εNd and REE signatures of the bottom water influenced by the marginal sediments are preserved when LCDW reaches station SO202-32 and prevails over the influence from the seafloor sediments.

The resuspended particles in the nepheloid layer could also impact the bottom water εNd. Nepheloid layers near the seafloor sometimes have very high particle concentrations (100s-1000s μg/L; (Gardner et al., 2018)). Resuspended particles in the nepheloid layer could potentially add external Nd to the seawater and modified εNd

signal of the bottom water. However, the nepheloid layer at the five stations in this study are very thin (≤ 50 m) with extremely low particle concentrations (≤ 10 μg/L) (Gardner et al., 2018). Therefore, the nepheloid layer is ruled out to be the source of any changes in εNd and REE signatures of the bottom water.

## 7. Conclusions

This paper presents five vertical water column profiles of the seawater Nd isotopic compositions and REEs from the INOPEX SO202 cruise across the subarctic North Pacific Ocean. For the surface water (~10 m), Northwest station SO202-5 (closest to the Aleutian-Kamchatka volcanic margin) shows the highest εNd, highest $Yb_n/Nd_n$, and highest $Eu/Eu^*$ compared to near Japan stations SO202-44, 41, and 39 and open ocean Northeast station SO202-32, indicating higher contribution of external REEs from volcanic ashes compared to the other stations. In the shallow water (100-400 m, depending on location), increasing εNd with depth at Northwest station SO202-5 and near Japan stations SO202-44, 41, and 39 indicates remineralization of REEs from volcanic ashes prevailing over Asian dusts, whereas decreasing εNd with depth at Northeast station SO202-32 indicates remineralization of REEs from Asian dusts prevailing over volcanic ashes. Based on the comparisons of εNd and REEs with water mass tracers, εNd and REEs of seawater between the depths of NPIW and NPDW show conservative water mass mixing of NPIW-NPDW. εNd and REEs also behave conservatively along the water mass transport paths of NPIW and NPDW. Below the depths of NPDW, addition of external REEs is observed when εNd and REEs are

compared with water mass tracers as well as along the transport path of LCDW. The potential sources of external REEs to the bottom water are (1) sediments on the Kuril-Kamchatka-Aleutian volcanic margin along the LCDW transport path, and (2) sediments on the seafloor, both of which could interact with seawater and modify the seawater εNd and REE signatures.

**Acknowledgements**

We thank the German Ministry of Education and Research (BmBF) for supporting the INOPEX SO202 cruise.

**References**

Abouchami, W., Goldstein, S., Gazer, S., Eisenhauer, A. and Mangini, A. (1997) Secular changes of lead and neodymium in central Pacific seawater recorded by a Fe-Mn crust. Geochimica et Cosmochimica Acta 61, 3957-3974.

Alibo, D.S. and Nozaki, Y. (1999) Rare earth elements in seawater: particle association, shale-normalization, and Ce oxidation. Geochimica et Cosmochimica Acta 63, 363-372.

Amakawa, H., Nozaki, Y., Alibo, D.S., Zhang, J., Fukugawa, K. and Nagai, H. (2004) Neodymium isotopic variations in Northwest Pacific waters1. Geochimica et Cosmochimica Acta 68, 715-727.

Amakawa, H., Sasaki, K. and Ebihara, M. (2009) Nd isotopic composition in the central North Pacific. Geochimica et Cosmochimica Acta 73, 4705-4719.

Behrens, M.K., Muratli, J., Pradoux, C., Wu, Y., Böning, P., Brumsack, H.-J., Goldstein, S.L., Haley, B., Jeandel, C. and Paffrath, R. (2016) Rapid and precise analysis of rare earth elements in small volumes of seawater-Method and intercomparison. Marine Chemistry 186, 110-120.

Bertram, C. and Elderfield, H. (1993) The geochemical balance of the rare earth elements and neodymium isotopes in the oceans. Geochimica et Cosmochimica Acta 57, 1957-1986.

Bory, A.-M., Biscaye, P.E., Svensson, A. and Grousset, F.E. (2002) Seasonal variability in the origin of recent atmospheric mineral dust at NorthGRIP, Greenland. Earth and Planetary Science Letters 196, 123-134.

Broecker, W.S., Blanton, S., Smethie, W.M. and Ostlund, G. (1991) Radiocarbon decay and oxygen utilization in the Deep Atlantic Ocean. Global Biogeochemical Cycles 5, 87-117.

Byrne, R.H. (2002) Inorganic speciation of dissolved elements in seawater: the influence of pH on concentration ratios. Geochemical Transactions 3, 11.

Byrne, R.H. and Kim, K.-H. (1990) Rare earth element scavenging in seawater. Geochimica et Cosmochimica Acta 54, 2645-2656.

Byrne, R.H. and Li, B. (1995) Comparative complexation behavior of the rare earths. Geochimica et Cosmochimica Acta 59, 4575-4589.

Churikova, T., Dorendorf, F. and Wörner, G. (2001) Sources and fluids in the mantle wedge below Kamchatka, evidence from across-arc geochemical variation. Journal of Petrology 42, 1567-1593.

De Baar, H., Schijf, J. and Byrne, R. (1991) Solution chemistry of the rare earth elements in seawater. European Journal of Solid State Inorganic Chemistry 28.

De Baar, H.J.W., Bacon, M.P., Brewer, P.G. and Bruland, K.W. (1985) Rare earth elements in the Pacific and Atlantic Oceans. Geochimica et Cosmochimica Acta 49, 1943-1959.

Dreyer, B.á., Morris, J. and Gill, J. (2010) Incorporation of subducted slab-derived sediment and fluid in arc magmas: B–Be–10Be–εNd systematics of the Kurile convergent margin, Russia. Journal of Petrology 51, 1761-1782.

Eguchi, K., Uno, I., Yumimoto, K., Takemura, T., Shimizu, A., Sugimoto, N. and Liu, Z. (2009) Trans-pacific dust transport: integrated analysis of NASA/CALIPSO and a global aerosol transport model. Atmospheric Chemistry and Physics 9, 3137-3145.

Elderfield, H., Whitfield, M., Burton, J., Bacon, M. and Liss, P. (1988) The oceanic chemistry of the rare-earth elements [and discussion]. Philosophical Transactions of the Royal Society of London A: Mathematical, Physical and Engineering Sciences 325, 105-126.

Ferrat, M., Weiss, D.J., Strekopytov, S., Dong, S., Chen, H., Najorka, J., Sun, Y., Gupta, S., Tada, R. and Sinha, R. (2011) Improved provenance tracing of Asian dust sources using rare earth elements and selected trace elements for palaeomonsoon studies on the eastern Tibetan Plateau. Geochimica et Cosmochimica Acta 75, 6374-6399.

Frank, M. (2002) Radiogenic isotopes: tracers of past ocean circulation and erosional input. Reviews of geophysics 40.

Garcia, H.E., Locarnini, R.A., Boyer, T.P., Antonov, J.I., Baranova, O.K., Zweng, M.M., Reagan, J.R. and Johnson, D.R. (2013) World Ocean Atlas 2013, Volume 4: Dissolved Inorganic Nutrients (phosphate, nitrate, silicate). NOAA Atlas NESDIS 76, 25.

Gardner, W.D., Richardson, M.J. and Mishonov, A.V. (2018) Global assessment of benthic nepheloid layers and linkage with upper ocean dynamics. Earth and Planetary Science Letters 482, 126-134.

GEOROC (2007) GEOROC, Geochemistry of rocks of the oceans and continents, database. Max-Planck-Institut für Chemie.

German, C., Masuzawa, T., Greaves, M., Elderfield, H. and Edmond, J. (1995) Dissolved rare earth elements in the Southern Ocean: Cerium oxidation and the influence of hydrography. Geochimica et Cosmochimica Acta 59, 1551-1558.

Goldstein, S., O'nions, R. and Hamilton, P. (1984) A Sm-Nd isotopic study of atmospheric dusts and particulates from major river systems. Earth and Planetary Science Letters 70, 221-236.

Goldstein, S.L. and Hemming, S.R. (2003) Long-lived isotopic tracers in oceanography, paleoceanography, and ice-sheet dynamics. Treatise on geochemistry 6, 453-489.

Grenier, M., Jeandel, C., Lacan, F., Vance, D., Venchiarutti, C., Cros, A. and Cravatte, S. (2013) From the subtropics to the central equatorial Pacific Ocean: Neodymium isotopic composition and rare earth element concentration variations. Journal of Geophysical Research: Oceans 118, 592-618.

Haley, B.A., Du, J., Abbott, A.N. and McManus, J. (2017) The Impact of Benthic Processes on Rare Earth Element and Neodymium Isotope Distributions in the Oceans. Frontiers in Marine Science 4, 426.

Haley, B.A., Frank, M., Hathorne, E. and Pisias, N. (2014) Biogeochemical implications from dissolved rare earth element and Nd isotope distributions in the Gulf of Alaska. Geochimica et Cosmochimica Acta 126, 455-474.

Hanawa, K. and Talley, L.D. (2001) Mode waters. International Geophysics Series 77, 373-386.

Harrison, P.J., Whitney, F.A., Tsuda, A., Saito, H. and Tadokoro, K. (2004) Nutrient and plankton dynamics in the NE and NW gyres of the subarctic Pacific Ocean. Journal of Oceanography 60, 93-117.

Hathorne, E.C., Stichel, T., Brück, B. and Frank, M. (2015) Rare earth element distribution in the Atlantic sector of the Southern Ocean: the balance between particle scavenging and vertical supply. Marine Chemistry 177, 157-171.

Hayes, C.T., Anderson, R.F., Fleisher, M.Q., Serno, S., Winckler, G. and Gersonde, R. (2013) Quantifying lithogenic inputs to the North Pacific Ocean using the long-lived thorium isotopes. Earth and Planetary Science Letters 383, 16-25.

Hu, R., Chen, T. and Ling, H. (2012) Late Cenozoic history of deep water circulation in the western North Pacific: Evidence from Nd isotopes of ferromanganese crusts. Chinese science bulletin 57, 4077-4086.

Husar, R.B., Tratt, D., Schichtel, B.A., Falke, S., Li, F., Jaffe, D., Gasso, S., Gill, T., Laulainen, N.S. and Lu, F. (2001) Asian dust events of April 1998. Journal of Geophysical Research: Atmospheres 106, 18317-18330.

Jacobsen, S.B. and Wasserburg, G. (1980) Sm-Nd isotopic evolution of chondrites. Earth and Planetary Science Letters 50, 139-155.

Jeandel, C. (1993) Concentration and isotopic composition of Nd in the South Atlantic Ocean. Earth and Planetary Science Letters 117, 581-591.

Jeandel, C., Bishop, J. and Zindler, A. (1995) Exchange of neodymium and its isotopes between seawater and small and large particles in the Sargasso Sea. Geochimica et Cosmochimica Acta 59, 535-547.

Jeandel, C., Thouron, D. and Fieux, M. (1998) Concentrations and isotopic compositions of neodymium in the eastern Indian Ocean and Indonesian straits. Geochimica et Cosmochimica Acta 62, 2597-2607.

Jones, C.E., Halliday, A.N., Rea, D.K. and Owen, R.M. (1994) Neodymium isotopic variations in North Pacific modern silicate sediment and the insignificance of detrital REE contributions to seawater. Earth and Planetary Science Letters 127, 55-66.

Jones, K.M., Khatiwala, S.P., Goldstein, S.L., Hemming, S.R. and van de Flierdt, T. (2008) Modeling the distribution of Nd isotopes in the oceans using an ocean general circulation model. Earth and Planetary Science Letters 272, 610-619.

Kawabe, M. and Fujio, S. (2010) Pacific Ocean circulation based on observation. Journal of oceanography 66, 389-403.

Lacan, F. and Jeandel, C. (2004) Denmark Strait water circulation traced by heterogeneity in neodymium isotopic compositions. Deep Sea Research Part I: Oceanographic Research Papers 51, 71-82.

Lambelet, M., van de Flierdt, T., Crocket, K., Rehkämper, M., Kreissig, K., Coles, B., Rijkenberg, M.J., Gerringa, L.J., de Baar, H.J. and Steinfeldt, R. (2016) Neodymium isotopic composition and concentration in the western North Atlantic Ocean: Results from the GEOTRACES GA02 section. Geochimica et Cosmochimica Acta 177, 1-29.

Lee, J.H. and Byrne, R.H. (1993) Complexation of trivalent rare earth elements (Ce, Eu, Gd, Tb, Yb) by carbonate ions. Geochimica et Cosmochimica Acta 57, 295-302.

Lehnert, K., Su, Y., Langmuir, C., Sarbas, B. and Nohl, U. (2000) A global geochemical database structure for rocks. Geochemistry, Geophysics, Geosystems 1.

Ling, H., Burton, K., O'nions, R., Kamber, B., Von Blanckenburg, F., Gibb, A. and Hein, J. (1997) Evolution of Nd and Pb isotopes in Central Pacific seawater from ferromanganese crusts. Earth and Planetary Science Letters 146, 1-12.

Ling, H.-F., Jiang, S.-Y., Frank, M., Zhou, H.-Y., Zhou, F., Lu, Z.-L., Chen, X.-M., Jiang, Y.-H. and Ge, C.-D. (2005) Differing controls over the Cenozoic Pb and Nd isotope evolution of deepwater in the central North Pacific Ocean. Earth and Planetary Science Letters 232, 345-361.

Locarnini, R.A., Mishonov, A.V., Antonov, J.I., Boyer, T.P., Garcia, H.E., Baranova, O.K., Zweng, M.M., Paver, C.R., Reagan, J.R., Johnson, D.R., Hamilton, M. and Seidov, D. (2013a) World Ocean Atlas 2013, Volume 1: Temperature.

Locarnini, R.A., Mishonov, A.V., Antonov, J.I., Boyer, T.P., Garcia, H.E., Baranova, O.K., Zweng, M.M., Paver, C.R., Reagan, J.R., Johnson, D.R., Hamilton, M. and Seidov, D. (2013b) World Ocean Atlas 2013, Volume 1: Temperature. NOAA Atlas NESDIS 73, 40.

Luo, Y.-R. and Byrne, R.H. (2004) Carbonate complexation of yttrium and the rare earth elements in natural waters. Geochimica et Cosmochimica Acta 68, 691-699.

Macdonald, A.M., Mecking, S., Robbins, P., Toole, J., Johnson, G.C., Talley, L., Cook, M. and Wijffels, S. (2009) The WOCE-era 3-D Pacific Ocean circulation and heat budget. Progress in Oceanography 82, 281-325.

Moffett, J.W. (1990) Microbially mediated cerium oxidation in sea water. Nature 345, 421.

Molina-Kescher, M., Frank, M. and Hathorne, E. (2014) South Pacific dissolved Nd isotope compositions and rare earth element distributions: water mass mixing versus biogeochemical cycling. Geochimica et Cosmochimica Acta 127, 171-189.

Nagashima, K., Tada, R., Matsui, H., Irino, T., Tani, A. and Toyoda, S. (2007) Orbital- and millennial-scale variations in Asian dust transport path to the Japan Sea. Palaeogeography, Palaeoclimatology, Palaeoecology 247, 144-161.

Nagashima, K., Tada, R., Tani, A., Sun, Y., Isozaki, Y., Toyoda, S. and Hasegawa, H. (2011) Millennial-scale oscillations of the westerly jet path during the last glacial period. Journal of Asian Earth Sciences 40, 1214-1220.

Nakai, S.i., Halliday, A.N. and Rea, D.K. (1993) Provenance of dust in the Pacific Ocean. Earth and Planetary Science Letters 119, 143-157.

Orsi, A., Johnson, G. and Bullister, J. (1999) Circulation, mixing, and production of Antarctic Bottom Water. Progress in Oceanography 43, 55-109.

Orsi, A.H., Whitworth, T. and Nowlin, W.D. (1995) On the meridional extent and fronts of the Antarctic Circumpolar Current. Deep Sea Research Part I: Oceanographic Research Papers 42, 641-673.

Osborne, A.H., Haley, B.A., Hathorne, E.C., Plancherel, Y. and Frank, M. (2015) Rare earth element distribution in Caribbean seawater: Continental inputs versus lateral transport of distinct REE compositions in subsurface water masses. Marine Chemistry 177, 172-183.

Osborne, A.H., Hathorne, E.C., Schijf, J., Plancherel, Y., Böning, P. and Frank, M. (2017) The potential of sedimentary foraminiferal rare earth element patterns to trace water masses in the past. Geochemistry, Geophysics, Geosystems 18, 1550-1568.

Pahnke, K., Van de Flierdt, T., Jones, K.M., Lambelet, M., Hemming, S.R. and Goldstein, S.L. (2012) GEOTRACES intercalibration of neodymium isotopes and rare earth element concentrations in seawater and suspended particles. Part 2: Systematic tests and baseline profiles. Limnology and Oceanography: Methods 10, 252-269.

Piepgras, D. and Wasserburg, G. (1987) Rare earth element transport in the western North Atlantic inferred from Nd isotopic observations. Geochimica et Cosmochimica Acta 51, 1257-1271.

Piepgras, D.J. and Jacobsen, S.B. (1988) The isotopic composition of neodymium in the North Pacific. Geochimica et Cosmochimica Acta 52, 1373-1381.

Piepgras, D.J. and Jacobsen, S.B. (1992) The behavior of rare earth elements in seawater: Precise determination of variations in the North Pacific water column. Geochimica et Cosmochimica Acta 56, 1851-1862.

Piepgras, D.J. and Wasserburg, G. (1980) Neodymium isotopic variations in seawater. Earth and Planetary Science Letters 50, 128-138.

Qiu, B. (2001) Kuroshio and Oyashio currents. Academic Press.

Rempfer, J., Stocker, T.F., Joos, F., Dutay, J.-C. and Siddall, M. (2011) Modelling Nd-isotopes with a coarse resolution ocean circulation model: Sensitivities to model parameters and source/sink distributions. Geochimica et Cosmochimica Acta 75, 5927-5950.

Schlitzer, R. (2012) Ocean data view.

Serno, S., Winckler, G., Anderson, R.F., Hayes, C.T., McGee, D., Machalett, B., Ren, H., Straub, S.M., Gersonde, R. and Haug, G.H. (2014) Eolian dust input to the Subarctic North Pacific. Earth and Planetary Science Letters 387, 252-263.

Shabani, M.B., Akagi, T. and Masuda, A. (1992) Preconcentration of trace rare-earth elements in seawater by complexation with bis (2-ethylhexyl) hydrogen phosphate and 2-ethylhexyl dihydrogen phosphate adsorbed on a C18 cartridge and determination by inductively coupled plasma mass spectrometry. Analytical Chemistry 64, 737-743.

Shimizu, H., Tachikawa, K., Masuda, A. and Nozaki, Y. (1994) Cerium and neodymium isotope ratios and REE patterns in seawater from the North Pacific Ocean. Geochimica et Cosmochimica Acta 58, 323-333.

Sholkovitz, E. and Schneider, D. (1991) Cerium redox cycles and rare earth elements in the Sargasso Sea. Geochimica et Cosmochimica Acta 55, 2737-2743.

Singer, B.S., Jicha, B.R., Leeman, W.P., Rogers, N.W., Thirlwall, M.F., Ryan, J. and Nicolaysen, K.E. (2007) Along‐strike trace element and isotopic variation in Aleutian Island arc basalt: Subduction melts sediments and dehydrates serpentine. Journal of Geophysical Research: Solid Earth 112.

Stichel, T., Frank, M., Rickli, J. and Haley, B.A. (2012a) The hafnium and neodymium isotope composition of seawater in the Atlantic sector of the Southern Ocean. Earth and Planetary Science Letters 317, 282-294.

Stichel, T., Frank, M., Rickli, J., Hathorne, E.C., Haley, B.A., Jeandel, C. and Pradoux, C. (2012b) Sources and input mechanisms of hafnium and neodymium in surface waters of the Atlantic sector of the Southern Ocean. Geochimica et Cosmochimica Acta 94, 22-37.

Sun, J., Zhang, M. and Liu, T. (2001) Spatial and temporal characteristics of dust storms in China and its surrounding regions, 1960–1999: Relations to source area and climate. Journal of Geophysical Research: Atmospheres 106, 10325-10333.

Talley, L.D. (1993) Distribution and formation of North Pacific intermediate water. Journal of Physical Oceanography 23, 517-537.

Talley, L.D. (2011) Descriptive physical oceanography: an introduction. Academic press.

Tanaka, T., Togashi, S., Kamioka, H., Amakawa, H., Kagami, H., Hamamoto, T., Yuhara, M., Orihashi, Y., Yoneda, S., Shimizu, H., Kunimaru, T., Takahashi, K., Yanagi, T., Nakano, T., Fujimaki, H., Shinjo, R., Asahara, Y., Tanimizu, M. and Dragusanu, C. (2000) JNdi-1: a neodymium isotopic reference in consistency with LaJolla neodymium. Chemical Geology 168, 279-281.

Taylor, S.R. and McLennan, S.M. (1985) The continental crust: its composition and evolution. Blackwell Scientific Pub.,Palo Alto, CA, United States.

Uno, I., Eguchi, K., Yumimoto, K., Liu, Z., Hara, Y., Sugimoto, N., Shimizu, A. and Takemura, T. (2011) Large Asian dust layers continuously reached North America in April 2010. Atmospheric Chemistry and Physics 11, 7333.

van de Flierdt, T., Griffiths, A.M., Lambelet, M., Little, S.H., Stichel, T. and Wilson, D.J. (2016) Neodymium in the oceans: a global database, a regional comparison and implications for palaeoceanographic research. Phil. Trans. R. Soc. A 374, 20150293.

van de Flierdt, T., Pahnke, K., Amakawa, H., Andersson, P., Basak, C., Coles, B., Colin, C., Crocket, K., Frank, M., Frank, N., Goldstein, S.L., Goswami, V., Haley, B.A., Hathorne, E.C., Hemming, S.R., Henderson, G.M., Jeandel, C., Jones, K., Kreissig, K., Lacan, F., Lambelet, M., Martin, E.E., Newkirk, D.R., Obata, H., Pena, L., Piotrowski, A.M., Pradoux, C., Scher, H.D., Schöberg, H., Singh, S.K., Stichel, T., Tazoe, H., Vance, D. and Yang, J. (2012) GEOTRACES intercalibration of neodymium isotopes and rare earth element concentrations in seawater and suspended particles. Part 1: reproducibility of results for the international intercomparison. Limnology and Oceanography: Methods 10, 234-251.

von Blanckenburg, F. (1999) Tracing past ocean circulation? Science 286, 1862-1863.

Whitworth, T., Orsi, A., Kim, S.J., Nowlin, W. and Locarnini, R. (1998) Water masses and mixing near the Antarctic Slope Front. Ocean, ice, and atmosphere: interactions at the Antarctic continental margin, 1-27.

Yasuda, I. (2004) North Pacific intermediate water: Progress in SAGE (subarctic gyre experiment) and related projects. Journal of oceanography 60, 385-395.

You, Y. (2003) The pathway and circulation of North Pacific intermediate water. Geophysical Research Letters 30.

Yumimoto, K., Eguchi, K., Uno, I., Takemura, T., Liu, Z., Shimizu, A. and Sugimoto, N. (2009) An elevated large-scale dust veil from the Taklimakan Desert: Intercontinental transport and three-dimensional structure as captured by CALIPSO and regional and global models. Atmospheric Chemistry and Physics 9, 8545-8558.

Zhang, J. and Nozaki, Y. (1998) Behavior of rare earth elements in seawater at the ocean margin: a study along the slopes of the Sagami and Nankai troughs near Japan. Geochimica et Cosmochimica Acta 62, 1307-1317.

Zhao, T., Gong, S., Zhang, X., Blanchet, J.-P., McKendry, I. and Zhou, Z. (2006) A simulated climatology of Asian dust aerosol and its trans-Pacific transport. Part I: Mean climate and validation. Journal of Climate 19, 88-103.

Zheng, X.-Y., Plancherel, Y., Saito, M.A., Scott, P.M. and Henderson, G.M. (2016) Rare earth elements (REEs) in the tropical South Atlantic and quantitative deconvolution of their non-conservative behavior. Geochimica et Cosmochimica Acta 177, 217-237.

Zimmermann, B., Porcelli, D., Frank, M., Rickli, J., Lee, D.-C. and Halliday, A.N. (2009) The hafnium isotope composition of Pacific Ocean water. Geochimica et Cosmochimica Acta 73, 91-101.

Zweng, M.M., Reagan, J.R., Antonov, J.I., Locarnini, R.A., Mishonov, A.V., Boyer, T.P., Garcia, H.E., Baranova, O.K., Johnson, D.R., Seidov, D. and Biddle, M.M. (2013) World Ocean Atlas 2013, Volume 2: Salinity.

Figure 1. Map of the five sampling locations from the SO202 cruise in the North Pacific Ocean. (a) Surface currents in the North Pacific Ocean (after (Qiu, 2001; Harrison et al., 2004)). (b) Transport paths of intermediate and deep water in the North Pacific Ocean (after (Kawabe and Fujio, 2010)). The map was made using ODV software (Schlitzer, 2012). KC: Kuroshio Current; KE: Kuroshio Extension; NPC: North Pacific Current; OC: Oyashio Current; SAF: Subarctic Front; AS: Alaska Stream; EKC: East Kamchatka Current; WSG: West Subarctic Gyre; AG: Alaska Gyre; NPIW: North Pacific Intermediate Water; NPDW: North Pacific Deep Water; LCDW: Lower Circumpolar Deep Water.

Figure 2. Diagrams of hydrographic properties for the five SO202 stations. (a) Potential temperature vs. salinity. (b) is the enlargement of panel (a). (c) Depth vs. salinity. (d) Depth vs. potential temperature.

Figure 3. PAAS-normalized REE patterns of the five SO202 stations. (a) Station SO202-5. (b) Station SO202-32. (c) Station SO202-39. (d) Station SO202-41. (e) Station SO202-44. They show typical seawater characteristics: increasing REE concentrations with depth, enriched HREEs relative to LREEs, and depleted Ce compared to its neighbors.

Figure 4. REE patterns of intermediate and deep water in the North Atlantic (blue), Southern Ocean (green), and North Pacific (red). (a) Intermediate water (square). (b) Deep water (circle). (c) Bottom water: LCDW (triangle) and AABW (diamond). REE patterns show that deep water masses generally have higher REE abundances than intermediate water masses and REE abundances in the North Pacific are higher than that in the North Atlantic and Southern Ocean.

Figure 5. Depth profiles of Nd isotopic composition (εNd), dissolved $^{232}$Th concentration, and Nd concentration ([Nd]) for the five SO202 stations. (a) Depth vs. εNd (0-600 m). (b) Depth vs. εNd (0-6000 m). (c) Depth vs. $^{232}$Th (0-600 m). (d) Depth vs. $^{232}$Th (0-6000 m). (e) Depth vs. [Nd] (0-600 m). (f) Depth vs. [Nd] (0-6000 m).

Figure 6. Neutral density ($\gamma^n$) profiles of εNd, dissolved $^{232}$Th concentration, and [Nd] for the five SO202 stations. (d) $\gamma^n$ vs. εNd ($\gamma^n$ = 22.0-28.5 kg/m$^3$). (f) $\gamma^n$ vs. εNd ($\gamma^n$ = 27.75-28.15 kg/m$^3$). (g) $\gamma^n$ vs. $^{232}$Th ($\gamma^n$ = 22.0-28.5 kg/m$^3$). (i) $\gamma^n$ vs. $^{232}$Th ($\gamma^n$ = 27.75-28.15 kg/m$^3$). (a) $\gamma^n$ vs. [Nd] ($\gamma^n$ = 22.0-28.5 kg/m$^3$). (c) $\gamma^n$ vs. [Nd] ($\gamma^n$ = 27.75-28.15 kg/m$^3$).

Figure 7. Depth profiles of Ce concentration ([Ce]), Ce anomaly (Ce/Ce$^*$) and oxygen concentration for the five SO202 stations. (a) Depth vs. [Ce] (0-600 m). (b) Depth vs. [Ce] (0-6000 m). (c) Depth vs. Ce/Ce$^*$ (0-600 m). (d) Depth vs. Ce/Ce$^*$ (0-6000 m). (e) Depth vs. oxygen (0-600 m). (f) Depth vs. oxygen (0-6000 m).

Figure 8. Neutral density profiles of [Ce], Ce/Ce$^*$ and oxygen concentration for the five SO202 stations. (a) $\gamma^n$ vs. [Ce] ($\gamma^n$ = 22.0-28.5 kg/m$^3$). (b) $\gamma^n$ vs. [Ce] ($\gamma^n$ = 27.75-28.15 kg/m$^3$). (c) $\gamma^n$ vs. Ce/Ce$^*$ ($\gamma^n$ = 22.0-28.5 kg/m$^3$). (d) $\gamma^n$ vs. Ce/Ce$^*$ ($\gamma^n$ = 27.75-28.15

kg/m$^3$). (e) $\gamma^n$ vs. oxygen ($\gamma^n$ = 22.0-28.5 kg/m$^3$). (f) $\gamma^n$ vs. oxygen ($\gamma^n$ = 27.75-28.15 kg/m$^3$).

Figure 9. Depth profiles of $Yb_n/Nd_n$ and $La_n/Nd_n$ for the five SO202 stations. (a) Depth vs. $Yb_n/Nd_n$ (0-600 m). (b) Depth vs. $Yb_n/Nd_n$ (0-6000 m). (c) Depth vs. $La_n/Nd_n$ (0-600 m). (d) Depth vs. $La_n/Nd_n$ (0-6000 m).

Figure 10. Neutral density profiles of $Yb_n/Nd_n$ and $La_n/Nd_n$ for the five SO202 stations. (a) $\gamma^n$ vs. $Yb_n/Nd_n$ ($\gamma^n$ = 22.0-28.5 kg/m$^3$). (b) $\gamma^n$ vs. $Yb_n/Nd_n$ ($\gamma^n$ = 27.75-28.15 kg/m$^3$). (c) $\gamma^n$ vs. $La_n/Nd_n$ ($\gamma^n$ = 22.0-28.5 kg/m$^3$). (d) $\gamma^n$ vs. $La_n/Nd_n$ ($\gamma^n$ = 27.75-28.15 kg/m$^3$).

Figure 11. Depth profiles of MREE/MREE$^*$ and Eu/Eu$^*$ for the five SO202 stations. (a) Depth vs. MREE/MREE$^*$ (0-600 m). (b) Depth vs. MREE/MREE$^*$ (0-6000 m). (c) Depth vs. Eu/Eu$^*$ (0-600 m). (d) Depth vs. Eu/Eu$^*$ (0-6000 m).

Figure 12. Neutral density profiles of MREE/MREE$^*$ and Eu/Eu$^*$ for the five SO202 stations. (a) $\gamma^n$ vs. MREE/MREE$^*$ ($\gamma^n$ = 22.0-28.5 kg/m$^3$). (b) $\gamma^n$ vs. MREE/MREE$^*$ ($\gamma^n$ = 27.75-28.15 kg/m$^3$). (c) $\gamma^n$ vs. Eu/Eu$^*$ ($\gamma^n$ = 22.0-28.5 kg/m$^3$). (d) $\gamma^n$ vs. Eu/Eu$^*$ ($\gamma^n$ = 27.75-28.15 kg/m$^3$).

Figure 13. Double-normalized REE patterns of sources of Asian dusts transported over Asia and the Pacific Ocean (a), volcanic ashes (a), core-top sediments of the five SO202 stations (b), and surface water of the five SO202 stations (c). (a) REE values of sources of Asian dusts are average REE concentrations of sediments (< 16 μm) from Taklamakan desert and Tengger desert (Ferrat et al., 2011; Serno et al., 2014). The Taklimakan desert and Tengger desert are sources for long-range eolian dust transport over Asia and the Pacific Ocean (e.g. (Husar et al., 2001; Sun et al., 2001; Bory et al., 2002; Zhao et al., 2006; Nagashima et al., 2007; Eguchi et al., 2009; Yumimoto et al., 2009; Nagashima et al., 2011; Uno et al., 2011)). Ferrat et al. (2011) reported that there are significant differences in REE compositions between the coarse and fine fractions of the surface sands from the Taklimakan desert and Tengger desert. The < 4 μm fraction best represents the bulk REE geochemistry of the samples and REE concentrations in the < 4 μm fraction and 4-16 μm fraction are almost identical (Ferrat et al., 2011). Therefore, fractions < 16 μm are used to represent the sources of dusts transported over Asia and the Pacific Ocean. REE values of North Pacific volcanics are average REE concentrations of Aleutian, Kamchatka and Kurile basalts (Churikova et al., 2001; Singer et al., 2007; Dreyer et al., 2010). Compared to sources of Asian dusts, North Pacific volcanics are relatively depleted in LREEs and enriched in Eu. (b) REE pattern of the core-top sediments at Northwest station SO202-5 shows more depletion in LREEs and more enrichment of HREEs compared to the other stations. Therefore, Northwest station SO202-5 shows more similarity to North Pacific volcanics compared to the other stations. (c) REE patterns of the surface seawater of the five stations do not resemble that of core-top sediments and are overprinted by seawater signatures: (1) the negative Ce anomalies, and (2) much higher enrichments in HREEs (Er to Lu: 1.48-1.93) compared to core-top

sediments (Er to Lu: 0.91-1.24) because in seawater HREEs are more soluble than LREEs and LREEs are more preferentially scavenged than HREEs.

Figure 14. Comparison of εNd and REEs from the five SO202 stations with published data from nearby stations for NPIW. (a) Map of stations with NPIW εNd and REE data. SO202 stations are in red. The other stations are from (Amakawa et al., 2004) (dark blue), (Amakawa et al., 2009) (light blue), (Zimmermann et al., 2009) (yellow), (Zhang and Nozaki, 1998) (light green), (Alibo and Nozaki, 1999) (brown). The NPIW pathways are shown in white. The map was made using ODV software (Schlitzer, 2012). (b) Potential temperature vs. salinity. The filtered samples are shown with marker lines and the unfiltered samples are shown without marker lines. Data points with solid color are NPIW samples of each station. Data points with transparent color are the remaining samples of that station. (c) Depth vs. εNd. (d) Depth vs. [Nd].

Figure 15. Comparison of εNd and REEs from the five SO202 stations with published data from nearby stations for NPDW. (a) Map of stations with NPDW εNd and REE data. SO202 stations are in red. The other stations are from (Piepgras and Jacobsen, 1988, 1992) (dark green), (Amakawa et al., 2004) (dark blue), (Shimizu et al., 1994) (light grey), (Amakawa et al., 2009) (light blue), (Zimmermann et al., 2009) (yellow), (Haley et al., 2014) (white). The NPDW pathways are shown in white. The map was made using ODV software (Schlitzer, 2012). (b) Potential temperature vs. salinity. The filtered samples are shown with marker lines and the unfiltered samples are shown without marker lines. Data points with solid color are NPDW samples of each station. Data points with transparent color are the remaining samples of that station. (c) Depth vs. εNd. (d) Depth vs. [Nd].

Figure 16. Comparison of εNd and REEs from the five SO202 stations with published data from nearby stations for LCDW. (a) Map of stations with LCDW εNd and REE data. SO202 stations are in red. The other stations are from (Piepgras and Jacobsen, 1988, 1992) (dark green), (Amakawa et al., 2004) (dark blue), (Shimizu et al., 1994) (light grey), (Amakawa et al., 2009) (light blue), (Zimmermann et al., 2009) (yellow), (Haley et al., 2014) (white). The LCDW pathways are shown in white. The map was made using ODV software (Schlitzer, 2012). (b) Potential temperature vs. salinity. The filtered samples are shown with marker lines and the unfiltered samples are shown without marker lines. Data points with solid color are LCDW samples of each station. Data points with transparent color are the remaining samples of that station. (c) Depth vs. εNd. (d) Depth vs. [Nd].

Figure 17. Comparison of εNd, dissolved $^{232}$Th and Nd concentration with salinity below the depths of NPIW. (a) εNd vs. salinity. (b) $^{232}$Th vs. salinity. (c) [Nd] vs. salinity. Between the depths of NPIW and NPDW, they generally show water mass mixing of NPIW-NPDW. Below the depths of NPDW, they show addition of external Nd with high εNd signal.

Figure 18. Comparison of REE ratios with salinity below the depths of NPIW. (a) $Yb_n/Nd_n$ vs. salinity. (b) $La_n/Nd_n$ vs. salinity. (c) MREE/MREE$^*$ vs. salinity. (d) Eu/Eu$^*$ vs. salinity. Between the depths of NPIW and NPDW, they generally show water mass mixing of NPIW-NPDW. Below the depths of NPDW, they show addition of external REEs.

Figure 19. Map of εNd of marine sediments in the North Pacific Ocean. εNd-values of marine sediments are from geochemical data EarthChem (http://www.earthchem.org).

Figure 1. Map of the five sampling locations from the SO202 cruise in the North Pacific Ocean

a

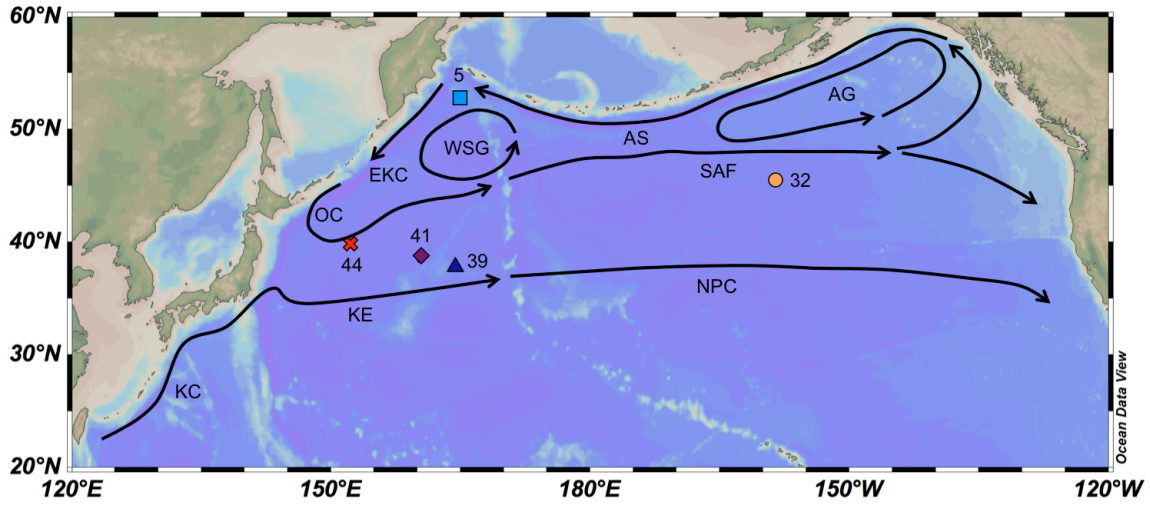


b

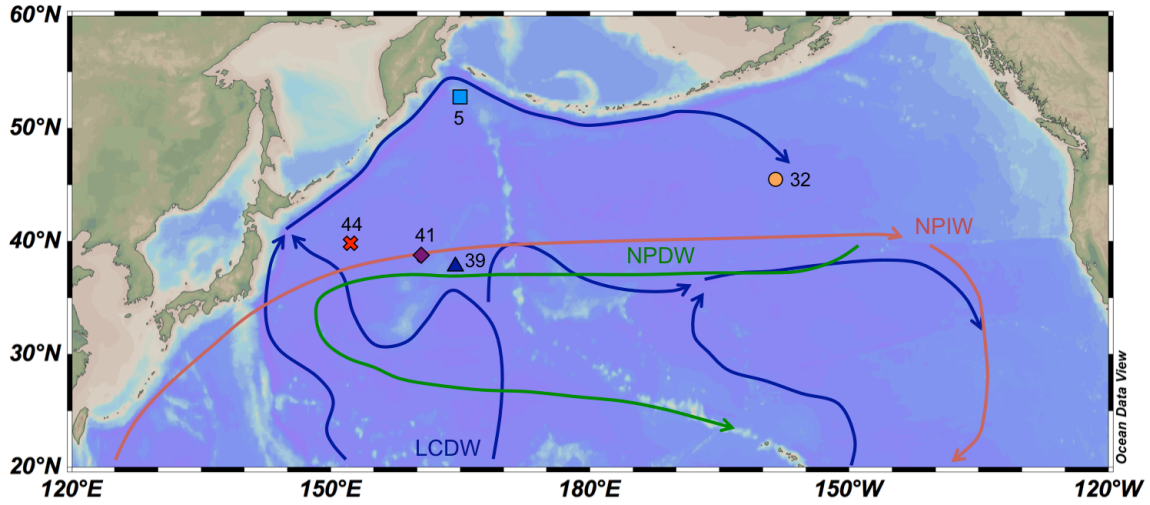

Figure 2. Diagrams of hydrographic properties for SO202 stations

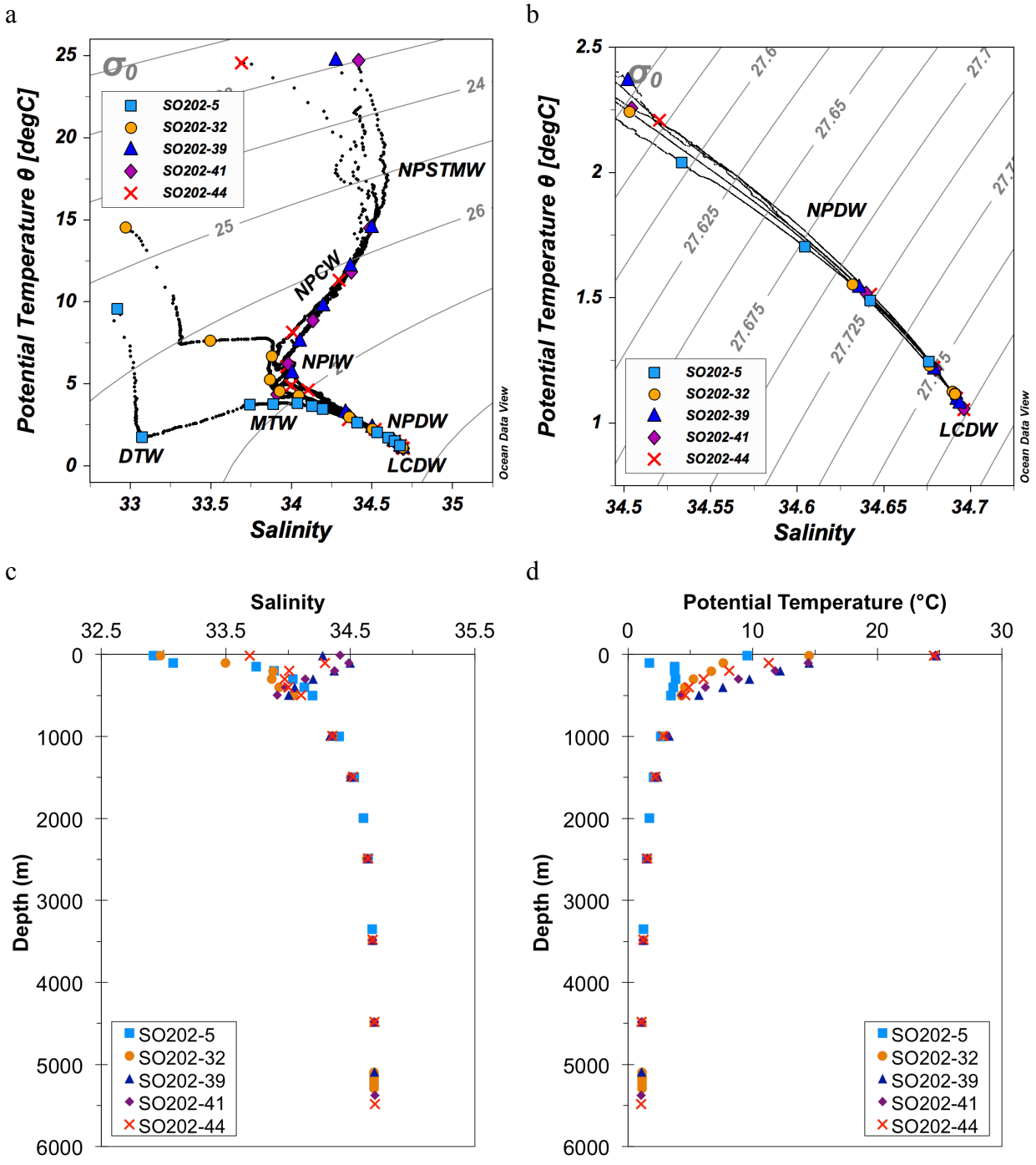

Figure 3. PAAS-normalized REE patterns of SO202 stations

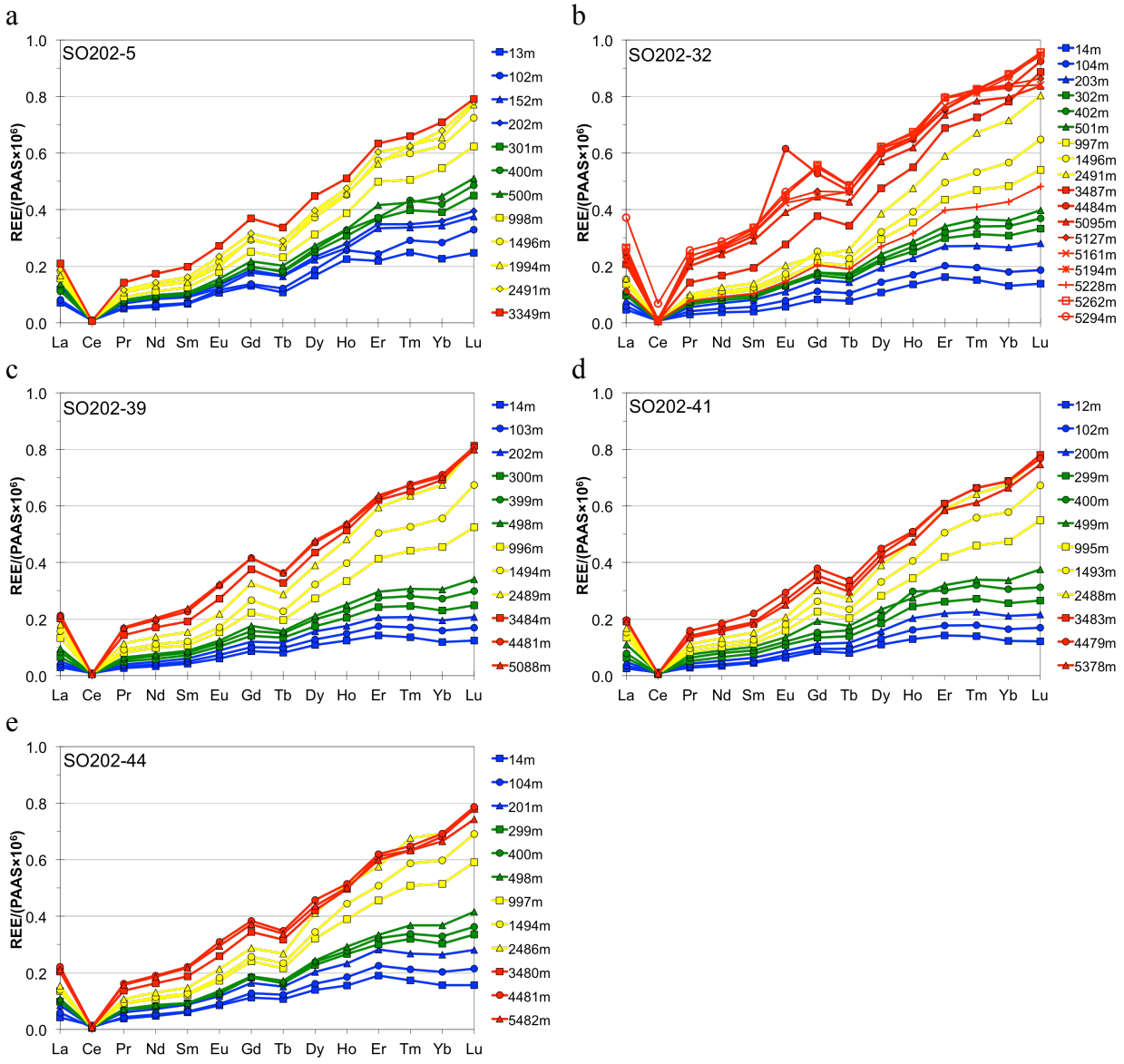

Figure 4. REE patterns of intermediate and deep water in the North Atlantic, Southern Ocean, and North Pacific

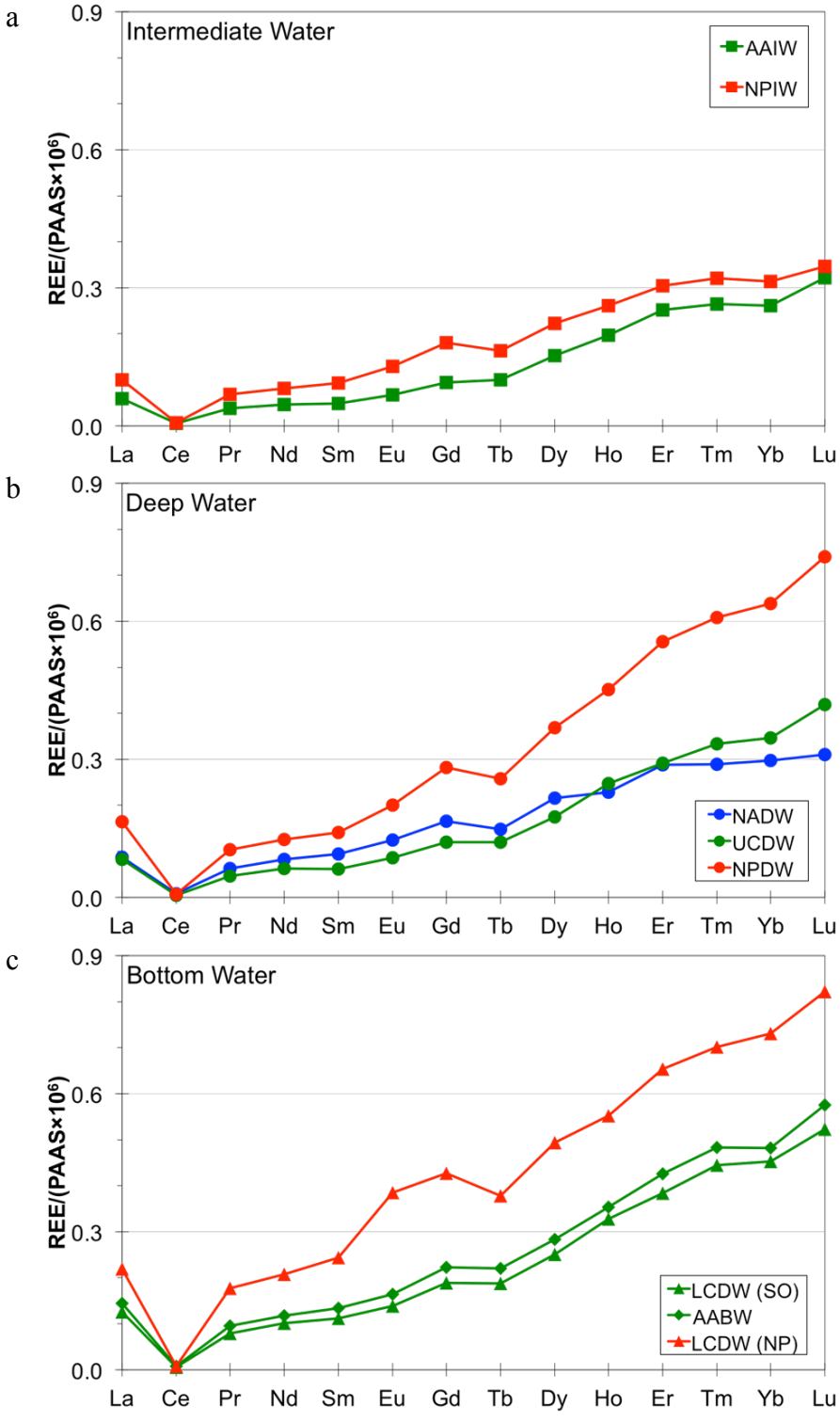

Figure 5. Depth profiles of εNd, dissolved $^{232}$Th concentration, and [Nd] for SO202 stations

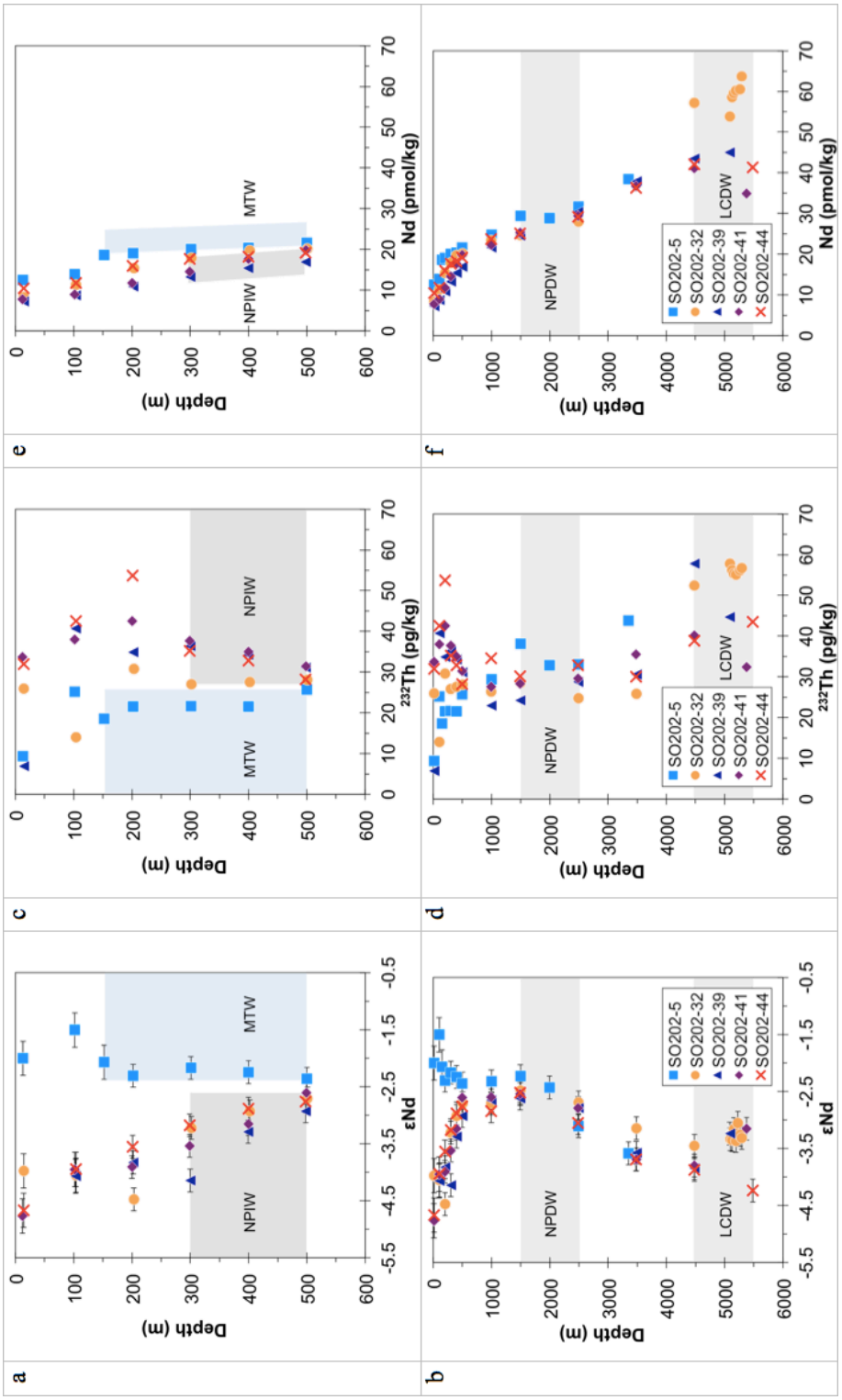

Figure 6. Neutral density profiles of εNd, dissolved $^{232}$Th concentration, and [Nd] for SO202 stations

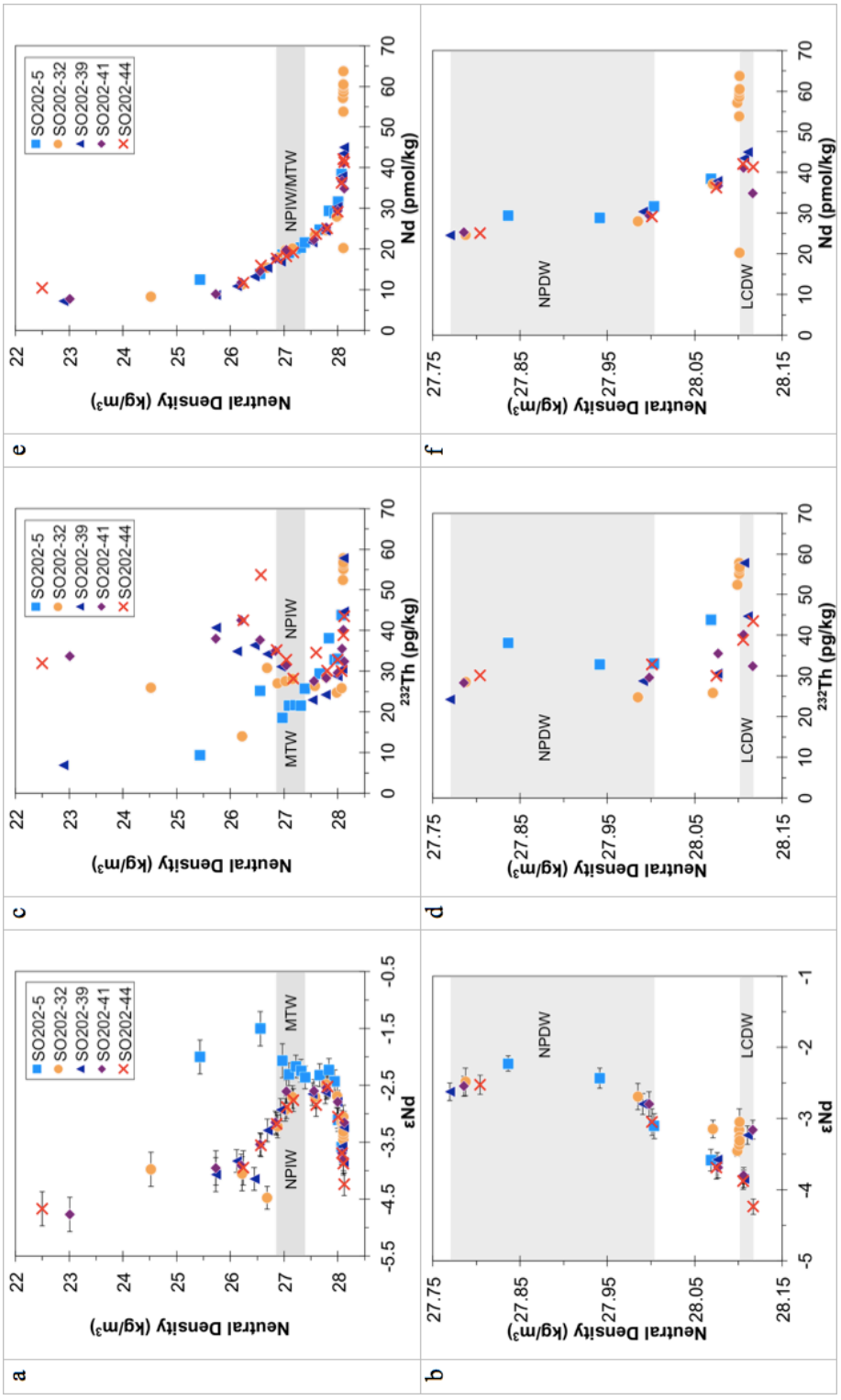

Figure 7. Depth profiles of [Ce], Ce anomaly and [Oxygen] for SO202 stations

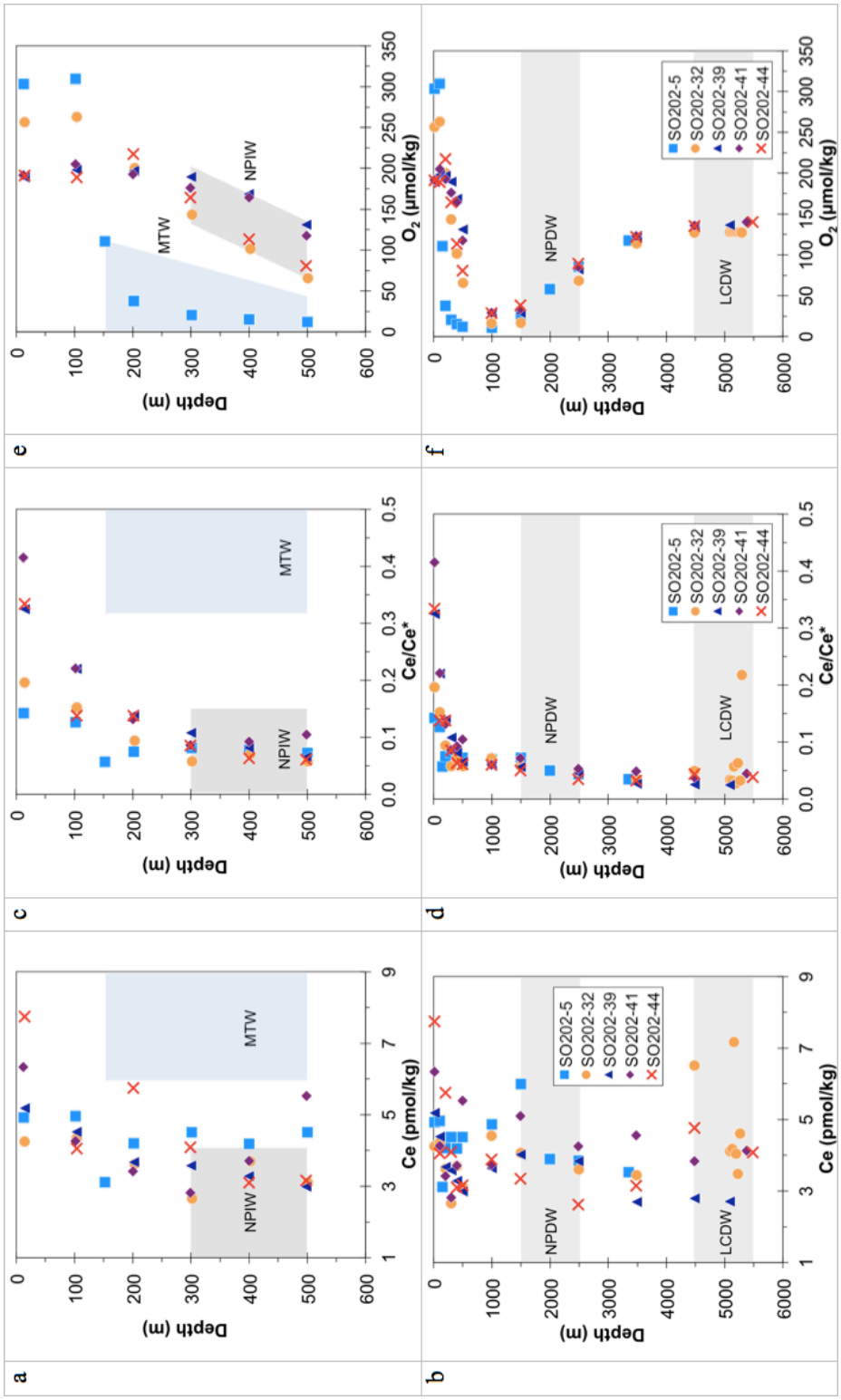

Figure 8. Neutral density profiles of [Ce], Ce anomaly and [Oxygen] for SO202 stations

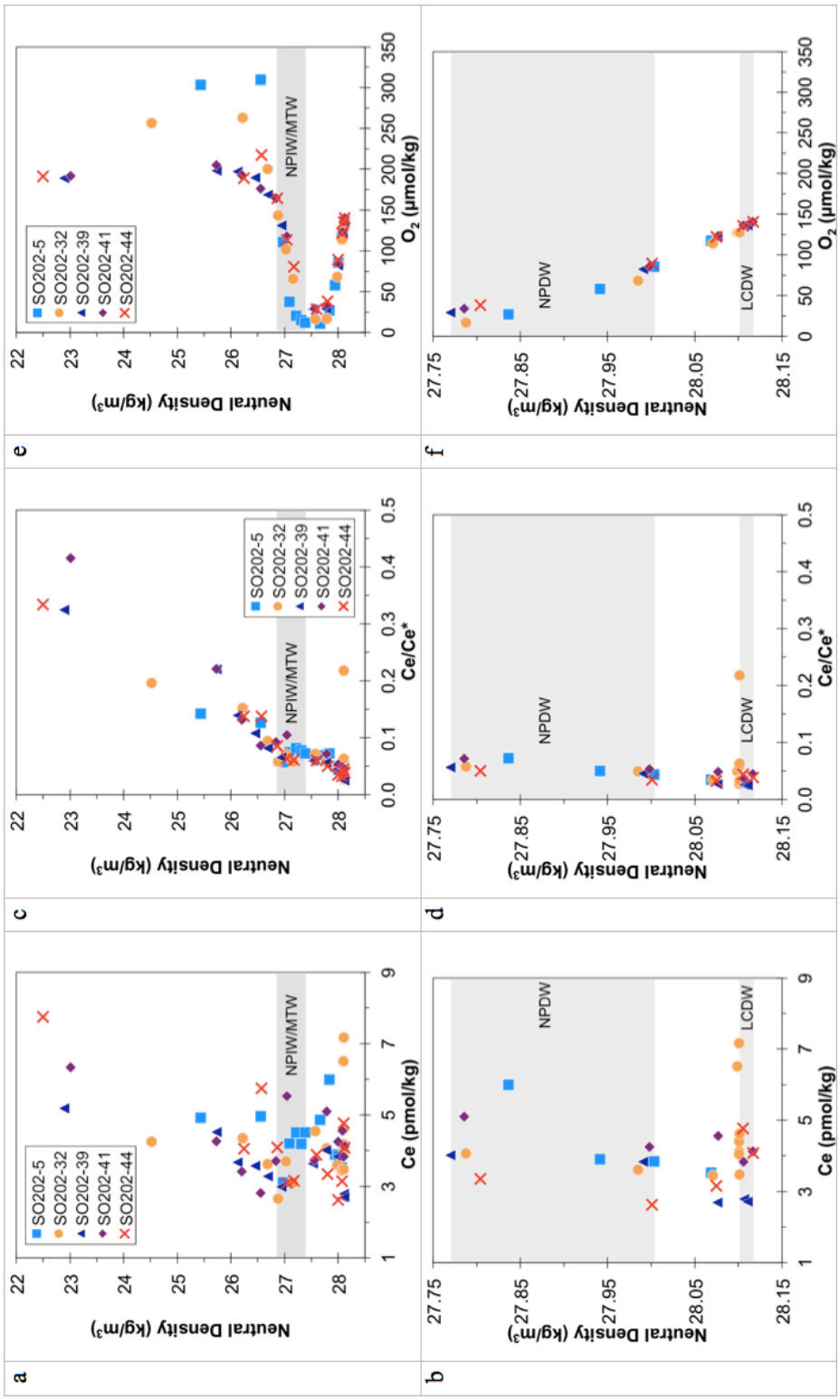

Figure 9. Depth profiles of $Yb_n/Nd_n$ and $La_n/Nd_n$ for SO202 stations

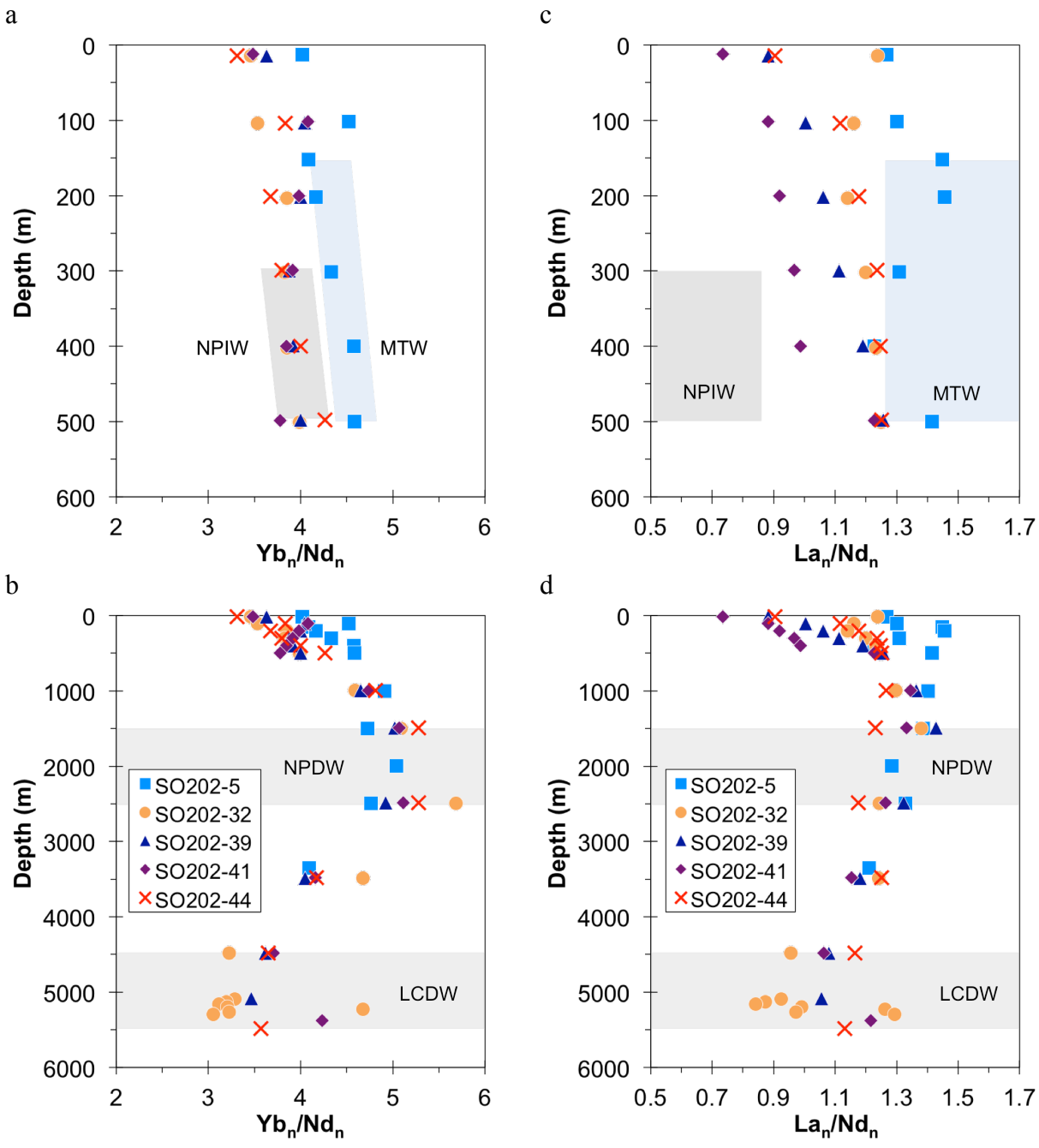

Figure 10. Neutral density profiles of $Yb_n/Nd_n$ and $La_n/Nd_n$ for SO202 stations

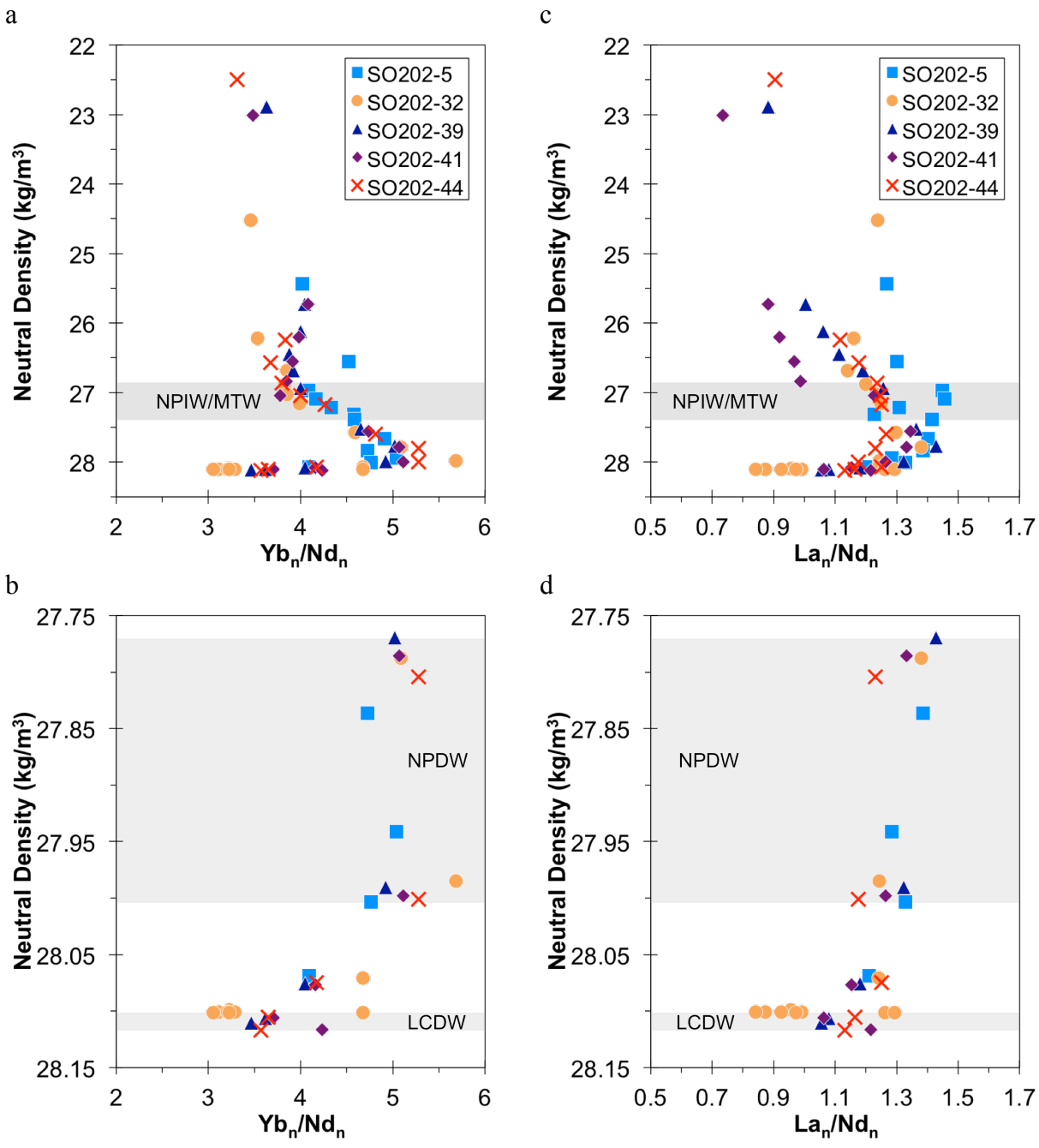

Figure 11. Depth profiles of MREE/MREE* and Eu/Eu* for SO202 stations

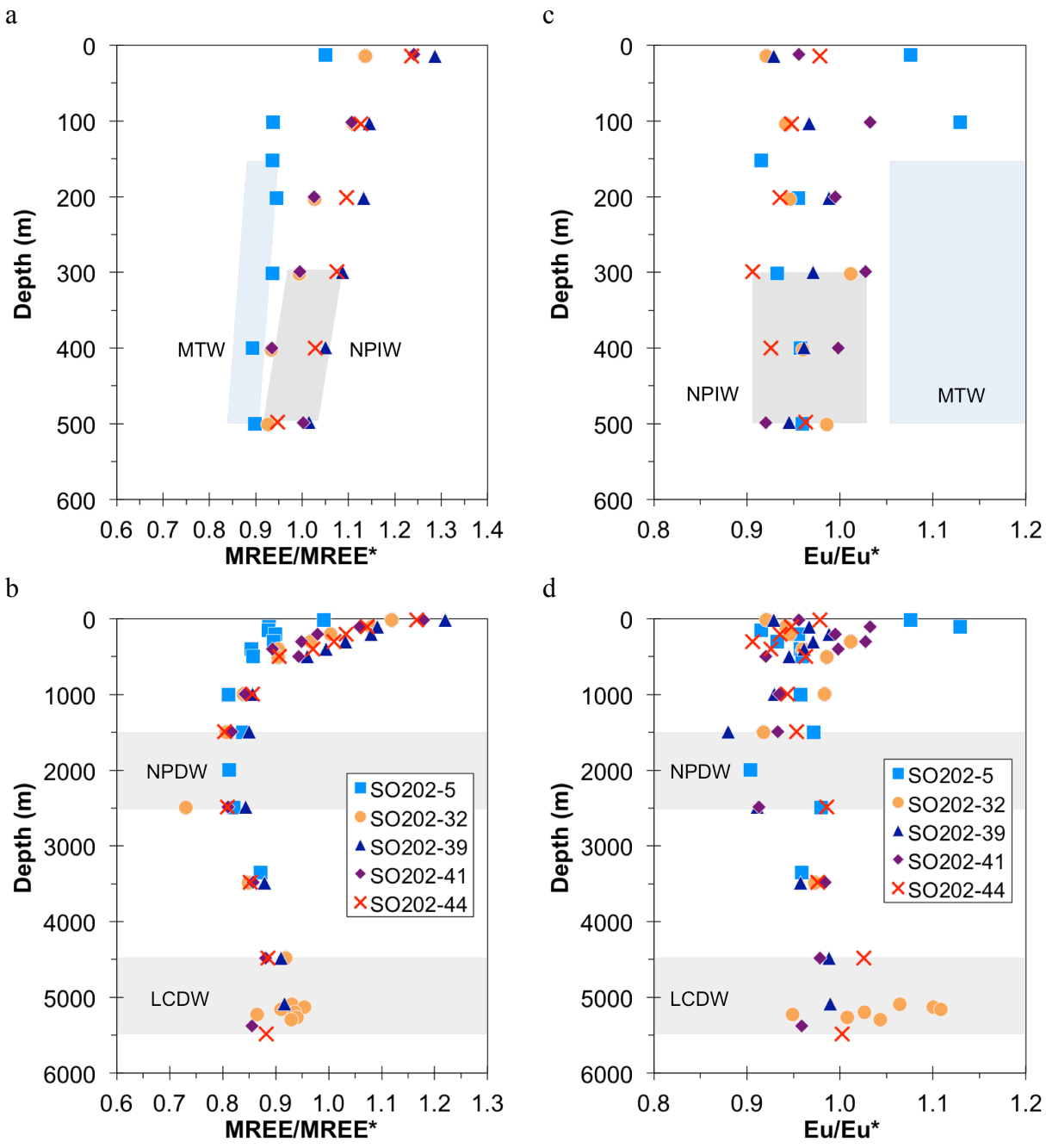

Figure 12. Neutral density profiles of MREE/MREE* and Eu/Eu* for SO202 stations

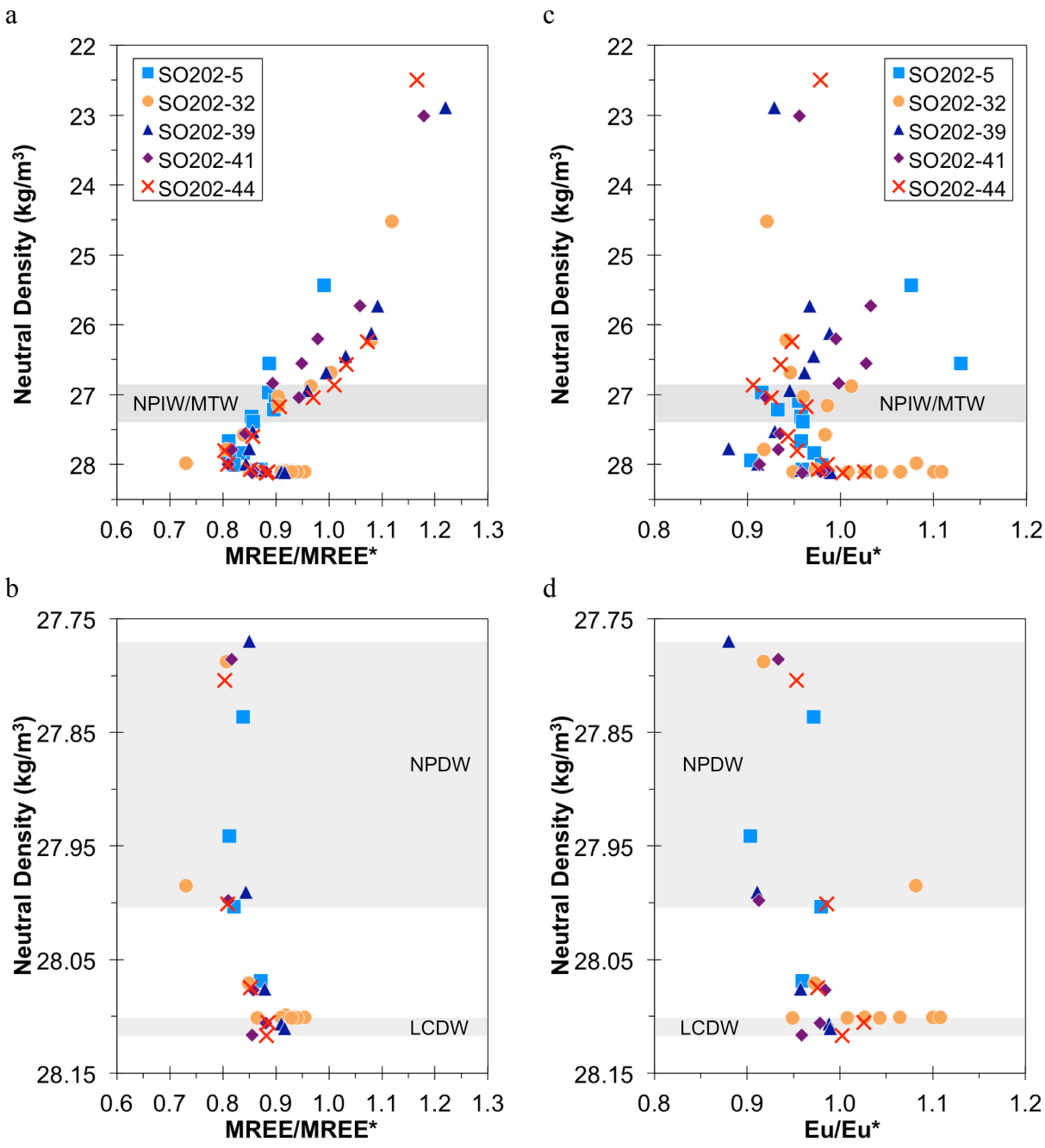

Figure 13. Double-normalized REE patterns of sources of Asian dusts transported over Asia and the Pacific Ocean, volcanic ashes, core-top sediments of SO202 stations, and surface water of SO202 stations

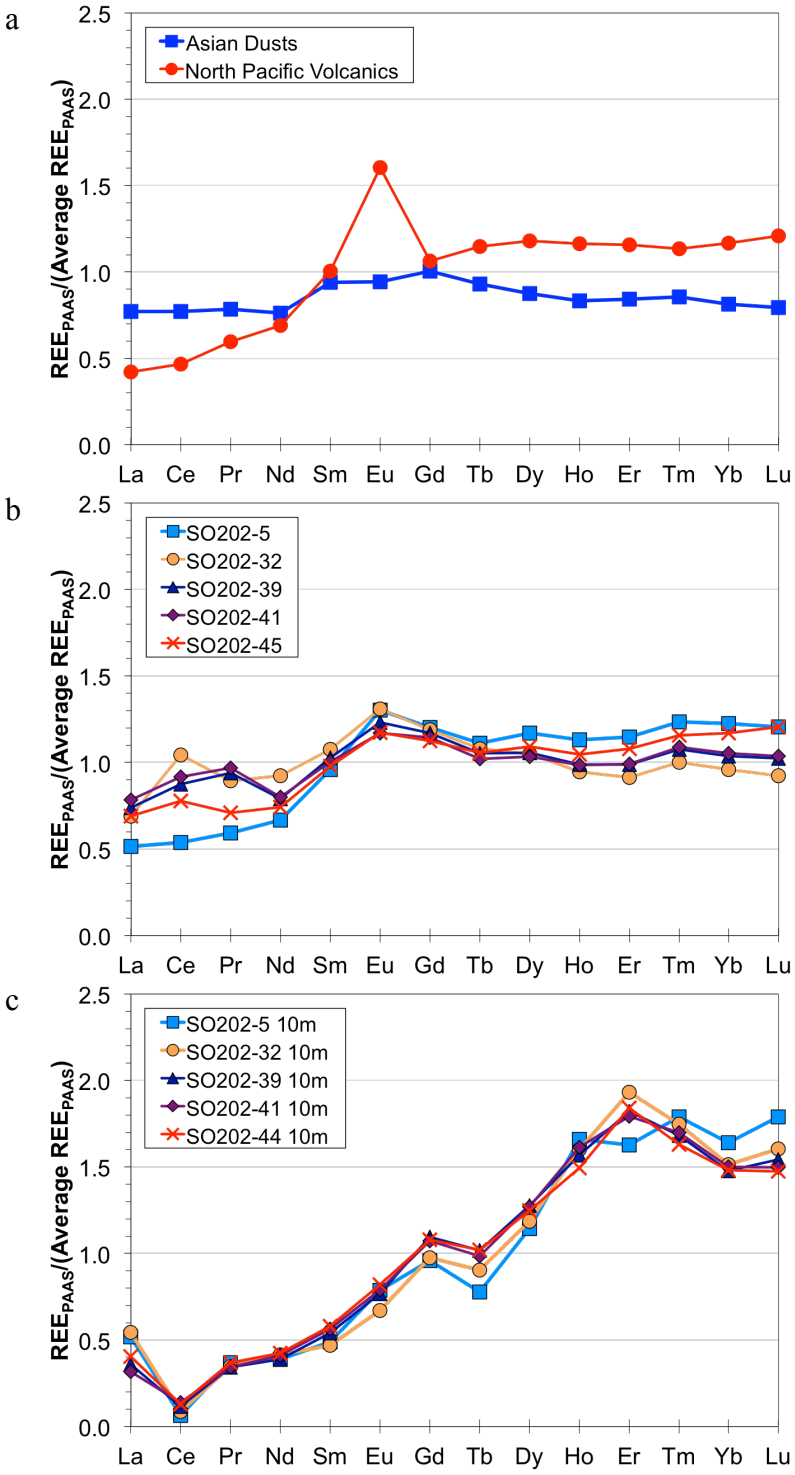

Figure 14. Comparison of εNd and REEs from SO202 stations with published data from nearby stations for NPIW

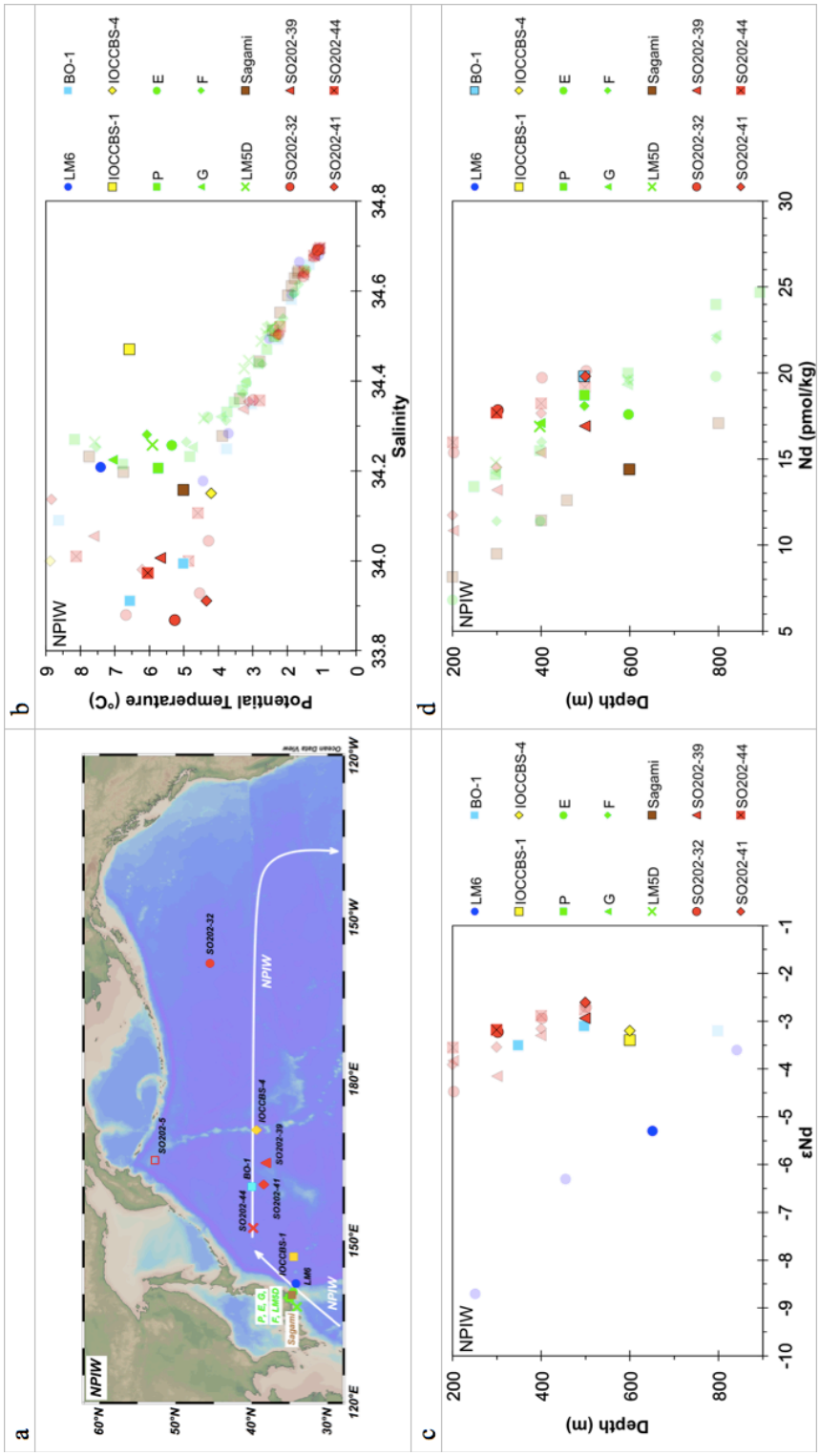

Figure 15. Comparison of εNd and REEs from SO202 stations with published data from nearby stations for NPDW

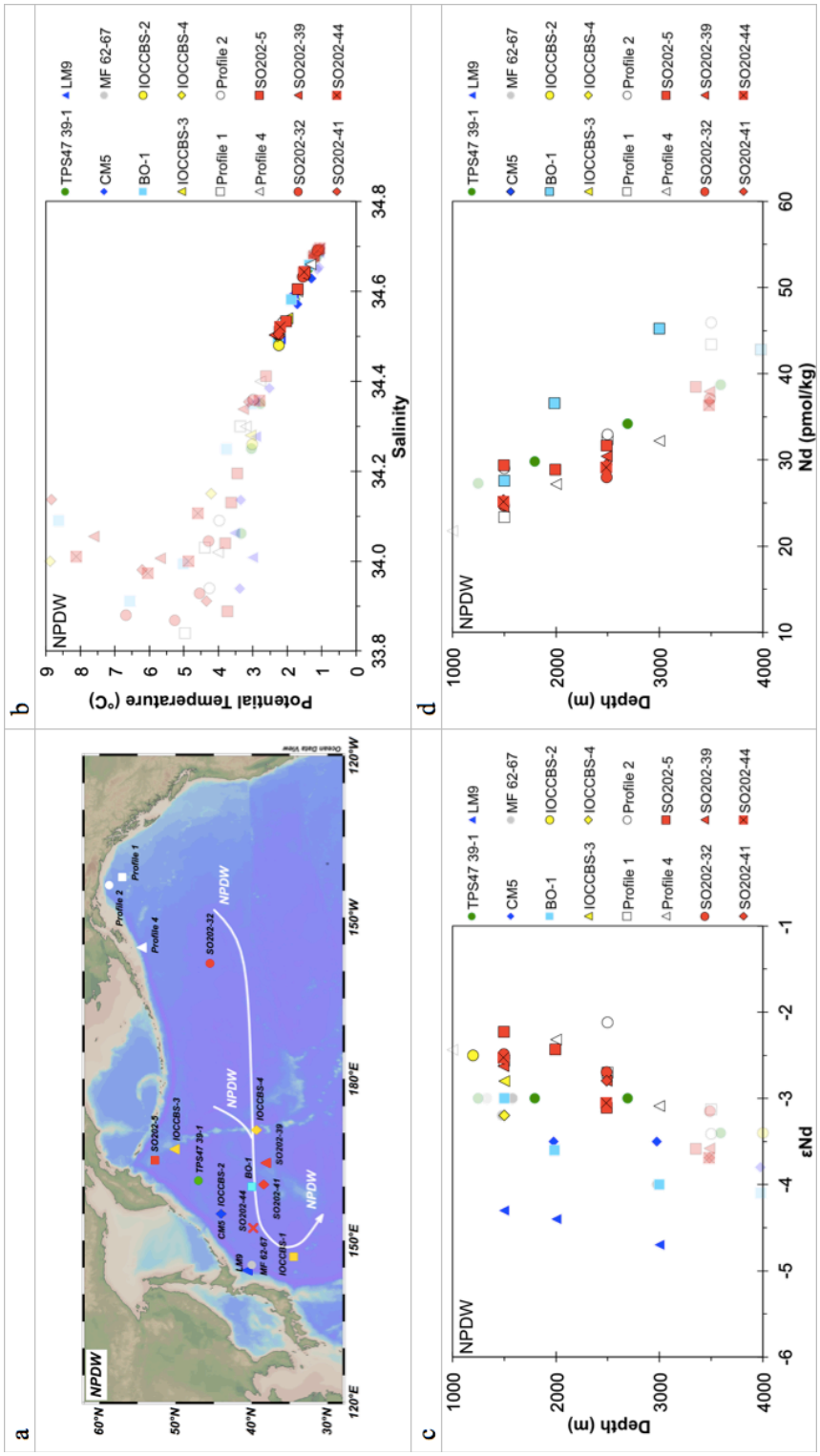

Figure 16. Comparison of εNd and REEs from SO202 stations with published data from nearby stations for LCDW

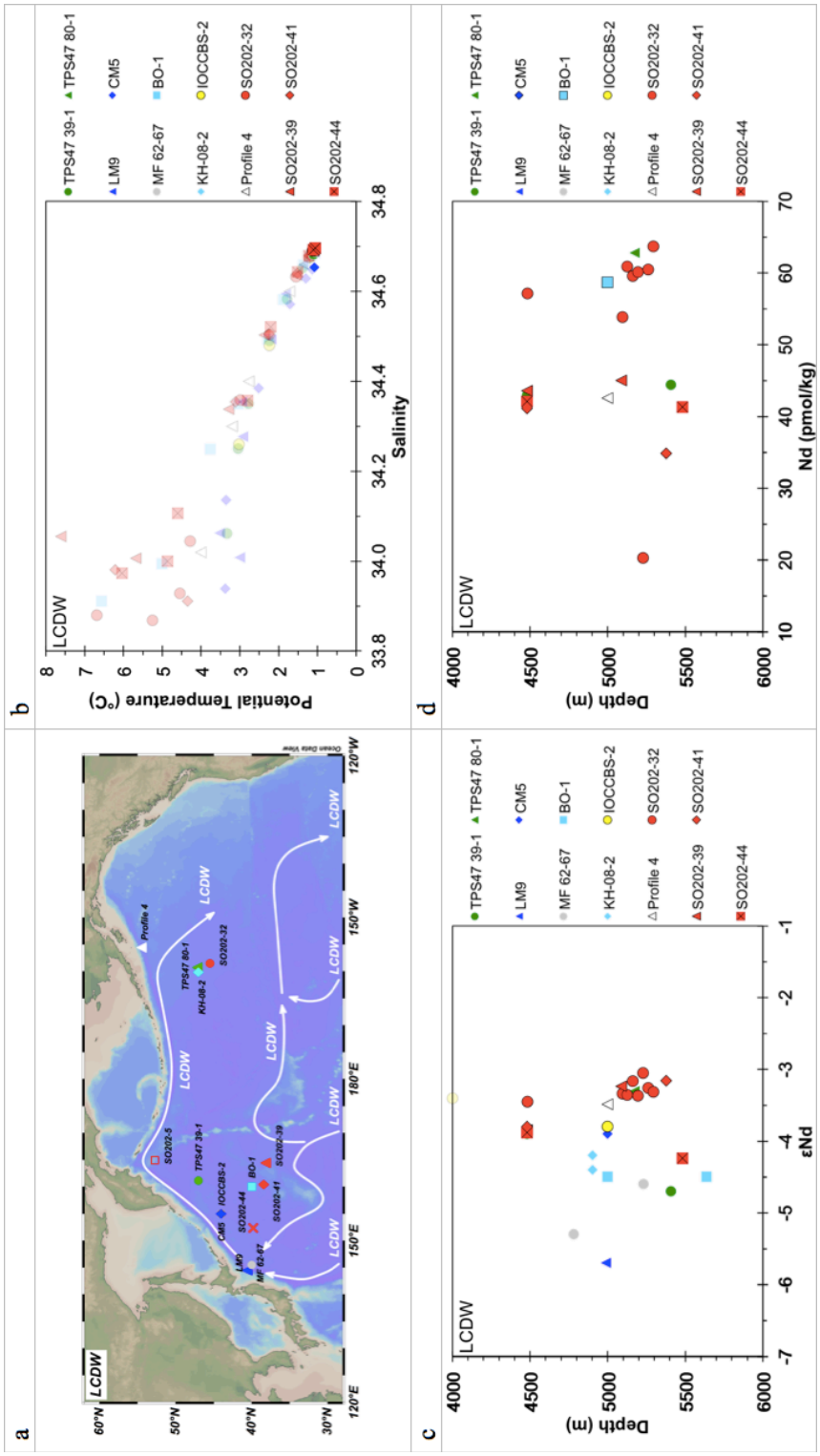

Figure 17. Comparison of εNd, dissolved $^{232}$Th and Nd concentration with salinity below the depths of NPIW

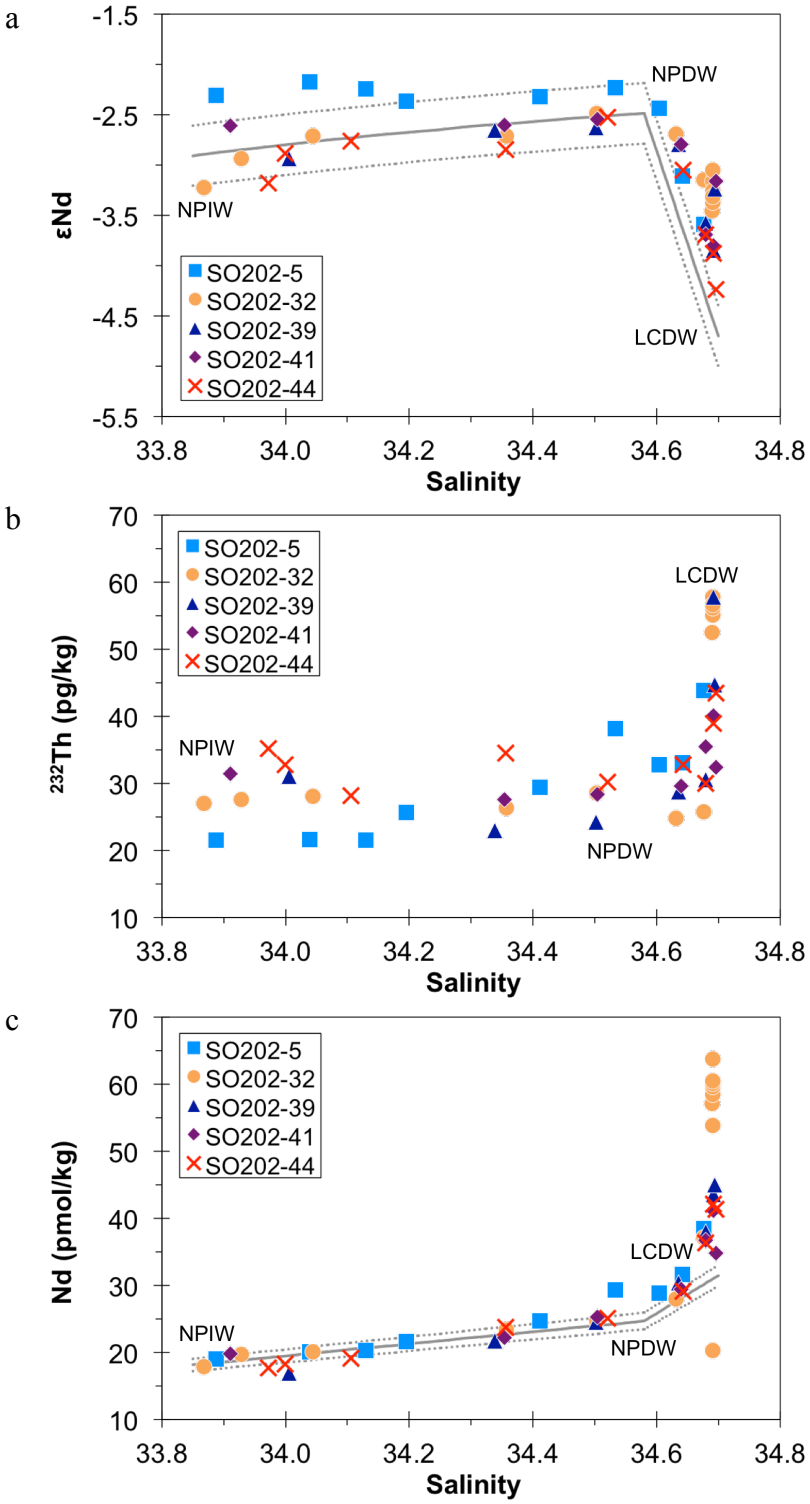

Figure 18. Comparison of REE ratios with salinity below the depths of NPIW

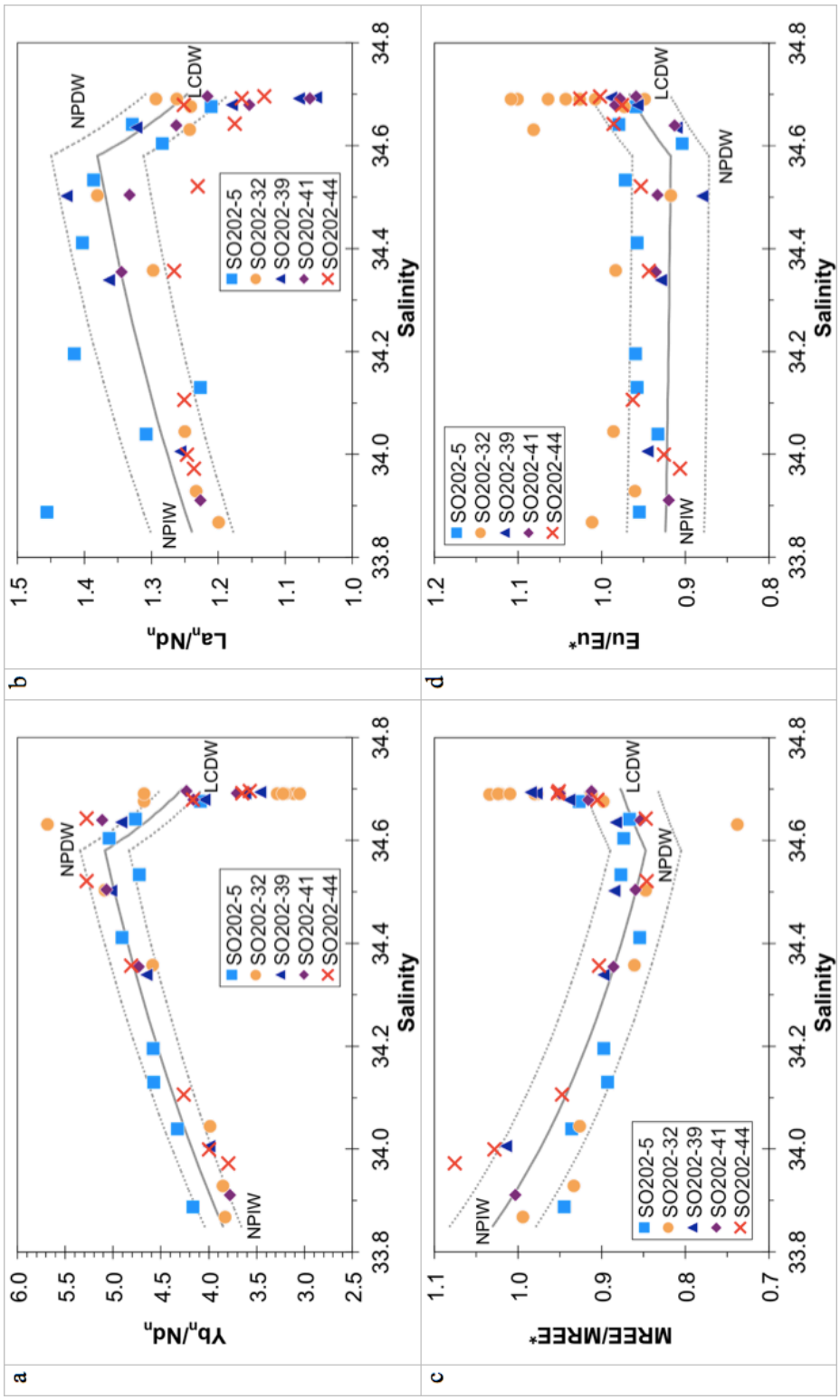

Figure 19. Map of εNd of marine sediments in the North Pacific Ocean

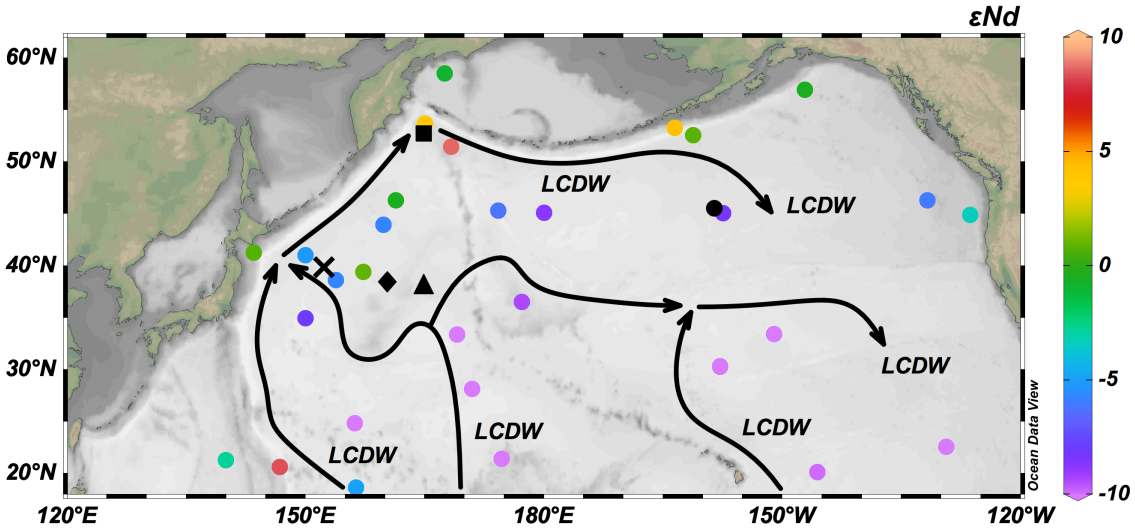

Table 1. Isotope concentrations and natural abundances for DKM spike and diluted spike solution (dilution factor = 16152).

Table 2. Seawater REE concentrations of GEOTRACES station BATS at 20 m and 2000 m analyzed in this study with two standard deviations (2σ SD) and relative two standard deviations (2σ RSD). REE concentrations at 2000 m of BATS analyzed in this study are compared with GEOTRACES intercalibration values (van de Flierdt et al., 2012).

Table 3. Profile data of five stations from the SO202 cruise. (a) latitude, longitude, depth, salinity, temperature, potential temperature, oxygen concentration, εNd value, εNd external 2 standard deviation. (b) REE concentration, Ce anomaly, $Yb_n/Nd_n$ and MREE anomaly. Errors for REE concentrations represent 2σ external errors in percent. Table 3 is in the Appendix 3.

Table 4. North Pacific water mass end-member compositions based on hydrographic data from World Ocean Atlas 2013 and εNd and REE data in the water mass formation regions.

Table 1. Isotope concentrations and natural abundances for DKM spike and diluted spike solution

| Isotope | DKM Spike Concentration μmol/g | Diluted Spike Concentration μmol/g | Natural Abundance |
|---|---|---|---|
| $^{138}$La | 5.64E-04 | 3.49E-08 | 0.0009 |
| $^{139}$La | 7.77E-03 | 4.81E-07 | 0.9991 |
| $^{140}$Ce | 1.27E-02 | 7.86E-07 | 0.8848 |
| $^{142}$Ce | 1.45E-01 | 8.99E-06 | 0.1108 |
| $^{143}$Nd | 7.46E-04 | 4.62E-08 | 0.1218 |
| $^{144}$Nd | 8.93E-02 | 5.53E-06 | 0.0830 |
| $^{147}$Sm | 1.82E-04 | 1.12E-08 | 0.1500 |
| $^{149}$Sm | 4.81E-02 | 2.98E-06 | 0.1380 |
| $^{151}$Eu | 7.92E-04 | 4.90E-08 | 0.4780 |
| $^{153}$Eu | 1.39E-02 | 8.59E-07 | 0.5220 |
| $^{155}$Gd | 2.72E-02 | 1.68E-06 | 0.1480 |
| $^{157}$Gd | 3.73E-04 | 2.31E-08 | 0.1565 |
| $^{161}$Dy | 2.84E-02 | 1.76E-06 | 0.1889 |
| $^{163}$Dy | 4.55E-04 | 2.81E-08 | 0.2490 |
| $^{166}$Er | 4.38E-04 | 2.71E-08 | 0.3360 |
| $^{167}$Er | 1.38E-02 | 8.51E-07 | 0.2295 |
| $^{171}$Yb | 1.52E-02 | 9.38E-07 | 0.1430 |
| $^{174}$Yb | 1.55E-04 | 9.62E-09 | 0.3180 |
| $^{175}$Lu | 1.22E-04 | 7.55E-09 | 0.9741 |
| $^{176}$Lu | 3.08E-04 | 1.91E-08 | 0.0259 |

Table 2. Seawater REE concentrations of GEOTRACES station BATS at 20 m and 2000 m

| | La | Ce | Pr | Nd | Sm | Eu | Gd | Tb | Dy | Ho | Er | Tm | Yb | Lu |
|---|---|---|---|---|---|---|---|---|---|---|---|---|---|---|
| BATS 20 m | | | | | | | | | | | | | | |
| Average of this study (pmol/kg) (n = 16) | 14.30 | 10.33 | 3.28 | 14.09 | 3.15 | 0.87 | 4.33 | 0.77 | 5.99 | 1.45 | 4.80 | 0.64 | 4.20 | 0.66 |
| 2σ SD (pmol/kg) | 0.72 | 0.50 | 0.22 | 0.49 | 0.16 | 0.06 | 0.27 | 0.04 | 0.28 | 0.09 | 0.21 | 0.03 | 0.14 | 0.05 |
| 2σ RSD (%) | 5.00 | 4.81 | 6.77 | 3.49 | 5.13 | 6.84 | 6.13 | 5.32 | 4.72 | 6.35 | 4.35 | 4.03 | 3.43 | 7.22 |
| | | | | | | | | | | | | | | |
| BATS 2000 m | | | | | | | | | | | | | | |
| Average of this study (pmol/kg) (n = 14) | 23.54 | 4.24 | 4.21 | 17.23 | 3.38 | 0.87 | 4.20 | 0.74 | 5.76 | 1.44 | 4.91 | 0.68 | 4.72 | 0.78 |
| 2σ SD (pmol/kg) | 1.21 | 0.15 | 0.07 | 0.49 | 0.13 | 0.05 | 0.25 | 0.03 | 0.25 | 0.03 | 0.23 | 0.02 | 0.22 | 0.03 |
| 2σ RSD (%) | 5.14 | 3.45 | 1.71 | 2.83 | 3.98 | 5.51 | 5.94 | 4.69 | 4.39 | 2.29 | 4.78 | 3.28 | 4.57 | 4.35 |
| GEOTRACES intercalibration value (pmol/kg) | 23.61 | 5.12 | 4.03 | 17.32 | 3.45 | 0.91 | 4.84 | 0.79 | 5.80 | 1.52 | 5.04 | 0.74 | 4.76 | 0.81 |
| 2σ SD (pmol/kg) | 2.79 | 2.27 | 0.36 | 1.22 | 0.34 | 0.10 | 0.53 | 0.08 | 0.38 | 0.09 | 0.25 | 0.05 | 0.25 | 0.04 |
| 2σ RSD (%) | 11.83 | 44.42 | 8.88 | 7.04 | 9.74 | 11.17 | 10.91 | 9.69 | 6.53 | 5.83 | 4.97 | 6.82 | 5.28 | 4.53 |

Table 4. North Pacific water mass end-member compositions

| | Salinity | Potential Temperature | εNd | La | Ce | Pr | Nd | Sm | Eu | Gd | Tb | Dy | Ho | Er | Tm | Yb | Lu |
|---|---|---|---|---|---|---|---|---|---|---|---|---|---|---|---|---|---|
| | | | | pmol/kg | pmol/kg | pmol/kg | pmol/kg | pmol/kg | pmol/kg | pmol/kg | pmol/kg | pmol/kg | pmol/kg | pmol/kg | pmol/kg | pmol/kg | pmol/kg |
| NPIW | 33.85 | 5.24 | -2.91 | 27.73 | 4.20 | 4.42 | 18.14 | 3.50 | 0.93 | 5.51 | 0.80 | 6.07 | 1.60 | 5.30 | 0.76 | 5.10 | 0.86 |
| NPDW | 34.58 | 1.82 | -2.49 | 42.04 | 4.06 | 5.86 | 24.70 | 4.65 | 1.25 | 7.56 | 1.10 | 8.70 | 2.38 | 8.61 | 1.26 | 9.17 | 1.59 |
| LCDW | 34.70 | 1.05 | -4.70 | 48.40 | 4.58 | 7.54 | 31.49 | 5.96 | 1.57 | 8.61 | 1.32 | 9.99 | 2.58 | 9.00 | 1.41 | 9.82 | 1.82 |

**Supplementary Information**

# Chapter 4. Constraining the Source of Neodymium Isotopic Composition in North Pacific Seawater

This supplementary information includes (1) comparison of εNd and REE data of intermediate and deep water from the INOPEX (Innovative North Pacific Experiment) SO202 cruise with published data in the North Pacific and (2) a description of how εNd and REEs change for each intermediate and deep water mass along their transport paths.

**1. Comparison of εNd and REE data of intermediate and deep water from SO202 stations with published data in the North Pacific**

To investigate whether filtration has any impact on εNd and REEs of seawater samples in the North Pacific, we compare our εNd and REE data of filtered samples for North Pacific Intermediate Water (NPIW), North Pacific Deep Water (NPDW) and Lower Circumpolar Deep Water (LCDW) from SO202 stations with published data of filtered and unfiltered samples in the North Pacific. The published εNd and REE data of North Pacific seawater samples used in this comparison are from 20°N to 59°N (Piepgras and Jacobsen, 1988, 1992; Shimizu et al., 1994; Zhang and Nozaki, 1998; Alibo and Nozaki, 1999; Amakawa et al., 2004; Vance et al., 2004; Amakawa et al., 2009; Zimmermann et al., 2009; Pahnke et al., 2012; Haley et al., 2014; Behrens et al., 2016; Fröllje et al., 2016; Behrens et al., 2018a; Behrens et al., 2018b). The water masses of these samples are defined based on the same hydrographic properties as that of SO202 stations: the salinity minimum for NPIW in the North Pacific (Fig. S1b), NPDW with salinity of 34.48-34.68 and potential temperature of 1.3-2.6 °C in the North Pacific (Fig. S2b), and the lowest potential temperature for LCDW (Fig. S3b) in the North Pacific.

Hydrographic properties of these samples for different water masses are shown in diagrams of potential temperature vs. salinity (Fig. S1b,S2b,S3b).

### *1.1. North Pacific Intermediate Water*

NPIW with the salinity minimum (33.9-34.0) is observed in near Japan stations SO202-44, 41 and 39 and Northeast station SO202-32 (Fig. S1a,S1b). εNd-values of NPIW from SO202 stations range from −3.2 to −2.6 (Fig. S1c), which are consistent with published values of filtered samples (−4.2 to −2.4, symbols with marker lines in Fig. S1c) and higher than the published values of unfiltered samples (−5.3 to −3.1, symbols without marker lines in Fig. S1c) in the North Pacific. Nd concentrations of NPIW from SO202 range from 16.9 to 19.8 pmol/kg (Fig. S1d), which are similar to the published values of filtered samples (10.9 to 19.8 pmol/kg, symbols with marker lines in Fig. S1d) and unfiltered samples (15.1 to 18.7 pmol/kg, symbols without marker lines in Fig. S1d) in the North Pacific.

Near Japan station SO202-41 is very close to a published station BO-1 (Fig. S1a), where samples are filtered for εNd measurements and unfiltered for Nd concentration measurements (Amakawa et al., 2009). NPIW at station SO202-41 has higher εNd (−2.6, filtered) compared to that at station BO-1 (−3.5 to −3.1, unfiltered) (Fig. S4a). NPIW at these two stations have the same Nd concentrations (19.8 pmol/kg, both filtered) (Fig. S4b).

εNd of unfiltered seawater is the mixture between seawater and particle εNd signals. In the above observations, lower εNd-values of the unfiltered seawater compared to the filtered seawater (0.7-1.1 εNd units lower) indicate release of unradiogenic Nd

from particle leaching. Nd concentrations of the unfiltered seawater are expected to show higher values compared to the filtered seawater due to particle leaching. However, filtered and unfiltered seawater show similar Nd concentrations suggesting that particle leaching does not impact Nd concentrations significantly.

REEs of NPIW from SO202 stations show similar PAAS (Post-Archean Australian Shale; (Taylor and McLennan, 1985)) normalized patterns compared to the published filtered and unfiltered data in the North Pacific (Fig. S1e). REEs of NPIW from SO202 stations have lower abundances compared to that of NPDW and LCDW (Fig. S1e).

***1.2. North Pacific Deep Water***

NPDW is observed in all five stations from the SO202 cruise (Fig. S2a,S2b). εNd-values of NPDW from SO202 stations range from −3.1 to −2.2 (Fig. S2c), which are consistent with the published values of filtered samples (−3.7 to −0.7, symbols with marker lines in Fig. S2c) and higher than the published values of unfiltered samples (−6.0 to −3.0, symbols without marker lines in Fig. S2c) in the North Pacific. Nd concentrations of NPDW from SO202 stations range from 24.6 to 31.7 pmol/kg (Fig. S2d), which are consistent with the published values of filtered samples (15.4 to 47.3 pmol/kg, symbols with marker lines in Fig. S2d) and unfiltered samples (24.5 to 41.6 pmol/kg, symbols without marker lines in Fig. S2d) in the North Pacific.

Near Japan station SO202-41 is very close to the published station BO-1 (Amakawa et al., 2009) (Fig. S2a). NPDW at station SO202-41 shows higher εNd-values (−2.8 to −2.6, filtered) compared to that at BO-1 (−4.0 to −3.0, filtered) (Fig. S4a) and

lower Nd concentrations (25.3 to 29.5 pmol/kg, filtered) compared to that at BO-1 (27.6 to 45.2 pmol/kg, unfiltered) (Fig. S4b). Northwest station SO202-5 is close to two published stations IOCCBS-3 (filtered) (Zimmermann et al., 2009) and TPS47 39-1 (unfiltered) (Piepgras and Jacobsen, 1988) (Fig. S2a). NPDW at station SO202-5 has similar εNd (−3.1 to −2.2, filtered) compared to that at stations IOCCBS-3 (−2.8, filtered) and TPS47 39-1 (−3.0, unfiltered) (Fig. S5a). Nd concentrations of NPDW at station SO202-5 (29.4 to 31.7 pmol/kg, filtered) are similar to that at station TPS47 39-1 (29.8 to 34.2 pmol/kg, filtered) (Fig. S5b). Nd concentrations are not analyzed at IOCCBS stations.

Similar to NPIW, the above observations for NPDW also show lower εNd-values of the unfiltered seawater compared to the filtered seawater (2.3 εNd units lower), which indicates release of unradiogenic Nd from particle leaching. The filtered seawater samples show similar Nd concentrations compared to the unfiltered seawater suggesting that particle leaching does not impact Nd concentrations significantly.

REEs of NPDW from SO202 stations show similar PAAS normalized patterns compared to the published filtered and unfiltered data in the North Pacific (Fig. S2e). REEs of NPDW from SO202 stations have abundances higher than that of NPIW and lower than that of LCDW (Fig. S2e).

***1.3. Lower Circumpolar Deep Water***

LCDW is observed in near Japan stations SO202-44, 41 and 39 and Northeast station SO202-32 (Fig. S3a,S3b). εNd-values of LCDW from SO202 stations range from −4.2 to −3.1 (Fig. S3c), which are consistent with the published values of filtered samples

(−4.8 to −3.5, symbols with marker lines in Fig. S3c) and higher than the published values of unfiltered samples (−6.5 to −3.8, symbols without marker lines in Fig. S3c) in the North Pacific. Nd concentrations of LCDW from SO202 stations range from 34.8 to 63.7 pmol/kg (except 20.3 pmol/kg at ~5228 m) (Fig. S3d), which are consistent with the published values of filtered samples (30.7 to 58.7 pmol/kg, symbols with marker lines in Fig. S3d) and unfiltered samples (35.0 to 62.8 pmol/kg, symbols without marker lines in Fig. S3d) in the North Pacific.

Near Japan station SO202-41 is very close to the published station BO-1 (Amakawa et al., 2009) (Fig. S3a). LCDW at station SO202-41 shows higher εNd-values (−3.8 to −3.2, filtered) compared to that at station BO-1 (−4.5, unfiltered) (Fig. S4a) and lower Nd concentrations (34.8 to 41.1 pmol/kg, filtered) compared to that at station BO-1 (58.7 pmol/kg, filtered) (Fig. S4b). Northeast station SO202-32 is close to two published stations TPS47 80-1 (unfiltered) (Piepgras and Jacobsen, 1988, 1992) and KH-08-2 (unfiltered) (Amakawa et al., 2009) (Fig. S3a). LCDW at station SO202-32 has εNd of −3.5 to −3.1 (filtered), similar to that at station TPS47 80-1 (−3.3, unfiltered) and higher than that at station KH-08-2 (−4.4 to −4.2, unfiltered) (Fig. S6a). Nd concentrations of NPDW at station SO202-32 are 53.8 to 63.7 pmol/kg (filtered, except 20.3 pmol/kg at ~5228 m), which are close to that at station TPS47 80-1 (62.8 pmol/kg, filtered) (Fig. S6b). Nd concentrations are not analyzed at KH-08-2.

Similar to NPIW and NPDW, the above observations for LCDW also show lower εNd-values of the unfiltered seawater compared to the filtered seawater (0.7-1.7 εNd units lower) and indicate release of unradiogenic Nd from particle leaching. The filtered

seawater samples show similar Nd concentrations compared to the unfiltered seawater suggesting that particle leaching does not impact Nd concentrations significantly.

REEs of LCDW from SO202 stations show similar PAAS normalized patterns compared to the published filtered and unfiltered data in the North Pacific (Fig. S3e). REEs of LCDW from SO202 stations have higher abundances compared to that of NPIW and NPDW (Fig. S3e). LCDW at Northeast station SO202-32 show europium enrichments (Fig. S3e).

**2. How εNd and REEs change along the water mass transport paths**

To investigate how well εNd and REEs trace the intermediate and deep water masses along their transport paths, we discuss whether and how εNd and REEs change along each water mass transport path in this section. Increasing location numbers are used to show the progressing water mass transport paths (Fig. S7a,S8a,S9a). Here location numbers are not station numbers. They are locations where εNd and/or REE data are available. Changes of εNd and REEs along each water mass pathway are shown in Fig. S7b-g,S8b-g,S9b-g. NPIW and NPDW of the filtered samples show conservative behavior of εNd and REEs (Supplementary Information Section 2.1 and 2.2), whereas εNd and REEs of the filtered samples for LCDW indicate addition of external REEs from volcanic sources along the transport path of LCDW (Supplementary Information Section 2.3).

### *2.1. North Pacific Intermediate Water*

After NPIW is formed in the mixed water region between the Kuroshio Extension and Oyashio front (location 1; Fig. S7a), it circulates clockwise in the subtropical North Pacific (location 1 to 10; Fig. S7a). Along the transport path of NPIW, εNd-values of the filtered samples range from −4.2 to −2.6 and do not change much (Fig. S7b), indicating conservative behavior of εNd.

Both Nd and Yb concentrations of the filtered samples show a decreasing trend along the NPIW pathway (Fig. S7c,d). The unfiltered samples at stations along the slopes of the Sagami and Nankai troughs near Japan show higher Nd and Yb concentrations (Fig. S7c,d) due to release of REEs from slope sediments (Zhang and Nozaki, 1998). Often REEs accumulate along water mass transport path resulting in increasing concentrations. However, they are scavenged onto the particles at the same time resulting in decreasing concentrations. Here both Nd and Yb concentrations decrease along the NPIW pathway, indicating that scavenging prevails over accumulation. Here $Yb_n/Nd_n$ ratios of NPIW of the filtered samples increase along the NPIW pathway (Fig. S7e). Since light REEs (LREEs, e.g. Nd) are more preferentially scavenged onto particles compared to heavy REEs (HREEs, e.g. Yb), the resulting HREE/LREE ratios (e.g. $Yb_n/Nd_n$) would increase along the water mass transport path. The unfiltered samples at stations along the slopes of the Sagami and Nankai troughs near Japan show lower $Yb_n/Nd_n$ ratios (Fig. S7e) due to preferential release of LREEs than HREEs from slope sediments (Zhang and Nozaki, 1998).

Ce/Ce* ratios are usually constant along water mass transport path of intermediate and deep water. Here Ce/Ce* ratios of NPIW of the filtered samples range from 0.05 to 0.10 and do not change much along the transport path of NPIW (Fig. S7f). The unfiltered samples at stations along the slopes of the Sagami and Nankai troughs near Japan show higher Ce/Ce* ratios (Fig. S7f) due to release of REEs from slope sediments enriched in Ce compared to seawater (Zhang and Nozaki, 1998).

Eu/Eu* ratios are usually constant along water mass transport path if there is no influence from lithogenic input of volcanic sources (enriched in Eu). Here Eu/Eu* ratios of NPIW of the filtered samples do not show an increasing trend along the transport path of NPIW (Fig. S7g), indicating no addition of lithogenic input from volcanic sources along the NPIW pathway. The unfiltered samples at stations along the slopes of the Sagami and Nankai troughs near Japan have Eu/Eu* ratios of 0.97-1.05, consistent with values of the filtered samples.

***2.2. North Pacific Deep Water***

NPDW is formed from the upwelled LCDW in the central and eastern subarctic North Pacific (location 1; Fig. S8a). It is transported westward to the Japan Sea before turning southeastward (location 1 to 10; Fig. S8a). In the formation regions, NPDW from the unfiltered samples in the central subarctic North Pacific (station DE-4; location 1C; Fig. S8a) shows lower εNd (−6.0; Fig. S8b) than that from the filtered samples in the eastern subarctic North Pacific (−2.7 to −2.5; station SO202-32; location 1E; Fig. S8b). Then εNd-values of NPDW are almost constant (−3.2 to −2.5) along the NPDW transport path compared to its value in the formation region of eastern subarctic North Pacific (Fig.

S8b), indicating conservative behavior of εNd. The only exception is at station IOCCBS-1 (location 7), where NPDW has εNd of −0.7 (Fig. S8b). When NPDW reaches the Hawaii Islands, εNd-values have a larger range from −3.5 to −1.5 compared to previous locations (location 9) (Fig. S8b).

Nd concentrations of NPDW are almost constant from the formation region of eastern subarctic North Pacific to station SO202-44 (location 5) (Fig. S8c), indicating that scavenging equals accumulation. Similar to εNd, Nd concentrations of NPDW have a larger range near the Hawaiian Islands (location 9) (Fig. S8c). Yb concentrations of NPDW do not change much along the transport path of NPDW (Fig. S8d), indicating that scavenging equals accumulation. Similar to NPIW, $Yb_n/Nd_n$ ratios of NPDW show an increasing trend (except for one sample at 2500 m of SO202-32) along the transport path of NPDW (Fig. S8e) due to preferential scavenging of LREEs compared to HREEs. $Ce/Ce^*$ ratios of NPDW do not change much along the transport path of NPDW (Fig. S8f). $Eu/Eu^*$ ratios of NPDW do not show an increasing trend along the transport path (Fig. S7g), indicating no addition of lithogenic input from volcanic sources along the NPDW pathway.

### *2.3. Lower Circumpolar Deep Water*

LCDW enters the North Pacific in two northward braches (Fig. S9a). At ~10°N, the two branches become three northward branches at ~150°E (location 2W), ~170°E (location 2M), and ~150°W (location 2E) (Fig. S9a). The middle branch separates into westward and eastward directions at ~30°N (Fig. S9a). The eastward water at ~30°N joins the westernmost branch in the Japan Sea and they move northward along Kuril

Island and Kamchatka Peninsula (Fig. S9a). Then it flows along the Aleutian Islands and southeastward to the Eastern Pacific (Fig. S9a). The westward water at ~30°N joins the easternmost branch and they flow eastward to the Eastern Pacific (Fig. S9a). Along the transport path of LCDW, εNd-values of the filtered samples show an increasing trend (Fig. S7b), indicating addition of radiogenic Nd from volcanic sources.

Both Nd and Yb concentrations of the filtered samples show increasing trends along the transport path of LCDW (Fig. S9c,d). $Yb_n/Nd_n$ ratios of LCDW show a decreasing trend along the LCDW pathway (Fig. S9e), which could be explained by addition of external REEs from lithogenic input along the LCDW pathway. Since LREEs are more preferentially released compared to HREEs, the resulting $Yb_n/Nd_n$ ratios would decrease. Similar to εNd, $Eu/Eu^*$ ratios of LCDW also increase along the transport path of LCDW indicating addition of external REEs from volcanic sources (Fig. S9g). $Ce/Ce^*$ ratios of LCDW range from 0.05 to 0.07 and do not change much along the LCDW pathway (Fig. S9f).

**References**

Alibo, D.S. and Nozaki, Y. (1999) Rare earth elements in seawater: particle association, shale-normalization, and Ce oxidation. Geochimica et Cosmochimica Acta 63, 363-372.

Amakawa, H., Nozaki, Y., Alibo, D.S., Zhang, J., Fukugawa, K. and Nagai, H. (2004) Neodymium isotopic variations in Northwest Pacific waters1. Geochimica et Cosmochimica Acta 68, 715-727.

Amakawa, H., Sasaki, K. and Ebihara, M. (2009) Nd isotopic composition in the central North Pacific. Geochimica et Cosmochimica Acta 73, 4705-4719.

Behrens, M.K., Muratli, J., Pradoux, C., Wu, Y., Böning, P., Brumsack, H.-J., Goldstein, S.L., Haley, B., Jeandel, C. and Paffrath, R. (2016) Rapid and precise analysis of rare

earth elements in small volumes of seawater-Method and intercomparison. Marine Chemistry 186, 110-120.

Behrens, M.K., Pahnke, K., Paffrath, R., Schnetger, B. and Brumsack, H.-J. (2018a) Rare earth element distributions in the West Pacific: Trace element sources and conservative vs. non-conservative behavior. Earth and Planetary Science Letters 486, 166-177.

Behrens, M.K., Pahnke, K., Schnetger, B. and Brumsack, H.-J. (2018b) Sources and processes affecting the distribution of dissolved Nd isotopes and concentrations in the West Pacific. Geochimica et Cosmochimica Acta 222, 508-534.

Fröllje, H., Pahnke, K., Schnetger, B., Brumsack, H.-J., Dulai, H. and Fitzsimmons, J.N. (2016) Hawaiian imprint on dissolved Nd and Ra isotopes and rare earth elements in the central North Pacific: local survey and seasonal variability. Geochimica et Cosmochimica Acta 189, 110-131.

Haley, B.A., Frank, M., Hathorne, E. and Pisias, N. (2014) Biogeochemical implications from dissolved rare earth element and Nd isotope distributions in the Gulf of Alaska. Geochimica et Cosmochimica Acta 126, 455-474.

Pahnke, K., Van de Flierdt, T., Jones, K.M., Lambelet, M., Hemming, S.R. and Goldstein, S.L. (2012) GEOTRACES intercalibration of neodymium isotopes and rare earth element concentrations in seawater and suspended particles. Part 2: Systematic tests and baseline profiles. Limnology and Oceanography: Methods 10, 252-269.

Piepgras, D.J. and Jacobsen, S.B. (1988) The isotopic composition of neodymium in the North Pacific. Geochimica et Cosmochimica Acta 52, 1373-1381.

Piepgras, D.J. and Jacobsen, S.B. (1992) The behavior of rare earth elements in seawater: Precise determination of variations in the North Pacific water column. Geochimica et Cosmochimica Acta 56, 1851-1862.

Schlitzer, R. (2012) Ocean data view.

Shimizu, H., Tachikawa, K., Masuda, A. and Nozaki, Y. (1994) Cerium and neodymium isotope ratios and REE patterns in seawater from the North Pacific Ocean. Geochimica et Cosmochimica Acta 58, 323-333.

Taylor, S.R. and McLennan, S.M. (1985) The continental crust: its composition and evolution. Blackwell Scientific Pub.,Palo Alto, CA, United States.

Vance, D., Scrivner, A.E., Beney, P., Staubwasser, M., Henderson, G.M. and Slowey, N.C. (2004) The use of foraminifera as a record of the past neodymium isotope composition of seawater. Paleoceanography 19.

Zhang, J. and Nozaki, Y. (1998) Behavior of rare earth elements in seawater at the ocean margin: a study along the slopes of the Sagami and Nankai troughs near Japan. Geochimica et Cosmochimica Acta 62, 1307-1317.

Zimmermann, B., Porcelli, D., Frank, M., Rickli, J., Lee, D.-C. and Halliday, A.N. (2009) The hafnium isotope composition of Pacific Ocean water. Geochimica et Cosmochimica Acta 73, 91-101.

Figure S1. Comparison of εNd and REEs of the INOPEX (Innovative North Pacific Experiment) SO202 cruise with published REE data of seawater samples between 20°N and 59°N for NPIW. (a) Map of stations with NPIW εNd and REE data. Stations in red are from SO202. The other stations are from (Piepgras and Jacobsen, 1988, 1992) (dark green), (Amakawa et al., 2004) (dark blue), (Vance et al., 2004) (violet), (Amakawa et al., 2009) (light blue), (Zimmermann et al., 2009) (yellow), (Zhang and Nozaki, 1998) (light green), (Alibo and Nozaki, 1999) (brown), (Fröllje et al., 2016) (purple), (Pahnke et al., 2012) (Black), (Behrens et al., 2018a; Behrens et al., 2018b) (orange). The NPIW pathways are shown in white. The map was made using ODV software (Schlitzer, 2012). (b) Potential temperature (θ) vs. salinity (S). The filtered samples are shown in marker lines and the unfiltered samples are shown without marker lines. Data points with solid color are NPIW samples of each station. Data points with transparent color are the remaining samples of that station. (c) Depth vs. εNd. (d) Depth vs. [Nd]. (e) PAAS-normalized REE patterns. NPDW and LCDW REE patterns (light blue) are based on published and unpublished REE data.

Figure S2. Comparison of εNd and REEs of SO202 stations with published REE data of seawater samples between 20°N and 59°N for NPDW. (a) Map of stations with NPDW εNd and REE data. Stations in red are from SO202. The other stations are from (Piepgras and Jacobsen, 1988, 1992) (dark green), (Amakawa et al., 2004) (dark blue), (Shimizu et al., 1994) (light grey), (Vance et al., 2004) (violet), (Amakawa et al., 2009) (light blue), (Zimmermann et al., 2009) (yellow), (Haley et al., 2014) (white), (Zhang and Nozaki, 1998) (light green), (Alibo and Nozaki, 1999) (brown), (Fröllje et al., 2016) (purple), (Pahnke et al., 2012; Behrens et al., 2016) (Black), (Behrens et al., 2018a; Behrens et al., 2018b) (orange). The NPDW pathways are shown in white. The map was made using ODV software (Schlitzer, 2012). (b) Potential temperature (θ) vs. salinity (S). The filtered samples are shown in marker lines and the unfiltered samples are shown without marker lines. Data points with solid color are NPIW samples of each station. Data points with transparent color are the remaining samples of that station. (c) Depth vs. εNd. (d) Depth vs. [Nd]. (e) PAAS-normalized REE patterns. NPIW and LCDW REE patterns (light blue) are based on published and unpublished REE data.

Figure S3. Comparison of εNd and REEs of SO202 stations with published REE data of seawater samples between 20°N and 59°N for LCDW. (a) Map of stations with LCDW εNd and REE data. Stations in red are from SO202. The other stations are from (Piepgras and Jacobsen, 1988, 1992) (dark green), (Amakawa et al., 2004) (dark blue), (Shimizu et al., 1994) (light grey), (Vance et al., 2004) (violet), (Amakawa et al., 2009) (light blue), (Zimmermann et al., 2009) (yellow), (Haley et al., 2014) (white), (Fröllje et al., 2016) (purple), (Pahnke et al., 2012) (Black), (Behrens et al., 2018a; Behrens et al., 2018b) (orange). The LCDW pathways are shown in white. The map was made using ODV software (Schlitzer, 2012). (b) Potential temperature (θ) vs. salinity (S). The filtered samples are shown in marker lines and the unfiltered samples are shown without marker lines. Data points with solid color are NPIW samples of each station. Data points with transparent color are the remaining samples of that station. (c) Depth vs. εNd. (d) Depth

vs. [Nd]. (e) PAAS-normalized REE patterns. NPIW and NPDW REE patterns (light blue) are based on published and unpublished REE data.

Figure S4. Depth profiles of εNd and [Nd] for near Japan station SO202-41 and a nearby published station BO-1 (Amakawa et al., 2009). (a) Depth vs. εNd. (b) Depth vs. [Nd].

Figure S5. Depth profiles of εNd and [Nd] for Northwest station SO202-5 and nearby published stations TPS47 80-1 (Piepgras and Jacobsen, 1988, 1992) and IOCCBS-3 (Zimmermann et al., 2009). (a) Depth vs. εNd. (b) Depth vs. [Nd].

Figure S6. Depth profiles of εNd and [Nd] for Northeast station SO202-32 and nearby published stations TPS47 80-1 (Piepgras and Jacobsen, 1988, 1992) and KH-08-2 (Amakawa et al., 2009). (a) Depth vs. εNd. (b) Depth vs. [Nd].

Figure S7. Changes of εNd and REEs along the NPIW pathway. (a) Map showing the transport path of NPIW. Location numbers are not station numbers. They indicate locations where REE and εNd data are available. The map was made using the ODV software (Schlitzer, 2012). (b) εNd vs. location number. (c) [Nd] vs. location number. (d) [Yb] vs. location number. (e) $Yb_n/Nd_n$ vs. location number. (f) $Ce/Ce^*$ vs. location number. (g) $Eu/Eu^*$ vs. location number.

Figure S8. Changes of εNd and REEs along the NPDW pathway. (a) Map showing the transport path of NPDW. Location numbers are not station numbers. They indicate locations where REE and εNd data are available. The map was made using the ODV software (Schlitzer, 2012). (b) εNd vs. location number. (c) [Nd] vs. location number. (d) [Yb] vs. location number. (e) $Yb_n/Nd_n$ vs. location number. (f) $Ce/Ce^*$ vs. location number. (g) $Eu/Eu^*$ vs. location number.

Figure S9. Changes of εNd and REEs along the LCDW pathway. (a) Map showing the transport path of LCDW. Location numbers are not station numbers. They indicate locations where REE and εNd data are available. The map was made using the ODV software (Schlitzer, 2012). (b) εNd vs. location number. (c) [Nd] vs. location number. (d) [Yb] vs. location number. (e) $Yb_n/Nd_n$ vs. location number. (f) $Ce/Ce^*$ vs. location number. (g) $Eu/Eu^*$ vs. location number.

Figure S10. Comparison of εNd, dissolved $^{232}Th$ and Nd concentration with potential temperature below the depths of NPIW. (a) εNd vs. potential temperature. (b) $^{232}Th$ vs. potential temperature. (c) [Nd] vs. potential temperature.

Figure S11. Comparison of REE ratios with potential temperature below the depths of NPIW. (a) $Yb_n/Nd_n$ vs. potential temperature. (b) $La_n/Nd_n$ vs. potential temperature. (c) $MREE/MREE^*$ vs. potential temperature. (d) $Eu/Eu^*$ vs. potential temperature.

Figure S1. Comparison of εNd and REEs of SO202 stations with published REE data of seawater samples for NPIW

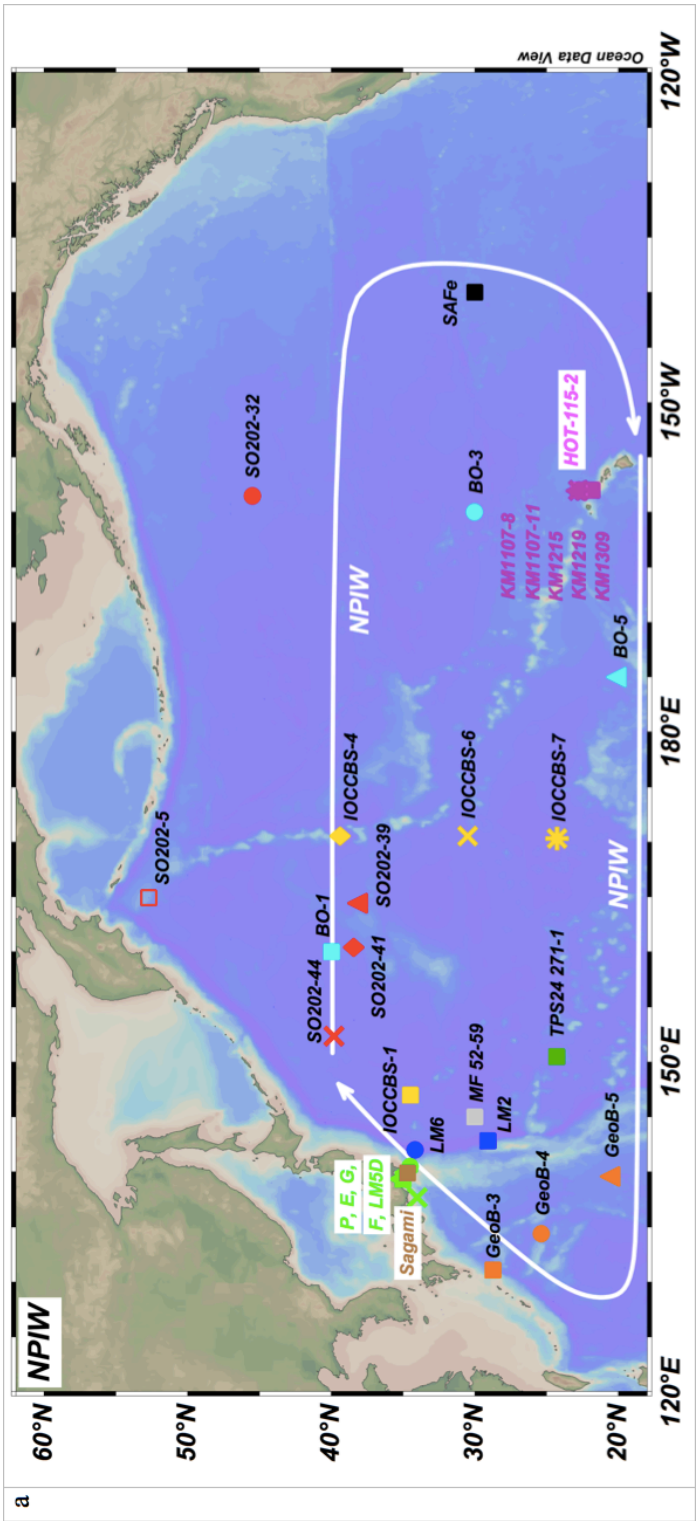

Figure S1. continued

b

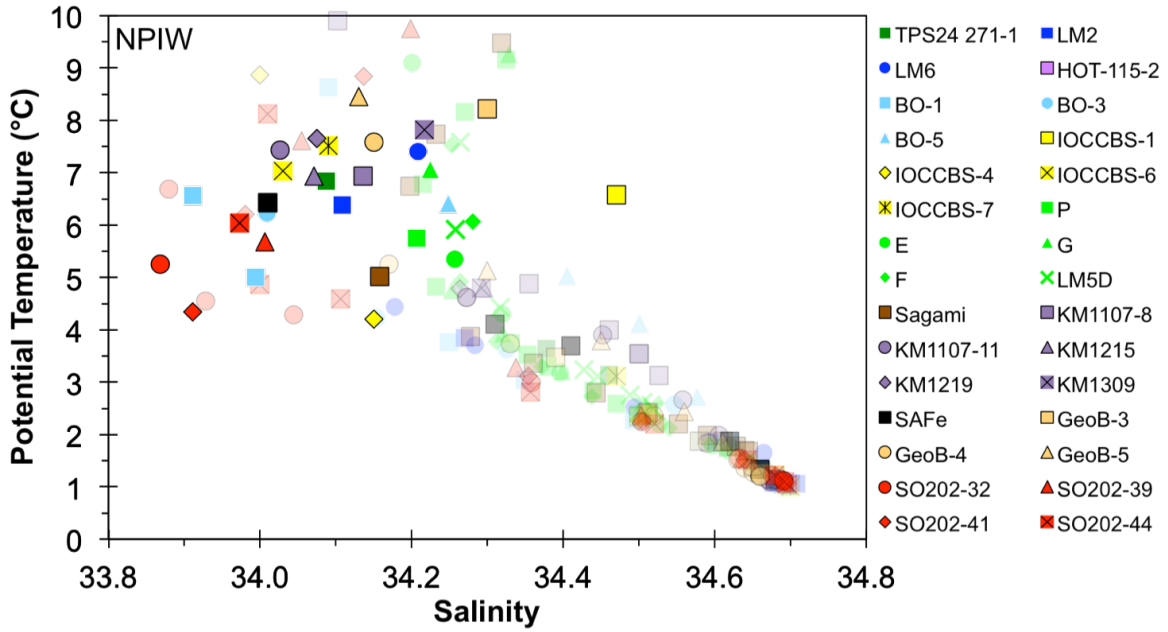


c

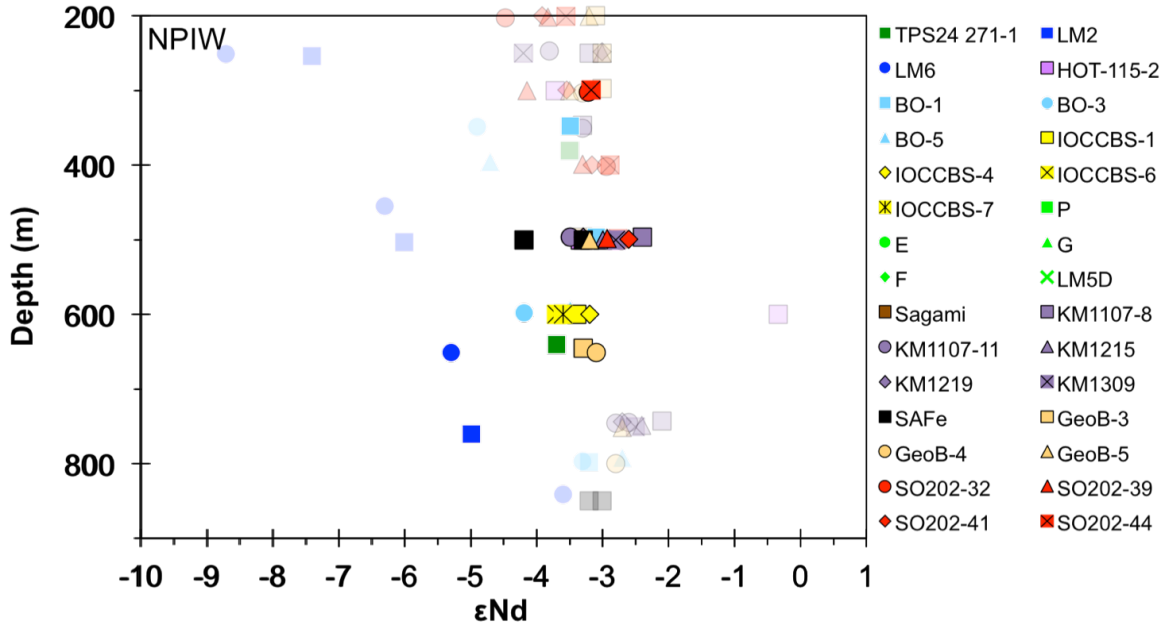

Figure S1. continued

d

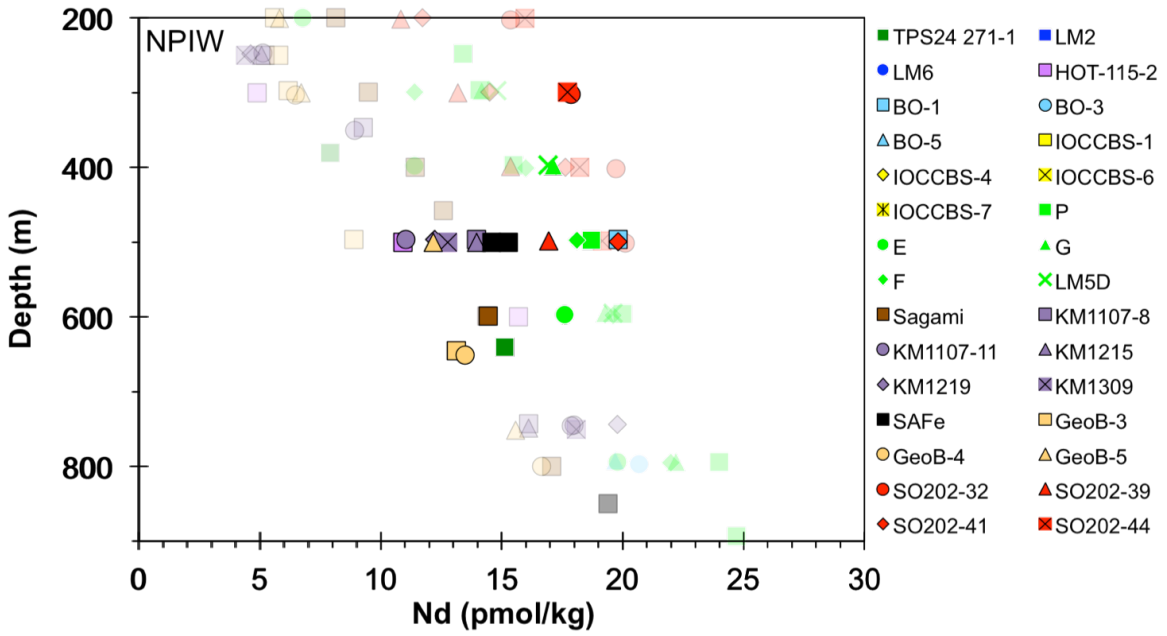


e

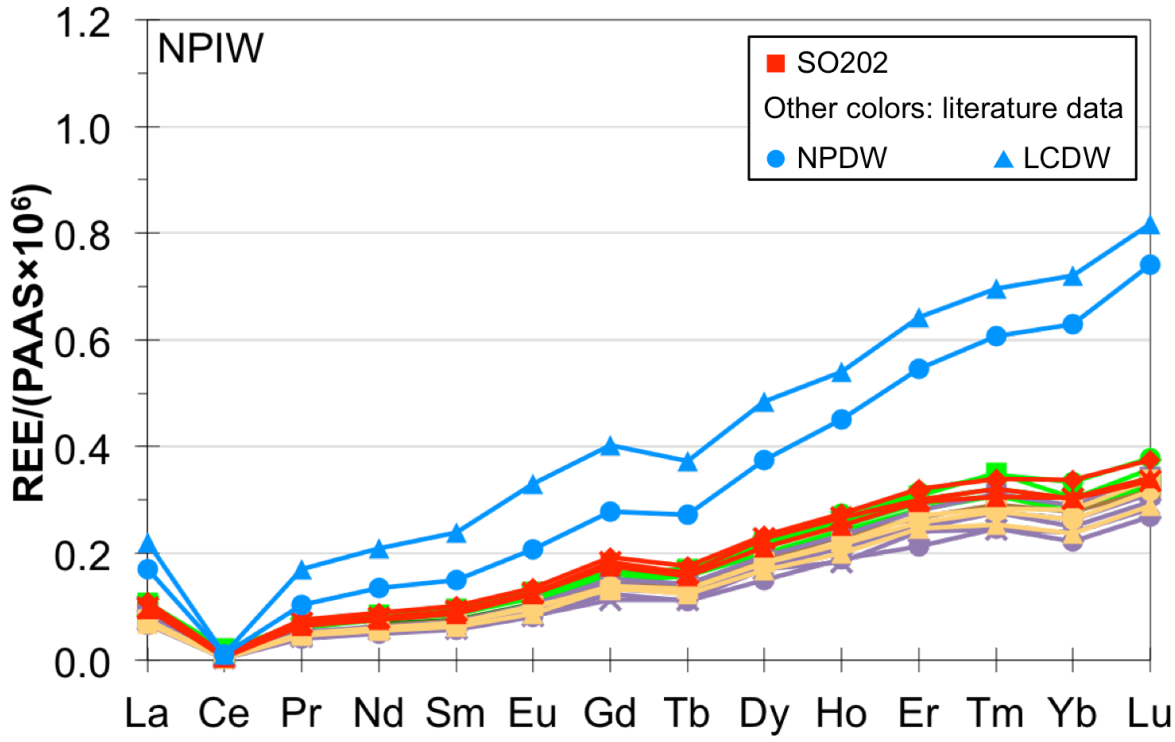

Figure S2. Comparison of εNd and REEs of SO202 stations with published REE data of seawater samples for NPDW

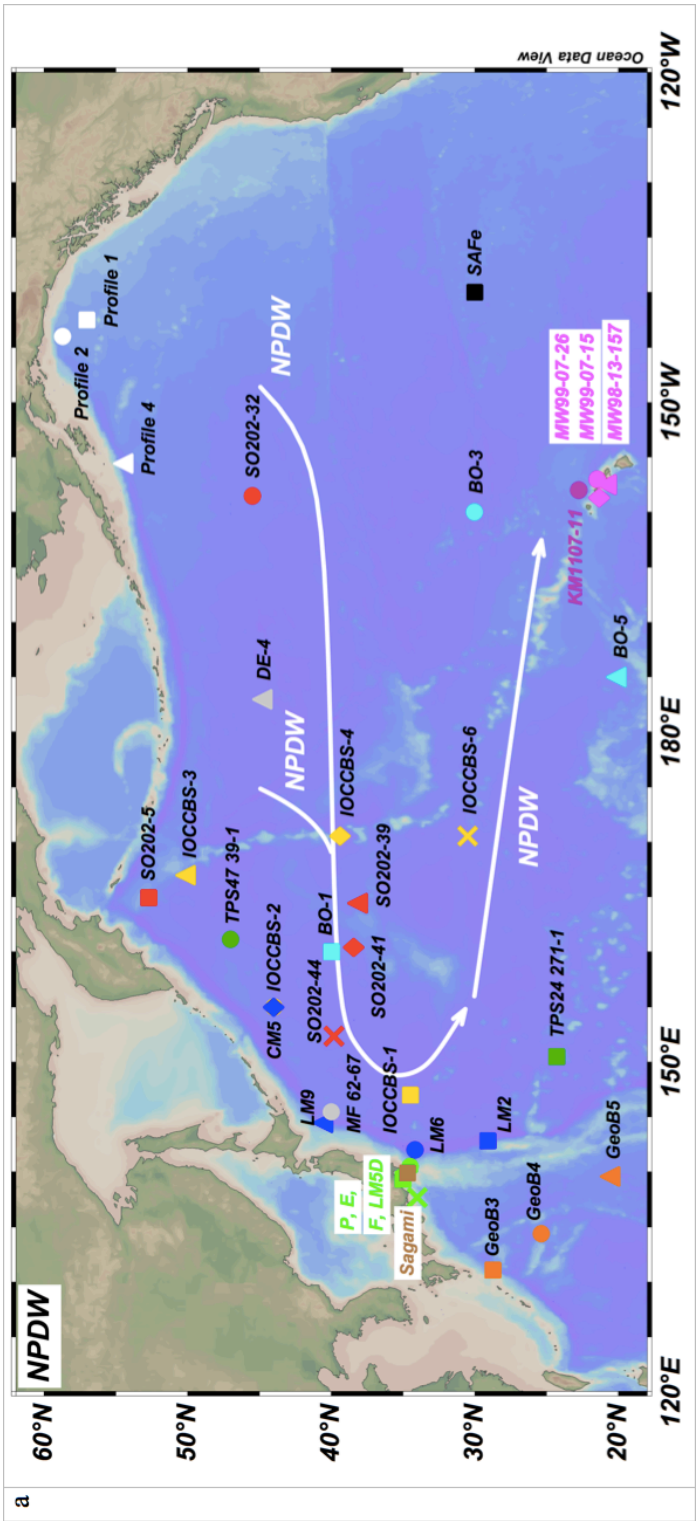

Figure S2. continued

b

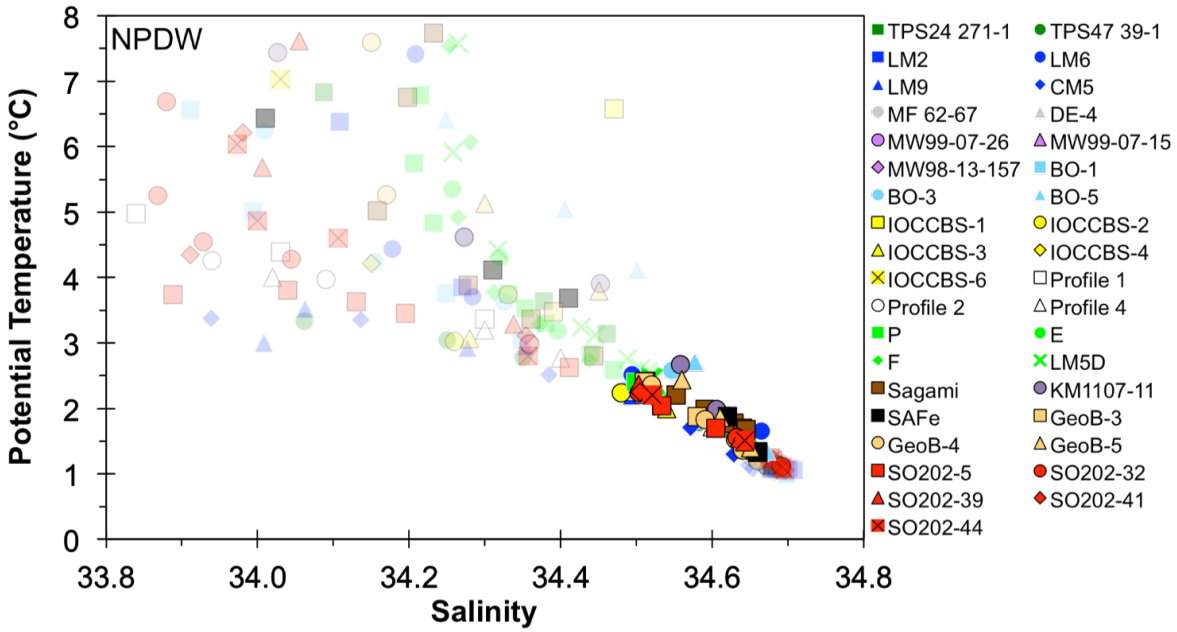


c

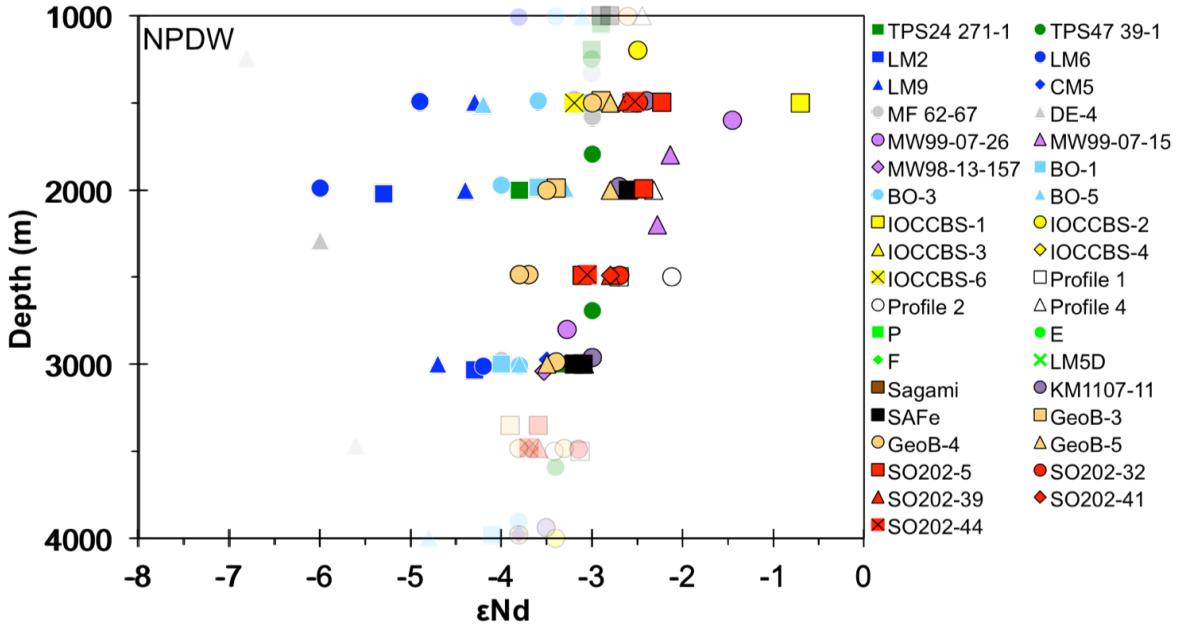

Figure S2. continued

d

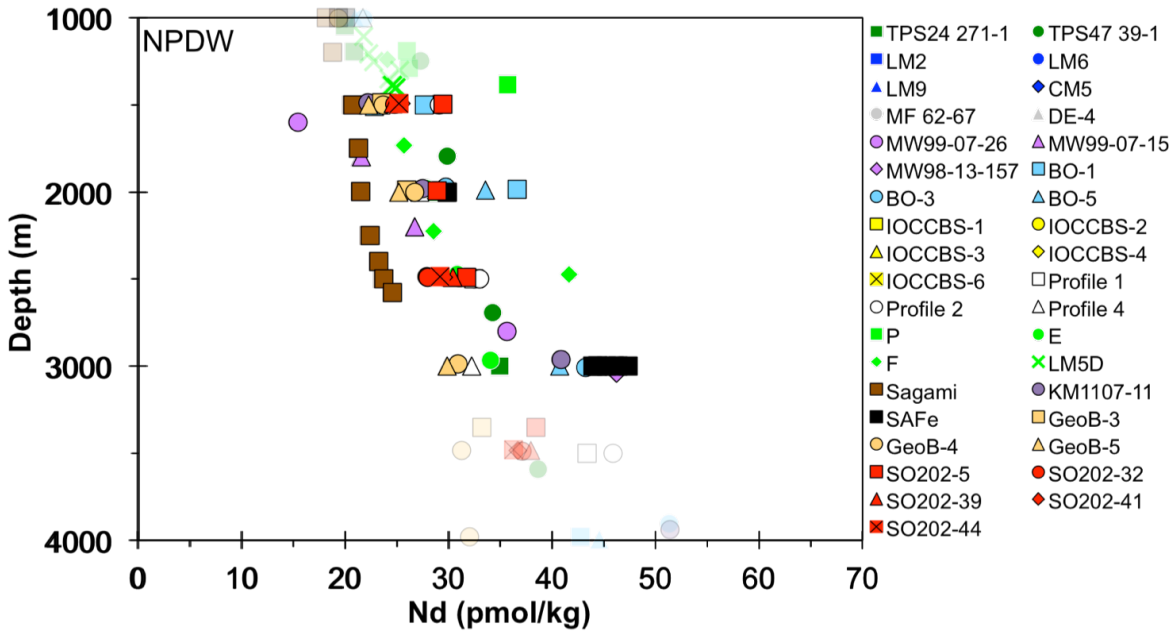


e

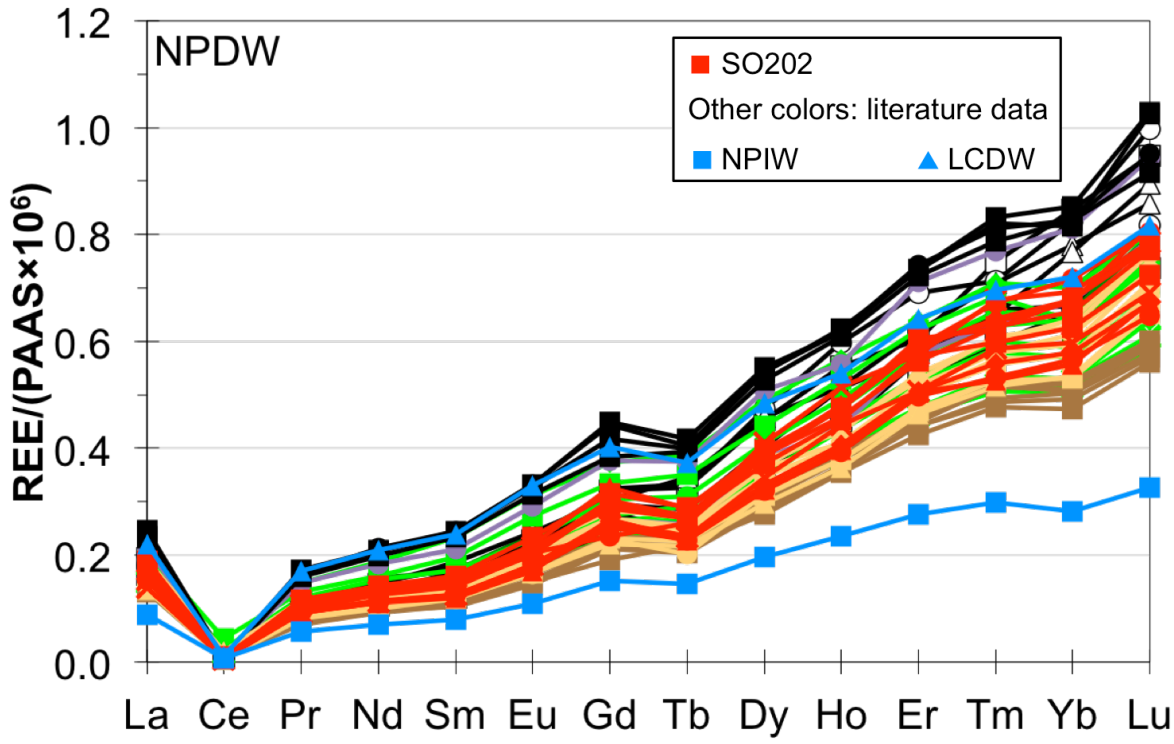

Figure S3. Comparison of εNd and REEs of SO202 stations with published REE data of seawater samples for LCDW

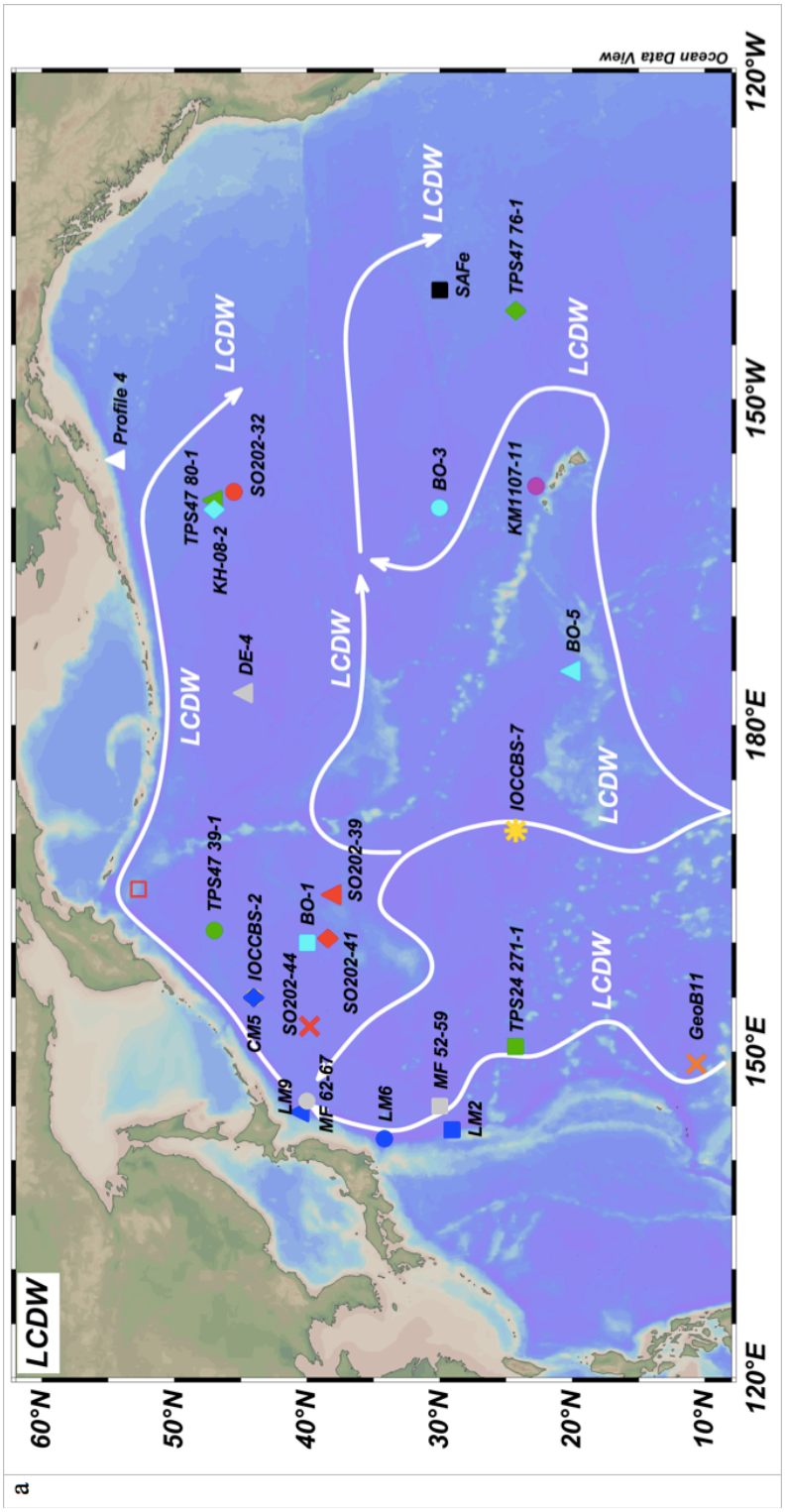

Figure S3. continued

b

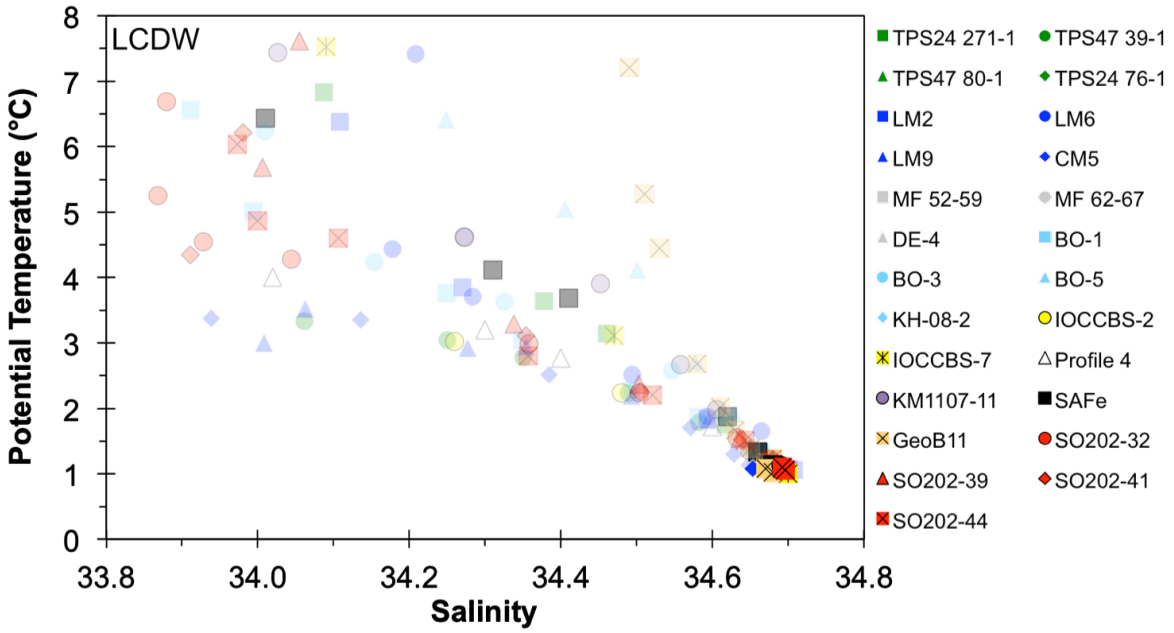


c

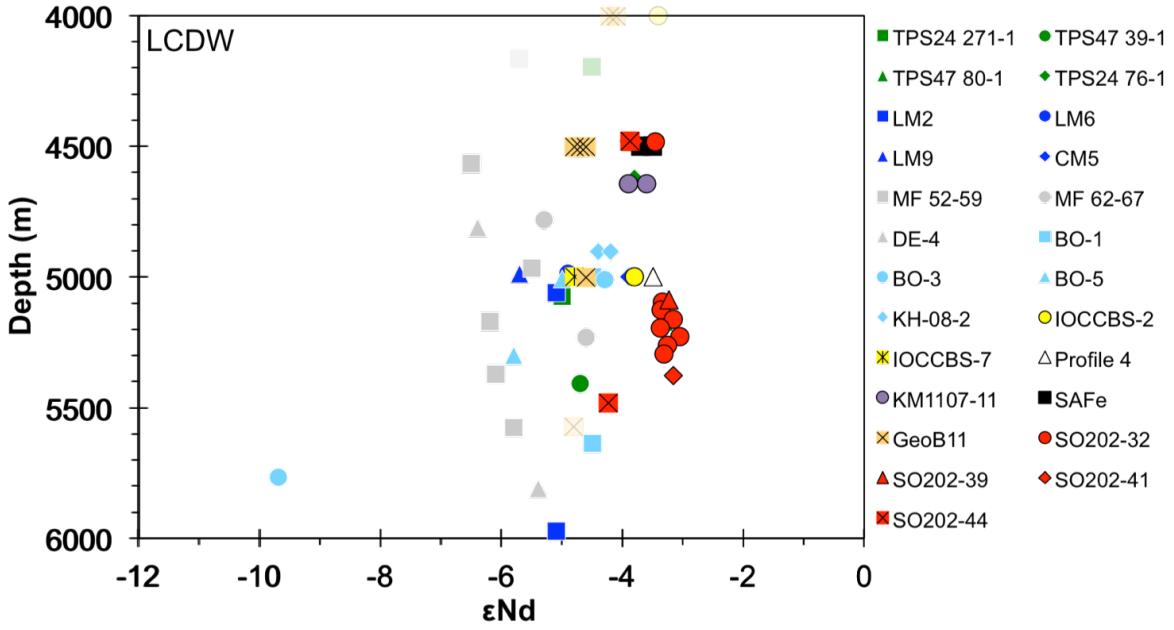

Figure S3. continued

d

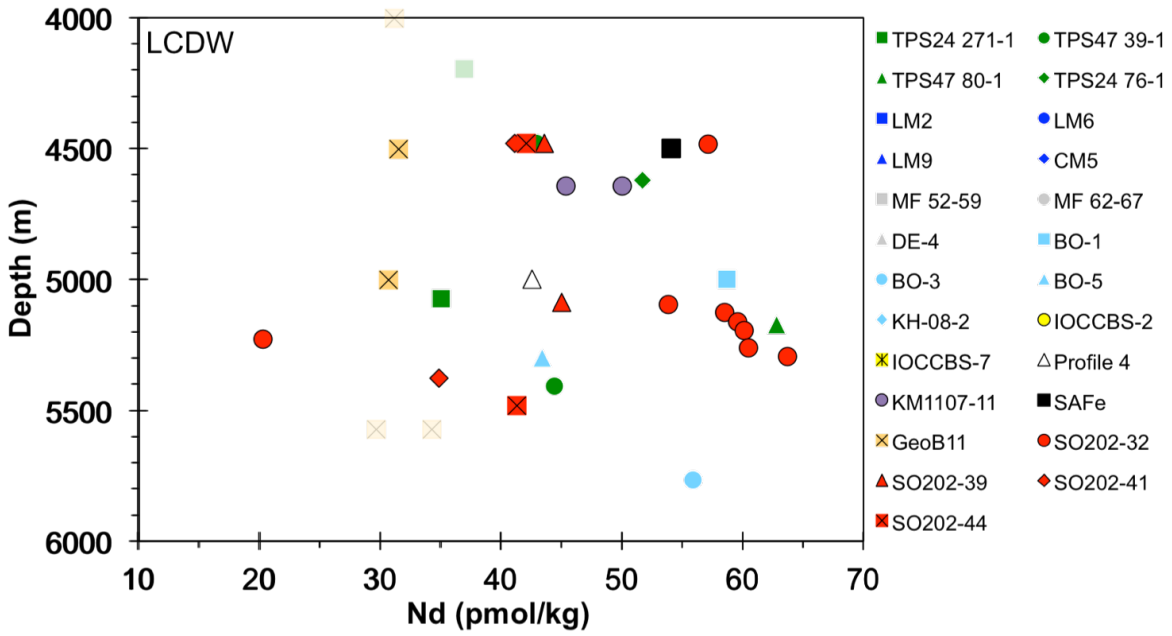


e

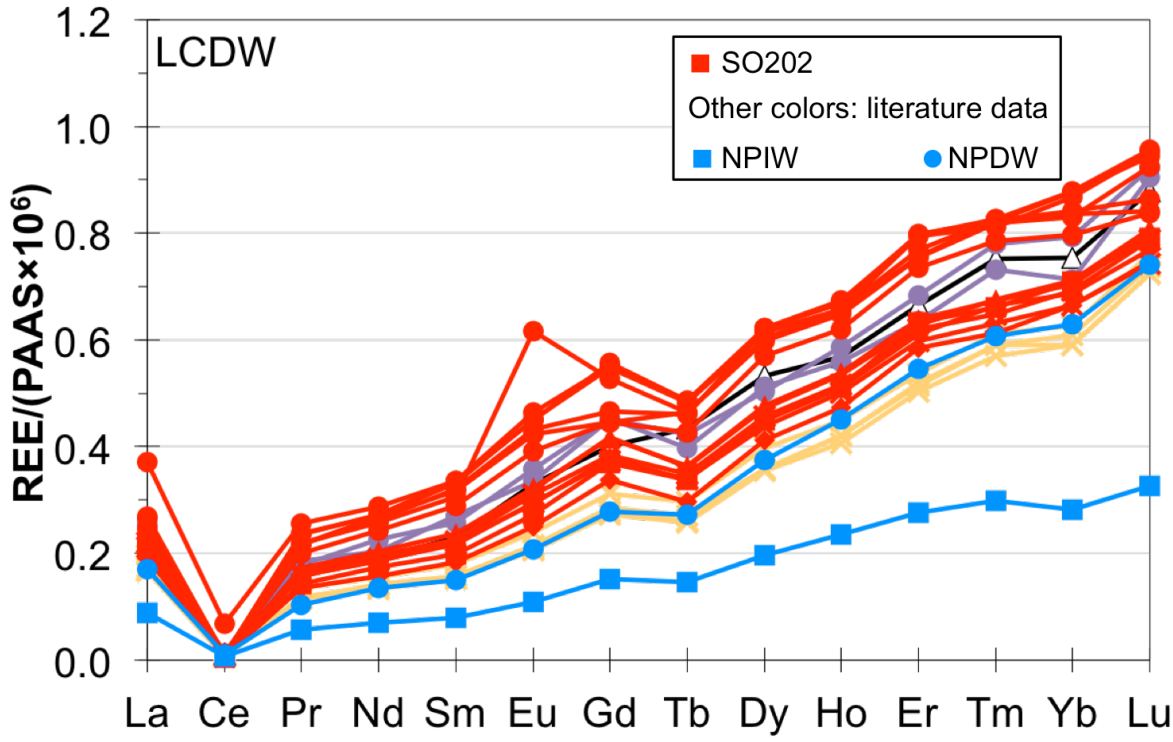

Figure S4. Depth profiles of εNd and [Nd] for near Japan station SO202-41 and a nearby published station

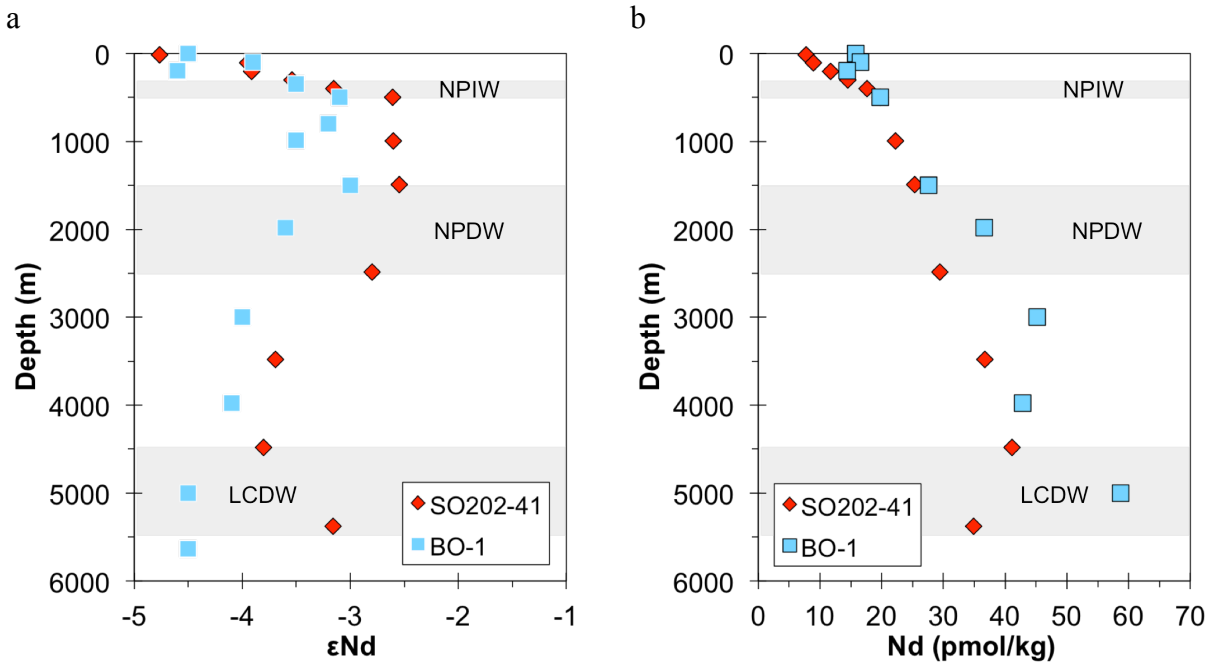

Figure S5. Depth profiles of εNd and [Nd] for Northwest station SO202-5 and nearby published stations

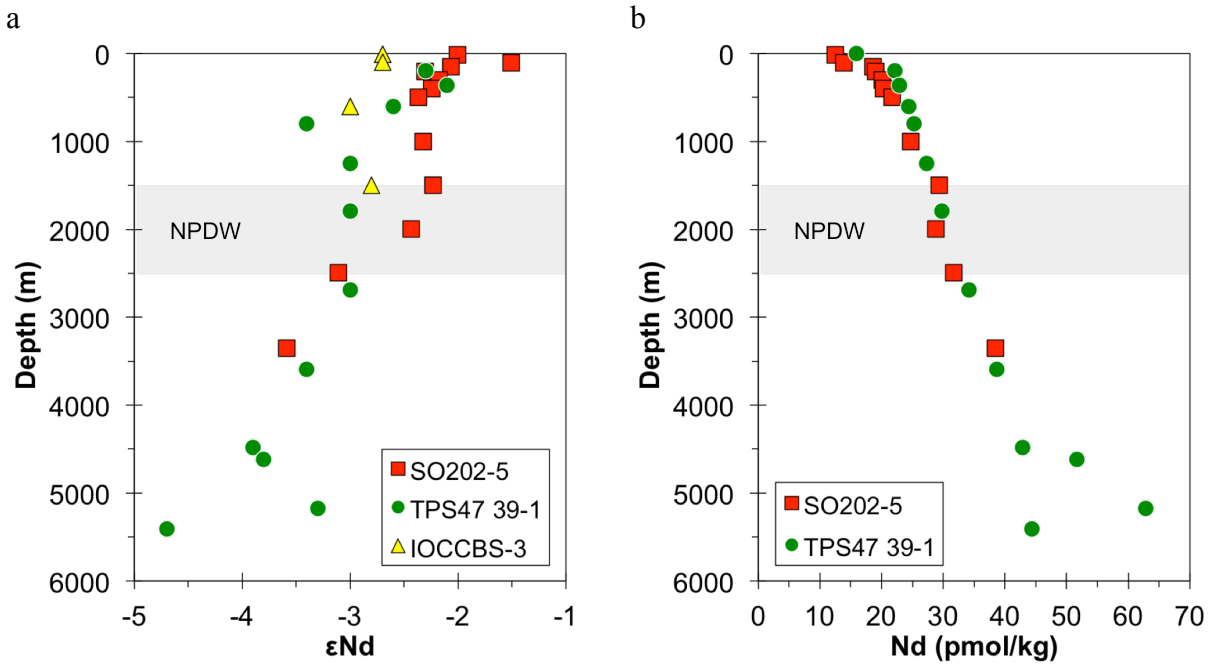

Figure S6. Depth profiles of εNd and [Nd] for Northeast station SO202-32 and nearby published stations

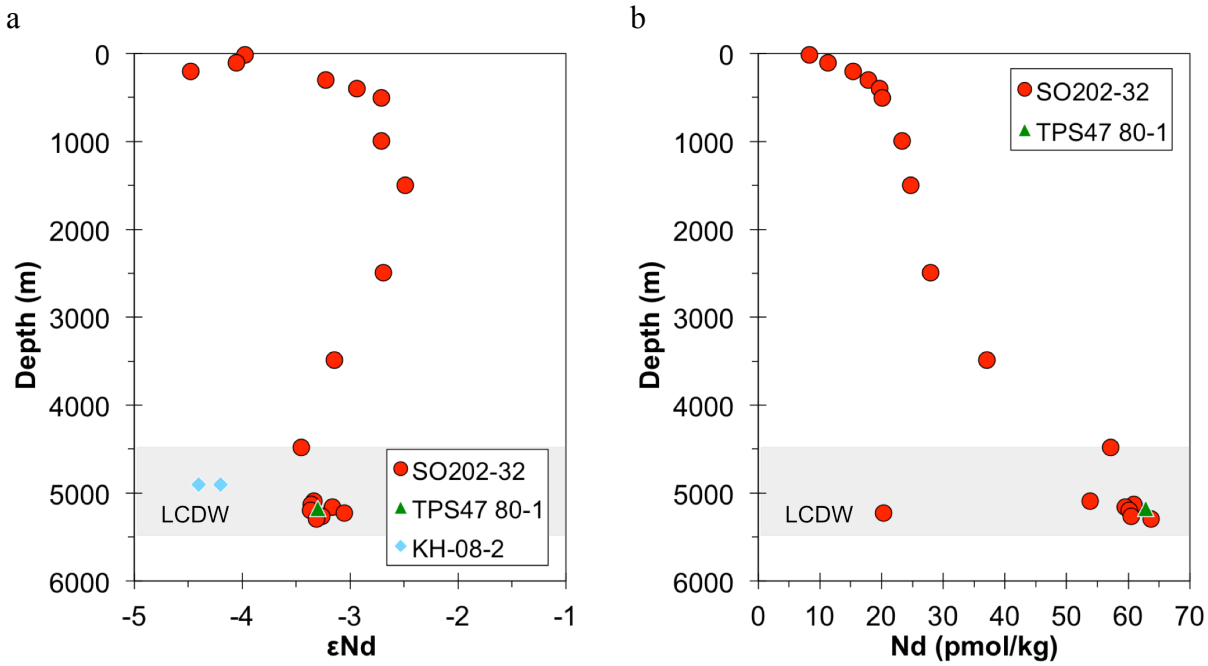

Figure S7. Changes of εNd and REEs along the NPIW pathway

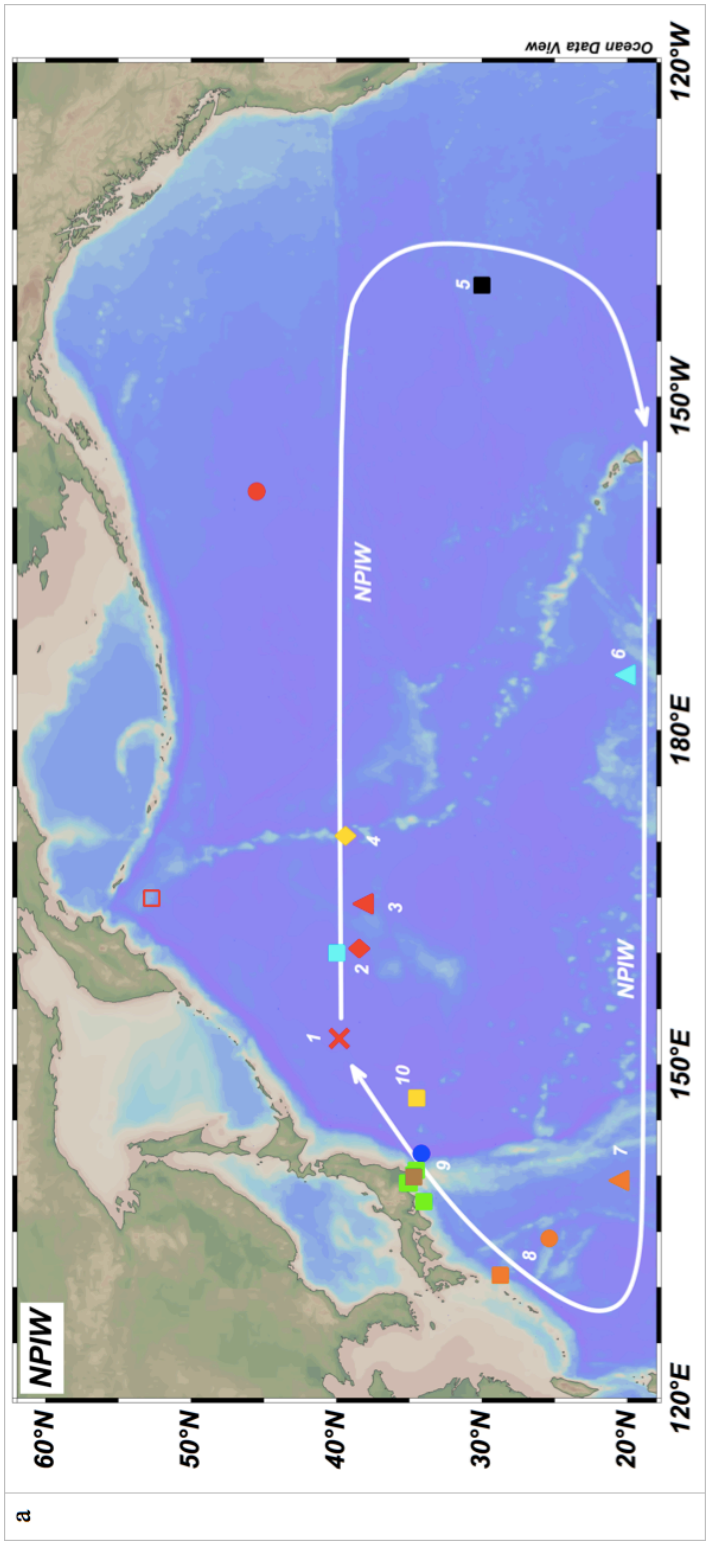

Figure S7. continued

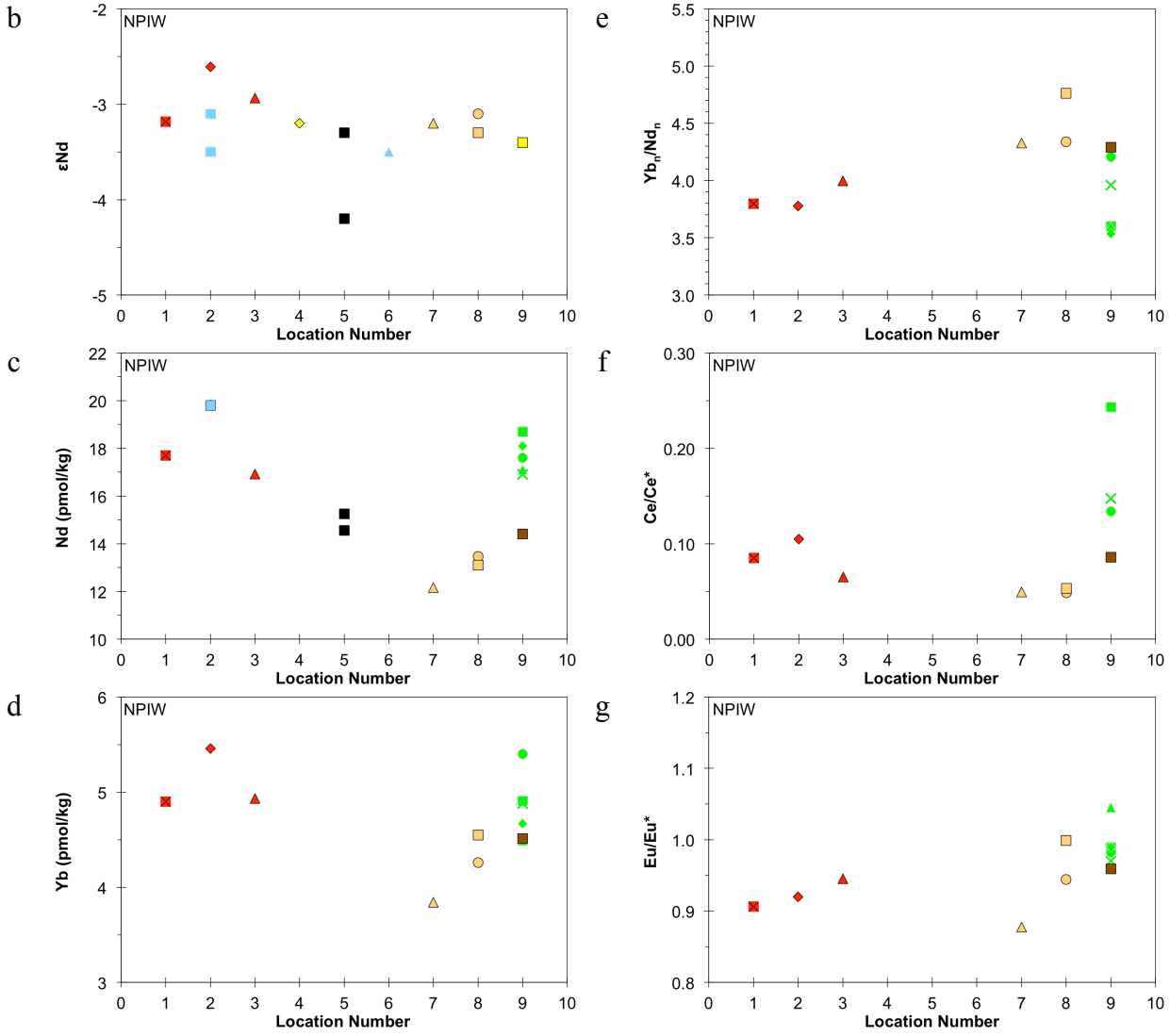

Figure S8. Changes of εNd and REEs along the NPDW pathway

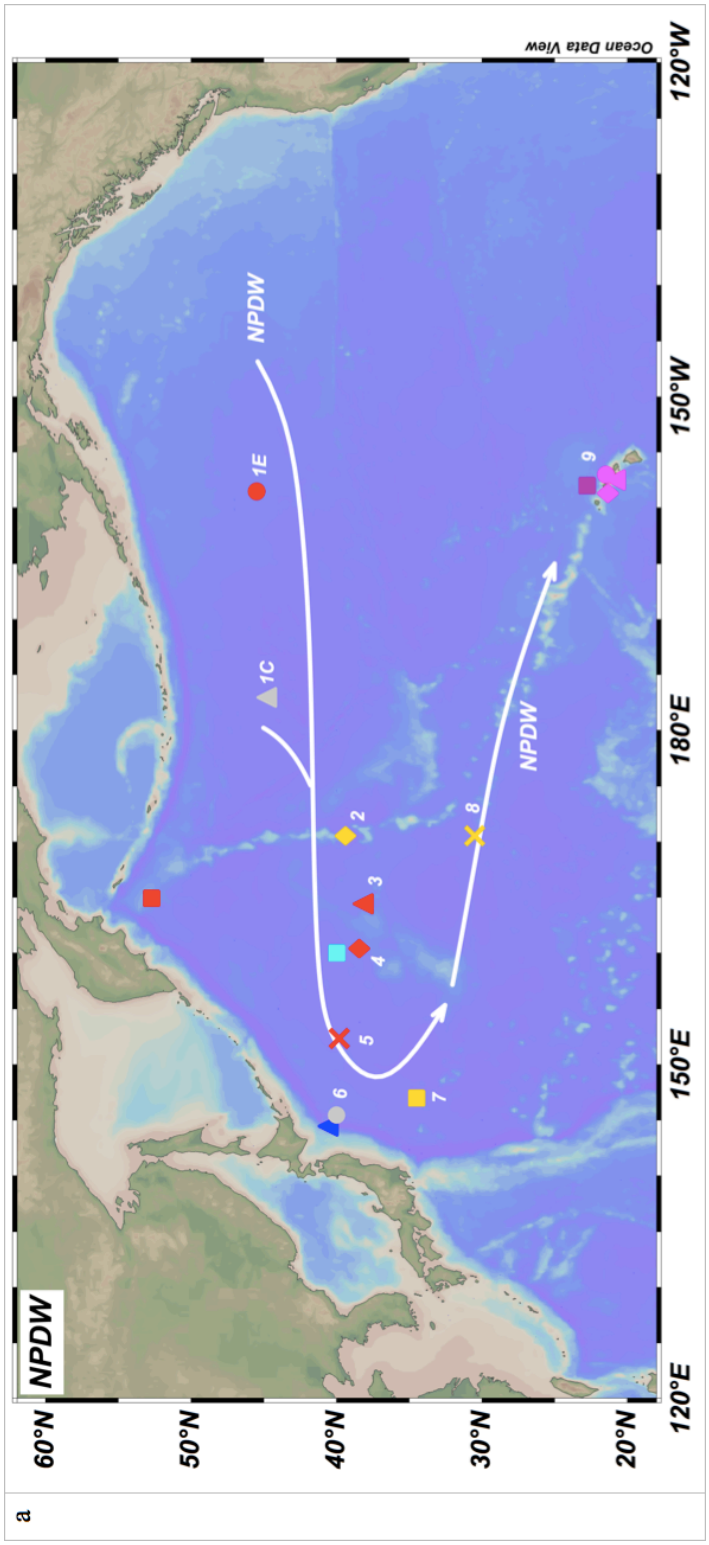

Figure S8. continued

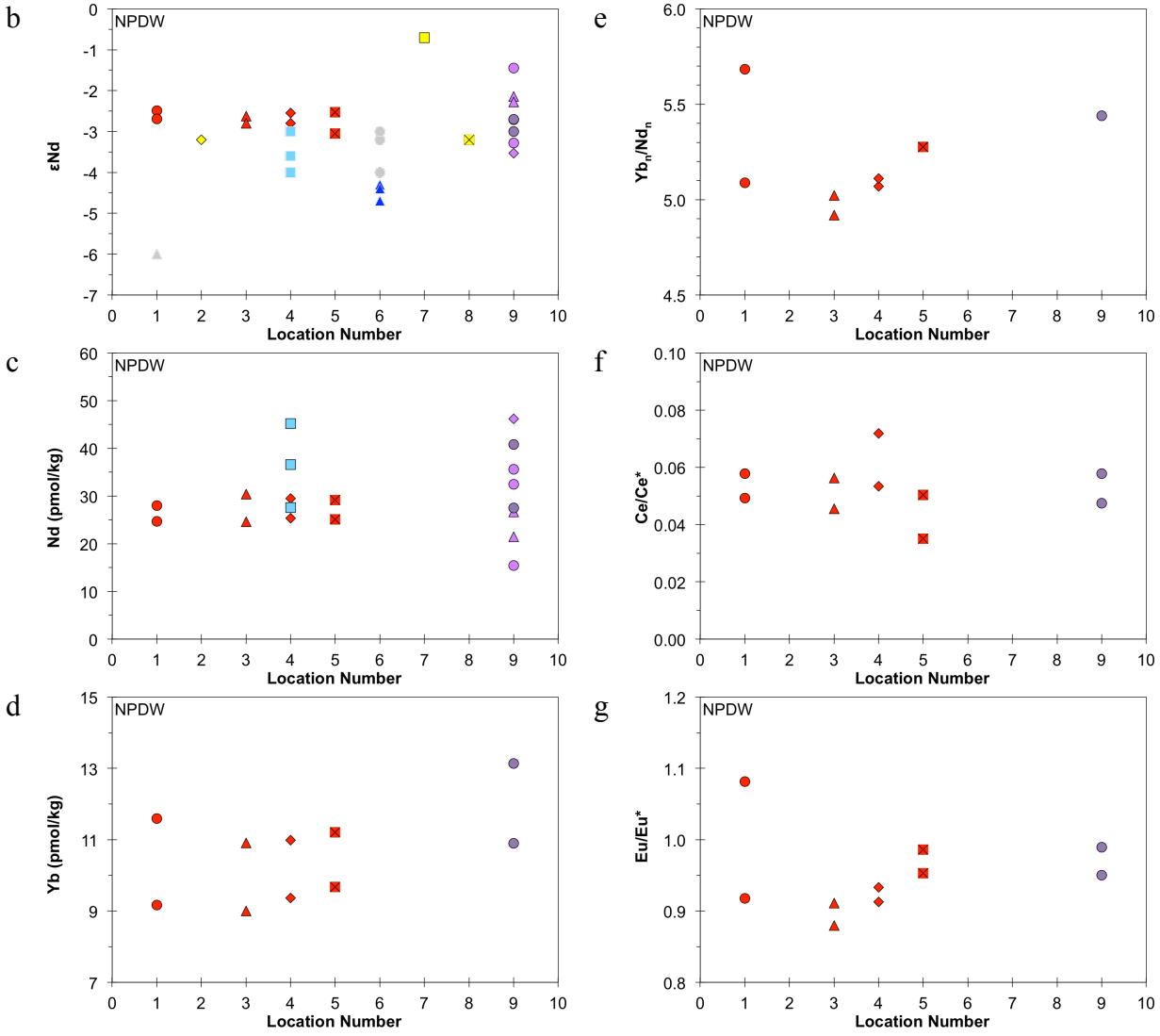

Figure S9. Changes of εNd and REEs along the LCDW pathway

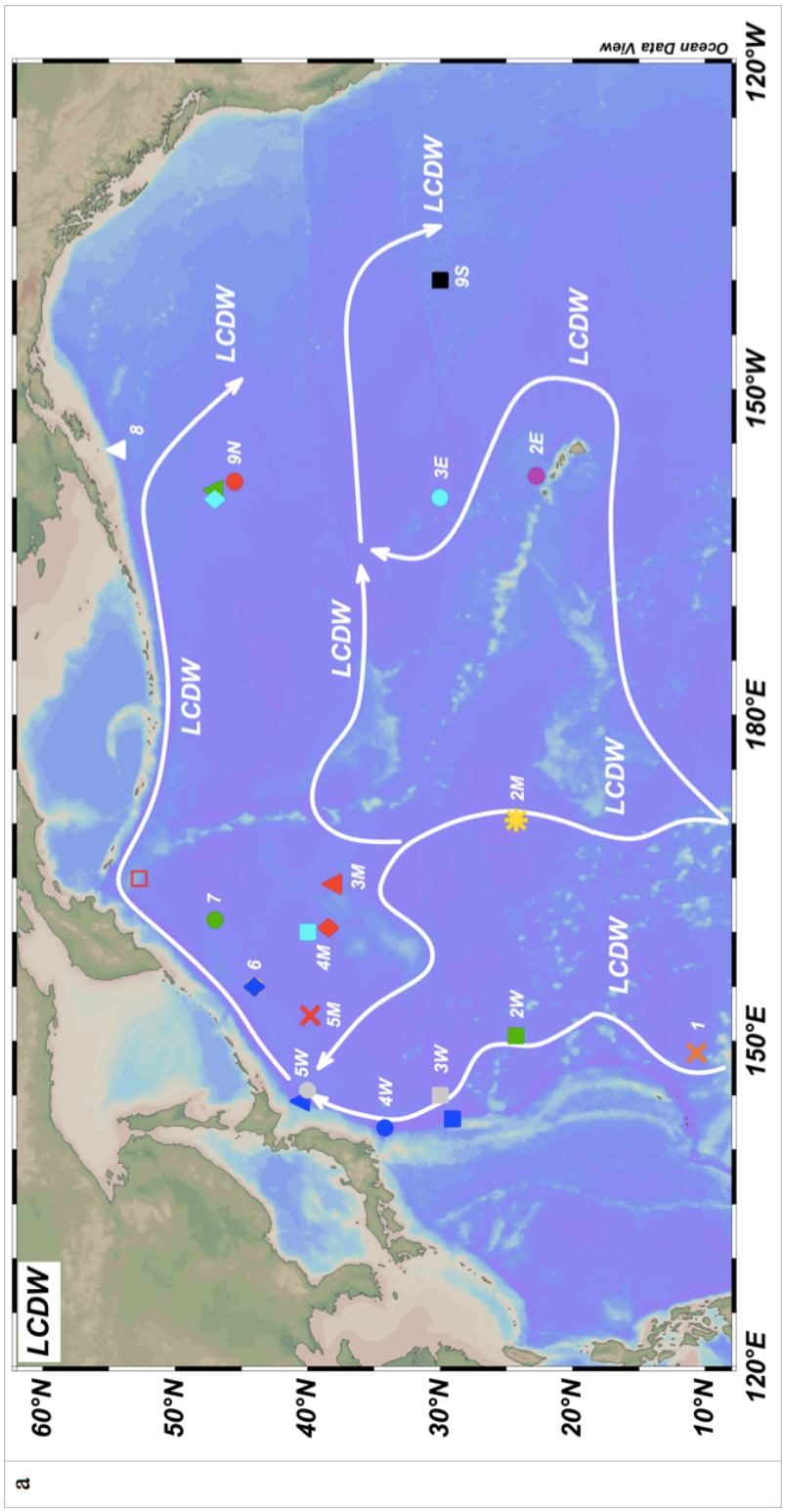

Figure S9. continued

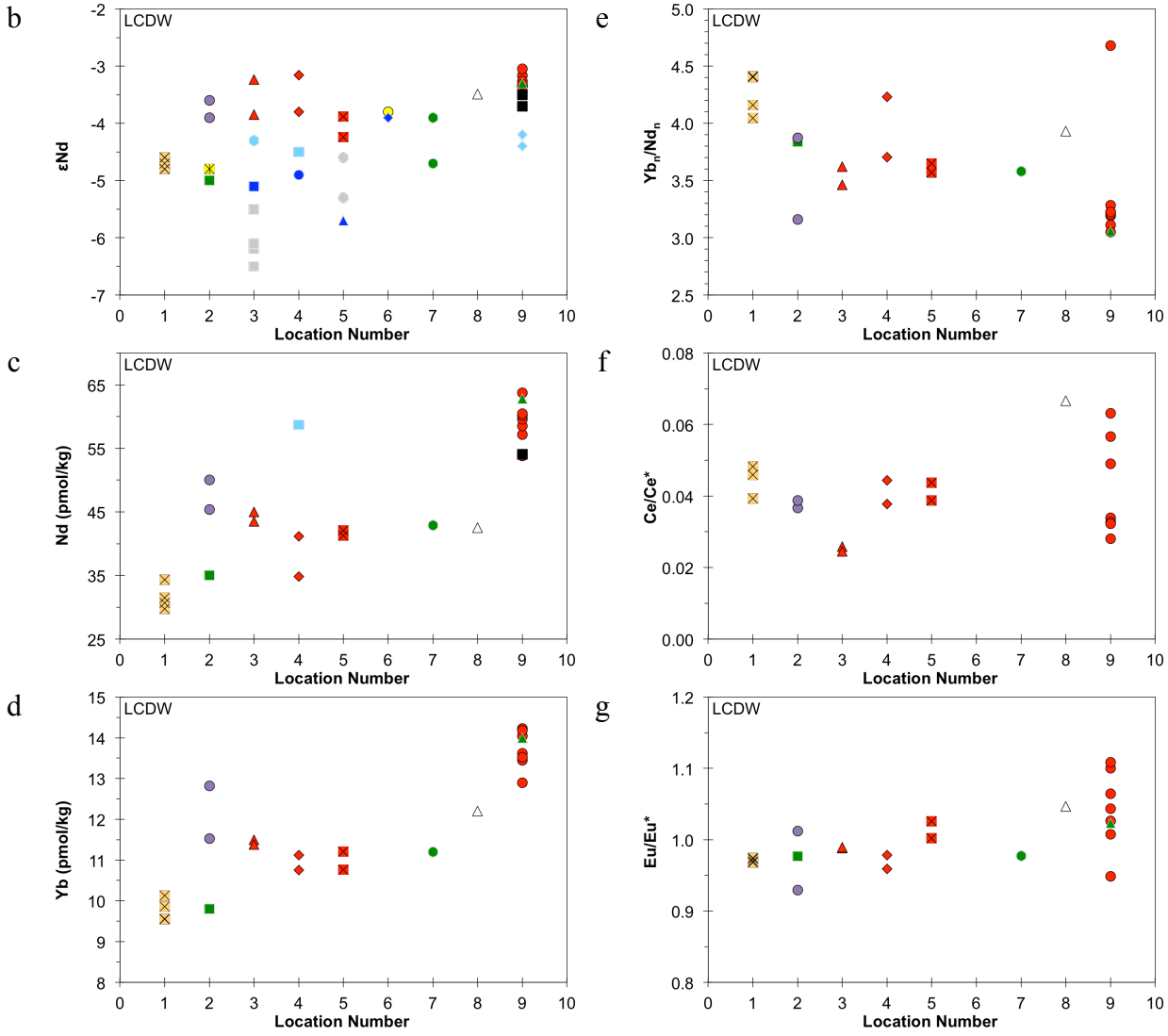

Figure S10. Comparison of εNd, dissolved $^{232}$Th and [Nd] with potential temperature below the depths of NPIW

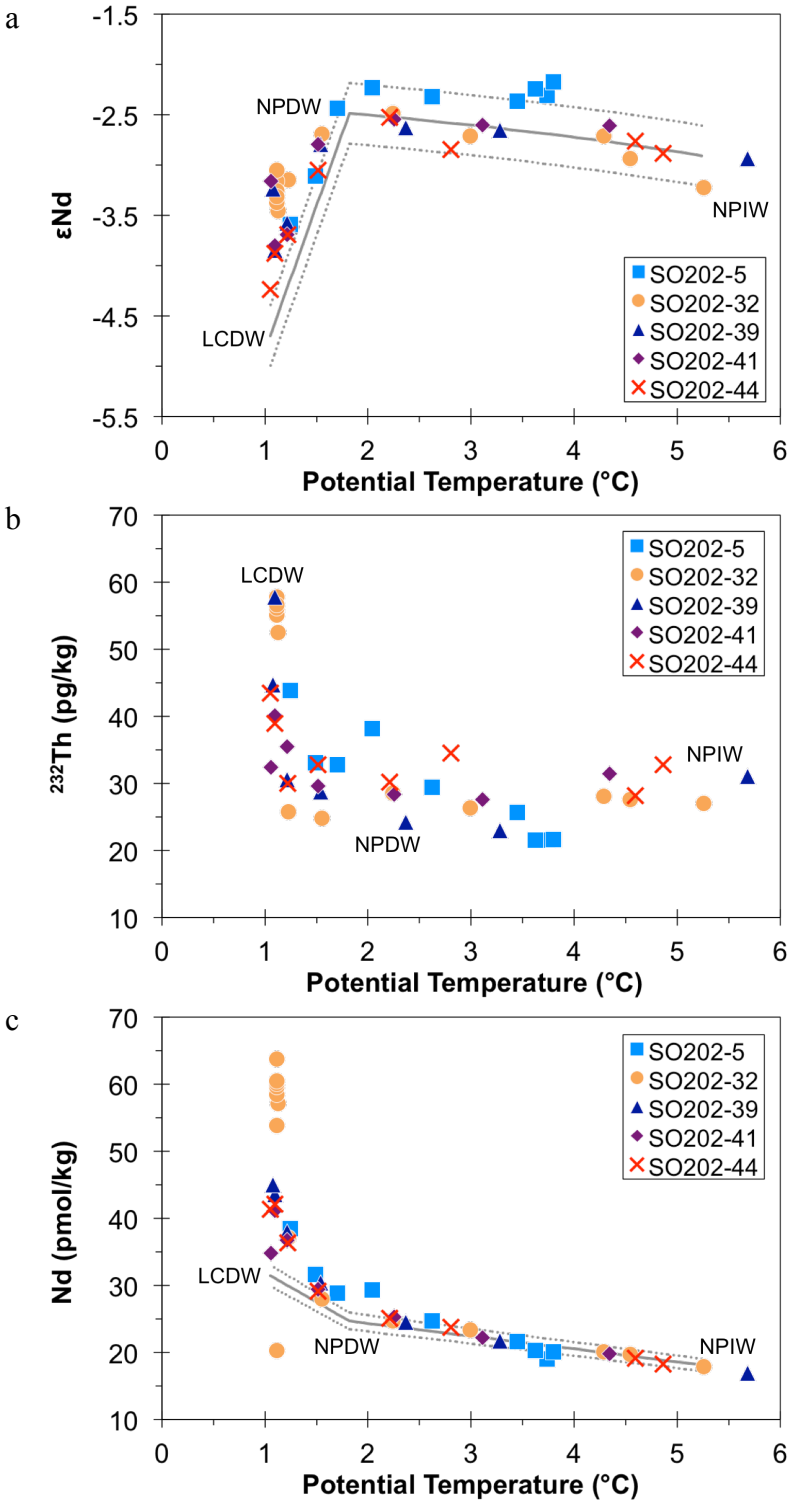

Figure S11. Comparison of REE ratios with potential temperature below the depths of NPIW

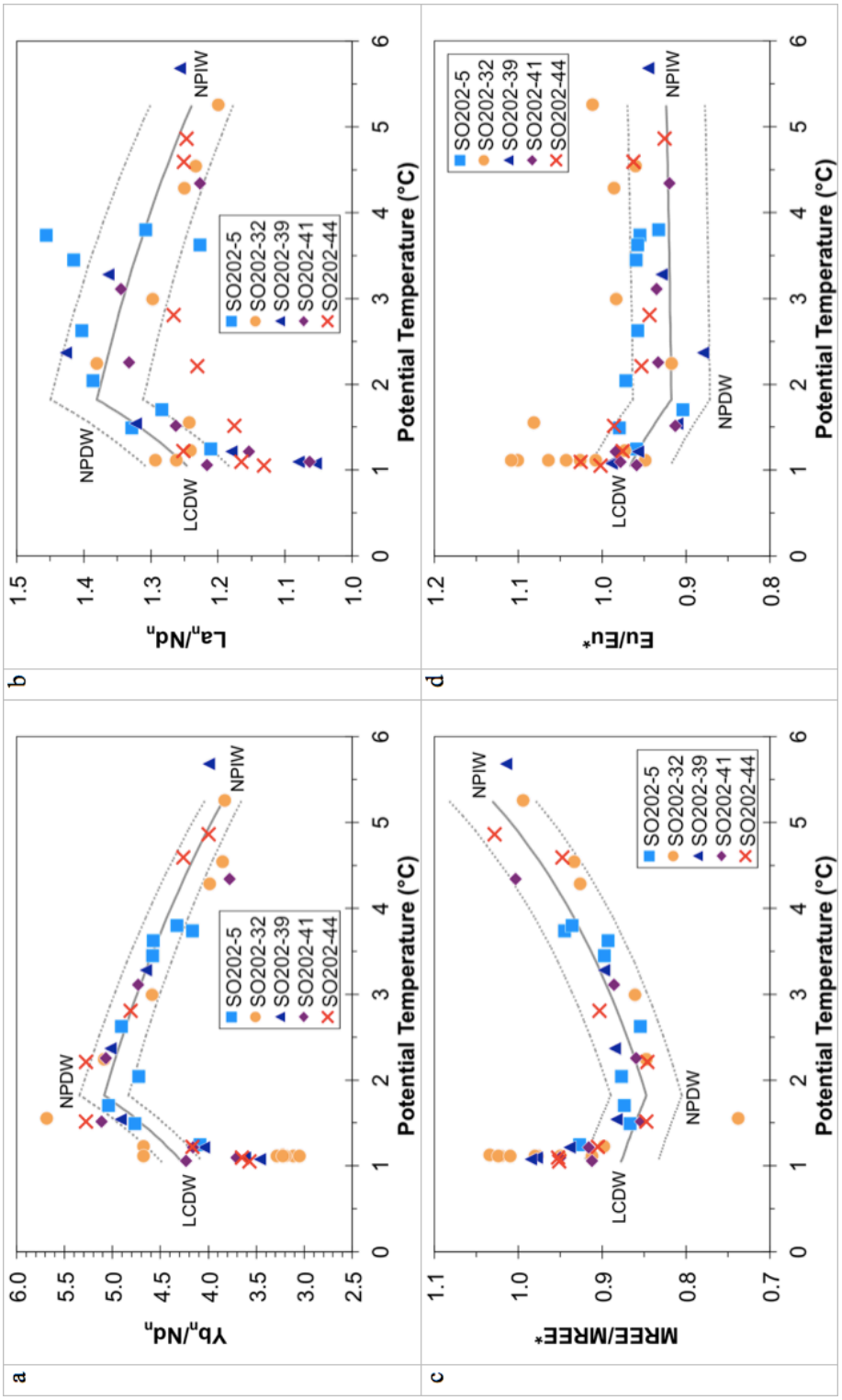

## Appendix 1. Table 1 of Chapter 2

Table 1 of Chapter 2. Data for the 17 seawater profiles collected from the Southwest Atlantic Meridional Transect (SAMT). Sampling location, depth, salinity, potential temperature, neutral density, oxygen concentration, silicate concentration, nutrient concentration, εNd, external 2 standard deviation of εNd, fractional contributions of water masses calculated based on potential temperature and salinity, predicted εNd based on water mass mixing calculations, and ΔεNd-value (= measured εNd – expected εNd).

Table 1. Data for the 17 seawater profiles collected from the Southwest Atlantic Meridional Transect

| Depth | Salinity | Potential Temperature | Neutral Density | Oxygen | Silicate | Nitrate | Phosphate | $PO_4^*$ | εNd | Ext. 2sd | SACW | aAAIW | iAAIW | UCDW | UNADW | MNADW | LNADW | LCDW | AABW | Calculated εNd | ΔεNd |
|---|---|---|---|---|---|---|---|---|---|---|---|---|---|---|---|---|---|---|---|---|---|
| m | | °C | kg/m$^3$ | µmol/kg | µmol/kg | µmol/kg | µmol/kg | µmol/kg | | | | | | | | | | | | | |
| Station 1 (-49.55°N -52.69°E) | | | | | | | | | | | | | | | | | | | | | |
| 2312 | 34.72 | 1.11 | 28.12 | 203.2 | 107.95 | 32.21 | 2.19 | 1.40 | -8.60 | 0.26 | | | | | | | | 100.0% | | -8.50 | -0.10 |
| 2248 | 34.72 | 1.19 | 28.11 | 200.6 | 106.38 | 32.29 | 2.19 | 1.39 | -8.48 | 0.26 | | | | | | | | 100.0% | | -8.50 | 0.02 |
| 2123 | 34.72 | 1.53 | 28.05 | 191.3 | 100.10 | 32.50 | 2.21 | 1.36 | -8.29 | 0.26 | | | | 24.5% | | 8.9% | | 66.6% | | -8.76 | 0.46 |
| 1874 | 34.70 | 1.79 | 27.99 | 184.0 | 94.49 | 32.91 | 2.24 | 1.34 | -8.02 | 0.26 | | | | 43.2% | | 12.3% | | 44.5% | | -8.84 | 0.82 |
| 1497 | 34.67 | 2.03 | 27.93 | 177.4 | 87.45 | 33.58 | 2.29 | 1.35 | -8.04 | 0.26 | | | | 70.8% | | 8.9% | | 20.2% | | -8.59 | 0.55 |
| 1248 | 34.62 | 2.21 | 27.87 | 175.0 | 81.01 | 34.28 | 2.34 | 1.39 | -7.96 | 0.26 | | | | 100.0% | | | | | | -8.00 | 0.04 |
| 987 | 34.53 | 2.41 | 27.78 | 176.5 | 72.08 | 34.95 | 2.37 | 1.43 | -7.75 | 0.26 | | 16.2% | | 83.8% | | | | | | -8.01 | 0.26 |
| 902 | 34.50 | 2.49 | 27.75 | 179.5 | 68.64 | 34.94 | 2.38 | 1.45 | -8.20 | 0.26 | | 21.5% | | 78.5% | | | | | | -8.02 | -0.19 |
| 800 | 34.44 | 2.59 | 27.69 | 186.1 | 62.53 | 34.82 | 2.36 | 1.47 | -7.92 | 0.26 | | 30.8% | | 69.2% | | | | | | -8.02 | 0.10 |
| 701 | 34.39 | 2.68 | 27.63 | 196.6 | 55.74 | 34.35 | 2.33 | 1.50 | -7.88 | 0.26 | | 41.0% | | 59.0% | | | | | | -8.03 | 0.15 |
| 599 | 34.32 | 2.65 | 27.58 | 212.3 | 48.90 | 33.63 | 2.27 | 1.54 | -7.97 | 0.26 | | 52.1% | | 47.9% | | | | | | -8.04 | 0.07 |
| 500 | 34.21 | 2.36 | 27.52 | 245.4 | 38.31 | 32.23 | 2.18 | 1.63 | -8.16 | 0.28 | | 72.4% | | 27.6% | | | | | | -8.06 | -0.10 |
| 300 | 34.09 | 2.78 | 27.36 | 282.3 | 22.78 | 29.10 | 1.96 | 1.63 | -8.04 | 0.26 | | 92.3% | | 7.7% | | | | | | -8.09 | 0.05 |
| 250 | 34.07 | 2.96 | 27.32 | 294.5 | 18.85 | 28.04 | 1.89 | 1.63 | -8.09 | 0.26 | | 100.0% | | | | | | | | -8.10 | 0.01 |
| 100 | 34.03 | 4.71 | 27.07 | 306.9 | 5.69 | 22.52 | 1.66 | 1.46 | -8.15 | 0.26 | | | | | | | | | | | |
| 24 | 34.00 | 9.51 | 26.29 | 295.7 | 0.00 | 13.06 | 1.03 | 0.77 | -7.52 | 0.26 | | | | | | | | | | | |
| Station 2 (-48.97°N -48.88°E) | | | | | | | | | | | | | | | | | | | | | |
| 5797 | 34.67 | -0.14 | 28.30 | 231.1 | 125.74 | 33.03 | 2.31 | 1.68 | -8.10 | 0.26 | | | | | | | | | 100.0% | -8.00 | -0.10 |
| 5497 | 34.67 | -0.12 | 28.29 | 230.7 | 125.35 | 32.97 | 2.30 | 1.67 | -8.12 | 0.26 | | | | | | | | 2.9% | 97.1% | -8.01 | -0.12 |
| 5000 | 34.67 | -0.08 | 28.28 | 228.0 | 124.84 | 32.98 | 2.29 | 1.64 | -8.13 | 0.26 | | | | | | | | 6.0% | 94.0% | -8.02 | -0.11 |
| 4001 | 34.69 | 0.24 | 28.24 | 219.4 | 119.73 | 32.65 | 2.26 | 1.57 | -8.27 | 0.26 | | | | | | | | 31.3% | 68.7% | -8.10 | -0.16 |
| 3004 | 34.73 | 1.06 | 28.14 | 205.0 | 103.77 | 31.59 | 2.18 | 1.40 | -8.60 | 0.26 | | | | | | | | 95.5% | 4.5% | -8.46 | -0.14 |
| 2509 | 34.75 | 1.57 | 28.07 | 199.6 | 92.09 | 30.93 | 2.12 | 1.31 | -8.98 | 0.31 | | | | 14.6% | | 18.1% | | 67.4% | | -9.14 | 0.16 |
| 2007 | 34.73 | 1.98 | 27.99 | 187.9 | 84.92 | 31.48 | 2.17 | 1.29 | -8.49 | 0.31 | | | | 44.5% | | 23.5% | | 32.1% | | -9.32 | 0.83 |
| 1504 | 34.69 | 2.47 | 27.90 | 184.6 | 70.97 | 31.90 | 2.18 | 1.29 | -8.62 | 0.31 | | | | 79.2% | | 20.8% | | | | -9.13 | 0.51 |
| 1253 | 34.63 | 2.68 | 27.83 | 182.6 | 63.95 | 32.60 | 2.23 | 1.33 | -8.87 | 0.31 | | | | 98.4% | | 1.6% | | | | -8.09 | -0.77 |
| 1003 | 34.51 | 2.69 | 27.73 | 182.4 | 61.96 | 34.04 | 2.34 | 1.43 | -8.32 | 0.31 | | 18.7% | | 81.3% | | | | | | -8.01 | -0.31 |
| 746 | 34.37 | 2.85 | 27.60 | 200.5 | 49.82 | 33.64 | 2.32 | 1.51 | -7.80 | 0.31 | | 43.5% | | 56.5% | | | | | | -8.04 | 0.24 |
| 497 | 34.21 | 3.00 | 27.45 | 241.1 | 31.69 | 31.18 | 2.12 | 1.55 | -7.94 | 0.31 | | 72.4% | | 27.6% | | | | | | -8.06 | 0.12 |
| 400 | 34.11 | 2.87 | 27.37 | 272.5 | 24.04 | 29.38 | 1.99 | 1.60 | -7.98 | 0.31 | | 88.8% | | 11.2% | | | | | | -8.08 | 0.11 |
| 248 | 34.06 | 3.28 | 27.28 | 300.3 | 14.95 | 26.64 | 1.83 | 1.59 | -8.08 | 0.31 | | 100.0% | | | | | | | | -8.10 | 0.02 |
| 99 | 33.99 | 5.05 | 26.99 | 304.2 | 4.11 | 21.27 | 1.61 | 1.39 | -8.22 | 0.26 | | | | | | | | | | | |

Table 1. continued

| Depth | Salinity | Potential Temperature | Neutral Density | Oxygen | Silicate | Nitrate | Phosphate | $PO_4^*$ | εNd | Ext. 2sd | SACW | aAAIW | iAAIW | UCDW | UNADW | MNADW | LNADW | LCDW | AABW | Calculated εNd | ΔεNd |
|---|---|---|---|---|---|---|---|---|---|---|---|---|---|---|---|---|---|---|---|---|---|
| m | | °C | $kg/m^3$ | µmol/kg | µmol/kg | µmol/kg | µmol/kg | µmol/kg | | | | | | | | | | | | | |
| 25 | 33.97 | 9.71 | 26.21 | 296.8 | 0.00 | 14.35 | 1.07 | 0.82 | -11.34 | 0.31 | | | | | | | | | | | |
| Station 3 (-46.93°N -47.22°E) | | | | | | | | | | | | | | | | | | | | | |
| 5715 | 34.67 | -0.16 | 28.30 | 229.3 | 126.90 | 32.95 | 2.26 | 1.62 | -8.12 | 0.30 | | | | | | | | | 100.0% | -8.00 | -0.12 |
| 5501 | 34.67 | -0.13 | 28.29 | 228.5 | 126.23 | 33.00 | 2.24 | 1.60 | -7.92 | 0.24 | | | | | | | | 2.1% | 97.9% | -8.01 | 0.09 |
| 4500 | 34.68 | 0.17 | 28.24 | 221.5 | 120.57 | 32.62 | 2.23 | 1.55 | -8.38 | 0.13 | | | | | | | | 25.9% | 74.1% | -8.08 | -0.30 |
| 4001 | 34.71 | 0.59 | 28.20 | 214.3 | 112.56 | 32.02 | 2.18 | 1.46 | -8.61 | 0.13 | | | | | | | | 58.5% | 41.5% | -8.22 | -0.38 |
| 3001 | 34.77 | 1.73 | 28.06 | 207.8 | 81.52 | 29.10 | 1.97 | 1.20 | -9.34 | 0.30 | | | | 12.1% | | 29.9% | | 58.0% | | -9.62 | 0.28 |
| 2502 | 34.83 | 2.50 | 28.00 | 218.4 | 55.23 | 25.91 | 1.74 | 1.04 | -10.59 | 0.30 | | | | 29.5% | | 65.5% | | 5.0% | | -11.16 | 0.57 |
| 2001 | 34.73 | 2.56 | 27.91 | 192.5 | 65.65 | 30.16 | 2.03 | 1.18 | -9.23 | 0.30 | | | | 65.1% | | 34.9% | | | | -9.83 | 0.60 |
| 1501 | 34.57 | 2.64 | 27.79 | 180.3 | 65.27 | 33.44 | 2.25 | 1.33 | -8.31 | 0.19 | | 8.1% | | 91.9% | | | | | | -8.01 | -0.30 |
| 1250 | 34.45 | 2.74 | 27.68 | 187.1 | 57.98 | 34.10 | 2.30 | 1.42 | -8.12 | 0.30 | | 30.5% | | 69.5% | | | | | | -8.02 | -0.09 |
| 1002 | 34.31 | 2.92 | 27.54 | 212.7 | 42.67 | 32.65 | 2.19 | 1.46 | -8.15 | 0.19 | | 54.4% | | 45.6% | | | | | | -8.05 | -0.10 |
| 751 | 34.21 | 3.43 | 27.39 | 244.8 | 26.93 | 30.01 | 2.01 | 1.46 | -8.15 | 0.19 | | 72.3% | | 27.7% | | | | | | -8.06 | -0.09 |
| 502 | 34.13 | 4.20 | 27.23 | 285.7 | 12.05 | 25.65 | 1.74 | 1.42 | -8.10 | 0.13 | 32.3% | 67.7% | | | | | | | | -8.26 | 0.16 |
| 401 | 34.16 | 4.70 | 27.19 | 282.5 | 9.93 | 24.91 | 1.70 | 1.37 | -8.16 | 0.30 | 40.0% | 60.0% | | | | | | | | -8.30 | 0.14 |
| 250 | 34.48 | 7.87 | 26.99 | 243.5 | 6.36 | 20.02 | 1.37 | 0.81 | -8.43 | 0.19 | | | | | | | | | | | |
| 99 | 35.10 | 12.61 | 26.61 | 223.6 | 2.81 | 10.52 | 0.78 | 0.10 | -9.03 | 0.30 | | | | | | | | | | | |
| 26 | 34.67 | 16.91 | 25.19 | 248.2 | 0.41 | 0.35 | 0.18 | -0.35 | -7.63 | 0.30 | | | | | | | | | | | |
| Station 5 (-42.38°N -44.02°E) | | | | | | | | | | | | | | | | | | | | | |
| 5146 | 34.67 | -0.16 | 28.29 | 228.3 | 126.93 | 32.82 | 2.25 | 1.61 | -8.05 | 0.30 | | | | | | | | 0.3% | 99.7% | -8.00 | -0.04 |
| 5001 | 34.67 | -0.15 | 28.29 | 228.4 | 126.48 | 32.90 | 2.24 | 1.59 | -8.22 | 0.26 | | | | | | | | 1.1% | 98.9% | -8.00 | -0.22 |
| 4000 | 34.69 | 0.25 | 28.24 | 219.3 | 119.20 | 32.37 | 2.20 | 1.51 | -8.24 | 0.26 | | | | | | | | 31.9% | 68.1% | -8.10 | -0.14 |
| 3502 | 34.72 | 0.80 | 28.17 | 212.3 | 107.73 | 31.44 | 2.14 | 1.40 | -8.59 | 0.30 | | | | | | | | 75.2% | 24.8% | -8.31 | -0.28 |
| 2503 | 34.82 | 2.20 | 28.03 | 219.1 | 62.80 | 26.61 | 1.79 | 1.10 | -10.34 | 0.30 | | | | 18.5% | | 54.6% | | 26.9% | | -10.64 | 0.30 |
| 2000 | 34.77 | 2.47 | 27.96 | 200.4 | 65.59 | 28.89 | 1.96 | 1.15 | -9.84 | 0.28 | | | | 53.4% | | 46.6% | | | | -10.37 | 0.53 |
| 1748 | 34.70 | 2.46 | 27.90 | 186.7 | 70.15 | 31.18 | 2.12 | 1.24 | -9.21 | 0.30 | | | | 74.9% | | 25.1% | | | | -9.35 | 0.14 |
| 1500 | 34.64 | 2.64 | 27.84 | 182.6 | 65.18 | 32.13 | 2.18 | 1.27 | -9.55 | 0.32 | | | | 95.0% | | 5.0% | | | | -8.28 | -1.27 |
| 1250 | 34.52 | 2.67 | 27.74 | 181.8 | 62.78 | 33.68 | 2.29 | 1.37 | -8.23 | 0.28 | | 18.0% | | 82.0% | | | | | | -8.01 | -0.22 |
| 999 | 34.38 | 2.85 | 27.60 | 198.8 | 50.38 | 33.64 | 2.26 | 1.45 | -7.98 | 0.28 | | 42.5% | | 57.5% | | | | | | -8.03 | 0.06 |
| 748 | 34.24 | 3.13 | 27.46 | 234.1 | 32.14 | 31.32 | 2.10 | 1.49 | -7.94 | 0.30 | | 67.3% | | 32.7% | | | | | | -8.06 | 0.12 |
| 500 | 34.15 | 3.89 | 27.29 | 270.3 | 15.89 | 27.30 | 1.82 | 1.41 | -8.79 | 0.32 | 37.9% | 62.1% | | | | | | | | -8.29 | -0.50 |
| 400 | 34.16 | 4.41 | 27.23 | 272.0 | 12.13 | 26.27 | 1.76 | 1.36 | -8.79 | 0.32 | 41.5% | 58.5% | | | | | | | | -8.31 | -0.49 |
| 247 | 34.31 | 6.26 | 27.10 | 254.5 | 7.56 | 22.85 | 1.55 | 1.05 | -8.15 | 0.30 | 100.0% | | | | | | | | | -8.59 | 0.44 |
| 100 | 34.64 | 9.51 | 26.84 | 253.2 | 2.95 | 13.51 | 1.00 | 0.49 | -7.59 | 0.28 | | | | | | | | | | | |
| 25 | 34.58 | 16.31 | 25.36 | 261.6 | 0.00 | 0.00 | 0.24 | -0.22 | -6.94 | 0.32 | | | | | | | | | | | |
| Station 6 (-39.97°N -42.49°E) | | | | | | | | | | | | | | | | | | | | | |

Table 1. continued

| Depth | Salinity | Potential Temperature | Neutral Density | Oxygen | Silicate | Nitrate | Phosphate | $PO_4^*$ | εNd | Ext. 2sd | SACW | aAAIW | iAAIW | UCDW | UNADW | MNADW | LNADW | LCDW | AABW | Calculated εNd | ΔεNd |
|---|---|---|---|---|---|---|---|---|---|---|---|---|---|---|---|---|---|---|---|---|---|
| m | | °C | kg/m$^3$ | µmol/kg | µmol/kg | µmol/kg | µmol/kg | µmol/kg | | | | | | | | | | | | | |
| 5132 | 34.67 | -0.16 | 28.30 | 227.5 | 127.25 | 33.13 | 2.30 | 1.65 | -7.97 | 0.18 | | | | | | | | 0.3% | 99.7% | -8.00 | 0.03 |
| 5000 | 34.67 | -0.14 | 28.29 | 227.7 | 126.67 | 33.11 | 2.29 | 1.64 | -8.18 | 0.18 | | | | | | | | 1.3% | 98.7% | -8.00 | -0.18 |
| 4001 | 34.69 | 0.22 | 28.24 | 220.1 | 119.63 | 32.75 | 2.25 | 1.55 | -8.42 | 0.18 | | | | | | | | 29.8% | 70.2% | -8.10 | -0.32 |
| 3501 | 34.72 | 0.82 | 28.17 | 211.1 | 107.82 | 31.65 | 2.17 | 1.43 | -8.72 | 0.18 | | | | | | | | 76.7% | 23.3% | -8.32 | -0.40 |
| 3002 | 34.75 | 1.44 | 28.10 | 206.8 | 91.64 | 30.32 | 2.08 | 1.31 | -10.17 | 0.18 | | | | | | 14.5% | | 85.5% | | -9.04 | -1.14 |
| 2000 | 34.82 | 2.90 | 27.93 | 213.2 | 48.98 | 26.51 | 1.79 | 1.06 | -10.55 | 0.18 | | | | 37.5% | | 62.5% | | | | -11.06 | 0.51 |
| 1751 | 34.76 | 3.04 | 27.87 | 201.1 | 49.60 | 28.56 | 1.92 | 1.12 | -10.27 | 0.18 | | | | 57.2% | | 42.8% | | | | -10.20 | -0.07 |
| 1499 | 34.63 | 2.84 | 27.81 | 188.6 | 57.34 | 31.99 | 2.15 | 1.28 | -8.98 | 0.18 | | | | 97.7% | | 2.3% | | | | -8.13 | -0.85 |
| 1250 | 34.48 | 2.82 | 27.69 | 188.8 | 55.85 | 33.68 | 2.28 | 1.41 | -8.35 | 0.18 | | 17.9% | 19.8% | 62.3% | | | | | | -8.45 | 0.10 |
| 1000 | 34.35 | 3.13 | 27.54 | 208.3 | 42.52 | 32.82 | 2.23 | 1.47 | -8.31 | 0.18 | | 39.7% | 24.2% | 36.1% | | | | | | -8.61 | 0.30 |
| 750 | 34.24 | 3.66 | 27.39 | 238.1 | 26.14 | 30.21 | 2.04 | 1.45 | -9.62 | 0.18 | | | | | | | | | | | |
| 500 | 34.17 | 4.38 | 27.25 | 274.3 | 13.05 | 26.09 | 1.77 | 1.39 | -8.36 | 0.18 | 45.8% | 54.2% | | | | | | | | -8.33 | -0.03 |
| 399 | 34.24 | 5.31 | 27.18 | 258.6 | 10.80 | 25.18 | 1.71 | 1.24 | -8.45 | 0.18 | 72.4% | 27.6% | | | | | | | | -8.46 | 0.01 |
| 250 | 34.52 | 8.09 | 26.99 | 229.0 | 7.41 | 20.63 | 1.41 | 0.77 | -9.04 | 0.18 | 100.0% | | | | | | | | | -8.59 | -0.44 |
| 101 | 35.17 | 13.03 | 26.58 | 221.4 | 2.48 | 9.71 | 0.72 | 0.04 | -9.09 | 0.18 | | | | | | | | | | | |
| 25 | 35.29 | 21.32 | 24.62 | 230.3 | 0.99 | 0.00 | 0.08 | -0.55 | -9.41 | 0.18 | | | | | | | | | | | |
| Station 7 (-37.83°N -41.12°E) | | | | | | | | | | | | | | | | | | | | | |
| 5023 | 34.67 | -0.15 | 28.29 | 227.5 | 126.70 | 33.09 | 2.27 | 1.62 | -8.01 | 0.28 | | | | | | | | 0.8% | 99.2% | -8.00 | 0.00 |
| 5000 | 34.67 | -0.15 | 28.29 | 227.6 | 126.97 | 33.04 | 2.27 | 1.62 | -8.18 | 0.37 | | | | | | | | 0.8% | 99.2% | -8.00 | -0.18 |
| 4000 | 34.69 | 0.34 | 28.23 | 218.3 | 116.90 | 32.42 | 2.20 | 1.50 | -9.88 | 0.37 | | | | | | | 1.9% | 35.5% | 62.6% | -8.18 | -1.71 |
| 3500 | 34.73 | 0.98 | 28.15 | 209.1 | 104.69 | 31.52 | 2.13 | 1.37 | -8.32 | 0.37 | | | | | | | 7.5% | 75.9% | 16.6% | -8.63 | 0.32 |
| 2501 | 34.82 | 2.47 | 27.99 | 216.0 | 57.66 | 26.65 | 1.80 | 1.09 | -10.28 | 0.28 | | | | 32.9% | | 61.6% | | 5.5% | | -11.00 | 0.72 |
| 2000 | 34.74 | 2.71 | 27.90 | 196.4 | 60.10 | 29.54 | 2.00 | 1.17 | -12.57 | 0.37 | | | | 65.0% | 22.9% | 12.1% | | | | -9.93 | -2.65 |
| 1748 | 34.64 | 2.73 | 27.83 | 184.9 | 61.83 | 31.94 | 2.17 | 1.27 | -9.22 | 0.37 | | | 12.3% | 75.2% | 12.4% | | | | | -8.99 | -0.23 |
| 1500 | 34.52 | 2.76 | 27.73 | 184.3 | 58.76 | 33.42 | 2.27 | 1.37 | -9.32 | 0.37 | | 11.1% | 19.9% | 69.1% | | | | | | -8.43 | -0.88 |
| 1249 | 34.36 | 3.01 | 27.57 | 203.5 | 45.54 | 33.10 | 2.23 | 1.44 | -8.30 | 0.28 | | 38.7% | 19.4% | 41.8% | | | | | | -8.49 | 0.18 |
| 1000 | 34.24 | 3.59 | 27.40 | 237.0 | 27.37 | 30.22 | 2.03 | 1.43 | -7.93 | 0.37 | | 54.1% | 38.3% | 7.7% | | | | | | -9.02 | 1.09 |
| 751 | 34.20 | 4.55 | 27.25 | 261.6 | 14.15 | 26.46 | 1.77 | 1.32 | -8.46 | 0.37 | 40.4% | 48.2% | 11.4% | | | | | | | -8.60 | 0.14 |
| 409 | 34.91 | 10.82 | 26.82 | 217.7 | 4.51 | 14.83 | 1.04 | 0.33 | -9.23 | 0.28 | | | | | | | | | | | |
| 349 | 35.19 | 12.66 | 26.68 | 221.7 | 3.00 | 10.66 | 0.78 | 0.09 | -10.24 | 0.37 | | | | | | | | | | | |
| 249 | 35.52 | 14.35 | 26.57 | 227.5 | 1.94 | 6.46 | 0.53 | -0.12 | -10.53 | 0.37 | | | | | | | | | | | |
| 101 | 35.67 | 15.43 | 26.44 | 230.0 | 1.59 | 3.15 | 0.34 | -0.30 | -10.06 | 0.37 | | | | | | | | | | | |
| 24 | 35.47 | 20.04 | 25.12 | 234.4 | 0.87 | 0.00 | 0.07 | -0.54 | -10.55 | 0.37 | | | | | | | | | | | |
| Station 8 (-35.01°N -39.44°E) | | | | | | | | | | | | | | | | | | | | | |
| 4838 | 34.67 | -0.13 | 28.29 | 226.1 | 126.81 | 33.16 | 2.25 | 1.60 | -8.70 | 0.32 | | | | | | | | 2.0% | 98.0% | -8.01 | -0.70 |
| 4787 | 34.67 | -0.13 | 28.29 | 226.5 | 126.78 | 33.14 | 2.27 | 1.61 | -8.59 | 0.26 | | | | | | | | 2.1% | 97.9% | -8.01 | -0.58 |

Table 1. continued

| Depth | Salinity | Potential Temperature | Neutral Density | Oxygen | Silicate | Nitrate | Phosphate | $PO_4^*$ | εNd | Ext. 2sd | SACW | aAAIW | iAAIW | UCDW | UNADW | MNADW | LNADW | LCDW | AABW | Calculated εNd | ΔεNd |
|---|---|---|---|---|---|---|---|---|---|---|---|---|---|---|---|---|---|---|---|---|---|
| m | | °C | kg/m$^3$ | µmol/kg | µmol/kg | µmol/kg | µmol/kg | µmol/kg | | | | | | | | | | | | | |
| 4000 | 34.70 | 0.43 | 28.22 | 217.0 | 114.90 | 32.26 | 2.18 | 1.47 | -8.30 | 0.28 | | | | | | | 3.7% | 39.5% | 56.9% | -8.25 | -0.04 |
| 3501 | 34.80 | 1.53 | 28.12 | 229.2 | 74.33 | 26.69 | 1.80 | 1.16 | -10.07 | 0.28 | | | | | | | 48.7% | 45.4% | 5.9% | -10.22 | 0.15 |
| 2500 | 34.90 | 2.84 | 28.00 | 242.1 | 34.43 | 22.19 | 1.47 | 0.90 | -11.57 | 0.26 | | | | 13.4% | 12.4% | 74.2% | | | | -12.07 | 0.51 |
| 2001 | 34.81 | 2.94 | 27.92 | 215.9 | 45.70 | 26.31 | 1.75 | 1.03 | -11.24 | 0.32 | | | | 45.1% | 31.2% | 23.7% | | | | -10.88 | -0.36 |
| 1749 | 34.70 | 2.85 | 27.86 | 195.5 | 54.69 | 29.82 | 2.01 | 1.17 | -9.65 | 0.28 | | | 7.5% | 68.1% | 24.4% | | | | | -9.56 | -0.09 |
| 1501 | 34.54 | 2.81 | 27.74 | 188.2 | 56.47 | 32.97 | 2.21 | 1.33 | -9.10 | 0.30 | | 5.6% | 24.2% | 70.2% | | | | | | -8.52 | -0.59 |
| 1251 | 34.38 | 3.11 | 27.57 | 203.1 | 44.56 | 32.77 | 2.20 | 1.41 | -8.71 | 0.28 | | 32.6% | 26.1% | 41.3% | | | | | | -8.63 | -0.08 |
| 1001 | 34.26 | 3.87 | 27.38 | 232.8 | 25.32 | 29.96 | 2.00 | 1.38 | -7.88 | 0.32 | | 45.0% | 54.3% | 0.7% | | | | | | -9.41 | 1.54 |
| 751 | 34.25 | 5.24 | 27.21 | 252.6 | 11.95 | 25.56 | 1.71 | 1.21 | -8.57 | 0.26 | 63.1% | 27.1% | 9.8% | | | | | | | -8.67 | 0.09 |
| 501 | 34.97 | 11.07 | 26.83 | 211.4 | 4.75 | 14.95 | 1.05 | 0.31 | -10.35 | 0.32 | | | | | | | | | | | |
| 400 | 35.33 | 13.23 | 26.67 | 218.4 | 2.70 | 9.38 | 0.70 | 0.00 | -10.24 | 0.28 | | | | | | | | | | | |
| 251 | 35.63 | 15.06 | 26.50 | 221.7 | 1.75 | 5.35 | 0.43 | -0.25 | -10.35 | 0.28 | | | | | | | | | | | |
| 100 | 35.82 | 16.63 | 26.28 | 234.9 | 0.48 | 0.00 | 0.13 | -0.48 | -11.42 | 0.28 | | | | | | | | | | | |
| 24 | 35.73 | 21.98 | 24.78 | 225.2 | 0.47 | 0.00 | 0.03 | -0.63 | -11.43 | 0.26 | | | | | | | | | | | |
| Station 9 (-32.09°N -37.46°E) | | | | | | | | | | | | | | | | | | | | | |
| 4121 | 34.69 | 0.21 | 28.25 | 220.7 | 119.19 | 32.29 | 2.23 | 1.54 | -7.77 | 0.32 | | | | | | | 3.0% | 23.3% | 73.7% | -8.16 | 0.40 |
| 4085 | 34.69 | 0.29 | 28.23 | 220.1 | 116.58 | 32.03 | 2.21 | 1.52 | -8.55 | 0.13 | | | | | | | 4.8% | 27.0% | 68.2% | -8.23 | -0.32 |
| 3498 | 34.82 | 1.55 | 28.13 | 239.0 | 67.86 | 25.51 | 1.72 | 1.13 | -10.43 | 0.19 | | | | | | | 61.4% | 24.7% | 13.9% | -10.48 | 0.05 |
| 2999 | 34.91 | 2.44 | 28.06 | 250.0 | 37.27 | 21.57 | 1.43 | 0.91 | -11.88 | 0.24 | | | | | | 72.2% | 15.1% | 12.7% | | -11.90 | 0.02 |
| 2500 | 34.92 | 2.81 | 28.02 | 246.2 | 32.71 | 21.50 | 1.44 | 0.90 | -11.88 | 0.19 | | | | 8.8% | 8.1% | 83.0% | | | | -12.22 | 0.34 |
| 1999 | 34.82 | 2.88 | 27.94 | 221.4 | 44.16 | 25.72 | 1.74 | 1.06 | -9.95 | 0.19 | | | | 40.6% | 25.1% | 34.3% | | | | -11.04 | 0.77 |
| 1749 | 34.71 | 2.77 | 27.87 | 201.7 | 53.59 | 29.48 | 1.98 | 1.18 | -9.32 | 0.19 | | | 2.0% | 71.5% | 26.6% | | | | | -9.57 | -0.38 |
| 1499 | 34.57 | 2.84 | 27.76 | 191.2 | 54.78 | 31.93 | 2.18 | 1.32 | -8.52 | 0.19 | | | 25.6% | 74.4% | | | | | | -8.53 | -0.79 |
| 1249 | 34.41 | 3.12 | 27.59 | 199.4 | 46.63 | 32.95 | 2.23 | 1.42 | -8.68 | 0.19 | | 25.8% | 29.3% | 44.9% | | | | | | -8.69 | 0.17 |
| 1001 | 34.29 | 3.91 | 27.40 | 225.1 | 28.08 | 30.30 | 2.05 | 1.39 | -9.41 | 0.32 | | 37.1% | 59.0% | 3.9% | | | | | | -9.49 | 0.08 |
| 752 | 34.33 | 5.76 | 27.20 | 237.3 | 12.77 | 25.45 | 1.71 | 1.11 | -8.68 | 0.19 | 74.3% | 3.7% | 22.0% | | | | | | | -9.02 | 0.34 |
| 500 | 34.99 | 11.21 | 26.81 | 211.8 | 4.73 | 14.32 | 0.99 | 0.25 | -10.08 | 0.22 | | | | | | | | | | | |
| 401 | 35.29 | 13.03 | 26.68 | 217.7 | 3.05 | 9.94 | 0.72 | 0.01 | -10.16 | 0.22 | | | | | | | | | | | |
| 250 | 35.60 | 15.02 | 26.48 | 222.1 | 1.77 | 5.15 | 0.43 | -0.25 | -10.74 | 0.13 | | | | | | | | | | | |
| 101 | 35.89 | 17.41 | 26.13 | 235.1 | 0.74 | 0.00 | 0.09 | -0.52 | -11.86 | 0.22 | | | | | | | | | | | |
| 26 | 35.97 | 23.71 | 24.46 | 217.8 | 0.35 | 0.00 | 0.00 | -0.71 | -12.87 | 0.19 | | | | | | | | | | | |
| Station 10 (-29.06°N -35.78°E) | | | | | | | | | | | | | | | | | | | | | |
| 3835 | 34.78 | 1.09 | 28.17 | 235.5 | 82.95 | 27.56 | 1.86 | 1.26 | -9.90 | 0.13 | | | | | | | 3.0% | 23.3% | 73.7% | -8.16 | 0.40 |
| 3786 | 34.79 | 1.13 | 28.17 | 236.2 | 81.63 | 27.50 | 1.84 | 1.24 | -10.06 | 0.22 | | | | | | | 4.8% | 27.0% | 68.2% | -8.23 | -0.32 |
| 3502 | 34.85 | 1.68 | 28.13 | 246.3 | 58.08 | 24.04 | 1.61 | 1.07 | -11.06 | 0.19 | | | | | | | 61.4% | 24.7% | 13.9% | -10.48 | 0.05 |

Table 1. continued

| Depth | Salinity | Potential Temperature | Neutral Density | Oxygen | Silicate | Nitrate | Phosphate | $PO_4^*$ | εNd | Ext. 2sd | SACW | aAAIW | iAAIW | UCDW | UNADW | MNADW | LNADW | LCDW | AABW | Calculated εNd | ΔεNd |
|---|---|---|---|---|---|---|---|---|---|---|---|---|---|---|---|---|---|---|---|---|---|
| m | | °C | $kg/m^3$ | µmol/kg | µmol/kg | µmol/kg | µmol/kg | µmol/kg | | | | | | | | | | | | | |
| 2999 | 34.91 | 2.38 | 28.07 | 252.9 | 35.97 | 21.18 | 1.42 | 0.92 | -11.52 | 0.32 | | | | | | 55.6% | 36.7% | 7.6% | | -12.03 | 0.51 |
| 2502 | 34.91 | 2.69 | 28.03 | 249.2 | 32.85 | 21.44 | 1.42 | 0.90 | -12.07 | 0.22 | | | | | | 92.2% | 7.8% | | | -12.46 | 0.40 |
| 2001 | 34.84 | 2.75 | 27.97 | 230.1 | 42.04 | 24.53 | 1.64 | 1.00 | -11.08 | 0.19 | | | | 31.8% | 12.6% | 55.6% | | | | -11.35 | 0.27 |
| 1750 | 34.77 | 2.73 | 27.92 | 214.1 | 48.84 | 27.17 | 1.82 | 1.10 | -10.66 | 0.37 | | | | 56.6% | 20.6% | 22.9% | | | | -10.31 | -0.34 |
| 1501 | 34.65 | 2.81 | 27.83 | 196.9 | 53.78 | 30.40 | 2.05 | 1.22 | -9.79 | 0.19 | | | 12.6% | 71.4% | 16.0% | | | | | -9.20 | -0.58 |
| 1296 | 34.54 | 2.95 | 27.72 | 191.1 | 52.86 | 32.44 | 2.18 | 1.33 | -9.17 | 0.37 | | 3.9% | 30.7% | 65.4% | | | | | | -8.65 | -0.51 |
| 1003 | 34.32 | 3.57 | 27.46 | 215.5 | 34.47 | 31.68 | 2.12 | 1.40 | -8.32 | 0.19 | | 36.4% | 44.5% | 19.1% | | | | | | -9.10 | 0.78 |
| 751 | 34.34 | 5.51 | 27.24 | 226.6 | 15.95 | 26.94 | 1.83 | 1.17 | -8.83 | 0.37 | 60.4% | 4.4% | 35.2% | | | | | | | -9.26 | 0.43 |
| 500 | 34.84 | 10.14 | 26.90 | 211.2 | 5.89 | 16.93 | 1.17 | 0.43 | -9.81 | 0.22 | | | | | | | | | | | |
| 402 | 35.22 | 12.60 | 26.71 | 217.1 | 3.25 | 11.00 | 0.80 | 0.09 | -10.53 | 0.37 | | | | | | | | | | | |
| 252 | 35.54 | 14.64 | 26.52 | 221.4 | 1.91 | 6.14 | 0.48 | -0.20 | -10.53 | 0.22 | | | | | | | | | | | |
| 107 | 35.84 | 17.21 | 26.14 | 237.5 | 0.61 | 0.00 | 0.07 | -0.52 | -11.54 | 0.22 | | | | | | | | | | | |
| 25 | 35.69 | 24.05 | 24.14 | 216.7 | 0.27 | 0.00 | 0.01 | -0.70 | -12.95 | 0.37 | | | | | | | | | | | |
| Station 11 (-26.09°N -34.26°E) | | | | | | | | | | | | | | | | | | | | | |
| 4548 | 34.67 | -0.06 | 28.29 | 224.9 | 124.47 | 32.79 | 2.24 | 1.58 | -8.37 | 0.37 | | | | | | | | 7.6% | 92.4% | -8.02 | -0.35 |
| 4001 | 34.78 | 1.04 | 28.18 | 235.2 | 85.16 | 27.71 | 1.87 | 1.26 | -10.72 | 0.37 | | | | | | | 42.9% | 17.5% | 39.5% | -9.50 | -1.22 |
| 3493 | 34.88 | 2.03 | 28.10 | 252.9 | 44.49 | 22.03 | 1.47 | 0.96 | -11.80 | 0.30 | | | | | | 4.1% | 85.1% | 10.9% | | -11.75 | -0.05 |
| 3000 | 34.92 | 2.49 | 28.06 | 254.6 | 32.63 | 20.59 | 1.38 | 0.89 | -12.16 | 0.30 | | | | | | 69.7% | 24.1% | 6.2% | | -12.13 | -0.03 |
| 2503 | 34.93 | 2.82 | 28.02 | 252.9 | 28.15 | 20.36 | 1.36 | 0.86 | -12.50 | 0.30 | | | | | | 79.3% | 20.7% | | | -12.40 | -0.10 |
| 2000 | 34.93 | 3.18 | 27.98 | 246.8 | 26.32 | 20.98 | 1.40 | 0.86 | -11.94 | 0.37 | | | | 9.1% | 34.5% | 56.5% | | | | -12.34 | 0.40 |
| 1749 | 34.88 | 3.24 | 27.94 | 231.5 | 32.24 | 23.33 | 1.56 | 0.93 | -11.80 | 0.30 | | | | 26.4% | 45.5% | 28.1% | | | | -11.72 | -0.08 |
| 1501 | 34.75 | 3.13 | 27.86 | 206.2 | 43.94 | 27.92 | 1.86 | 1.09 | -10.80 | 0.30 | | | 7.9% | 54.0% | 38.1% | | | | | -10.31 | -0.49 |
| 1249 | 34.53 | 3.04 | 27.70 | 190.9 | 51.03 | 32.28 | 2.17 | 1.31 | -9.46 | 0.30 | | 3.1% | 35.0% | 61.9% | | | | | | -8.75 | -0.71 |
| 998 | 34.38 | 3.68 | 27.50 | 201.2 | 37.83 | 32.16 | 2.16 | 1.36 | -9.22 | 0.30 | | 23.7% | 54.5% | 21.8% | | | | | | -9.29 | 0.07 |
| 750 | 34.36 | 5.57 | 27.24 | 218.6 | 17.50 | 27.52 | 1.85 | 1.14 | -9.87 | 0.37 | 54.7% | | 45.3% | | | | | | | -9.46 | -0.41 |
| 501 | 34.92 | 10.85 | 26.83 | 206.5 | 5.59 | 15.65 | 1.10 | 0.33 | -10.69 | 0.30 | | | | | | | | | | | |
| 403 | 35.20 | 12.83 | 26.65 | 214.6 | 3.13 | 10.30 | 0.78 | 0.05 | -10.97 | 0.30 | | | | | | | | | | | |
| 249 | 35.61 | 15.98 | 26.26 | 211.6 | 1.64 | 4.11 | 0.41 | -0.33 | -12.61 | 0.28 | | | | | | | | | | | |
| 100 | 36.64 | 21.31 | 25.68 | 218.2 | 0.77 | 0.00 | 0.08 | -0.62 | -13.73 | 0.37 | | | | | | | | | | | |
| 25 | 36.51 | 25.90 | 24.20 | 207.1 | 0.35 | 0.00 | 0.01 | -0.76 | -16.37 | 0.37 | | | | | | | | | | | |
| Station 12 (-22.47°N -32.73°E) | | | | | | | | | | | | | | | | | | | | | |
| 4510 | 34.69 | 0.10 | 28.28 | 224.1 | 120.55 | 32.92 | 2.19 | 1.52 | -8.50 | 0.24 | | | | | | | 4.0% | 13.2% | 82.8% | -8.15 | -0.35 |
| 4002 | 34.78 | 1.05 | 28.18 | 236.1 | 83.56 | 27.59 | 1.87 | 1.27 | -12.63 | 0.37 | | | | | | | 46.1% | 12.4% | 41.4% | -9.57 | -3.06 |
| 3499 | 34.89 | 2.06 | 28.10 | 252.8 | 42.41 | 21.75 | 1.44 | 0.94 | -11.52 | 0.28 | | | | | | 4.2% | 88.3% | 7.5% | | -11.87 | 0.34 |
| 3002 | 34.92 | 2.51 | 28.06 | 254.1 | 32.09 | 20.71 | 1.37 | 0.87 | -12.11 | 0.24 | | | | | | 70.4% | 25.0% | 4.6% | | -12.19 | 0.09 |
| 2501 | 34.94 | 2.83 | 28.03 | 253.7 | 27.48 | 20.28 | 1.33 | 0.83 | -12.50 | 0.37 | | | | | | 91.0% | 9.0% | | | -12.46 | -0.05 |

Table 1. continued

| Depth | Salinity | Potential Temperature | Neutral Density | Oxygen | Silicate | Nitrate | Phosphate | $PO_4^*$ | εNd | Ext. 2sd | SACW | aAAIW | iAAIW | UCDW | UNADW | MNADW | LNADW | LCDW | AABW | Calculated εNd | ΔεNd |
|---|---|---|---|---|---|---|---|---|---|---|---|---|---|---|---|---|---|---|---|---|---|
| m | | °C | kg/m$^3$ | µmol/kg | µmol/kg | µmol/kg | µmol/kg | µmol/kg | | | | | | | | | | | | | |
| 1999 | 34.95 | 3.29 | 27.98 | 251.5 | 22.20 | 20.13 | 1.32 | 0.81 | -12.34 | 0.28 | | | | 1.9% | 39.2% | 58.9% | | | | -12.62 | 0.28 |
| 1751 | 34.95 | 3.55 | 27.95 | 242.2 | 22.05 | 21.09 | 1.37 | 0.81 | -12.30 | 0.24 | | | | 7.3% | 59.8% | 33.0% | | | | -12.53 | 0.23 |
| 1502 | 34.86 | 3.65 | 27.87 | 217.9 | 29.67 | 24.77 | 1.63 | 0.93 | -11.80 | 0.28 | | | 5.2% | 26.9% | 67.9% | | | | | -11.71 | -0.09 |
| 1250 | 34.66 | 3.43 | 27.76 | 193.7 | 41.31 | 29.98 | 1.99 | 1.15 | -10.54 | 0.26 | | | 29.8% | 42.5% | 27.7% | | | | | -10.23 | -0.31 |
| 999 | 34.45 | 3.66 | 27.56 | 187.6 | 40.01 | 32.81 | 2.18 | 1.30 | -10.00 | 0.24 | | 9.1% | 59.5% | 31.4% | | | | | | -9.34 | -0.66 |
| 752 | 34.39 | 5.23 | 27.31 | 196.9 | 22.79 | 30.09 | 2.01 | 1.19 | -9.67 | 0.28 | 24.0% | | 76.0% | | | | | | | -9.96 | 0.28 |
| 502 | 34.81 | 9.98 | 26.90 | 199.7 | 7.58 | 18.51 | 1.27 | 0.46 | -10.47 | 0.24 | | | | | | | | | | | |
| 401 | 35.12 | 12.40 | 26.68 | 208.0 | 3.97 | 11.93 | 0.87 | 0.11 | -11.26 | 0.24 | | | | | | | | | | | |
| 250 | 35.63 | 16.03 | 26.27 | 214.4 | 1.83 | 3.81 | 0.37 | -0.35 | -12.69 | 0.24 | | | | | | | | | | | |
| 100 | 36.76 | 22.04 | 25.56 | 216.1 | 0.75 | 0.00 | 0.05 | -0.66 | -13.71 | 0.37 | | | | | | | | | | | |
| 24 | 36.49 | 26.35 | 24.04 | 206.7 | 0.46 | 0.00 | 0.03 | -0.73 | -13.87 | 0.24 | | | | | | | | | | | |
| Station 13 (-17.02°N -30.59°E) | | | | | | | | | | | | | | | | | | | | | |
| 4893 | 34.68 | 0.02 | 28.28 | 224.3 | 122.80 | 32.73 | 2.26 | 1.59 | -8.73 | 0.37 | | | | | | | 1.5% | 11.3% | 87.1% | -8.08 | -0.66 |
| 4844 | 34.68 | 0.04 | 28.28 | 224.6 | 121.97 | 32.63 | 2.22 | 1.56 | -8.44 | 0.17 | | | | | | | 2.7% | 11.2% | 86.2% | -8.11 | -0.34 |
| 3999 | 34.84 | 1.59 | 28.14 | 246.4 | 59.71 | 24.02 | 1.60 | 1.06 | -11.81 | 0.37 | | | | | | | 74.0% | 5.5% | 20.5% | -10.73 | -1.08 |
| 3503 | 34.89 | 2.14 | 28.09 | 252.7 | 40.89 | 21.69 | 1.44 | 0.94 | -11.94 | 0.17 | | | | | | 16.4% | 76.0% | 7.5% | | -11.90 | -0.04 |
| 2501 | 34.92 | 2.66 | 28.04 | 248.7 | 32.77 | 21.38 | 1.39 | 0.87 | -12.47 | 0.20 | | | | | | 100.0% | | | | -12.50 | 0.03 |
| 2002 | 34.93 | 3.05 | 28.00 | 248.1 | 27.24 | 21.10 | 1.38 | 0.85 | -12.02 | 0.17 | | | | 6.2% | 23.9% | 69.9% | | | | -12.39 | 0.37 |
| 1749 | 34.92 | 3.30 | 27.96 | 239.7 | 26.26 | 22.02 | 1.45 | 0.87 | -12.42 | 0.17 | | | | 12.6% | 44.4% | 43.0% | | | | -12.26 | -0.16 |
| 1502 | 34.91 | 3.77 | 27.89 | 228.3 | 23.65 | 22.99 | 1.51 | 0.86 | -12.16 | 0.17 | | | 0.5% | 20.0% | 79.5% | | | | | -12.13 | -0.02 |
| 1251 | 34.76 | 3.86 | 27.78 | 196.0 | 30.89 | 28.16 | 1.87 | 1.04 | -12.48 | 0.17 | | | 27.3% | 20.1% | 52.6% | | | | | -11.47 | -0.49 |
| 1000 | 34.51 | 3.70 | 27.60 | 183.6 | 38.29 | 32.54 | 2.19 | 1.29 | -10.81 | 0.17 | | | 60.8% | 34.8% | 4.5% | | | | | -9.60 | -1.20 |
| 750 | 34.42 | 4.52 | 27.42 | 180.2 | 30.10 | 32.69 | 2.20 | 1.28 | -10.27 | 0.17 | | | 100.0% | | | | | | | -10.30 | 0.03 |
| 500 | 34.67 | 8.22 | 27.09 | 155.3 | 13.91 | 26.99 | 1.75 | 0.69 | -14.38 | 0.37 | | | | | | | | | | | |
| 401 | 34.93 | 10.89 | 26.82 | 166.6 | 7.93 | 20.16 | 1.33 | 0.33 | -13.20 | 0.37 | | | | | | | | | | | |
| 250 | 35.60 | 15.99 | 26.25 | 194.7 | 2.36 | 6.30 | 0.52 | -0.31 | -13.68 | 0.37 | | | | | | | | | | | |
| 100 | 37.07 | 24.18 | 25.16 | 223.4 | 0.69 | 0.00 | 0.08 | -0.60 | -14.38 | 0.17 | | | | | | | | | | | |
| 24 | 37.44 | 27.85 | 24.28 | 198.2 | 0.67 | 0.00 | 0.02 | -0.80 | -13.20 | 0.17 | | | | | | | | | | | |
| Station 14 (-12.89°N -29.22°E) | | | | | | | | | | | | | | | | | | | | | |
| 5435 | 34.69 | 0.15 | 28.27 | 225.9 | 117.67 | 32.01 | 2.16 | 1.50 | -8.24 | 0.26 | | | | | | | 6.8% | 12.3% | 80.9% | -8.23 | -0.01 |
| 4999 | 34.71 | 0.33 | 28.25 | 227.6 | 110.92 | 31.22 | 2.13 | 1.48 | -9.21 | 0.30 | | | | | | | 15.3% | 10.9% | 73.8% | -8.47 | -0.74 |
| 4000 | 34.82 | 1.40 | 28.15 | 241.5 | 68.07 | 25.25 | 1.71 | 1.14 | -10.43 | 0.20 | | | | | | | 64.8% | 7.2% | 27.9% | -10.31 | -0.11 |
| 3502 | 34.89 | 2.12 | 28.10 | 250.3 | 41.84 | 21.84 | 1.45 | 0.93 | -12.01 | 0.30 | | | | | | 14.0% | 78.2% | 7.8% | | -11.88 | -0.12 |
| 2500 | 34.91 | 2.61 | 28.04 | 244.5 | 35.79 | 21.89 | 1.45 | 0.90 | -13.07 | 0.37 | | | | | | 100.0% | | | | -12.50 | -0.57 |
| 1999 | 34.95 | 3.17 | 27.99 | 250.0 | 23.86 | 20.36 | 1.34 | 0.82 | -12.48 | 0.26 | | | | 2.9% | 31.5% | 65.6% | | | | -12.55 | 0.06 |
| 1748 | 34.95 | 3.57 | 27.94 | 242.6 | 21.10 | 20.97 | 1.39 | 0.82 | -12.50 | 0.30 | | | | 6.1% | 61.0% | 32.9% | | | | -12.58 | 0.08 |

Table 1. continued

| Depth | Salinity | Potential Temperature | Neutral Density | Oxygen | Silicate | Nitrate | Phosphate | $PO_4^*$ | εNd | Ext. 2sd | SACW | aAAIW | iAAIW | UCDW | UNADW | MNADW | LNADW | LCDW | AABW | Calculated εNd | ΔεNd |
|---|---|---|---|---|---|---|---|---|---|---|---|---|---|---|---|---|---|---|---|---|---|
| m | | °C | $kg/m^3$ | µmol/kg | µmol/kg | µmol/kg | µmol/kg | µmol/kg | | | | | | | | | | | | | |
| 1497 | 34.91 | 4.06 | 27.86 | 218.5 | 21.49 | 23.53 | 1.55 | 0.84 | -11.57 | 0.37 | | | 7.6% | 1.1% | 91.2% | | | | | -12.80 | 1.23 |
| 1250 | 34.74 | 3.99 | 27.75 | 188.4 | 29.72 | 28.96 | 1.92 | 1.05 | -12.08 | 0.26 | | | 43.3% | | 56.7% | | | | | -12.04 | -0.04 |
| 998 | 34.53 | 3.95 | 27.59 | 169.7 | 35.39 | 33.20 | 2.21 | 1.23 | -11.59 | 0.20 | | | 80.7% | | 19.3% | | | | | -10.97 | -0.62 |
| 749 | 34.43 | 4.49 | 27.44 | 171.8 | 30.62 | 33.54 | 2.20 | 1.23 | -10.70 | 0.26 | | | 97.4% | | 2.6% | | | | | -10.40 | -0.31 |
| 500 | 34.54 | 6.50 | 27.25 | 155.3 | 19.25 | 30.96 | 2.02 | 0.95 | -11.29 | 0.26 | | | | | | | | | | | |
| 401 | 34.71 | 8.52 | 27.07 | 147.4 | 13.33 | 27.04 | 1.77 | 0.66 | -11.50 | 0.37 | | | | | | | | | | | |
| 250 | 35.38 | 14.08 | 26.52 | 150.2 | 4.68 | 15.51 | 1.06 | -0.03 | -14.12 | 0.28 | | | | | | | | | | | |
| 100 | 37.10 | 24.30 | 25.15 | 218.8 | 0.58 | 0.00 | 0.10 | -0.59 | -17.74 | 0.37 | | | | | | | | | | | |
| 25 | 37.04 | 27.81 | 23.99 | 201.8 | 0.48 | 0.00 | 0.10 | -0.70 | -15.45 | 0.37 | | | | | | | | | | | |
| Station 15 (-9.15°N -28.00°E) | | | | | | | | | | | | | | | | | | | | | |
| 5607 | 34.69 | 0.18 | 28.27 | 225.7 | 116.35 | 31.86 | 2.19 | 1.53 | -9.00 | 0.20 | | | | | | | 8.1% | 12.4% | 79.5% | -8.26 | -0.74 |
| 5001 | 34.72 | 0.38 | 28.25 | 228.5 | 107.94 | 30.83 | 2.11 | 1.46 | -8.73 | 0.32 | | | | | | | 18.7% | 8.9% | 72.4% | -8.56 | -0.17 |
| 4000 | 34.83 | 1.42 | 28.16 | 242.9 | 66.97 | 25.42 | 1.68 | 1.12 | -10.77 | 0.28 | | | | | | | 67.2% | 4.3% | 28.5% | -10.37 | -0.39 |
| 3498 | 34.91 | 2.21 | 28.10 | 256.2 | 35.12 | 20.38 | 1.38 | 0.89 | -11.99 | 0.32 | | | | | | 16.1% | 83.9% | | | -12.15 | 0.17 |
| 2499 | 34.93 | 2.76 | 28.03 | 247.5 | 30.77 | 20.99 | 1.41 | 0.87 | -13.69 | 0.37 | | | | | | 100.0% | | | | -12.50 | -1.19 |
| 2003 | 34.95 | 3.23 | 27.99 | 247.1 | 23.94 | 20.68 | 1.37 | 0.83 | -12.57 | 0.17 | | | | 3.2% | 35.4% | 61.4% | | | | -12.56 | -0.02 |
| 1750 | 34.97 | 3.66 | 27.95 | 244.7 | 18.89 | 20.40 | 1.35 | 0.80 | -12.60 | 0.30 | | | | 2.1% | 65.3% | 32.6% | | | | -12.75 | 0.15 |
| 1500 | 34.94 | 4.01 | 27.88 | 226.3 | 19.86 | 22.51 | 1.49 | 0.84 | -12.68 | 0.30 | | | 3.2% | 5.8% | 91.0% | | | | | -12.69 | 0.01 |
| 1252 | 34.80 | 4.13 | 27.77 | 191.5 | 26.53 | 27.76 | 1.85 | 1.00 | -12.25 | 0.32 | | | 33.4% | | 66.6% | | | | | -12.28 | 0.03 |
| 1000 | 34.58 | 3.98 | 27.62 | 170.4 | 34.47 | 32.72 | 2.19 | 1.22 | -11.27 | 0.26 | | | 72.6% | | 27.4% | | | | | -11.23 | -0.04 |
| 750 | 34.47 | 4.75 | 27.43 | 149.7 | 29.66 | 35.02 | 2.33 | 1.23 | -11.78 | 0.32 | 16.0% | | 71.9% | | 12.1% | | | | | -10.53 | -1.24 |
| 499 | 34.58 | 6.60 | 27.27 | 113.5 | 20.92 | 34.98 | 2.27 | 0.96 | -11.98 | 0.30 | | | | | | | | | | | |
| 400 | 34.55 | 7.73 | 27.07 | 100.4 | 17.37 | 33.86 | 2.19 | 0.81 | -12.39 | 0.32 | | | | | | | | | | | |
| 249 | 35.05 | 10.97 | 26.90 | 95.8 | 10.33 | 27.33 | 1.75 | 0.34 | -13.10 | 0.28 | | | | | | | | | | | |
| 100 | 36.86 | 24.49 | 24.91 | 209.6 | 0.26 | 0.00 | 0.10 | -0.65 | -12.29 | 0.37 | | | | | | | | | | | |
| 25 | 36.69 | 28.70 | 23.42 | 197.3 | 0.21 | 0.00 | 0.09 | -0.73 | -12.86 | 0.17 | | | | | | | | | | | |
| Station 16 (-5.67°N -28.46°E) | | | | | | | | | | | | | | | | | | | | | |
| 5519 | 34.70 | 0.24 | 28.26 | 226.0 | 114.46 | 31.74 | 2.18 | 1.52 | -9.19 | 0.30 | | | | | | | 10.5% | 12.5% | 77.0% | -8.33 | -0.86 |
| 4999 | 34.72 | 0.38 | 28.25 | 226.8 | 108.99 | 30.99 | 2.14 | 1.48 | -9.63 | 0.24 | | | | | | | 17.0% | 11.7% | 71.3% | -8.53 | -1.10 |
| 3998 | 34.84 | 1.51 | 28.15 | 247.0 | 59.64 | 23.93 | 1.62 | 1.09 | -11.26 | 0.30 | | | | | | | 72.0% | 2.9% | 25.1% | -10.58 | -0.68 |
| 3500 | 34.91 | 2.24 | 28.09 | 259.3 | 31.64 | 19.92 | 1.35 | 0.88 | -12.46 | 0.17 | | | | | | 20.0% | 80.0% | | | -12.17 | -0.29 |
| 2500 | 34.92 | 2.69 | 28.04 | 245.0 | 33.71 | 21.51 | 1.44 | 0.89 | -12.35 | 0.30 | | | | | | 91.5% | 8.5% | | | -12.46 | 0.11 |
| 2000 | 34.96 | 3.31 | 27.98 | 249.5 | 21.98 | 20.20 | 1.34 | 0.82 | -12.73 | 0.24 | | | | 1.7% | 40.8% | 57.5% | | | | -12.64 | -0.09 |
| 1751 | 34.97 | 3.78 | 27.93 | 244.7 | 17.90 | 20.30 | 1.35 | 0.80 | -12.84 | 0.24 | | | | 2.2% | 73.8% | 24.0% | | | | -12.78 | -0.05 |
| 1499 | 34.95 | 4.08 | 27.88 | 226.3 | 19.42 | 22.40 | 1.52 | 0.86 | -12.67 | 0.17 | | | 4.1% | 1.7% | 94.2% | | | | | -12.85 | 0.18 |
| 1247 | 34.82 | 4.25 | 27.77 | 190.8 | 25.10 | 27.53 | 1.86 | 1.00 | -11.96 | 0.17 | | | 29.8% | | 70.2% | | | | | -12.37 | -0.11 |

Table 1. continued

| Depth | Salinity | Potential Temperature | Neutral Density | Oxygen | Silicate | Nitrate | Phosphate | $PO_4^*$ | εNd | Ext. 2sd | SACW | aAAIW | iAAIW | UCDW | UNADW | MNADW | LNADW | LCDW | AABW | Calculated εNd | ΔεNd |
|---|---|---|---|---|---|---|---|---|---|---|---|---|---|---|---|---|---|---|---|---|---|
| m | | °C | $kg/m^3$ | µmol/kg | µmol/kg | µmol/kg | µmol/kg | µmol/kg | | | | | | | | | | | | | |
| 999 | 34.55 | 4.10 | 27.59 | 166.6 | 33.61 | 33.25 | 2.25 | 1.26 | -11.75 | 0.24 | | | 76.6% | | 23.4% | | | | | -11.10 | -0.65 |
| 749 | 34.48 | 4.98 | 27.41 | 146.9 | 28.22 | 35.09 | 2.35 | 1.24 | -11.48 | 0.30 | 29.9% | | 53.9% | | 16.2% | | | | | -10.50 | -0.98 |
| 499 | 34.58 | 6.66 | 27.26 | 118.1 | 20.86 | 34.66 | 2.26 | 0.98 | -11.64 | 0.17 | | | | | | | | | | | |
| 376 | 34.75 | 8.41 | 27.12 | 81.3 | 16.64 | 34.62 | 2.18 | 0.70 | -12.63 | 0.24 | | | | | | | | | | | |
| 250 | 34.94 | 10.22 | 26.95 | 100.9 | 11.74 | 28.54 | 1.82 | 0.44 | -12.23 | 0.30 | | | | | | | | | | | |
| 109 | 36.35 | 21.71 | 25.34 | 169.1 | 1.48 | 3.17 | 0.48 | -0.51 | -13.79 | 0.30 | | | | | | | | | | | |
| 25 | 36.36 | 28.78 | 23.15 | 200.0 | 0.28 | 0.00 | 0.09 | -0.72 | -12.61 | 0.24 | | | | | | | | | | | |
| Station 17 (-2.64°N -28.91°E) | | | | | | | | | | | | | | | | | | | | | |
| 4891 | 34.71 | 0.37 | 28.24 | 225.7 | 110.34 | 31.12 | 2.14 | 1.48 | -10.19 | 0.32 | | | | | | | 16.2% | 12.7% | 71.2% | -8.51 | -1.68 |
| 4840 | 34.71 | 0.37 | 28.25 | 225.2 | 110.37 | 31.13 | 2.14 | 1.47 | -9.53 | 0.26 | | | | | | | 16.5% | 12.5% | 71.1% | -8.51 | -1.02 |
| 4000 | 34.85 | 1.61 | 28.14 | 252.4 | 52.90 | 22.64 | 1.53 | 1.02 | -8.86 | 0.30 | | | | | | | 77.8% | | 22.2% | -10.81 | 1.95 |
| 3500 | 34.91 | 2.19 | 28.10 | 260.3 | 31.56 | 19.79 | 1.31 | 0.85 | -12.43 | 0.30 | | | | | | 13.1% | 86.9% | | | -12.14 | -0.29 |
| 2502 | 34.93 | 2.76 | 28.03 | 246.0 | 32.21 | 21.31 | 1.40 | 0.86 | -12.52 | 0.26 | | | | | | 100.0% | | | | -12.50 | -0.02 |
| 2001 | 34.97 | 3.51 | 27.96 | 254.0 | 17.92 | 19.38 | 1.27 | 0.77 | -12.61 | 0.26 | | | | | 64.1% | 45.5% | | | | -12.79 | 0.18 |
| 1750 | 34.98 | 3.72 | 27.95 | 249.9 | 17.09 | 19.70 | 1.29 | 0.77 | -12.80 | 0.26 | | | | | 81.3% | 31.2% | | | | -12.86 | 0.06 |
| 1501 | 34.98 | 4.07 | 27.90 | 239.9 | 16.26 | 20.39 | 1.35 | 0.77 | -12.81 | 0.32 | | | | | 100.0% | | | | | -13.00 | 0.19 |
| 1251 | 34.87 | 4.39 | 27.79 | 197.0 | 22.93 | 26.21 | 1.75 | 0.93 | -12.10 | 0.26 | | | 21.8% | | 78.2% | | | | | -12.55 | 0.44 |
| 1000 | 34.62 | 4.30 | 27.62 | 161.4 | 31.33 | 32.83 | 2.21 | 1.18 | -11.76 | 0.26 | | | 65.4% | | 34.6% | | | | | -11.44 | -0.32 |
| 750 | 34.48 | 4.83 | 27.43 | 154.9 | 29.16 | 34.36 | 2.29 | 1.23 | -12.89 | 0.32 | 20.9% | | 64.9% | | 14.2% | | | | | -10.54 | -2.35 |
| 499 | 34.68 | 7.71 | 27.18 | 99.7 | 17.85 | 34.14 | 2.15 | 0.77 | -9.41 | 0.32 | | | | | | | | | | | |
| 374 | 34.93 | 10.05 | 26.98 | 78.9 | 13.06 | 31.27 | 1.93 | 0.43 | -13.11 | 0.26 | | | | | | | | | | | |
| 249 | 35.17 | 12.10 | 26.77 | 97.7 | 9.26 | 25.18 | 1.60 | 0.21 | -14.68 | 0.32 | | | | | | | | | | | |
| 100 | 35.49 | 14.61 | 26.49 | 120.0 | 5.73 | 18.63 | 1.22 | -0.04 | -12.28 | 0.32 | | | | | | | | | | | |
| 17 | 35.73 | 28.75 | 22.68 | 199.6 | 0.37 | 0.00 | 0.03 | -0.78 | -12.35 | 0.26 | | | | | | | | | | | |
| Station 18 (-0.18°N -32.88°E) | | | | | | | | | | | | | | | | | | | | | |
| 4338 | 34.77 | 0.83 | 28.20 | 234.8 | 88.12 | 27.92 | 1.89 | 1.28 | -10.24 | 0.26 | | | | | | | 40.0% | 6.7% | 53.3% | -9.27 | -0.98 |
| 3999 | 34.87 | 1.74 | 28.14 | 256.9 | 45.19 | 21.42 | 1.44 | 0.96 | -12.25 | 0.32 | | | | | | | 83.8% | | 16.2% | -11.13 | -1.13 |
| 3249 | 34.91 | 2.27 | 28.09 | 254.6 | 34.30 | 20.55 | 1.35 | 0.86 | -12.11 | 0.13 | | | | | | 26.0% | 74.0% | | | -12.19 | 0.08 |
| 2994 | 34.92 | 2.41 | 28.08 | 255.5 | 32.17 | 20.42 | 1.33 | 0.84 | -12.51 | 0.32 | | | | | | 47.4% | 52.6% | | | -12.27 | -0.24 |
| 2498 | 34.94 | 2.74 | 28.05 | 254.3 | 27.38 | 20.03 | 1.30 | 0.81 | -12.27 | 0.13 | | | | | | 100.0% | | | | -12.50 | 0.23 |
| 2000 | 34.96 | 3.29 | 27.99 | 252.0 | 21.45 | 19.93 | 1.30 | 0.79 | -12.62 | 0.13 | | | | | 50.7% | 61.1% | | | | -12.72 | 0.10 |
| 1750 | 34.98 | 3.79 | 27.94 | 249.0 | 16.50 | 19.66 | 1.28 | 0.75 | -14.16 | 0.32 | | | | | 81.8% | 26.0% | | | | -12.87 | -1.29 |
| 1500 | 34.99 | 4.16 | 27.90 | 239.9 | 15.92 | 20.20 | 1.33 | 0.75 | -13.60 | 0.32 | | | | | 100.0% | | | | | -13.00 | -0.60 |
| 1252 | 34.87 | 4.46 | 27.78 | 194.7 | 22.66 | 26.35 | 1.74 | 0.90 | -12.04 | 0.26 | | | 21.2% | | 78.8% | | | | | -12.56 | 0.52 |
| 998 | 34.61 | 4.43 | 27.59 | 160.9 | 30.70 | 32.76 | 2.17 | 1.14 | -11.64 | 0.32 | | | 66.0% | | 34.0% | | | | | -11.43 | -0.22 |
| 750 | 34.51 | 5.18 | 27.41 | 151.6 | 27.09 | 33.97 | 2.23 | 1.14 | -10.75 | 0.32 | | | | | | | | | | | |

Table 1. continued

| Depth | Salinity | Potential Temperature | Neutral Density | Oxygen | Silicate | Nitrate | Phosphate | $PO_4^*$ | εNd | Ext. 2sd | SACW | aAAIW | iAAIW | UCDW | UNADW | MNADW | LNADW | LCDW | AABW | Calculated εNd | ΔεNd |
|---|---|---|---|---|---|---|---|---|---|---|---|---|---|---|---|---|---|---|---|---|---|
| m | | °C | $kg/m^3$ | µmol/kg | µmol/kg | µmol/kg | µmol/kg | µmol/kg | | | | | | | | | | | | | |
| 499 | 34.61 | 6.96 | 27.23 | 132.3 | 19.57 | 32.39 | 2.06 | 0.87 | -11.43 | 0.32 | | | | | | | | | | | |
| 400 | 34.71 | 8.02 | 27.15 | 119.8 | 16.77 | 31.38 | 1.97 | 0.71 | -11.85 | 0.32 | | | | | | | | | | | |
| 244 | 35.17 | 12.12 | 26.77 | 111.6 | 9.03 | 23.91 | 1.51 | 0.20 | -12.20 | 0.13 | | | | | | | | | | | |
| 150 | 35.40 | 14.08 | 26.54 | 165.3 | 5.07 | 14.28 | 0.99 | -0.02 | -13.38 | 0.32 | | | | | | | | | | | |
| 22 | 35.79 | 28.45 | 22.83 | 201.5 | 0.47 | 0.00 | 0.03 | -0.77 | -12.09 | 0.13 | | | | | | | | | | | |

## Appendix 2. Table 3 of Chapter 3

Table 3 of Chapter 3. Sampling location, depth, REE concentration, Ce anomaly, and $Yb_n/Nd_n$ for the 17 seawater profiles collected from the Southwest Atlantic Meridional Transect (SAMT). Errors for REE concentrations represent 2σ external errors in percent.

Table 3. Sampling location, depth, REE concentration, Ce anomaly, and $Yb_n/Nd_n$ for the 17 seawater profiles collected from the Southwest Atlantic Meridional Transect

| Depth | La | Ce | Pr | Nd | Sm | Eu | Gd | Tb | Dy | Ho | Er | Tm | Yb | Lu | Ce/Ce* | $Yb_n/Nd_n$ |
|---|---|---|---|---|---|---|---|---|---|---|---|---|---|---|---|---|
| m | pmol/kg | pmol/kg | pmol/kg | pmol/kg | pmol/kg | pmol/kg | pmol/kg | pmol/kg | pmol/kg | pmol/kg | pmol/kg | pmol/kg | pmol/kg | pmol/kg | | |
| | 5.1% | 3.4% | 1.7% | 2.8% | 4.0% | 5.5% | 5.9% | 4.7% | 4.4% | 2.3% | 4.8% | 3.3% | 4.6% | 4.3% | | |
| Station 1 (-49.55°N -52.69°E) | | | | | | | | | | | | | | | | |
| 2312 | 32.40 | 4.95 | 5.51 | 21.86 | 3.92 | 1.05 | 6.68 | 0.95 | 7.34 | 2.08 | 6.96 | 1.12 | 7.64 | 1.41 | 0.08 | 4.79 |
| 2248 | 33.60 | 4.15 | 5.22 | 21.45 | 3.83 | 1.02 | 5.89 | 0.93 | 7.30 | 1.99 | 6.94 | 1.04 | 7.26 | 1.37 | 0.07 | 4.64 |
| 2123 | 31.20 | 3.57 | 4.72 | 19.58 | 3.56 | 0.97 | 5.32 | 0.85 | 6.53 | 1.93 | 6.77 | 1.00 | 7.12 | 1.36 | 0.07 | 4.98 |
| 1874 | 29.36 | 3.67 | 4.32 | 17.68 | 3.22 | 0.82 | 5.26 | 0.82 | 6.27 | 1.84 | 6.46 | 1.00 | 6.86 | 1.29 | 0.07 | 5.32 |
| 1497 | 26.69 | 3.99 | 3.88 | 16.13 | 2.92 | 0.83 | 4.66 | 0.74 | 5.96 | 1.74 | 6.25 | 0.94 | 6.48 | 1.22 | 0.09 | 5.51 |
| 1248 | 24.93 | 4.08 | 3.58 | 14.85 | 2.70 | 0.75 | 4.35 | 0.70 | 5.56 | 1.65 | 5.85 | 0.89 | 6.14 | 1.19 | 0.10 | 5.66 |
| 987 | 22.44 | 3.73 | 3.23 | 13.35 | 2.45 | 0.67 | 4.03 | 0.64 | 5.16 | 1.54 | 5.55 | 0.82 | 5.74 | 1.10 | 0.10 | 5.90 |
| 902 | 21.96 | 3.51 | 3.12 | 13.12 | 2.49 | 0.66 | 3.53 | 0.62 | 5.03 | 1.52 | 5.56 | 0.83 | 6.01 | 1.12 | 0.09 | 6.27 |
| 800 | 21.67 | 3.60 | 3.11 | 12.80 | 2.34 | 0.65 | 3.90 | 0.61 | 4.91 | 1.46 | 5.36 | 0.79 | 5.56 | 1.04 | 0.10 | 5.96 |
| 701 | 21.44 | 3.63 | 3.10 | 12.84 | 2.30 | 0.63 | 3.79 | 0.61 | 4.82 | 1.44 | 5.17 | 0.78 | 5.38 | 1.02 | 0.10 | 5.75 |
| 599 | 19.82 | 2.89 | 2.87 | 11.85 | 2.15 | 0.60 | 3.58 | 0.57 | 4.57 | 1.38 | 5.09 | 0.74 | 5.10 | 0.97 | 0.09 | 5.90 |
| 500 | 19.05 | 3.08 | 2.76 | 11.34 | 2.09 | 0.60 | 3.50 | 0.56 | 4.51 | 1.33 | 4.83 | 0.69 | 4.94 | 0.93 | 0.10 | 5.97 |
| 300 | 17.26 | 2.91 | 2.56 | 10.67 | 1.93 | 0.52 | 3.20 | 0.51 | 4.14 | 1.24 | 4.56 | 0.64 | 4.42 | 0.83 | 0.10 | 5.67 |
| 250 | 16.83 | 2.95 | 2.51 | 10.47 | 1.91 | 0.52 | 3.21 | 0.50 | 4.07 | 1.20 | 4.39 | 0.63 | 4.32 | 0.82 | 0.10 | 5.65 |
| 100 | 14.90 | 3.79 | 2.34 | 9.84 | 1.72 | 0.50 | 2.93 | 0.47 | 3.90 | 1.14 | 4.13 | 0.60 | 4.00 | 0.74 | 0.15 | 5.57 |
| 24 | 10.26 | 3.56 | 1.99 | 8.62 | 1.52 | 0.45 | 2.84 | 0.41 | 3.69 | 1.10 | 3.91 | 0.59 | 3.60 | 0.66 | 0.18 | 5.72 |
| Station 2 (-48.97°N -48.88°E) | | | | | | | | | | | | | | | | |
| 5797 | 48.70 | 6.82 | 10.01 | 40.67 | 7.91 | 1.97 | 11.14 | 1.56 | 11.09 | 2.92 | 9.39 | 1.49 | 10.23 | 1.81 | 0.07 | 3.45 |
| 5497 | 49.06 | 4.91 | 9.16 | 35.94 | 6.85 | 1.69 | 8.85 | 1.31 | 9.76 | 2.48 | 8.47 | 1.22 | 8.67 | 1.46 | 0.05 | 3.31 |
| 5000 | 47.63 | 4.83 | 8.76 | 34.65 | 6.55 | 1.68 | 8.95 | 1.29 | 9.39 | 2.41 | 8.14 | 1.22 | 8.66 | 1.49 | 0.05 | 3.43 |
| 4001 | 42.16 | 4.51 | 7.36 | 29.31 | 5.42 | 1.40 | 7.38 | 1.11 | 8.66 | 2.19 | 7.57 | 1.12 | 8.12 | 1.37 | 0.06 | 3.80 |
| 3004 | 35.56 | 3.89 | 5.65 | 22.96 | 4.29 | 1.10 | 5.88 | 0.88 | 7.18 | 1.92 | 6.96 | 0.97 | 7.03 | 1.23 | 0.06 | 4.20 |
| 2509 | 31.77 | 3.80 | 4.92 | 20.10 | 3.70 | 1.00 | 5.48 | 0.84 | 6.68 | 1.86 | 6.60 | 0.95 | 7.03 | 1.24 | 0.07 | 4.80 |
| 2007 | 27.70 | 3.27 | 4.12 | 17.12 | 3.12 | 0.87 | 4.80 | 0.76 | 6.20 | 1.73 | 6.06 | 0.92 | 6.86 | 1.19 | 0.07 | 5.50 |
| 1504 | 24.97 | 3.78 | 3.66 | 15.48 | 2.82 | 0.75 | 4.31 | 0.70 | 5.56 | 1.61 | 5.69 | 0.86 | 6.33 | 1.10 | 0.09 | 5.61 |
| 1253 | 23.68 | 3.83 | 3.50 | 14.81 | 2.60 | 0.78 | 4.37 | 0.68 | 5.35 | 1.55 | 5.58 | 0.81 | 5.79 | 1.06 | 0.09 | 5.36 |
| 1003 | 21.96 | 3.49 | 3.19 | 13.71 | 2.36 | 0.66 | 4.18 | 0.65 | 5.23 | 1.46 | 5.55 | 0.76 | 5.55 | 0.99 | 0.09 | 5.55 |
| 746 | 20.54 | 2.95 | 2.88 | 12.36 | 2.06 | 0.64 | 3.81 | 0.60 | 4.78 | 1.38 | 4.82 | 0.69 | 5.17 | 0.94 | 0.09 | 5.74 |
| 497 | 17.64 | 2.59 | 2.60 | 11.23 | 1.81 | 0.59 | 3.41 | 0.54 | 4.39 | 1.23 | 4.80 | 0.65 | 4.80 | 0.85 | 0.09 | 5.86 |
| 400 | 16.80 | 2.56 | 2.49 | 10.72 | 1.82 | 0.53 | 3.29 | 0.52 | 4.46 | 1.26 | 4.46 | 0.66 | 4.75 | 0.82 | 0.09 | 6.08 |
| 248 | 15.38 | 2.73 | 2.34 | 10.32 | 1.68 | 0.46 | 3.11 | 0.47 | 4.08 | 1.19 | 4.39 | 0.62 | 4.13 | 0.76 | 0.10 | 5.49 |
| 99 | 13.83 | 2.94 | 2.24 | 9.67 | 1.73 | 0.48 | 3.05 | 0.46 | 4.06 | 1.11 | 4.05 | 0.57 | 3.96 | 0.71 | 0.12 | 5.61 |
| 25 | 10.85 | 3.65 | 2.10 | 9.39 | 1.65 | 0.41 | 3.14 | 0.42 | 3.63 | 1.14 | 3.81 | 0.58 | 3.64 | 0.64 | 0.18 | 5.32 |
| Station 3 (-46.93°N -47.22°E) | | | | | | | | | | | | | | | | |
| 5715 | 53.89 | 5.38 | 10.35 | 40.37 | 7.86 | 1.92 | 10.98 | 1.51 | 10.98 | 2.73 | 9.20 | 1.32 | 9.46 | 1.64 | 0.05 | 3.21 |
| 5501 | 51.92 | 4.75 | 9.50 | 38.04 | 7.50 | 1.84 | 9.41 | 1.39 | 10.14 | 2.47 | 8.64 | 1.22 | 8.91 | 1.48 | 0.05 | 3.21 |
| 4500 | 44.68 | 4.57 | 7.54 | 30.37 | 5.76 | 1.38 | 7.88 | 1.16 | 8.83 | 2.27 | 8.00 | 1.16 | 8.32 | 1.40 | 0.06 | 3.76 |
| 4001 | 40.78 | 4.22 | 6.47 | 26.53 | 4.90 | 1.23 | 6.92 | 1.04 | 7.82 | 2.08 | 7.30 | 1.06 | 7.79 | 1.31 | 0.06 | 4.02 |

Table 3. continued

| Depth | La | Ce | Pr | Nd | Sm | Eu | Gd | Tb | Dy | Ho | Er | Tm | Yb | Lu | Ce/Ce* | $Yb_n/Nd_n$ |
|---|---|---|---|---|---|---|---|---|---|---|---|---|---|---|---|---|
| m | pmol/kg | pmol/kg | pmol/kg | pmol/kg | pmol/kg | pmol/kg | pmol/kg | pmol/kg | pmol/kg | pmol/kg | pmol/kg | pmol/kg | pmol/kg | pmol/kg | | |
| | 5.1% | 3.4% | 1.7% | 2.8% | 4.0% | 5.5% | 5.9% | 4.7% | 4.4% | 2.3% | 4.8% | 3.3% | 4.6% | 4.3% | | |
| 3001 | 31.91 | 4.41 | 4.85 | 20.03 | 3.79 | 1.00 | 5.66 | 0.83 | 6.67 | 1.78 | 6.59 | 0.94 | 6.75 | 1.15 | 0.08 | 4.62 |
| 2502 | 26.91 | 4.15 | 4.23 | 17.59 | 3.40 | 0.91 | 5.06 | 0.77 | 6.06 | 1.60 | 5.83 | 0.84 | 5.93 | 0.99 | 0.09 | 4.62 |
| 2001 | 25.58 | 4.13 | 3.78 | 15.95 | 2.88 | 0.77 | 4.62 | 0.73 | 5.81 | 1.61 | 5.87 | 0.85 | 6.04 | 1.03 | 0.09 | 5.19 |
| 1501 | 22.34 | 3.56 | 3.23 | 13.75 | 2.50 | 0.68 | 4.13 | 0.67 | 5.22 | 1.50 | 5.59 | 0.82 | 5.92 | 1.05 | 0.09 | 5.91 |
| 1250 | 20.84 | 3.44 | 3.01 | 12.63 | 2.25 | 0.63 | 3.72 | 0.62 | 5.00 | 1.42 | 5.28 | 0.78 | 5.69 | 1.02 | 0.10 | 6.18 |
| 1002 | 18.98 | 2.88 | 2.79 | 12.12 | 2.22 | 0.59 | 3.70 | 0.56 | 4.60 | 1.32 | 4.99 | 0.71 | 5.06 | 0.90 | 0.09 | 5.72 |
| 751 | 17.07 | 2.74 | 2.54 | 10.71 | 1.98 | 0.56 | 3.27 | 0.52 | 4.25 | 1.23 | 4.63 | 0.66 | 4.67 | 0.84 | 0.09 | 5.98 |
| 502 | 14.72 | 3.32 | 2.27 | 9.85 | 1.78 | 0.48 | 2.94 | 0.49 | 3.91 | 1.12 | 4.07 | 0.59 | 4.12 | 0.73 | 0.13 | 5.73 |
| 401 | 14.54 | 3.53 | 2.27 | 9.96 | 1.79 | 0.51 | 2.97 | 0.49 | 3.84 | 1.11 | 4.04 | 0.59 | 4.05 | 0.71 | 0.14 | 5.58 |
| 250 | 14.17 | 4.55 | 2.51 | 10.54 | 2.00 | 0.55 | 3.08 | 0.48 | 3.87 | 1.06 | 3.87 | 0.53 | 3.53 | 0.61 | 0.17 | 4.59 |
| 99 | 14.55 | 8.22 | 2.90 | 12.09 | 2.40 | 0.62 | 3.54 | 0.53 | 4.09 | 1.07 | 3.69 | 0.50 | 3.26 | 0.52 | 0.29 | 3.70 |
| 26 | 11.28 | 9.34 | 2.71 | 11.18 | 2.16 | 0.56 | 3.54 | 0.49 | 3.78 | 1.07 | 3.38 | 0.51 | 2.87 | 0.48 | 0.39 | 3.52 |
| Station 5 (-42.38°N -44.02°E) | | | | | | | | | | | | | | | | |
| 5146 | 51.84 | 6.65 | 10.54 | 41.82 | 8.07 | 2.13 | 11.09 | 1.62 | 11.36 | 2.89 | 9.40 | 1.39 | 9.94 | 1.75 | 0.07 | 3.26 |
| 5001 | 44.91 | 4.45 | 8.89 | 35.28 | 6.78 | 1.70 | 9.73 | 1.37 | 9.86 | 2.45 | 7.91 | 1.18 | 8.37 | 1.47 | 0.05 | 3.25 |
| 4000 | 39.26 | 4.53 | 6.89 | 27.12 | 5.08 | 1.35 | 7.45 | 1.09 | 8.15 | 2.11 | 6.97 | 1.07 | 7.65 | 1.39 | 0.06 | 3.87 |
| 3502 | 34.15 | 3.74 | 5.83 | 23.11 | 4.23 | 1.14 | 6.75 | 0.98 | 7.37 | 2.00 | 6.62 | 1.01 | 7.32 | 1.32 | 0.06 | 4.34 |
| 2503 | 25.17 | 3.49 | 4.20 | 16.98 | 3.22 | 0.88 | 5.15 | 0.76 | 5.97 | 1.60 | 5.67 | 0.84 | 5.84 | 1.04 | 0.08 | 4.71 |
| 2000 | 23.83 | 3.59 | 3.68 | 15.08 | 2.83 | 0.75 | 4.59 | 0.70 | 5.72 | 1.58 | 5.47 | 0.81 | 5.74 | 1.05 | 0.09 | 5.22 |
| 1748 | 29.78 | 4.54 | 4.45 | 18.94 | 3.51 | 0.95 | 5.38 | 0.84 | 7.03 | 1.93 | 6.99 | 1.04 | 7.64 | 1.34 | 0.09 | 5.53 |
| 1500 | 21.75 | 3.53 | 3.26 | 13.68 | 2.52 | 0.70 | 3.99 | 0.62 | 5.13 | 1.44 | 5.36 | 0.77 | 5.64 | 0.99 | 0.09 | 5.65 |
| 1250 | 25.22 | 4.02 | 3.73 | 15.36 | 2.82 | 0.78 | 4.53 | 0.71 | 5.86 | 1.69 | 6.34 | 0.92 | 6.72 | 1.18 | 0.09 | 6.00 |
| 999 | 18.40 | 2.79 | 2.73 | 11.23 | 2.13 | 0.60 | 3.65 | 0.56 | 4.59 | 1.32 | 4.73 | 0.71 | 4.94 | 0.92 | 0.09 | 6.02 |
| 748 | 19.10 | 4.82 | 3.05 | 12.48 | 2.36 | 0.65 | 3.99 | 0.63 | 5.17 | 1.45 | 5.25 | 0.77 | 5.39 | 0.96 | 0.14 | 5.92 |
| 500 | 15.65 | 2.94 | 2.47 | 10.51 | 1.89 | 0.50 | 3.20 | 0.51 | 4.21 | 1.23 | 4.35 | 0.65 | 4.41 | 0.80 | 0.11 | 5.76 |
| 400 | 14.92 | 3.60 | 2.39 | 10.25 | 1.82 | 0.50 | 2.94 | 0.49 | 3.88 | 1.12 | 4.14 | 0.57 | 4.11 | 0.71 | 0.14 | 5.49 |
| 247 | 14.09 | 3.66 | 2.45 | 10.32 | 1.87 | 0.52 | 2.91 | 0.48 | 3.88 | 1.09 | 3.95 | 0.54 | 3.70 | 0.64 | 0.14 | 4.92 |
| 100 | 13.93 | 7.65 | 2.72 | 11.27 | 2.09 | 0.54 | 3.12 | 0.48 | 3.81 | 1.04 | 3.61 | 0.49 | 3.22 | 0.51 | 0.29 | 3.92 |
| 25 | 11.00 | 6.73 | 2.27 | 9.07 | 1.54 | 0.40 | 2.52 | 0.33 | 2.37 | 0.66 | 1.80 | 0.24 | 1.24 | 0.20 | 0.31 | 1.88 |
| Station 6 (-39.97°N -42.49°E) | | | | | | | | | | | | | | | | |
| 5132 | 50.30 | 3.81 | 10.09 | 39.23 | 7.63 | 1.88 | 10.23 | 1.44 | 10.88 | 2.70 | 8.76 | 1.32 | 9.10 | 1.59 | 0.04 | 3.18 |
| 5000 | 50.82 | 4.48 | 9.08 | 37.83 | 7.42 | 1.73 | 9.22 | 1.38 | 10.17 | 2.55 | 8.42 | 1.25 | 8.91 | 1.49 | 0.05 | 3.23 |
| 4001 | 42.26 | 5.04 | 6.90 | 29.16 | 5.70 | 1.38 | 7.60 | 1.13 | 8.45 | 2.22 | 7.83 | 1.13 | 8.06 | 1.36 | 0.07 | 3.79 |
| 3501 | 37.43 | 4.05 | 5.76 | 24.45 | 4.63 | 1.15 | 6.49 | 0.97 | 7.65 | 2.01 | 6.94 | 1.04 | 7.42 | 1.24 | 0.06 | 4.16 |
| 3002 | 27.73 | 4.24 | 4.29 | 18.61 | 3.58 | 0.91 | 5.12 | 0.80 | 6.26 | 1.67 | 5.85 | 0.86 | 6.03 | 1.01 | 0.09 | 4.44 |
| 2000 | 24.51 | 4.44 | 3.74 | 16.16 | 3.19 | 0.81 | 4.75 | 0.73 | 5.85 | 1.53 | 5.57 | 0.83 | 5.77 | 0.96 | 0.10 | 4.89 |
| 1751 | 23.21 | 4.41 | 3.59 | 15.61 | 2.88 | 0.77 | 4.44 | 0.68 | 5.50 | 1.54 | 5.42 | 0.82 | 5.53 | 0.94 | 0.11 | 4.86 |
| 1499 | 22.56 | 3.95 | 3.19 | 14.01 | 2.57 | 0.72 | 4.14 | 0.63 | 5.33 | 1.50 | 5.39 | 0.81 | 5.74 | 0.99 | 0.10 | 5.62 |
| 1250 | 21.41 | 3.56 | 2.96 | 13.11 | 2.46 | 0.65 | 3.86 | 0.59 | 4.95 | 1.42 | 5.14 | 0.77 | 5.48 | 0.94 | 0.10 | 5.73 |

Table 3. continued

| Depth | La | Ce | Pr | Nd | Sm | Eu | Gd | Tb | Dy | Ho | Er | Tm | Yb | Lu | Ce/Ce* | $Yb_n/Nd_n$ |
|---|---|---|---|---|---|---|---|---|---|---|---|---|---|---|---|---|
| m | pmol/kg | pmol/kg | pmol/kg | pmol/kg | pmol/kg | pmol/kg | pmol/kg | pmol/kg | pmol/kg | pmol/kg | pmol/kg | pmol/kg | pmol/kg | pmol/kg | | |
| | 5.1% | 3.4% | 1.7% | 2.8% | 4.0% | 5.5% | 5.9% | 4.7% | 4.4% | 2.3% | 4.8% | 3.3% | 4.6% | 4.3% | | |
| 1000 | 19.61 | 3.28 | 2.81 | 12.16 | 2.28 | 0.62 | 3.56 | 0.55 | 4.65 | 1.32 | 4.76 | 0.73 | 4.98 | 0.87 | 0.10 | 5.62 |
| 500 | 15.24 | 4.19 | 2.38 | 10.35 | 1.95 | 0.53 | 3.26 | 0.47 | 4.17 | 1.16 | 4.25 | 0.61 | 4.21 | 0.72 | 0.16 | 5.58 |
| 399 | 14.20 | 3.08 | 2.32 | 10.19 | 1.89 | 0.50 | 3.09 | 0.47 | 3.90 | 1.10 | 4.01 | 0.59 | 3.94 | 0.67 | 0.12 | 5.31 |
| 250 | 14.09 | 3.93 | 2.45 | 10.47 | 2.03 | 0.56 | 3.09 | 0.47 | 3.90 | 1.06 | 3.79 | 0.55 | 3.61 | 0.59 | 0.15 | 4.73 |
| 101 | 14.31 | 7.80 | 2.86 | 12.39 | 2.45 | 0.62 | 3.55 | 0.54 | 4.11 | 1.08 | 3.64 | 0.51 | 3.18 | 0.52 | 0.28 | 3.52 |
| 25 | 16.65 | 15.32 | 4.17 | 16.92 | 3.49 | 0.77 | 5.20 | 0.71 | 5.72 | 1.42 | 4.55 | 0.67 | 3.86 | 0.64 | 0.42 | 3.13 |
| Station 7 (-37.83°N -41.12°E) | | | | | | | | | | | | | | | | |
| 5023 | 51.64 | 3.78 | 9.25 | 37.34 | 7.21 | 1.82 | 9.18 | 1.41 | 9.78 | 2.48 | 8.61 | 1.19 | 8.64 | 1.45 | 0.04 | 3.17 |
| 5000 | 51.52 | 3.73 | 9.22 | 37.92 | 7.21 | 1.82 | 9.27 | 1.41 | 10.05 | 2.47 | 8.67 | 1.18 | 8.58 | 1.44 | 0.04 | 3.10 |
| 4000 | 41.97 | 4.50 | 6.75 | 27.69 | 5.15 | 1.37 | 7.55 | 1.10 | 8.18 | 2.08 | 7.55 | 1.04 | 7.77 | 1.31 | 0.06 | 3.85 |
| 3500 | 36.89 | 3.77 | 5.68 | 23.91 | 4.28 | 1.15 | 5.99 | 0.96 | 7.22 | 1.89 | 6.84 | 0.98 | 7.04 | 1.20 | 0.06 | 4.03 |
| 2501 | 24.35 | 3.99 | 4.07 | 16.80 | 3.15 | 0.88 | 5.40 | 0.76 | 5.85 | 1.64 | 5.71 | 0.86 | 5.89 | 1.04 | 0.09 | 4.81 |
| 2000 | 22.24 | 4.09 | 3.61 | 15.26 | 2.85 | 0.76 | 4.91 | 0.69 | 5.72 | 1.58 | 5.60 | 0.85 | 5.78 | 1.02 | 0.10 | 5.19 |
| 1748 | 21.22 | 3.73 | 3.38 | 14.04 | 2.63 | 0.76 | 4.61 | 0.64 | 5.25 | 1.53 | 5.44 | 0.83 | 5.77 | 1.04 | 0.10 | 5.64 |
| 1500 | 20.11 | 3.62 | 3.08 | 12.96 | 2.36 | 0.67 | 4.37 | 0.61 | 5.00 | 1.45 | 5.10 | 0.79 | 5.51 | 0.97 | 0.10 | 5.83 |
| 1249 | 18.52 | 3.16 | 2.81 | 11.78 | 2.17 | 0.63 | 3.95 | 0.55 | 4.68 | 1.31 | 4.88 | 0.70 | 4.88 | 0.90 | 0.10 | 5.68 |
| 1000 | 16.22 | 2.85 | 2.62 | 10.80 | 2.01 | 0.54 | 3.54 | 0.51 | 4.25 | 1.26 | 4.41 | 0.68 | 4.52 | 0.82 | 0.10 | 5.74 |
| 751 | 14.16 | 2.78 | 2.41 | 9.92 | 1.85 | 0.51 | 3.45 | 0.47 | 3.95 | 1.15 | 4.09 | 0.60 | 4.03 | 0.72 | 0.11 | 5.57 |
| 409 | 13.70 | 3.25 | 2.58 | 10.66 | 2.07 | 0.57 | 3.32 | 0.48 | 3.81 | 1.04 | 3.70 | 0.53 | 3.46 | 0.57 | 0.13 | 4.45 |
| 349 | 13.77 | 4.19 | 2.76 | 11.51 | 2.24 | 0.59 | 3.42 | 0.49 | 3.91 | 1.06 | 3.62 | 0.50 | 3.21 | 0.54 | 0.16 | 3.83 |
| 249 | 13.97 | 8.24 | 2.99 | 12.38 | 2.46 | 0.66 | 3.82 | 0.52 | 4.05 | 1.09 | 3.63 | 0.48 | 2.98 | 0.48 | 0.29 | 3.30 |
| 101 | 13.27 | 9.93 | 2.84 | 12.10 | 2.30 | 0.66 | 3.65 | 0.50 | 3.92 | 1.05 | 3.44 | 0.45 | 2.87 | 0.45 | 0.37 | 3.25 |
| 24 | 14.02 | 11.74 | 3.03 | 12.47 | 2.46 | 0.65 | 3.80 | 0.52 | 3.90 | 1.02 | 3.41 | 0.44 | 2.70 | 0.42 | 0.41 | 2.97 |
| Station 8 (-35.01°N -39.44°E) | | | | | | | | | | | | | | | | |
| 4838 | 47.27 | 4.85 | 9.78 | 39.13 | 7.34 | 1.86 | 9.66 | 1.46 | 10.53 | 2.76 | 8.88 | 1.32 | 9.17 | 1.61 | 0.05 | 3.21 |
| 4787 | 52.31 | 4.83 | 9.56 | 37.62 | 7.52 | 1.85 | 9.32 | 1.43 | 10.13 | 2.57 | 8.44 | 1.22 | 8.94 | 1.65 | 0.05 | 3.26 |
| 4000 | 49.01 | 4.95 | 8.61 | 34.08 | 6.54 | 1.60 | 8.84 | 1.34 | 9.46 | 2.45 | 8.11 | 1.15 | 8.70 | 1.59 | 0.05 | 3.50 |
| 3501 | 35.94 | 4.27 | 5.99 | 23.71 | 4.65 | 1.16 | 6.16 | 0.98 | 7.24 | 1.91 | 6.50 | 0.92 | 6.77 | 1.23 | 0.07 | 3.91 |
| 2500 | 25.39 | 4.21 | 4.21 | 17.42 | 3.52 | 0.90 | 4.65 | 0.78 | 5.86 | 1.58 | 5.31 | 0.77 | 5.34 | 0.97 | 0.09 | 4.20 |
| 2001 | 24.14 | 4.20 | 3.77 | 15.46 | 3.17 | 0.76 | 4.37 | 0.71 | 5.49 | 1.53 | 5.05 | 0.76 | 5.50 | 1.03 | 0.10 | 4.88 |
| 1749 | 21.48 | 3.99 | 3.55 | 14.96 | 2.61 | 0.68 | 4.14 | 0.72 | 5.47 | 1.61 | 5.33 | 0.88 | 5.81 | 1.12 | 0.10 | 5.33 |
| 1501 | 20.25 | 3.60 | 3.16 | 13.53 | 2.41 | 0.66 | 4.06 | 0.64 | 5.22 | 1.55 | 5.09 | 0.81 | 5.45 | 1.08 | 0.10 | 5.52 |
| 1251 | 18.82 | 3.48 | 2.96 | 12.20 | 2.18 | 0.85 | 3.37 | 0.61 | 4.70 | 1.40 | 4.61 | 0.75 | 5.26 | 1.01 | 0.11 | 5.92 |
| 1001 | 15.70 | 2.83 | 2.59 | 10.74 | 1.87 | 0.52 | 3.13 | 0.51 | 4.18 | 1.25 | 4.30 | 0.69 | 4.38 | 0.85 | 0.10 | 5.59 |
| 751 | 13.92 | 3.16 | 2.48 | 10.04 | 1.88 | 0.55 | 2.96 | 0.50 | 3.91 | 1.19 | 3.89 | 0.62 | 3.99 | 0.78 | 0.12 | 5.45 |
| 501 | 12.92 | 3.27 | 2.77 | 11.20 | 2.22 | 0.56 | 3.24 | 0.52 | 3.86 | 1.11 | 3.68 | 0.51 | 3.22 | 0.58 | 0.13 | 3.94 |
| 400 | 13.23 | 5.75 | 2.80 | 11.69 | 2.18 | 0.59 | 3.12 | 0.54 | 3.93 | 1.09 | 3.46 | 0.50 | 3.11 | 0.54 | 0.22 | 3.64 |
| 251 | 13.55 | 8.93 | 3.02 | 12.12 | 2.33 | 0.59 | 3.24 | 0.56 | 4.08 | 1.09 | 3.51 | 0.50 | 2.88 | 0.52 | 0.32 | 3.26 |
| 100 | 10.54 | 9.16 | 2.38 | 9.86 | 1.78 | 0.46 | 2.58 | 0.44 | 3.38 | 0.94 | 3.07 | 0.42 | 2.38 | 0.43 | 0.42 | 3.31 |

Table 3. continued

| Depth | La | Ce | Pr | Nd | Sm | Eu | Gd | Tb | Dy | Ho | Er | Tm | Yb | Lu | Ce/Ce* | $Yb_n/Nd_n$ |
|---|---|---|---|---|---|---|---|---|---|---|---|---|---|---|---|---|
| m | pmol/kg | pmol/kg | pmol/kg | pmol/kg | pmol/kg | pmol/kg | pmol/kg | pmol/kg | pmol/kg | pmol/kg | pmol/kg | pmol/kg | pmol/kg | pmol/kg | | |
| | 5.1% | 3.4% | 1.7% | 2.8% | 4.0% | 5.5% | 5.9% | 4.7% | 4.4% | 2.3% | 4.8% | 3.3% | 4.6% | 4.3% | | |
| 24 | 11.72 | 11.76 | 2.73 | 11.29 | 2.14 | 0.71 | 3.47 | 0.51 | 3.78 | 1.01 | 2.97 | 0.45 | 2.62 | 0.42 | 0.48 | 3.18 |
| Station 9 (-32.09°N -37.46°E) | | | | | | | | | | | | | | | | |
| 4121 | 42.56 | 4.39 | 7.91 | 32.18 | 6.16 | 1.49 | 8.95 | 1.19 | 9.13 | 2.35 | 7.83 | 1.17 | 8.14 | 1.42 | 0.05 | 3.47 |
| 4085 | 44.21 | 4.43 | 7.45 | 30.95 | 5.66 | 1.40 | 8.17 | 1.17 | 8.62 | 2.27 | 7.66 | 1.14 | 8.00 | 1.37 | 0.06 | 3.54 |
| 3498 | 35.42 | 4.03 | 6.11 | 25.32 | 4.62 | 1.17 | 6.68 | 1.00 | 7.21 | 1.88 | 6.44 | 0.92 | 6.39 | 1.08 | 0.06 | 3.46 |
| 2999 | 27.19 | 3.26 | 4.75 | 19.79 | 3.61 | 0.95 | 5.55 | 0.82 | 6.03 | 1.63 | 5.52 | 0.78 | 5.30 | 0.90 | 0.07 | 3.67 |
| 2500 | 24.86 | 3.88 | 4.25 | 17.72 | 3.38 | 0.89 | 5.25 | 0.79 | 5.76 | 1.55 | 5.31 | 0.76 | 5.12 | 0.86 | 0.09 | 3.96 |
| 1999 | 23.40 | 4.24 | 3.67 | 15.69 | 2.83 | 0.75 | 4.76 | 0.72 | 5.50 | 1.51 | 5.33 | 0.78 | 5.37 | 0.92 | 0.10 | 4.69 |
| 1749 | 22.89 | 3.74 | 3.41 | 14.71 | 2.58 | 0.74 | 4.53 | 0.70 | 5.29 | 1.50 | 5.36 | 0.80 | 5.48 | 0.97 | 0.10 | 5.11 |
| 1499 | 21.56 | 3.89 | 3.11 | 13.25 | 2.31 | 0.65 | 4.20 | 0.63 | 5.01 | 1.43 | 5.22 | 0.76 | 5.44 | 0.95 | 0.11 | 5.63 |
| 1249 | 19.57 | 3.17 | 2.90 | 12.51 | 2.20 | 0.61 | 3.81 | 0.59 | 4.62 | 1.38 | 4.91 | 0.73 | 5.13 | 0.91 | 0.09 | 5.62 |
| 1001 | 16.98 | 2.70 | 2.65 | 11.31 | 2.07 | 0.56 | 3.47 | 0.55 | 4.27 | 1.25 | 4.39 | 0.66 | 4.43 | 0.79 | 0.09 | 5.36 |
| 752 | 14.79 | 2.34 | 2.42 | 10.36 | 1.89 | 0.52 | 3.17 | 0.49 | 3.82 | 1.13 | 4.00 | 0.58 | 3.87 | 0.68 | 0.09 | 5.13 |
| 500 | 13.92 | 3.57 | 2.65 | 11.22 | 2.07 | 0.56 | 3.24 | 0.50 | 3.75 | 1.03 | 3.51 | 0.49 | 3.04 | 0.50 | 0.13 | 3.71 |
| 401 | 13.60 | 5.23 | 2.73 | 11.30 | 2.15 | 0.57 | 3.37 | 0.51 | 3.86 | 1.03 | 3.49 | 0.48 | 2.95 | 0.47 | 0.20 | 3.58 |
| 250 | 13.20 | 8.11 | 2.72 | 11.46 | 2.14 | 0.56 | 3.30 | 0.51 | 3.78 | 1.00 | 3.37 | 0.45 | 2.74 | 0.43 | 0.31 | 3.27 |
| 101 | 11.53 | 9.06 | 2.45 | 10.02 | 1.90 | 0.51 | 2.96 | 0.44 | 3.32 | 0.91 | 3.12 | 0.40 | 2.42 | 0.39 | 0.39 | 3.32 |
| 26 | 12.34 | 13.23 | 2.63 | 10.69 | 2.12 | 0.57 | 3.25 | 0.46 | 3.44 | 0.94 | 3.15 | 0.43 | 2.45 | 0.39 | 0.53 | 3.14 |
| Station 10 (-29.06°N -35.78°E) | | | | | | | | | | | | | | | | |
| 3835 | 38.45 | 4.22 | 7.76 | 31.39 | 5.67 | 1.43 | 8.65 | 1.19 | 8.53 | 2.33 | 7.34 | 1.15 | 7.62 | 1.32 | 0.06 | 3.33 |
| 3786 | 39.94 | 4.15 | 7.46 | 30.17 | 5.67 | 1.37 | 7.72 | 1.13 | 8.40 | 2.18 | 7.16 | 1.07 | 7.30 | 1.23 | 0.06 | 3.32 |
| 3502 | 34.97 | 4.25 | 6.57 | 25.99 | 4.97 | 1.22 | 6.71 | 1.00 | 7.57 | 1.93 | 6.43 | 0.94 | 6.40 | 1.06 | 0.06 | 3.38 |
| 2999 | 27.20 | 3.35 | 5.05 | 20.39 | 3.88 | 0.95 | 5.57 | 0.83 | 6.35 | 1.68 | 5.54 | 0.83 | 5.53 | 0.93 | 0.07 | 3.72 |
| 2502 | 24.43 | 3.63 | 4.38 | 17.93 | 3.39 | 0.84 | 5.32 | 0.78 | 6.03 | 1.64 | 5.52 | 0.80 | 5.45 | 0.91 | 0.08 | 4.17 |
| 2001 | 24.90 | 3.61 | 4.03 | 16.72 | 3.17 | 0.83 | 4.74 | 0.74 | 5.80 | 1.56 | 5.45 | 0.80 | 5.57 | 0.96 | 0.08 | 4.57 |
| 1750 | 24.18 | 3.57 | 3.75 | 15.61 | 2.97 | 0.82 | 4.52 | 0.69 | 5.60 | 1.52 | 5.43 | 0.80 | 5.69 | 0.96 | 0.08 | 5.00 |
| 1501 | 23.25 | 3.77 | 3.47 | 14.56 | 2.71 | 0.75 | 4.16 | 0.67 | 5.48 | 1.51 | 5.44 | 0.81 | 5.75 | 1.00 | 0.09 | 5.42 |
| 1296 | 22.13 | 3.76 | 3.29 | 13.68 | 2.53 | 0.69 | 3.91 | 0.62 | 5.04 | 1.44 | 5.27 | 0.78 | 5.49 | 0.97 | 0.10 | 5.50 |
| 1003 | 18.69 | 3.02 | 2.79 | 11.89 | 2.19 | 0.61 | 3.48 | 0.54 | 4.45 | 1.28 | 4.63 | 0.69 | 4.82 | 0.84 | 0.09 | 5.56 |
| 751 | 15.86 | 2.44 | 2.58 | 10.91 | 1.99 | 0.54 | 3.09 | 0.49 | 4.15 | 1.15 | 4.06 | 0.60 | 4.12 | 0.71 | 0.09 | 5.18 |
| 500 | 14.66 | 3.15 | 2.75 | 11.35 | 2.12 | 0.57 | 3.08 | 0.50 | 3.91 | 1.06 | 3.73 | 0.51 | 3.34 | 0.54 | 0.11 | 4.04 |
| 402 | 14.90 | 4.87 | 2.97 | 12.06 | 2.29 | 0.59 | 3.39 | 0.51 | 3.91 | 1.06 | 3.52 | 0.48 | 2.94 | 0.47 | 0.17 | 3.34 |
| 252 | 13.83 | 7.84 | 2.88 | 11.77 | 2.37 | 0.61 | 3.42 | 0.51 | 3.93 | 1.02 | 3.50 | 0.47 | 2.95 | 0.47 | 0.29 | 3.44 |
| 107 | 10.91 | 8.98 | 2.32 | 9.61 | 1.81 | 0.47 | 2.82 | 0.42 | 3.38 | 0.90 | 3.04 | 0.41 | 2.45 | 0.38 | 0.41 | 3.50 |
| 25 | 10.26 | 10.64 | 2.33 | 9.64 | 1.80 | 0.49 | 2.73 | 0.43 | 3.13 | 0.90 | 2.82 | 0.41 | 2.25 | 0.36 | 0.50 | 3.20 |
| Station 11 (-26.09°N -34.26°E) | | | | | | | | | | | | | | | | |
| 4548 | 42.38 | 4.56 | 9.17 | 36.82 | 7.04 | 1.76 | 10.11 | 1.40 | 10.14 | 2.69 | 8.78 | 1.37 | 9.24 | 1.58 | 0.05 | 3.44 |
| 4001 | 42.00 | 4.58 | 7.99 | 31.74 | 5.90 | 1.48 | 8.29 | 1.22 | 8.90 | 2.25 | 7.28 | 1.10 | 7.77 | 1.37 | 0.06 | 3.36 |
| 3493 | 30.61 | 3.83 | 6.12 | 24.76 | 4.58 | 1.16 | 6.60 | 0.98 | 6.94 | 1.89 | 5.94 | 0.89 | 6.07 | 1.04 | 0.06 | 3.36 |

Table 3. continued

| Depth | La | Ce | Pr | Nd | Sm | Eu | Gd | Tb | Dy | Ho | Er | Tm | Yb | Lu | Ce/Ce* | $Yb_n/Nd_n$ |
|---|---|---|---|---|---|---|---|---|---|---|---|---|---|---|---|---|
| m | pmol/kg | pmol/kg | pmol/kg | pmol/kg | pmol/kg | pmol/kg | pmol/kg | pmol/kg | pmol/kg | pmol/kg | pmol/kg | pmol/kg | pmol/kg | pmol/kg | | |
| | 5.1% | 3.4% | 1.7% | 2.8% | 4.0% | 5.5% | 5.9% | 4.7% | 4.4% | 2.3% | 4.8% | 3.3% | 4.6% | 4.3% | | |
| 3000 | 25.70 | 3.11 | 4.95 | 19.58 | 3.67 | 0.91 | 5.26 | 0.88 | 6.02 | 1.78 | 5.19 | 0.82 | 5.27 | 1.03 | 0.06 | 3.69 |
| 2503 | 23.17 | 3.55 | 4.57 | 18.25 | 3.35 | 0.81 | 5.15 | 0.82 | 5.80 | 1.81 | 5.25 | 0.79 | 5.13 | 1.00 | 0.08 | 3.85 |
| 2000 | 21.59 | 4.16 | 4.21 | 16.69 | 3.21 | 0.80 | 4.79 | 0.82 | 5.53 | 1.68 | 5.06 | 0.78 | 5.04 | 0.97 | 0.10 | 4.14 |
| 1749 | 21.76 | 4.03 | 4.01 | 15.72 | 2.89 | 0.78 | 4.61 | 0.75 | 5.39 | 1.61 | 5.11 | 0.77 | 5.19 | 1.06 | 0.10 | 4.53 |
| 1501 | 20.96 | 3.86 | 3.49 | 14.04 | 2.79 | 0.72 | 4.10 | 0.69 | 5.37 | 1.51 | 5.18 | 0.78 | 5.48 | 1.00 | 0.10 | 5.36 |
| 1249 | 19.95 | 3.62 | 3.07 | 12.60 | 2.48 | 0.67 | 3.82 | 0.60 | 4.83 | 1.43 | 4.91 | 0.75 | 5.31 | 1.02 | 0.10 | 5.78 |
| 998 | 18.27 | 3.35 | 2.84 | 11.68 | 2.21 | 0.59 | 3.45 | 0.56 | 4.45 | 1.30 | 4.46 | 0.69 | 4.82 | 0.90 | 0.10 | 5.66 |
| 750 | 15.21 | 2.68 | 2.58 | 10.55 | 2.01 | 0.55 | 3.11 | 0.49 | 3.91 | 1.14 | 3.91 | 0.58 | 3.98 | 0.74 | 0.10 | 5.17 |
| 501 | 13.68 | 3.39 | 2.60 | 10.46 | 2.09 | 0.53 | 2.99 | 0.48 | 3.71 | 1.02 | 3.39 | 0.49 | 3.18 | 0.57 | 0.13 | 4.17 |
| 403 | 13.28 | 5.08 | 2.64 | 10.73 | 2.19 | 0.56 | 3.07 | 0.49 | 3.67 | 1.02 | 3.33 | 0.46 | 2.97 | 0.51 | 0.20 | 3.80 |
| 249 | 10.90 | 6.74 | 2.24 | 9.03 | 1.72 | 0.47 | 2.59 | 0.42 | 3.23 | 0.87 | 2.83 | 0.38 | 2.33 | 0.39 | 0.31 | 3.53 |
| 100 | 9.91 | 7.93 | 2.00 | 8.25 | 1.49 | 0.39 | 2.35 | 0.37 | 2.89 | 0.76 | 2.43 | 0.32 | 1.90 | 0.30 | 0.41 | 3.16 |
| 25 | 10.69 | 10.25 | 2.13 | 9.04 | 1.61 | 0.46 | 2.59 | 0.40 | 3.02 | 0.82 | 2.62 | 0.35 | 1.99 | 0.31 | 0.49 | 3.02 |
| Station 12 (-22.47°N -32.73°E) | | | | | | | | | | | | | | | | |
| 4510 | 48.51 | 5.07 | 8.85 | 35.03 | 6.69 | 1.69 | 8.85 | 1.29 | 9.59 | 2.37 | 8.21 | 1.20 | 8.59 | 1.46 | 0.06 | 3.36 |
| 4002 | 38.01 | 4.28 | 7.53 | 29.42 | 5.72 | 1.36 | 7.55 | 1.15 | 8.31 | 2.15 | 6.97 | 1.03 | 6.99 | 1.30 | 0.06 | 3.26 |
| 3499 | 30.13 | 3.76 | 5.74 | 22.85 | 4.16 | 1.07 | 5.92 | 0.90 | 6.60 | 1.71 | 5.61 | 0.83 | 5.56 | 1.03 | 0.07 | 3.33 |
| 3002 | 26.20 | 3.26 | 4.79 | 19.01 | 3.72 | 0.95 | 5.02 | 0.80 | 5.81 | 1.57 | 5.13 | 0.76 | 5.26 | 0.94 | 0.07 | 3.79 |
| 2501 | 23.96 | 3.66 | 4.35 | 17.36 | 3.37 | 0.91 | 4.98 | 0.79 | 5.69 | 1.52 | 5.05 | 0.72 | 5.03 | 0.92 | 0.08 | 3.97 |
| 1999 | 25.23 | 5.04 | 4.46 | 17.75 | 3.50 | 0.91 | 5.08 | 0.81 | 6.01 | 1.58 | 5.30 | 0.76 | 5.20 | 0.95 | 0.11 | 4.02 |
| 1751 | 23.26 | 4.81 | 4.24 | 16.97 | 3.45 | 0.87 | 5.14 | 0.79 | 6.01 | 1.59 | 5.46 | 0.78 | 5.26 | 0.94 | 0.11 | 4.25 |
| 1502 | 22.77 | 4.66 | 3.95 | 16.00 | 3.16 | 0.83 | 4.76 | 0.75 | 5.82 | 1.57 | 5.40 | 0.79 | 5.42 | 0.97 | 0.11 | 4.65 |
| 1250 | 21.97 | 4.28 | 3.55 | 14.50 | 2.79 | 0.73 | 4.37 | 0.67 | 5.49 | 1.52 | 5.29 | 0.80 | 5.56 | 1.01 | 0.11 | 5.25 |
| 999 | 19.50 | 3.09 | 3.10 | 12.76 | 2.35 | 0.65 | 3.86 | 0.63 | 5.03 | 1.40 | 5.07 | 0.75 | 5.33 | 0.98 | 0.09 | 5.72 |
| 752 | 17.69 | 2.61 | 2.83 | 11.60 | 2.22 | 0.59 | 3.56 | 0.55 | 4.45 | 1.25 | 4.36 | 0.65 | 4.44 | 0.80 | 0.08 | 5.24 |
| 502 | 13.44 | 3.39 | 2.69 | 11.36 | 2.09 | 0.56 | 3.16 | 0.54 | 4.07 | 1.35 | 3.50 | 0.56 | 3.70 | 0.69 | 0.13 | 4.46 |
| 401 | 12.80 | 5.32 | 2.78 | 11.23 | 2.16 | 0.56 | 3.28 | 0.54 | 4.16 | 1.32 | 3.49 | 0.52 | 3.48 | 0.62 | 0.21 | 4.25 |
| 250 | 11.12 | 7.41 | 2.41 | 10.06 | 1.82 | 0.46 | 2.80 | 0.47 | 3.39 | 1.04 | 2.94 | 0.44 | 2.66 | 0.47 | 0.33 | 3.63 |
| 100 | 10.20 | 9.65 | 2.34 | 9.22 | 1.73 | 0.45 | 2.67 | 0.43 | 3.11 | 0.95 | 2.60 | 0.37 | 2.08 | 0.36 | 0.45 | 3.10 |
| 24 | 10.01 | 9.40 | 2.10 | 8.56 | 1.56 | 0.43 | 2.45 | 0.38 | 2.96 | 0.78 | 2.67 | 0.33 | 2.01 | 0.31 | 0.47 | 3.22 |
| Station 13 (-17.02°N -30.59°E) | | | | | | | | | | | | | | | | |
| 4893 | 49.21 | 4.97 | 9.33 | 36.53 | 7.13 | 1.74 | 9.25 | 1.31 | 9.81 | 2.43 | 8.66 | 1.20 | 8.73 | 1.47 | 0.05 | 3.28 |
| 4844 | 46.57 | 5.15 | 9.39 | 38.25 | 7.25 | 1.63 | 8.64 | 1.43 | 10.25 | 2.67 | 8.54 | 1.31 | 8.82 | 1.54 | 0.06 | 3.16 |
| 3999 | 35.40 | 4.96 | 7.36 | 28.68 | 5.44 | 1.32 | 7.24 | 1.11 | 7.87 | 2.08 | 6.84 | 1.01 | 6.69 | 1.17 | 0.07 | 3.20 |
| 3503 | 29.71 | 3.42 | 5.94 | 23.26 | 4.41 | 1.10 | 5.82 | 0.94 | 7.01 | 1.82 | 6.05 | 0.88 | 5.90 | 1.04 | 0.06 | 3.48 |
| 2501 | 24.79 | 3.11 | 4.69 | 19.65 | 3.60 | 0.97 | 4.72 | 0.84 | 6.24 | 1.67 | 5.64 | 0.84 | 5.56 | 1.01 | 0.07 | 3.88 |
| 2002 | 23.37 | 3.79 | 4.46 | 18.29 | 3.55 | 1.00 | 4.83 | 0.80 | 5.96 | 1.64 | 5.44 | 0.82 | 5.41 | 1.00 | 0.08 | 4.05 |
| 1749 | 23.72 | 4.12 | 4.31 | 17.39 | 3.48 | 0.88 | 4.78 | 0.81 | 6.06 | 1.64 | 5.51 | 0.81 | 5.42 | 0.95 | 0.09 | 4.27 |
| 1502 | 23.11 | 4.65 | 4.24 | 17.15 | 3.27 | 0.83 | 4.61 | 0.78 | 5.89 | 1.59 | 5.35 | 0.79 | 5.40 | 0.96 | 0.11 | 4.32 |

Table 3. continued

| Depth | La | Ce | Pr | Nd | Sm | Eu | Gd | Tb | Dy | Ho | Er | Tm | Yb | Lu | Ce/Ce* | $Yb_n/Nd_n$ |
|---|---|---|---|---|---|---|---|---|---|---|---|---|---|---|---|---|
| m | pmol/kg | pmol/kg | pmol/kg | pmol/kg | pmol/kg | pmol/kg | pmol/kg | pmol/kg | pmol/kg | pmol/kg | pmol/kg | pmol/kg | pmol/kg | pmol/kg | | |
| | 5.1% | 3.4% | 1.7% | 2.8% | 4.0% | 5.5% | 5.9% | 4.7% | 4.4% | 2.3% | 4.8% | 3.3% | 4.6% | 4.3% | | |
| 1251 | 23.07 | 4.28 | 3.90 | 15.84 | 3.03 | 0.77 | 4.44 | 0.73 | 5.64 | 1.57 | 5.55 | 0.81 | 5.56 | 1.05 | 0.10 | 4.82 |
| 1000 | 22.49 | 3.72 | 3.61 | 14.44 | 2.68 | 0.70 | 3.88 | 0.65 | 5.02 | 1.45 | 5.17 | 0.76 | 5.34 | 1.00 | 0.09 | 5.07 |
| 750 | 17.34 | 2.53 | 3.13 | 12.38 | 2.47 | 0.64 | 3.42 | 0.60 | 4.42 | 1.39 | 4.73 | 0.70 | 5.06 | 0.96 | 0.08 | 5.60 |
| 500 | 15.92 | 2.75 | 3.06 | 12.54 | 2.27 | 0.59 | 3.46 | 0.58 | 4.27 | 1.24 | 4.10 | 0.64 | 4.17 | 0.74 | 0.09 | 4.56 |
| 401 | 14.93 | 3.97 | 2.97 | 12.06 | 2.26 | 0.63 | 3.31 | 0.54 | 4.04 | 1.16 | 3.79 | 0.55 | 3.59 | 0.64 | 0.14 | 4.08 |
| 250 | 12.35 | 7.33 | 2.60 | 10.58 | 1.91 | 0.52 | 2.85 | 0.48 | 3.53 | 1.00 | 3.14 | 0.44 | 2.58 | 0.45 | 0.30 | 3.34 |
| 100 | 11.87 | 9.12 | 2.47 | 10.16 | 1.82 | 0.50 | 2.75 | 0.43 | 3.12 | 0.89 | 2.76 | 0.35 | 1.92 | 0.33 | 0.39 | 2.60 |
| 24 | 15.14 | 12.45 | 3.33 | 13.60 | 2.46 | 0.68 | 3.65 | 0.54 | 3.99 | 1.00 | 3.30 | 0.40 | 2.36 | 0.36 | 0.40 | 2.38 |
| Station 14 (-12.89°N -29.22°E) | | | | | | | | | | | | | | | | |
| 5435 | 50.23 | 5.16 | 9.43 | 37.45 | 7.04 | 1.76 | 9.07 | 1.33 | 9.86 | 2.45 | 8.45 | 1.21 | 8.62 | 1.47 | 0.05 | 3.15 |
| 4999 | 45.45 | 6.09 | 9.24 | 36.49 | 7.29 | 1.81 | 8.99 | 1.35 | 9.90 | 2.47 | 8.15 | 1.22 | 8.63 | 1.47 | 0.07 | 3.24 |
| 4000 | 35.95 | 4.37 | 7.38 | 29.37 | 5.81 | 1.44 | 7.50 | 1.06 | 8.25 | 2.09 | 6.88 | 1.06 | 6.88 | 1.15 | 0.06 | 3.21 |
| 3502 | 30.11 | 3.59 | 5.89 | 23.71 | 4.33 | 1.09 | 6.12 | 0.89 | 6.91 | 1.77 | 5.98 | 0.86 | 5.97 | 1.02 | 0.06 | 3.45 |
| 2500 | 26.08 | 2.66 | 4.67 | 19.05 | 3.63 | 0.98 | 5.31 | 0.80 | 6.22 | 1.66 | 5.71 | 0.83 | 5.66 | 0.99 | 0.05 | 4.08 |
| 1999 | 23.05 | 4.19 | 4.39 | 17.96 | 3.44 | 0.88 | 5.15 | 0.77 | 5.94 | 1.58 | 5.42 | 0.78 | 5.27 | 0.90 | 0.10 | 4.02 |
| 1748 | 23.16 | 4.45 | 4.29 | 17.30 | 3.42 | 0.91 | 4.96 | 0.77 | 5.98 | 1.55 | 5.47 | 0.76 | 5.17 | 0.89 | 0.10 | 4.10 |
| 1497 | 22.38 | 4.86 | 4.19 | 16.67 | 3.39 | 0.88 | 4.85 | 0.75 | 5.65 | 1.54 | 5.36 | 0.77 | 5.22 | 0.90 | 0.11 | 4.30 |
| 1250 | 20.80 | 4.61 | 3.79 | 15.17 | 2.94 | 0.80 | 4.57 | 0.73 | 5.64 | 1.59 | 5.43 | 0.81 | 5.80 | 1.03 | 0.12 | 5.24 |
| 998 | 20.60 | 3.83 | 3.59 | 14.09 | 2.64 | 0.74 | 4.39 | 0.65 | 5.29 | 1.47 | 5.07 | 0.79 | 5.63 | 1.03 | 0.10 | 5.48 |
| 749 | 19.98 | 3.02 | 3.42 | 13.63 | 2.59 | 0.67 | 4.09 | 0.60 | 4.82 | 1.37 | 4.83 | 0.73 | 5.12 | 0.92 | 0.08 | 5.15 |
| 500 | 19.40 | 3.01 | 3.35 | 13.41 | 2.54 | 0.66 | 3.89 | 0.58 | 4.49 | 1.27 | 4.45 | 0.65 | 4.54 | 0.84 | 0.09 | 4.64 |
| 401 | 18.14 | 2.71 | 3.27 | 13.11 | 2.47 | 0.64 | 3.70 | 0.55 | 4.26 | 1.19 | 4.07 | 0.60 | 4.05 | 0.74 | 0.08 | 4.23 |
| 250 | 16.41 | 6.95 | 3.18 | 12.68 | 2.35 | 0.59 | 3.43 | 0.51 | 3.90 | 1.06 | 3.60 | 0.49 | 3.21 | 0.54 | 0.22 | 3.47 |
| 100 | 13.85 | 10.36 | 2.85 | 11.80 | 2.21 | 0.59 | 3.12 | 0.48 | 3.55 | 0.95 | 2.96 | 0.40 | 2.30 | 0.36 | 0.38 | 2.67 |
| 25 | 17.80 | 13.62 | 3.88 | 15.70 | 2.89 | 0.75 | 4.10 | 0.63 | 4.33 | 1.08 | 3.42 | 0.41 | 2.48 | 0.37 | 0.38 | 2.16 |
| Station 15 (-9.15°N -28.00°E) | | | | | | | | | | | | | | | | |
| 5607 | 49.20 | 4.63 | 9.61 | 37.76 | 7.15 | 1.78 | 9.67 | 1.36 | 9.89 | 2.49 | 8.59 | 1.20 | 8.65 | 1.47 | 0.05 | 3.14 |
| 5001 | 50.49 | 6.60 | 10.00 | 38.41 | 7.49 | 1.82 | 9.69 | 1.42 | 10.34 | 2.60 | 8.43 | 1.25 | 8.69 | 1.54 | 0.07 | 3.10 |
| 4000 | 41.89 | 5.58 | 7.79 | 30.73 | 5.82 | 1.40 | 7.62 | 1.16 | 8.51 | 2.13 | 7.19 | 1.03 | 7.07 | 1.28 | 0.07 | 3.15 |
| 3498 | 31.63 | 3.55 | 5.91 | 23.00 | 4.54 | 1.15 | 6.43 | 0.97 | 6.86 | 1.82 | 5.92 | 0.84 | 5.79 | 1.04 | 0.06 | 3.45 |
| 2499 | 26.14 | 4.08 | 4.69 | 18.82 | 3.68 | 0.94 | 5.32 | 0.83 | 6.32 | 1.66 | 5.66 | 0.81 | 5.53 | 0.99 | 0.08 | 4.03 |
| 2003 | 24.50 | 4.62 | 4.39 | 17.46 | 3.53 | 0.91 | 5.13 | 0.81 | 6.21 | 1.62 | 5.59 | 0.79 | 5.30 | 0.96 | 0.10 | 4.16 |
| 1750 | 24.31 | 5.08 | 4.15 | 17.26 | 3.58 | 0.94 | 5.19 | 0.81 | 5.83 | 1.55 | 5.30 | 0.72 | 5.13 | 0.89 | 0.12 | 4.08 |
| 1500 | 25.72 | 4.96 | 4.03 | 16.98 | 3.26 | 0.89 | 4.83 | 0.79 | 5.45 | 1.49 | 5.23 | 0.71 | 4.85 | 0.87 | 0.11 | 3.92 |
| 1252 | 20.61 | 4.80 | 3.97 | 16.18 | 3.03 | 0.84 | 4.73 | 0.73 | 5.67 | 1.56 | 5.20 | 0.81 | 5.57 | 0.98 | 0.12 | 4.72 |
| 1000 | 20.13 | 4.29 | 3.63 | 14.86 | 2.52 | 0.72 | 3.63 | 0.65 | 5.24 | 1.47 | 5.88 | 0.83 | 5.64 | 1.00 | 0.11 | 5.20 |
| 750 | 19.80 | 3.37 | 3.60 | 15.05 | 2.77 | 0.68 | 3.91 | 0.64 | 4.79 | 1.43 | 5.16 | 0.78 | 5.16 | 0.92 | 0.09 | 4.70 |
| 499 | 21.18 | 3.31 | 3.79 | 15.74 | 2.91 | 0.79 | 4.06 | 0.63 | 4.74 | 1.43 | 4.77 | 0.72 | 4.88 | 0.85 | 0.08 | 4.25 |
| 400 | 20.37 | 3.84 | 3.86 | 15.72 | 2.90 | 0.66 | 4.11 | 0.64 | 4.71 | 1.34 | 4.62 | 0.70 | 4.51 | 0.80 | 0.10 | 3.93 |

Table 3. continued

| Depth | La | Ce | Pr | Nd | Sm | Eu | Gd | Tb | Dy | Ho | Er | Tm | Yb | Lu | Ce/Ce* | $Yb_n/Nd_n$ |
|---|---|---|---|---|---|---|---|---|---|---|---|---|---|---|---|---|
| m | pmol/kg | pmol/kg | pmol/kg | pmol/kg | pmol/kg | pmol/kg | pmol/kg | pmol/kg | pmol/kg | pmol/kg | pmol/kg | pmol/kg | pmol/kg | pmol/kg | | |
| | 5.1% | 3.4% | 1.7% | 2.8% | 4.0% | 5.5% | 5.9% | 4.7% | 4.4% | 2.3% | 4.8% | 3.3% | 4.6% | 4.3% | | |
| 249 | 18.84 | 3.44 | 3.47 | 14.22 | 2.66 | 0.71 | 3.68 | 0.58 | 4.42 | 1.23 | 4.31 | 0.61 | 3.95 | 0.66 | 0.10 | 3.81 |
| 100 | 16.64 | 12.82 | 3.59 | 15.32 | 2.77 | 0.70 | 3.85 | 0.59 | 4.22 | 1.13 | 3.34 | 0.45 | 2.47 | 0.38 | 0.38 | 2.21 |
| 25 | 17.81 | 15.16 | 4.08 | 16.17 | 2.94 | 0.80 | 4.22 | 0.64 | 4.43 | 1.07 | 3.50 | 0.42 | 2.61 | 0.39 | 0.41 | 2.21 |
| Station 16 (-5.67°N -28.46°E) | | | | | | | | | | | | | | | | |
| 5519 | 57.29 | 7.62 | 11.40 | 44.57 | 8.61 | 2.13 | 10.88 | 1.56 | 11.39 | 2.81 | 9.72 | 1.36 | 9.69 | 1.64 | 0.07 | 2.98 |
| 4999 | 52.58 | 6.20 | 10.31 | 40.16 | 7.46 | 1.87 | 9.32 | 1.46 | 10.11 | 2.59 | 8.45 | 1.24 | 8.66 | 1.65 | 0.06 | 2.96 |
| 3998 | 39.66 | 5.53 | 7.80 | 30.45 | 5.57 | 1.45 | 7.37 | 1.16 | 8.25 | 2.14 | 6.85 | 0.99 | 6.83 | 1.26 | 0.07 | 3.07 |
| 3500 | 31.57 | 3.45 | 5.99 | 23.66 | 4.55 | 1.15 | 6.03 | 0.95 | 6.83 | 1.78 | 5.88 | 0.85 | 5.64 | 1.06 | 0.06 | 3.27 |
| 2500 | 27.14 | 4.58 | 4.90 | 19.26 | 3.68 | 0.95 | 5.39 | 0.84 | 6.26 | 1.70 | 5.67 | 0.84 | 5.70 | 1.07 | 0.09 | 4.06 |
| 2000 | 25.00 | 4.88 | 4.59 | 18.68 | 3.51 | 0.91 | 4.96 | 0.81 | 6.04 | 1.61 | 5.23 | 0.79 | 5.40 | 1.00 | 0.10 | 3.96 |
| 1751 | 21.85 | 5.21 | 4.28 | 17.41 | 3.45 | 0.86 | 5.15 | 0.81 | 6.07 | 1.59 | 5.32 | 0.76 | 5.23 | 0.98 | 0.12 | 4.12 |
| 1499 | 21.03 | 5.43 | 4.12 | 16.66 | 3.55 | 0.84 | 4.79 | 0.80 | 5.86 | 1.59 | 5.05 | 0.78 | 5.37 | 0.98 | 0.13 | 4.42 |
| 1247 | 21.61 | 5.19 | 4.18 | 17.06 | 3.14 | 0.90 | 4.67 | 0.79 | 5.59 | 1.66 | 5.28 | 0.84 | 5.65 | 1.04 | 0.13 | 4.55 |
| 999 | 21.84 | 4.35 | 3.90 | 15.47 | 2.91 | 0.72 | 3.93 | 0.72 | 5.12 | 1.58 | 5.21 | 0.84 | 5.87 | 1.11 | 0.11 | 5.20 |
| 749 | 20.41 | 3.81 | 3.74 | 15.02 | 2.82 | 0.76 | 4.01 | 0.66 | 4.88 | 1.40 | 4.65 | 0.74 | 5.04 | 0.96 | 0.10 | 4.60 |
| 499 | 21.02 | 3.51 | 3.88 | 15.78 | 2.84 | 0.72 | 4.11 | 0.66 | 4.80 | 1.33 | 4.56 | 0.69 | 4.64 | 0.88 | 0.09 | 4.03 |
| 376 | 23.11 | 4.29 | 4.25 | 16.83 | 3.07 | 0.76 | 4.23 | 0.67 | 5.09 | 1.35 | 4.47 | 0.69 | 4.55 | 0.85 | 0.10 | 3.71 |
| 250 | 23.22 | 6.62 | 4.45 | 17.70 | 3.33 | 0.90 | 4.69 | 0.72 | 5.21 | 1.42 | 4.86 | 0.72 | 4.77 | 0.88 | 0.15 | 3.69 |
| 109 | 15.07 | 9.10 | 3.12 | 12.63 | 2.33 | 0.58 | 3.37 | 0.52 | 3.77 | 1.00 | 3.04 | 0.45 | 2.59 | 0.47 | 0.31 | 2.81 |
| 25 | 18.11 | 16.90 | 4.19 | 17.03 | 3.15 | 0.84 | 4.32 | 0.65 | 4.68 | 1.10 | 3.55 | 0.44 | 2.73 | 0.41 | 0.45 | 2.20 |
| Station 17 (-2.64°N -28.91°E) | | | | | | | | | | | | | | | | |
| 4891 | 50.35 | 5.50 | 9.96 | 38.88 | 7.29 | 1.87 | 9.31 | 1.35 | 9.89 | 2.51 | 8.44 | 1.20 | 8.53 | 1.43 | 0.06 | 3.01 |
| 4840 | 51.46 | 5.72 | 10.14 | 38.75 | 7.40 | 1.84 | 9.56 | 1.36 | 10.05 | 2.46 | 8.37 | 1.17 | 8.58 | 1.48 | 0.06 | 3.03 |
| 4000 | 38.10 | 5.79 | 7.58 | 28.87 | 5.58 | 1.39 | 7.50 | 1.06 | 7.89 | 1.95 | 6.68 | 0.93 | 6.56 | 1.13 | 0.08 | 3.12 |
| 3500 | 31.23 | 3.77 | 6.05 | 23.30 | 4.54 | 1.16 | 6.32 | 0.89 | 6.82 | 1.67 | 5.84 | 0.79 | 5.62 | 0.93 | 0.06 | 3.31 |
| 2502 | 26.04 | 4.70 | 4.75 | 18.42 | 3.73 | 0.99 | 5.33 | 0.78 | 6.17 | 1.57 | 5.57 | 0.77 | 5.52 | 0.95 | 0.10 | 4.11 |
| 2001 | 23.67 | 5.17 | 4.57 | 17.93 | 3.65 | 0.95 | 5.21 | 0.76 | 6.01 | 1.51 | 5.21 | 0.72 | 4.97 | 0.85 | 0.11 | 3.80 |
| 1750 | 22.31 | 6.94 | 4.65 | 18.42 | 3.64 | 0.95 | 5.21 | 0.78 | 6.11 | 1.58 | 5.09 | 0.77 | 5.17 | 0.87 | 0.16 | 3.85 |
| 1501 | 21.31 | 5.18 | 4.51 | 17.61 | 3.56 | 0.95 | 5.30 | 0.79 | 6.01 | 1.58 | 5.24 | 0.77 | 5.17 | 0.86 | 0.12 | 4.03 |
| 1251 | 20.77 | 5.97 | 4.22 | 16.85 | 3.37 | 0.90 | 4.89 | 0.74 | 5.71 | 1.59 | 5.41 | 0.79 | 5.45 | 0.95 | 0.15 | 4.44 |
| 1000 | 21.02 | 5.22 | 4.05 | 15.95 | 3.12 | 0.85 | 4.51 | 0.68 | 5.48 | 1.52 | 5.22 | 0.81 | 5.58 | 0.97 | 0.13 | 4.80 |
| 750 | 19.53 | 3.98 | 3.73 | 14.94 | 2.81 | 0.80 | 4.27 | 0.63 | 4.92 | 1.38 | 4.79 | 0.73 | 5.16 | 0.90 | 0.11 | 4.73 |
| 499 | 21.03 | 3.88 | 4.11 | 16.23 | 2.98 | 0.80 | 4.13 | 0.65 | 4.94 | 1.36 | 4.61 | 0.68 | 4.71 | 0.81 | 0.10 | 3.98 |
| 374 | 21.42 | 4.31 | 4.18 | 16.49 | 3.11 | 0.80 | 4.19 | 0.64 | 4.78 | 1.29 | 4.30 | 0.64 | 4.29 | 0.73 | 0.10 | 3.57 |
| 249 | 19.19 | 4.39 | 3.90 | 15.31 | 2.83 | 0.76 | 4.03 | 0.60 | 4.58 | 1.22 | 4.06 | 0.59 | 3.88 | 0.64 | 0.12 | 3.48 |
| 100 | 16.91 | 7.66 | 3.43 | 13.60 | 2.58 | 0.66 | 3.58 | 0.54 | 4.05 | 1.09 | 3.68 | 0.50 | 3.27 | 0.54 | 0.23 | 3.30 |
| 17 | 20.11 | 21.25 | 5.00 | 19.83 | 3.87 | 0.95 | 4.96 | 0.74 | 4.89 | 1.17 | 3.87 | 0.48 | 2.93 | 0.44 | 0.49 | 2.02 |
| Station 18 (-0.18°N -32.88°E) | | | | | | | | | | | | | | | | |
| 4338 | 45.91 | 5.90 | 8.84 | 34.60 | 6.50 | 1.60 | 8.47 | 1.22 | 8.96 | 2.25 | 7.79 | 1.09 | 7.71 | 1.29 | 0.07 | 3.05 |

Table 3. continued

| Depth | La | Ce | Pr | Nd | Sm | Eu | Gd | Tb | Dy | Ho | Er | Tm | Yb | Lu | Ce/Ce* | $Yb_n/Nd_n$ |
|---|---|---|---|---|---|---|---|---|---|---|---|---|---|---|---|---|
| m | pmol/kg | pmol/kg | pmol/kg | pmol/kg | pmol/kg | pmol/kg | pmol/kg | pmol/kg | pmol/kg | pmol/kg | pmol/kg | pmol/kg | pmol/kg | pmol/kg | | |
| | 5.1% | 3.4% | 1.7% | 2.8% | 4.0% | 5.5% | 5.9% | 4.7% | 4.4% | 2.3% | 4.8% | 3.3% | 4.6% | 4.3% | | |
| 3999 | 36.40 | 5.71 | 7.47 | 28.69 | 5.37 | 1.34 | 7.35 | 1.02 | 7.64 | 1.95 | 6.49 | 0.92 | 6.38 | 1.05 | 0.08 | 3.05 |
| 3249 | 29.91 | 4.28 | 5.83 | 22.69 | 4.28 | 1.09 | 6.06 | 0.86 | 6.65 | 1.69 | 5.79 | 0.82 | 5.80 | 0.97 | 0.07 | 3.51 |
| 2994 | 28.12 | 3.94 | 5.46 | 21.14 | 4.03 | 1.07 | 5.70 | 0.84 | 6.39 | 1.64 | 5.50 | 0.79 | 5.56 | 0.91 | 0.07 | 3.61 |
| 2498 | 26.45 | 4.14 | 5.01 | 19.47 | 3.72 | 0.98 | 5.38 | 0.80 | 6.18 | 1.60 | 5.53 | 0.77 | 5.35 | 0.91 | 0.08 | 3.77 |
| 2000 | 24.13 | 5.52 | 4.67 | 18.37 | 3.57 | 0.93 | 5.23 | 0.78 | 6.04 | 1.58 | 5.33 | 0.75 | 5.30 | 0.89 | 0.12 | 3.95 |
| 1750 | 23.58 | 5.50 | 4.58 | 18.01 | 3.52 | 0.93 | 5.28 | 0.76 | 5.97 | 1.55 | 5.26 | 0.73 | 5.07 | 0.86 | 0.12 | 3.86 |
| 1500 | 23.12 | 5.26 | 4.59 | 17.99 | 3.64 | 0.94 | 5.27 | 0.77 | 5.94 | 1.54 | 5.24 | 0.73 | 5.02 | 0.85 | 0.12 | 3.83 |
| 1252 | 21.36 | 5.89 | 4.41 | 17.37 | 3.44 | 0.84 | 4.71 | 0.74 | 5.65 | 1.57 | 5.45 | 0.77 | 5.14 | 0.88 | 0.14 | 4.06 |
| 998 | 21.00 | 5.48 | 4.07 | 15.91 | 3.08 | 0.79 | 4.25 | 0.65 | 5.08 | 1.41 | 5.30 | 0.76 | 5.12 | 0.92 | 0.14 | 4.41 |
| 750 | 20.71 | 4.51 | 3.94 | 15.56 | 3.00 | 0.75 | 4.06 | 0.61 | 4.88 | 1.32 | 4.84 | 0.70 | 4.79 | 0.84 | 0.11 | 4.23 |
| 499 | 20.54 | 4.59 | 4.06 | 15.65 | 3.01 | 0.79 | 3.98 | 0.60 | 4.83 | 1.25 | 4.57 | 0.64 | 4.36 | 0.77 | 0.12 | 3.82 |
| 400 | 20.44 | 4.88 | 4.10 | 16.04 | 3.00 | 0.79 | 4.18 | 0.62 | 4.74 | 1.27 | 4.20 | 0.64 | 4.04 | 0.73 | 0.12 | 3.45 |
| 244 | 19.42 | 4.79 | 4.03 | 15.61 | 2.97 | 0.75 | 4.04 | 0.60 | 4.36 | 1.21 | 3.92 | 0.57 | 3.60 | 0.63 | 0.12 | 3.16 |
| 150 | 15.01 | 6.53 | 3.13 | 12.56 | 2.30 | 0.61 | 3.23 | 0.52 | 3.85 | 1.06 | 3.57 | 0.49 | 3.06 | 0.52 | 0.22 | 3.34 |
| 22 | 18.95 | 19.84 | 4.62 | 18.30 | 3.60 | 0.89 | 4.58 | 0.66 | 4.74 | 1.13 | 3.63 | 0.46 | 2.82 | 0.42 | 0.49 | 2.11 |

## Appendix 3. Table 3 of Chapter 4

Table 3 of Chapter 4. Profile data of five stations from the SO202 cruise. (a) latitude, longitude, depth, salinity, temperature, potential temperature, oxygen concentration, εNd value, εNd external 2 standard deviation. (b) REE concentrations. Errors for REE concentrations represent 2σ external errors in percent.

Panel a

| Depth | Salinity | Potential Temperature | Potential Density | Neutral Density | Oxygen | εNd | Ext. 2sd |
|---|---|---|---|---|---|---|---|
| m | | °C | kg/m$^3$ | kg/m$^3$ | ml/l | | |
| SO202-5 (52.70°N 164.92°E) | | | | | | | |
| 13 | 32.92 | 9.57 | 25.40 | 25.43 | 6.97 | -2.00 | 0.30 |
| 102 | 33.08 | 1.73 | 26.45 | 26.56 | 7.12 | -1.51 | 0.30 |
| 152 | 33.74 | 3.73 | 26.82 | 26.97 | 2.54 | -2.07 | 0.30 |
| 202 | 33.89 | 3.74 | 26.93 | 27.09 | 0.87 | -2.31 | 0.20 |
| 301 | 34.04 | 3.80 | 27.04 | 27.22 | 0.47 | -2.17 | 0.20 |
| 400 | 34.13 | 3.63 | 27.13 | 27.31 | 0.35 | -2.25 | 0.20 |
| 500 | 34.20 | 3.45 | 27.20 | 27.39 | 0.28 | -2.36 | 0.20 |
| 998 | 34.41 | 2.62 | 27.45 | 27.66 | 0.26 | -2.32 | 0.20 |
| 1496 | 34.53 | 2.04 | 27.59 | 27.84 | 0.62 | -2.23 | 0.20 |
| 1994 | 34.60 | 1.70 | 27.68 | 27.94 | 1.34 | -2.43 | 0.20 |
| 2491 | 34.64 | 1.49 | 27.72 | 28.00 | 1.97 | -3.11 | 0.20 |
| 3349 | 34.68 | 1.25 | 27.77 | 28.07 | 2.70 | -3.59 | 0.20 |
| SO202-32 (45.50°N 201.50°E) | | | | | | | |
| 14 | 32.97 | 14.54 | 24.51 | 24.52 | 5.89 | -3.97 | 0.30 |
| 104 | 33.50 | 7.62 | 26.15 | 26.22 | 6.04 | -4.06 | 0.30 |
| 203 | 33.88 | 6.68 | 26.58 | 26.69 | 4.60 | -4.48 | 0.20 |
| 302 | 33.87 | 5.26 | 26.75 | 26.88 | 3.30 | -3.22 | 0.20 |
| 402 | 33.93 | 4.54 | 26.88 | 27.03 | 2.34 | -2.93 | 0.20 |
| 501 | 34.04 | 4.29 | 27.00 | 27.16 | 1.52 | -2.71 | 0.20 |
| 997 | 34.36 | 2.99 | 27.37 | 27.58 | 0.38 | -2.71 | 0.20 |
| 1496 | 34.50 | 2.24 | 27.55 | 27.79 | 0.38 | -2.49 | 0.20 |
| 2491 | 34.63 | 1.55 | 27.71 | 27.98 | 1.57 | -2.69 | 0.20 |
| 3487 | 34.68 | 1.23 | 27.77 | 28.07 | 2.62 | -3.15 | 0.20 |
| 4484 | 34.69 | 1.13 | 27.79 | 28.10 | 2.94 | -3.45 | 0.20 |
| 5095 | 34.69 | 1.12 | 27.79 | 28.10 | 2.95 | -3.34 | 0.20 |
| 5127 | 34.69 | 1.12 | 27.79 | 28.10 | 2.95 | -3.36 | 0.20 |
| 5161 | 34.69 | 1.12 | 27.79 | 28.10 | 2.94 | -3.16 | 0.20 |
| 5194 | 34.69 | 1.12 | 27.79 | 28.10 | 2.94 | -3.37 | 0.20 |
| 5228 | 34.69 | 1.12 | 27.79 | 28.10 | 2.94 | -3.05 | 0.20 |
| 5262 | 34.69 | 1.12 | 27.79 | 28.10 | 2.94 | -3.26 | 0.20 |
| 5294 | 34.69 | 1.12 | 27.79 | 28.10 | 2.94 | -3.31 | 0.20 |
| SO202-39 (38.01°N 164.45°E) | | | | | | | |
| 14 | 34.28 | 24.71 | 22.88 | 22.89 | 4.33 | | |
| 103 | 34.50 | 14.52 | 25.69 | 25.73 | 4.55 | -4.07 | 0.30 |
| 202 | 34.37 | 12.19 | 26.06 | 26.12 | 4.53 | -3.83 | 0.30 |
| 300 | 34.20 | 9.75 | 26.37 | 26.44 | 4.35 | -4.15 | 0.20 |
| 399 | 34.05 | 7.61 | 26.59 | 26.69 | 3.88 | -3.30 | 0.20 |
| 498 | 34.01 | 5.68 | 26.81 | 26.94 | 3.02 | -2.93 | 0.20 |

Panel a. continued

| Depth | Salinity | Potential Temperature | Potential Density | Neutral Density | Oxygen | εNd | Ext. 2sd |
|---|---|---|---|---|---|---|---|
| m | | °C | $kg/m^3$ | $kg/m^3$ | ml/l | | |
| 996 | 34.34 | 3.28 | 27.33 | 27.52 | 0.66 | -2.65 | 0.20 |
| 1494 | 34.50 | 2.37 | 27.54 | 27.77 | 0.67 | -2.63 | 0.20 |
| 2489 | 34.64 | 1.54 | 27.71 | 27.99 | 1.90 | -2.80 | 0.20 |
| 3484 | 34.68 | 1.21 | 27.77 | 28.08 | 2.81 | -3.58 | 0.20 |
| 4481 | 34.69 | 1.09 | 27.79 | 28.11 | 3.13 | -3.85 | 0.20 |
| 5088 | 34.69 | 1.08 | 27.79 | 28.11 | 3.14 | -3.24 | 0.20 |
| SO202-41 (38.41°N 160.34°E) | | | | | | | |
| 12 | 34.42 | 24.67 | 23.00 | 23.01 | 4.39 | -4.77 | 0.30 |
| 102 | 34.49 | 14.47 | 25.69 | 25.73 | 4.71 | -3.95 | 0.30 |
| 200 | 34.37 | 11.79 | 26.14 | 26.20 | 4.43 | -3.91 | 0.20 |
| 299 | 34.14 | 8.84 | 26.47 | 26.55 | 4.04 | -3.54 | 0.20 |
| 400 | 33.98 | 6.21 | 26.72 | 26.84 | 3.78 | -3.16 | 0.20 |
| 499 | 33.91 | 4.34 | 26.88 | 27.04 | 2.71 | -2.61 | 0.20 |
| 995 | 34.35 | 3.11 | 27.36 | 27.56 | 0.67 | -2.60 | 0.20 |
| 1493 | 34.50 | 2.26 | 27.55 | 27.79 | 0.78 | -2.55 | 0.20 |
| 2488 | 34.64 | 1.52 | 27.72 | 28.00 | 1.97 | -2.80 | 0.20 |
| 3483 | 34.68 | 1.21 | 27.77 | 28.08 | 2.84 | -3.69 | 0.20 |
| 4479 | 34.69 | 1.10 | 27.79 | 28.11 | 3.13 | -3.80 | 0.20 |
| 5378 | 34.70 | 1.06 | 27.80 | 28.12 | 3.23 | -3.16 | 0.20 |
| SO202-44 (39.80°N 152.35°E) | | | | | | | |
| 14 | 33.69 | 24.54 | 22.49 | 22.50 | 4.37 | -4.67 | 0.30 |
| 104 | 34.30 | 11.30 | 26.18 | 26.24 | 4.34 | -3.95 | 0.30 |
| 201 | 34.01 | 8.12 | 26.48 | 26.57 | 5.00 | -3.55 | 0.20 |
| 299 | 33.97 | 6.04 | 26.74 | 26.86 | 3.78 | -3.18 | 0.20 |
| 400 | 34.00 | 4.86 | 26.90 | 27.05 | 2.61 | -2.89 | 0.20 |
| 498 | 34.11 | 4.60 | 27.01 | 27.17 | 1.86 | -2.76 | 0.20 |
| 997 | 34.36 | 2.81 | 27.39 | 27.60 | 0.66 | -2.85 | 0.20 |
| 1494 | 34.52 | 2.21 | 27.57 | 27.80 | 0.88 | -2.53 | 0.20 |
| 2486 | 34.64 | 1.51 | 27.72 | 28.00 | 2.06 | -3.05 | 0.20 |
| 3480 | 34.68 | 1.22 | 27.77 | 28.07 | 2.81 | -3.69 | 0.20 |
| 4481 | 34.69 | 1.10 | 27.79 | 28.11 | 3.12 | -3.88 | 0.20 |
| 5482 | 34.70 | 1.05 | 27.80 | 28.12 | 3.23 | -4.24 | 0.20 |

Panel b

| Depth | La | Ce | Pr | Nd | Sm | Eu | Gd | Tb | Dy | Ho | Er | Tm | Yb | Lu |
|---|---|---|---|---|---|---|---|---|---|---|---|---|---|---|
| m | pmol/kg | pmol/kg | pmol/kg | pmol/kg | pmol/kg | pmol/kg | pmol/kg | pmol/kg | pmol/kg | pmol/kg | pmol/kg | pmol/kg | pmol/kg | pmol/kg |
| | 5.1% | 3.4% | 1.7% | 2.8% | 4.0% | 5.5% | 5.9% | 4.7% | 4.4% | 2.3% | 4.8% | 3.3% | 4.6% | 4.3% |
| SO202-5 (52.70°N 164.92°E) | | | | | | | | | | | | | | |
| 13 | 19.54 | 4.93 | 3.16 | 12.51 | 2.48 | 0.77 | 3.89 | 0.52 | 4.51 | 1.37 | 3.81 | 0.59 | 3.66 | 0.61 |
| 102 | 22.37 | 4.96 | 3.52 | 13.94 | 2.59 | 0.84 | 4.10 | 0.59 | 5.09 | 1.55 | 4.22 | 0.69 | 4.59 | 0.81 |
| 152 | 33.28 | 3.11 | 4.31 | 18.64 | 3.35 | 0.88 | 5.28 | 0.80 | 6.03 | 1.60 | 5.80 | 0.80 | 5.55 | 0.92 |
| 202 | 34.26 | 4.20 | 4.53 | 19.08 | 3.48 | 0.97 | 5.57 | 0.81 | 6.33 | 1.69 | 6.04 | 0.83 | 5.80 | 0.97 |
| 301 | 32.38 | 4.50 | 4.78 | 20.08 | 3.71 | 1.01 | 5.97 | 0.87 | 6.81 | 1.87 | 6.38 | 0.94 | 6.34 | 1.11 |
| 400 | 30.77 | 4.18 | 4.76 | 20.34 | 3.81 | 1.04 | 5.87 | 0.89 | 7.04 | 1.99 | 6.45 | 1.02 | 6.79 | 1.20 |
| 500 | 37.81 | 4.51 | 5.03 | 21.67 | 3.95 | 1.12 | 6.49 | 0.98 | 7.38 | 2.00 | 7.22 | 1.01 | 7.24 | 1.26 |
| 998 | 42.82 | 4.87 | 5.70 | 24.75 | 4.68 | 1.31 | 7.50 | 1.13 | 8.45 | 2.35 | 8.66 | 1.20 | 8.86 | 1.53 |
| 1496 | 50.20 | 5.99 | 6.77 | 29.37 | 5.54 | 1.55 | 8.75 | 1.31 | 10.07 | 2.74 | 9.96 | 1.42 | 10.12 | 1.78 |
| 1994 | 45.68 | 3.90 | 6.76 | 28.85 | 5.37 | 1.45 | 8.92 | 1.30 | 10.50 | 2.77 | 9.75 | 1.49 | 10.60 | 1.90 |
| 2491 | 51.88 | 3.84 | 7.32 | 31.67 | 6.02 | 1.69 | 9.44 | 1.40 | 10.75 | 2.88 | 10.48 | 1.48 | 11.00 | 1.92 |
| 3349 | 57.45 | 3.52 | 8.99 | 38.48 | 7.39 | 1.97 | 11.04 | 1.63 | 12.16 | 3.10 | 10.99 | 1.56 | 11.48 | 1.95 |
| SO202-32 (45.50°N 201.50°E) | | | | | | | | | | | | | | |
| 14 | 12.74 | 4.25 | 1.86 | 8.34 | 1.48 | 0.41 | 2.47 | 0.38 | 2.92 | 0.82 | 2.81 | 0.36 | 2.11 | 0.34 |
| 104 | 16.14 | 4.35 | 2.58 | 11.27 | 2.11 | 0.57 | 3.34 | 0.51 | 3.90 | 1.03 | 3.51 | 0.46 | 2.90 | 0.46 |
| 203 | 21.62 | 3.62 | 3.52 | 15.37 | 3.01 | 0.80 | 4.53 | 0.69 | 5.25 | 1.38 | 4.70 | 0.64 | 4.32 | 0.69 |
| 302 | 26.41 | 2.66 | 4.12 | 17.85 | 3.31 | 0.94 | 5.05 | 0.76 | 5.89 | 1.54 | 5.20 | 0.74 | 4.99 | 0.82 |
| 402 | 30.00 | 3.70 | 4.58 | 19.73 | 3.59 | 0.95 | 5.28 | 0.81 | 6.11 | 1.63 | 5.55 | 0.81 | 5.54 | 0.91 |
| 501 | 31.03 | 3.10 | 4.69 | 20.13 | 3.79 | 0.99 | 5.29 | 0.84 | 6.56 | 1.73 | 5.90 | 0.87 | 5.86 | 0.98 |
| 997 | 37.39 | 4.54 | 5.36 | 23.36 | 4.29 | 1.16 | 6.30 | 0.99 | 8.01 | 2.15 | 7.54 | 1.11 | 7.82 | 1.33 |
| 1496 | 42.04 | 4.06 | 5.86 | 24.70 | 4.65 | 1.25 | 7.56 | 1.10 | 8.70 | 2.38 | 8.61 | 1.26 | 9.17 | 1.59 |
| 2491 | 42.85 | 3.60 | 6.28 | 27.95 | 5.22 | 1.47 | 7.04 | 1.26 | 10.44 | 2.89 | 10.22 | 1.59 | 11.59 | 1.98 |
| 3487 | 56.81 | 3.44 | 9.03 | 37.12 | 7.23 | 2.01 | 11.26 | 1.67 | 12.89 | 3.33 | 11.95 | 1.72 | 12.66 | 2.18 |
| 4484 | 67.32 | 6.51 | 13.86 | 57.15 | 11.42 | 4.46 | 15.76 | 2.25 | 16.19 | 3.93 | 13.08 | 1.94 | 13.45 | 2.27 |
| 5095 | 61.34 | 4.11 | 12.69 | 53.82 | 10.80 | 2.83 | 13.32 | 2.07 | 15.43 | 3.76 | 12.75 | 1.86 | 12.90 | 2.06 |
| 5127 | 62.92 | 4.18 | 13.74 | 58.50 | 11.99 | 3.13 | 13.90 | 2.23 | 16.74 | 3.96 | 13.10 | 1.95 | 13.62 | 2.12 |
| 5161 | 61.81 | 7.16 | 13.70 | 59.57 | 11.84 | 3.06 | 13.33 | 2.25 | 16.33 | 3.99 | 13.31 | 1.96 | 13.52 | 2.07 |
| 5194 | 73.41 | 4.04 | 14.94 | 60.12 | 12.37 | 3.27 | 16.38 | 2.34 | 16.66 | 3.99 | 13.79 | 1.92 | 14.05 | 2.34 |
| 5228 | 31.57 | 3.48 | 4.91 | 20.29 | 3.86 | 1.06 | 6.12 | 0.93 | 7.28 | 1.91 | 6.90 | 0.97 | 6.92 | 1.19 |

Panel b. continued

| Depth | La | Ce | Pr | Nd | Sm | Eu | Gd | Tb | Dy | Ho | Er | Tm | Yb | Lu |
|---|---|---|---|---|---|---|---|---|---|---|---|---|---|---|
| m | pmol/kg | pmol/kg | pmol/kg | pmol/kg | pmol/kg | pmol/kg | pmol/kg | pmol/kg | pmol/kg | pmol/kg | pmol/kg | pmol/kg | pmol/kg | pmol/kg |
| | 5.1% | 3.4% | 1.7% | 2.8% | 4.0% | 5.5% | 5.9% | 4.7% | 4.4% | 2.3% | 4.8% | 3.3% | 4.6% | 4.3% |
| 5262 | 72.48 | 4.61 | 14.92 | 60.47 | 12.48 | 3.25 | 16.65 | 2.36 | 16.84 | 4.09 | 13.82 | 1.96 | 14.23 | 2.35 |
| 5294 | 101.63 | 38.96 | 16.17 | 63.71 | 12.53 | 3.35 | 16.50 | 2.35 | 16.85 | 4.05 | 13.84 | 1.95 | 14.18 | 2.32 |
| SO202-39 (38.01°N 164.45°E) | | | | | | | | | | | | | | |
| 14 | 7.90 | 5.19 | 1.71 | 7.25 | 1.59 | 0.43 | 2.59 | 0.40 | 2.93 | 0.75 | 2.48 | 0.32 | 1.92 | 0.30 |
| 103 | 10.84 | 4.52 | 2.05 | 8.76 | 1.89 | 0.53 | 3.00 | 0.48 | 3.46 | 0.90 | 3.03 | 0.40 | 2.58 | 0.42 |
| 202 | 14.20 | 3.67 | 2.54 | 10.85 | 2.26 | 0.65 | 3.60 | 0.56 | 4.24 | 1.07 | 3.56 | 0.49 | 3.17 | 0.51 |
| 300 | 18.14 | 3.58 | 3.15 | 13.22 | 2.71 | 0.75 | 4.23 | 0.65 | 4.73 | 1.24 | 4.21 | 0.58 | 3.74 | 0.61 |
| 399 | 22.57 | 3.28 | 3.68 | 15.38 | 3.04 | 0.83 | 4.73 | 0.72 | 5.41 | 1.40 | 4.77 | 0.66 | 4.39 | 0.74 |
| 498 | 26.23 | 2.99 | 4.10 | 16.92 | 3.26 | 0.90 | 5.26 | 0.76 | 5.71 | 1.52 | 5.14 | 0.73 | 4.93 | 0.84 |
| 996 | 36.48 | 3.64 | 5.16 | 21.70 | 4.00 | 1.11 | 6.65 | 0.95 | 7.41 | 2.03 | 7.17 | 1.05 | 7.36 | 1.29 |
| 1494 | 43.24 | 4.01 | 5.78 | 24.57 | 4.51 | 1.24 | 7.99 | 1.11 | 8.75 | 2.41 | 8.75 | 1.25 | 9.00 | 1.66 |
| 2489 | 49.61 | 3.83 | 7.17 | 30.40 | 5.76 | 1.59 | 9.76 | 1.39 | 10.56 | 2.92 | 10.32 | 1.51 | 10.91 | 2.00 |
| 3484 | 55.21 | 2.69 | 9.04 | 37.94 | 7.15 | 1.97 | 11.22 | 1.59 | 11.79 | 3.11 | 10.77 | 1.54 | 11.21 | 2.00 |
| 4481 | 58.00 | 2.79 | 10.53 | 43.54 | 8.45 | 2.30 | 12.46 | 1.76 | 12.74 | 3.24 | 10.89 | 1.60 | 11.50 | 1.99 |
| 5088 | 58.57 | 2.71 | 10.83 | 45.03 | 8.84 | 2.34 | 12.45 | 1.76 | 12.90 | 3.26 | 11.06 | 1.59 | 11.38 | 1.96 |
| SO202-41 (38.41°N 160.34°E) | | | | | | | | | | | | | | |
| 12 | 7.06 | 6.33 | 1.74 | 7.79 | 1.69 | 0.45 | 2.57 | 0.39 | 2.96 | 0.79 | 2.47 | 0.33 | 1.98 | 0.30 |
| 102 | 9.70 | 4.26 | 2.03 | 8.91 | 1.83 | 0.54 | 2.82 | 0.47 | 3.56 | 0.98 | 3.08 | 0.42 | 2.65 | 0.42 |
| 200 | 13.30 | 3.41 | 2.65 | 11.74 | 2.35 | 0.63 | 3.36 | 0.57 | 4.27 | 1.23 | 3.83 | 0.53 | 3.41 | 0.53 |
| 299 | 17.30 | 2.82 | 3.24 | 14.52 | 2.87 | 0.79 | 4.04 | 0.68 | 5.01 | 1.48 | 4.54 | 0.64 | 4.14 | 0.65 |
| 400 | 21.51 | 3.71 | 3.95 | 17.66 | 3.31 | 0.87 | 4.55 | 0.78 | 5.64 | 1.81 | 5.21 | 0.76 | 4.95 | 0.77 |
| 499 | 29.97 | 5.53 | 4.76 | 19.81 | 3.79 | 0.98 | 5.78 | 0.85 | 6.34 | 1.67 | 5.56 | 0.80 | 5.46 | 0.92 |
| 995 | 36.89 | 3.74 | 5.32 | 22.26 | 4.26 | 1.16 | 6.79 | 0.99 | 7.65 | 2.09 | 7.29 | 1.09 | 7.69 | 1.35 |
| 1493 | 41.61 | 5.10 | 6.09 | 25.33 | 4.70 | 1.32 | 7.87 | 1.14 | 9.00 | 2.46 | 8.78 | 1.32 | 9.36 | 1.65 |
| 2488 | 45.87 | 4.25 | 7.02 | 29.45 | 5.67 | 1.50 | 9.04 | 1.32 | 10.58 | 2.87 | 10.20 | 1.52 | 10.98 | 1.91 |
| 3483 | 52.26 | 4.56 | 8.87 | 36.74 | 7.03 | 1.93 | 10.56 | 1.52 | 11.63 | 3.05 | 10.53 | 1.57 | 11.15 | 1.92 |
| 4479 | 53.96 | 3.84 | 10.04 | 41.14 | 8.22 | 2.12 | 11.33 | 1.63 | 12.18 | 3.09 | 10.58 | 1.57 | 11.12 | 1.89 |
| 5378 | 52.27 | 4.12 | 8.48 | 34.84 | 6.80 | 1.81 | 10.09 | 1.44 | 11.15 | 2.87 | 10.15 | 1.45 | 10.75 | 1.84 |
| SO202-44 (39.80°N 152.35°E) | | | | | | | | | | | | | | |
| 14 | 11.72 | 7.74 | 2.42 | 10.51 | 2.25 | 0.61 | 3.37 | 0.52 | 3.78 | 0.94 | 3.30 | 0.41 | 2.54 | 0.38 |

Panel b. continued

| Depth | La | Ce | Pr | Nd | Sm | Eu | Gd | Tb | Dy | Ho | Er | Tm | Yb | Lu |
|---|---|---|---|---|---|---|---|---|---|---|---|---|---|---|
| m | pmol/kg | pmol/kg | pmol/kg | pmol/kg | pmol/kg | pmol/kg | pmol/kg | pmol/kg | pmol/kg | pmol/kg | pmol/kg | pmol/kg | pmol/kg | pmol/kg |
| | 5.1% | 3.4% | 1.7% | 2.8% | 4.0% | 5.5% | 5.9% | 4.7% | 4.4% | 2.3% | 4.8% | 3.3% | 4.6% | 4.3% |
| 104 | 16.24 | 4.05 | 2.75 | 11.79 | 2.35 | 0.66 | 3.83 | 0.60 | 4.36 | 1.12 | 3.91 | 0.50 | 3.30 | 0.53 |
| 201 | 23.18 | 5.75 | 3.87 | 15.97 | 3.26 | 0.85 | 4.92 | 0.74 | 5.52 | 1.41 | 4.90 | 0.63 | 4.28 | 0.69 |
| 299 | 26.99 | 4.09 | 4.40 | 17.70 | 3.45 | 0.91 | 5.50 | 0.79 | 6.16 | 1.62 | 5.21 | 0.76 | 4.90 | 0.82 |
| 400 | 28.05 | 3.10 | 4.43 | 18.25 | 3.46 | 0.93 | 5.53 | 0.80 | 6.44 | 1.68 | 5.58 | 0.80 | 5.32 | 0.89 |
| 498 | 29.59 | 3.16 | 4.59 | 19.18 | 3.48 | 0.98 | 5.61 | 0.83 | 6.59 | 1.77 | 5.81 | 0.87 | 5.96 | 1.02 |
| 997 | 37.06 | 3.88 | 5.76 | 23.74 | 4.59 | 1.24 | 7.19 | 1.05 | 8.69 | 2.37 | 7.92 | 1.20 | 8.33 | 1.45 |
| 1494 | 38.14 | 3.35 | 5.88 | 25.12 | 4.72 | 1.32 | 7.65 | 1.13 | 9.35 | 2.70 | 8.80 | 1.39 | 9.67 | 1.70 |
| 2486 | 42.22 | 2.63 | 6.81 | 29.13 | 5.48 | 1.55 | 8.59 | 1.30 | 11.12 | 3.12 | 9.98 | 1.60 | 11.21 | 1.93 |
| 3480 | 56.03 | 3.15 | 8.66 | 36.30 | 6.98 | 1.88 | 10.29 | 1.54 | 11.41 | 3.01 | 10.62 | 1.50 | 11.04 | 1.91 |
| 4481 | 60.46 | 4.77 | 10.18 | 42.10 | 8.26 | 2.25 | 11.46 | 1.69 | 12.38 | 3.12 | 10.75 | 1.54 | 11.21 | 1.93 |
| 5482 | 57.63 | 4.08 | 9.97 | 41.31 | 8.10 | 2.14 | 11.14 | 1.64 | 11.84 | 3.04 | 10.38 | 1.50 | 10.76 | 1.83 |